A Low Cycle Fatigue Testing Framework for Evaluating the Effect of Artifacts on the Seismic Behavior of Moment Frames

Ebrahim K. Abbas

Dissertation submitted to the faculty of the Virginia Polytechnic Institute and State University in partial fulfillment of the requirements for the degree of

Doctor of Philosophy
In
Civil Engineering

Matthew R. Eatherton, Chair

Norman E. Dowling

Ioannis Koutromanos

Roberto T. Leon

October 21, 2015

Blacksburg, Virginia

Keywords: Low-cycle Fatigue, Finite Element Modeling, Seismic Behavior

A Low Cycle Fatigue Testing Framework for Evaluating the Effect of Artifacts on the Seismic Behavior of Moment Frames

Ebrahim K. Abbas

ABSTRACT

Structural steel components erected in real buildings include a wide range of artifacts. In this case, the word artifact is used to describe both defects and fasteners that create discontinuities in the steel such as notches, nicks, welds, powder actuated fasteners, self-drilling screws, repaired defects, and others. Although artifacts occur in real structures and their presence may affect the ductility of elements subjected to large inelastic strains, there is a dearth of experimental data on the seismic behavior of structural systems with artifacts. For instance, full-scale testing of moment resisting connections is expensive which makes it economically infeasible to experimentally examine the wide range of possible artifact types, artifact locations, and structural configurations. A framework has been developed for evaluating the effect of artifacts on special moment resisting frame (SMRF) plastic hinge regions using relatively economical coupon tests. Cyclic bend tests and monotonic tension tests on flat plate coupons that include artifacts are used to calibrate fracture parameters for different low cycle fatigue models such as the Cyclic Void Growth Model (CVGM), Stress-Weighted Damage Model (SWDM) and Cyclic Damage Plasticity Model (CDPM) which are then used in conjunction with finite element (FE) models to predict fracture initiation in full-scale SMRF connections. The framework is general and can be applied to many types of artifacts and seismic structural systems. Fracture propagation has been studied also using CDPM for full-scale tests using FE finite element software LS-DYNA. Alternatively, recommendations for future work is proposed for developing a new test setup, studying artifacts sensitivity to material thickness, and a method of demonstrating equivalence for the artifacts.

ACKNOWLEDGEMENTS

This material is based on work supported by the American Institute of Steel Construction and Hilti. The authors appreciate the input from the AISC advisory committee consisting of Tom Schlafly, Jie Zuo, Keith Landwehr, Jim Malley, John Barsom, Leigh Arber, Tim Fraser, and Duane Miller. In-kind funding was provided by Banker Steel Company.

First, I would like to take this opportunity and thank my committee members Dr. Matthew R. Eatherton, Dr. Roberto T. Leon, Dr. Norman E. Dowling, and Dr. Ioannis Koutromanos for giving me their trust and continuous support from the first day on this research. Their doors were always open for any guidance, assistance, questions, and concerns.

Valuable assistance in the preparation and conducting of tests was provided by Andrew Garrison, Osama Bukhamseen, and Ammar Motorwala as well as lab technicians Dennis Huffman and Brett Farmer.

I would like to acknowledge and thank Kuwait University for funding and giving me this valuable opportunity to finish my graduate studies in one of the top respected schools.

Finally, I would like to thank and dedicate this work for my parents, Khaleel Abbas and Wafaa Al-Sabaghah, and my wife, Noha Mohamed, and our children, Mohammad, Dana and Yaqoub. Their continuous support, care, and prayers were a strong motivation throughout my life and career.

TABLE OF CONTENTS

Contents

ABSTRACT ..... **ii**

ACKNOWLEDGEMENTS ..... **iii**

TABLE OF CONTENTS ..... **iv**

CHAPTER 1 INTRODUCTION **1**

1.1 Overview 1

1.2 Scope of Work 4

1.3 Organization of This Dissertation 6

CHAPTER 2 LITERATURE REVIEW **9**

2.1 Fracture of Steel Components Due to Earthquake Loading 9

2.1.1 Fracture in Moment Connections in Northridge Earthquake 9

2.1.2 Testing of Moment Connections 10

2.2 Effect of Defects and Stress Concentrations on Fracture 12

2.3 Overview of Cyclic Fatigue 15

2.4 LCF Models to Predict Fracture (CVGM) 21

2.5 Stress-Weighted Damage Model to Predict Fracture 24

2.6 Cyclic Damage Plasticity Model to Predict Fracture 25

2.7 Comparison and Limitations of the LCF Models 26

CHAPTER 3 EXPERIMENTAL TESTING PROGRAM **29**

3.1 Introduction 29

3.2 Round Notched Bar Tests 29

3.3 Overview of Testing Approach with Flat Plate Specimens 31

3.4 Monotonic Uniaxial Tension Tests 32

3.5 Cyclic Bend Tests 34
3.6 Specimen Preparation with Artifacts 39
3.6.1 Powder Actuated Fasteners (PAF) 39
3.6.2. Puddle Welds (PW) 40
3.6.3. Ground Fillet Weld (GFW) 41
3.6.4. Notch Ground to Taper (NGT) 41
3.6.5. Notch Welded and Ground Smooth (NWG) 42
CHAPTER 4 TEST RESULTS 45
4.1 Introduction 45
4.2 Circumferentially Notched Round Bar Test Results and Fracture Parameters 45
4.3 Charpy V-Notch Tests 49
4.4 Monotonic Axial Tests 50
4.5 Cyclic Bend Test Results 55
CHAPTER 5 FE MODELS, AND CALIBRATION OF FRACTURE PARAMETERS FOR ULCF MODELS 65
5.1 Introduction 65
5.2 FE Models Mesh Refinement Study 65
5.3 Complimentary FE Models and Calibration of Fracture Parameters from Flat Plate Coupon Tests 67
5.3.1 Monotonic Uniaxial Tests FE Models 68
5.3.2 Cyclic Bend Tests FE Models 70
5.3.3 Calibrating Fracture Parameters 72
5.4 Improvements to CVGM Calibration 76
5.4.1 Monotonic Uniaxial Tests FE Models with Artifacts 76
5.4.2 Cyclic Bend Tests FE Models with Artifacts 80

5.4.3 Calibrating Fracture Parameters using FE Models with Artifacts 81
5.4.4 Width Effect on Monotonic Uniaxial FE Models with Artifacts 84
5.4.5 Proposed CVGM Modified Fracture Parameters Calibration Method 89
5.5 Stress-Weighted Damage Model Calibration 91
5.6 Cyclic Damage Plasticity Model Calibration 92
5.6.1 Monotonic Uniaxial Tests Calibration Using LS-DYNA 92
5.6.2 CDPM Calibration Using Cyclic Bend Tests 96
5.7 Cumulative Extreme Fiber Strain 97
CHAPTER 6 FRACTURE BEHAVIOR OF FULL-SCALE MOMENT CONNECTION TESTS 101
6.1 Introduction 101
6.2 Full-Scale Special Moment Resisting Frames (SMRF) Tests 101
6.3 Full-Scale Tests Results and Fracture Study 108
6.3.1 Behavior of W24x62 Specimens with RBS 108
6.3.2 Behavior of W24x62 Specimens with RBS 117
6.3.3 Behavior of W36x150 Specimens with RBS 120
6.3.4 Behavior of Non-RBS W36x150 Specimens 130
6.3.5 Discussion of Full-Scale Tests Fracture Behavior 135
CHAPTER 7 PREDICTING FRACTURE IN THE FULL-SCALE TESTS 139
7.1 Introduction 139
7.2 Full-Scale Tests FEM Analysis 139
7.3 CVGM Fracture Initiation Prediction for Full-Scale Tests 140
7.4 Modified CVGM Fracture Initiation Prediction for Full-Scale Tests 147
7.5 SWDM Fracture Initiation Prediction for Full-Scale Tests 148

7.6 CDPM Fracture Initiation and Propagation for Full-Scale Tests 150
CHAPTER 8 RECOMMENDATIONS OF FUTURE WORK 155
8.1 Introduction 155
8.2 New Monotonic and Cyclic Bend Test 155
8.3 Artifact Sensitivity to Material Thickness 157
8.4 Method of Demonstrating Equivalence 162
CHAPTER 9 SUMMARY AND CONCLUSIONS 164
9.1 Summary 164
9.1.1 Monotonic Uniaxial and Cyclic Bend Tests 165
9.1.2 Calibration of LCF Fracture Parameters to Predict Fracture 167
9.1.3 Recommendations of Future Work 171
9.2 Conclusion 172
REFERENCES 174
APPENDIX A DESCRIPTION OF BEND TEST FRACTURES 179
A.1 No Artifact (B) 179
A.2 Powder Actuated Fasteners (PAF) 184
A.3 Puddle Welds (PW) 191
A.4 Ground Fillet Weld (GFW) 196
A.5 Notch Ground to Taper (NGT) 202
A.6 Notch Welded and Ground Smooth (NWG) 208
A.7 W24 and W36 Specimens Dimensions 214
APPENDIX B TESTING DATA 216
B.1 Monotonic Axial Tests Data 216
B.2 Cyclic Bend Tests Data 222

APPENDIX C CALIBRATION OF DEGRADATION COEFFICIENT 241

APPENDIX D FULL-SCALE FRACTURE INITIATION 247

D.1 Fracture Initiation Location Based on Worst Case 247

D.2 Fracture Initiation at the Center of the Flange 260

APPENDIX E STRAIN GRADIENTS FROM STRAIN GAGES 275

APPENDIX F FULL-SCALE TEST VALIDATION HYSTERESIS PLOTS 346

APPENDIX G LCF MODELS CALCULATION DEMONSTRATION 349

CHAPTER 1 INTRODUCTION

1.1 Overview

After the 1994 Northridge Earthquake and the 1995 Kobe Earthquake, unexpected fractures were observed in steel beam-to-column moment-resisting connections. This led to many experimental programs focused on a range of topics including reduced beam section connections (e.g. Chi and Uang 2002), extended end plate connections (e.g. Adey et al. 2000), effect of composite slabs (e.g. Hajjar et al. 1998), panel zone strength (e.g. Lee et al. 2005) and more. A subset of these testing programs included a composite slab with welded shear studs attached to the beam in the plastic hinge region causing geometric and material discontinuities (e.g. Chi and Uang 2002, Hajjar et al. 1998, Ricles et al. 2002). One of the beam-to-column connection specimens with welded shear studs in the plastic hinge region experienced fracture of the flange initiating at the shear stud (Ricles et al. 2002). It was concluded that the fracture of the beam flange was a direct result of the reduced notch toughness of the base metal caused by shear stud welding.

The AISC Seismic Provisions for Structural Steel Buildings (AISC 2010a) define the locations where large inelastic strains are expected to occur as protected zones in which welded, bolted, screwed or shot-in attachments are not allowed. However, during construction, structural steel components erected in real buildings are subjected to a wide range of artifacts including, but not limited to: notches, nicks, welds, powder actuated fasteners, and self-drilling screws. In this report, the word artifact is used to describe discontinuities in the steel due to defects, fasteners, or repairs intended to mitigate defects. Almost no tests have been conducted on moment resisting connections with these types of artifacts. Full-scale testing of moment resisting connections is expensive which makes it economically infeasible to experimentally examine the wide range of possible structural configurations, artifact types, and artifact locations.

A framework has been developed for evaluating the acceptance of artifacts in special moment resisting frames (SMRF) using the results of relatively economical coupon tests. See Figure 1.1 for a schematic example for part of the proposed framework to predict fracture initiation using the cyclic void growth model (CVGM) which one of the low cycle fatigue models used.

Cyclic bend tests and monotonic axial tension tests are conducted on plate material with artifacts, the results of which are used to calibrate fracture parameters for the cyclic void growth model (CVGM), stress-weighted damage model (SWDM), and cyclic damage plasticity model (CDPM). Finite element (FE) models are used to get stress and strain histories in full-scale moment connections which can be used to characterize fracture demand. The fracture resistance can then be evaluated relative to the fracture demand to determine acceptability. Fracture propagation also has been studied using CDPM which is implemented in FE software LS-DYNA (LSTC 2015). An alternate method for demonstrating equivalence to artifacts already proven acceptable through full-scale testing is also presented at the end of this dissertation.

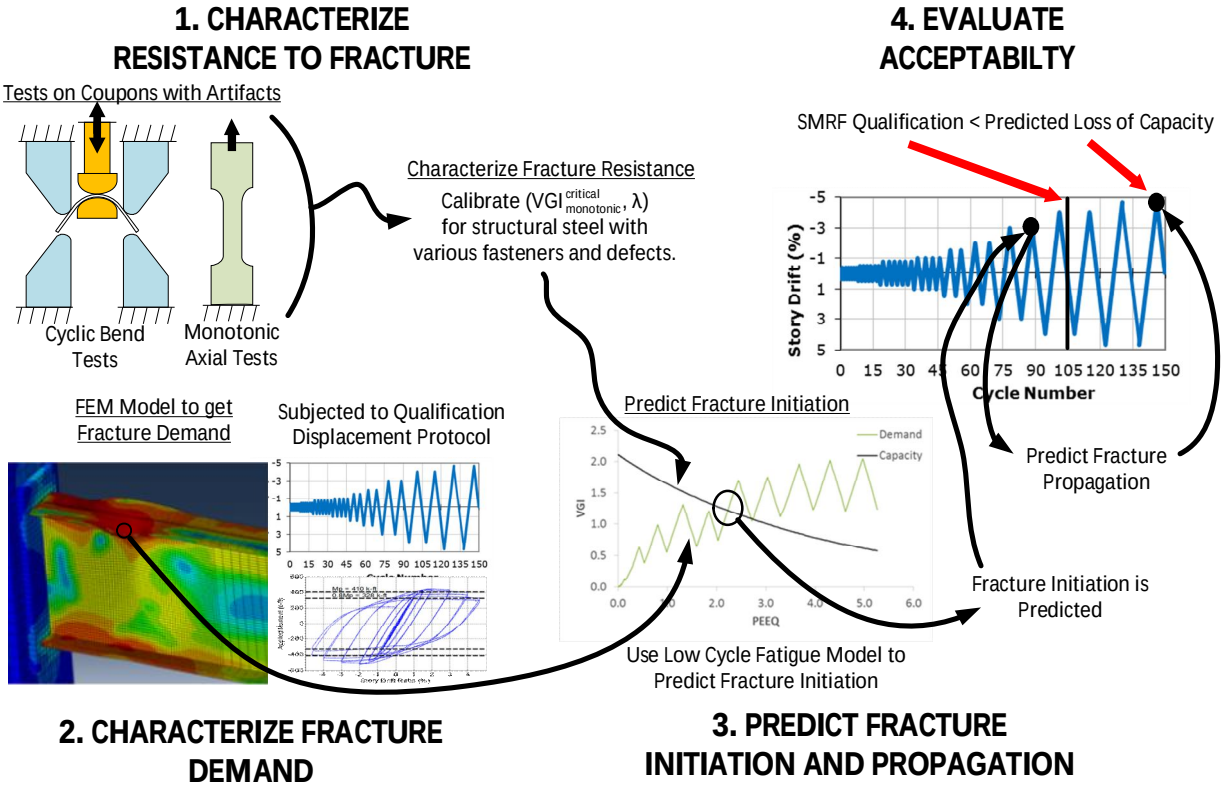


Figure 1.1 – Proposed framework for evaluating the acceptability of artifacts in the protected zone of moment resisting frames.

In the literature, there has been considerable research on fracture due to both high cycle fatigue and low cycle fatigue. Fatigue fracture after more than 10^4 cycles is usually considered high cycle fatigue, while fatigue fracture between 10^2 and 10^4 cycles is often considered low cycle

fatigue. Failure of structural steel components during an earthquake can occur after relatively few severe inelastic loading cycles. This type of failure (usually less than 20 cycles) can be classified as Ultra Low Cycle Fatigue (ULCF). Classical fracture mechanics approaches are not appropriate to predict ULCF, primarily due to large scale yielding which invalidates stress intensity approaches such as the plastic zone adjustment, J-integral, and crack tip opening displacement (CTOD). Ductile fracture often dominates in ULCF consisting of a progression from void nucleation, to growth and coalescence as shown schematically in Figure 1.2. In earthquakes brittle fracture is observed in steel beam-to-column moment-resisting connections. Meanwhile, ductile fracture controls in bracings only. After the 1994 Northridge Earthquake and the 1995 Kobe Earthquake, there has not been many earthquakes after the intense research on beam-to-column moment-resisting connections to test the integrity of RBS. There is a possibility that ductile failure mechanism would control in beams instead of brittle failures.

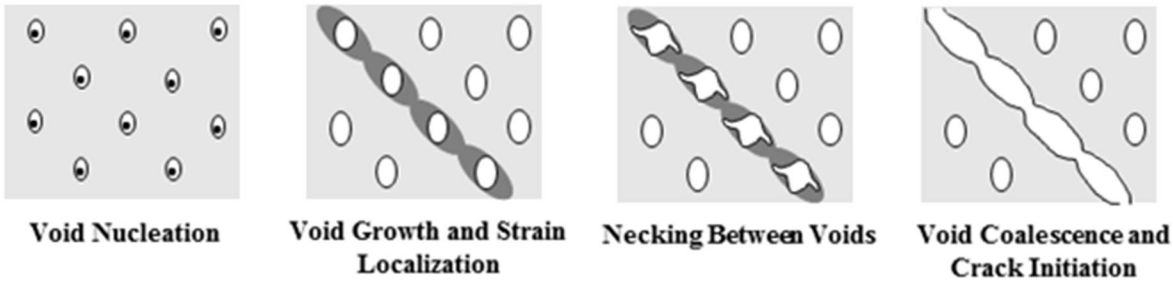


Figure 1.2 – Graphical representation of low cycle fatigue fracture (adapted from Anderson 2004).

The Cyclic Void Growth Model (CVGM) described by Kanvinde and Deierlein (2007) and modified by Myers (2009) is adapted from the monotonic Void Growth Model (VGM) developed by Rice and Tracey (1969), to predict fracture initiation during cyclic loading. CVGM has been used by researchers to predict fracture initiation in ductile metals subjected to ULCF. CVGM is attractive in part because it attempts to capture the mechanism of ULCF through fracture parameters representing void growth. Those parameters are presented in Equations 1.1, 1.2, and 1.3. Fracture initiation occurs when the cyclic void growth index demand, VGI_{cyclic}, is greater than the cyclically degraded critical void growth index capacity, $VGI_{cyclic}^{critical}$, as described in Equation 1.1. The demand is defined by the cyclic void growth index, VGI_{cyclic}, in Equation 1.2,

and the capacity for fracture resistance is defined as the critical cyclic void index, $VGI_{cyclic}^{critical}$, as given in Equation 1.3. For further information about the CVGM refer to Myers (2009).

$$VGI_{cyclic} > VGI_{cyclic}^{critical} \tag{1.1}$$

$$VGI_{cyclic} = \sum_{tensile\ cycles} \int_{\varepsilon_1}^{\varepsilon_2} exp\left(\left|1.5\frac{\sigma_m}{\sigma_e}\right|\right) d\bar{\varepsilon}_p - \sum_{compressive\ cycles} \int_{\varepsilon_1}^{\varepsilon_2} exp\left(\left|1.5\frac{\sigma_m}{\sigma_e}\right|\right) d\bar{\varepsilon}_p \tag{1.2}$$

$$VGI_{cyclic}^{critical} = VGI_{monotonic}^{critical}\, exp\left(-\lambda\, \bar{\varepsilon}_p^{accumulated}\right) \tag{1.3}$$

$$VGI_{monotonic}^{critical} = \int_0^{\varepsilon_p^{critical}} exp\left(1.5\frac{\sigma_m}{\sigma_e}\right) d\bar{\varepsilon}_p \tag{1.4}$$

The cyclic void growth index, VGI_{cyclic}, is a function of the stress triaxiality ratio, σ_m/σ_e, (hydrostatic stress, σ_m, divided by the von Mises stress, σ_e), and incremental equivalent plastic strain, $d\bar{\varepsilon}_p$. The critical cyclic void growth index, $VGI_{cyclic}^{critical}$, is a function of the accumulated equivalent plastic strain, $\bar{\varepsilon}_p^{accumulated}$, and calibrated fracture parameters: the critical monotonic void growth index, $VGI_{monotonic}^{critical}$, and the degradation coefficient, λ. The critical monotonic void growth index, $VGI_{monotonic}^{critical}$, is calibrated using Equation 1.4 based on monotonic test results (to get strain at fracture initiation) and complimentary FE models (to get equivalent plastic strain and stress triaxiality). Once $VGI_{monotonic}^{critical}$ is found, a regression analysis can be performed using the values of $VGI_{cyclic}^{critical}$ obtained from cyclic tests to calibrate the cyclic degradation coefficient, λ, using the relationship given in Equation 1.3.

1.2 Scope of Work

A total of forty-eight cyclic bend tests and monotonic axial tests, were conducted at the Thomas M. Murray Structural Engineering Laboratory at Virginia Tech. The specimens were cut

from W24x62 and W36x150 beams used in full-scale SMRF moment connection tests (Eatherton et al. 2013). Six types of specimens were tested including bare specimens with no artifacts, powder actuated fasteners, puddle welds, ground fillet welds, notches ground to taper, and notches filled with weld and ground smooth. Bare steel specimens are used as benchmark behavior and their results were also compared with results from conventional test methods for calculating CVGM, SWDM, and CDPM fracture parameters. Powder actuated fasteners and puddle welds represent typical deck attachments that may occur in the plastic hinge region of a SMRF connection. These types of fasteners also represent typical connection of nonstructural elements such as partition walls, pipe racks, and ductwork to the structural steel. The last three artifact types (ground fillet welds, notches ground to taper, and notches filled with weld and ground smooth) are methods described in AWS D1.8 (AWS 2012) for repairing notches, nicks, and gouges in the protected zone of seismic resisting structural systems. No previous testing data exists as to how these repair methods affect the low cycle fatigue resistance of steel sections.

For the coupon bend tests, the coupons were cyclically bent around a roller with a diameter of 11 in. causing cycles with constant peak strain gradient. Specimen dimensions were selected to have an aspect ratio of 1:5 with respect to the thickness and width. Therefore, the coupons cut from the flanges of W24x62 sections were 0.59 in. thick x 2.95 in. wide and the coupons cut from W36x150 flanges were 0.94 in. thick x 4.7 in. wide. CVGM fracture parameters including the void growth index, $VGI_{monotonic}^{critical}$, and degradation coefficient, λ, were calibrated based on monotonic uniaxial tension tests and cyclic bend tests. Also, a total of eight conventional circumferentially notched bar tests were conducted to validate the fracture parameters ($VGI_{monotonic}^{critical}$ and λ) for bare steel specimens.

The calibrated fracture parameters were used to predict fracture initiation in full-scale specimens tested by Eatherton et al. (2013). In Eatherton et al. (2013), full-scale connection specimens were subjected to the SMRF qualification loading protocol given in the AISC Seismic Provisions. In this study, FE models were conducted on the same specimens using the same loading protocol to obtain stress and strain histories in critical parts of the plastic hinge region. The calibrated fracture parameters for all five artifacts were used to predict when fracture would initiate at the worst case location in the SMRF connection (inside of the local buckle), and the worst case

location along the centerline of the beam flange (representing the location of artifacts in some full-scale tests simulating deck attachments).

Two type of artifacts, powder actuated fasteners and ground notched to taper, were modeled in the FE models of the uniaxial monotonic and cyclic bend tests. Those artifacts were modeled to obtain stress and strain histories in critical locations to calibrate fracture parameters. Also, a width effect study was conducted for the monotonic tests to measure the impact of width results to the actual tests.

Fracture initiation and propagation was studied on one of the full-scale specimens tested by Eatherton et al. (2013). This study was conducted using the CDPM which is implemented in FE software LS-DYNA (LSTC 2015). The CDPM parameters were calibrated using the bare cyclic bend test specimens with the support of the monotonic uniaxial tests CDPM calibration. Later the results were compared to the full-scale results in predicting fracture initiation and propagation.

Finally, recommendations for future work are presented such as a new cyclic and monotonic bend tests proposes, recommendations for number of tests recommended based on different artifacts sensitivity to material thickness, and a method of demonstrating equivalence is proposed instead of using ULCF models.

1.3 Organization of This Dissertation

This dissertation describes relevant background, details of the framework developed in testing different types of artifacts, results from the tests, development of fracture parameters for the artifacts tested, fracture initiation prediction for different artifacts in full-scale SMRF, and a summary of the findings including additional future research needs. The report is organized into the following chapters:

- Chapter 1 describes the motivation for and an introduction to the proposed framework for investigating the effect of artifacts on seismic behavior of moment connections using low cycle fatigue models. It also summarizes what is included in this document.

- Chapter 2 provides a discussion of the literature review of work related to the proposed work. It describes the type of failures in moment connections at the Northridge Earthquake. Discussion is also provided about different types of fatigue with focus on ULCF models. Also, the effect of defects and stress concentrations are discussed.

- Chapter 3 discusses the testing program consisting of round circumferentially notched bars tests, cyclic bend tests, and uniaxial monotonic tests. Information is included such as goals of the testing, test matrix, and dimensions and details of the test setup and specimens.

- Chapter 4 presents the results from all the tests conducted such as the circumferentially notched bar tests, monotonic axial tests, cyclic bend tests and charpy v-notch tests.

- Chapter 5 presents the complimentary FE models used in this work to for the monotonic uniaxial, and cyclic bend tests. Fracture parameters calibration for all of the fracture models is presented using the cyclic bend test data. Also, the process and the related assumptions are presented.

- Chapter 6 presents briefly the testing program for the full-scale moment connection tests conducted previously by Eatherton et al. (2013) with a detailed discussion of fracture analysis for each failed specimen. Also, a discussion about the strain gages and how they are used to provide “strain line” profiles is presented.

- Chapter 7 presents complimentary FEM models used in this work for full-scale tests. Also the fracture parameters calibrated for each artifact previously is used to predict fracture initiation in full-scale SMRF. Different fracture models are applied on full-scale moment connection tests with no artifacts conducted previously by Eatherton et al. (2013).

- Chapter 8 includes the recommendations for future work are summarized in this chapter. The following topics will be discussed, a new generation of cyclic and monotonic tests, recommendations and considerations for the next phase of testing based on artifacts sensitivity to material thickness, and a method of demonstrating equivalence is proposed instead of using ULCF models.

- Chapter 9 includes the summary of the work and conclusions reached in this study. Also, it contains the overall observations that were found in this study.

Appendices provide all of the monotonic uniaxial and cyclic bend tests data plots, curve fitting scatter plots of the cyclic bend test data to calibrate λ for each artifact, prediction of fracture initiation for full-scale tests for each artifact tested, and strain gradient from strain gages for full-scale tests.

CHAPTER 2 LITERATURE REVIEW

2.1 Fracture of Steel Components Due to Earthquake Loading

During an earthquake, buildings face tremendous forces which can cause catastrophic damage. Understanding the different types of damage that occur during an earthquake will help to ensure safety of infrastructure during future earthquakes. This can be accomplished by properly documenting and investigating failures in the aftermath of an earthquake. There might be many factors that were the root causes of those failures from inappropriate design to constructability issues. This can lead to many experimental programs to further investigate and develop structural members for better performance during future earthquakes.

2.1.1 Fracture in Moment Connections in Northridge Earthquake

The damage caused to the steel moment frame structures by the 1994 Northridge Earthquake has raised many questions related to the behavior and reliability of connections used for the decades leading up to Northridge. The pre-Northridge moment connections were developed in the late 1960s until early 1990s by testing. Those earlier tests consisted of both monotonic (e.g. Parfitt and Chen 1976, and Chen and Patel 1981) and cyclic tests (e.g, Popov and Pinkey 1969, and Engelhardt and Husain 1993). Steel moment frames, prior to the Northridge Earthquake, were thought to be the most reliable structural system for resisting seismic loads based on the conducted tests. Although, adequate strength and plastic rotation capacity for specific beams were achieved, different types of failures were observed but were not a concern prior to the Northridge Earthquake. Some of those failures were weld cracks, column flange tearing, and bolt failure. In previous earthquakes, those failures were not noticed since beam-column connections are mostly hidden behind ceilings or fireproofing. A schematic of a typical connection detail most commonly used in the buildings being effected by the Northridge Earthquake is shown in Figure 2.1.

During the Northridge Earthquake, many different types of damage were discovered during the aftermath inspections. Although there were not any catastrophic failures in the moment

resisting frames, the most common failure modes were either severe buckling (in the flange and web), or brittle fractures at or near the beam flange complete penetration groove welds. In many cases, both of the most common failure modes were seen together after further investigation. This showed that there was a lack of evidence of plastic deformation in beams, and also in the types of failure modes (Youssef et al. 1995).

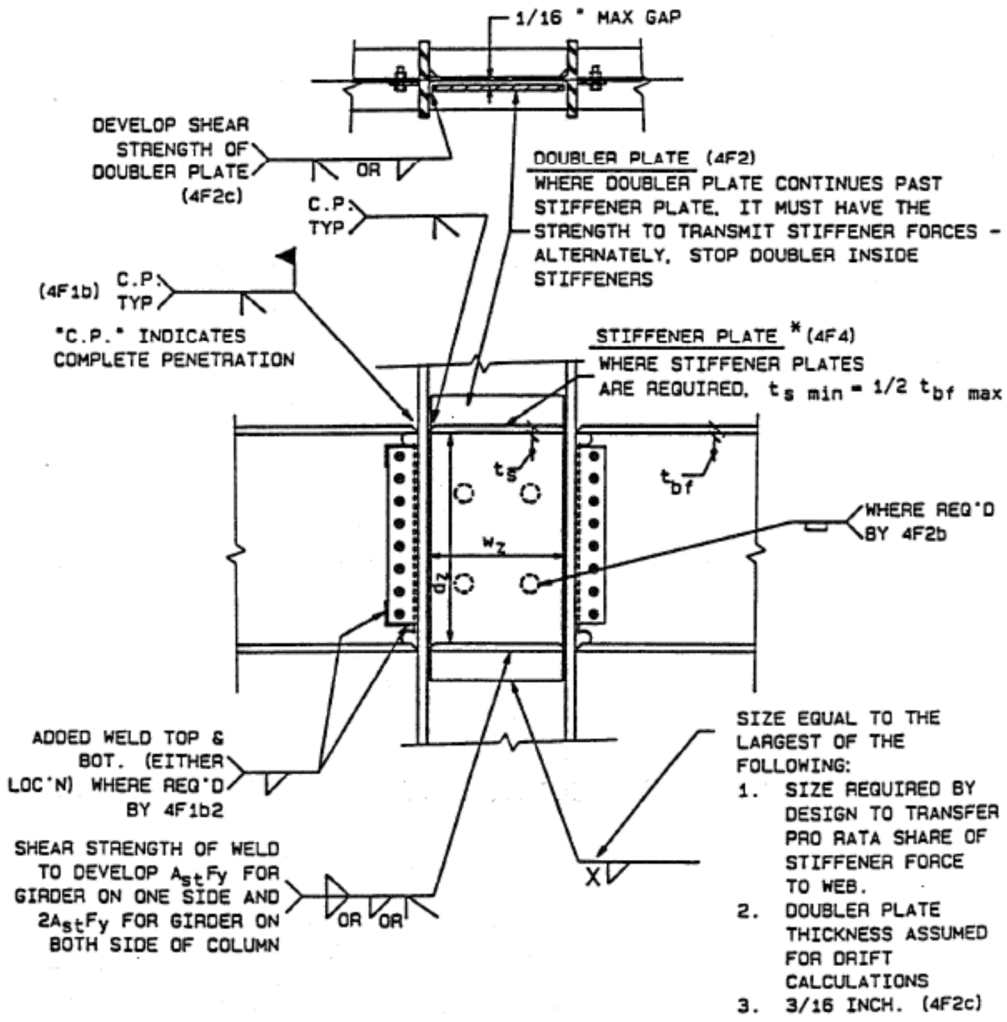


Figure 2.1 – Schematic of a typical moment connection prior to the 1994 Northridge Earthquake (Youssef et al 1995).

2.1.2 Testing of Moment Connections

There was a great focus on different topics for moment connections experimental testing. This was based on types of unexpected fractures observed in steel beam-to-column moment

resisting connections in the aftermath of the 1994 Northridge Earthquake and the 1995 Kobe Earthquake. Chi and Uang (2002) studied reduced beam section (RBS) connections with no artifacts. The SAC Joint Venture initiated a testing program to test those type of connections after the 1994 Northridge Earthquake. They became popular after Northridge because the testing results by SAC showed that they mitigate issues related to pre-Northridge moment connections. In the three specimens tested, yielding was observed in the panel zone, followed by web local buckling in the RBS region causing lateral-torsional buckling accompanied with flange local buckling. On the other hand, Uang el al. (2000) and Civjan et al. (2000) studied RBS section at the bottom flange only with concrete slabs attached. Uang el al. (2000) conducted a set of six full-scale specimens, three of the specimens with light weight concrete slabs. Brittle fracture was noticed at the weld metal of the top flange, also ductile tearing occurred at the weld access hole of the flange. Six full-scale specimens were conducted by Civjan et al. (2000), three of those specimens were composite slabs and three were bare (two specimens RBS at bottom flange and four haunch at bottom). Most of the specimens fractured at the bottom flange weld with a gradual deterioration in strength due to local and lateral buckling. Only one specimen fractured at the top flange weld.

More composite full-scale tests were conducted with welded shear studs attached to the beam in the plastic hinge region causing geometric and material discontinuities (e.g. (Leon et al. 1998), (Chen and Chao 2001), (Engelhardt et al. 2000) and (Ricles et al. 2002)). In Leon et al. (1998) one bare and two composite full-scale specimens (55% composite and 35% composite floor slab) were tested. All specimens failed at the bottom flange access hole or weld column interface. The tests conducted by Chen and Chao (2001) consisted of a total of four composite full-scale specimens (two with 3 ksi and two with 6 ksi concrete). All specimens failed at the bottom flange by fracture at the CJP weld or on the base metal near the weld access hole. Engelhardt et al. (2000) tested eight full-scale RBS specimens (four composite slabs and four bare). Most of the specimens fractured at the bottom flange near the weld, and gradual deterioration in strength occurred due to beam instability. Only one specimen fractured at the top and bottom flange near weld. The researchers observed that the presence of the slab contributed to enhanced beam stability and delayed strength degradation. Engelhardt also avoided placing any shear studs as well as other sources of heat input and local stress riser within the RBS region to avoid fracture initiation at

those locations. Ricles et al. (2002) tested a total of eleven full-scale specimens one of the specimens had a composite slab and the other ten were bare. Only one of the specimens (Specimen C5) with welded shear studs in the plastic hinge region experienced fracture of the flange initiating at the shear stud. Based on this failed specimen, it was concluded that the fracture of the beam flange was a direct result of the reduced notch toughness of the base metal caused by shear stud welding. It can be clearly noted that most of the specimens excluding Ricles et al. (2002) failed at the access hole or the weld column interface.

A recent study conducted by Eatherton et al. (2014) consisted of twelve specimens (six RBS and six non-RBS sections) which examined the effects of powder actuated fasteners (PAF) and puddle welds at the protected zone region with no composite slabs. All of the specimens satisfied the SMRF qualification criteria in AISC 341-10 Chapter K. The SMRF qualification criteria is used to evaluate acceptance for qualification in industrial testing. It was also found that the achieved moment capacities during the qualification cycle and maximum moment capacities were unaffected by the puddle welds and PAF. Also, the effect of puddle welds and PAF on strength degradation and energy dissipation were similarly found to be negligible prior to fracture.

2.2 Effect of Defects and Stress Concentrations on Fracture

There are many factors which effect the behavior of structural steel materials. Those factors can occur during the manufacturing of structural steel or during construction by construction practices. In both cases, this will affect the steel behavior by changing the stress concentrations and the material microstructural properties. This can lead to unpredicted failures from stable ductile failures to unstable brittle sudden failures. Usually structural steel exhibits ductile fracture under large plasticity with a failure progression starting from void nucleation, to growth and coalescence as shown schematically in Figure 1.2.

In many cases stress concentrations is one of the main factors that cause early failures. Although, in some cases residual compressive stresses are preferred to increase the resistivity of fatigue using such as shot peening or hole expansions. There are many methods which determine

the stress concentrations such as finite elements (FE), strain gages, and photoelasticity. Each of those methods has its limitations which leads to different results for complicated geometries. Photoelasticity has been used since the 1800's by Sir David Brewster (Brewster 1816). It involves the retardation of light in which it creates black and white interference which are called fringes. Those fringes are proportional to the stresses within the material. Figure 2.2 shows a photoelastic picture of a plate with three different cracks showing a similar butterfly pattern at each crack tip. Another method is using strain gages, the challenge in using strain gages on small specimens is protecting the gages from getting damaged during testing and also using the right strain gage for the application being tested. The most reliable and cost effective method is using FE which requires experience and a critical view on the FE-model adopted to simulate a component. On the other hand, loads, boundary conditions and mesh distributions should be studied carefully to achieve accurate results.

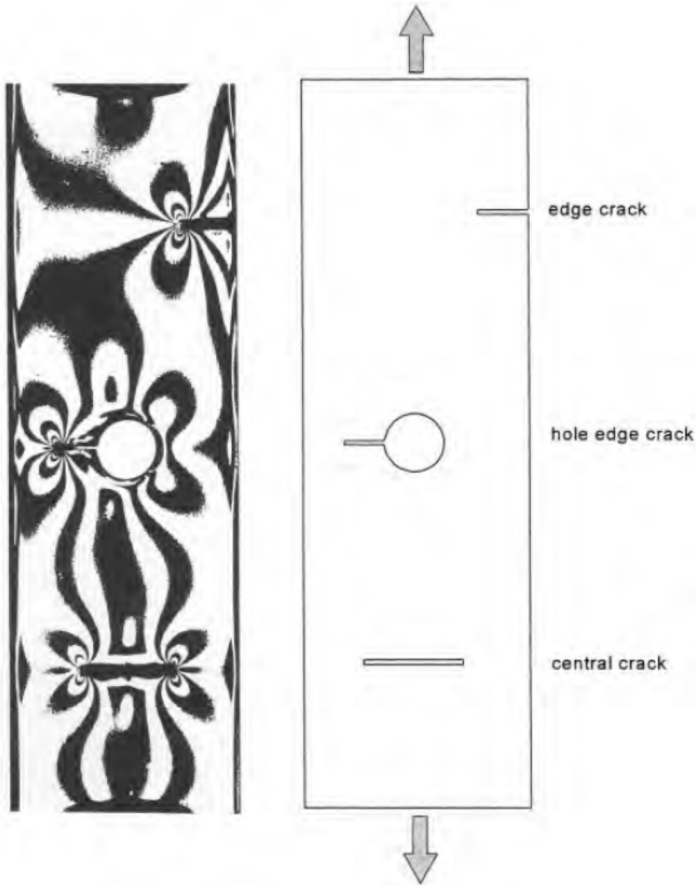


Figure 2.2 – An example of three different types of crack using photoelasticity (Schijve 2001).

Residual stresses can be present in materials as a results of different processes. Some of those cases are notches, occurring during production, shot peening, plastic hole expansion, heat treatment, assembling components, differential cooling of hot rolled sections, and plastic deformation during col-rolling. There are no simple techniques in measuring residual stresses. A non-destructive method to measure residual stresses is by using X-ray diffraction techniques. The disadvantage of this method is that it cannot be adopted on routine basis. It can get even more complicated if the residual stresses need to be measured at the root of a notch in which high strain gradients are usually present. A common destructive method uses strain gages in the area of interest and then cutting the material around the strain gage. This will release or remove the residual strains and the residual stresses can be calculated using the strain variations. Measuring the residual stresses with a reliable practical method is challenging. Analytical calculations using FE can be used in calculating residual stresses but it requires experience and high level of competency especially when dealing with plastic deformation.

Any type of artifact or defect in a structural member will cause micro or macro cracks, even if it was repaired as per any standard. A study by Lee et al. (2012) focused on studying the tensile properties and the hardness of steel around the powder actuated fastener (PAF) and welded shear stud. Also, the metal structure around the artifacts tested was observed using an optical and a scanning electron microscope. The PAFs used in this study were manufactured by HILTI Corp. with a model number “X-ENP-19-L15”. For the tensile tests, there were no differences in the yield stress but a slight difference in the ultimate stress with lower value for the PAF results. The optical microscope showed that the PAF is strongly fixed in the base material with a high residual stress confirmed by the change of hardness surrounding the PAF. Also, traces of melted zinc from the galvanized surface of the PAF which melted due to the heat exhibited by the friction between the PAF and base material during installation were noticed. The effected zone for a PAF and a welded shear stud is 0.24 in. measured from the face of the PAF and shear stud and this was measured by the difference in hardness values.

2.3 Overview of Cyclic Fatigue

Fracture mechanics started back in the early 1900's by Griffith which was the first to propose the concept of the strain energy release rate. It was related to the effects of scratches (filing, grinding or polishing) on the mechanical strength of solids using energy release rate (Griffith 1921) which is known as linear elastic fracture mechanics at the current time. In the literature, there has been considerable research on fracture due to both high cycle fatigue and low cycle fatigue. Fatigue fracture after more than 10^4 cycles is usually considered high cycle fatigue, while fatigue fracture between 10^2 and 10^4 cycles is often considered low cycle fatigue. High cycle fatigue occurs by applying small elastic amplitudes of stress and strain to cause failure, while for the low cycle fatigue much higher stress and strain amplitudes are applied which leads to less cycles towards fracture. Also, another difference between the high and low cycle fatigue is that the high cycle fatigue is related to elastic behavior on a macro scale of the material. While the low cycle fatigue is more associated with macroplastic deformation in each cycle.

Failure of structural steel components during an earthquake can occur after relatively few severe inelastic loading cycles. This type of failure (usually less than 20 cycles) can be classified as Ultra Low Cycle Fatigue (ULCF). Classical fracture mechanics approaches are not appropriate to predict ULCF, primarily due to large scale yielding which invalidates stress intensity approaches such as the plastic zone adjustment, J-integral, and crack tip opening displacement (CTOD). Ductile fracture often dominates in ULCF consisting of a progression from void nucleation, to growth and coalescence as shown schematically in Figure 1.2.

Linear elastic behavior is assumed in linear elastic fracture mechanics (LEFM). It works well in materials that remain elastic until the point of fracture which is the case in most brittle materials. Also, it is assumed to be valid if it the specimen dimensions are about fifty times the dimension of the plastic zone (Anderson 2004). Nucleation of microcracks generally occur very early in the fatigue life. They may occur immediately if a cyclic stress above the fatigue limit is applied. The fatigue limit is the cyclic stress level below which a fatigue failure does not occur. Microcracks remain invisible for a considerable part of the total fatigue life. Grain boundaries affect the crack growth after a microcrack has been nucleated. There are two important periods

during the fatigue life until failure, fracture initiation period and fracture propagation period. Differentiating between the two periods is importance because several surface conditions do affect the initiation period. The fatigue prediction methods are different for those two periods. The classic fracture mechanics models are more geared towards simplified analysis which focus on the global behavior, with the modern computational capabilities more localized behavior is being in focus.

Fatigue can be characterized as being Stage I, II or III, as shown in Figure 2.3 from Kanvinde (2004), which presents a log-log plot of stress range versus the crack growth rate. The stress applied at the crack tip control the three stages of different fatigue mechanism. Moving from Stages I throughout III is caused by the crack growth which will lead to an increase in the stress intensity factor and will cause fracture when the propagation rate reaches infinite.

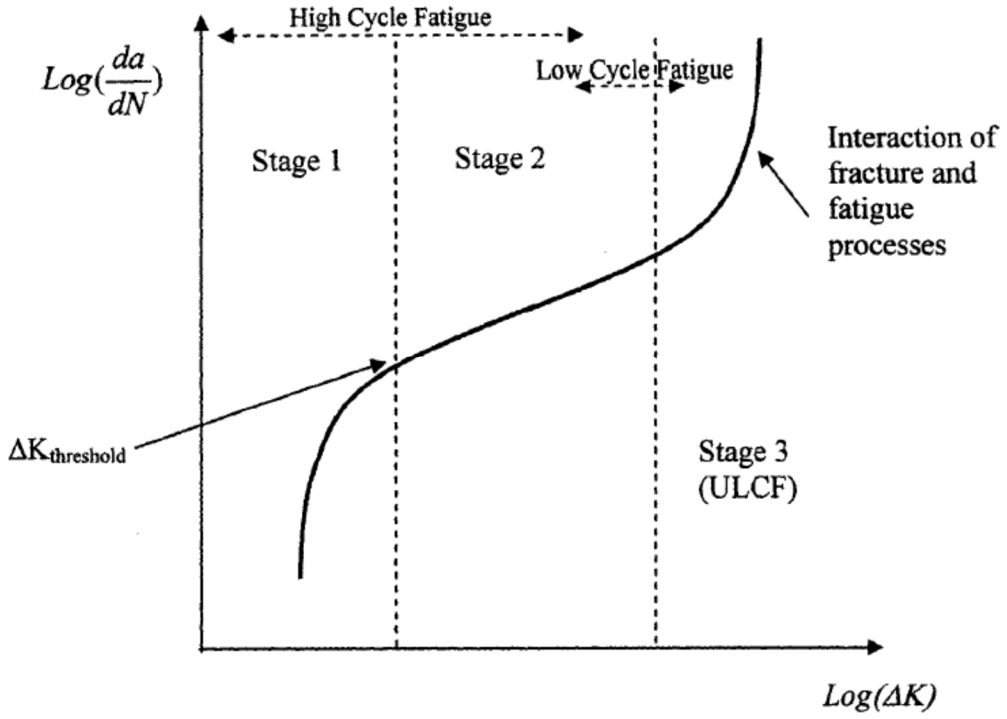


Figure 2.3 – Three stages of fatigue crack growth (Kanvinde 2004)

Fracture can occur with stresses under the yielding stress if a crack is present. Artifacts such as surface scratches, gouges, voids in welds, inclusions and delaminations in materials can easily develop into cracks. It is impossible to avoid crack occurrence despite how detailed or

frequent inspections are conducted. There are many methods of crack examination from simple visual examination to more sophisticated X-ray photography and ultrasonic. If a crack is noticed, depending on the size and severity, the section can be replaced, machining the crack to create a smooth surface or to reinforce it. Although, those methods are used in repairing as per the standards but they are causing additional residual stresses which will have influence on the fatigue life of the structure.

Despite the accuracy of classical fracture mechanics, such as fatigue crack growth, hardness and notch-impact tests, they are limited to certain specimen geometry such as a sharp stress concentration or are valid only if the material is within the elastic limit or even to certain level of plasticity and also for certain materials. While in structural components there are many factors which void the use of classical fracture mechanics in fracture prediction for either high or low cycle fatigue. For earthquake structural engineering the failure is expected only after few highly plastic cycles which classifies it in a category below low cycle fatigue. This type of cyclic loading is called ultra-low cycle fatigue (ULCF). It causes a ductile fracture in less than 20 constant amplitude loading cycles (Kanvinde and Deierlein 2004). Also, the mechanisms for ULCF are similar to monotonic fracture and are different from other types of fatigue. Ductile fracture initiation is the growth and coalescence of microvoids around secondary particles. Those particles are inclusions, which are impurities such as carbides, which are part of the crystalline structure and the grains of the steel matrix. Inclusions, grains and dislocations are visible in the scale of polycrystalline level. A simplified classical illustration of the void growth and coalescence process is shown in Figure 1.2. The growth of voids occur around the inclusions causing loss in the net section. This leads to softening of the materials and coalescence between the microvoids. Varying the stress triaxiality level controls the rate and shape of the void growth. As per Rice and Tracey (1969), low stress triaxiality causes elongated voids around inclusions, while for higher stress triaxiality values the voids are more symmetric around the inclusions. This phenomenon have been validated by experimental fracture data.

Murdy (1983) developed the field of damage mechanics which is also known as the local approach of fracture. Murdy's main focus was on the predication of fracture initiation and stable crack growth. It uses continuum mechanics to predict the behavior of cracks in structures using a

combination of local stresses and strains also known as fracture initiation (Lemaitré 1986). The local approach of fracture was used by many researchers such as, Murdy (1983), Pineau (1992), Berdin and Besson (2004), to predict fracture initiation. There are also different levels of cracks which are defined in details by Lemaitré (1986).

Many different local approach of fracture models have been developed, the most popular one is Stress Modified Critical Strain (SMCS) which depends on the equivalent plastic strain and the stress state or also known as triaxiality ratio (Hancock and Mackenzie 1977). The SMCS is based on analytical work studies conducted previously (McClintock 1968, Rice and Tracey 1969). Also, it predicts ductile fracture in steels under monotonic loads. For cyclic loading, a model called Cyclic Void Growth Model (CVGM) (Kanvinde and Deierlein 2007) is used to predict ductile fracture in steels under ULCF loading. Rice and Tracey (1969) stated that void growth is often not equiaxial and depends strongly on the level of stress triaxiality ratio. Stress triaxiality ratio, T, is the ratio of the hydrostatic stress or mean normal stress, σ_m, to the effective or the Von Mises stress, σ_e, as shown in Equation 2.1.

$$T = \frac{\sigma_m}{\sigma_e} \tag{2.1}$$

A high stress triaxiality ratio, between 0.75 and 1.5, can cause a large reduction in the rupture strain. Values of stress triaxiality ratio greater than 1.5 can result in brittle behavior (LeMaitre 1986). Those stress triaxiality limits do not represent a fixed limit and there are some minor variations in the literature. The voids grow asymmetrically into a prolate shape such that the major axis is aligned along the direction of remote plastic strain for triaxiality ratios less than 1.0. In cases with triaxiality ratios greater than 3, which are considered large, the void growth is oblate shape with larger dimension being normal to the axis of straining (Kanvinde 2004). Equations 2.2 and 2.3 presents the mean normal stress, σ_m, and the effective stress, σ_e, respectively. Stress triaxiality is affected by cyclic loading, causing a change in sign during tension (positive) or compression (negative).

$$\sigma_m = \frac{(\sigma_1+\sigma_2+\sigma_3)}{3} \tag{2.2}$$

$$\sigma_e = \sqrt{\frac{1}{2}(\sigma_1 - \sigma_2)^2(\sigma_2 - \sigma_3)^2(\sigma_3 - \sigma_1)^2} \quad (2.3)$$

Another important parameter which is used to measure fracture damage which occurs under plastic strain is the equivalent plastic strain. It is presented in its incremental format as shown in Equation 2.4. It represents the total amount of plastic strain sustained by the material while the specimen is in tensile during cyclic loading.

$$d\bar{\varepsilon}_p = \sqrt{\frac{2}{3} d\varepsilon_p^{ij} d\varepsilon_p^{ij}} \quad (2.4)$$

Equations were derived by Rice and Tracey (1969) for the growth of spherical voids in an elastically rigid and incompressible plastic material under uniform plastic strain in presence of stress triaxiality. The conclusion was that the growth rate is exponentially related to stress triaxiality for spherical voids as shown in Equation 2.5.

$$\frac{dR}{R} = 0.283 \exp\left(\frac{3\sigma_m}{2\sigma_y}\right) d\bar{\varepsilon}_p \quad (2.5)$$

Where R is the void radius, σ_m is the mean normal stress defined in Equation 2.2, σ_y is the yield stress, and $d\varepsilon_p$ is the incremental equivalent plastic strain which defined in Equation 2.4. Rice and Tracey's Void Growth Model (VGM) can be derived by integrating Equation 2.5. It can only be applied for elastically perfectly plastic material and does not account for multiple void interaction. D'Escata and Devaux (1979) modified the VGM by Rice and Tracey (1969) to account for hardening behavior by replacing the yield stress, σ_y, with the effective stress, σ_e, as shown in Equation 2.6.

$$ln\left(\frac{R}{R_0}\right)_{critical} = 0.283 \int_0^{\varepsilon_p} exp\left(\frac{3\sigma_m}{2\sigma_e}\right) d\bar{\varepsilon}_p \quad (2.6)$$

Equation 2.1 presents the stress triaxiality ratio which is the defined by the mean normal stress, σ_m, divided by the effective stress, σ_e. This ratio σ_m/σ_e in Equation 2.6 can be replaced with stress trixiality ratio, T. From Equation 2.6, it can be clearly concluded that crack initiation occurs under uniform plastic strain which causes the voids to reach a critical size or ratio. The calibration factor 0.283, in Equations 2.5 and 2.6, was obtained by curve fitting data by Rice and Tracey

(1969). This factor can be replaced with constant, *c*, to represent the material capacity in terms of void growth normalized by coefficient, c, to control void growth rate, as shown in Equation 2.7. Equation 2.7 accounts only for one void and does not account for multiple void interaction.

$$\frac{ln\left(\frac{R}{R_0}\right)_{critical}}{c} = \int_0^{\varepsilon_p^{critical}} exp(1.5T)d\bar{\varepsilon}_p \tag{2.7}$$

The SMCS Model can be derived by integrating Equation 2.7. It was derived by Hancock and Mackenzie (1976), and it enables direct calculation of critical plastic strain as a function of stress triaxiality ratio for monotonic loading, as shown in Equation 2.8. The SMCS Model is based on the assumption that the triaxiality does not change with respect to increasing plastic strain, so the critical plastic strain depends on the current level of stress triaxiality. SMCS Model parameter α is calculated for each test individually and then an average is taken. While testing different size specimens, it was noticed that α was size dependent and that it is not capable of capturing all aspects of behavior responsible for fracture. For further detailed information about the SMCS Model refer to Kanvinde and Deierlein (2006) and Myers (2009).

$$\varepsilon_p^{critical} = \alpha\, exp(-1.5T) < \varepsilon_p \tag{2.8}$$

As mentioned previously the SMCS Model is the base of the VGM which is presented in Equation 2.9. The VGM is an expansion on the derivation by Rice and Tracey (1969). The VGM incorporates a full plastic strain history in relation with the triaxiality ratio for monotonic loading.

$$VGI = \int_0^{\varepsilon_p^{critical}} exp(-1.5T)d\bar{\varepsilon}_p > VGI_{critical} \tag{2.9}$$

A comparison between the SMCS Model and VGM was conducted by Kanvinde and Deierlein (2006). They used seven different types of steel in this study with notched coupon specimens with different notch sizes to vary stress triaxiality. It was concluded that the VGM is more accurate in large triaxiality changes compared to the SMCS Model, while the SMCS Model is more convenient to use than the VGM. Also, both models are reliable for use in situations without very sharp stress or strain gradient.

2.4 LCF Models to Predict Fracture (CVGM)

The fracture mechanisms controlling ULCF are similar to monotonic fracture mechanisms in the manner of void growth and coalescence. ULCF does not obey the classical high or low cycle fatigue fracture mechanisms nor models. A common approach to predict the crack growth behavior is Paris Law which was derived by Paul Paris in the 1960's (Paris and Erdogan 1963). It is a relation between cyclic crack growth, *da/dN*, and stress intensity range, ΔK, as shown in Equation 2.10. Where *C* is a constant and *m* is the slope on the log-log plot (constant).

$$\frac{da}{dN} = C(\Delta K)^m \tag{2.10}$$

Figure 2.3 presents the three stages of fatigue crack growth, and Paris Law is valid only for Stage 2 which is mostly the high cycle fatigue region (linear part). For low and high growth rates (Stage 1 and 3) the curve generally is steep which invalidates the use of Paris Law. Replacing the ΔK with the range of J-integral, ΔJ which is a nonlinear energy parameter, provides better results for low cycle fatigue but still the equation is invalid to use for ULCF. ULCF is considered more of a fracture problem rather than fatigue problem due to the very low cycles to failure due to the observed high strains. Also, with high and low cycle fatigue, the crack growth is more consistent for each cycle as long as the stresses are above the threshold. For these reasons, new models to simulate ULCF failures in metals have been developed.

ULCF can be classified as Stage 3 as per Figure 2.3 due to the high plastic strains and low cycles to failure. As mentioned previously that ULCF failure mechanism is similar to monotonic fracture mechanisms which is related to the void growth and coalescence. The only difference is that the ULCF model needs to capture the growth of voids under reversed loading and accumulate the damage due to the high plasticity being applied through cycling.

The Degraded Significant Plastic Strain (DSPS) Model is one of the models which is used to predict fracture initiation in ductile metals subjected to ULCF. The model is simple and easy to calibrate. It is derived from the SMCS Model used for monotonic loading with some modifications to encounter cyclic loading and a newly developed strain measure. Also, it is referred to in the literature as Cyclic SMCS Model. There are many assumptions made in the DSPS Model. Under

high plastic strains, the stress triaxiality does not change significantly. Also, it assumes that the positive and negative mean stress is nearly equal for the same cycle. The stress triaxiality is dependent on the specimen geometry and it assumes that the stress triaxiality at failure are similar for the cyclic and monotonic cases. Highly ductile material are not the best candidates to be used with the DSPS Model due to high triaxiality stress conditions. A set of monotonic and cyclic tests needs to be conducted to calibrate the DSPS Model. The material toughness parameter α is calculated using the SMCS Model, which is discussed previously, using monotonic tests, then the damageability parameter ,λ_{DSPS}, is calibrated by curve fitting the cyclic test data using Equation 2.11.

$$\varepsilon^{*}_{critical} = exp\left(-\lambda_{DSPS}\varepsilon_p\right)\varepsilon_p^{critical} \tag{2.11}$$

The Cyclic Void Growth Model (CVGM) described by Kanvinde and Deierlein (2007) and modified by Myers (2009) is adapted from the monotonic Void Growth Model (VGM) developed by Rice and Tracey (1969), to predict fracture initiation during cyclic loading. CVGM has been used by researchers to predict fracture initiation in ductile metals subjected to ULCF. CVGM is attractive in part because it attempts to capture the mechanism of ULCF through fracture parameters representing void growth. Those parameters are presented in Equations 2.12 through 2.15. Fracture initiation occurs when the cyclic void growth index demand, VGI_{cyclic}, is greater than the cyclically degraded critical void growth index capacity, $VGI_{cyclic}^{critical}$, as described in Equation 2.12. The demand is defined by the cyclic void growth index, VGI_{cyclic}, in Equation 2.13, and the capacity for fracture resistance is defined as the critical cyclic void index, $VGI_{cyclic}^{critical}$, as given in Equation 2.14. Myers (2009) proposed refinements for the CVGM described by Kanvinde and Deierlein (2007). Those refinements were proposed to increase the accuracy and the calibration framework consistency of the model. For further information about the CVGM refer to Myers (2009).

$$VGI_{cyclic} > VGI_{cyclic}^{critical} \tag{2.12}$$

$$VGI_{cyclic} = \sum_{tensile\ cycles} \int_{\varepsilon_1}^{\varepsilon_2} exp\left(\left|1.5\frac{\sigma_m}{\sigma_e}\right|\right) d\bar{\varepsilon}_p - \sum_{compressive\ cycles} \int_{\varepsilon_1}^{\varepsilon_2} exp\left(\left|1.5\frac{\sigma_m}{\sigma_e}\right|\right) d\bar{\varepsilon}_p \quad (2.13)$$

$$VGI_{cyclic}^{critical} = VGI_{monotonic}^{critical}\, exp\left(-\lambda\, \bar{\varepsilon}_p^{accumulated}\right) \quad (2.14)$$

$$VGI_{monotonic}^{critical} = \int_0^{\varepsilon_p^{critical}} exp\left(1.5\frac{\sigma_m}{\sigma_e}\right) d\bar{\varepsilon}_p \quad (2.15)$$

The cyclic void growth index, VGI_{cyclic}, is a function of the stress triaxiality ratio, σ_m/σ_e, (hydrostatic stress, σ_m, divided by the von Mises stress, σ_e), and incremental equivalent plastic strain, $d\bar{\varepsilon}_p$. The critical cyclic void growth index, $VGI_{cyclic}^{critical}$, is a function of the accumulated equivalent plastic strain, $\varepsilon_p^{accumulated}$, and calibrated fracture parameters: the critical monotonic void growth index, $VGI_{monotonic}^{critical}$, and the degradation coefficient, λ. The critical monotonic void growth index, $VGI_{monotonic}^{critical}$, is calibrated using Equation 2.15 based on monotonic test results (to get strain at fracture initiation) and complimentary FE models (to get equivalent plastic strain and stress triaxiality). Once $VGI_{monotonic}^{critical}$ is found, a regression analysis can be performed using the values of $VGI_{cyclic}^{critical}$ obtained from cyclic tests to calibrate the cyclic degradation coefficient, λ, using the relationship given in Equation 2.14. Looking closely at Equation 2.13, it quantifies the effects of voids growth and shrinkage, voids grow during tensile cycles and shrink during compressive cycles. Voids growth is defined as whenever the mean stress is positive and void shrinkage is defined as whenever the mean stress is negative.

Recent work conducted by Saykin et al. (2014) used the VGM and Hillerborg Model to study fracture initiation and propagation in moment resisting beam to column connections. The FEM captured the material softening followed by element removal to simulate fracture propagation using the VGM and Hillerborg Model. Calibration of the VGM and Hillerborg Model was conducted using circumferential notched tensile coupon specimens with different notch sizes similar to Kanvinde and Deierlein (2007). The proposed approach has shown its effectiveness in predicting fracture initiation and propagation.

2.5 Stress-Weighted Damage Model to Predict Fracture

A new model called the Stress-Weighted Damage Model (SWDM) has been developed by Smith et al. (2014). This model is a modified model of the CVGM which was developed by Kanvinde and Deierlein (2007). The SWDM uses different parameters that were derived from three different models Full Axisymmetric Model, the Lode Angle Model, and the Capacity Degradation Model originating in the CVGM by Kanvinde and Deierlein (2007). Full Axisymmetric Model is a fracture model valid for axisymmetric stress states with a complete range of triaxiality levels ranging from -2 to 2 triaxiality. In other hand, the Lode Angle Model is valid for a non-axisymmetric stress with high triaxiality only. Incorporating the Full Axisymmetric Model in the SWDM enables the prediction of ductile fracture under all relevant structural conditions especially with low triaxiality.

For more information about the derivation and background of the SWDM refer to Smith et al. (2014). Equation 2.16 presents the final derived version of the SWDM that is used in the next chapters.

$$1 < D_{SWDM} = e^{-\lambda \bar{\varepsilon}_p} \int_{\varepsilon_1}^{\varepsilon_2} C \left(\beta e^{A^+ T} - e^{-A^- T} \right) e^{\kappa |\xi|} \, d\bar{\varepsilon}_p \tag{2.16}$$

Where λ is the degradation coefficient that controls the rate of degradation during compressive loading. C is a material parameter that controls mainly the overall ductility of the material. β controls the relative rate of damage accumulation (during tension loading) and reduction (during compression loading). In Smith et al. (2014) it is recommended to use $\beta = 1$, this is based on the success of the CVGM. In cases with geometric nonlinearity it is recommended to use higher values of $1.05 < \beta < 1.3$. A^+, A^- are dependent on the voids behavior under negative or positive stress triaxiality. They control the growth and reduction of damage due to the stress triaxiality, Smith et al. (2014) used a value of $A^+ = A^- = 1.3$ based on calibration procedure that was used in his work. In a previous study by Rice and Tracey (1969) those parameters for a rigid-plastic material is 1.5. T is the stress triaxiality ratio, σ_m/σ_e. κ is material dependent that effects the Lode angle parameter, ξ, it can also be negative or positive. If there is an increase in ductility $\kappa <$

0, while if there is a decrease in ductility κ >0 for an axisymmetric stress condition relative to a plane strain condition. ξ is the Lode angle parameter for material ductility.

2.6 Cyclic Damage Plasticity Model to Predict Fracture

Cyclic Damage Plasticity Model (CDPM) is a numerical model that predicts the fracture initiation and propagation during cyclic loading. This model has been developed by Dufailly and Lemaitre (1995) and it involves multi-axial states of material nonlinearity, both local and global buckling, and material fatigue under inelastic cycling loading. It is a numerically efficient continuum damage mechanics material model that has been implemented in finite element software LS-DYNA by Huang and Mahin (2010).

Usually when metal-like materials are under complex plastic loading isotropic, kinematic or combined hardening is used to simulate the actual behavior using finite element software. The material model that is used in the CDPM is the Lemaitre and Chaboche (1994) plasticity model with combined nonlinear isotropic and kinematic hardening which was derived from multiaxial formulations by Armstrong and Fredrick (1966). It is a pressure-independent plasticity model and it captures the nonlinear Bauschinger effect, cyclic hardening and ratcheting. Also, it has two back stress terms for kinematic hardening combined with isotropic hardening and a damage model for modeling low cycle fatigue and failure. The advantages of defining back stress in the model accurately models larger strain range and ratcheting. Both of the isotropic and kinematic component of the combined hardening model are presented in Equations 2.17 and 2.18 respectively.

$$\sigma^0 = \sigma|_0 + Q_\infty\left(1 - e^{-b\bar{\varepsilon}_p}\right) \tag{2.17}$$

Where σ^0 is the instantaneous yield surface, $\sigma|_0$ is the initial yield surface size, $Q_\infty$and b are material parameters, and $\bar{\varepsilon}_p$ is the equivalent plastic strain.

$$\dot{\tilde{\alpha}} = C\dot{\bar{\varepsilon}}_p \frac{1}{\sigma_0}(\tilde{\sigma} - \tilde{\alpha}) - \gamma\tilde{\alpha}\dot{\bar{\varepsilon}}_p \tag{2.18}$$

Where $\dot{\tilde{\alpha}}$ is the incremental change in back stress tensor, $\tilde{\alpha}$ is back stress tensor, C and γ are material parameters, and $\dot{\bar{\varepsilon}}_p$ is incremental change in the equivalent plastic strain.

When isotropic damage, D, is $D = 0$ it defines a damage free material, however when $D = 1$ it defines a fully broken material. When the critical damage, D_c, is between 0 and 1 it defines element removal and the element is deleted from the model. The removal of the first element in the FE model is considered that fracture has initiated in the section. The default value of D_c in LS-DYNA is 0.5. The isotropic damage is presented in Equation 2.19.

$$0 \leq D \leq 1 \tag{2.19}$$

$$D = \begin{cases} \left(\frac{Y}{S}\right)^t \bar{\varepsilon}_p & \bar{\varepsilon}_p > \bar{\varepsilon}_{pd} \text{ and } \frac{\sigma_m}{\sigma_e} > -\frac{1}{3} \\ 0 & Otherwise \end{cases} \tag{2.20}$$

Where Y is strain energy density release rate, t is a material constant (Default = 1 in LS-DYNA), S is a damage material constant with units of energy density (Default = $\sigma_{y0}/200$ in LS-DYNA), σ_m/σ_e is stress triaxiality, $\bar{\varepsilon}_p$ is the equivalent plastic strain, and $\bar{\varepsilon}_{pd}$ is the damage threshold. The name of this material model in LS-DYNA is MAT_DAMAGE_3 (MAT_153) it is revised for simpler implementation than other similar models. This model is valid to be used for beam, shell and solid elements.

2.7 Comparison and Limitations of the LCF Models

Each of the three LCF Models presented in previous sections has their advantages and limitations. A summary and conclusion of the three LCF Models is presented in this section.

CVGM which was refined by Myers (2009) is limited for high stress triaxiality conditions. Only two fracture parameters are calibrated in the CVGM compared to other models, and it is valid

for conditions with high stress triaxiality. The SWDM was later developed by Smith et al. (2014) and it involves five fracture parameters that require calibration. Also, a new specimen geometry is used in calibrating the fracture parameters that enables fracture initiation in low stress triaxiality conditions. This damage model predicts ductile fracture initiation under all relevant structural conditions especially low triaxiality. While, the CDPM is a numerical LCF model that predicts fracture initiation and propagation. Dufailly and Lemaitre (1995) developed the model and it was implanted in FE software LS-DYNA by Huang and Mahin (2010). This model does not require special calibration procedures as the previous two models and the calibration process can be done using FE modeling. It involves multi-axial states of material nonlinearity, both local and global buckling, and material fatigue under inelastic cycling loading. Also, it this damage model predicts fracture initiation under all relevant structural conditions and does not have any limitations to any stress triaxiality conditions.

All of the LCF models discussed previously require stress triaxiality and equivalent plastic strain to predict fracture initiation. Choosing a LCF model relies on two main factors, the stress triaxiality condition of the problem or structure that is studied, and the available resources for material testing versus computational calibration. Also, all of the models discussed can be used to study fracture propagation. The only model that is currently implemented in FE software is the CDPM. Although the CVGM and SWDM were developed to predict fracture initiation, recently Saykin et al. (2014) used the VGM and Hillerborg Model to study fracture initiation and propagation in moment resisting beam to column connections using element removal.

When the CVGM and SWDM were developed they were geared toward studying ductile fracture initiation for different materials with no artifacts. The geometry of the specimens that are used to calibrate the fracture parameters for the CVGM and SWDM cannot incorporate artifacts. In this work the LCF models discussed previously will be used to calibrate fracture parameters for each LCF model using modified cyclic bend test to encounter artifacts. Flat plate coupons that include artifacts are used to calibrate fracture parameters for different LCF models to predict fracture initiation for different artifacts using the proposed testing procedure. Also, understanding the fracture propagation and the failure mechanism is necessary in the case of artifacts. The CDPM will be calibrated using the cyclic bend tests and will be used to study fracture initiation and

propagation. Then the calibrated fracture parameters will be used in conjunction with FE models to predict fracture initiation and the effect of artifacts in SMRF connections in the plastic hinge region. The framework is general and can be applied to many types of artifacts and seismic structural systems.

CHAPTER 3 EXPERIMENTAL TESTING PROGRAM

3.1 Introduction

This chapter will present the testing program. Tests were conducted to validate the proposed framework and apply the framework for five artifact types. The parts of the experimental program that will be discussed are the round notched bar tests which were conducted as a benchmark to validate the bend test approach, the monotonic uniaxial tension tests on flat plates, and the cyclic bend tests on flat plates. Then, the detailed procedures for implementing each artifact are described.

3.2 Round Notched Bar Tests

The majority of the testing used to calibrate low cycle fatigue models has been conducted using circumferentially notched (CN) round bars. Myers (2009) includes a summary of numerous monotonic and cyclic tests on these types of CN specimens. Monotonic tension and cyclic axial tests of CN specimens are typically used to characterize ductile fracture initiation for a relatively homogenous metal material. To validate the proposed test methods using flat plate specimens, it was necessary to conduct testing on a series of round CN specimens to act as a benchmark. The conventional CN specimens were used to obtain calibrated CVGM fracture parameters (presented in the next chapter), to compare with fracture parameters calibrated using bare steel (no artifact) flat plate specimens tested using the proposed bend test methods.

Round CN bar tests were conducted on A992 steel extracted from the flanges of the W36x150 beams used in full-scale tests (Eatherton et al. 2013). The geometries of the round specimens were in accordance with ASTM A370-12a (ASTM 2012), while the notch sizes were adapted from Kanvinde and Deierlein (2007) and Myers (2009). A total of eight CN round bar tests (three monotonic and five cyclic) were conducted. Figure 3.1 shows a diagram of the round notched bars including the Notched Diameter, D_N, and Unnotched Diameter, D_{UN}, which were the

same for all specimens with values of 0.25 in. and 0.5 in. respectively. Three different notch radii, R_N = 0.060, 0.125, and 0.250 in., were tested to vary the stress triaxiality to aid in calibrating the fracture parameters, $VGI_{monotonic}^{critical}$ and λ. Kanvinde and Deierlein (2007) recommend a total of 6-9 notched bar tests (three monotonic and three to six cyclic) to calibrate fracture parameters for use with the CVGM.

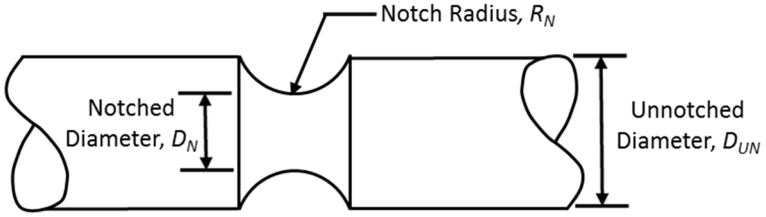


Figure 3.1 – Round notched bar schematic.

Tests consisted of both monotonic and cyclic loading. The monotonic tests are used to calculate the critical monotonic void growth index, $VGI_{monotonic}^{critical}$, while the cyclic tests are used to calculate the critical cyclic void growth index, $VGI_{cyclic}^{critical}$, which in turn is used to calibrate the degradation coefficient, λ. Calibrating the fracture parameters relies on knowing the stress triaxiality history and equivalent plastic strain history at the fracture initiation location. Stress and strain histories are calculated using complimentary FEM analyses described in more detail in the next chapter. A total of five cyclic CN round bar tests were conducted as presented in Table 3.1 with their notch radii and displacement range between which they were cycled. A MTS Model 380.10 uniaxial testing machine was used with a load capacity of 22 kips. Displacement was measured using MTS Model 632.11B-20 extensometer with a gage length of 1 in. and a maximum displacement of 0.15 in. (15% of gage length). Load, crosshead displacement, and extensometer displacement were recorded. The tests were displacement controlled wherein the displacement of the 1 in. gage length extensometer was used for control. The results of round notched bar tests are discussed in the next chapter.

Table 3.1 – Cyclic notched round bar test matrix for A992 steel.

Specimen	**R060**	**R125**	**R250-1**	**R250-2**	**R250-3**
Notch Radius, R_N (in.)	0.060	0.125	0.250	0.250	0.250
Displacement Limits* (in.)	-0.005↔0.01	-0.005↔0.015	0.000↔0.02	0.000↔0.02	0.000↔0.015

* Tests are displacement controlled using a 1.0 in. gage length extensometer. Numbers given are the lower and upper bounds of displacement for each cycle. Cycles were constant amplitude up to failure.

3.3 Overview of Testing Approach with Flat Plate Specimens

While round CN bar specimens have been used to characterize the fracture behavior of many types of material, it is not possible to use these types of specimens to characterize the effect of macroscopic artifacts on fracture behavior. The main focus of this report is developing a new test method to expand the applicability of the CVGM to consider common artifacts encountered in steel construction. A test on flat plate coupons that represent the web or flange of steel wide flange sections was selected. If fracture occurs in a steel component away from a connection, it typically occurs at the location of a buckle such as the buckling and creasing of HSS braces in concentrically braced frames, or local buckles in a moment frame plastic hinge region. In these cases, fracture occurs in portions of steel plate subjected to a steep strain gradient associated with bending. A cyclic bend test setup using flat plate material was therefore chosen.

It is not, however, the intent of these bend tests to exactly replicate the stress and strain histories in a local buckle. The stress and strain states at a flange local buckle in ductile moment frame connection are very complex. Several attempts were made to develop a test method that recreates the stress and strain conditions of a local buckle with little success (see Toellner 2013). Replicating the exact strain histories expected in a local buckle is not necessary in the calibration of fracture parameters, however, since the stress and strain states at critical fracture locations will be explicitly considered in the calculation of fracture demand. As such, the coupon tests will be used to characterize fracture resistance (as embodied in the calibrated fracture parameters), as opposed to developing acceptability criteria based on the coupon tests alone.

The development of the bend test approach to predict fracture initiation consists of two sets of tests on flat plate specimens: monotonic uniaxial tension tests and cyclic bend tests. Each type

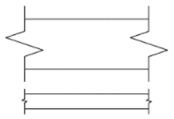
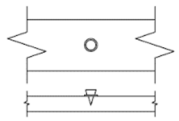
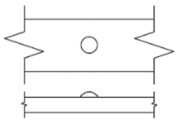
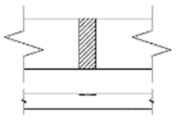
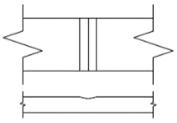
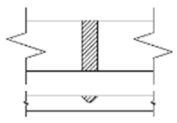
of test is used to calibrate the two fracture parameters used in the CVGM. The two fracture parameters are the critical monotonic void growth index, $VGI_{monotonic}^{critical}$, and the degradation coefficient, λ. FE models are used to obtain the equivalent plastic strain, $\varepsilon_p^{accumulated}$, and stress triaxiality that are required in the calculation of fracture parameters. See section 1.1 for the CVGM equations.

3.4 Monotonic Uniaxial Tension Tests

Calculating the critical monotonic void growth index, $VGI_{monotonic}^{critical}$, for a particular artifact is done using monotonic tension tests on flat plate specimens containing the artifact. The specimens were cut from the flanges of beams used in full-scale tests (Eatherton et al. 2013). The specimens were taken from the middle of the beam where no inelastic deformations occurred. The geometry of the coupons and testing rate were conducted as per A370-12a (ASTM 2012) with a total length of 18 in., a gage length of 8 in, and a width of 1.5 in.

A total of 12 monotonic uniaxial tests were conducted with different artifacts to calibrate $VGI_{monotonic}^{critical}$ for use in the CVGM. Six were cut from the flanges of the W24x62 and the other six were cut from the flanges of the W36x150 specimens. Table 3.2 presents the monotonic uniaxial testing matrix. Results and pictures are presented in the next chapter.

Table 3.2 – Monotonic test matrix.

Artifact Type		Flange Thickness	Specimen Name
1) No Artifact		W24x62 (0.59 in.)	W24-B-Mono-T59
		W36x150 (0.94 in.)	W36-B-Mono-T94
2) Powder Actuated Fasteners (PAF)		W24x62 (0.59 in.)	W24-PAF-Mono-T59
		W36x150 (0.94 in.)	W36-PAF-Mono-T94
3) Puddle Welds (PW)		W24x62 (0.59 in.)	W24-PW-Mono-T59
		W36x150 (0.94 in.)	W36-PW-Mono -T94
4) Ground Fillet Weld (GFW)		W24x62 (0.59 in.)	W24-GFW-Mono-T59
		W36x150 (0.94 in.)	W36-GFW-Mono -T94
5) Notch Ground to Taper (NGT)		W24x62 (0.59 in.)	W24-NGT-Mono-T59
		W36x150 (0.94 in.)	W36-NGT-Mono-T94
6) Notch Welded and Ground Smooth (NWG)		W24x62 (0.59 in.)	W24-NWG-Mono-T59
		W36x150 (0.94 in.)	W36-NWG-Mono-T94

3.5 Cyclic Bend Tests

A cyclic bend test setup was designed and built. As shown in Figure 3.2, a plate specimen is cyclically bent around opposing rollers creating a constant peak curvature which implies cycles with constant strain amplitude assuming uniform strain distribution.

Two loading arms are connected to the actuator to hold the two 11 in. diameter rollers as shown in Figure 2.2. The specimen is clamped between the two rollers and moved back and forth. As shown in Figure 2.2(b), Figure 2.2(c), and Figure 2.3, the specimen is forced to bend around the rollers as the specimen is pushed between two guides. The moving parts are shown in green in Figure 2.2(b) and the fixed parts are shown in blue. The roller diameter of 11 in. was used since it was predicted to cause ULCF in less than 30 cycles for a range of 0.5 in. to 1.0 in. For the 0.59 in. and 0.94 in. thick specimens, the calculated strain at the extreme fiber was 0.051 in./in. and 0.079 in./in. respectively, and the calculated radius of curvature was 5.795 in. and 5.97 in. respectively

The coupon is held between the two 11 in. diameter rollers and displaced using a loading arm connected to the actuator. AISI 12L14 carbon steel with Birnell hardness of 163 is used for the rollers material. A 1 3/8 inch bolt is used to hold the top roller tight against the specimen while accommodating a range of 0.5 to 1.0 in. plates through use of slotted holes in the loading arms. The bolt is designed to be slip critical and thus prevent slippage during loading. To ensure that the specimen was secured between the rollers, a jack was used to apply loading on the top roller while tensioning the 1 3/8 in. bolt. The load applied by the jack was 9 kips. A schematic example of the bending action during one cycle is shown in Figure 3.3. The test setup was designed to withstand four times the maximum expected loading associated with the thicker specimens (0.94 in. thick x 4.7 in. wide).

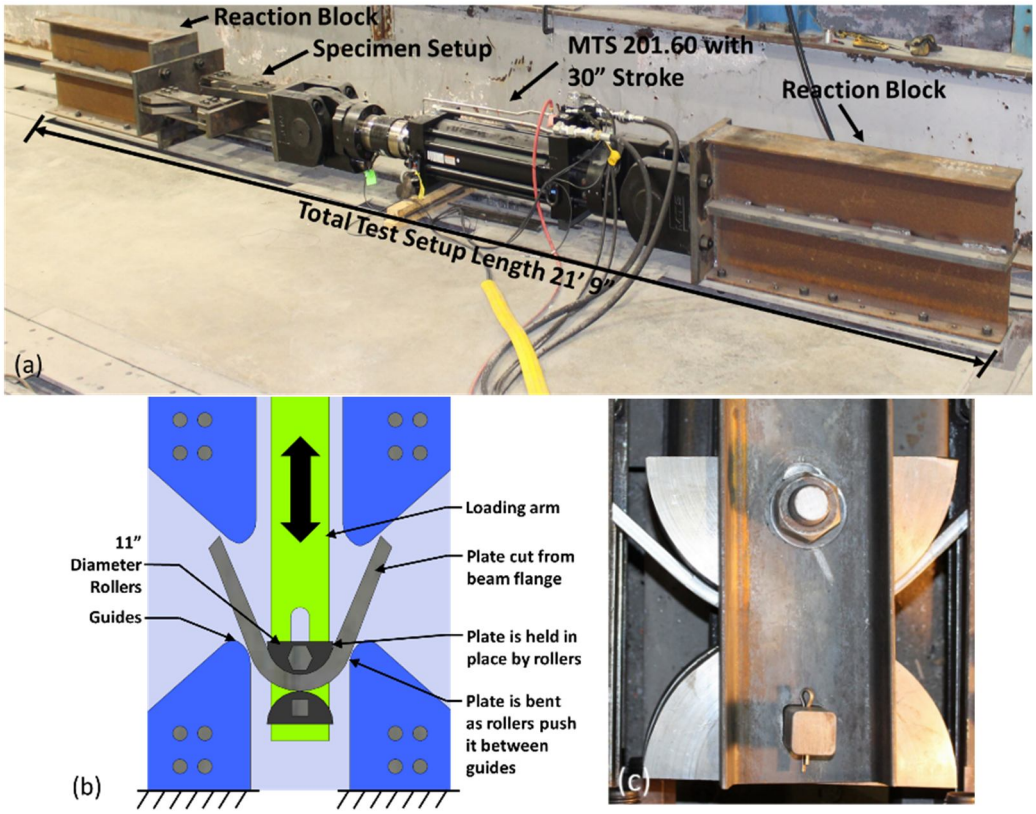


Figure 3.2 (a) Cyclic bend test overall view, (b) top view, and (c) photograph of test setup top view.

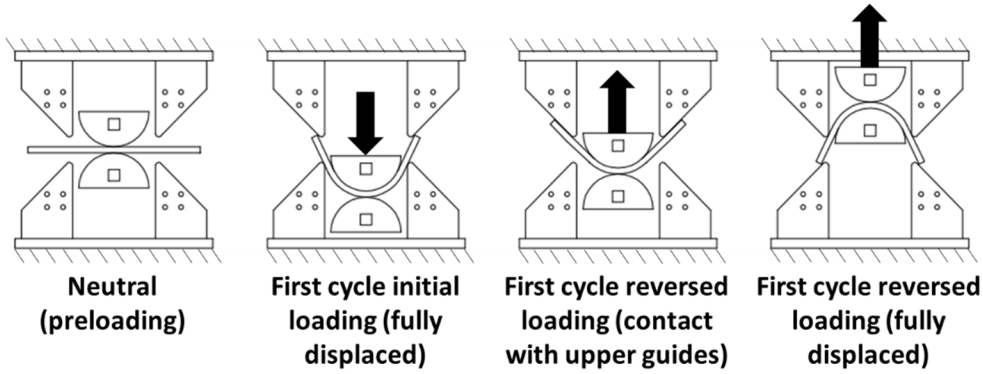


Figure 3.3 – Cyclic bend test bending steps for first cycle.

A total of 36 specimens were tested as part of this study, 18 cut from the flanges of W24x62 beams and the other 18 were cut from the flanges of W36x150 beams. Specimen dimensions were selected to have an aspect ratio of 1:5 with respect to the thickness and width. Therefore, the

coupons cut from the flange of a W24x62 section are 0.59 in. x 2.95 in. and the coupons cut from W36x150 are 0.94 in. x 4.7 in. From a study by Lee et al. (2012), the effected zone for a PAF and a welded shear stud is 0.24 in. measured from the face of the PAF and shear stud. This was considered in selecting the aspect ratio of the specimens to maintain a distance approximately two times the thickness between the artifact and the edges of the specimens. Three different specimen geometries were tested an unnotched specimen, a small notch (R = 0.25 in.) and a large notch (R = 1.00 in.) as shown in Figure 3.5. Notches were used to vary the stress triaxiality and equivalent plastic strain which results in a wider distribution of points for calibration of the fracture parameters. The specimens were cycled with a constant displacement protocol between -5 in. and +5 in. using a MTS 201.60 actuator with a stroke length of 30 in. Loading rates for the 0.59 in. and 0.94 in. thick specimens were 10 in./min and 5 in./min respectively. Those rates were selected based on trial tests (not reported here) to check the integrity of the test setup and mitigate the possibility of early damage due to rapid loading. The rollers are split into two parts (front and back pieces) with a 1 in. gap in between as shown in Figure 3.4 (a). Six high definition cameras were mounted in the gap to monitor both faces of the specimens as shown in Figure 3.4 (b). The cameras were used to record the time and location of fracture initiation as well as recording the fracture propagation and full section fracture.

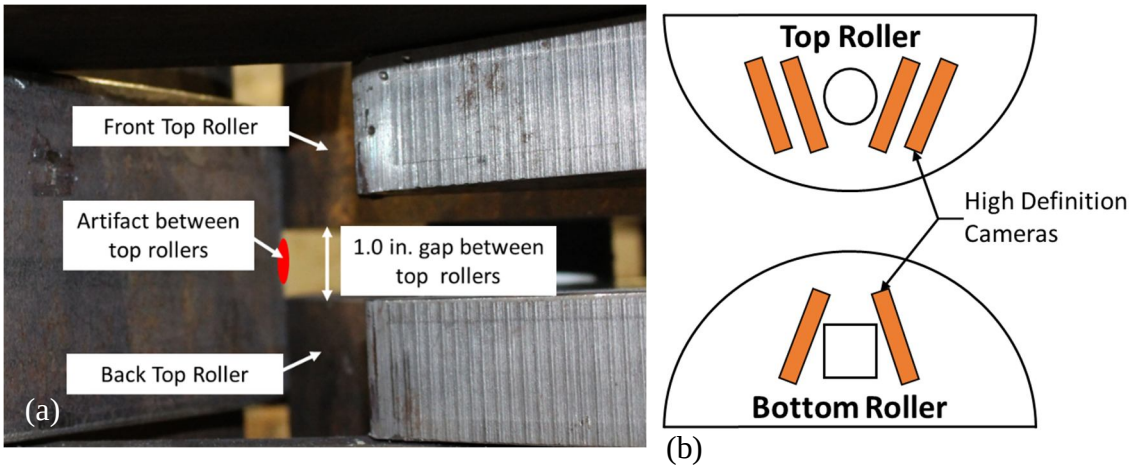


Figure 3.4 – (a) Close up side view of top front and back rollers with 1 in. gap between them, (b) high definition cameras layout on the back top and bottom rollers.

The side referred to as the top side in the results section corresponds to the top side of the flange when it was cut from the wide flange section. The artifacts were placed on the top side of the coupon and the displacement protocol was configured so that the top side of the specimen underwent tension in the first half cycle.

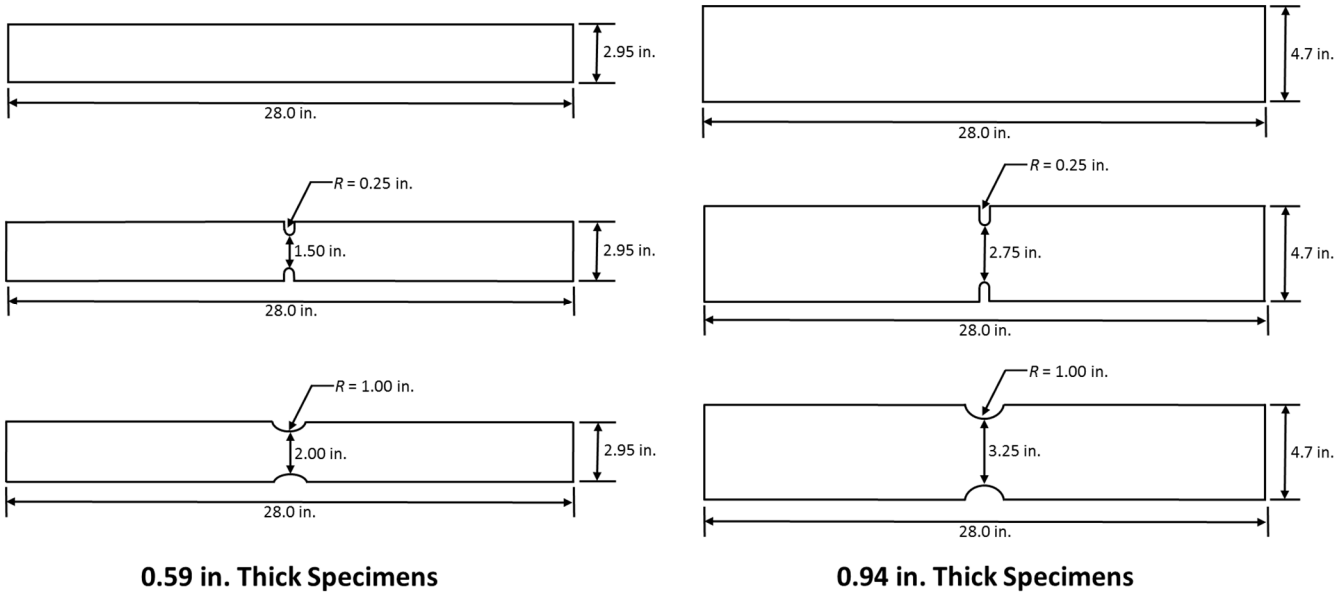
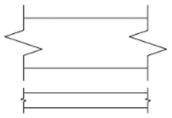
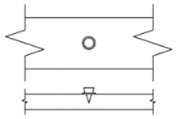
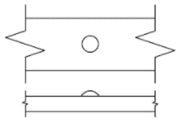
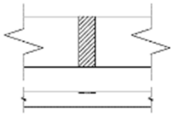
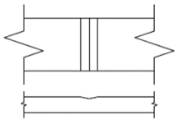
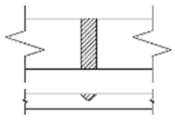


Figure 3.5 – Cyclic bend test specimens for both W24x62 and W36x150.

Table 3.3 – Bend test testing matrix

Artifact Type		Specimen Thickness	Specimen Name	Notched Radius (in.)
1) No Artifact		W24x62 (0.59 in.)	W24-B1-T59-R000	N/A
			W24-B2-T59-R025	0.25
			W24-B3-T59-R100	1.00
		W36x150 (0.94 in.)	W36-B1-T94-R000	N/A
			W36-B2-T94-R025	0.25
			W36-B3-T94-R100	1.00
2) Powder Actuated Fasteners (PAF)		W24x62 (0.59 in.)	W24-PAF1-T59-R000	N/A
			W24-PAF2-T59-R025	0.25
			W24-PAF3-T59-R100	1.00
		W36x150 (0.94 in.)	W36-PAF1-T94-R000	N/A
			W36-PAF2-T94-R025	0.25
			W36-PAF3-T94-R100	1.00
3) Puddle Welds (PW)		W24x62 (0.59 in.)	W24-PW1-T59-R000	N/A
			W24-PW2-T59-R025	0.25
			W24-PW3-T59-R100	1.00
		W36x150 (0.94 in.)	W36-PW1-T94-R000	N/A
			W36-PW2-T94-R025	0.25
			W36-PW3-T94-R100	1.00
4) Ground Fillet Weld (GFW)		W24x62 (0.59 in.)	W24-GFW1-T59-R000	N/A
			W24-GFW2-T59-R025	0.25
			W24-GFW3-T59-R100	1.00
		W36x150 (0.94 in.)	W36-GFW1-T94-R000	N/A
			W36-GFW2-T94-R025	0.25
			W36-GFW3-T94-R100	1.00
5) Notch Ground to Taper (NGT)		W24x62 (0.59 in.)	W24-NGT1-T59-R000	N/A
			W24-NGT2-T59-R025	0.25
			W24-NGT3-T59-R100	1.00
		W36x150 (0.94 in.)	W36-NGT1-T94-R000	N/A
			W36-NGT2-T94-R025	0.25
			W36-NGT3-T94-R100	1.00
6) Notch Welded and Ground Smooth (NWG)		W24x62 (0.59 in.)	W24-NWG1-T59-R000	N/A
			W24-NWG2-T59-R025	0.25
			W24-NWG3-T59-R100	1.00
		W36x150 (0.94 in.)	W36-NWG1-T94-R000	N/A
			W36-NWG2-T94-R025	0.25
			W36-NWG3-T94-R100	1.00

3.6 Specimen Preparation with Artifacts

Five different artifacts were studied: Powder Actuated Fasteners (PAF), Puddle Welds (PW), Ground Fillet Weld (GFW), Notch Ground to Taper (NGT), and Notch Welded and Ground Smooth (NWG). Also, bare control specimens with no artifacts (B) were tested to study the relative impact of the artifacts compared to bare steel specimens. The application of each artifact is presented in this section. Any artifact which required welding such as the PW, GFW, and NWG were conducted by a certified lab technician with substantial previous welding experience including experience making puddle welds for deck attachment.

3.6.1 Powder Actuated Fasteners (PAF)

The PAFs used in this study were Hilti X-ENP-19 L15 Nails. The PAFs were shot into test specimens with a 0.22 caliber Hilti DX 76-PTR tool. Successful installation of a PAF is determined by three criteria. First is a depth of penetration check which is done by a card gage with an indicator on how far the fastener should penetrate the steel. It cannot be too deep or too shallow as shown in Figure 3.6a. The second check is the hammer mark check. After the fastener is installed, a "C" shaped hammer mark should be on the top of the fastener as shown in Figure 3.6 (c). Finally, the third check is a contact test wherein the two washers on the PAF must be fully in contact with each other all the way around the fastener which can also be clearly shown in Figure 3.6 (b). Checking for this contact can be done by sliding a thin piece of paper between the washers. A PAF has three variables that determine how far the fastener penetrates into the steel. These include: the toughness of the steel, strength setting on the gun itself, and strength of the powder cartridges. In order to ensure the PAF is installed properly, practice shots were taken on scrap steel of the same type and thickness. The toughness of the steel was found to be relatively constant so only the strength of the cartridges and the strength setting of the gun affected penetration.

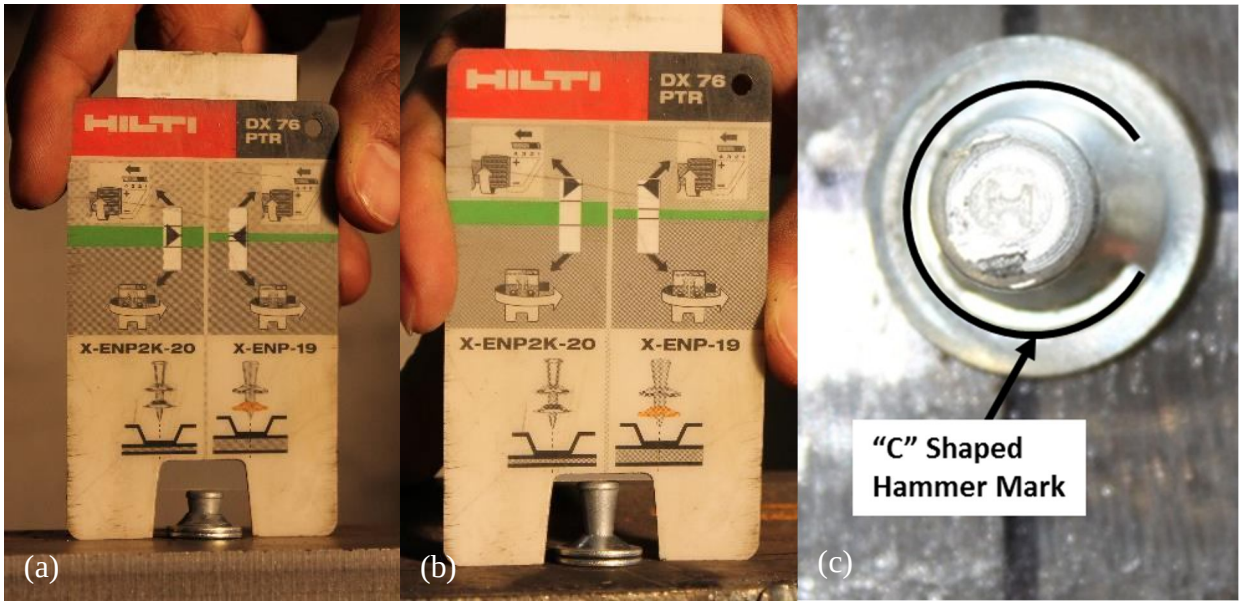


Figure 3.6 – PAF application check of (a) sufficient, (b) insufficient penetration, and (c) "C" shaped hammer mark.

3.6.2. Puddle Welds (PW)

Puddle welds are the only type of deck attachment method allowed in the protected zone region. A 5/8 in. puddle weld was applied to simulate typical deck attachment. The puddle welds were applied through pieces of galvanized 20 gage metal decking secured to the specimen. After welding, the decking was trimmed around the welds using a torch to allow the surface of the specimen to be monitored during testing for fracture initiating at or around the weld area. Shielded Metal Arc Welding (SMAW) was used with a 1/8 in. 6010 5p+ rod (60 – 60 ksi, 1 – any weld position, and 10 – high cellulose sodium coating)) with 85 amps – DC+ (direct current positive).

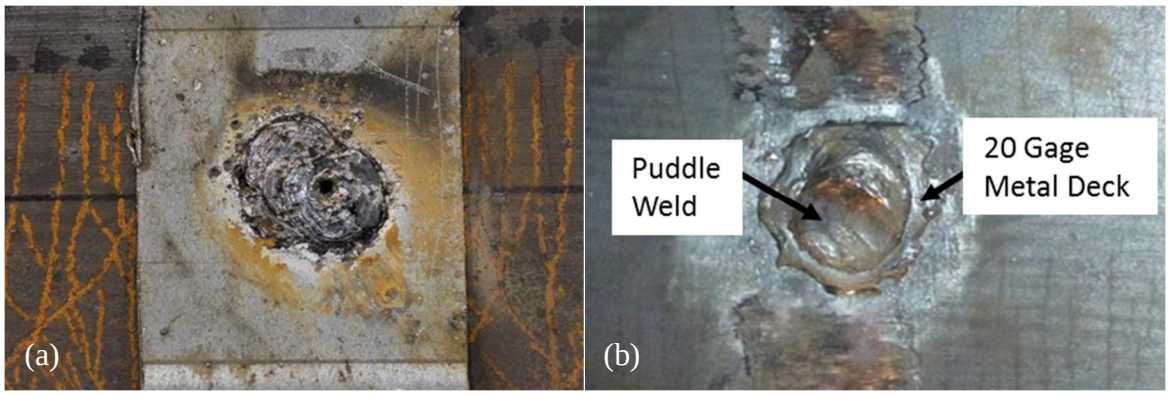


Figure 3.7 – Typical puddle weld (a) with 20 gage metal deck and (b) after torching the metal deck.

3.6.3. Ground Fillet Weld (GFW)

A 1/4 in. bead of weld was applied at the center of the specimens to simulate a typical fillet weld. Gas Metal Arc Welding (GMAW) was used for the NWG specimens with a 70 ksi wire (70c-6) and a wire speed of 350 Amps with 30 volts with 85/15 argon shielding gas (85% argon and 15% CO_2). After the welding was complete it was left to cool and then ground until the specimen was back to its original thickness as shown in Figure 3.8. As per AWS D1.8 (2009) section 6.15.3, the removal of the weld must be done by air carbon arc cutting (CAC-A), grinding, chipping or thermal cutting. For all of the specimens, the weld was ground with care taken to minimize errant gouging. After removal, the area must be ground smooth and free of defect. Also, the surface roughness for each specimen was checked using a surface roughness scale. The roughness of each ground surface was 67 μin.

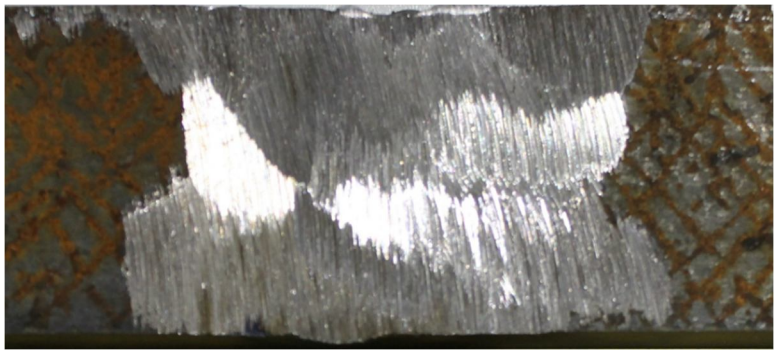


Figure 3.8 – Fillet weld after grinding.

3.6.4. Notch Ground to Taper (NGT)

A 1/8 in. deep notch was used to simulate the limitation of grinding as per AISC 358-10 section 5.7. When repairing the notches or gouges, the ground area shall provide a gradual taper to the surface of the base metal. In the direction parallel to the member axis, the taper shall not be greater than 1:5. The recommendations from AWS D1.8 section 6.15.4.1 were followed in the preparation of the specimens.

A hand grinder and two different grinding attachments were used to make the 1/8th in. deep V-notch. The attachments were: a metal grinding wheel for a majority of the grinding, and a

sanding wheel for finishing. First the center of the specimen was marked. After marking the center, the depth of the notch was marked on both edges of the specimen. The dimensions of the notch are 1/8 in. deep and 1-1/4 in. wide. The metal grinding wheel was then used, holding it parallel with the center mark and perpendicular to the face of the specimen. The wheel was used to grind a divot roughly the width of the wheel to the desired depth. When the 1/8th in. depth was reached, the grinder was used to start grinding off the corners created by the divot starting at a 45 degree angle and then slowly decreasing the angle until the width of the notch was about 5/8 in. The process was repeated for the other side of the notch until the total width of the notch was 1-1/4 inch. Then the grinder was switched to the sanding wheel to smooth out the surface of the slopes. The roughness of each grinded surface was measured using a surface roughness gauge as shown in Figure 3.9 and the value for all of the specimens was approximately 67µin.

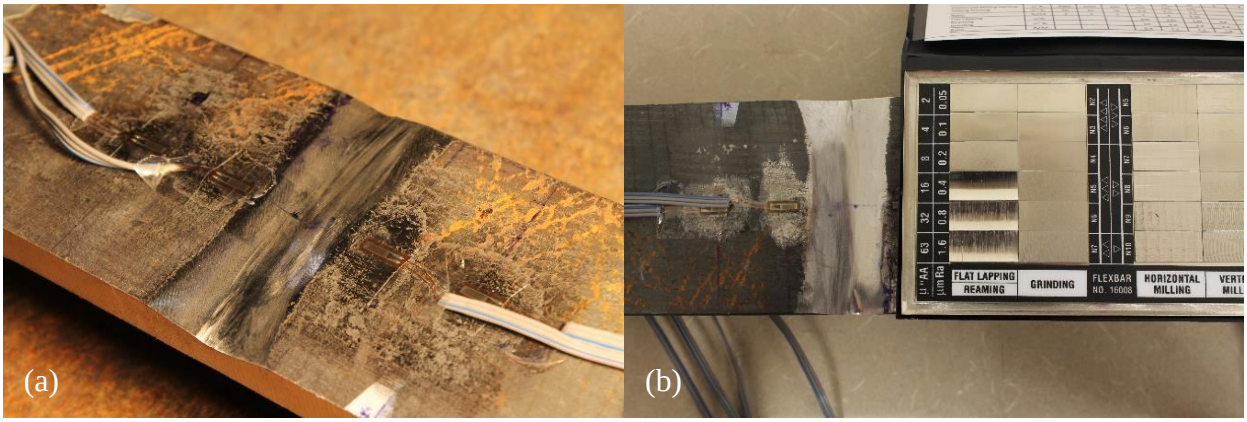


Figure 3.9 – NGT specimen (a) over all view, and (b) surface roughness check.

3.6.5. Notch Welded and Ground Smooth (NWG)

Repair methods for deeper notches or gouges in the protected zone can be done by filling with weld and grinding smooth according to AWS D1.8. When repairs require filling with weld, the notch or gouge shall be removed and ground to provide a smooth radius of not less than 1/4 in. in preparation for welding. Following welding, the repair weld shall be ground to a smooth contour with a surface roughness not to exceed 500 µin. The resultant thickness of the repaired area shall be no less than the base metal thickness less 1/16 in. This type of specimen will simulate a 1/4 in.

deep notch that is repaired by grinding it into a u-notch, filling the notch with weld, and finally grinding it smooth.

For the u-notch, a hand grinder with a metal grinding wheel and a hand file were used. The u-notch was 1/4 in. deep and roughly 3/8 in. wide. First the center of the specimen was marked where the notch was to be created. On the sides of the specimen, the 1/4 in. depth was marked at the center line. The hand grinder was held parallel with the center line mark of the specimen and perpendicular to the face of the specimen. After the notch was the correct dimensions, a hand file was used to round the edges of the notch. After the notch was prepared, it was filled with weld. Gas Metal Arc Welding (GMAW) was used for the NWG specimens with a 70 ksi wire (70c-6) and a wire speed of 350 Amps with 30 volts and 85/15 argon shielding gas (85% argon and 15% CO_2). The same welding setup was used for the GFW and NWG specimens. Small runoff plates were placed on the each side of the specimen to achieve a continuous weld with the same thickness throughout the specimen as shown in Figure 3.10 (b). Figure 3.11 shows the surface roughness scale used to measure the roughness of the ground surface. The surface roughness was approximately 67 μin.

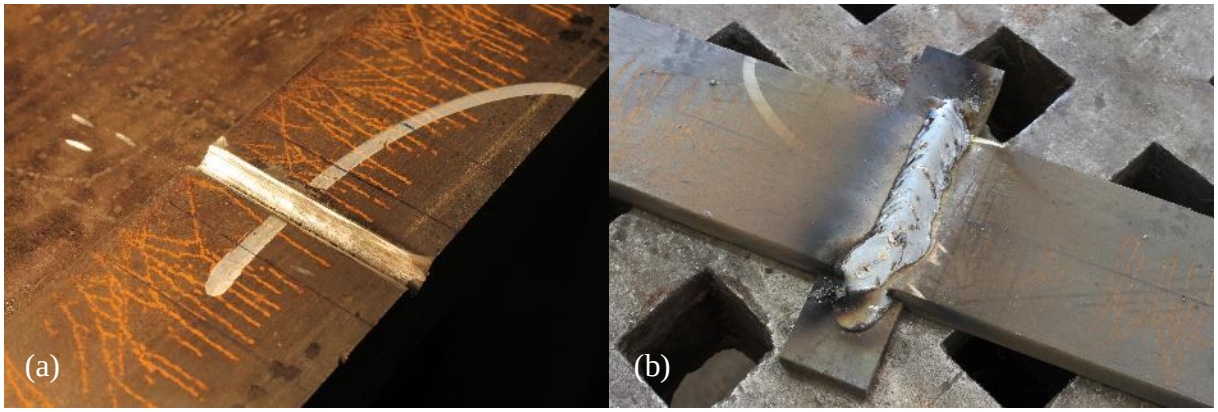


Figure 3.10 – (a) Preparation of the 1/4 in. u-notch, and (b) u-notch filled with fillet weld.



Figure 3.11 – Grinded fillet weld with surface roughness scale.

CHAPTER 4 TEST RESULTS

4.1 Introduction

This chapter presents the results from the testing program. First, the results from circumferentially notched round bar tests are presented along with the complimentary FE models and calibration of fracture parameters for the steel material At the end of the chapter, the monotonic test results are presented followed by a description of behavior for each bend test specimen. The cyclic bend tests are then summarized with number of cycles to fracture initiation and full fracture.

4.2 Circumferentially Notched Round Bar Test Results and Fracture Parameters

Circumferentially notched round bar tests were conducted to obtain baseline fracture parameters for the A992 steel extracted from the flanges of the W36x150 using conventional methods typical in the literature. As described in Chapter 2, a total of eight notched round bar tests (three monotonic and five cyclic) were conducted. A picture of the test setup is shown in Figure 4.1 (a).

A yield plateau was observed in the force-displacement response as shown in Figure 4.3 and Figure 4.4 for both monotonic and cyclic loading. After one or two cycles of constant displacement amplitude cyclic loading, a stable hysteric response developed as shown in Figure 4.4. This stabile hysteretic behavior continued until a sudden change in slope that indicated the occurrence of fracture initiation and a loss in cross sectional area. An example of fracture propagation before full fracture occurred is shown in Figure 4.1 (b).

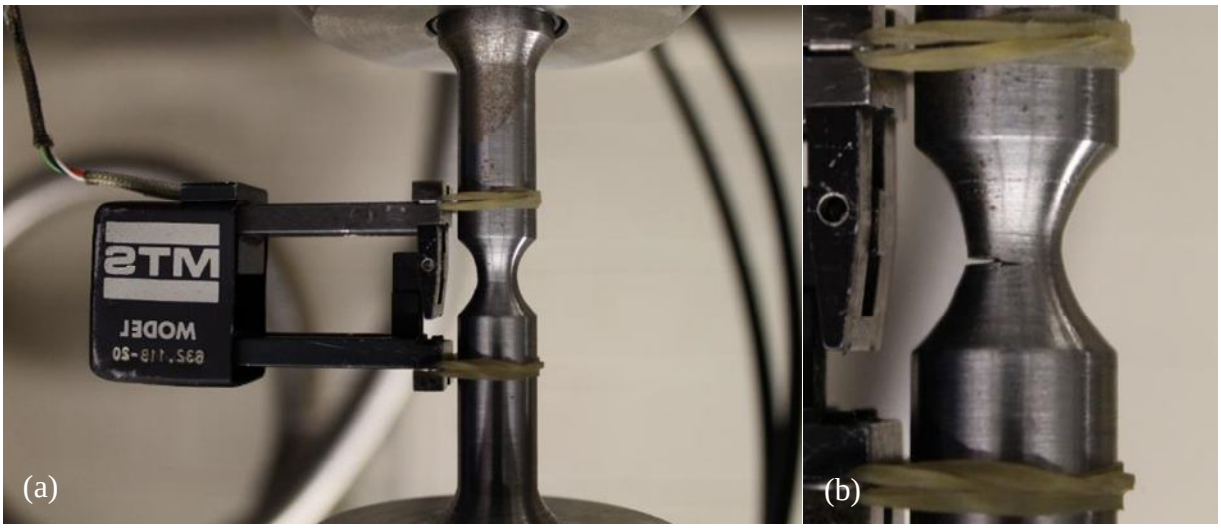


Figure 4.1 – (a) Notched round bar test setup, and (b) fracture propagation at the center of the notch.

A complimentary finite element model was analyzed using ABAQUS 6.13 (Simulia 2012) software. Axisymmetric elements were used to model both the monotonic and cyclic tests with a combined nonlinear isotropic/kinematic hardening model. For further information about the hardening model refer to the ABAQUS Manual (Simulia 2012) and Lemaitre and Chaboche (1994) which was derived from multiaxial formulations by Armstrong and Fredrick (1966). The modulus of elasticity was set to 29,000 ksi and the five other material parameters were calibrated to capture the load-deformation behavior including isotropic hardening parameters (Q_{inf} and b) and kinematic hardening parameters (C, γ, and σ_o). A separate calibration of material parameters was conducted for monotonic and cyclic tests. The calibrated constitutive material parameters are shown in Table 4.1 and their efficacy in capturing coupon load-deformation behavior is demonstrated in Figure 4.3 and Figure 4.4.

Table 4.1 – Constitutive material parameters for A992 steel cut from W36x150 flanges

Monotonic Parameters					**Cyclic Parameters**				
σ_o **(ksi)**	C **(ksi)**	γ	Q_{inf} **(ksi)**	b	σ_o **(ksi)**	C **(ksi)**	γ	Q_{inf} **(ksi)**	b
50	700	35	45	4	55	700	40	20	4

The specimens were modeled only for the length of the extensometer which was one inch as shown in Figure 4.2. Material and geometric non-linear effects were incorporated for all finite element simulations. Mesh size has a strong influence on the accuracy of the local stress and strain results, therefore a refined mesh with a size of 0.01 in. was selected (see Figure 4.2) and, through a sensitivity study, found to sufficiently capture the cumulative strain and stress triaxiality. The finite-element model was subjected to the same displacement protocol followed during testing.

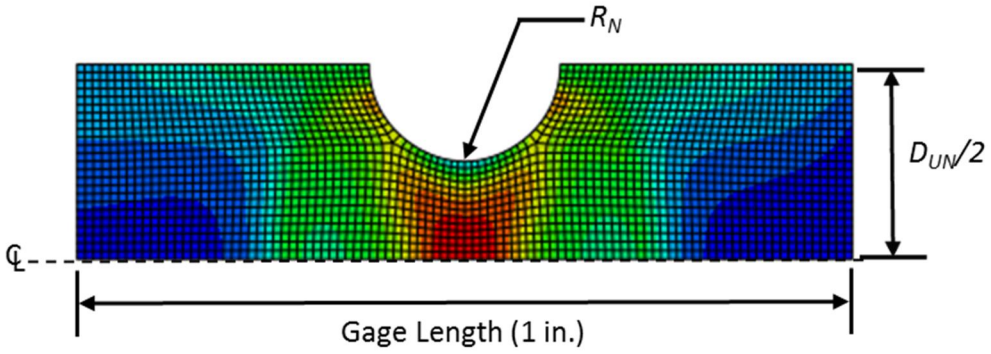


Figure 4.2 – Deformed geometry of axisymmetric FEM model.

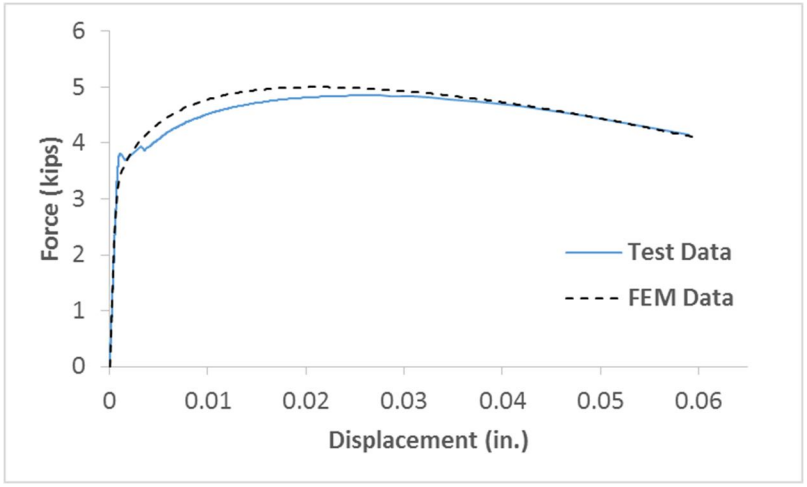


Figure 4.3 – Load displacement curve for R125 specimen compared to FEM data.

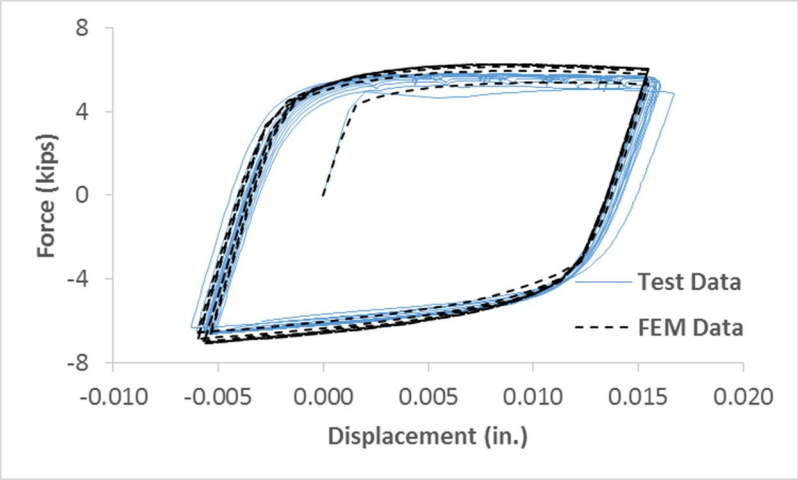


Figure 4.4 – Shows cyclic test for R125 specimen compared to FEM data

Table 4.2 – Monotonic notched round bar test matrix and results for A992 steel.

Specimen	**R060**	**R125**	**R250**
Notch Radius, R_N (in.)	0.060	0.125	0.250
Displacement Limits (in.)	0.051	0.060	0.076
$VGI_{monotonic}^{critical}$	2.20	1.87	1.74

Table 4.3 – Cyclic notched round bar test matrix and results for A992 steel.

Specimen	**R060**	**R125**	**R250-1**	**R250-2**	**R250-3**
Notch Radius, R_N (in.)	0.060	0.125	0.250	0.250	0.250
Displacement Limits (in.)	-0.005↔0.01	-0.005↔0.015	0.000↔0.02	0.000↔0.02	0.000↔0.015
Fracture Cycle	8	9	10	10	18
$VGI_{cyclic}^{critical}$	1.45	1.07	0.89	0.89	0.69

The fracture parameters were calibrated using the approach described briefly in Section 1.1 and given in more detail in Meyers (2009). The value of $VGI_{monotonic}^{critical}$ ranged from 1.74 to 2.2 with an average value of 1.94 and are presented in Table 4.2. The average value was used to

calculate λ. For the cyclic tests, $VGI_{cyclic}^{critical}$ was taken at the tension peak of the cycle before the sudden change in slope that indicated occurrence of fracture initiation. The values of $VGI_{cyclic}^{critical}$ were computed for each cyclic test and are presented in Table 4.3. Figure 4.5 shows the regression analysis that was conducted to calculate λ by curve fitting the damage function (Equation 1.3) to the data. The resulting value for the cyclic degradation coefficient, λ, was 0.25. For the calibration of λ, the curve fitting starts at the vertical axis of $VGI_{monotonic}^{critical}$ / $VGI_{cyclic}^{critical}$ at a value of 1.0. This calibration method is used to be consistent with all of the materials. Only the equivalent plastic strain values for the cyclic tests are used for each test, while the monotonic test equivalent plastic strain values are excluded in the calibration method. If the monotonic test values exceed the cyclic tests values this will contradict the degradation law of the CVGM.

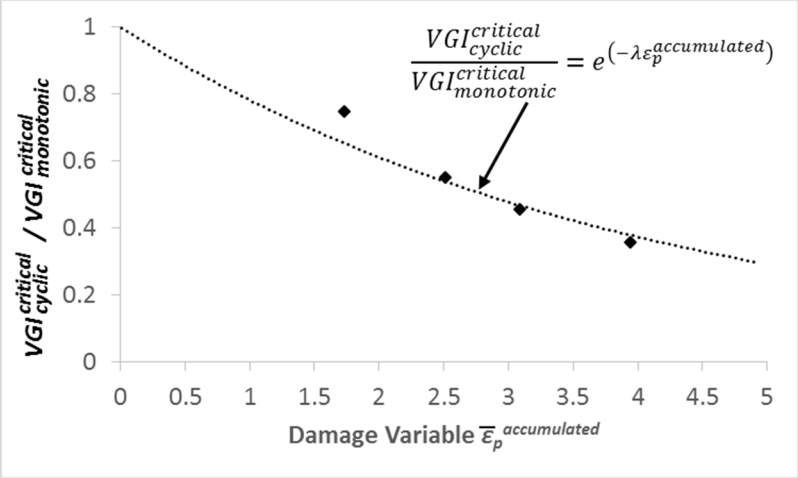


Figure 4.5 – Scatter plot and curve fit to calculate λ for A992 steel

4.3 Charpy V-Notch Tests

A total of six CVN specimens were conducted to measure the toughness of A992 steel. The specimens were cut from the flanges of beams used in full-scale tests (Eatherton et al. 2013), three were machined from W24x62 flanges and three were machined from W36x150 flanges. All of the machine were machined from the center of the flange tip. The specimens were taken from the middle of the beam where no inelastic deformations occurred. Specimen geometry and testing was

conducted as per ASTM E23-12c (ASTM 2012b). The geometry of the specimens is shown in Figure 4.6. All of the six specimens were tested using a friction compensated Tinius Olsen impact testing machine with a maximum capacity of 300 ft-lb at room temperature. The impact test machine was previously calibrated using NIST low and high energy specimens.

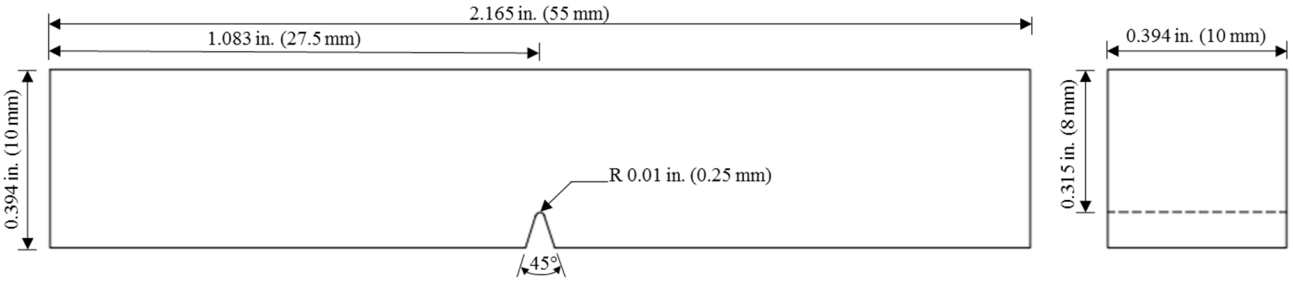


Figure 4.6 - CVN specimen geometry

Tests were conducted at a temperature of 70 F which is similar to the temperature at which all of the other tests were conducted in. The W36x150 specimens showed higher average Charpy Energy values compared to the W24x62 specimens with an average of 157 ft-lb and 187 ft-lb respectively. Usually, A992 steel absorbs energy more than 78 ft-lb at a temperature 70 F. Fracture appearance of the specimens were compared with the fracture appearance chart in ASTM E23-12c (ASTM 2012b) to find the observed shear area for each specimen. The results for the CVN tests is presented in Table 4.4.

Table 4.4 – CVN test results for W24x62 and W36x150 specimens.

	W24x62			**W36x150**		
Specimen Name	**S1**	**S2**	**S3**	**T1**	**T2**	**T3**
Charpy Energy, ft-lb	130	162	180	217	181	164
Observed Shear Area, %	75	80	80	90	80	80

4.4 Monotonic Axial Tests

A total of 12 monotonic axial tests were conducted with different artifacts to calibrate $VGI_{monotonic}^{critical}$ for the CVGM. Section 2.4 gives details of the test specimens which included 0.59 in. thick specimens cut from W24x62 flanges and 0.94 in. thick specimens cut from W36x150

flanges. Figure 4.7 shows a typical test setup. It was noticed that there was some variability in the measured thickness before testing.

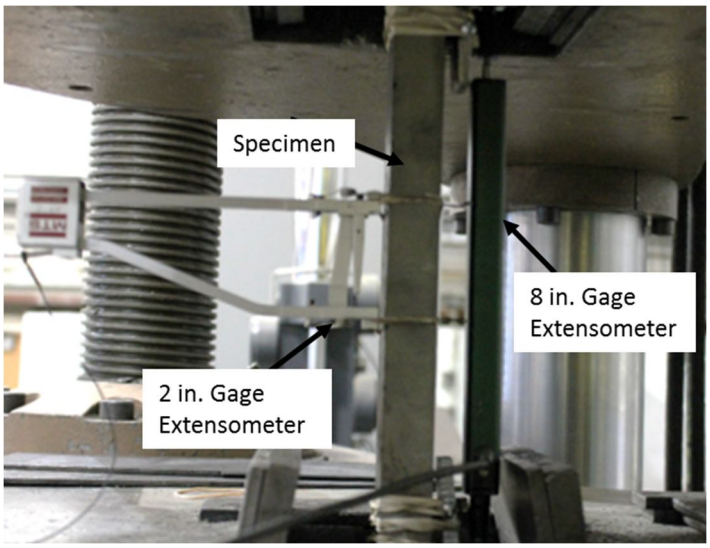


Figure 4.7 – Tensile monotonic test setup with two extensometers mounted one at each side of the specimen.

Figure 4.8 and Figure 4.9 show the load-displacement data for the 0.59 in. thick and 0.94 in. thick specimens with different artifacts. The twelve specimens produced yield stresses ranging from 49 to 54 ksi, and ultimate stresses ranging from 64 to 70 ksi. Detailed yield stress, ultimate stress and elongation data for each specimen is presented in

Table 4.5.

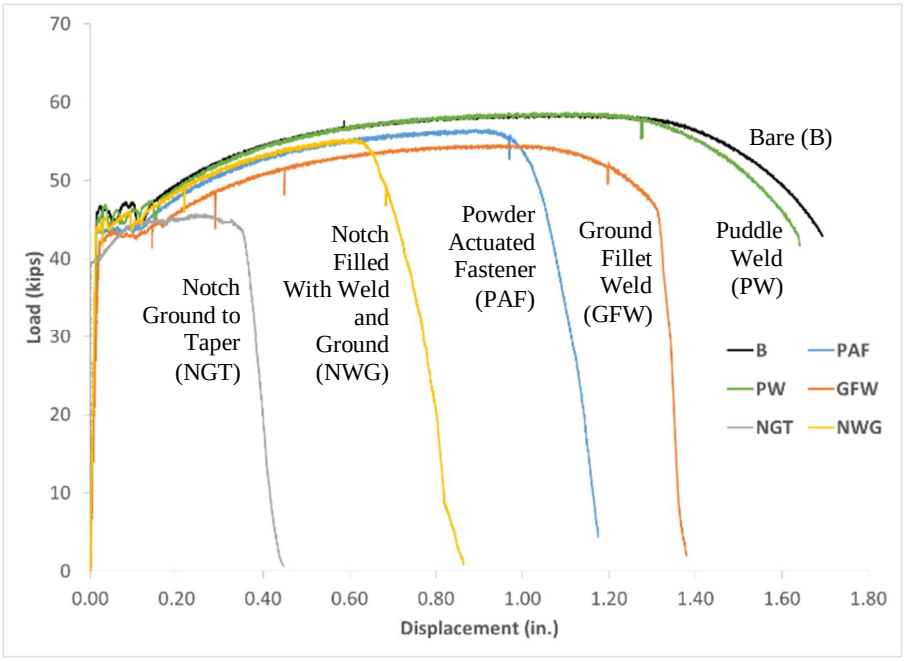


Figure 4.8 – Monotonic 0.59 in. thick tension coupon test data with various artifacts.

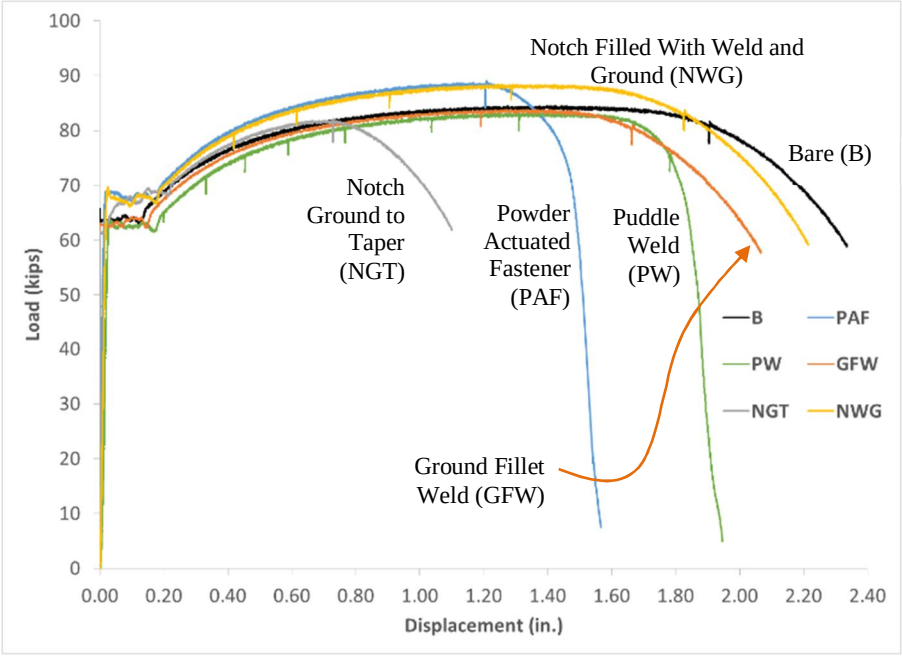
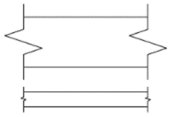
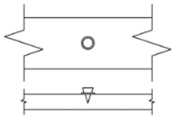
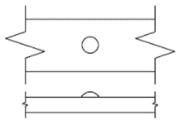
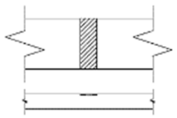
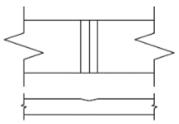
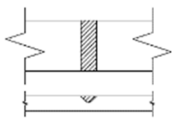


Figure 4.9 – Monotonic 0.94 in. thick tension coupon test data with various artifacts.

Elongations at fracture are given in Table 4.5. The bare specimens had an average elongation at fracture of 25.3%. Both the puddle weld (PW) and fillet weld ground smooth (GFW) reached consistently large elongations with average values of 22.4% and 21.5%, respectively. This represents 89% and 85% of the elongation capacity of the bare specimen for the puddle weld and ground fillet weld specimens, respectively. The specimen that experienced the largest reduction in elongation capacity was the notch ground to taper (NGT) which had an average fracture elongation of 14.6%. The two powder actuated fastener (PAF) specimens had similar reduction in elongation capacity to 69% and 67% of the bare specimen for the 0.59 in. thick and 0.94 in. thick specimens, respectively. The notch filled with weld and ground smooth (NWG) gave quite different results for the two thicknesses and appeared to be the most sensitive to thickness. For the 0.59 in. thick specimen, the elongation was only 51% of the bare specimen while the 0.94 in. thick specimen achieved 94% of the bare specimen elongation. The calibration of $VGI_{monotonic}^{critical}$ for use in the CVGM is presented in Section 5.3.

Table 4.5 – Monotonic test results for W24x62 and W36x150 specimens with artifacts.

Artifact Type		Flange Thickness	Artifact Name	F_y (ksi)	F_u (ksi)	Elongation (%)
1) No Artifact (B)		W24x62 (0.59 in.)	W24-B-Mono-T59	54	69	21.2
		W36x150 (0.94 in.)	W36-B-Mono-T94	51	66	29.4
2) Powder Actuated Fasteners (PAF)		W24x62 (0.59 in.)	W24-PAF-Mono-T59	52	67	14.7
		W36x150 (0.94 in.)	W36-PAF-Mono-T94	51	66	19.6
3) Puddle Welds (PW)		W24x62 (0.59 in.)	W24-PW-Mono-T59	54	70	20.5
		W36x150 (0.94 in.)	W36-PW-Mono -T94	50	65	24.3
4) Ground Fillet Weld (GFW)		W24x62 (0.59 in.)	W24-GFW-Mono-T59	53	68	17.2
		W36x150 (0.94 in.)	W36-GFW-Mono -T94	49	65	25.8
5) Notch Ground to Taper (NGT)		W24x62 (0.59 in.)	W24-NGT-Mono-T59	51	68	5.6
		W36x150 (0.94 in.)	W36-NGT-Mono-T94	49	64	13.7
6) Notch Welded and Ground Smooth (NWG)		W24x62 (0.59 in.)	W24-NWG-Mono-T59	52	65	10.8
		W36x150 (0.94 in.)	W36-NWG-Mono-T94	51	65	27.7

4.5 Cyclic Bend Test Results

Thirty-six bend tests were conducted using different artifacts to calibrate the fracture parameter λ by obtaining the $VGI_{cylic}^{critical}$ as described in Section 1.1. Photographs showing fracture initiation and final fracture for each specimen are included in APPENDIX A. Results for the cyclic bend tests are summarized in Table 4.6 including the cycle when fracture initiated and the cycle when complete fracture occurred. It is noted that while the cycle number when the specimen fully fractured was recorded and is reported in Table 4.6, only the initiation of fracture is used to calibrate CVGM fracture parameters since the method is intended to predict fracture initiation, not fracture propagation or final fracture. For each artifact an average of the fracture initiation and final fracture is presented. This was done for an easier comparison between all of the artifacts tested although it is not ideal statistical approach because the data distribution is highly skewed.

Specimen dimensions were measured and significant variations in thickness were noted. For the nominal 0.94 in. thick flanges cut from W36x150 beams, the measured thickness ranged from 0.82 to 1.02 in. with an average of 0.92 in. across 36 specimens. The width of the specimens ranged from 4.57 to 4.78 in. with an average of 4.69 in. For the nominal 0.59 in. thick flanges cut from W24x62 the measured thickness ranged from 0.53 to 0.59 in. with an average of 0.56 in. for 36 specimens. The width of the specimens ranged from 2.88 to 3.08 in. with an average of 2.97 in. The data for each specimen is presented in APPENDIX A.7.

Table 4.6 – Bend test results for W24x62 and W36x150 specimens with different artifacts.

Artifact Type	Flange Thickness	Artifact Name	Notched Radius (in.)	Fracture Initiation Cycle	Average Initiation Cycle	Final Fracture Cycle	Average Fracture Cycle
1) No Artifact	0.59 in. (W24x62)	W24-B1-T59-R000	N/A	18	8.3	28	13.3
		W24-B2-T59-R025	0.25	3		5	
		W24-B3-T59-R100	1.00	4		7	
	0.94 in. (W36x150)	W36-B1-T94-R000	N/A	4	2.3	7	4.0
		W36-B2-T94-R025	0.25	1		2	
		W36-B3-T94-R100	1.00	2		3	
2) Powder Actuated Fasteners (PAF)	0.59 in. (W24x62)	W24-PAF1-T59-R000	N/A	3	2.3	18	9.0
		W24-PAF2-T59-R025	0.25	2		4	
		W24-PAF3-T59-R100	1.00	3		5	
	0.94 in. (W36x150)	W36-PAF1-T94-R000	N/A	4	2.7	6	3.7
		W36-PAF2-T94-R025	0.25	2		2	
		W36-PAF3-T94-R100	1.00	2		3	
3) Puddle Welds (PW)	0.59 in. (W24x62)	W24-PW1-T59-R000	N/A	5	3.3	9	6.3
		W24-PW2-T59-R025	0.25	2		5	
		W24-PW3-T59-R100	1.00	3		5	
	0.94 in. (W36x150)	W36-PW1-T94-R000	N/A	4	2.7	7	3.7
		W36-PW2-T94-R025	0.25	2		2	
		W36-PW3-T94-R100	1.00	2		2	
4) Ground Fillet Weld (GFW)	0.59 in. (W24x62)	W24-GFW1-T59-R000	N/A	4	3.0	9	5.3
		W24-GFW2-T59-R025	0.25	2		2	
		W24-GFW3-T59-R100	1.00	3		5	
	0.94 in. (W36x150)	W36-GFW1-T94-R000	N/A	3	1.7	6	3.3
		W36-GFW2-T94-R025	0.25	1		2	
		W36-GFW3-T94-R100	1.00	1		2	
5) Notch Ground to Taper (NGT)	0.59 in. (W24x62)	W24-NGT1-T59-R000	N/A	2	1.3	5	3.0
		W24-NGT2-T59-R025	0.25	1		2	
		W24-NGT3-T59-R100	1.00	1		2	
	0.94 in. (W36x150)	W36-NGT1-T94-R000	N/A	2	1.7	3	2.3
		W36-NGT2-T94-R025	0.25	2		2	
		W36-NGT3-T94-R100	1.00	1		2	
6) Notch Welded and Ground (NWG)	0.59 in. (W24x62)	W24-NWG1-T59-R000	N/A	4	2.7	14	6.7
		W24-NWG2-T59-R025	0.25	2		3	
		W24-NWG3-T59-R100	1.00	2		3	
	0.94 in. (W36x150)	W36-NWG1-T94-R000	N/A	2	2.0	3	2.3
		W36-NWG2-T94-R025	0.25	2		2	
		W36-NWG3-T94-R100	1.00	2		2	

Bare Specimens (B)

Bare steel specimens that were 0.59 in. thick underwent an average of 8.3 cycles prior to fracture initiation and 13.3 cycles before full fracture. As expected, thicker specimens experienced fracture initiation and propagation in less cycles because the extreme fiber strains were larger for the nominally equal imposed curvature associated with an 11 in. roller. The 0.94 in. thick specimens experienced fracture initiation and full fracture after an average of 2.3 and 4.0 cycles, respectively.

Fracture initiation was observed to occur in many locations across the face of the bare specimens as shown in Figure 4.10(a). The cycle associated with fracture initiation was determined visually using six high definition cameras. Upon further bend cycles, the fractures propagated and linked up until one fracture line reached a critical length and the fracture propagated through the rest of the specimen in a sudden and brittle fashion as shown in Figure 4.10(b).

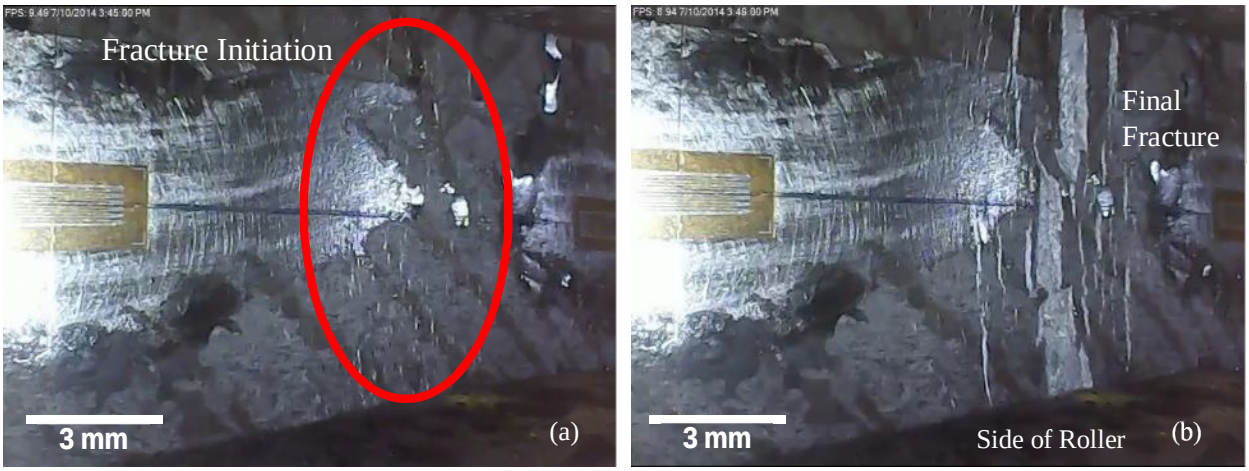


Figure 4.10 – Fracture initiation at multiple locations at the bottom of Specimen W24-B2-T59-R025 on cycle 3, complete fracture at the bottom side of the specimen at cycle 5.

The 1.0 in. radius side notches caused fracture initiation and final fracture at cycles that were approximately 28% of the cycle number for un-notched specimens. The sharper 0.25” radius notches reduced the number of cycles to fracture initiation and final fracture to approximately 19% of the un-notched specimens. The side notches increased the stress triaxiality and the plastic equivalent strain as demonstrated in the next section. As discussed in previous chapters, this variation is useful for a more robust calibration of fracture parameters.

Powder Actuated Fastener Specimens (PAF)

The behavior of the powder actuated fastener bend specimens was sensitive to specimen thickness. When the PAF were installed in 0.59 in. thick specimens in the top side of the specimen, the tip of the fastener was close to the surface of the bottom side of the specimen. An observable bump formed on the bottom side as shown in Figure 4.11(a). See Section 3.5 for a definition of the top side and bottom side of a specimen. During cyclic bend testing, fracture initiated at the bump on the back side of the specimen. The fracture propagated relatively slowly compared to other artifacts, and then final fracture through the thickness of the specimen occurred at the location of the PAF tip. The local effect due to the PAF tip was likely the reason that fracture initiated at an average of 2.3 cycles as compared to 8.3 cycles for bare steel specimens. Even though the fracture formed earlier than some other artifact types, the slow fracture propagation led to an average cycle at full fracture of 9.0 as compared to 13.3 average cycles to failure for the bare steel specimens. Although fractures also formed on the top side of the specimen around the head of the PAF, the final fracture occurred when the bottom side of the specimen was in tension.

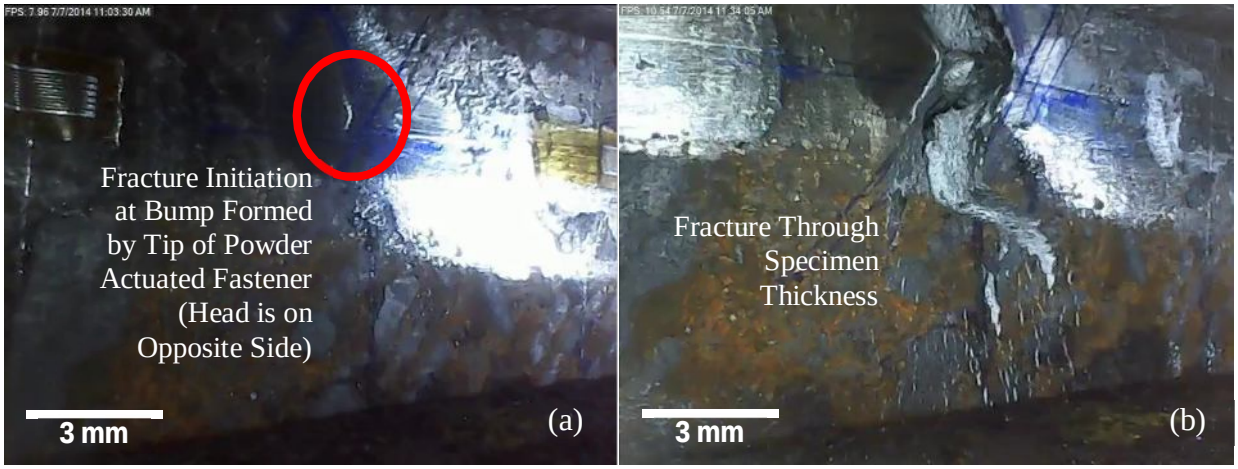


Figure 4.11 – Fracture initiation on Specimen W24-PAF1-T59-R000 at the bottom of the PAF at cycle 3, cycle 18

Thicker specimens with 0.94 in. thickness behaved differently than thinner specimens. Multiple cracks formed in the areas adjacent to the PAF as shown in Figure 4.12(a). Fracture

propagation was observed to happen on the top side around the PAF head until final fracture occurred through the PAF location as shown in Figure 4.12(b). For the 0.94 in. thick specimens, the tip of the PAF was more in the center of the specimen closer to the neutral axis. In the absence of local effects described above for thinner specimens, fracture initiation occurred in a similar cycle as the bare specimen. The average cycle at fracture initiation was 2.7 as compared to 2.3 for bare steel specimens. Since 0.94 in. thick specimens with puddle welds had the same average cycle at fracture initiation as PAF, it is likely that the difference in fracture initiation cycle between PAF and bare specimens was due to variability in the material. The cycle at final fracture was 3.7 on average for PAF compared to 4.0 for bare steel specimens. This implies that for the 0.94 in. thick specimens, PAF had little effect on the cycle number when fracture initiated or the cycle when fracture propagated through the specimen.

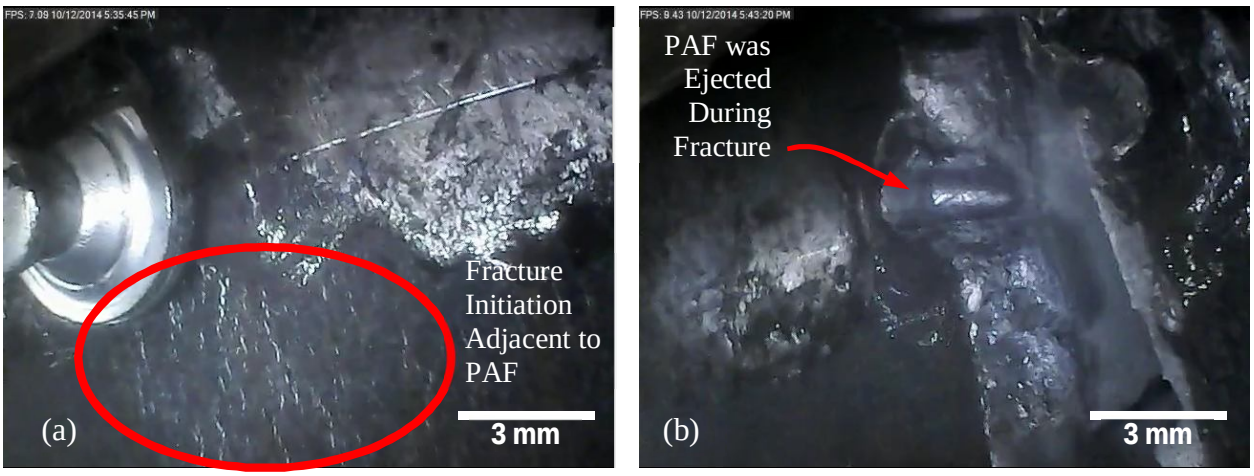


Figure 4.12 – Fracture initiation on Specimen W36-PAF1-T94-R000 at the top of the PAF at cycle 4, complete fracture occurred at the top side of the specimen near the PAF at the beginning of cycle 6.

Puddle Weld Specimens (PW)

Similar to powder actuated fasteners, the effect of puddle welds on fracture behavior of the bend test specimens was highly sensitive to thickness. For two of the three 0.59 in. thick specimens, fracture was observed to initiate on the bottom side of the specimen (side opposite the puddle weld) as shown in Figure 4.13(a). Fracture initiation and final fracture both occurred while the bottom

side was in tension and the puddle weld side was in compression. The average cycle when fracture initiation was 3.3 compared to 8.3 for the bare steel specimens while the average cycle at full fracture was 6.3 compared to 13.3 for bare steel specimens. Based on the reduced number of cycles to failure, the fact that fractures formed in the side of the specimen opposite the puddle weld, and because fractures occurred when the puddle weld side was in compression, it is hypothesized that reduced low cycle fatigue fracture resistance of puddle weld specimens may have been due to a redistribution of plastic strains. With stronger material and more cross-sectional area at the puddle weld side, more inelastic strain may have been forced to occur on the face of the specimen opposite the puddle weld. These increased plastic strains led to earlier fracture initiation and propagation in the face opposite the puddle weld.

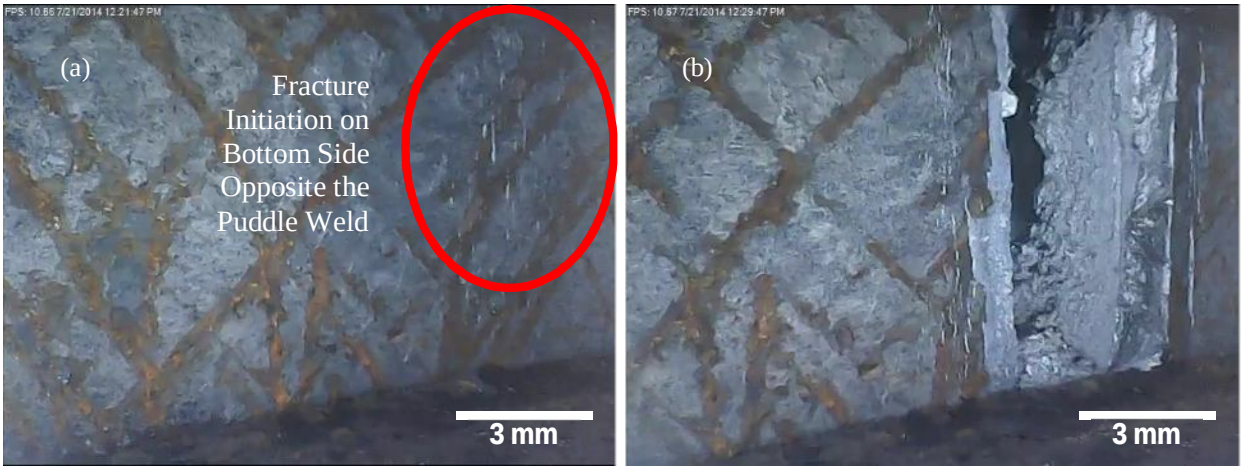


Figure 4.13 – Multiple fracture initiation on Specimen W24-PW1-T59-R000 at the bottom of the PW at cycle 5 while at tension, complete fracture occurred on Specimen W24-PW1-T59-R000 at the bottom of the PW at cycle 9 while at tension.

Fracture of the thicker specimens were not as affected by puddle welds. In 0.94 in. thick specimens, fractures initiated around the puddle weld as shown in Figure 4.14(a). Fractures initiated and propagated when the top side (puddle weld side) was in tension. For two of the three specimens, final fracture through the thickness of the specimen occurred when the puddle weld side was in compression (see Figure 4.14(b)). With an average fracture initiation cycle of 2.7 and average final fracture cycle of 3.7, which are similar to the values for bare steel specimens, the

effect of the puddle weld on cycles to fracture initiation and final fracture were found to be small for the thicker specimens.

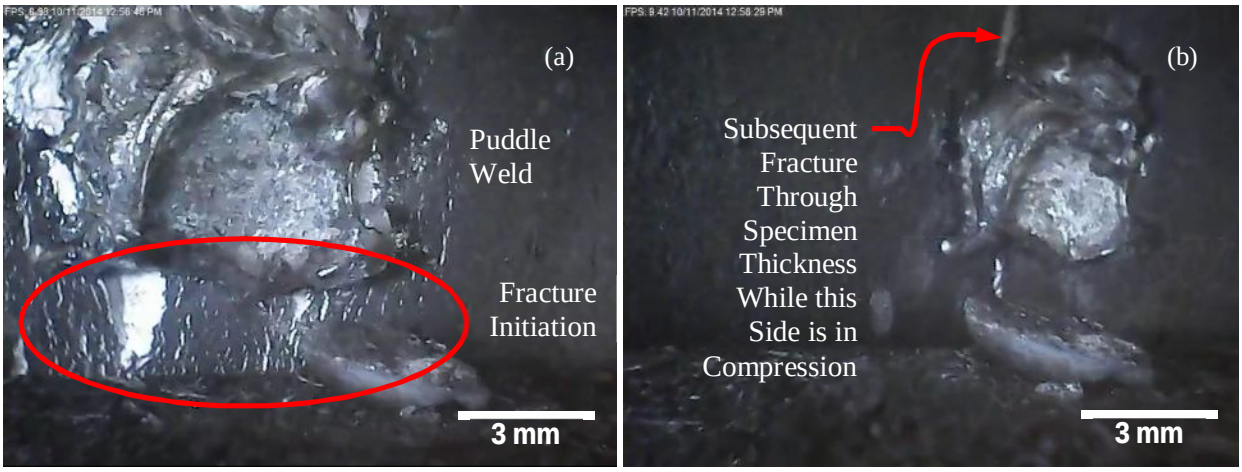


Figure 4.14 – Fracture initiation and propagation on Specimen W36-PW3-T94-R100 at the sides of the HAZ of the PW at cycle 2 while at tension, complete fracture at the side of the PW at cycle 2 while the top side of the spcecimen is at compression.

Ground Fillet Weld Specimens (GFW)

The number of cycles to fracture initiation and propagation was found to be sensitive to specimen thickness even though the fracture behavior of 0.59 in. and 0.94 in. thick specimens was similar. Cracks formed throughout the ground region, propagated, linked up, and resulted in a final brittle fracture through the thickness of the specimen. Figure 4.15 shows photographs for a 0.59 in. thick specimen and Figure 4.16 shows photographs for a 0.94 in. thick specimen. The average cycle number at fracture initiation and final fracture was 3.0 and 5.3 respectively for the 0.59 in. thick specimens, as compared to 8.3 and 13.3 for bare steel specimens. Fracture of the specimens with ground fillet welds occurred at approximately 38% of the cycle number for bare steel specimens. For the 0.94 in. thick specimens, the average cycle at fracture initiation and final fracture was 1.7 and 3.3 compared to 2.3 and 4.0 for bare steel specimens. This represents a reduction to 78% of the average fracture cycle associated with bare steel specimens. Ground fillet welds therefore have a smaller effect on fracture for thicker specimens.

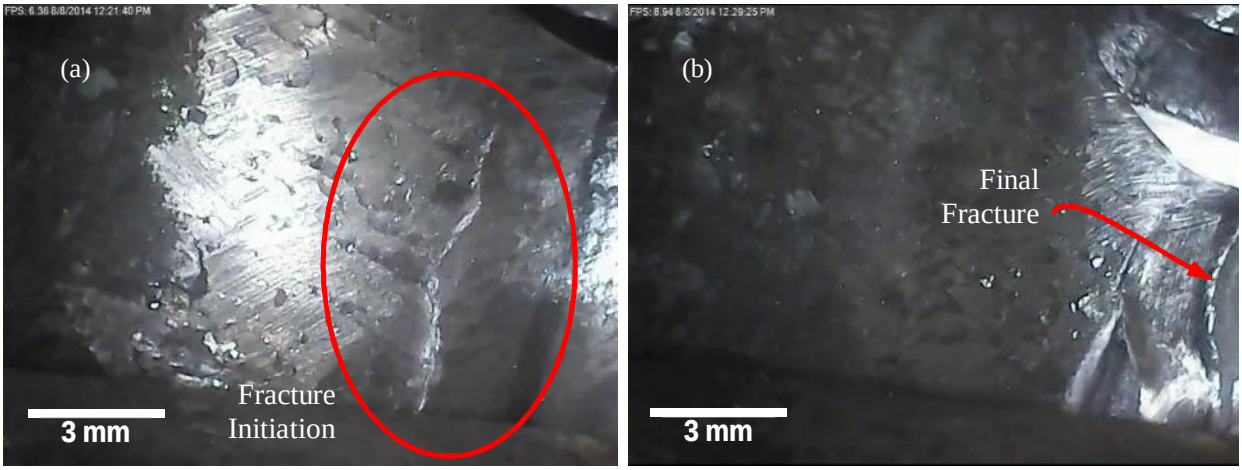


Figure 4.15 – Fracture propagation on Specimen W24-GFW3-T59-R100 at the top of the side of the weld at cycle 3 while at tension in the HAZ, Top of the specimen showing complete fracture at cycle 5 around the weld in the HAZ.

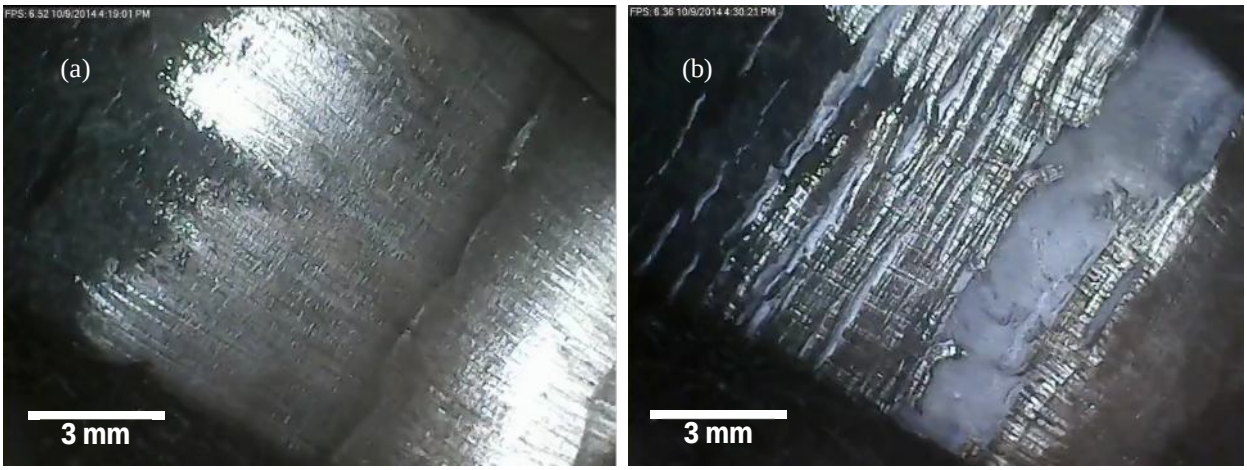


Figure 4.16 – Fracture initiation on Specimen W36-GFW1-T94-R000 at the top of the side of the weld at cycle 3 while at tension, complete fracture occurred at cycle 6 while top of the specimen was at tension.

Notch Ground to Taper Specimens (NGT)

Similar behavior was observed for 0.59 in. thick and 0.94 in. thick specimens that included a notch ground to a taper. Cracks formed in the tapered region and propagated during cycles in which the ground side was in tension. Figure 3.16 shows photographic examples of the behavior.

The average number of cycles for fracture initiation and final fracture was 1.3 and 3.0, respectively for 0.59 in. thick specimens as compared to 8.3 and 13.3 for bare steel specimens.

Fracture in the 0.59 in. thick notch ground to taper specimens therefore occurred at 19% of the cycles that caused fracture in bare steel specimens. The average number of cycles to fracture initiation and final fracture for 0.94 in. thick specimens was 1.7 and 2.3, respectively as compared to bare steel specimens that underwent 2.3 and 4.0 cycles prior to fracture initiation and final fracture. For the 0.94 in. thick specimens, the notch ground to taper specimens experienced fracture in 66% of the cycles required to cause fracture in bare steel specimens.

The notch ground to taper was found to cause the largest reduction in cycles to fracture of all five artifacts investigated herein. Unlike other artifacts including weld wherein stronger material on the artifact side caused fracture initiation on the side opposite the artifact, the notch ground to taper is primarily a geometric discontinuity. Fractures initiated and propagated on the ground side.

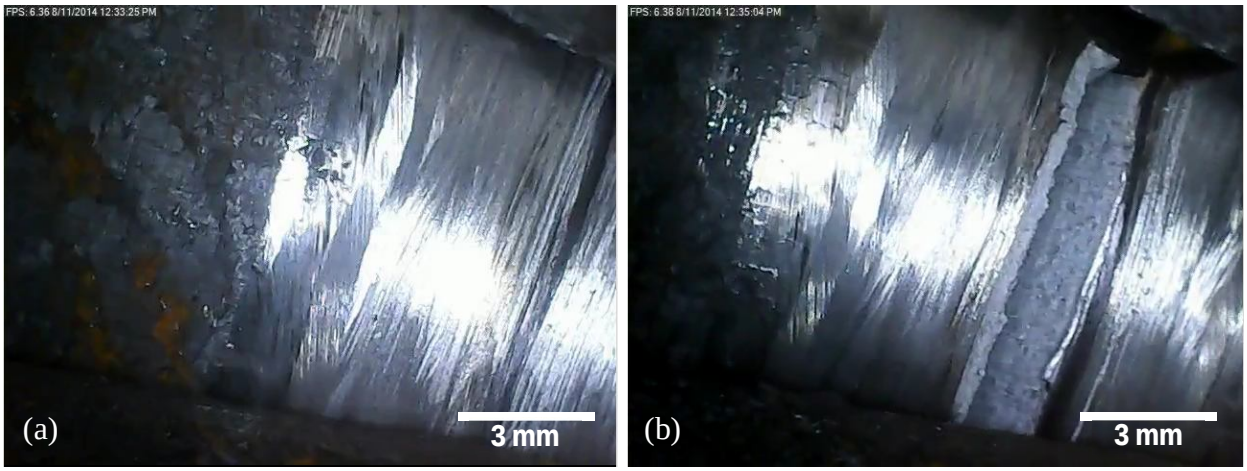


Figure 4.17 – Fracture initiation at the edge and center of Specimen W24-NGT2-T59-R025 at the ground notch located at the top of the specimen at cycle 1 while at tension, complete fracture at the center of the ground notch on cycle 2 while at tension.

Notches Filled with Weld and Ground Smooth Specimens (NWG)

Specimens with notches that were filled with weld and ground smooth typically experienced fracture initiation at the edges of the specimen around the welds. Although no video cameras captured the edges of the specimen, visual observations were made. Fractures initiated on

the top side (weld side) at the intersection between the weld metal and base metal and then propagated from the edges toward the center of the specimen until complete section fracture. Fractures propagated and caused complete fracture during parts of the cycle when the weld side of the specimen was in tension. See Figure 4.18.

The average cycle number at fracture initiation and final fracture was 2.7 and 6.7 respectively for the 0.59 in. thick specimens, as compared to 8.3 and 13.3 for bare steel specimens. Fracture of the specimens with notches welded and ground occurred at approximately 41% of the cycle number for bare steel specimens. For the 0.94 in. thick specimens, the average cycle at fracture initiation and final fracture was 2.0 and 2.3 compared to 2.3 and 4.0 for bare steel specimens. This represents a reduction to 72% of the average fracture cycle associated with bare steel specimens. Similar to other artifacts, notches filled with weld and ground smooth have a smaller effect on fracture for thicker specimens.

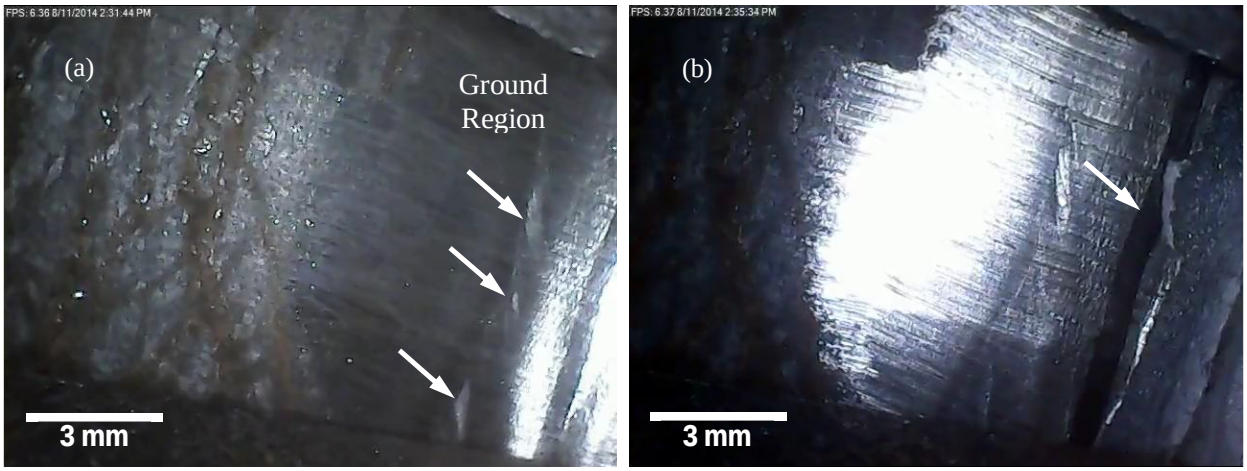


Figure 4.18 – (a) Fracture initiated at the edge of the top side of Specimen W24-NWG3-T59-R100 at the region between the weld and the base metal on cycle 2 at tension. (b) Complete fracture occurred at cycle 4 while the top side of the specimen was in tension.

CHAPTER 5 FE MODELS, AND CALIBRATION OF FRACTURE PARAMETERS FOR ULCF MODELS

5.1 Introduction

This chapter presents the calibration of the fracture parameters. First, a mesh refinement study is conducted using a sensitivity analysis to choose the optimum mesh size. Next, FE models for the monotonic and cyclic tests are presented along with the calibration of fracture parameters using different ULCF fracture models. At the end of the chapter an introduction to the CDPM calibration process using monotonic axial tests using LS-DYNA is presented.

5.2 FE Models Mesh Refinement Study

Mesh size has a strong influence on the accuracy of the stress and strain results and therefore was carefully chosen. A sensitivity study was conducted to examine convergence of cumulative plastic strain and stress triaxiality which are key quantities in the CVGM. The sensitivity study was conducted on SMRF connections with W24x62 and W36x150 beams as tested by Eatherton et al. (2013). To improve computational efficiency, a coarser mesh was used in the regions of the model expected to remain elastic.

The values for stress and strain at the locations with the largest equivalent plastic strain (PEEQ) values are included in Table 5.1 and Table 5.2. The effect of mesh refinement was examined for varying element size and separately by refining the number of elements within the flange thickness for fixed mesh size of 0.25 in.

All of the results are shown in Table 5.1 and Table 5.2 for the mesh refinement study. It is shown that the equivalent plastic strain (PEEQ), components of stresses (S_{11}, S_{22}, and S_{33}), and Von Mises equivalent stress (MISES) are converging with less than 5% difference. For the rest of the study a mesh size of 0.25 in. and elements through the flange thickness for the W24x62 and W36x150 are six and nine elements respectively. The PEEQ results changes by less than 2% and

the stress components changes by 1% to 4%, the expected low cycle fatigue fracture demands calculated using these values are expected to not vary by more than 1% to 2% for the mesh refinement from five to six elements through the flange thickness. Further refinement in the number of elements through the flange thickness are expected to have even less effect.

Table 5.1 - Mesh size study effects for W24x62 and W36x150 non-RBS with three and four elements through the flange thickness respectively.

	W24x62			**W36x150**		
Mesh Size, in.	0.15	0.25	0.50	0.15	0.25	0.50
Distance from End Plate, in.	9.75	10	7.5	16.92	16.25	16.67
Distance from Flange Tip, in.	0.6	0.51	0.47	2.25	2.52	2.52
PEEQ	0.3595	0.3221	0.3055	0.5692	0.5490	0.5173
S_{11}, ksi	-98.90	-96.45	-95.45	-102.09	-101.48	-100.93
S_{22}, ksi	-18.21	-16.26	-11.53	-12.25	-13.40	-13.95
S_{33}, ksi	-21.33	-18.77	-11.17	-36.48	-36.35	-36.60
MISES, ksi	84.12	82.97	82.62	85.94	84.14	83.38

Table 5.2 - Number of elements through the flange thickness effects with mesh size 0.25 in. (6.4 mm) for W24x62 and W36x150 non-RBS.

	W24x62			**W36x150**		
Elements	4	5	6	6	8	9
Distance from End Plate, in.	10.25	10.0	10.25	16.75	16.75	16.75
Distance from Flange Tip, in.	0.508	0.508	0.508	2.27	2.27	2.27
PEEQ	0.3656	0.3801	0.3868	0.5510	0.5832	0.5826
S_{11}, ksi	-97.14	-97.71	-99.02	-101.53	-101.91	-101.80
S_{22}, ksi	-13.33	-13.12	-12.59	-11.93	-11.58	-11.21
S_{33}, ksi	-19.63	-19.72	-20.05	-36.78	-37.12	-36.88
MISES, ksi	84.65	85.40	86.17	85.28	85.95	86.11

A mesh size of 0.25 in. wide x 0.25 in. long x 0.1 in. thick resulted in equivalent plastic strains and Von Mises stresses that were within 11% and 1%, respectively, of the values obtained using elements that were 36% of the selected element's volume. Because the coupon tests were smaller and computational expense was less, a smaller mesh size was chosen for the FE models of the monotonic uniaxial and cyclic bend tests, with elements that were typically 0.125 in. on a side and 0.1 in. thick. This fine mesh was used in the area of interest and slightly larger mesh was used in peripheral areas.

After the mesh refinement study, a comparison for peak moments between full-scale experiments and FEM results at 1%, 2%, 3% and 4% story drift was conducted as mean of model validation. The data of this study is presented in Table 5.3. The peak moments predicted by the model are shown to be within 3% of the experimentally obtained peak moments on average.

Table 5.3 - Comparison of peak moments (k-ft) between full-scale tests and FEM results at 1%, 2%, 3% and 4% story drift.

Story Drift	Cycle of Story Drift	W24x62 BUEEP		W24x62 RBS		W36x150 BSEEP		W36x150 RBS	
		Test	FEM	Test	FEM	Test	FEM	Test	FEM
1%	1st Cycle	438	435	378	375	1552	1541	1502	1443
2%	1st Cycle	716	732	498	530	2708	2845	2271	2210
3%	1st Cycle	760	781	491	516	3048	3094	2433	2243
4%	1st Cycle	633	635	462	472	3089	2505	2383	1990
4%	2nd Cycle	601	571	429	451	2866	2302	2243	1881

5.3 Complimentary FE Models and Calibration of Fracture Parameters from Flat Plate Coupon Tests

A set of FE analyses were conducted that simulated monotonic uniaxial and cyclic bend test specimens. FE analyses are necessary to get the equivalent plastic strain and stress triaxiality histories at the fracture initiation location. It is not possible to measure these quantities so FE models are created and calibrated to capture the behavior of the test specimens. Then, the equivalent plastic strain history and stress triaxiality history at the observed fracture initiation location are recorded up to the time of fracture initiation. These strain and stress histories are then used with the CVGM equations given in Section 1.1 to calibrate the fracture parameters, $VGI_{monotonic}^{critical}$ and λ. The FE models for monotonic and cyclic tests are first described, and then the calibration of fracture parameters is described at the end of this section.

The FE analyses were conducted using ABAQUS 6.13 software (Simulia 2012). An eight node brick element was used. The material model selected was the Armstrong-Frederick (1966) plasticity model with combined nonlinear isotropic and kinematic hardening. For further

information about the hardening model refer to the ABAQUS Manual (Simulia 2012) and Lemaitre and Chaboche (1994) which was derived from multiaxial formulations by Armstrong and Fredrick (1966). Geometric nonlinearity was also included in all analyses. In this section the simulated monotonic uniaxial and cyclic bend test specimens are modeled without artifacts. This assumption is supported by the relatively similar load-displacement curves prior to fracture for all of the specimens presented in Section 4.4.

5.3.1 Monotonic Uniaxial Tests FE Models

The monotonic specimens were modeled only for the length of the extensometer which was 8.0 in. As described in the previous subsection, a refined mesh with a size of 0.125 in. on each side and 0.1 in. thick was used at the center of the specimen where necking occurs. The mesh size at each end was increased to 0.25 in. by 0.125 in. The FE model was analyzed with an imposed monotonic elongation displacement history at one end while the other end was fixed. Figure 5.1 shows the mesh, boundary conditions, load application, and necking.

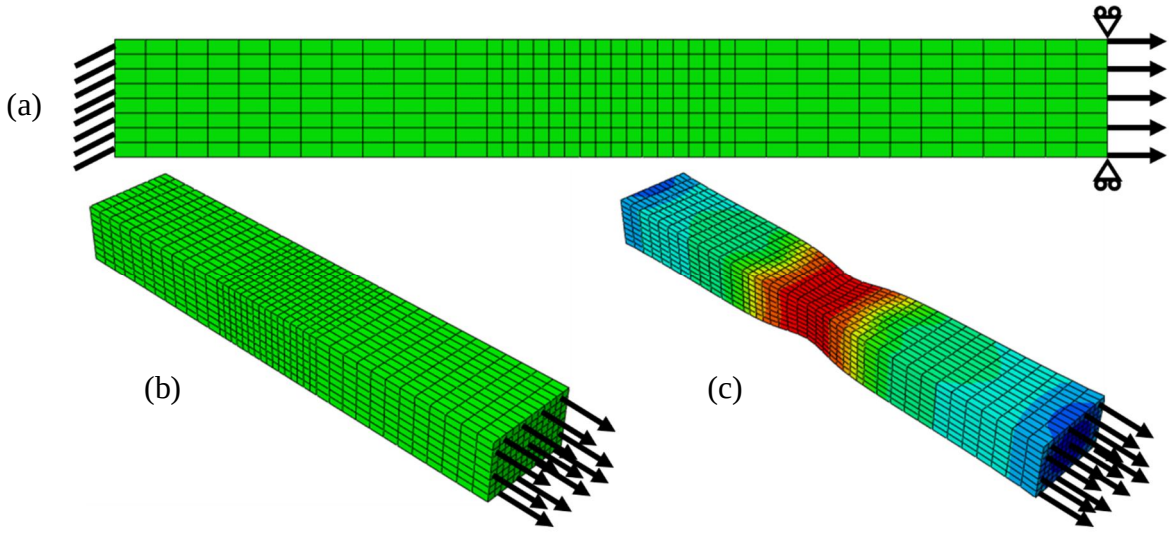


Figure 5.1 – FEM model of a monotonic uniaxial test for the W36x150 specimen showing the transition in mesh size (a) and boundary conditions of an undeformed specimen from side view, (b) an undeforrmed specimen loading and (c) deformed specimen showing necking at the center

Five material parameters were calibrated for the material model including two parameters for isotropic hardening (Q_{inf} and b) and three parameters for kinematic hardening (C, γ, and σ_o).

These material parameters, given in Table 5.4, were separately calibrated for the 0.54 in. thick specimen cut from the W24x62 and the 0.94 in. thick specimens cut from the W36x150. Material model parameters were calibrated against test data from the coupons with no artifacts and no side notches. The stress vs strain behavior for the 0.59 in. and 0.94 in. thick monotonic tests with no artifact are compared to FE results in Figure 5.2 and Figure 5.3, respectively.

Table 5.4 – Material model parameters for A992 steel cut fromW24x62 and W36x150 flanges

0.59 in. (W24x62)					**0.94 in. (W36x150)**				
σ_o **(ksi)**	C **(ksi)**	γ	Q_{inf} **(ksi)**	b	σ_o **(ksi)**	C **(ksi)**	γ	Q_{inf} **(ksi)**	b
50	660	45	36	4	50	250	45	47	4

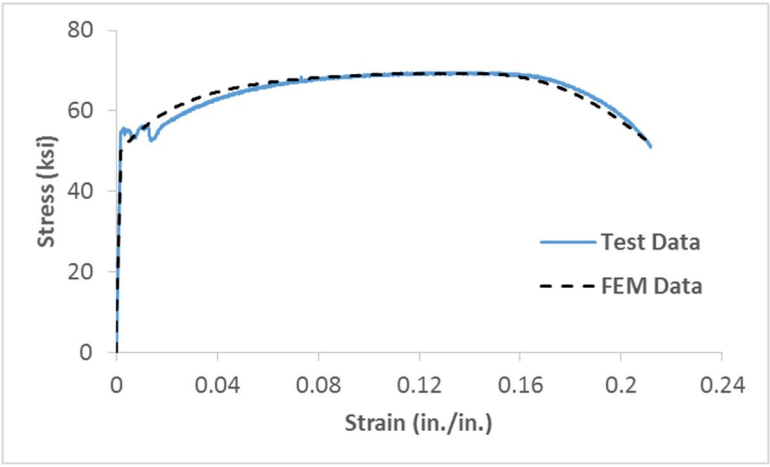


Figure 5.2 – Stress strain curve for W24x62 monotonic uniaxial test data with no artifact compared to FEM data.

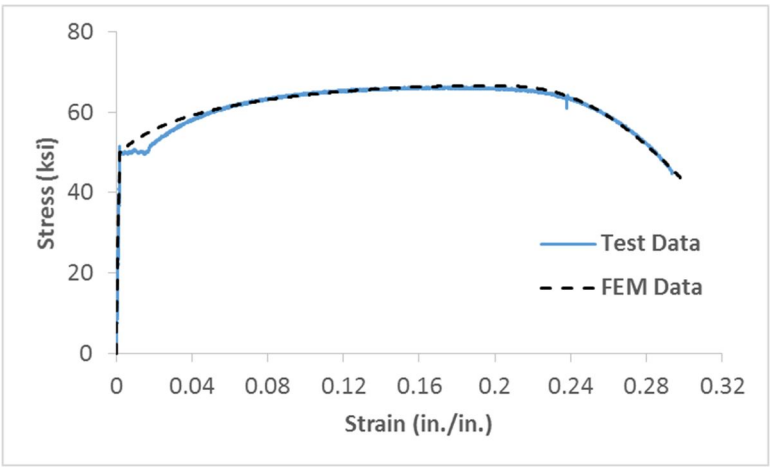


Figure 5.3 – Stress strain curve for W36x150 monotonic uniaxial test data with no artifact compared to FEM data.

Stress and strain data were extracted from these two models at the critical location in the middle of the necking region. This stress and strain data will be used in Section 5.3.3. It is noted that the artifacts were not modeled in the FE analysis. Instead, it is assumed that the stress and strain histories are relatively similar up to fracture initiation regardless of artifact type. This assumption is supported by the relatively similar load-displacement curves prior to fracture presented in Section 4.4.

5.3.2 Cyclic Bend Tests FE Models

As described previously, a refined mesh with a size of 0.125 in. x 0.125 in. x 0.1 in. thick elements (8 node brick elements) were used at the center of the specimen. To improve computational efficiency, a coarser mesh was used in the regions of the model expected to remain elastic. The same material model parameters calibrated in the monotonic uniaxial tests were used for the cyclic bend test as given in Table 5.4.

As described in Chapter 3, the two rollers clamped the specimen with a force of 9 kips to prevent the specimen from sliding around during testing. This clamping force was incorporated in the FE model as a pressure over the area of contact as highlighted in red in Figure 5.4. The width was taken as 0.25 in. with a varying length depending on the notch size (there is a 1 in. space between the rollers).

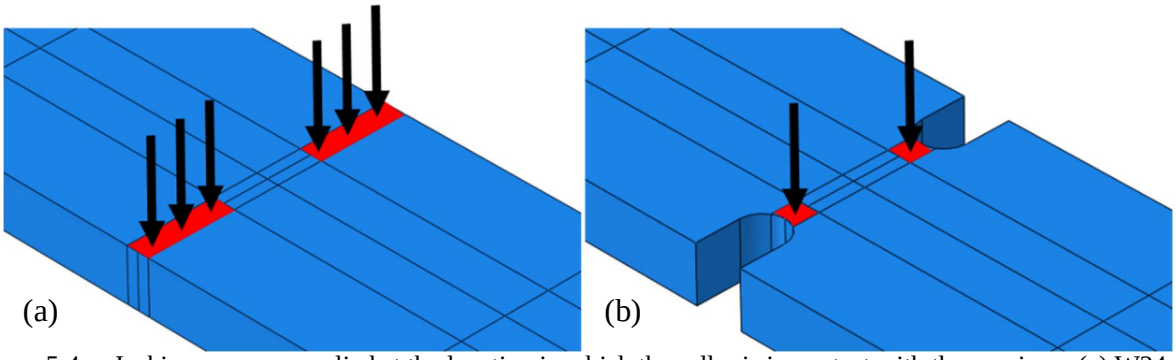


Figure 5.4 – Jacking pressure applied at the location in which the roller is in contact with the specimen (a) W24x62 unnotched specimen, and (b) W24x62 with notch radius of 0.25 in.

The contact region was defined as a surface-to-surface contact. This was done to create more accurate contact stresses without having to match meshes between the roller and specimen. The rollers were defined as the master surface and the specimens as the slave surface since the rollers are more rigid than the specimen. Figure 5.5 shows the boundary conditions for the FEM model and the location of the displacement increments were applied at the rollers.

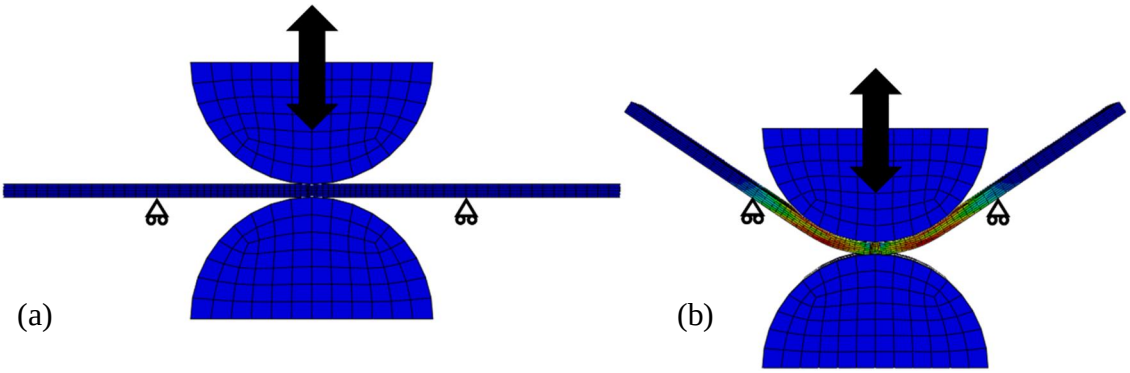


Figure 5.5 – (a) Undeformed and (b) deformed shape of the FEM model of the cyclic bend test for the W24x62 with notch radius of 0.25 in. specimen showing the transition in mesh size and boundary conditions.

Equivalent plastic strain histories and stress triaxiality histories were obtained from the model. Figure 5.6 shows a contour plot of the plastic equivalent strain (PEEQ) and the Von Mises stress (S. Mises) for a specimen with and without side notches. The stress and strain histories will be used in Section 5.3.3 to calibrate fracture parameters. Similar to the monotonic models, the

artifacts were not included in the FE model. It was assumed that the stress and strain histories prior to fracture would be similar with and without the artifacts. The stress and strain histories used for calibrating fracture parameters for a specific artifact were cut off at the time fracture initiation was observed in the test. In this way, the stress and strain histories were customized for each tested specimen.

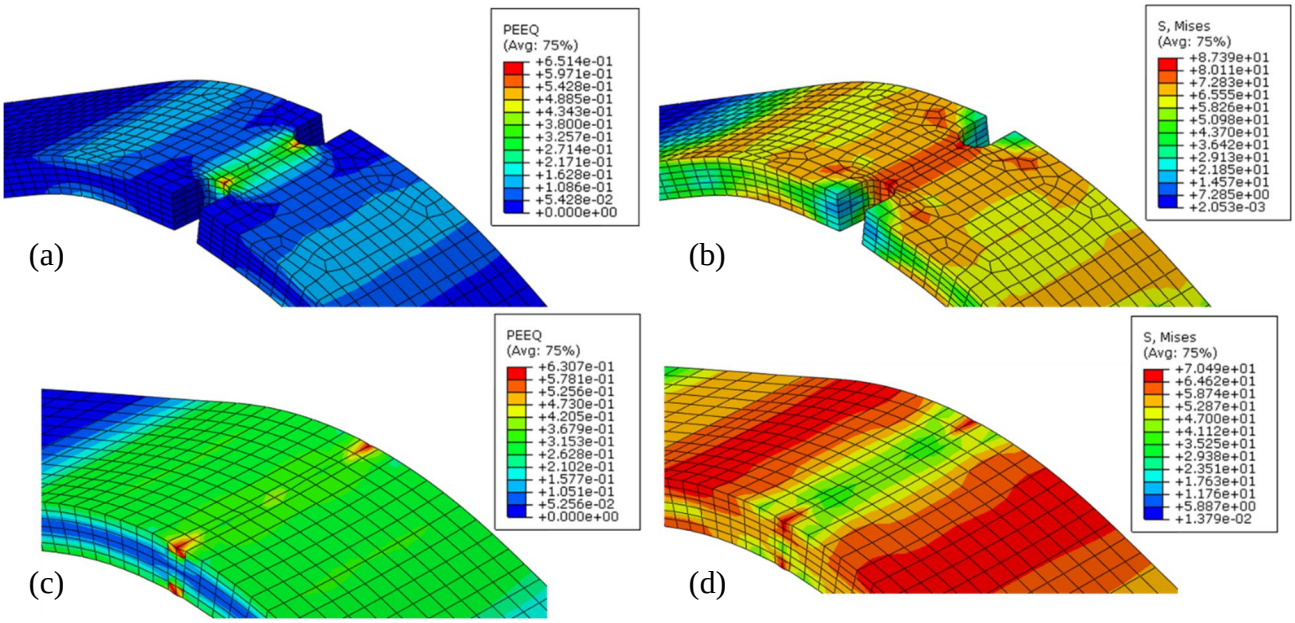


Figure 5.6 – PEEQ strain and Von Mises stresses contour at tension side of a cyclic bend test for W24x62 with notch radius of 0.25 in. (a) and (b), and a unotched specimen (c) and (d).

5.3.3 Calibrating Fracture Parameters

The critical monotonic void growth index was calculated using Equation 1.4 for each monotonic specimen. The integral was computed up until the time fracture initiation occurred which for monotonic specimens corresponded to a significant loss in load carrying capacity. The resulting values of $VGI_{monotonic}^{critical}$ for bare steel specimens were found to be 1.77 and 2.11 for 0.59 in. thick and 0.94 in. thick specimens respectively. The average $VGI_{monotonic}^{critical}$ value from three circumferentially notched round bar specimens taken from the same 0.94 in. thick flange material was 1.94. This difference between the two test methods (2.11 vs. 1.94) of 9% is well within the variability of the material as demonstrated by the range of values obtained for the three

circumferentially notched round bar specimens which ranged from 1.7 to 2.2. The calculated $VGI_{monotonic}^{critical}$ values for 0.59 in. specimens with artifacts were 0.23, 1.55, 0.23, 0.07, and 0.14 for the powder actuated fasteners, puddle welds, ground fillet weld, notch ground to taper, and notch welded and ground smooth, respectively. Similar trends were found for the 0.94 in. thick specimens with artifacts as the values for $VGI_{monotonic}^{critical}$ were found to be 0.26, 0.44, 0.36, 0.17, and 0.38 for the powder actuated fasteners, puddle welds, ground fillet weld, notch ground to taper, and notch welded and ground smooth, respectively.

The calibration of the other important fracture parameter, λ, starts by calculating the cyclic void growth index, VGI_{cyclic}, for each of the cyclic bend tests. Equation 1.2 was used and the summations were stopped at the tension peak of the cycle in which fracture initiation was observed. Equation 1.3 is then used to fit an appropriate value of λ to the data. A plot is made with $VGI_{cyclic}/VGI_{crtical}^{monotonic}$ on the vertical axis and the accumulated equivalent plastic strain, $\varepsilon_p^{accumulated}$ which is referred to as PEEQ in the Abaqus software. A regression analysis is performed to fit an equation of the form given by Equation 1.3 to the plotted data which results in the calibrated cyclic degradation term, λ.

Two examples of this process are shown in Figure 5.7 and Figure 5.8. For the specimens with no artifacts, λ for the 0.59 in. thick and 0.94 in. thick specimens with no artifacts was found to be 0.43 and 0.45 respectively. The circumferentially notched round bar specimens resulted in a calibrated cyclic strength degradation parameter, λ = 0.25 for the same 0.94 in. thick flange material. The difference between these values is not likely to be due just to material variability. More research is required.

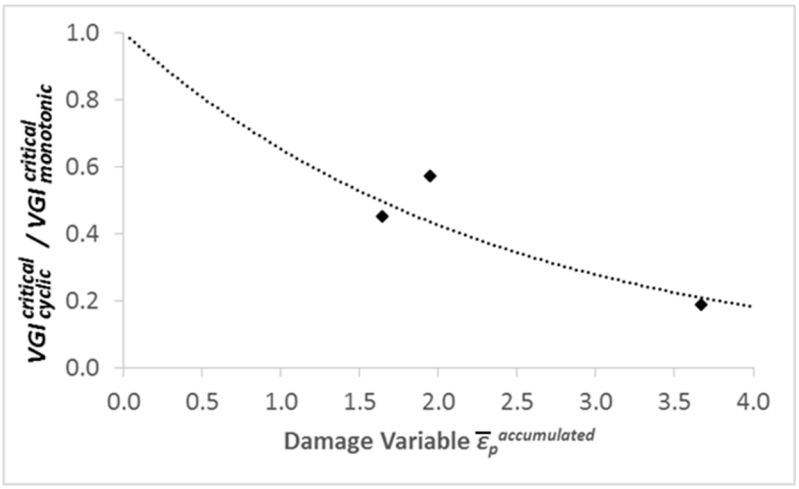


Figure 5.7 – Regression analysis to calculate λ for 0.59 in. thick (W24x62 flange) with no artifact.

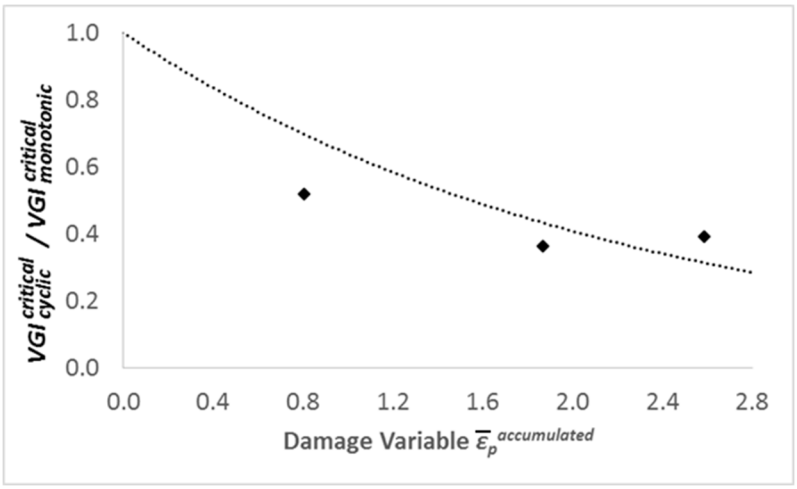


Figure 5.8 – Regression analysis to calculate λ for 0.94 in. thick (W36x150 flange) with no artifact.

The method described above to calculate values of the cyclic strength degradation parameter, λ, was unsuccessful for bend test specimens with artifacts. See Figure 5.9 for an example. In most cases, the calculated VGI_{cyclic} from bend tests was larger than the calculated $VGI_{monotonic}$ from monotonic axial tension tests. This results in a negative value of λ which implies that cyclic loading, instead of causing a degradation in fracture resistance, causes an increase in fracture resistance. This was considered implausible.

Improvements for the CVGM are presented in Section 5.4 to study the effect of modeling the artifacts in both the monotonic uniaxial and cyclic bend tests. Also, the width effect of the monotonic uniaxial tests is studied since the monotonic uniaxial and cyclic specimens had different widths. Another possibility is that the difference in the strain gradients between the monotonic tests which were uniaxial, and the cyclic tests which were flexural, are creating incompatible values of the void growth index. A new monotonic bend test is proposed in Chapter 8 to study this effect of strain gradients between a monotonic uniaxial and bend test. Meanwhile in this section, a value of λ equal to zero was conservatively assumed. The bend tests suggest that the fracture resistance with these artifacts was actually quite a bit larger than the values predicted using $\lambda = 0$.

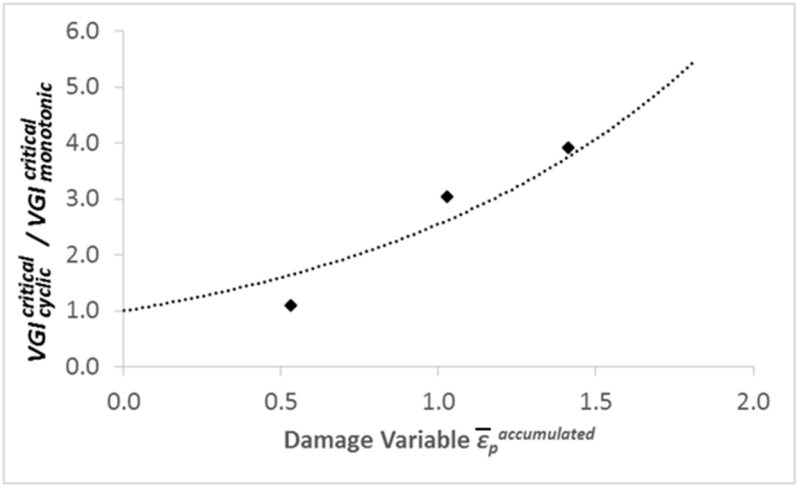


Figure 5.9 – Curve fit scatter plot and curve fit to calculate λ for W24x62 with PAF.

All of the calibrated fracture parameters are summarized in Table 5.5. A larger value of $VGI_{monotonic}^{critical}$ means the artifact is more resistance to fracture under monotonic loading. Conversely, a larger value of λ means more cyclic degradation in fracture resistance.

Table 5.5 – Calibrated fracture parameters for different artifacts from monotonic uniaxial and cyclic bend test results.

	W24x62		W36x150	
Artifact Type	$VGI_{monotonic}^{critical}$	λ	$VGI_{monotonic}^{critical}$	λ
No Artifact	1.77	0.43	2.11	0.45
Powder Actuated Fasteners (PAF)	0.23	INVALID Use λ=0.0	0.26	INVALID Use λ=0.0
Puddle Welds (PW)	1.55	1.15	0.44	INVALID Use λ=0.0
Ground Fillet Weld (GFW)	0.23	INVALID Use λ=0.0	0.36	INVALID Use λ=0.0
Notch Ground to Taper (NGT)	0.07	INVALID Use λ=0.0	0.17	INVALID Use λ=0.0
Notch Welded and Ground Smooth (NWG)	0.14	INVALID Use λ=0.0	0.38	INVALID Use λ=0.0

5.4 Improvements to CVGM Calibration

In this section the effect on two artifacts (PAF and NGT) will be studied using monotonic uniaxial tests and cyclic bend tests. This will be done using FE models and later the results will be used to calibrate the CVGM for those two artifacts. Also, a width study will be conducted on monotonic uniaxial tests and compared to the data from the monotonic uniaxial tests. Finally, a new calibration method for the CVGM will be explained with an example comparing results using the current CVGM with the CVGM new calibration method.

5.4.1 Monotonic Uniaxial Tests FE Models with Artifacts

After the fracture parameters unsuccessful calibration in the previous section for the specimens with artifacts, it was decided to study the effect of modeling the artifacts in the FE models. Only two artifacts were studied (PAF and NGT) out of the five artifacts tested in this

research. For the monotonic uniaxial tests FE models, the same model that was calibrated previously for the bare specimen with the same mesh size and calibration values of the material model, given in Table 5.4, was used for the 0.54 in. thick specimen cut from the W24x62 and the 0.94 in. thick specimens cut from the W36x150. Material model parameters were calibrated against test data from the coupons with no artifacts and no side notches.

The PAF was represented by a hole throughout the specimen with a diameter of 0.188 in. to mimic the material lose or damage caused by the insertion of the PAF. For the NGT it was modeled with a tapered ratio of 1:5 with a 1/8 in. deep notch. The dimensions of the notch are 1/8 in. deep and 1-1/4 in. wide. An example of the modeled artifacts are shown in Figure 5.10 and Figure 5.11 for a monotonic uniaxial test. The FE model was analyzed with an imposed monotonic elongation displacement history at one end while the other end was fixed and modeled only for the length of the extensometer which was 8.0 in.

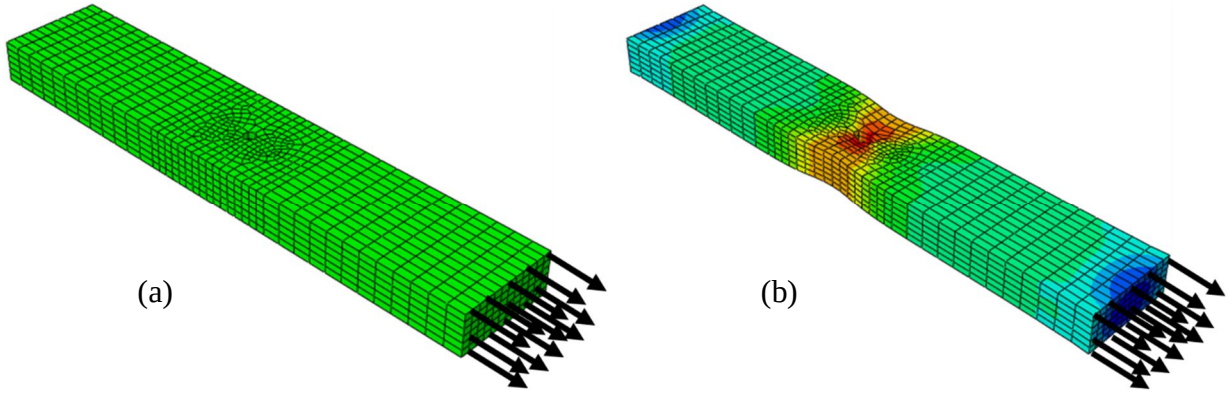


Figure 5.10 – FEM model of a monotonic uniaxial test for the W24x62 with PAF specimen showing the transition in mesh size (a) an undeforrmed specimen loading and (b) deformed specimen showing necking at the center

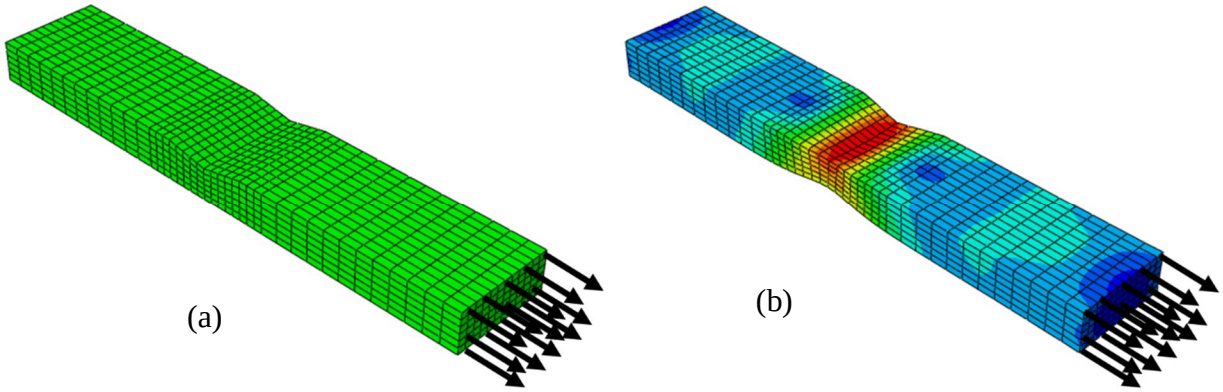


Figure 5.11 – FEM model of a monotonic uniaxial test for the W24x62 with NGT specimen showing the transition in mesh size (a) an undeforrmed specimen loading and (b) deformed specimen showing necking at the center

The stress vs strain behavior for the 0.59 in. and 0.94 in. thick monotonic tests with PAF and NGT are compared to FE results in Figure 5.12 through Figure 5.15. Stress and strain data were extracted from these four models at the critical location in the middle of the necking region. This stress and strain data will be used in Section 5.4.3.

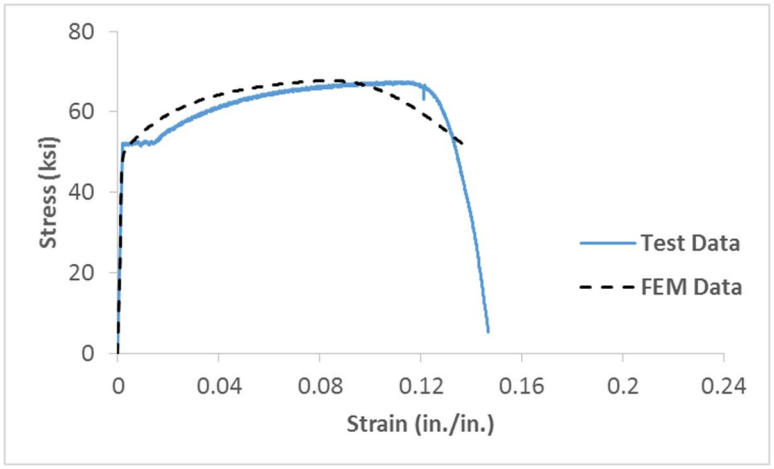


Figure 5.12 – Stress strain curve for W24x62 monotonic uniaxial test data with PAF compared to FEM data.

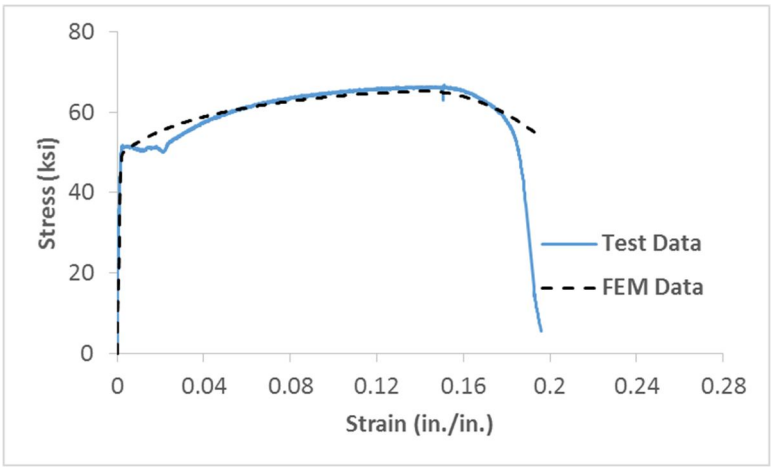


Figure 5.13 – Stress strain curve for W36x150 monotonic uniaxial test data with PAF compared to FEM data.

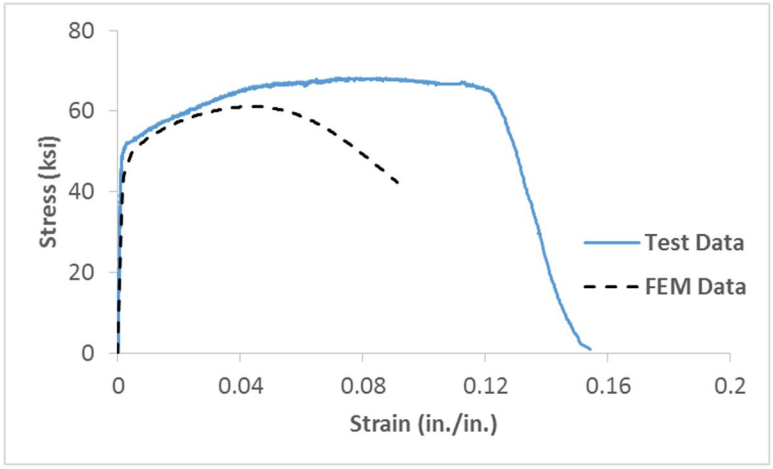


Figure 5.14 – Stress strain curve for W24x62 monotonic uniaxial test data with NGT compared to FEM data.

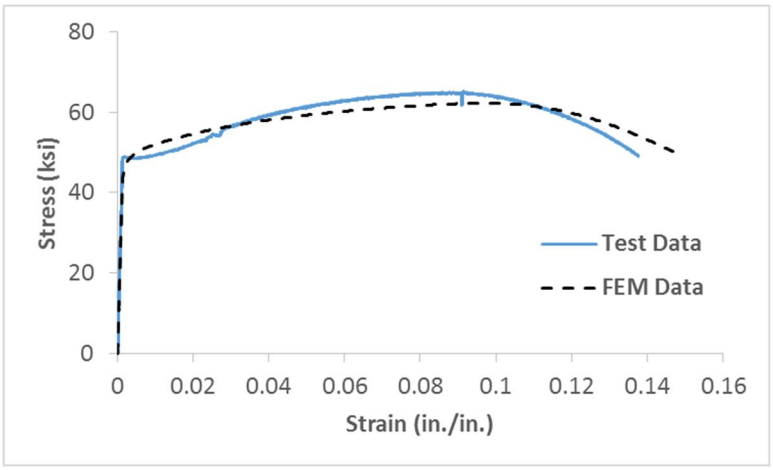


Figure 5.15 – Stress strain curve for W36x150 monotonic uniaxial test data with NGT compared to FEM data.

Three of the four FEM models with artifacts showed acceptable results matching the actual test data. Only one test was performed for each artifact and all of the material parameters calibration was calibrated for the bare specimens. Those differences between the FEM and test data results is likely to be due to material variability.

5.4.2 Cyclic Bend Tests FE Models with Artifacts

As described previously in Section 4.5.3, a refined mesh with a size of 0.125 in. x 0.125 in. x 0.1 in. thick elements (8 node brick elements) were used at the center of the specimen. Also, the same material model parameters calibrated in the monotonic uniaxial tests were used for the cyclic bend test as given in Table 5.4. The only difference is that two artifacts were modeled (PAF and NGT) at the center of the specimen. The PAF was represented by a hole throughout the specimen with a diameter of 0.188 in. to mimic the material lose or damage caused by the insertion of the PAF. For the NGT it was modeled with a tapered ratio of 1:5 with a 1/8 in. deep notch. The dimensions of the notch are 1/8 in. deep and 1-1/4 in. wide. Also, the same clamping forced, surface contacts, boundary conditions, and displacement increments described in previously in Section 4.5.3 are used in the cyclic bend tests FE models with artifacts.

Equivalent plastic strain histories and stress triaxiality histories were obtained from the model. Figure 5.16 shows a contour plot of the plastic equivalent strain (PEEQ) and the Von Mises stress (S. Mises) for a specimen with and without side notches for a W24x62 specimen with PAF. The stress and strain histories will be used in Section 4.5.7 to calibrate fracture parameters. The stress and strain histories used for calibrating fracture parameters for a specific artifact were run until the time of complete fracture was observed in the test. In this way, the stress and strain histories were the same observed for the tested artifact with the same geometry.

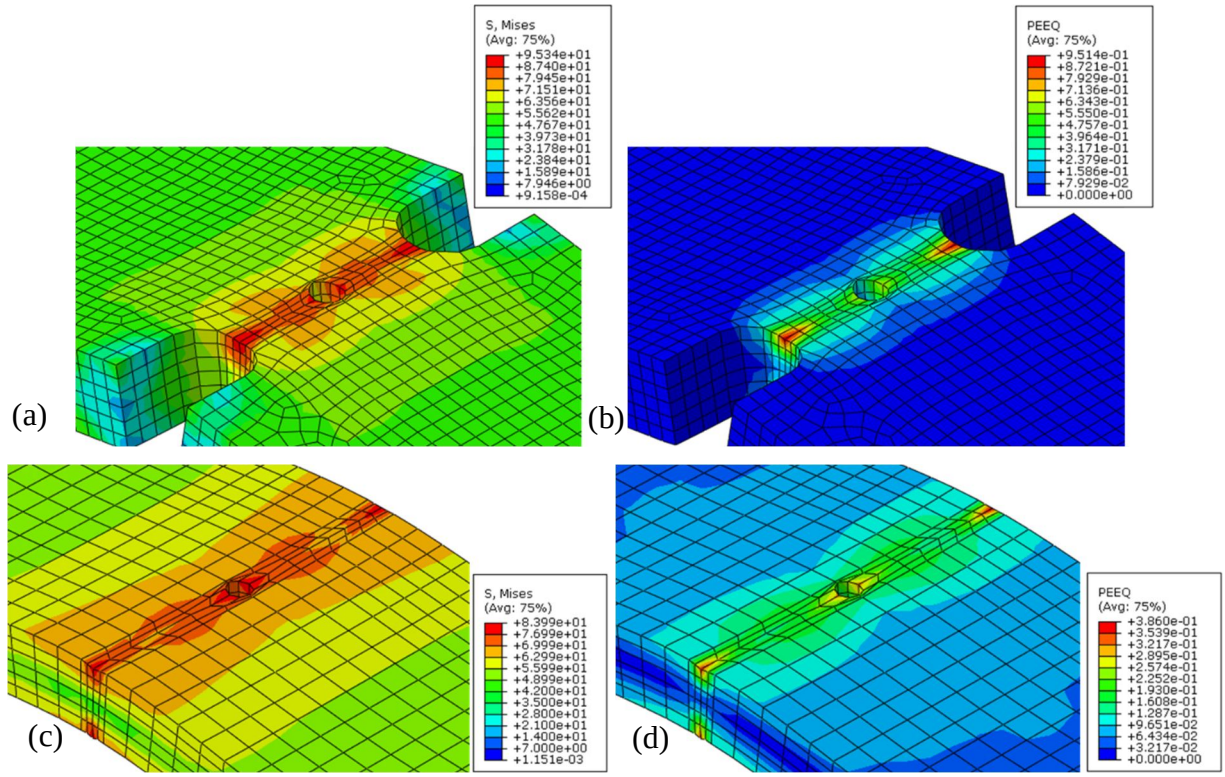


Figure 5.16 – PEEQ strain and Von Mises stresses contour at tension side of a cyclic bend test for W24x62 with PAF with notch radius of 0.25 in. (a) and (b), and a unotched specimen (c) and (d).

5.4.3 Calibrating Fracture Parameters using FE Models with Artifacts

The critical monotonic void growth index, $VGI_{monotonic}^{critical}$, and fracture parameter, λ, for cyclic degradation term for the specimens with PAF and NGT were calculated using the same

method used in Section 5.3.3. The only different is that those artifacts were modeled and the stresses and equivalent plastic strains in the critical locations were used.

Figure 5.17 through Figure 5.20 shows the calibration plots using regression analysis for cyclic degradation term, λ, for the PAF and NGT specimens with flange thickness of 059 in. and 0.94 in. Each artifact had different cyclic strength degradation parameter, λ. Also, by changing the thickness of the specimen while using the same artifact had different cyclic strength degradation parameter, λ.

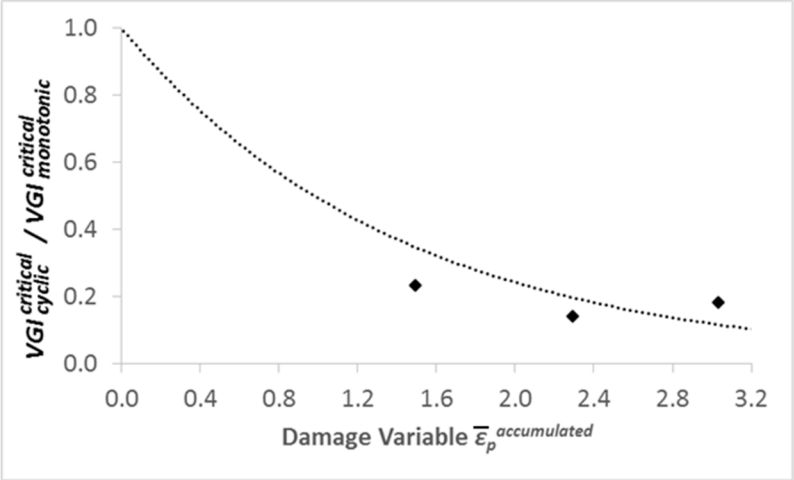


Figure 5.17 – Curve fit scatter plot and curve fit to calculate λ for W24x62 with PAF.

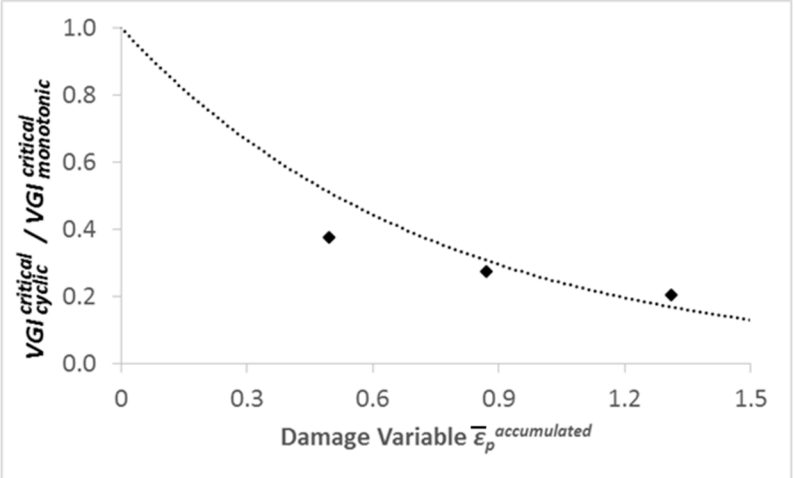


Figure 5.18 – Curve fit scatter plot and curve fit to calculate λ for W24x62 with NGT.

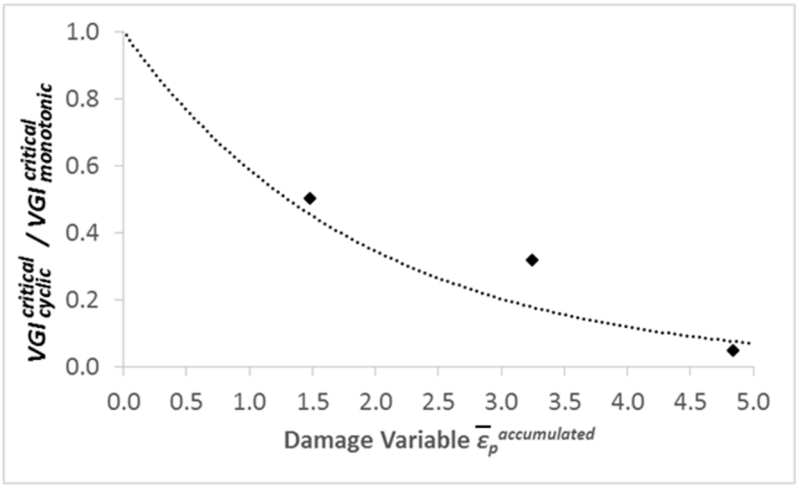


Figure 5.19 – Curve fit scatter plot and curve fit to calculate λ for W36x150 with NGT.

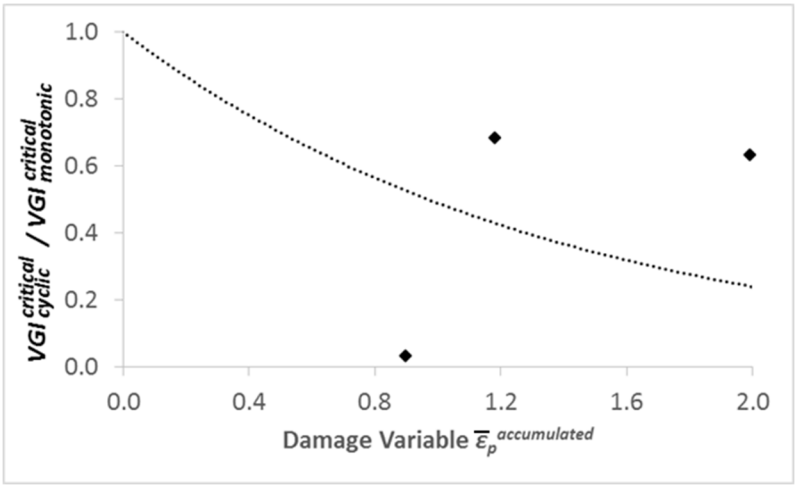


Figure 5.20 – Curve fit scatter plot and curve fit to calculate λ for W36x150 with NGT.

The calibrated fracture parameters for the PAF and NGT are summarized in Table 5.6. A larger value of $VGI_{monotonic}^{critical}$ means the artifact is more resistance to fracture under monotonic loading. Conversely, a larger value of λ means more cyclic degradation in fracture resistance.

Table 5.6 – Calibrated fracture parameters for different artifacts from monotonic uniaxial and cyclic bend test results.

	W24x62		W36x150	
Artifact Type	$VGI_{monotonic}^{critical}$	λ	$VGI_{monotonic}^{critical}$	λ
Powder Actuated Fasteners (PAF)	3.37	0.71	2.76	0.531
Notch Ground to Taper (NGT)	3.46	1.36	1.50	0.715

Modeling the artifacts (PAF and NGT) resulted in a positive value of λ rather than a negative value as in Section 4.5.4. Also modeling the artifacts led to an increase in the $VGI_{monotonic}^{critical}$ values in Table 5.6. In Section 4.5.4 all of the stresses and equivalent plastic strains were extracted from models for bare specimens only. In this part of the study it was decided to model two artifacts and use the stresses and equivalent plastic strains in the critical locations. This method led to a successful calibration of the cyclic strength degradation parameter, λ.

5.4.4 Width Effect on Monotonic Uniaxial FE Models with Artifacts

A width effect study on monotonic uniaxial testes was conducted to measure the impact of width results to the actual tests results since the monotonic uniaxial and cyclic specimens had different widths. Therefore, FE models were run with the same specimen width used for the unnotched bend tests having an aspect ratio of 1:5 with respect to the thickness and width. The coupons for the W24x62 specimens were 0.59 in. x 2.95 in. and the coupons for the W36x150 were 0.94 in. x 4.7 in. An imposed monotonic elongation displacement history was used in the FE model analysis at one end while the other end was fixed and modeled only for the length of the extensometer which was 8.0 in. As described in the previous subsection, a refined mesh with a size of 0.125 in. on each side and 0.1 in. thick was used at the center of the specimen where necking occurs. The mesh size at each end was increased to 0.25 in. by 0.125 in. This study was conducted

on W24x62 and W36x150 bare specimens and with artifacts (PAF and NGT). Figure 5.21 and Figure 5.22 shows the mesh, load application, and necking for a W24x62 with PAF and NGT respectively.

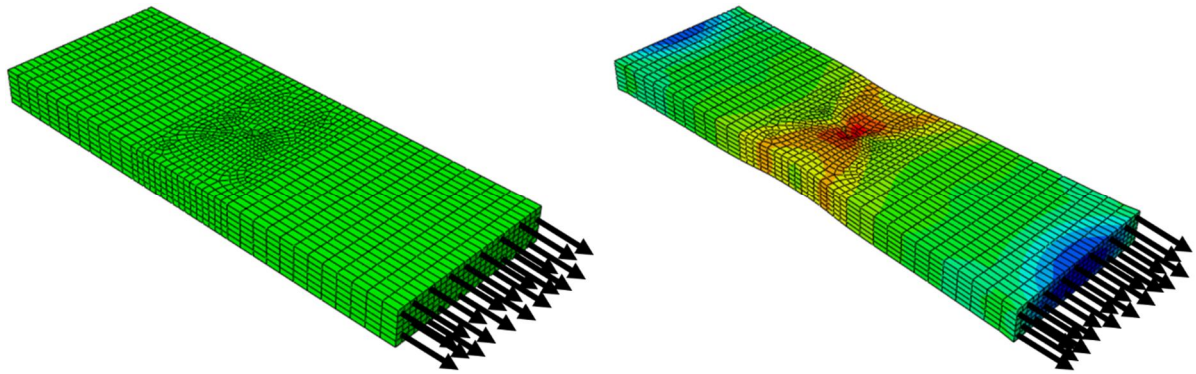


Figure 5.21 – FEM model of a wide monotonic uniaxial test for the W24x62 with PAF specimen showing the transition in mesh size (a) an undeforrmed specimen loading and (b) deformed specimen showing necking at the center

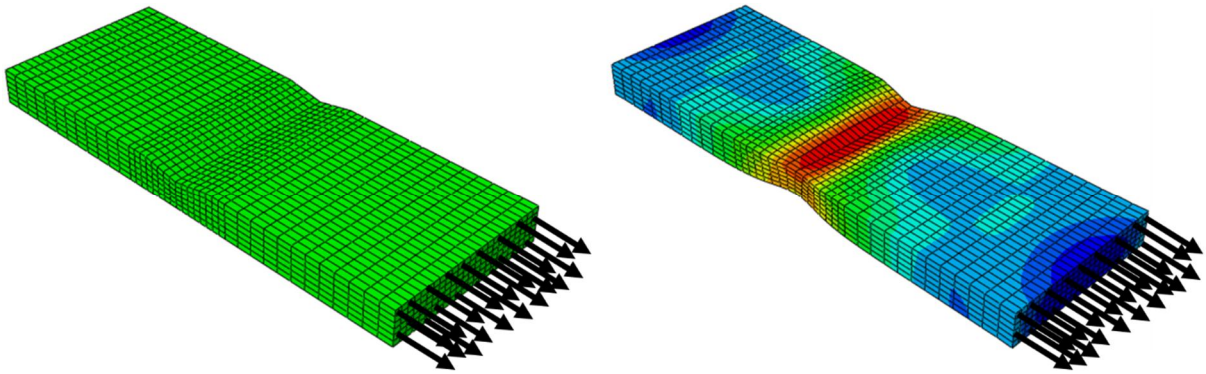


Figure 5.22 – FEM model of a wide monotonic uniaxial test for the W24x62 with NGT specimen showing the transition in mesh size (a) an undeforrmed specimen loading and (b) deformed specimen showing necking at the center

It is noted that the two artifacts studied were modeled in the FE analysis. Stress and strain data for the bare, PAF and NGT specimens were extracted from these six models at the critical location in the middle of the necking region. Instead, it is assumed that the stress and strain

histories are relatively similar up to fracture initiation regardless of artifact type. This assumption is supported by the relatively similar load-displacement curves prior to fracture presented in Section 4.4. The stress strain plots are presented in Figure 5.23 through Figure 5.28.

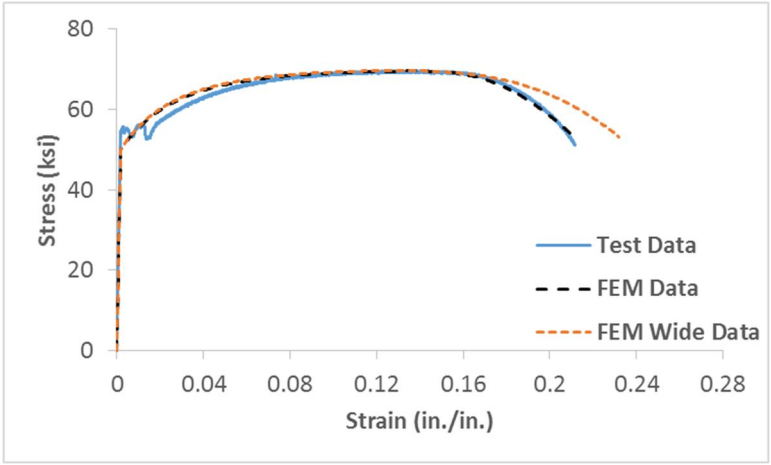


Figure 5.23 – Stress strain curve for W24x62 monotonic uniaxial test data with no Artifact compared to FEM data.

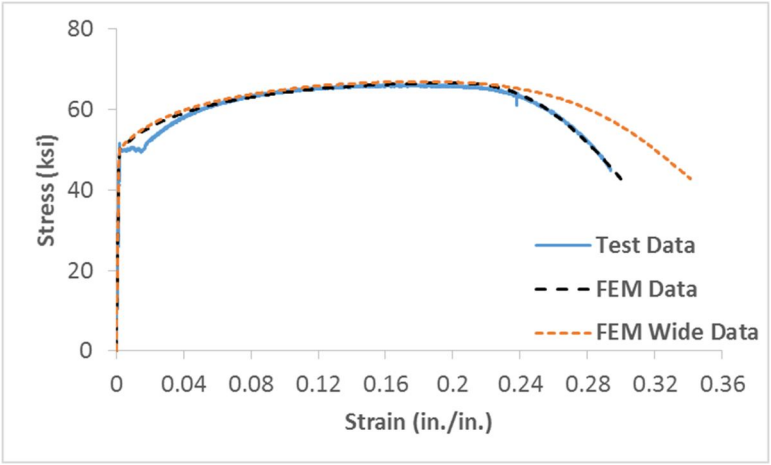


Figure 5.24 – Stress strain curve for W36x150 monotonic uniaxial test data with no Artifact compared to FEM data.

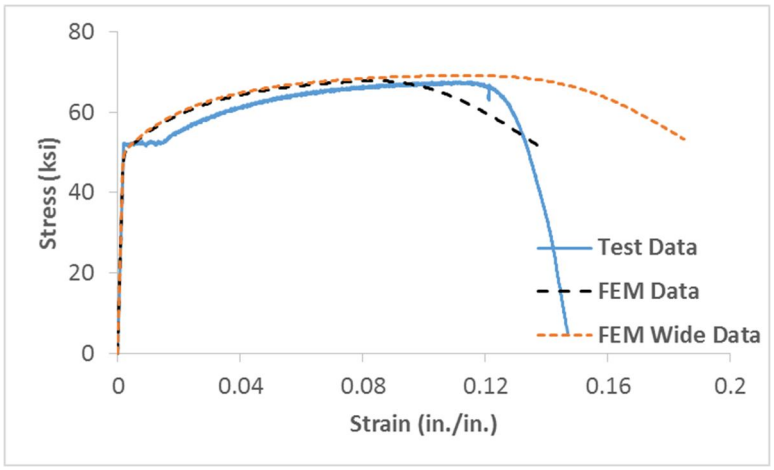


Figure 5.25 – Stress strain curve for W24x62 monotonic uniaxial test data with PAF compared to FEM data for wide and specimen.

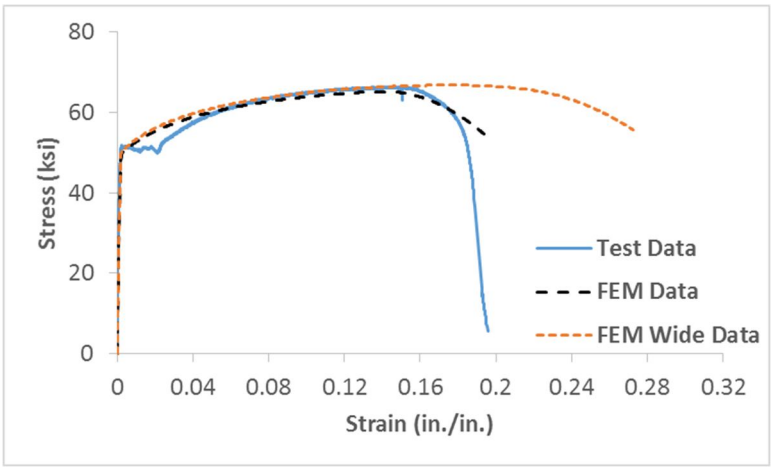


Figure 5.26 – Stress strain curve for W36x150 monotonic uniaxial test data with PAF compared to FEM data for wide and specimen.

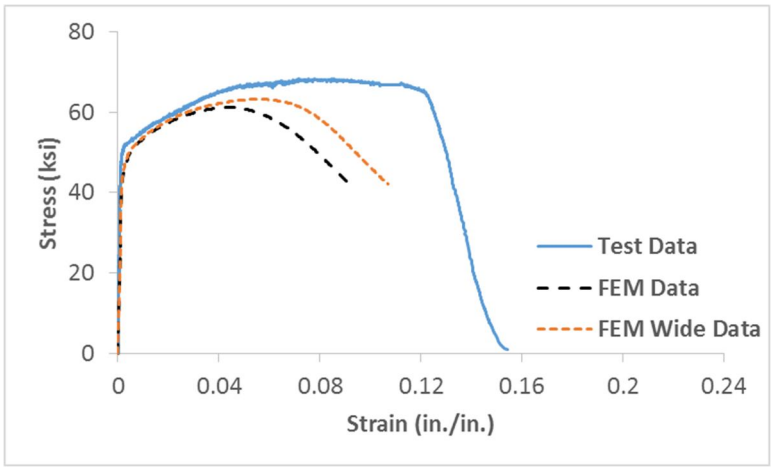


Figure 5.27 – Stress strain curve for W24x62 monotonic uniaxial test data with NGT compared to FEM data for wide specimen.

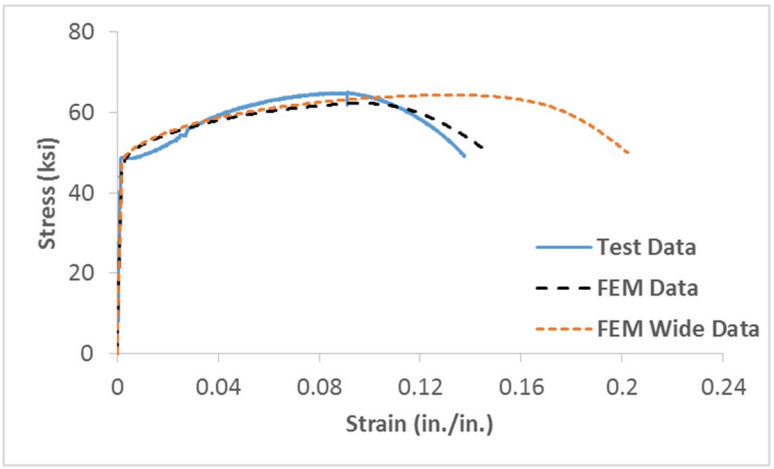


Figure 5.28 – Stress strain curve for W36x150 monotonic uniaxial test data with NGT compared to FEM data for wide specimen.

Increasing the width of the monotonic uniaxial coupons will result in higher failure strains and a slight increase in ultimate stress. The behavior of both FE models of the actual and wider width specimens has a decent match until the specimen with the actual width reaches ultimate stress. After that the wider specimen stress strain behavior increases until the new ultimate stress is reached. It was noticed that thicker specimens, W36x150, showed more elongation than the thinner specimens, W24x62.

Greater elongation will result in larger critical monotonic void growth index, $VGI_{monotonic}^{critical}$, would mean that the calibration of the cyclic degradation parameter, λ, may result in a positive value. It is recommended that in future testing to consider using the same width for both monotonic uniaxial and cyclic bend test specimens which may resolve the negative cyclic degradation parameter, λ, value for some of the artifacts calibrated in Section 5.3.3. This might also have an impact on the prediction of fracture initiation results.

5.4.5 Proposed CVGM Modified Fracture Parameters Calibration Method

In this section, a modified CVGM approach to calibrate the cyclic strength degradation parameter, λ, is proposed. Looking at Figure 5.7 and Figure 5.8 in Section 5.3, it can be noticed that the calibration of λ for the classical CVGM uses regression analysis by fitting the cyclic test data starting from accumulated plastic strain (PEEQ) value intercepting at zero and a $VGI_{cyclic}/VGI_{crtical}^{monotonic}$ value intercepting at 1.0. On the other hand, the modified CVGM approach accounts for the monotonic tests as cyclic tests failing at the first tensile cycle under extreme loading. Therefore, instead of calibrating λ for the accumulated plastic strain (PEEQ) value of zero, the calibration plot will start at the accumulated plastic strain (PEEQ) for the monotonic uniaxial tests. The $VGI_{cyclic}/VGI_{crtical}^{monotonic}$ values still start at 1.0 as to normalize the data points by dividing them by $VGI_{monotonic}^{critical}$.

This approach will be conducted using regression analysis by fitting Equation 1.3 to calibrate the modified cyclic degradation term, λ. The calibration of λ starts by calculating the cyclic void growth index, VGI_{cyclic}, for each of the circumferentially notched round bar tests and the cyclic bend tests. A plot is made with $VGI_{cyclic}/VGI_{crtical}^{monotonic}$ on the vertical axis and the accumulated equivalent plastic strain, $\varepsilon_p^{accumulated}$ which is referred to as PEEQ in ABAQUS software on the horizontal axis. The same value for the monotonic void growth index, $VGI_{monotonic}^{critical}$, with a value of 1.94 for the A992 steel circumferentially notched round bar tests and 1.77 for bare steel specimens of 0.59 in. thick calculated previously using Equation 1.4 is used.

An example of this process is shown in Figure 5.29 and Figure 5.30 for the circumferentially notched round bar tests and the W24x62 cyclic bend tests. The new value of λ for the circumferentially notched round bar tests and the 0.59 in. specimen with no artifacts are 0.30 and 0.63 respectively. Meanwhile, the value of λ using the previous calibration method was 0.25 and 0.43 respectively. It is clearly noticed an increase in the cyclic strength degradation parameter, λ, which means that fracture initiation will be predicted earlier using the modified CVGM approach.

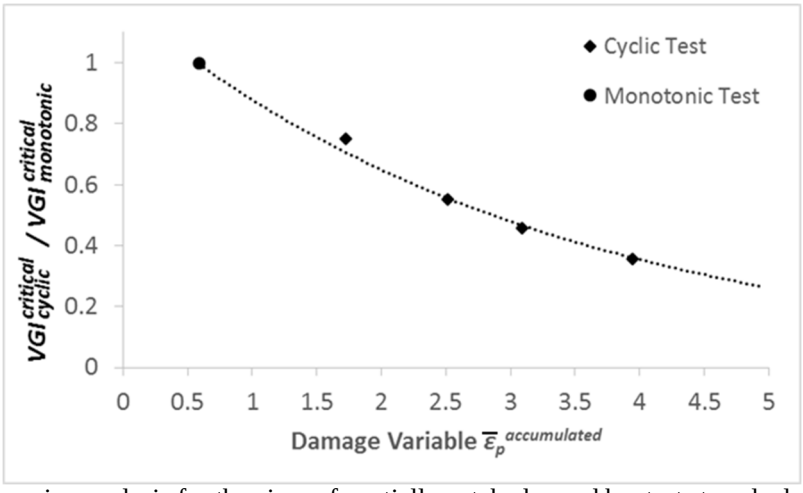


Figure 5.29 – Regression analysis for the circumferentially notched round bar tests to calculate λ for A992 steel using modified CVGM.

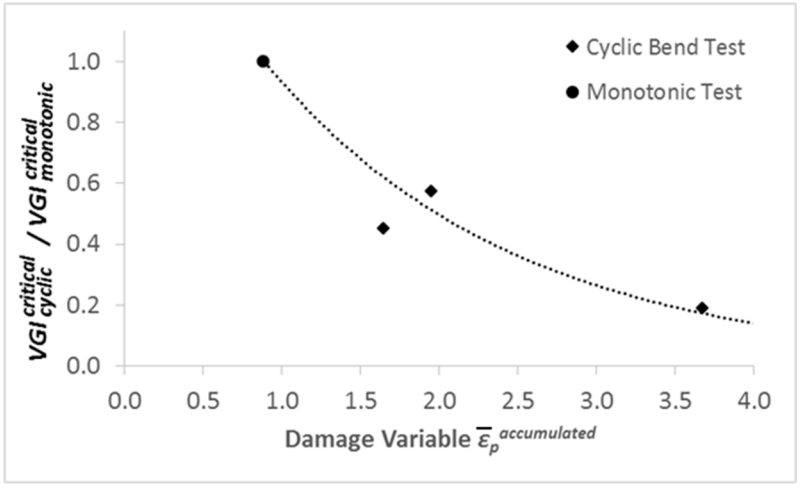


Figure 5.30 – Regression analysis to calculate λ for 0.59 in. thick (W24x62 flange) with no artifact using the modified CVGM.

5.5 Stress-Weighted Damage Model Calibration

In this section, the cyclic bend tests will be used to calibrate the SWDM. As mentioned previously the SWDM is a new fracture model developed by Smith et al. (2014). This model is a modified model of the CVGM which was developed by Kanvinde and Deierlein (2007). There are still two main fracture parameters being calibrated in the same method as they were calibrated using the CVGM, those two parameter are the monotonic void growth index, $VGI_{monotonic}^{critical}$, and the cyclic strength degradation parameter, λ. The monotonic void growth index, $VGI_{monotonic}^{critical}$, is incorporated in the SWDM using parameter ,*C*, which is a material parameter that controls mainly the overall ductility of the material and it is calculated by inverting $VGI_{monotonic}^{critical}$, ($C = 1/VGI_{monotonic}^{critical}$).

Since the SWDM is a new model which has been developed recently, Smith et al. (2014) have some recommended parameters values to be used. Those parameters were derived from three different models axisymmetric model, the Lode angle model, and the capacity degradation model originating in the CVGM by Kanvinde and Deierlein (2007). Also, the values of those parameters were supported by statistical and probabilistic studies using data from studies conducted by Kanvinde and Deierlein (2007), and Myers et al. (2009).

As a demonstration the two parameters which were calibrated by the cyclic bend test using the CVGM will be used with the other parameters values recommended by Smith et al. (2014) on the cyclic bend tests. Table 5.7 presents the values of the parameters used in the SWDM. An example of using the SWDM in predicting fracture initiation is presented in Figure 5.31 for W24-B3-T59-R100 specimen from cyclic bend tests. In the next chapter, the SWDM will applied the full-scale special moment resistance frame tests and compared with other fracture models used.

Table 5.7 – Parameters for SWDM from cyclic bend test and recommended parameters from Smith et al. (2014).

	C	***λ***	***β***	***A+, A-***	***ξ***	***κ***
0.59 in. (W24x62)	0.565	0.43	1.25	1.3	1.0	0.5
0.59 in. (W24x62)	0.474	0.45	1.25	1.3	1.0	0.5

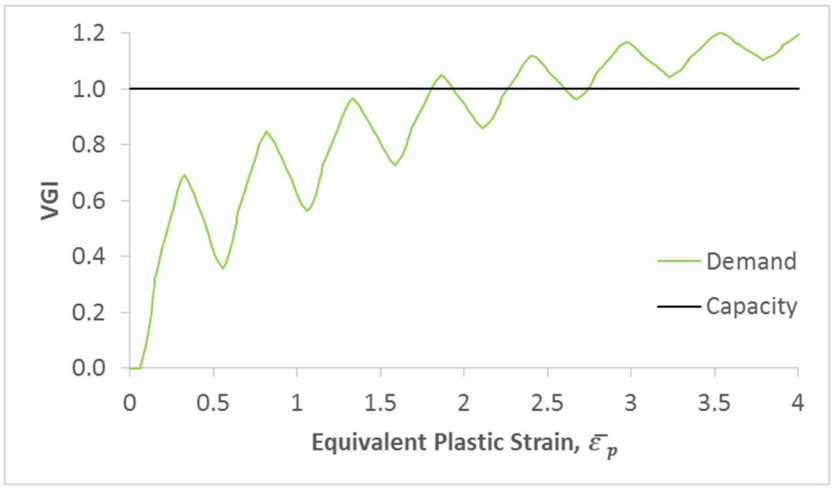


Figure 5.31 – Example of SWDM fracture initiation prediction for W24-B3-T59-R100 specimen from cyclic bend tests.

5.6 Cyclic Damage Plasticity Model Calibration

A numerical fracture model that is implemented in FE software LS-DYNA has been used to study the fracture initiation and propagation process. This model is called the Cyclic Damage Plasticity Model (CDPM). This model has been developed by Dufailly and Lemaitre (1995) and it involves multi-axial states of material nonlinearity.

In this section, an LS-DYNA model is used demonstrate and calibrate the CDPM which is implemented under the material model MAT_DAMAGE_3 (MAT_153) on monotonic uniaxial tests. Later the cyclic bend tests are used to calibrate the CDPM damage parameters to be used in a FE analysis using LS-DYNA for full-scale tests.

5.6.1 Monotonic Uniaxial Tests Calibration Using LS-DYNA

The FE analyses were conducted using LS-DYNA R8.0. All of the models that were used in this section were built and meshed using FE analysis software ABAQUS 6.13 (Simulia 2012). Those models were imported to LS-DYNA and later MAT_DAMAGE_3 (MAT_153) material model was selected. Lemaitre and Chaboche (1994) plasticity model with combined nonlinear

isotropic and kinematic hardening which was derived from multiaxial formulations by Armstrong and Fredrick (1966) is used in this material model in addition to the CDPM. All of the details related to the mesh size, boundary conditions, element type, and specimen dimensions in the FE model were discussed in Section 5.3.1. An example of the mesh, boundary conditions, load application, and necking for a W24x62 are presented in Figure 5.32 from LS-DYNA.

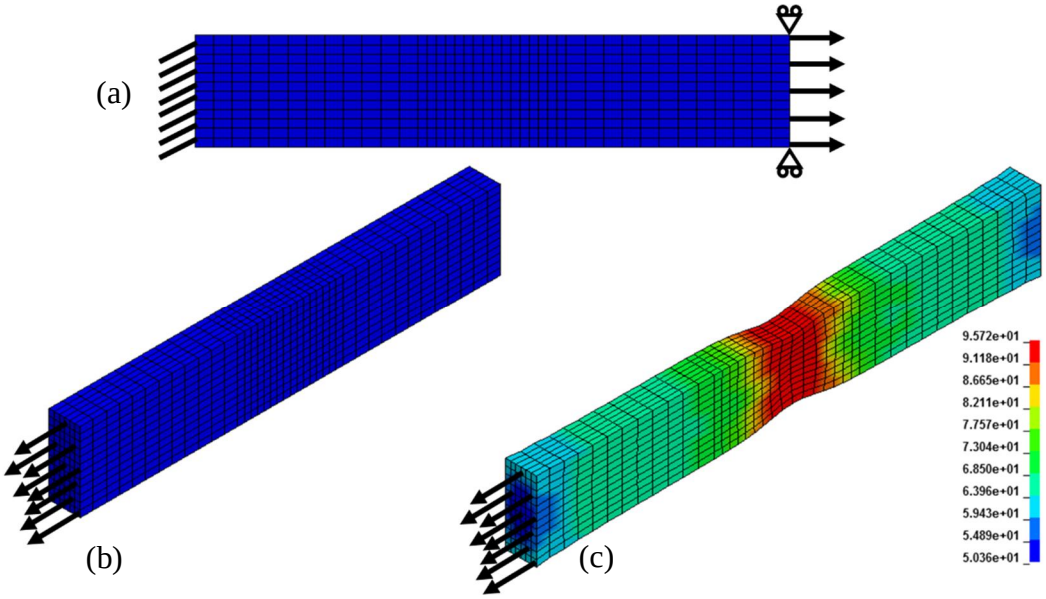


Figure 5.32 – FEM model of a monotonic uniaxial test for the W24x62 specimen in LS-DYNA showing the transition in mesh size (a) and boundary conditions of an undeformed specimen from side view, (b) an undeforrmed specimen loading and (c) deformed specimen showing necking at the center

Those models were previously calibrated using combined nonlinear isotropic and kinematic hardening using ABAQUS 6.13 (Simulia 2012) against from the coupons with no artifacts and no side notches. Five material parameters were calibrated for the material model including two parameters for isotropic hardening (Q_{inf} and b) and three parameters for kinematic hardening (C, γ, and σ_o). Those parameters are the same used in LS-DYNA, the only difference is in one of the isotropic parameters which is Q_{inf} that is defined as H/β in LS-DYNA rather than Q_{inf}. Given in Table 5.8 are the material parameters used in LS-DYNA for the combined hardening, the parameters used in ABAQUS are given in Table 5.8.

Table 5.8 – Material model parameters for A992 steel cut fromW24x62 and W36x150 flanges used in LS-DYNA.

0.59 in. (W24x62)					**0.94 in. (W36x150)**				
σ_o **(ksi)**	***C*** **(ksi)**	γ	***H*** **(ksi)**	***b***	σ_o **(ksi)**	***C*** **(ksi)**	γ	***H*** **(ksi)**	***b***
50	660	45	144	4	50	250	45	188	4

After validating the combined hardening parameters in LS-DYNA without activating the CDPM in the material model four fracture parameters were calibrated *EPSD*, *S*, *T*, and D_c. Given in Table 5.9 are the material fracture parameters for the CDPM. An example of the element removal and complete fracture of a W24x62 (0.59 in. thick) specimen is shown in Figure 5.33. The stress vs strain behavior for the 0.59 in. and 0.94 in. thick monotonic tests with no artifact are compared to FE results in Figure 5.34 and Figure 5.35, respectively.

Table 5.9 – CDPM parameters for A992 steel cut fromW24x62 and W36x150 flanges used in LS-DYNA.

0.59 in. (W24x62)					**0.94 in. (W36x150)**				
σ_o **(ksi)**	***EPSD***	***S***	***T***	D_c	σ_o **(ksi)**	***EPSD***	***S***	***T***	D_c
50	0.7	0.25	1.0	0.2	50	0.7	0.25	1.0	0.3

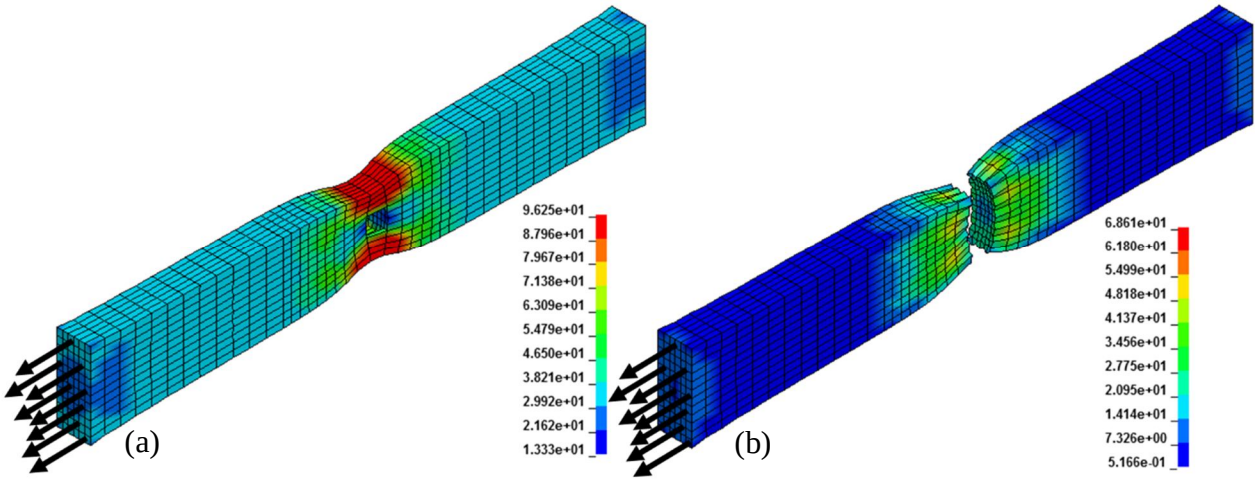


Figure 5.33 – FEM model of a monotonic uniaxial test for the W24x62 specimen showing (a) element removal at the center of the specimen and (b) complete fracture

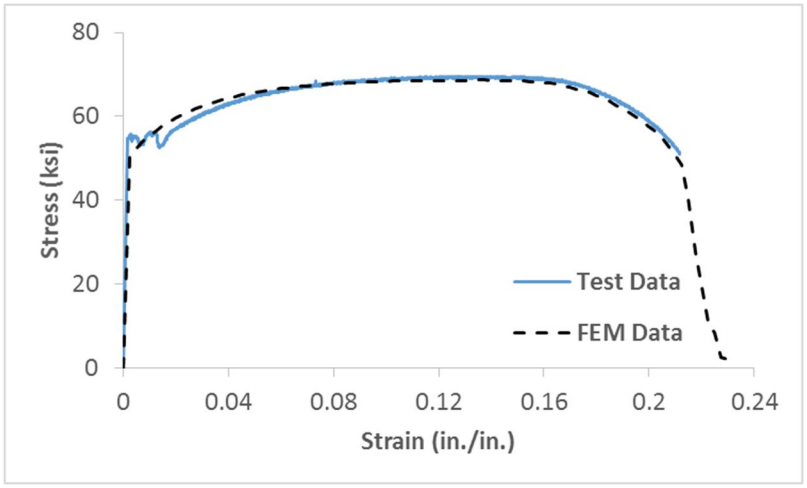


Figure 5.34 – Stress strain curve for W24x62 monotonic uniaxial test data with no artifact compared to LS-DYNA FEM data.

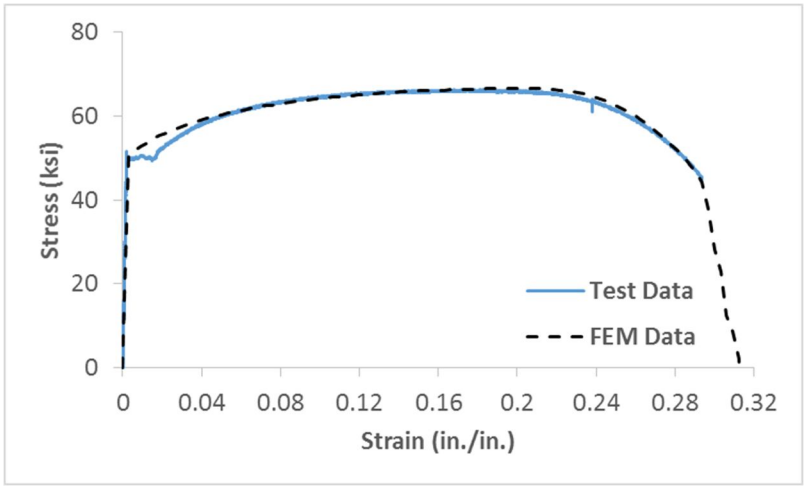


Figure 5.35 – Stress strain curve for W36x150 monotonic uniaxial test data with no artifact compared to LS-DYNA FEM data.

5.6.2 CDPM Calibration Using Cyclic Bend Tests

Cyclic bend tests are used in this section to calibrate some parameters of the CDPM to predict fracture initiation. Those parameters will be used to predict fracture initiation and propagation in FE software LS-DYNA for one of the full-scale models in the next chapter. Work from the previous section for calibrating the parameters of the monotonic uniaxial tests is used as a baseline in addition to recommendations by LS-DYNA for MAT_DAMAGE_3 (MAT_153). The parameters that the default value recommended by LS-DYNA user manual was used were *t* which is a material constant (Default T = 1 in LS-DYNA), and *S* which is a damage material constant with units of energy density (Default $S = \sigma_{y0}/200$ in LS-DYNA) are used. In other hand, two parameters were calibrated to match the fracture initiation in the cyclic bend tests and they are D_c which is the critical damage and *EPSD* which is the damage threshold value. Refer to Equation 2.17 for the CDPM model. The final calibrated values for the W24x62 bare cyclic bend test notched (*R025* and *R100*) and unnotched (*R000*) specimens are presented in Table 5.10. It is clearly noticed that the critical damage values for the notched and unnotched bare specimens is different. Those parameter will be used in the FE analysis of the full-scale specimen data of the W24x62 with RBS and no fasteners to predict fracture initiation and propagation. The CDPM results for the three cyclic bend tests specimens with the W24x62 bare specimens that were used to predict fracture initiation are presented in Figure 5.36 for both notched (*R025* and *R100*) and unnotched (*R000*) specimens.

Table 5.10 – Calibrated CDPM parameters for bare cyclic bend test specimens cut fromW24x62 flanges.

0.59 in. (W24x62)					
σ_0 (ksi)	***EPSD***	***S***	***T***	***D_c (R025 & R100)***	***D_c (R000)***
50	0.7	0.25	1.0	0.15	0.3

The proper methodology to calibrate the CDPM is to calibrate all of the parameters not only the critical damage parameter, D_c, as it was conducted in this section. A sensitivity analysis for each parameter must be conducted until the fracture initiation and propagation mechanism is

predicted in the FE analysis. This can be achieved by running multiple runs and setting different values of each parameter until the experimental behavior is captured.

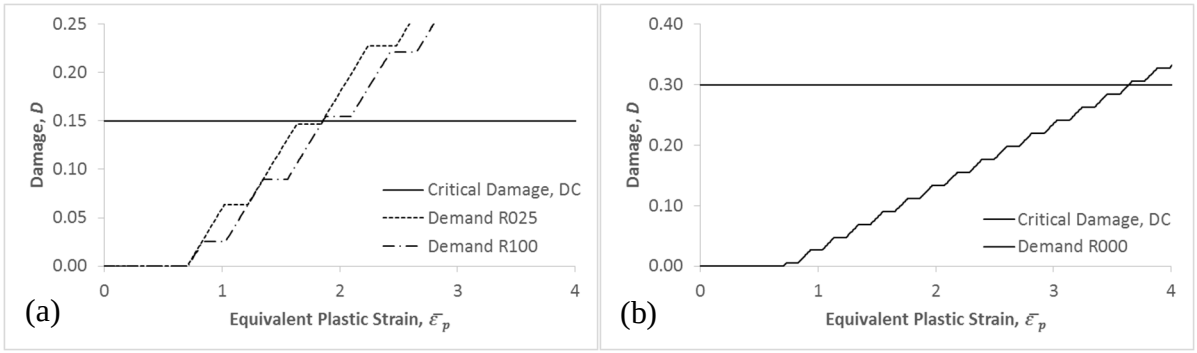


Figure 5.36 – Damage versus equivalent plastic strain for fracture initiation prediction for W24x62 bare cyclic bend tests specimens (a) notched specimens, and (b) unnotched specimen.

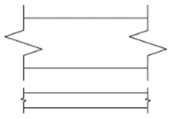
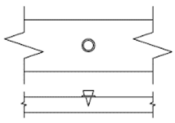
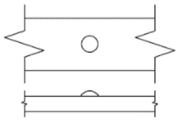
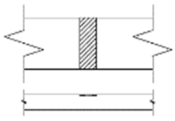
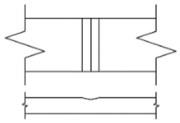
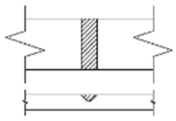
5.7 Cumulative Extreme Fiber Strain

A study was conducted to examine the cumulative theoretical fiber strain for the W24x62 and W36x150 to observe if there is any relation related to the thickness of the material and fracture initiation. Strain at the extreme fiber was calculated using the pure bend test curvature design method which assumes that plane sections remain plane for the first half cycle at the tension side. This approach was used since it is a quick and simple method to calculate strain theoretical rather than using more complex approaches. Also the curvature design method was previously used to determine the rollers diameter for the cyclic bend tests. The extreme fiber strain values for the first half cycle were 0.051 in./in. and 0.079 in./in. for the W24x62 and W36x150 specimens respectively. Cumulative strain was calculated using Equation 5.1, where $\Delta\varepsilon$ is the strain range from tension peak to compression peak, N is the number of cycles, and $\Sigma\varepsilon$ is the cumulative strain.

$$\Sigma\varepsilon = 2\,\Delta\varepsilon\,N \tag{5.1}$$

It can be clearly noticed that the thinner specimens (W24x62) sustained more cycles than thicker specimens (W36x150) for four out of six tested groups (Bare, PW, GFW, and NWG). The only two artifacts in which the W36x150 specimens outperformed the W24x62 specimens were the PAF and NGT specimens. Those two artifacts are dependent on the material thickness and the artifacts led to early fracture initiation for two different reasons. For the PAF, early fracture initiation for the W24x62 specimens was due to the PAF causing damage, a small hump, at the bottom side of the specimen. Fracture initiation occurred at the hump location at early cycles, but despite that there was an excessive resistance to final fracture and the PAF outperformed all of the other artifacts tested. While of the NGT, the amount of stress concertation for the W24x62 was higher than the W36x150 specimens. This added more stress at the v-notch leading the W24x62 for premature fracture initiation in relative to the W36x150 specimens. Overall, the strain at the extreme fiber of the thinner specimen, with a thickness of 0.59 in. (W24x62), is less than the thicker specimens, with a thickness of 0.94 in. (W36x150), but the thinner specimens require higher cumulative strain for fracture initiation to occur compared to the thicker specimens. The cumulative strain is dependent on the thickness of the specimen and the artifact which is also dependent on the material thickness. All of the average cumulative strain at fracture initiation for the six tested groups for the W24x62 and W36x150 specimens' results are presented in Table 5.11. The average cumulative strains values for the 0.59 in. (W24x62) and the 0.94 in. (W36x150) specimens are similar.

Table 5.11 – Artifacts effective damage depth relative to material thickness

Artifact Type		Specimen Flange Thickness (in.)	Average Initiation Cycle	Cumulative Strain (in./in.)
1) No Artifact		W24x62 t = 0.59	8.33	1.700
		W36x150 t = 0.94	2.33	0.737
2) Powder Actuated Fasteners (PAF)		W24x62 t = 0.59	2.67	0.544
		W36x150 t = 0.94	2.67	0.843
3) Puddle Welds (PW)		W24x62 t = 0.59	3.33	0.680
		W36x150 t = 0.94	2.67	0.843
4) Ground Fillet Weld (GFW)		W24x62 t = 0.59	3	0.612
		W36x150 t = 0.94	1.67	0.527
5) Notch Ground to Taper (NGT)		W24x62 t = 0.59	1.33	0.272
		W36x150 t = 0.94	1.67	0.527
6) Notch Welded and Ground Smooth (NWG)		W24x62 t = 0.59	2.67	0.544
		W36x150 t = 0.94	2	0.632
Cyclic Bend Test Average Results	N/A	W24x62 t = 0.59	3.56	0.725
		W36x150 t = 0.94	2.17	0.685

An exponential plot for peak tension to peak compression strain range versus average fracture initiation cycles for the W24x62 and W36x150 for the cyclic bend tests is shown in Figure 5.37. Material thickness is directly related to the cycles of failure while applying constant strain for cyclic bend tests. To have a better understanding of this relation more material thickness and different roller diameters needs to be tested and validated so we can compare the strain range number of cycles in which fracture initiates. The reason for using an exponential function to fit the two data points instead of a linear function is because the exponential curve simulates a coffin-manson relationship.

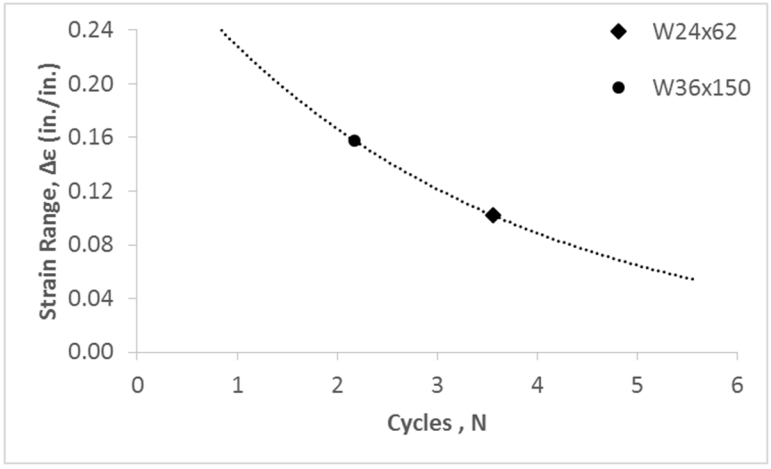


Figure 5.37 – Strain range for extreme fiber versus number of cycles to fracture initiation for a roller diameter of 11 in.

CHAPTER 6 FRACTURE BEHAVIOR OF FULL-SCALE MOMENT CONNECTION TESTS

6.1 Introduction

The testing program is briefly described for full-scale moment connection tests conducted previously by Eatherton et al. (2013). Also, a discussion about the strain gages and how they are used to provide "strain line" profiles at different locations to compare and measure strain concentrations due to PAFs and puddle welds. Finally, fracture analysis of the fracture surfaces is discussed for all of the twelve specimens.

6.2 Full-Scale Special Moment Resisting Frames (SMRF) Tests

Twelve full-scale experiments were conducted on moment resisting frame connections as shown in Figure 6.1. The full-scale tests produced key data for validation of the proposed fracture prediction framework since specimens included puddle welds and powder actuated fasteners. All twelve full-scale tests layout with the types of artifacts and their spacing is presented in Figure 6.2, and the test matrix with the artifact type in the protect zone is presented in Table 6.1.

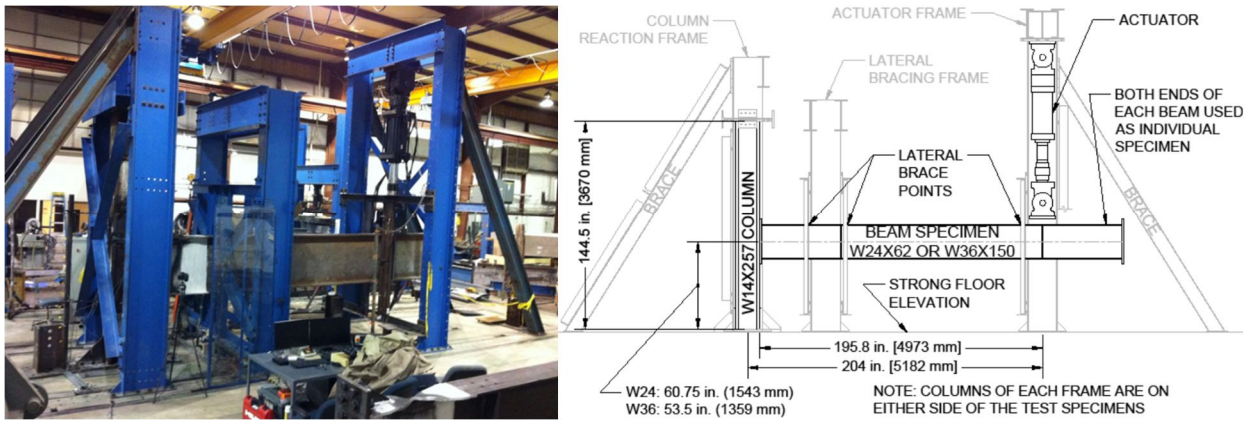


Figure 6.1 – Full-scale testing setup of moment connections.

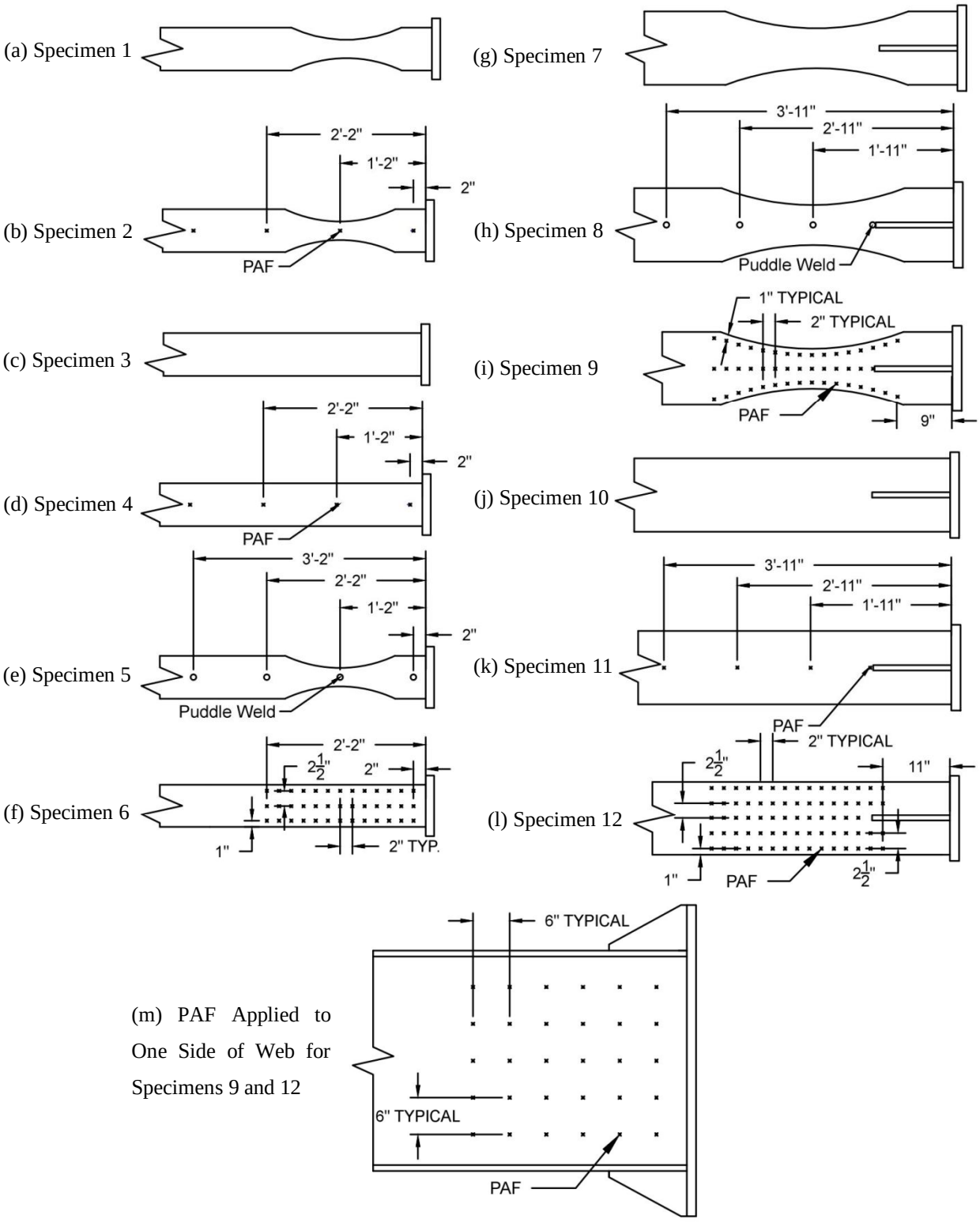
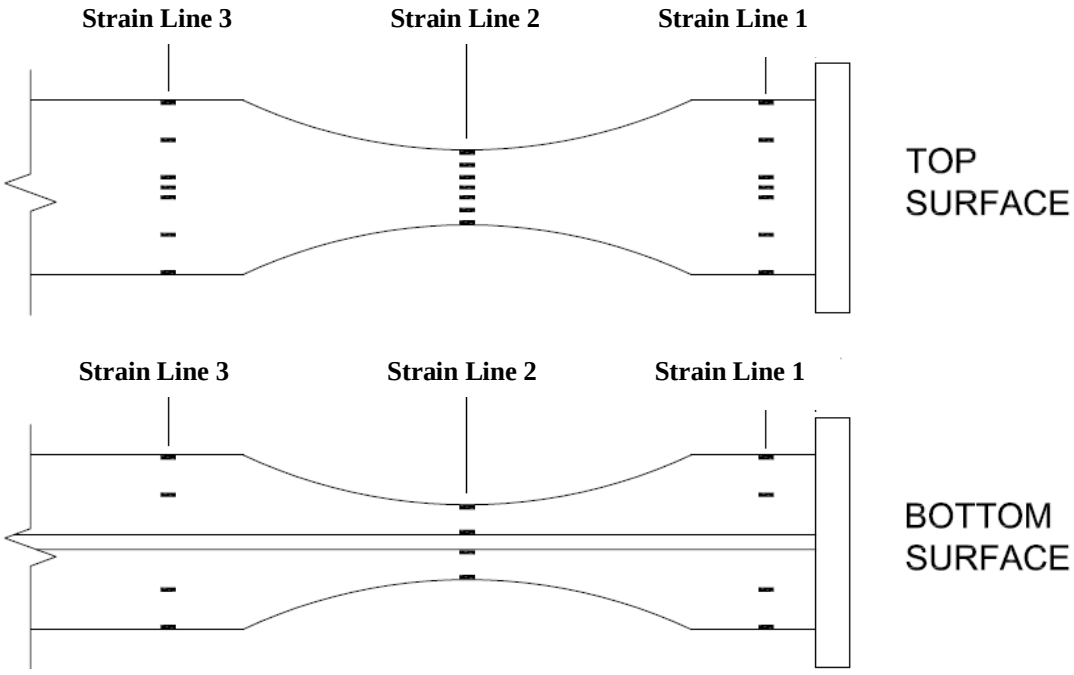


Figure 6.2 – Layout of fasteners for the 12 specimens.

Table 6.1 – Full-scale tests test matrix.

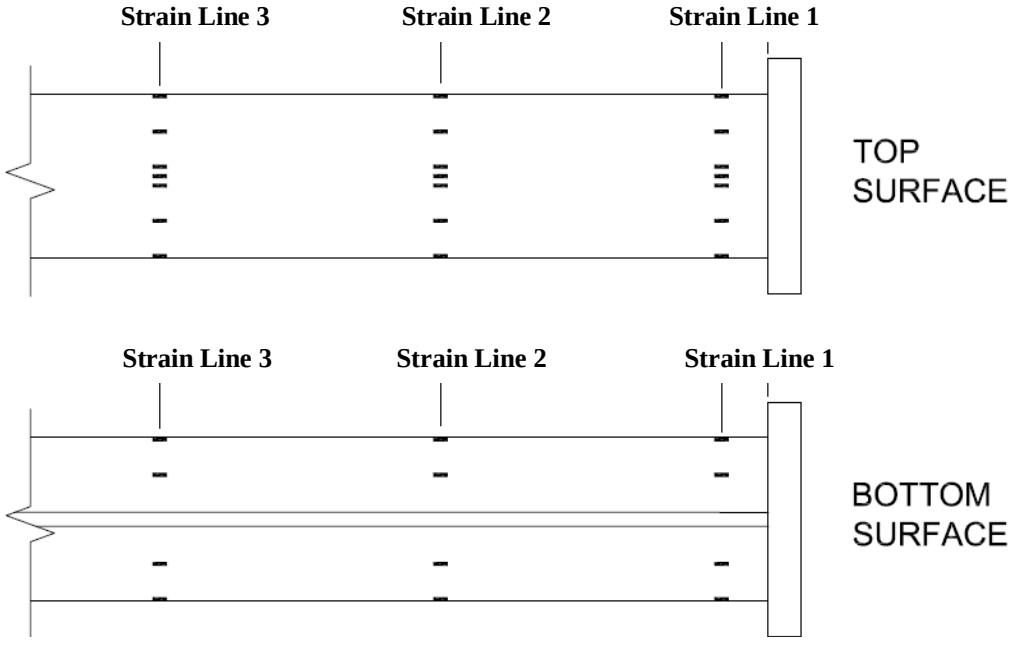
Specimen Number	Specimen Name	Beam Size	Connection Type	Artifact Type in the Protected Zone
1	RBS24	W24x62	RBS	No Artifact
2	RBS24-PAF12	W24x62	RBS	4 PAF @ 12"
3	W24	W24x62	BUEEP	No Artifact
4	W24-PAF12	W24x62	BUEEP	4 PAF @ 12"
5	RBS24-PW12	W24x62	RBS	4 PW @ 12"
6	W24-PAF_ARRAY	W24x62	BUEEP	Grid of PAF
7	RBS36	W36x150	RBS	No Artifact
8	RBS36-PW12	W36x150	RBS	4 PW @ 12"
9	RBS36-PAF_ARRAY	W36x150	RBS	Grid of PAF
10	W36	W36x150	BSEEP	No Artifact
11	W36-PAF12	W36x150	BSEEP	4 PAF @ 12"
12	W36-PAF_ARRAY	W36x150	BSEEP	Grid of PAF

Strain gages were attached along lines at the top and bottom of the top flange for both the RBS and non-RBS specimens at the protected zone for all of the twelve specimens. The intention of placing these strain gages is to provide “strain line” profiles at different locations to compare and measure strain concentrations due to PAFs and puddle welds. A typical strain gage layout for the RBS and non-RBS specimens is shown in Figure 6.3 and Figure 6.4. For the first six test it was noticed that the effect of PAFs and puddle welds were negligible. Based on those results only two strain gage lines were used for the W36 specimens instead of three strain gage lines used for the W24 specimens.



Note: For W36x150 RBS Specimens, Only Strain Line 1 and 2 Were Used

Figure 6.3 – Top and bottom of top flange of RBS specimens typical strain gage layout.



Note: For Specimens 10 and 11, Only Strain Line 1 and 2 Were Used

Figure 6.4 – Top and bottom of top flange of non-RBS specimens typical strain gage layout.

Figure 6.5 and Figure 6.6 shows a constant increase in strain as the story drift increases during the elastic cycles for a W24 and W36 specimen. Flange local buckling and deformation at the top flange can be clearly noticed after the strain profile starts deforming non-consistently. Figure 6.5 presents Specimen 3, non-RBS W24 specimen, strain data at strain line 1 through 3. Strain line 1 shows higher strain than strain line 2 which means that there is a higher potential for a fracture to occur in the region of strain line 1. Strain line 3, which is located further from the column connection, shows a more uniform strain gradient compared strain line 2 and 1 which are closer to the columns connection respectively. Figure 6.6 presents Specimen 12, non-RBS W36 specimen, showing a different behavior for the strain data compared to Specimen 3, non-RBS W24 specimen. Strain line 2 shows higher strain than strain line 1. Also, the W36 specimen exhibited larger strains than the W24 specimen. This due to the larger distance from the extreme fiber to the neutral axis. Surface fracture initiation for the W36 sections can be related to the high strains at the flange surface. The fracture study is discussed in depth in the following section for all of the failed specimens.

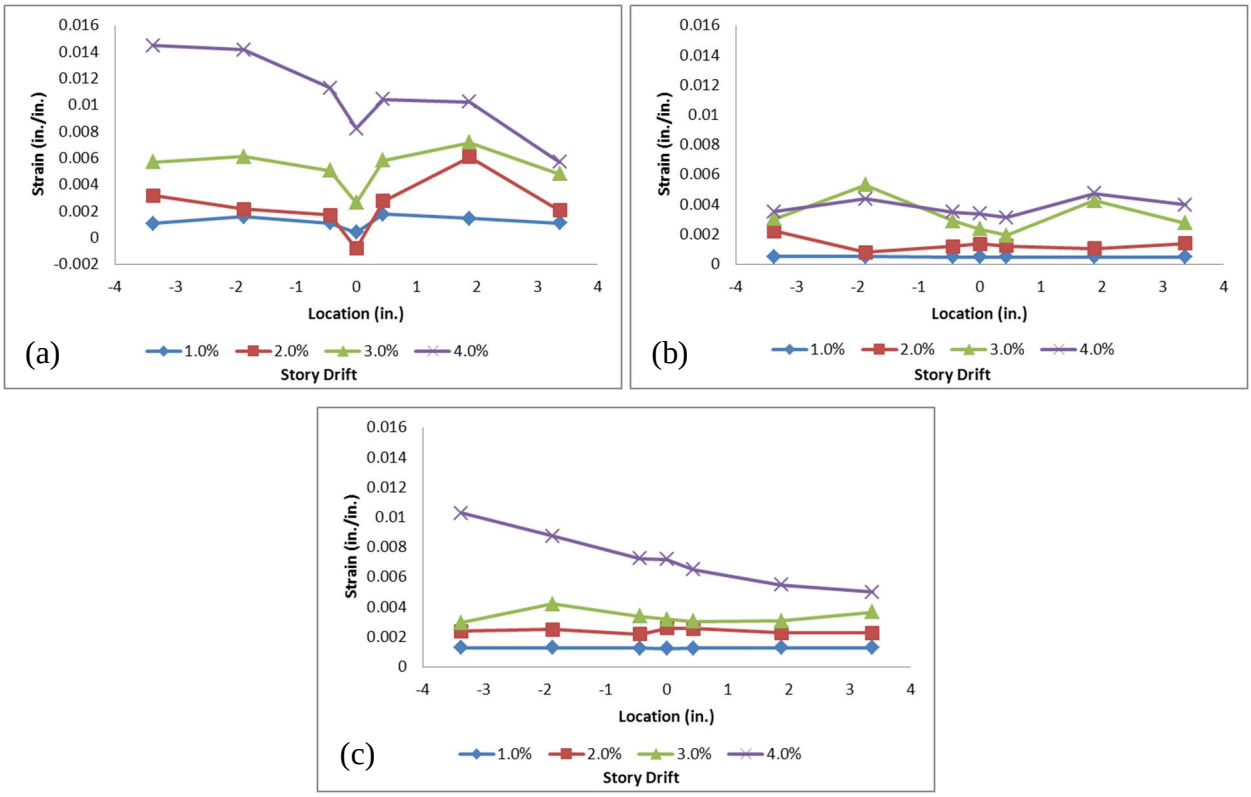


Figure 6.5 – Top Flange Strain Gradient for Specimen 3 (W24x62 without RBS or Fasteners) (a) Line 1, (b) Line 2, and (c) Line 3.

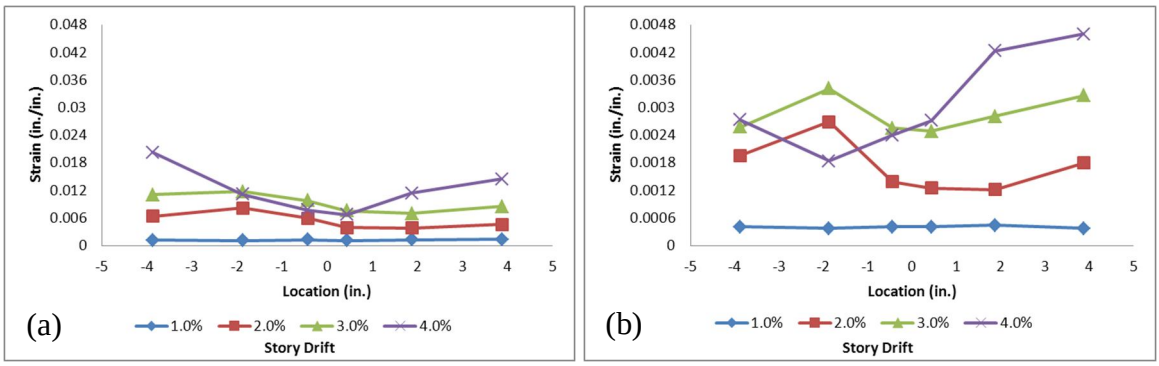


Figure 6.6 – Specimen 12 (W36x150 with No RBS and Grid of PAFs) Top Flange Strain Data (a) Line 1, and (b) Line 2.

A comparison for three W36 non-RBS specimens (Specimen 10, 11 and 12) strain data is shown in Figure 6.7. Specimen 10 contains no fasteners, Specimen 11 contains PAF spaced at 12 in., and Specimen 12 contains a grid of PAF. It was not possible to place strain gages at the center

of strain line 2 for Specimens 11 and 12 because a PAF was located in this location. This made it not possible to collect data at the actual location of the PAF but strain gages were placed closely on each side of the PAF. Each of the three specimens shown in Figure 6.7 had a unique strain profile as local buckling developed during the inelastic cycles. However, the inelastic strains were not found to concentrate in the vicinity of PAF or puddle welds.

Strain gages are useful in many applications but the can be unreliable for large inelastic strain cyclic loading. The reason is that strain gages a prone to delaminate from steel and loss of electrical continuity leading to loss of signal. All of the strain gradient plots for the twelve specimens are included in APPENDIX E. Similar trends can be seen for all twelve specimens.

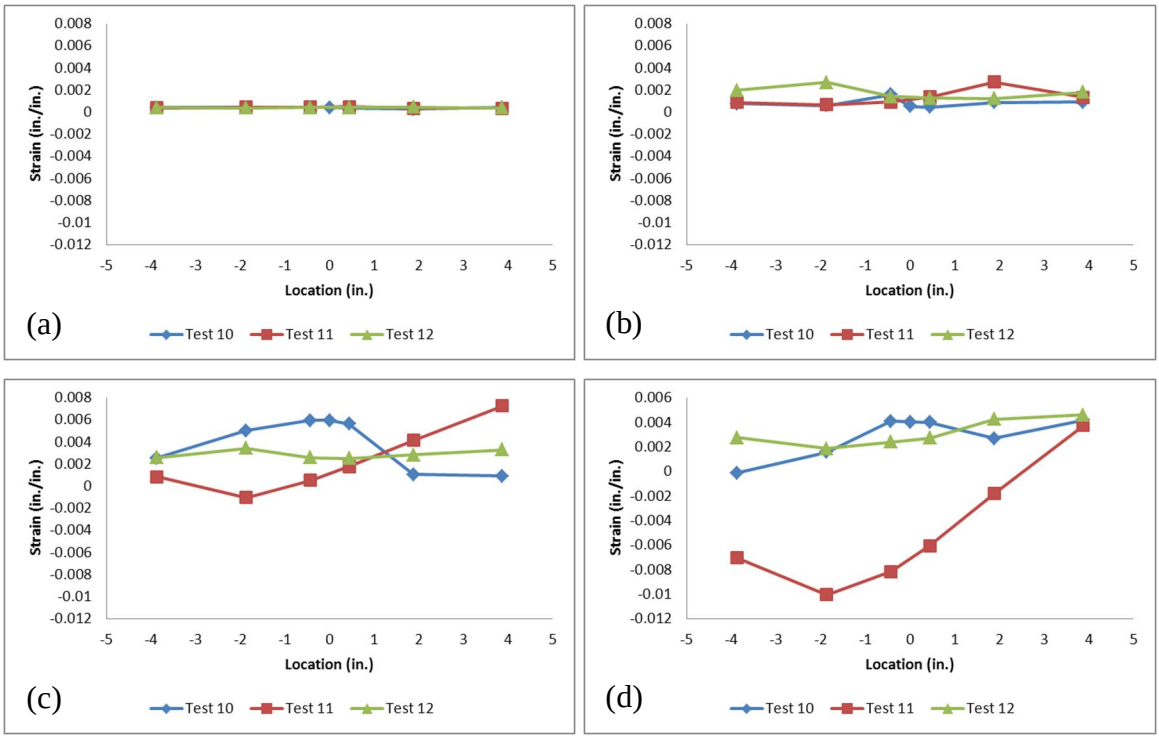


Figure 6.7 – W36x150 (Specimen 10, 11 and 12) Top Flange Strain Data Line 2 at (a) 1% Story Drift, and (b) 2% Story Drift, (c) 3% Story Drift, and (d) 4% Story Drift

6.3 Full-Scale Tests Results and Fracture Study

This section will focus on the analysis of the fracture surfaces. For further details of the testing program and associated results are presented in Eatherton et al. (2013) and are not repeated here except as necessary. All of the twelve specimens satisfied the qualification criteria for SMRF which states that the specimen must sustain a moment capacity at the face of the column that is at least 80% of the nominal plastic moment capacity during one complete cycle at 4% story drift. Although all of the specimens qualified and completed at least one full cycle of 4.7% story drift, fracture initiation was noticed at earlier inelastic story drifts before completing one complete cycle at 4% story drift.

6.3.1 Behavior of W24x62 Specimens with RBS

Specimen 1: W24x62 with RBS and No Fasteners

Specimen 1 served as the control test for the W24x62 specimens with RBS connections, PAFs or puddle welds were not present. The specimen completed two cycles of 4% story drift while maintaining a moment greater than 80% of the nominal plastic moment capacity. An overall picture of the protected zone before and after testing is shown in Figure 6.8.

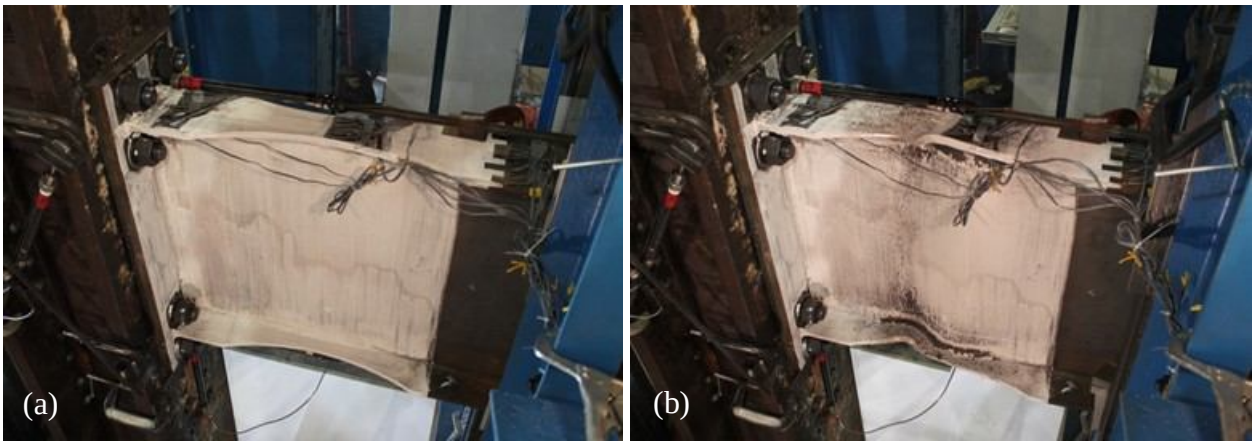


Figure 6.8 – Angled view of Specimen 1 (W24x62 with RBS) (a) before, and (b) after testing.

Crack initiation occurred at the middle of the reduced beam section at different locations of the bottom flange tip during the second cycle at 4.7% story drift. There were visible notches

and internal cracking at the flange tip, and the edge of the flange exhibited multiple failure origins at both sides of the bottom flange as shown in Figure 6.9. It is expected that these cracks were associated with large compressive plastic deformation, since they are at the compression side of the flange local buckle. Also, the crack initiation at the flange tips can be related to minor surface scratches caused by cutting and handling the RBS before testing. During the second cycle at 4.7% story drift, a ductile tear propagating from the tip of the bottom flange toward the middle of the flange, as shown in Figure 6.10, caused significant loss in strength. The propagation of the tear was not sudden, but instead a gradual, ductile process. Crack initiation was noted in several other locations typically initiating on the inside surface of local buckles at the flange tips where the greatest inelastic compressive strains due to local buckling had occurred. Although fracture initiation occurred at multiple locations at the bottom flange, fracture propagated primarily from one side leading to brittle fracture through half of the flange width and stopping at the web.

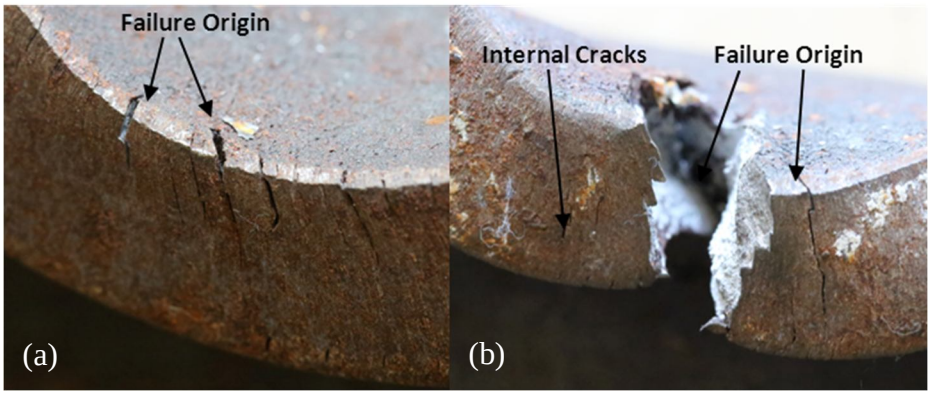


Figure 6.9 – Crack initiation at two different locations on both sides of the bottom flange. (a) Crack and fracture initiation, and (b) crack initiation at other side of the flange.



Figure 6.10 – Fracture propagation at flange surface.

Specimen 2: W24x62 with RBS and PAFs at 12 in.

Specimen 2 contained four PAFS spaced at 12 in. along the center of the top flange. Brittle fracture occurred through the top flange during the second cycle of 4.7% story drift after the qualification criteria was satisfied. The fracture occurred at the location were the minimum flange width at the RBS cut and also at the location were the second PAF which is spaced 14 in. from the endplate. An overall picture of the protected zone before and after testing is shown in Figure 6.11.

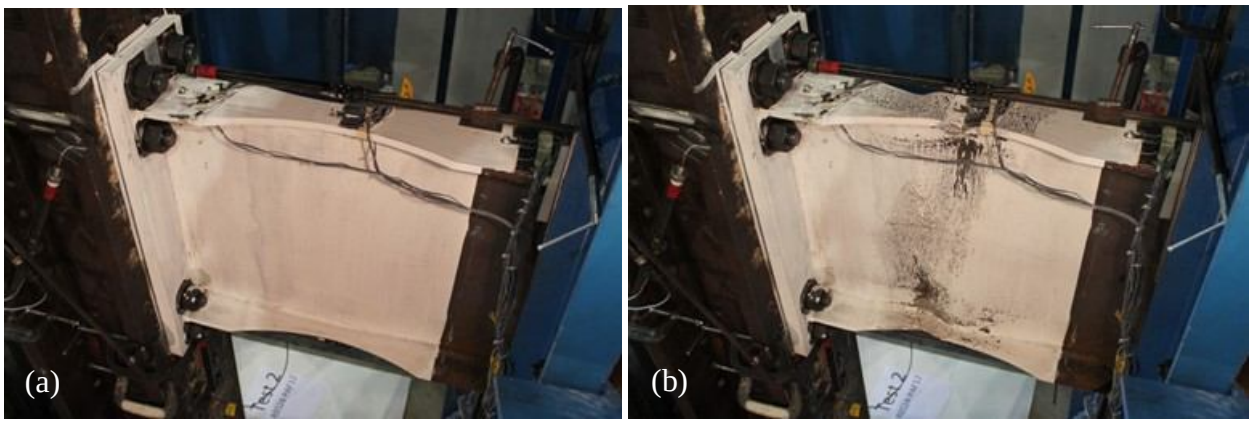


Figure 6.11 – Angled view of Specimen 2 (W24x62 with RBS and PAF at 12 in.) (a) before, and (b) after testing.

The fracture surface was analyzed to determine the location of crack initiation, direction of fracture propagation and the nature of the fracture process. Crack initiation occurred at the center of the reduced beam section at one side of the flange. There were visible notches and internal cracking at the flange tip. It is expected that these defects were related to surface scratches caused by cutting and handling the RBS before testing since they were observed only at one side of the top flange. The other side of the top flange did not show signs of notches and internal defects. The edge of the flange exhibited multiple failure origins as shown in Figure 6.12. This can also be illustrated by the smooth shiny texture at the tip of the fractured flange as shown in Figure 6.13 and Figure 6.14. The smooth shiny texture is suspected to be due to the rubbing of the crack during cyclic loading combined with a slow crack growth.

Non-uniform fatigue striations with smooth shiny texture were observed to be related to the last five cycles of the fatigue crack propagation before failure. The fatigue striations are numbered in Figure 6.13 and Figure 6.15 based on their sequence. The first striation, shown in Figure 6.14, had a different texture from the next four striations associated with a ductile overload fracture mode. The increase in flange thickness at the fillet caused more rubbing during cycles with local flange buckling, leading to the visual striations as shown in Figure 6.15.

Penetration of the PAF caused plastic displacement of the base material during installation. When the crack reached the plastically deformed area around the PAF, the section ruptured. The fracture mode was brittle overload. This type of failure occurs by rapid crack propagation with less expenditure of energy than in ductile fractures and without appreciable gross plastic deformations. The brittle overload fracture showed chevron marks pointing back to the fracture origin with coarse texture which can be seen in Figure 7.3b. Also, partial shear lips were observed on the edge where the brittle overload occurred and this shows that there was some ductility.

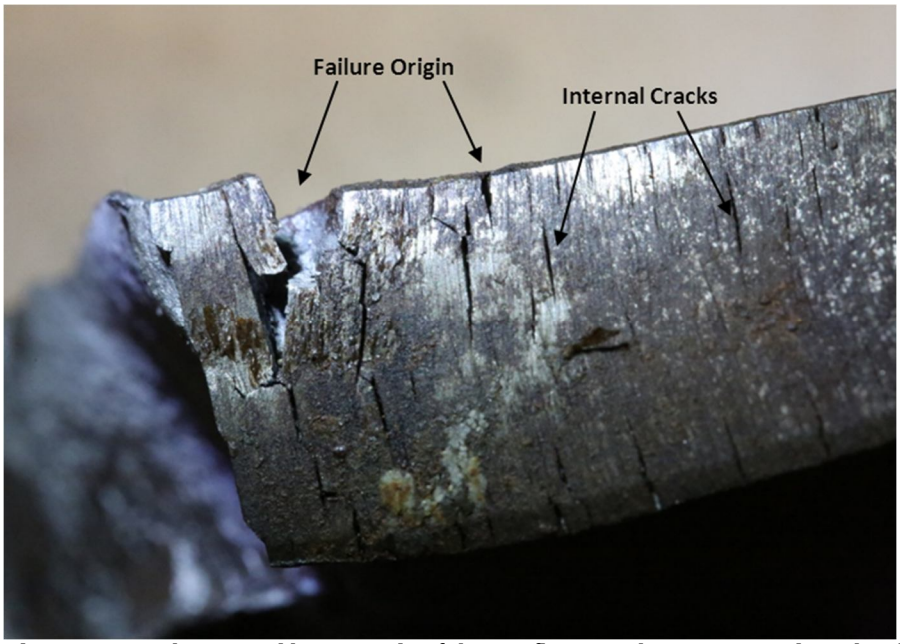


Figure 6.12 – Failure origin in the top and bottom side of the top flange with some internal cracks, this was noticed only on one side of the top flange.

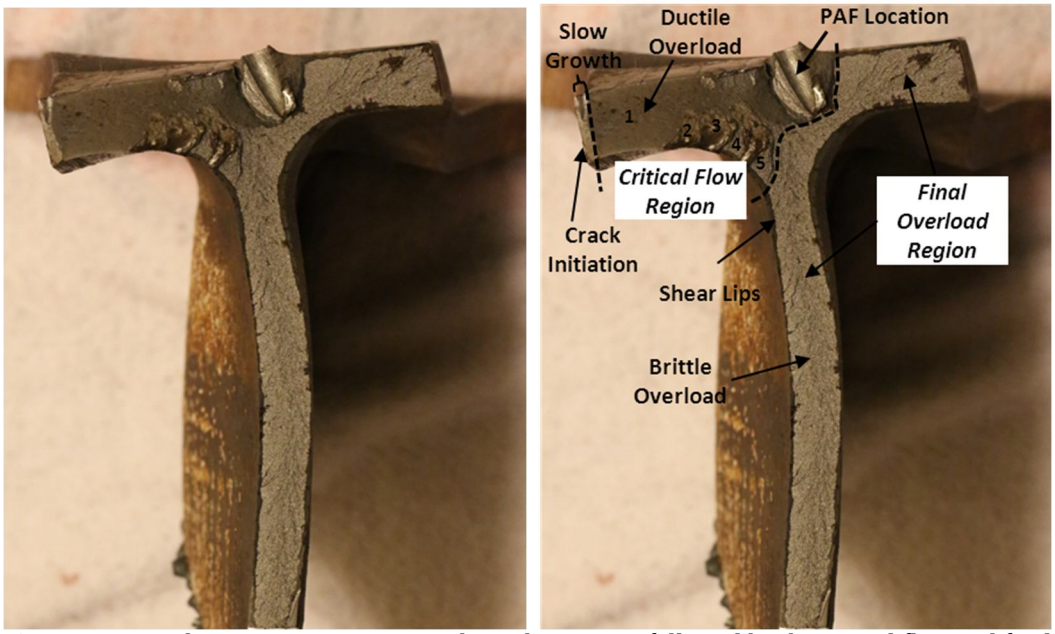


Figure 6.13 – Fatigue crack propagation starting with crack initiation followed by the critical flow and final overload regions.

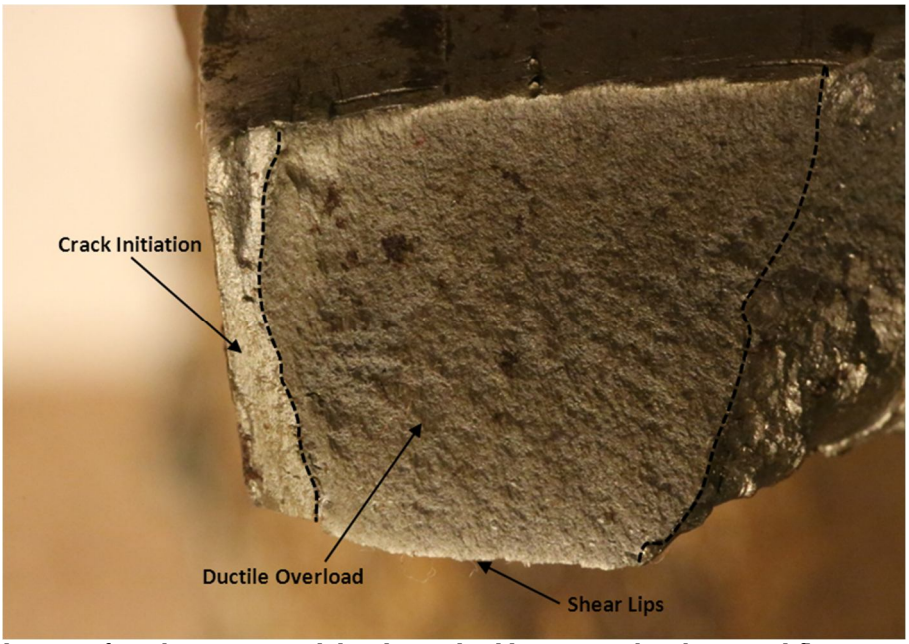


Figure 6.14 – Close-up of crack initiation and ductile overload location within the critical flow region, which shows two different surface textures and the striations.

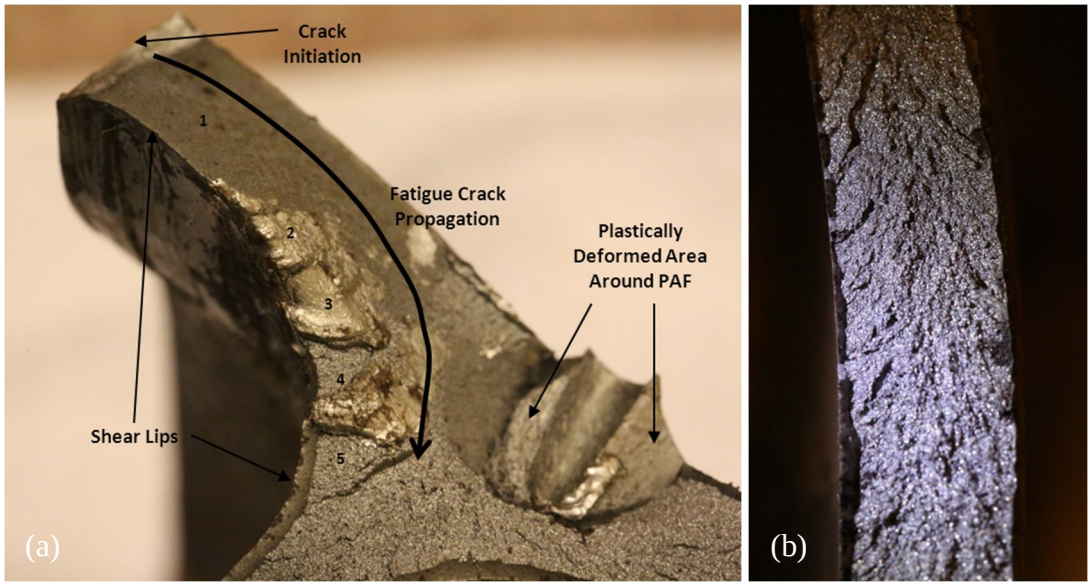


Figure 6.15 – (a) Close-up of striation locations and fatigue crack propagation and (b) chevron markings at the web pointing back to the fracture origin due to the brittle overload fracture mode.

Specimen 5: W24x62 with RBS and Puddle Welds at 12 in.

Specimen 5 included puddle welds on the top flange at 12 in. spacing. Brittle fracture of the bottom flange and several inches of the adjacent web occurred after the qualification criteria was satisfied during the third full cycle of 4.7% story drift. The fracture similarly as that of Specimen 2 in which the brittle fracture occurred after the bottom flange underwent the half cycle in compression and was beginning to be pulled into tension. Figure 6.17 shows the fracture of Specimen 5. Apart from the fracture, cracks were observed in the flange tips at the inner surface of local buckles as occurred with Specimens 1 and 2. An overall picture of the protected zone before and after testing is shown in Figure 6.16.

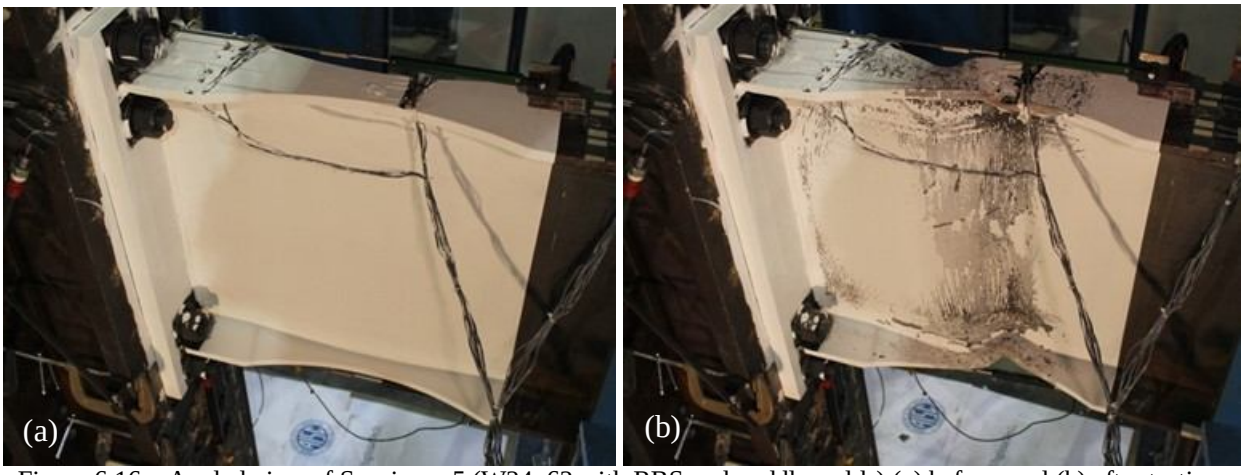


Figure 6.16 – Angled view of Specimen 5 (W24x62 with RBS and puddle welds) (a) before, and (b) after testing.

Crack initiation occurred at the center of the reduced beam section at different locations of the bottom flange away from the puddle welds during the third cycle at 4.7% story drift. There were visible notches and internal cracking at the flange tip and at the flange surface near the flange tip, and the edge of the flange exhibited multiple failure origins as shown in Figure 6.18. It is expected that these cracks were associated with the compressive plastic deformation, since they are at the compression side of the flange local buckle. Another factor for the crack initiation at the flange tips can be related to surface scratches caused by cutting and handling the RBS before testing since they were observed only at one side of the bottom flange.

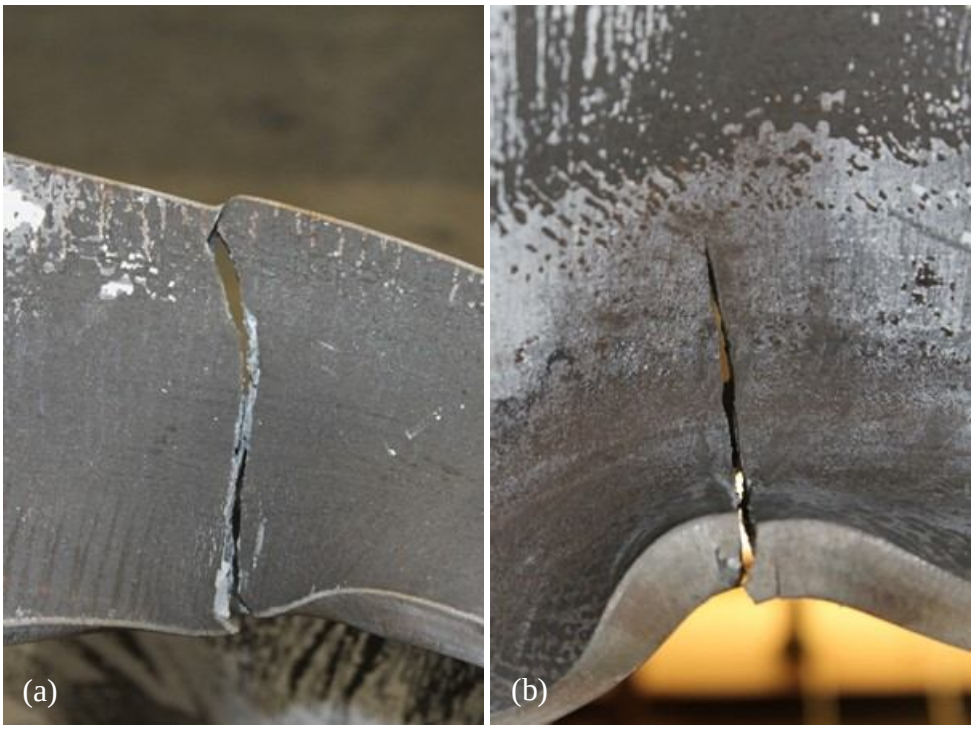


Figure 6.17 – Fracture of the bottom flange and web (a) bottom view, and (b) side view.

The other side of the bottom flange did not show significant signs of external notches and crack initiation at the flange tips and did not show any sign of visible notches or internal cracking at the top flange as the other side. There were signs of smooth shiny texture at the tip of the fractured flange as shown in Figure 6.19. The smooth shiny texture is suspected to be due to the rubbing of the crack during cyclic loading combined with a slow crack growth. Non-uniform fatigue striations with smooth shiny texture were observed to be related to the last two cycles of the fatigue crack propagation before failure. The fatigue striations are numbered in Figure 6.19 and Figure 6.20 based on their sequence.

The fracture mode was brittle overload which initiated as shown in Figure 6.19 and Figure 6.20. This type of failure occurs by rapid crack propagation with less expenditure of energy than in ductile fractures and without appreciable gross plastic deformations. The brittle overload fracture showed chevron marks pointing back to the fracture origin with coarse texture which can be seen in Figure 6.19 and Figure 6.20. Also, partial shear lips were observed on the edge where the brittle overload occurred and this shows that there was some ductility.

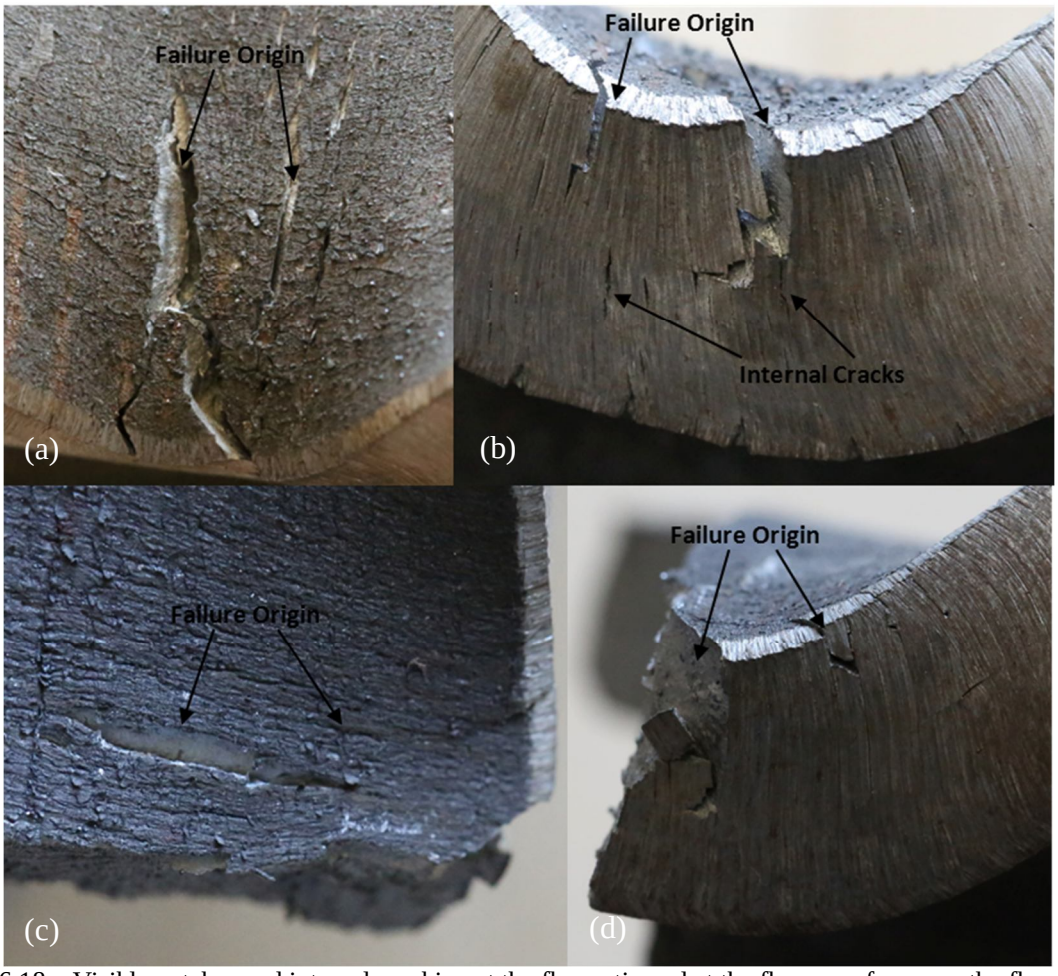


Figure 6.18 – Visible notches and internal cracking at the flange tip and at the flange surface near the flange tip at two different locations. (a) Surface view (b) and side view of the bottom flange with crack initiation. (c) Surface view (d) and side view of the bottom flange near the fractured area.

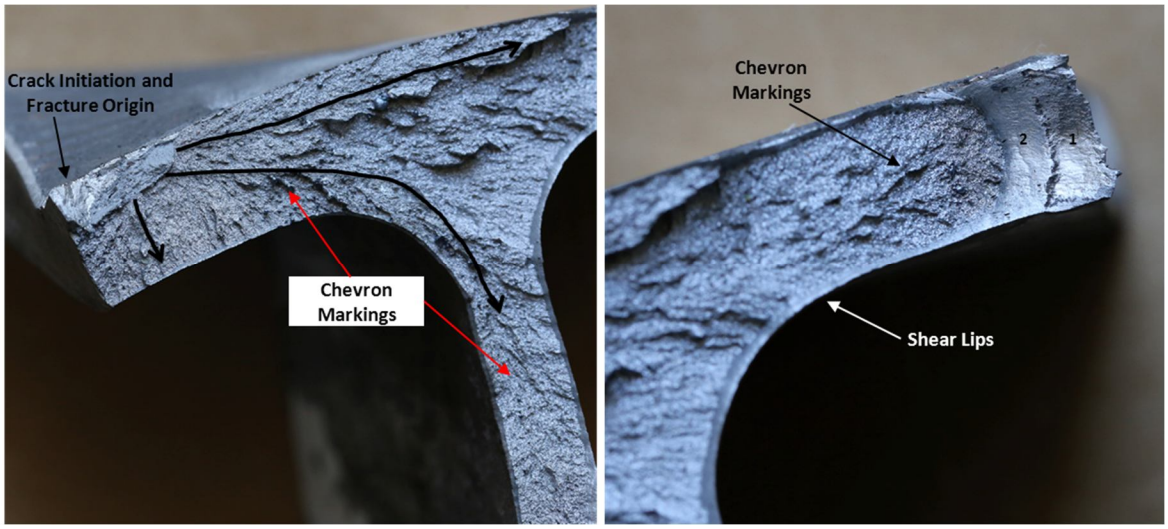


Figure 6.19 – (a) Close-up of crack initiation and fracture origin with chevron marking pointing back to the fracture origin due to the brittle overload fracture mode, and (b) close-up of striation locations at the other side with chevron markings pointing back to the fracture origin.

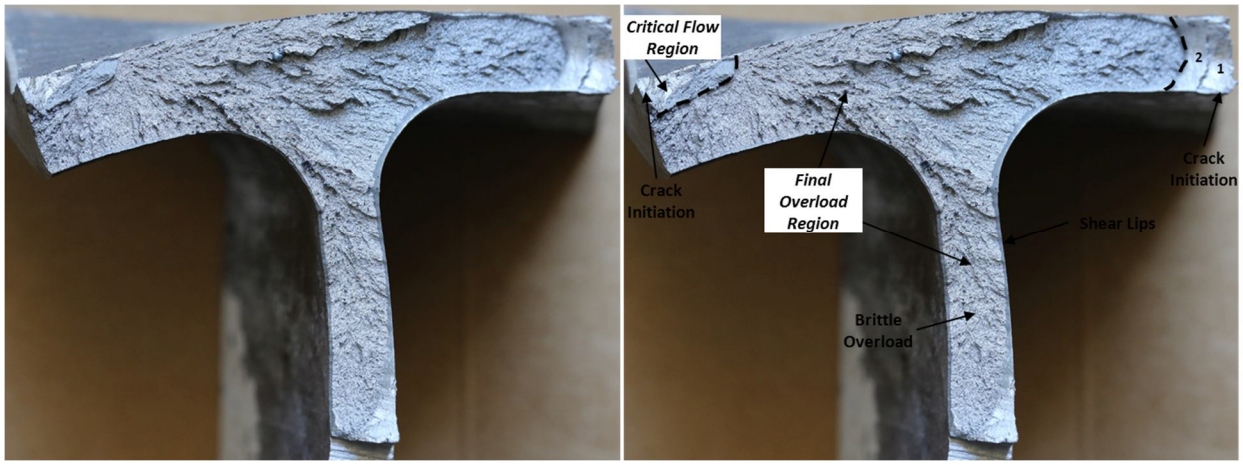


Figure 6.20 – Fatigue crack propagation starting with crack initiation at two locations followed by the critical flow and final overload regions. (a) Unmodified photograph, and (b) labeled photograph.

6.3.2 Behavior of W24x62 Specimens with RBS

Specimen 3: W24x62 with No RBS and No Fasteners

Specimen 3 served as the control test for the W24x62 specimens with no RBS connections, PAFs or puddle welds were not present. The specimen completed two cycles of 4% story drift

while maintaining a moment greater than 80% of the nominal plastic moment capacity. Since there were no signs of cracks or fracture with some degradation in the strength compared to the RBS specimens, the test was terminated after two cycles of 4.7% story drift. An overall picture of the protected zone before and after testing is shown in Figure 6.21.

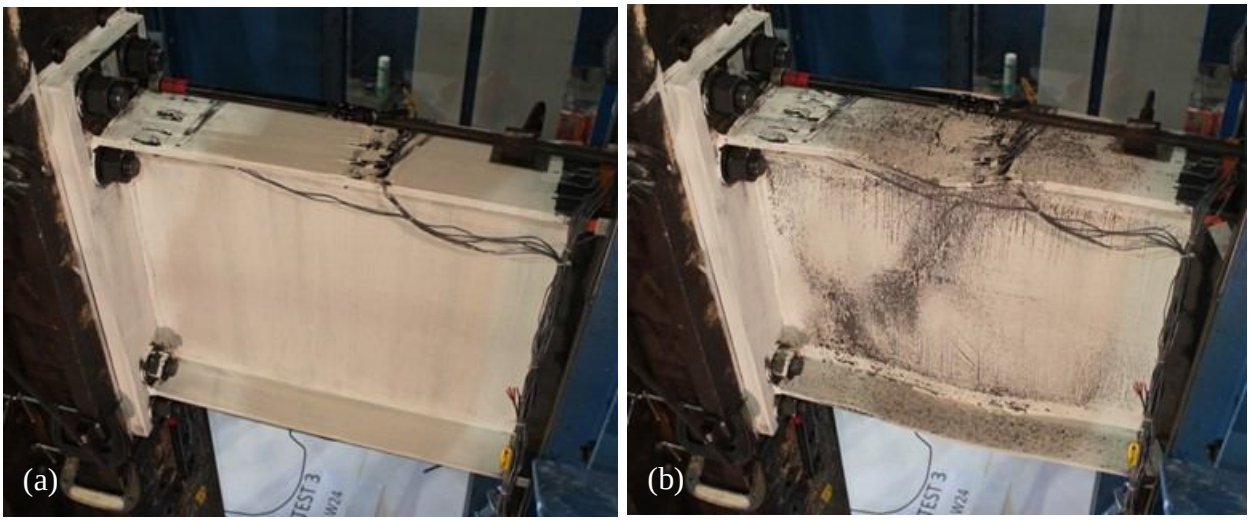


Figure 6.21 – Angled view of Specimen 3 (W24x62 with no RBS) (a) before, and (b) after testing.

Specimen 4: W24x62 with No RBS and PAFs at 12 in.

Specimen 4 contained four PAFS spaced at 12 in. along the center of the top flange, similar to Specimen 2. The qualification criteria was satisfied with no signs of cracks or fracture with some degradation in the strength compared to the RBS specimens, the test was terminated after two cycles of 4.7% story drift. An overall picture of the protected zone before and after testing is shown in Figure 6.22.

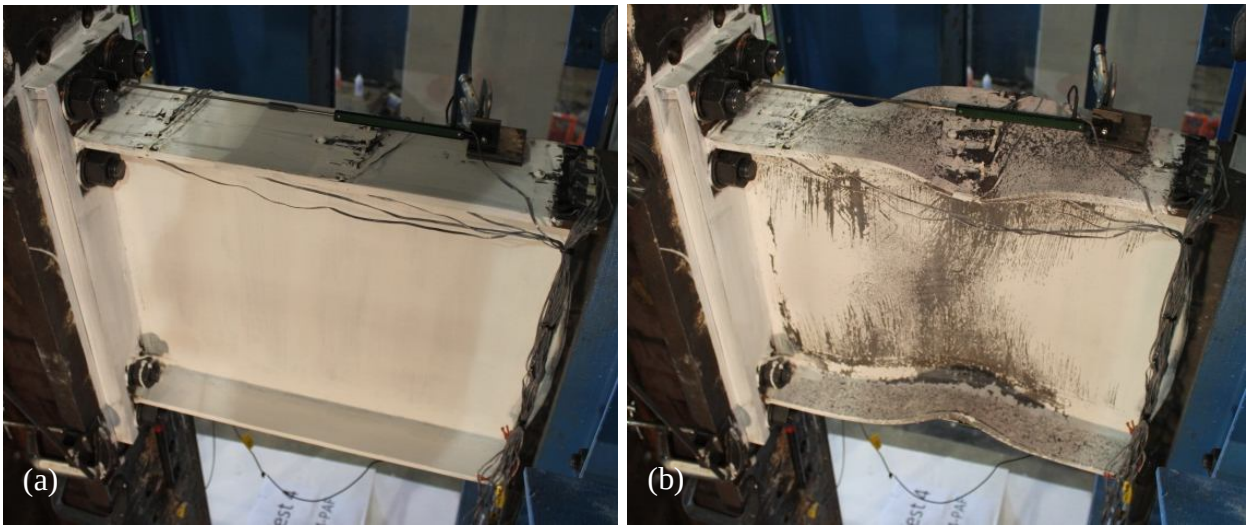


Figure 6.22 – Angled view of Specimen 4 (W24x62 with no RBS and PAF at 12 in.) (a) before, and (b) after testing.

Specimen 6: W24x62 with No RBS and Grid of PAFs

Specimen 6 contained an array of PAFs on both the top and bottom flange. The specimen maintained sufficient plastic moment capacity to pass qualification. After completing the first 4.7% story drift cycle, the applied moment fell below 80% of the nominal plastic moment capacity. Although the specimen was cycled with a total of five cycles at 4.7% story drift with strength degradation associated with local buckling, there was no significant loss in moment capacity associated with cracking initiating around several PAFs as shown in Figure 6.24. Some of those PAFs could be pulled easily which revealed small cracks around the PAFs holes. Those holes exhibited some stretching and elongation during cycling. Compared to the W24x62 RBS specimens, the fracture propagation was slow. An overall picture of the protected zone before and after testing is shown in Figure 6.23.

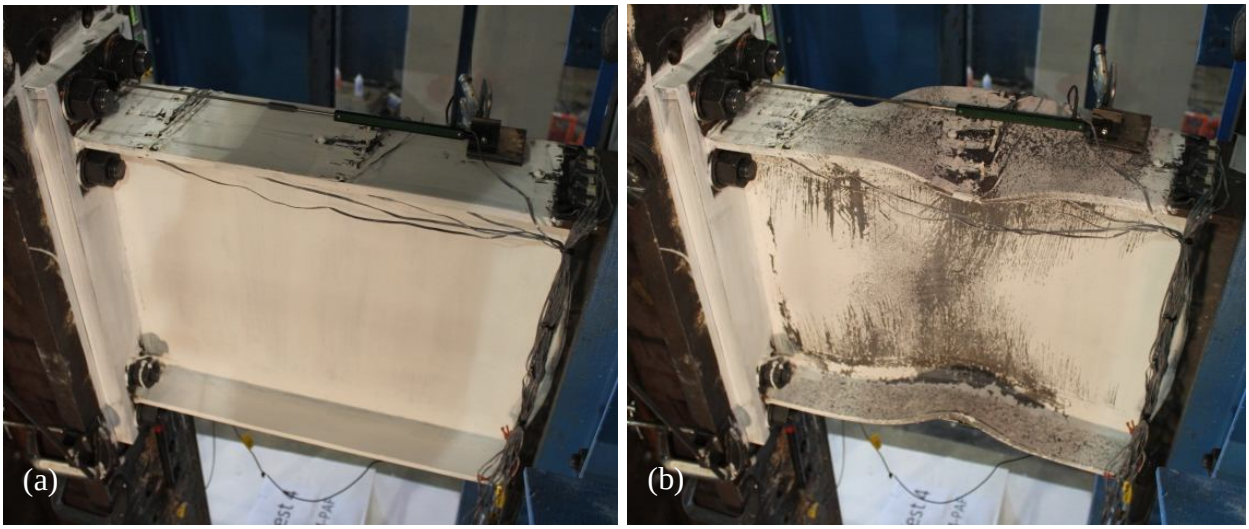


Figure 6.23 – Angled view of Specimen 4 (W24x62 with no RBS and grid of PAF) (a) before, and (b) after testing.

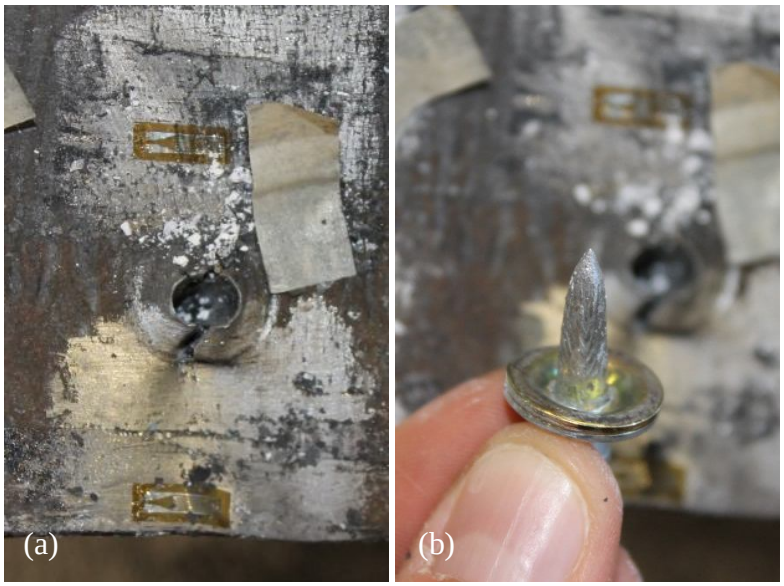


Figure 6.24 – An example of tearing around the PAF and a loose PAF.

6.3.3 Behavior of W36x150 Specimens with RBS

Specimen 7: W36x150 with RBS and No Fasteners

Specimen 7 served as the control test for the W36x150 specimens with RBS connections, PAFs or puddle welds were not present. The specimen completed two cycles of 4% story drift

while maintaining a moment greater than 80% of the nominal plastic moment capacity. An overall picture of the protected zone before and after testing is shown in Figure 6.25.

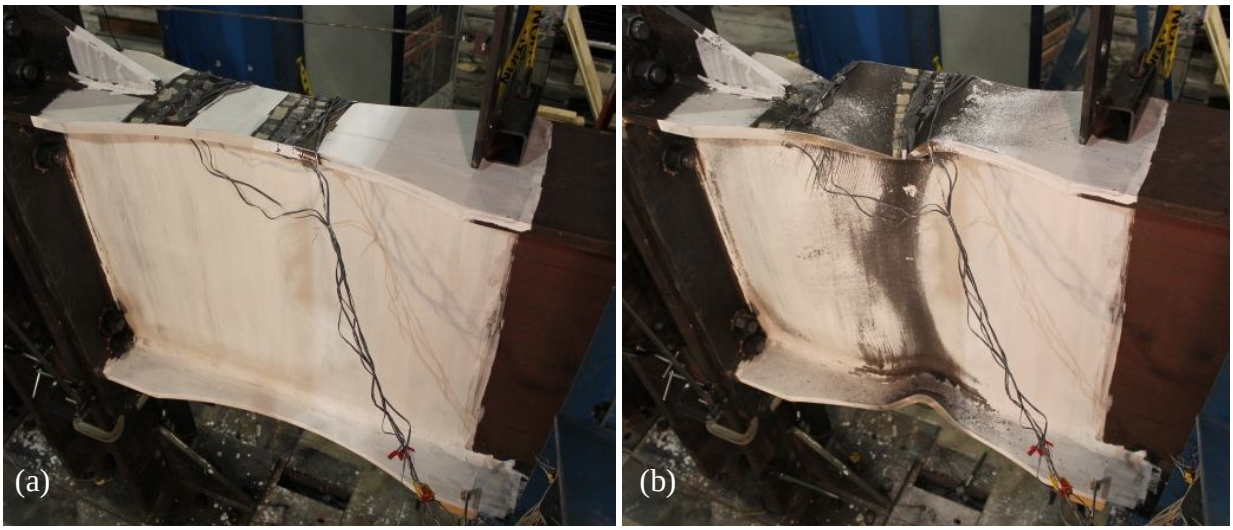


Figure 6.25 – Angled view of Specimen 7 (W36x150 with RBS) (a) before, and (b) after testing.

Multiple crack initiation locations were observed in Specimen 7 at different locations. They were located at the outer surface of the top and bottom flanges at the interior curvature of the local buckle, and at the top and bottom flanges at the weld metal at the junction of the toe of the end plates stiffeners. The crack initiation locations were noticed after the completion of the 4% story drift final cycle during the 4.7% cycle. After several cycles of 4.7% story drift, tearing was observed on the outer surfaces of both the top and bottom flange on the inside surface of local buckles (see Figure 6.26). These tears propagated during the half cycle in which the flanges were pulled in tension. The propagation was ductile and continued to propagate in width and through the depth of the flange as shown in Figure 6.27a. During the fifth cycle of 4.7% story drift, the specimen experienced a complete fracture of the top flange at the location of the RBS with multiple failure origins as shown in Figure 6.28. By this point, the tearing on the underside of the bottom flange was significant as well. In addition, tearing was observed on both top and bottom flanges at the junction of the endplate stiffeners to the flanges. It is expected that these cracks were due to the extreme compressive plastic loading, since they are at the compression buckled side of the flange due to the local flange buckling. Crack initiation was not noticed at the flange tips similar to the W24x62 RBS specimens. This can be related to polishing and smoothing the RBS edge

surface since scratches and dents were observed. While the other side of the top flange surface did not show any signs of crack initiation neither on the surface or the tip of the flange.

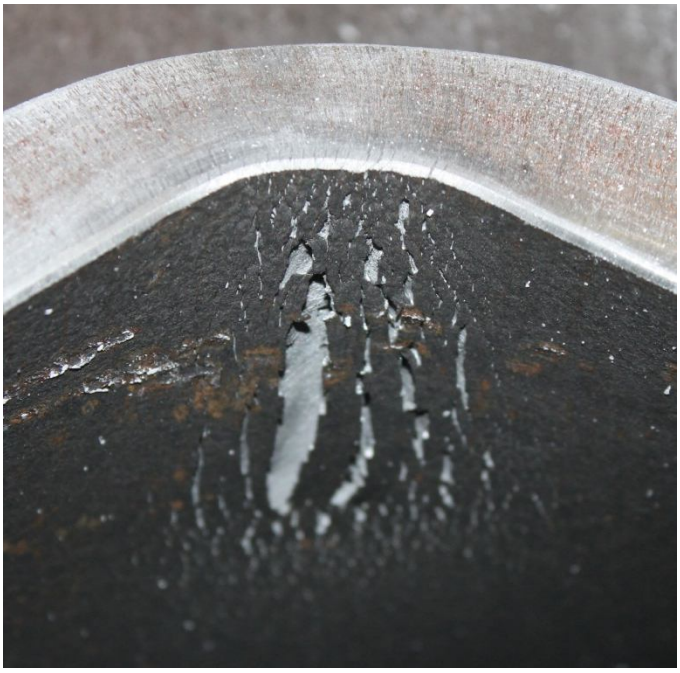


Figure 6.26 – Crack initiation on the surface of the bottom flange.

When the fracture surfaces were analyzed, the fracture mode was clearly brittle overload fracture which initiated as shown in Figure 6.29. This type of failure occurs by rapid crack propagation with less expenditure of energy than in ductile fractures and without appreciable gross plastic deformations. There were signs of bright coarse dimpled texture under the crack initiation location which can be related to brittle fracture as shown in Figure 6.29. The brittle overload fracture showed chevron marks pointing back to the fracture origin with coarse texture which can be seen in Figure 6.29. Also, shear lips were observed on the edge where the brittle overload occurred and this shows that there was significant amount of ductility.

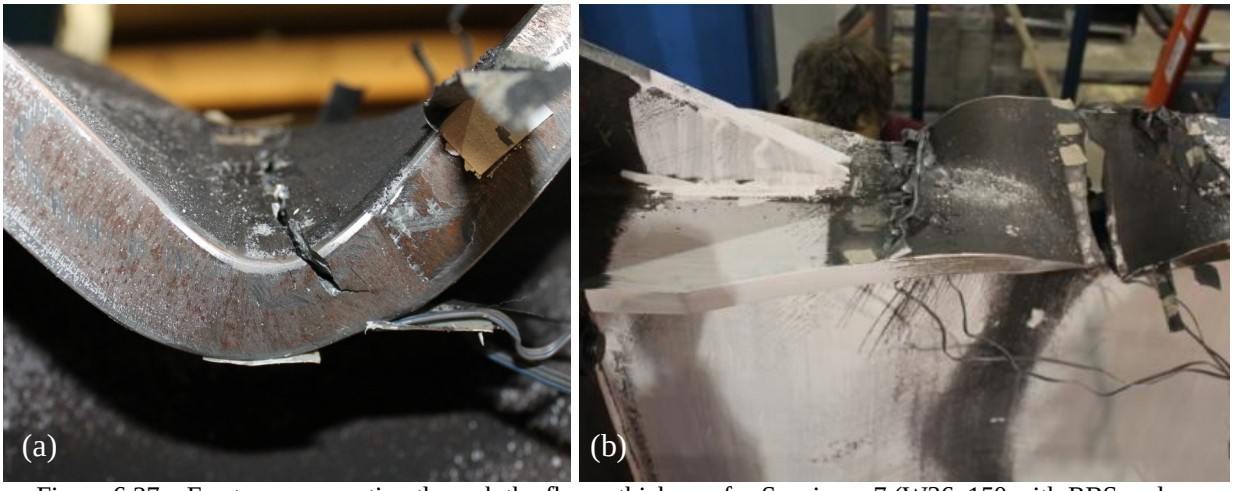


Figure 6.27 – Fracture propagation through the flange thickness for Specimen 7 (W36x150 with RBS and no fasteners) including (a) partial depth crack, and (b) final fracture through flange.

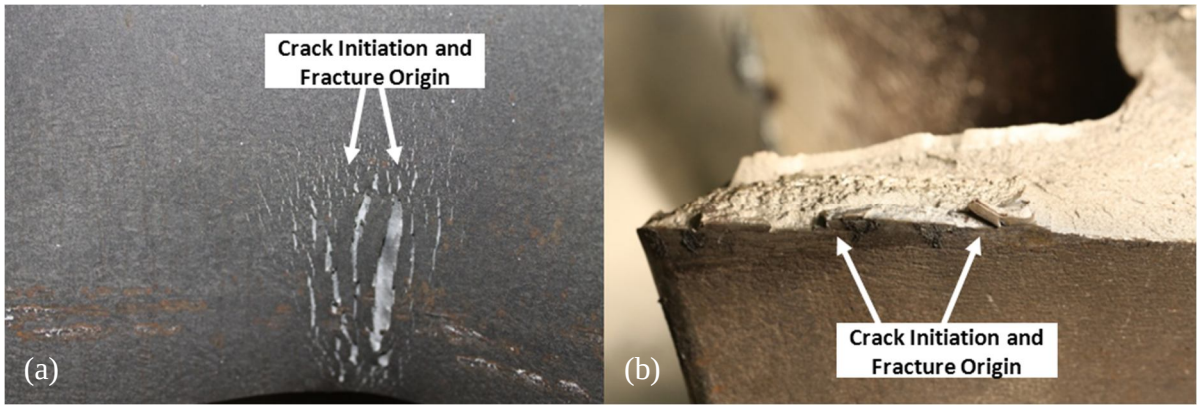


Figure 6.28 – (a) Crack initiation and failure origin in the top flange surface before fracture occurrence, and (b) after fracture occurrence of crack initiation and fracture origin location.

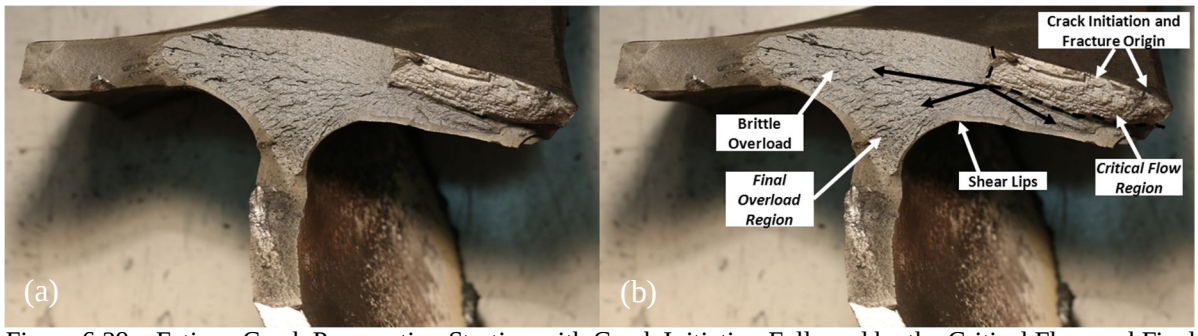


Figure 6.29 – Fatigue Crack Propagation Starting with Crack Initiation Followed by the Critical Flow and Final Overload Regions

Specimen 8: W36x150 with RBS and Puddle Welds at 12 in.

Specimen 8 was a W36x150 specimen with an RBS connection and puddle welds spaced at 12 in. along the top flange in the similar to Specimen 5. The specimen completed two cycles of 4% story drift while maintaining a moment greater than 80% of the nominal plastic moment capacity. Although during the 4% story drift tearing was observed at the junction between the end plate stiffener and the flange within the weld metal. However the specimen still passed qualifying requirements. An overall picture of the protected zone before and after testing is shown in Figure 6.30.

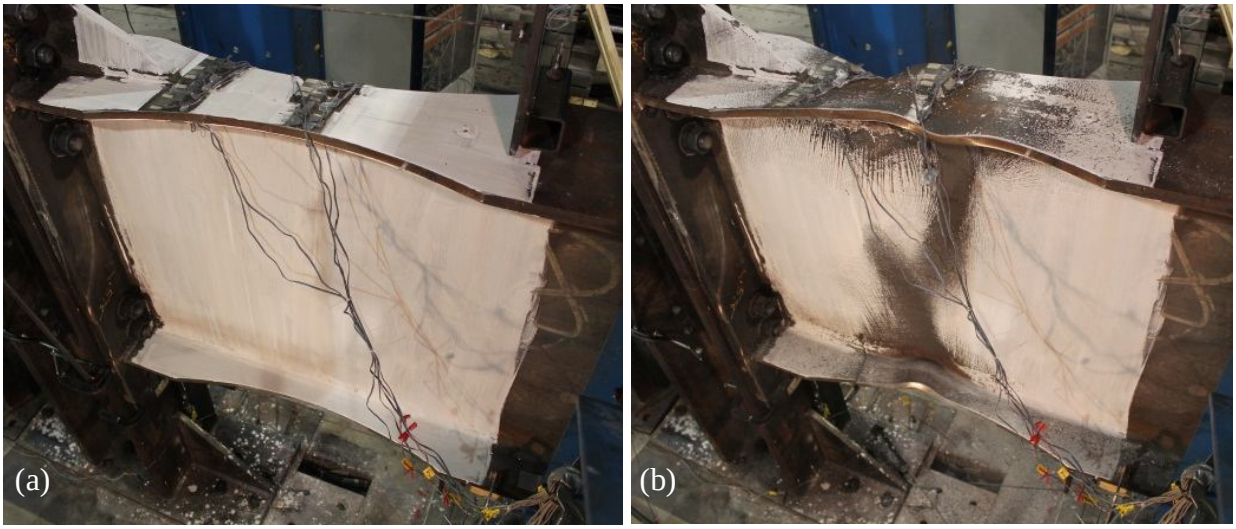


Figure 6.30 – Angled view of Specimen 8 (W36x150 with RBS and puddle welds) (a) before, and (b) after testing.

Tearing at the bottom flange stiffener weld metal propagated sufficiently to cause a complete fracture of the bottom flange at the location of the stiffener toe after completing the first 4.7% cycle. The fracture was related to the large stress triaxiality and plastic strains at the stiffener toe and it is unrelated to the puddle welds. Figure 6.31 shows the tearing at the top flange stiffener weld and the bottom flange fracture at the stiffener weld.

The fracture surface was and it was found that crack initiation occurred at the top and bottom flange at the weld metal at the junction of the toe of the end plates stiffeners during the 4%

story drift cycling, as shown in Figure 6.31. The location of the crack initiation is unrelated to the puddle welds, it is expected that these cracks were due to the high stress triaxiality and strain demand at the stiffener toe. Following the first cycle of 4.7% story drift the bottom flange fractured as shown in Figure 6.31. There were no signs of crack initiation noticed at other locations within the specimen.



Figure 6.31 – Cracks in Specimen 8 (W36x150 with RBS and puddle welds) including (a) initiation of crack at toe of stiffener weld to top flange, and (b) complete fracture at the bottom flange at the same location.

When the fracture was opened, it was clearly noticed that the fracture mode was brittle overload fracture that initiated at the weld metal at the junction of the toe of the end plates stiffeners as shown in Figure 6.32. This type of failure occurs by rapid crack propagation with less expenditure of energy than in ductile fractures and without appreciable gross plastic deformations. The brittle overload fracture showed chevron marks pointing back to the fracture origin with coarse texture that can be seen in Figure 6.32 and Figure 6.33. Also, partial shear lips were observed on the edge where the brittle overload occurred and this shows that there was some ductility.

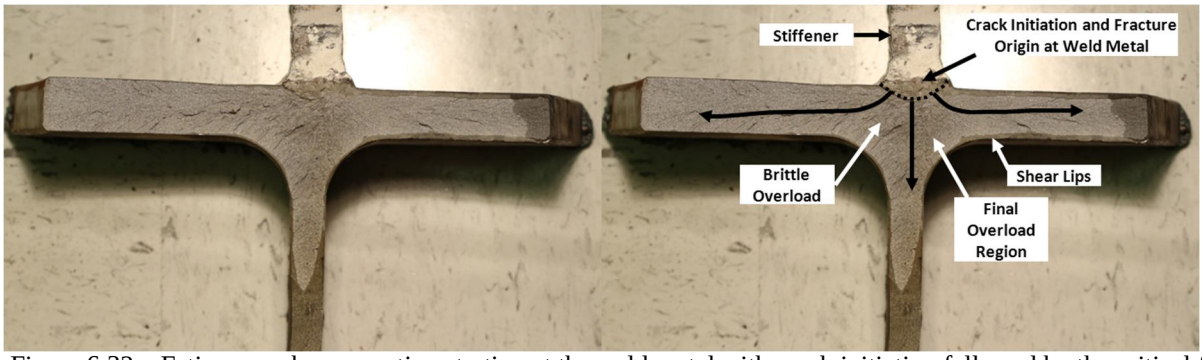


Figure 6.32 – Fatigue crack propagation starting at the weld metal with crack initiation followed by the critical flow and final overload regions.


Figure 6.33 – Close-up of chevron markings at the web and flange pointing back to the fracture origin at the weld metal of the stiffener due to the brittle overload fracture mode.

Specimen 9: W36x150 with RBS and Grid of PAFs

Specimen 9 was a W36x150 RBS specimen with a grid of PAFs. Although during the second cycle of 4% story drift, significant tearing was observed at the middle of the top flange RBS where one of the PAFs became dislodged as the hole enlarged during inelastic cycles as shown in Figure 6.35. However the specimen still passed qualifying requirements. Complete

fracture of the top flange occurred during the subsequent cycle which was the first cycle of 4.7% story drift. Figure 6.36 shows the fracture passed through two PAF holes in line with the minimum flange width and well into the web. An overall picture of the protected zone before and after testing is shown in Figure 6.34.

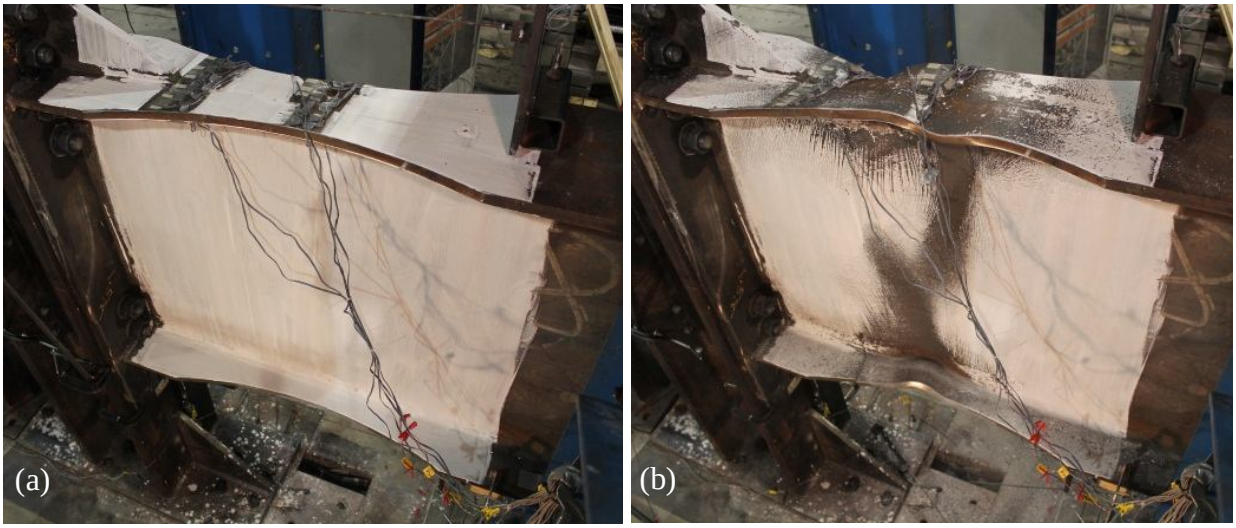


Figure 6.34 – Angled view of Specimen 9 (W36x150 with RBS and grid of PAFs) (a) before, and (b) after testing.

Crack initiation occurred at the top flange at the outer PAF located at the minimum flange width during the second cycle of the 4% story drift as shown in Figure 6.35. The weld metal at the junction of the toe of the end plates stiffeners at the top and bottom flanges also showed signs of crack initiation. During the first cycle of 4.7% story drift the PAF hole, which showed signs of crack initiation, fractured passing through a second PAF, which is located at the center of the RBS flange, and missing the third PAF located at the other side of the flange as shown in Figure 6.37.

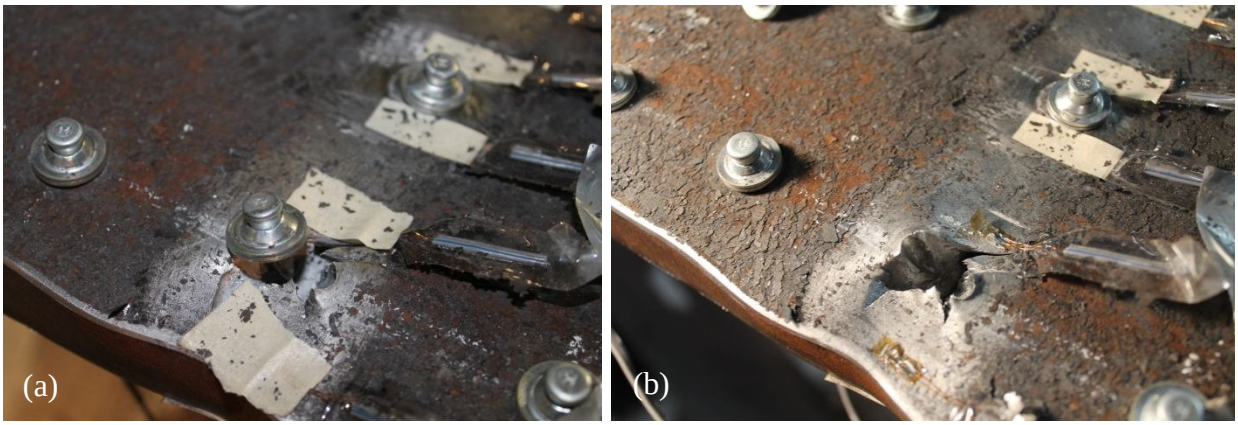


Figure 6.35 – Pictures of Tears Forming at PAF for Specimen 9 (W36x150 with RBS and Grid of PAF)



Figure 6.36 – Pictures of final top flange fracture for Specimen 9 (W36x150 with RBS and grid of PAF), (a) angle view, and (b) side view.

When the fracture was opened, there were signs of smooth shiny texture around the PAF where crack initiation was noticed as shown in Figure 6.38. The smooth shiny texture is suspected to be due to the rubbing of the crack during the final cycle loading combined with a rapid crack

growth. No fatigue striations with smooth shiny texture were observed which means failure occurred the next cycle or relatively shortly after the crack initiation was noticed. Followed by chevron marks pointing back to the fracture origin with coarse texture that refers to brittle overload fracture occurrence as shown in Figure 6.37. This type of failure occurs by rapid crack propagation with less expenditure of energy than in ductile fractures and without appreciable gross plastic deformations. Also, partial shear lips were observed on the edge where the brittle overload occurred and this shows that there was some ductility.

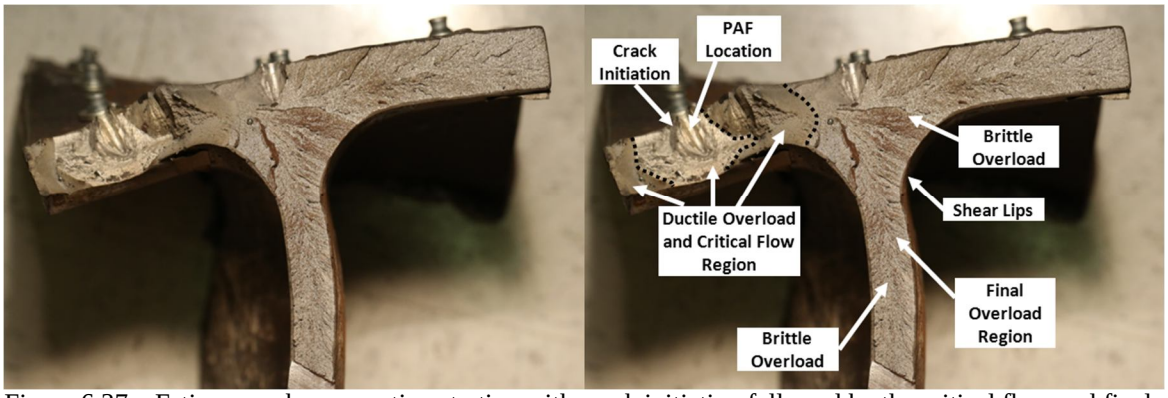


Figure 6.37 – Fatigue crack propagation starting with crack initiation followed by the critical flow and final overload regions.


Figure 6.38 – Close-up of fracture initiation location at outer PAF.

6.3.4 Behavior of Non-RBS W36x150 Specimens

Specimen 10: W36x150 with No RBS and No Fasteners

Specimen 10 served as the control test for the W36x150 specimens with no RBS connections, PAFs or puddle welds were not present. The specimen completed two cycles of 4% story drift while maintaining a moment greater than 80% of the nominal plastic moment capacity. At the start of the 4.7% story drift cycles, tearing was observed at the endplate stiffener toe weld metal similar to the tears observed in the W36x150 specimens with RBS. However, the tears did not propagate significantly through the five cycles at 4.7% story drift. An overall picture of the protected zone before and after testing is shown in Figure 6.39.

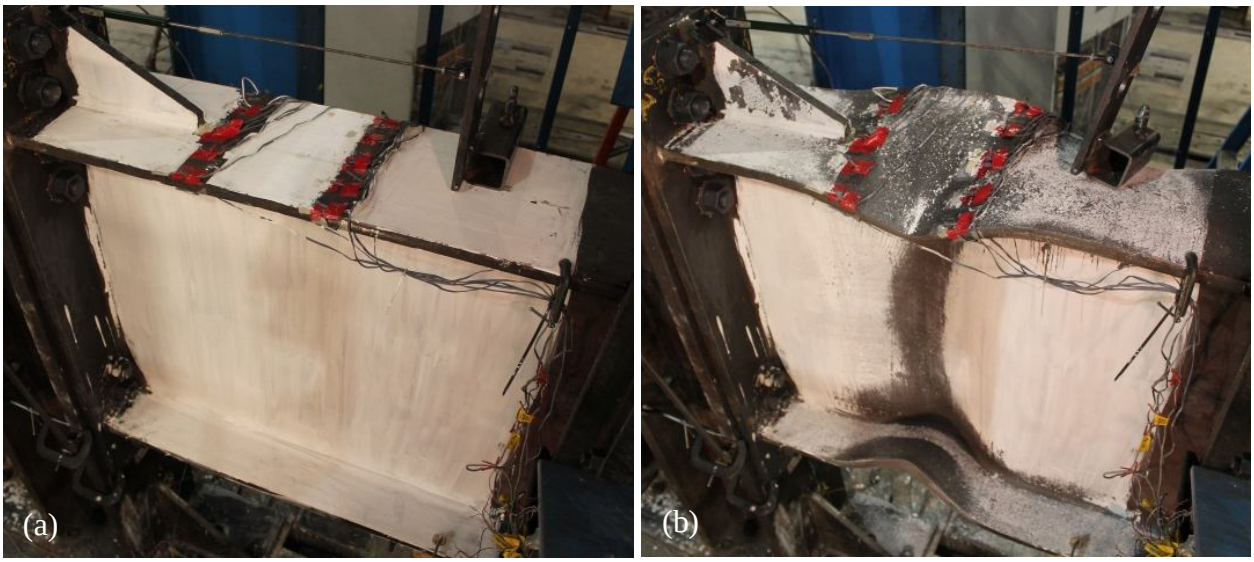


Figure 6.39 – Angled view of Specimen 10 (W36x150 with no RBS) (a) before, and (b) after testing.

Specimen 11: W36x150 with No RBS and PAFs at 12 in.

Specimen 11 was a W36x150 specimen without RBS and PAFs spaced at 12 in. along the center of the top flange, similar to Specimen 4. As in the previous test, qualification requirements were met and the test was ended after five cycles of 4.7%. The same endplate stiffener weld metal tearing observations were made as in previous tests. Figure 6.41 shows the tearing at both the top

and bottom endplate stiffener toe welds. The tears did not propagate significantly during the cycles at 4.7% story drift. An overall picture of the protected zone before and after testing is shown in Figure 6.40.

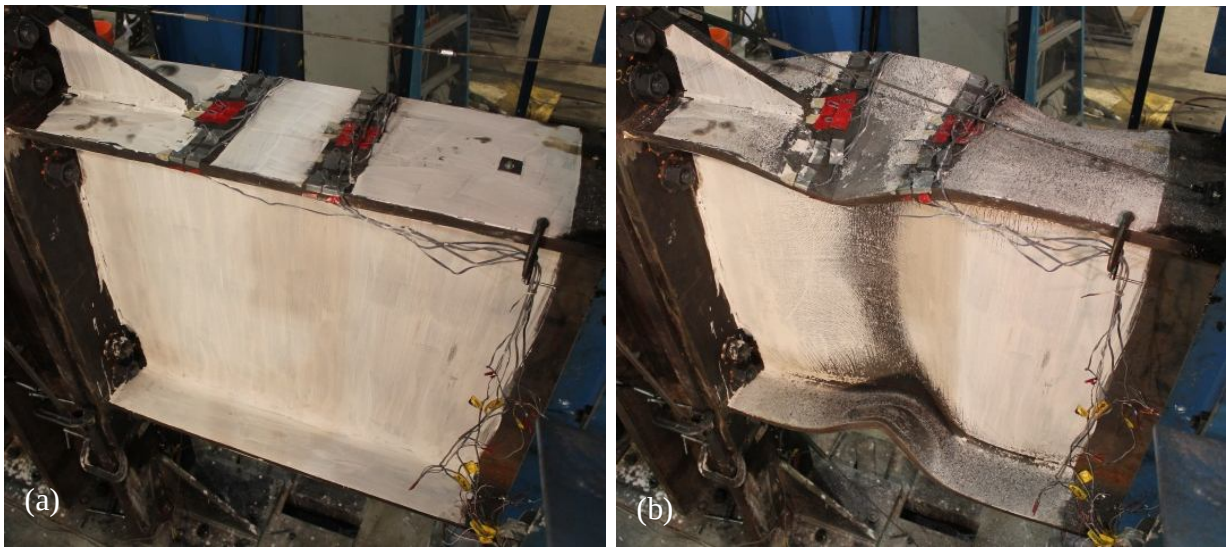


Figure 6.40 – Angled view of Specimen 11 (W36x150 with no RBS and PAF at 12 in.) (a) before, and (b) after testing.


Figure 6.41 – Tearing at endplate stiffener weld metal tearing (a) top flange, and (b) bottom flange.

Specimen 12: W36x150 with No RBS and Grid of PAFs

Specimen 12 was a W36x150 specimen with no RBS and a grid of PAFs. An overall picture of the protected zone before and after testing is shown in Figure 6.42.

An analysis of the fracture surface showed that crack initiation occurred at the bottom flange at multiple PAF. During the second cycle of 4.7% story drift, two PAFs on the underside of the bottom flange were observed to fall out of the beam as their holes began tearing and enlarging as shown in Figure 6.43. During the next cycle, significant tear propagation occurred, originating from a PAF hole 3.5 inches from the edge of the flange. During the extreme upward deflection of the fourth 4.7% cycle, the tear propagated to the flange edge. This was followed almost immediately by a full fracture of the bottom flange as shown in Figure 6.44. The fracture extended approximately six inches up the web intersecting one of the PAFs in the web this can be clearly seen in Figure 6.44b.

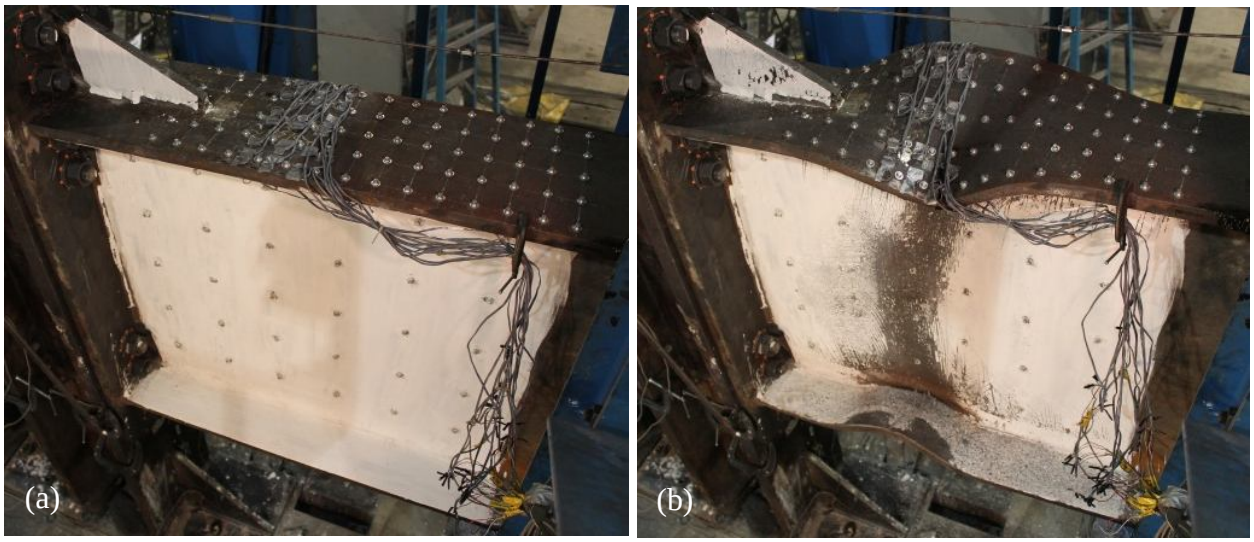


Figure 6.42 – Angled view of Specimen 12 (W36x150 with no RBS and grid of PAF) (a) before, and (b) after testing.



Figure 6.43 – Cracks forming on the surface of the bottom flange causing PAF to fall out.



Figure 6.44 – Fracture through the bottom flange as shown from the (a) bottom side view and (b) side view showing fracture extension to web PAF hole.

Two different brittle fracture textures were observed around the PAF located 3.5 inches and the first PAF from the flange edge as shown in Figure 6.45 and Figure 6.46. Both textures show signs of chevron marks pointing back to the fracture origin with coarse texture that refers to brittle overload fracture occurrence as shown in Figure 6.45, Figure 6.46, and Figure 6.47. No fatigue striations with smooth shiny texture were observed which means failure occurred the next cycle or relatively shortly after the crack initiation was noticed. This type of failure occurs by rapid

crack propagation with less expenditure of energy than in ductile fractures and without appreciable gross plastic deformations. Also, shear lips were observed on the edge where the brittle overload occurred and this shows that there was significant amount of ductility.

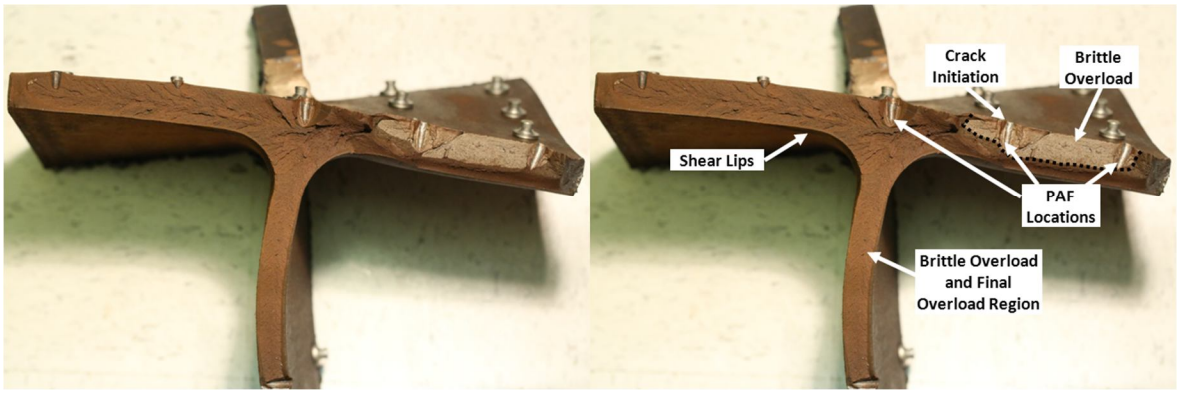


Figure 6.45 – Fatigue crack propagation with initial brittle overload followed by a final overload region.

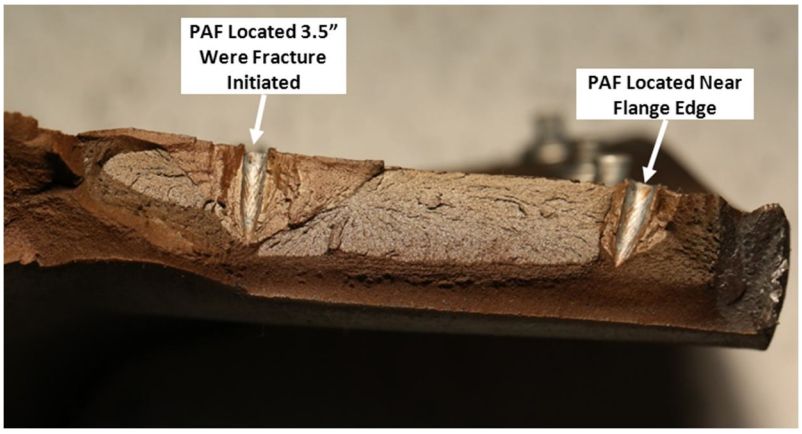


Figure 6.46 – Close-up of chevron markings at the web between PAF located 3.5 inches and the first PAF from the flange edge pointing back to the fracture origin due to the brittle overload fracture mode.



Figure 6.47 – Close-up of chevron markings at the web and flange pointing back to the fracture origin at the paf due to the brittle overload fracture mode.

6.3.5 Discussion of Full-Scale Tests Fracture Behavior

General observations regarding the fracture behavior of the twelve specimens were noticed. A summary of the fracture behavior for all of the twelve specimens is presented in Table 6.2. All of the six RBS specimens experienced some degree of fracture during 4.7% story drift cycling with Specimen 1 experiencing a ductile flange tear and the other five RBS specimens experiencing brittle fractures along an entire flange width and a portion of the web. The only non-RBS specimen to experience a fracture was Specimen 12 which contained a grid of PAF over both flanges and the web.

Table 6.2 – General observations of the twelve specimens.

Specimen Number	Specimen Description	Cycle at Significant Fracture	Fracture Location
1	W24x62 with RBS but No Fasteners	2nd Cycle at 4.7% Story Drift	Bottom Flange Near Center of RBS (Ductile tear, half the flange width, stopped at web)
2	W24x62 with RBS and PAF at 12	2nd Cycle at 4.7% Story Drift	Through PAF at Center of RBS on Top Flange
3	W24x62 without RBS or Fasteners	N/A	Test Stopped After Two Cycles at 4.7% No Fracture
4	W24x62 without RBS and PAF at 12	N/A	Test Stopped After Two Cycles at 4.7% No Fracture
5	W24x62 with RBS and Puddle Welds at 12 in.	3rd Cycle at 4.7% Story Drift	Bottom Flange, Away from Puddle Welds, Near Center of RBS
6	W24x62 without RBS and Grid of PAF	N/A	Test Stopped After Five Cycles at 4.7% No Fracture
7	W36x150 with RBS and No Fasteners	5th Cycle at 4.7% Story Drift	Top Flange at Center of RBS, Initial Fracture Partial Depth then Opened
8	W36x150 with RBS and Puddle Welds at 12	2nd Cycle at 4.7% Story Drift	Bottom Flange at Tip of End-Plate Stiffener, Not at Puddle Welds
9	W36x150 with RBS and Grid of PAF	1st Cycle at 4.7% Story Drift	Top Flange Near Center of RBS Through Two PAF
10	W36x150 without RBS and No Fasteners	N/A	Test Stopped After Five Cycles at 4.7% No Fracture
11	W36x150 without RBS and PAF at 12	N/A	Test Stopped After Five Cycles at 4.7% No Fracture
12	W36x150 without RBS and Grid of PAF	During 4th Cycle at 4.7% Story Drift	Bottom Flange Through Multiple PAF and Into a PAF Located on the Web

For the W24x62 beam specimens with RBS, the fractures occurred during the 2nd or 3rd cycle at 4.7% story drift regardless of whether there were PAF, puddle welds, or no fasteners included in the protected zone. The W36x150 RBS specimen with no fasteners fractured during the 5th cycle at 4.7% story drift whereas the specimens with a grid of PAF and puddle welds fractured in the 2nd and 1st cycles at 4.7% story drift respectively. However the fracture in the specimen with puddle welds (Specimen 8) was not related to the puddle welds, but instead occurred at the junction of the stiffener and flange. This implies some inherent variability in the cycle at which fracture occurs. Specimen 12 which included a grid of PAF fractured during the 4th cycle at 4.7% story drift whereas the other non-RBS specimens (Specimens 10 and 11) did not experience fracture through the 5th cycle at 4.7% story drift even though Specimen 11 included PAF at 12 in. spacing.

Although the W24x62 specimens suggest no difference, the results for the W36x150 specimens suggest that PAF may lead to fracture during an earlier cycle in the displacement protocol. The potential for fracture related to PAF is supported by the small tears that formed at PAF after a large number of inelastic strain cycles. It is noted, however, that fracture occurred well after SMRF qualification had been satisfied, the difference in the cycle number at fracture was small, and that the two W36x150 specimens that fractured included a grid of PAF that represent an extreme condition. Since the sample size is small and the difference in the cycle number at fracture is small, it was not possible to evaluate the difference in a statistically significant manner.

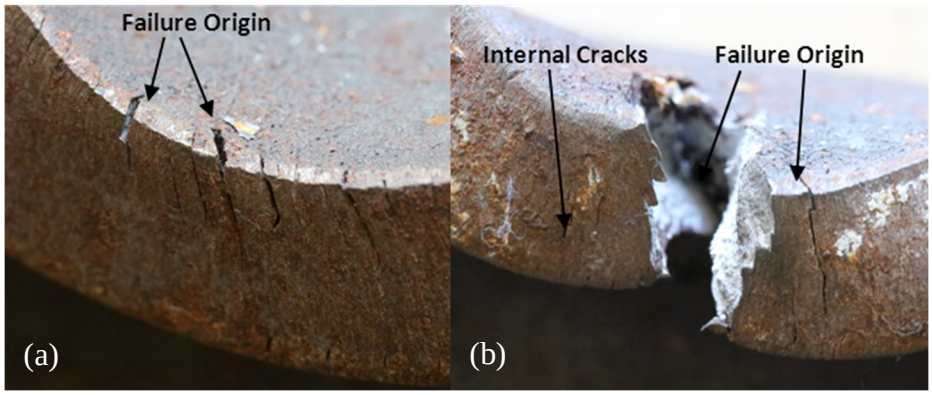


Figure 6.48 – Crack initiation at two different locations on both sides of the bottom flange. (a) Crack and fracture initiation, and (b) crack initiation at other side of the flange.

For the W24x62 beam specimens, multiple failure origins at different sides and locations were observed at the flange tip for all of the failed specimens (Specimen 1, 2, and 5) but only one of them controlled the fracture propagation for the fractured specimens. Some examples of the crack initiation and fracture origin for the W24x62 specimens are shown in Figure 6.48. For Specimens 2 and 5, it was noted that the specimens went through a ductile overload before the brittle failure. This can be clearly seen from the failed surface texture and striations as shown in Figure 6.49.

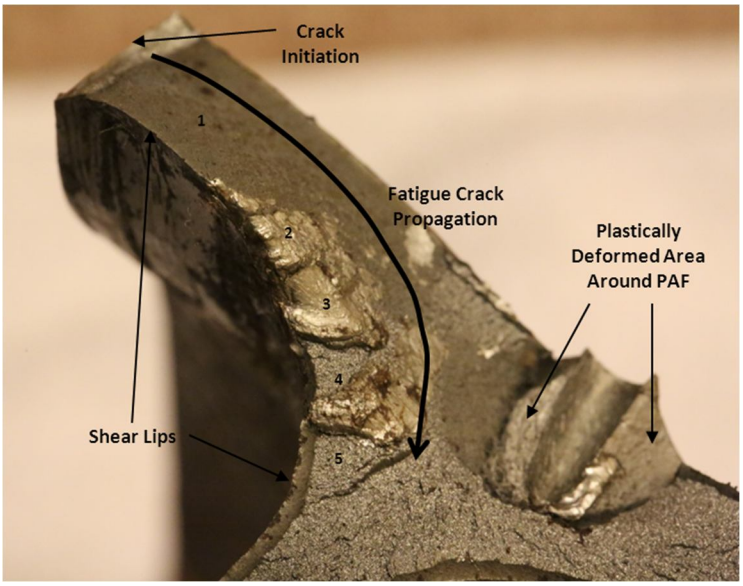


Figure 6.49 – Striation locations and fatigue crack propagation.

While for the W36x150 beam specimens, the crack initiation and fracture origin were observed at the surface of the flange near the tip of the flange, as shown in Figure 6.50, typically at one side only. This was most clearly observed in Specimen 7. Specimens 9 and 12 failure origins were similar to Specimen 7, the difference being that a PAF is located at the failure origin at the surface of the flange. The only specimen which showed a different fracture pattern was Specimen 8 in which fracture initiated at the toe of the flange stiffener. This fracture occurred due to high stress triaxiality at the stiffener toe.

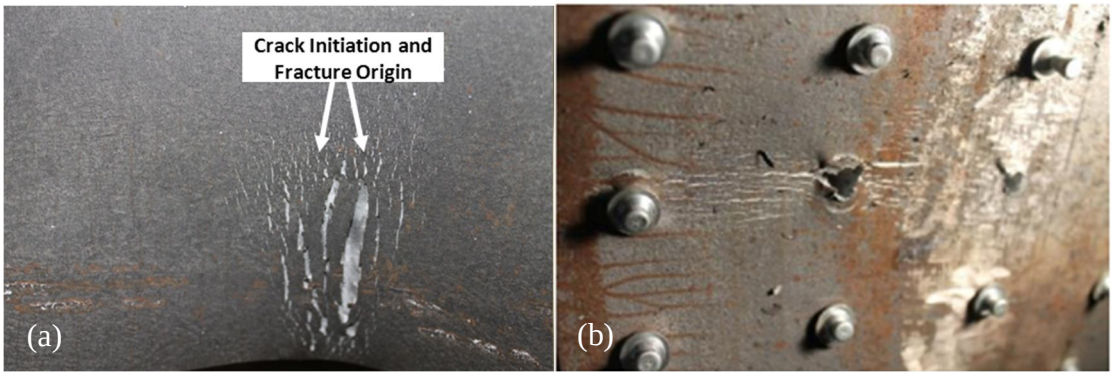


Figure 6.50 – Crack initiation and failure origin at the flange surface before fracture occurrence for Specimen 7 (a) and Specimen 12 (b)

CHAPTER 7 PREDICTING FRACTURE IN THE FULL-SCALE TESTS

7.1 Introduction

The fracture parameters calibrated in Chapter 5 are used to predict fracture initiation in full-scale moment connection tests conducted previously by Eatherton et al. (2013). First, the FE models are presented which can capture experimental behavior. Finally, calibrated fracture parameters for each artifact are used to predict when the moment connection tests would experience fracture initiation. The predicted cycle at fracture initiation is compared to experimental data for artifacts tested in the experimental program (puddle welds and powder actuated fasteners).

7.2 Full-Scale Tests FEM Analysis

The FE models of the full-scale tests were created using ABAQUS 6.13 software (Simulia 2012) as described in Abbas and Eatherton (2014). An eight node brick element was used. Similar to other FE models used in this study, the Armstrong Frederick material model was used which includes isotropic and kinematic hardening (Armstrong and Frederick 1966). Two material parameters were calibrated for the isotropic part of the hardening model: Q_{inf} = 7 and b= 4. For the kinematic part, tabulated data from tension monotonic tests cut from the W24x62 and W36x150 flange and web were used. A sensitivity analysis was conducted to examine convergence of cumulative plastic strain and stress triaxiality which resulted in elements that are 0.25 in. on a side and 0.1 in. thick. To improve computational efficiency, a coarser mesh was used in the regions of the model expected to remain elastic.

The computational model of the W24x62 RBS specimen is shown in Figure 7.1 (a). A horizontal linear spring was used at the column top support and calibrated to capture flexibility in the reaction frame and end plate connection. The load-deformation plot from the computational

model of the W24x62 RBS specimen is shown in Figure 7.1 (b) to exhibit good correlation with experimental behavior. All of the four validation plots are included in Appendix C. The peak moments predicted by the model are shown to be within 3% of the experimentally obtained peak moments on average.

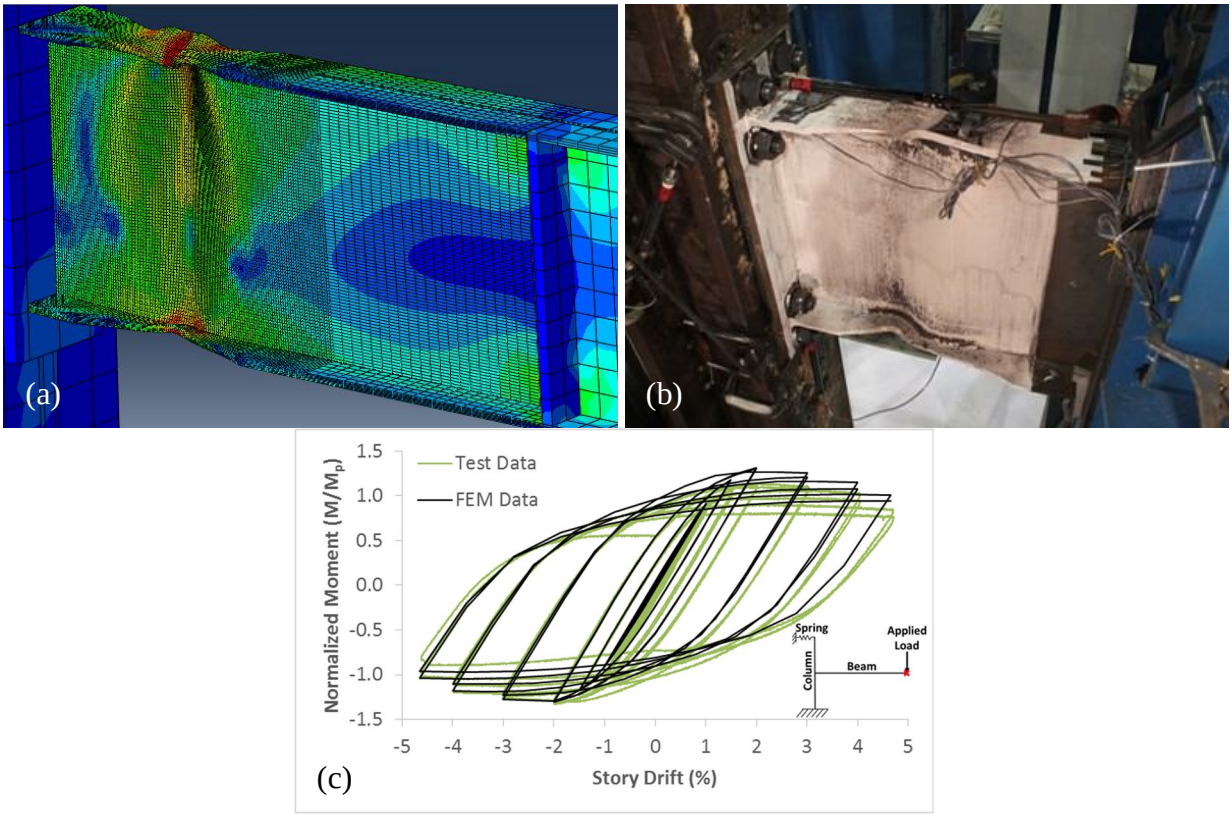


Figure 7.1 – (a) Deformed shape of the FEM model showing transition in mesh size, (b) angled view of deformed shape of full-scale test, and (c) validation of FEM analysis with experimental data for W24x62 specimen with RBS.

7.3 CVGM Fracture Initiation Prediction for Full-Scale Tests

An example application of the CVGM is shown in Figure 7.2 for the W24x62 specimen with RBS but no artifact (Specimen 1 from Eatherton et al. (2013)). The critical location from the FEM model was assumed as the location with the largest cumulative equivalent plastic strain (PEEQ). The critical location was found to be the flange tip on the inside of a local buckle which

matches observations of fracture initiation from the full-scale tests as shown in Figure 7.2. The cumulative plastic strains and stress triaxiality histories were extracted and used to calculate the void growth index shown in Figure 7.2. In this example the fracture parameters used are from Table 5.5 for the W24x62 no artifact specimen calibrated using the bend test approach ($VGI_{monotonic}^{critical}$ = 1.77 and λ = 0.43). In this case, fracture initiation was predicted approximately two cycles after fractures were observed to form. Fracture initiation occurred in the second cycle at 3% story drift in the SMRF qualification displacement protocol whereas fracture initiation was predicted in the second cycle at 4% story drift. The locations of these fractures, however, matched the predicted locations well in that fractures occurred at the flange tip at the inside of the worst local buckle.

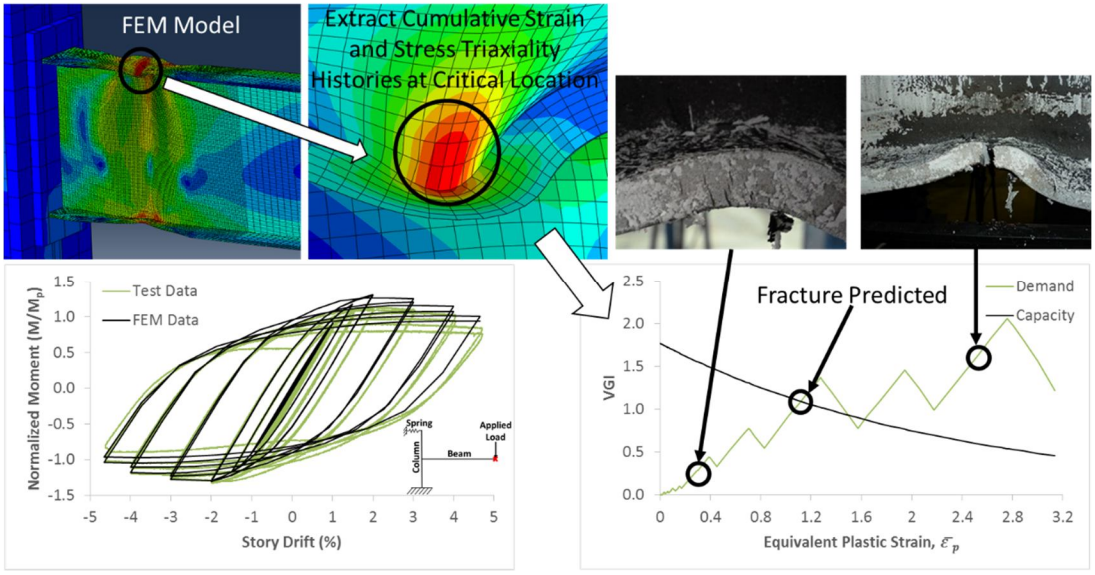


Figure 7.2 – Example of CVGM application predicting fracture for W24x62 RBS (Specimen 1).

Another comparison between the actual cycle in which fracture initiated in the full-scale tests compared to the CVGM predicted cycle is shown in Figure 7.3 for Specimen 10 (W36x160 BSEEP). The label "Test" refers to the time when fracture initiation was observed during the experiment and "CVGM" refers to the time when fracture initiation is predicted by the CVGM. Similar the previous example, the observed fracture initiation in the test was two cycles before the predicted fracture initiation using the CVGM.

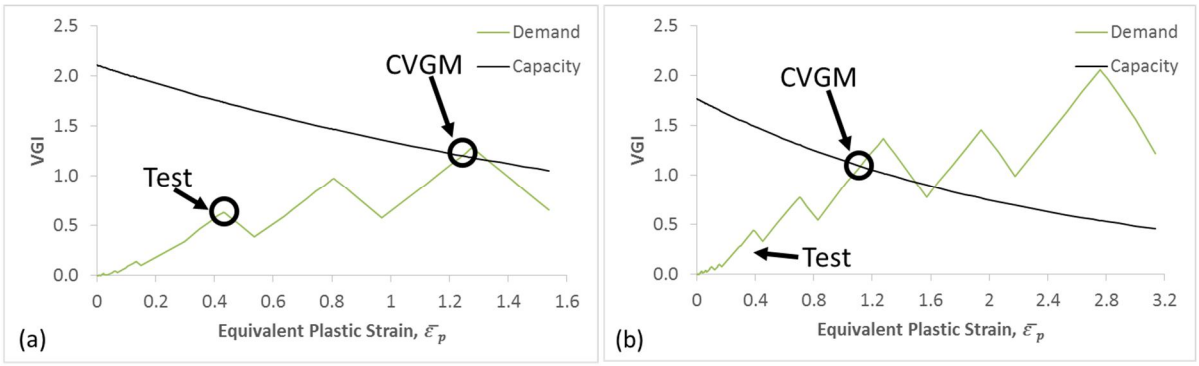


Figure 7.3 – Comparison of CVGM fracture initiation prediction with test results using fracture parameters from Table 5.5 (a) W36x150 BSEEP, and (b) W24x62 RBS.

The fracture parameters given in the previous chapter as calibrated using the bend test approach were used to predict fracture initiation at the worst case location at a local buckle, and the worst case location at the center of the beam in the plastic hinge region. The latter location along the centerline of the beam represents locations where artifacts were included in some of the full-scale testing program, but also simulate the intended fastener locations for decking attachment. The FE models were subjected to the SMRF qualification displacement protocol in AISC 341-10 chapter K with 2 additional cycles at each 1% story drift increment up to 8% story drift.

The fracture parameters calibrated for bare steel using conventional circumferentially notched round bar specimens ($VGI_{monotonic}^{critical}$=1.94, λ=0.45) had similar critical monotonic void growth index, but different degradation parameter than those calibrated using the proposed flat plate specimens ($VGI_{monotonic}^{critical}$=2.11, λ=0.25). A comparison of the fracture initiation prediction calculated based on the two sets of fracture parameters is shown in Figure 7.4 for the worst case location in the W36x150 Bolted Stiffened Extended End Plate (BSEEP) specimen. Fracture was predicted in the second cycle at 6% story drift with fracture parameters from conventional CN round bar tests and the second cycle at 5% story drift with fracture parameters from the bend tests on flat plates. It is demonstrated that although the cyclic degradation parameter takes a significantly different value between the two, the difference in the cycle when fracture initiation is predicted is only one cycle. In the experiment, the test setup was limited to 4.7% story drift and no fracture initiation was observed after five cycles at 4.7% story drift.

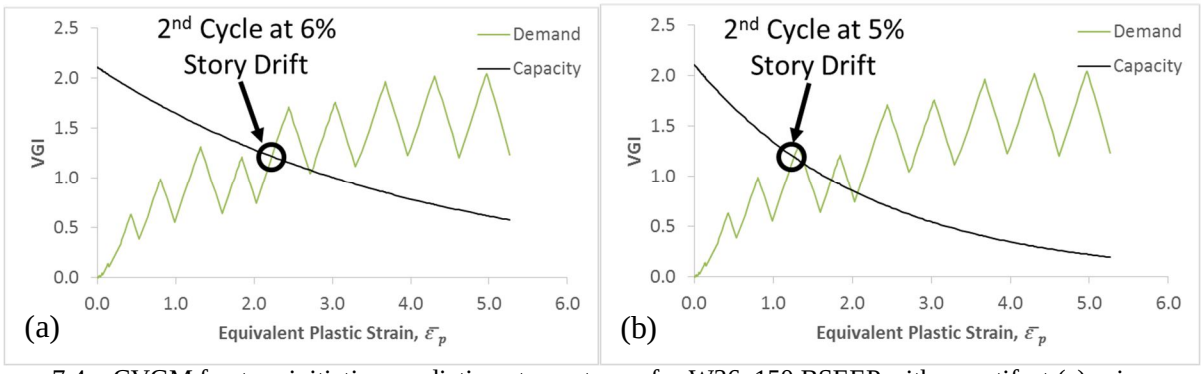


Figure 7.4 – CVGM fracture initiation prediction at worst case for W36x150 BSEEP with no artifact (a) using round notched tests, and (b) bend test approach fracture parameters.

Figure 7.5 shows a comparison between a W24x62 Bolted Unstiffened Extended End Plate (BUEEP) specimen and a W24x62 reduced beam section (RBS) specimen with no artifact. It can seen that the W24x62 RBS develops considerably larger void growth index (fracture demand) than the non-RBS specimen. The plastic strains at the inside of the local buckle are significantly larger in the RBS specimen. Even though the fracture resistance (as characterized by the calibrated fracture parameters) is the same for both specimens, fracture initiation is predicted in the first 6% story drift cycle for the non-RBS specimen and the second 4% story drift cycle for the RBS specimen.

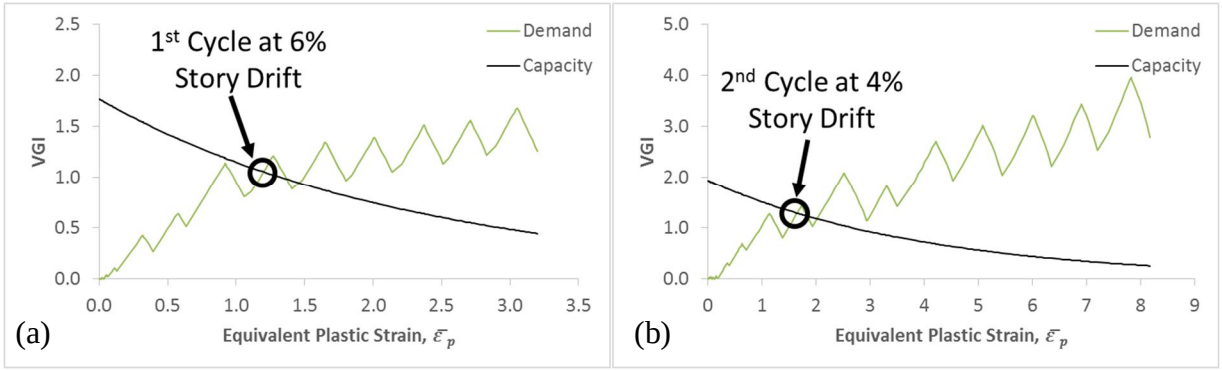


Figure 7.5 – CVGM fracture initiation prediction at worst case for (a) W24x62 BUEEP, and (b) W24x62 RBS with no artifact using bend test approach fracture parameters.

As described in the previous chapter, the calibration of the cyclic degradation parameter, λ, was unsuccessful for the majority of artifacts. As such, a value of $\lambda = 0$ was assumed. Examples of the CVGM fracture initiation for the W24x62 RBS with notch ground to taper (very low resistance to fracture) and a W36x150 with powder actuated fastener (higher resistance to fracture) are shown in Figure 7.6. The resulting fracture initiation predictions are expected to be conservative based on bend test results which suggest larger fracture resistance.

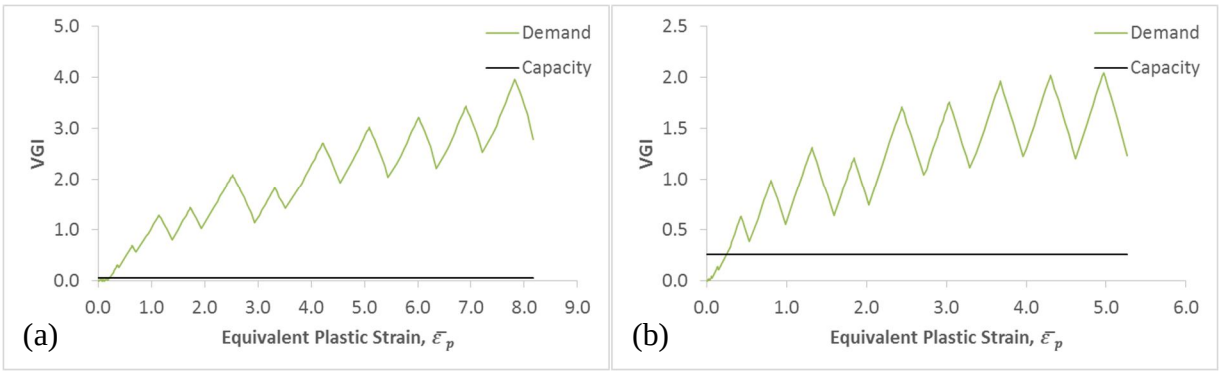


Figure 7.6 – CVGM fracture initiation prediction at worst case for (a) W24x62 RBS with NGT, and (b) W36x150 with PAF.

Table 7.1 and Table 7.2 give a summary of predicted fracture initiation at the worst case location at a local buckle, and at the worst case location along the centerline of the beam. Refer to Appendix C for the plots associated with these fracture predictions.

Table 7.1 – Fracture initiation prediction for W24x62 and W36x150 full-scale tests without RBS

	Worst Case at Local Buckle		**Worst Case at Middle**	
Artifact Type	**W24x62**	**W36x150**	**W24x62**	**W36x150**
No Artifact [1]	N/A	1st cycle at 6%	N/A	1st cycle at 7%
No Artifact [2]	1st cycle at 6%	2nd cycle at 5%	1st cycle at 7%	2nd cycle at 6%
Powder Actuated Fasteners (PAF)	1st cycle at 4%	1st cycle at 4%	2nd cycle at 5%	2nd cycle at 4%
Puddle Welds (PW)	1st cycle at 5%	1st cycle at 4%	1st cycle at 5%	1st cycle at 5%
Ground Fillet Weld (GFW)	1st cycle at 4%	1st cycle at 4%	2nd cycle at 5%	1st cycle at 5%
Notch Ground to Taper (NGT)	2nd cycle at 3%	1st cycle at 4%	1st cycle at 4%	1st cycle at 4%
Notch Welded and Ground Smooth (NWG)	1st cycle at 4%	1st cycle at 4%	2nd cycle at 4%	1st cycle at 5%

[1] Fracture parameters calibrated axially using round notch specimens cut from W36x150 flanges
[2] Fracture parameters calibrated using monotonic and cyclic bend tests for W24x62 and W36x150 flanges

Table 7.2 – Fracture initiation prediction for W24x62 RBS and W36x150 RBS full-scale tests for all artifacts.

	Worst Case at Local Buckle		**Worst Case at Middle**	
Artifact Type	**W24x62 RBS**	**W36x150 RBS**	**W24x62 RBS**	**W36x150 RBS**
No Artifact [1]	N/A	2nd cycle at 4%	N/A	1st cycle at 6%
No Artifact [2]	2nd cycle at 4%	1st cycle at 4%	1st cycle at 6%	2nd cycle at 5%
Powder Actuated Fasteners (PAF)	1st cycle at 3%	1st cycle at 3%	1st cycle at 4%	1st cycle at 4%
Puddle Welds (PW)	1st cycle at 4%	2nd cycle at 3%	1st cycle at 4%	2nd cycle at 4%
Ground Fillet Weld (GFW)	1st cycle at 3%	2nd cycle at 3%	1st cycle at 4%	1st cycle at 4%
Notch Ground to Taper (NGT)	1st cycle at 3%	1st cycle at 3%	1st cycle at 3%	2nd cycle at 3%
Notch Welded and Ground Smooth (NWG)	1st cycle at 3%	2nd cycle at 3%	2nd cycle at 3%	1st cycle at 4%

[1] Fracture parameters calibrated axially using round notch specimens cut from W36x150 flanges
[2] Fracture parameters calibrated using monotonic and cyclic bend tests for W24x62 and W36x150 flanges

Except for the notch ground to taper, all configurations without a reduced beam section (Table 7.1) are expected to initiate fracture during the SMRF qualification cycle (1st cycle at 4% story drift) or after. From the full-scale tests and the cyclic bend test program described herein, it was found that fracture initiation is not associated with a large reduction in load carrying capacity. That is, both the full-scale specimens and the bend test specimens survived several additional cycles before fracture propagation led to a large brittle fracture through the thickness of the flange material. It is therefore likely that specimens containing any of the tested artifacts, with the possible exception of the notch ground to taper, would satisfy SMRF qualification testing in AISC 341-10 chapter K. Full-scale tests on specimens with puddle welds and powder actuated fasteners were found to satisfy SMRF qualification criteria in the testing program conducted by Eatherton et al.

(2014). Some experimental specimens that passed SMRF qualification contained a grid of powder actuated fasteners in which PAF were near the worst case location.

Connection configurations with a reduced beam section (see Table 7.2) were predicted to experience fracture initiation as early as the 1st cycle at 3% story drift with some artifacts. Since the CVGM does not capture fracture propagation or loss of load carrying capacity, this fracture initiation prediction is not sufficient on its own to tell whether RBS connections with these artifacts would satisfy (or not satisfy) SMRF qualification criteria. More research is required to supplement the CVGM prediction with a fracture propagation models from conventional fracture mechanics to predict when significant loss of load carrying capacity would occur.

7.4 Modified CVGM Fracture Initiation Prediction for Full-Scale Tests

The calibrated cyclic degradation parameter, λ, in Section 7.3 is used to predict fracture initiation for the W24x62 specimen with RBS but no artifact (Specimen 1 from Eatherton et al. (2013)). In this case, fracture initiation was predicted approximately two cycles after fractures were observed to form similar to the classical CVGM prediction. Fracture initiation occurred in the second cycle at 3% story drift in the SMRF qualification displacement protocol whereas fracture initiation was predicted in the second cycle at 4% story drift. Both models use the same monotonic growth index, $VGI_{monotonic}^{critical}$, of 1.77. The cyclic strength degradation parameter, λ, values for the classical CVGM and the modified CVGM are 0.43 and 0.63 respectively. A higher cyclic strength degradation parameter, λ, value means that fracture initiation will be predicted earlier using the modified CVGM approach. A comparison between the classical CVGM and the modified CVGM results is presented in Figure 7.7 for the W24x62 specimen with RBS but no artifact. Although the modified CVGM shows fracture initiation earlier than the classical CVGM but both models show fracture initiation on the same cycle.

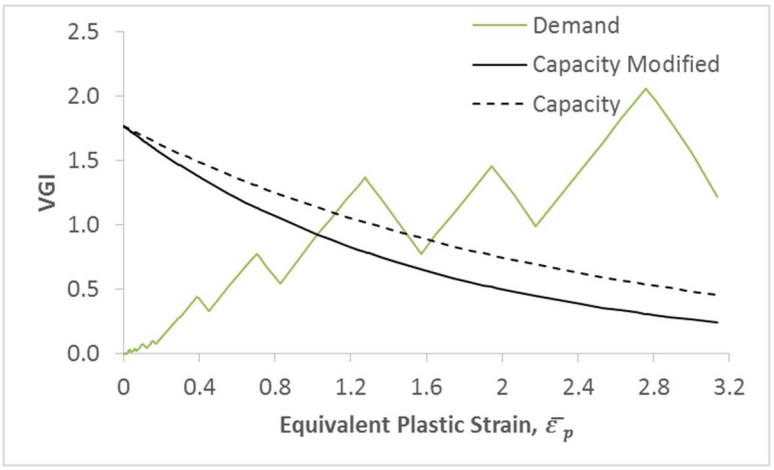


Figure 7.7 – Comparison of CVGM fracture initiation prediction using the modified approach and the classical approach at worst case for W24x62 RBS with no artifact using bend test approach fracture parameters.

7.5 SWDM Fracture Initiation Prediction for Full-Scale Tests

SWDM is a new ULCF that predicts fracture initiation and it was developed by Smith et al. (2014). The fracture parameters that were calibrated using the cyclic bend tests in Section 5.5 are used in this section to predict fracture initiation in full-scale tests from Eatherton et al. (2013). Fracture initiation using the SWDM will be studied in this section for the W24x62 specimen with RBS with no artifact (Specimen 1) and the W36x150 specimen with RBS with no artifact (Specimen 7).

Figure 7.8 presents the SWDM results in predicting fracture initiation for the W24x62 specimen with RBS with no artifact (Specimen 1). In this case, fracture initiation was predicted approximately two cycles after fractures were observed to perform similar to the classical CVGM prediction. Fracture initiation occurred in the second cycle at 3% story drift in the SMRF qualification displacement protocol whereas fracture initiation was predicted in the second cycle at 4% story drift.

Figure 7.9 presents the SWDM results in predicting fracture initiation for the W36x150 specimen with RBS but no artifact (Specimen 7). In this case, fracture initiation was predicted approximately one cycle before fractures were observed to perform similar to the classical CVGM prediction. Fracture initiation occurred in the second cycle at 4% story drift in the SMRF

qualification displacement protocol whereas fracture initiation was predicted in the first cycle at 4% story drift.

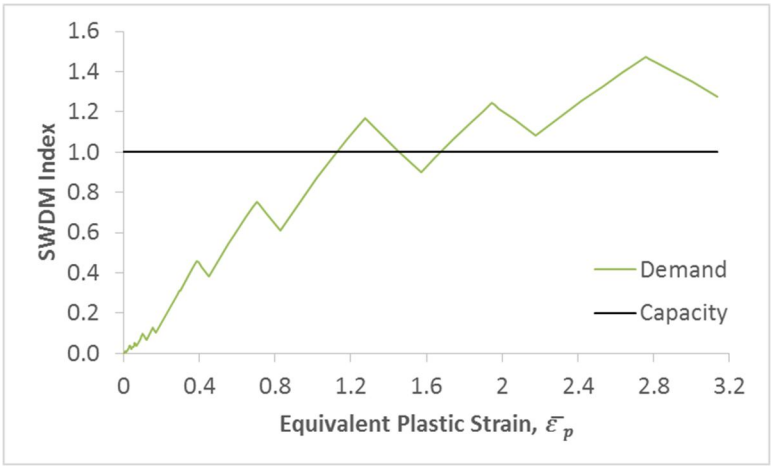


Figure 7.8 – SWDM application predicting fracture for W24x62 RBS (Specimen 1).

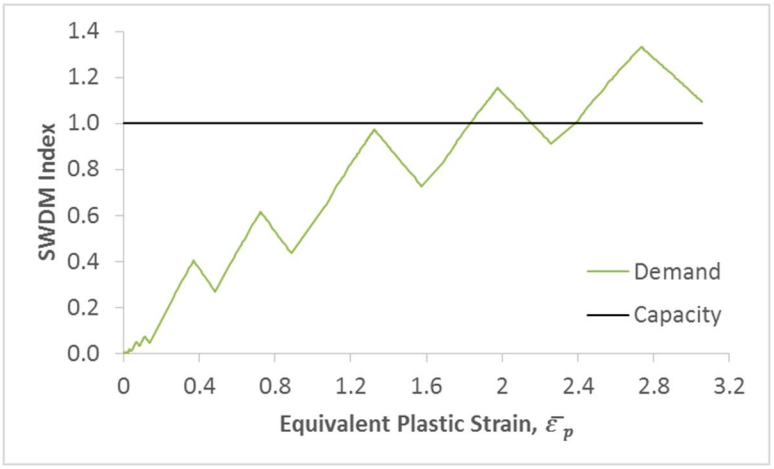


Figure 7.9 – SWDM application predicting fracture for W36x150 RBS (Specimen 7).

Both full-scale tests, the W24x62 with RBS (Specimen 1) and the W36x150 with RBS (Specimen 7) that are studied in this section using the SWDM to predict fracture initiation had similar results to the classical CVGM. The reason that the fracture initiation prediction matches the CVGM results in predicting fracture initiation at the same cycle is that the SWDM was

calibrated using the same data that the CVGM models were applied to previously which were from Kanvinde and Deierlein (2007), and Myers et al. (2009) work. Also, many parameter assumptions Smith et al. (2014) accounted for which makes the model similar to the CVGM with minor differences. Although the SWDM gave similar results to the CVGM but there are more parameters that can be calibrated so the SWDM that can account for low and high stress triaxiality for ULCF models.

7.6 CDPM Fracture Initiation and Propagation for Full-Scale Tests

CDPM is implemented in FE software LS-DYNA under few material models. It is a numerical fracture model that predicts fracture initiation and propagation. The FE analyses were conducted using LS-DYNA R8.0. In this section, the model that is used was built and meshed using FE analysis software ABAQUS 6.13 (Simulia 2012). Also, the plasticity model with combined nonlinear isotropic and kinematic hardening by Lemaitre and Chaboche (1994) was calibrated using the same FE analysis commercial program. Two material parameters were calibrated for the isotropic part of the hardening model: $H = 28$ and $b = 4$. For the kinematic part, tabulated data from tension monotonic tests cut from the W24x62 were used. This calibration process was discussed previously with all of the details related to the mesh size, boundary conditions, element type, and specimen dimensions in the FE model.

A numerical fracture model that is implemented in FE software LS-DYNA has been used to study the fracture initiation and propagation process. This model has been developed by Dufailly and Lemaitre (1995) and it involves multi-axial states of material nonlinearity. The CDPM parameter used in the FE model of the W24x62 RBS specimen were calibrated using the 0.59 in. bare specimens from the cyclic bend test, the calibration procedure is explained in Section 5.6.2. All of the CDPM parameters used to calibrate the cyclic bend tests were previously calibrated using uniaxial monotonic bare tests for 0.59 in. and 0.94 in. specimens except the critical damage, D_c. Two values for the critical damage, D_c, were calibrated for the cyclic bend tests. The specimens with notches (R025 and R100) shared the same D_c value of 0.15. While for the unnotched specimen (R000) had a different Dc value of 0.30. Refer to the values in Table 5.10 for the parameters used

in the material model MAT_DAMAGE_3 (MAT_153) for the W24x62 with RBS and no fasteners to predict fracture initiation and propagation using LS-DYNA.

In this study only one specimen out of the twelve specimens previously conducted by Eatherton et al. (2013) is studied. The W24x62 RBS specimen with no artifacts is studied since it exhibited fracture with proper support of the fracture initiation and propagation. For the critical damage, D_c, value of 0.15, fracture initiation was predicted approximately one cycle after fractures were observed to form. Fracture initiation occurred in the first cycle of 4% story drift. While for the critical damage, D_c, value of 0.30, fracture initiation was predicted approximately two cycles after fractures were observed to form. Fracture initiation occurred in the second cycle of 4% story drift. Crack initiation was noted in several locations at the compression side of the flange local buckle at the FE model and this behavior was observed in all of the three W24x62 RBS specimens tested by Eatherton et al. (2013). For the full-scale tests, internal cracking at the flange tip, and the edge of the flange exhibited multiple failure origins at both sides of the bottom and top flange. Those fracture initiation locations were followed by a ductile tear propagating from the tip of the flange toward the middle of the flange at the center of the RBS. This was simulated by multiple elements removed at the same time step in the FE model. The mechanism of fracture propagation in LS-DYNA is similar to the brittle fracture observed at the full-scale tests. Figure 7.10 and Figure 7.11 shows the fracture initiation and propagation for the W24x62 RBS with critical damage, D_c, values of 0.15 and 0.30 respectively.

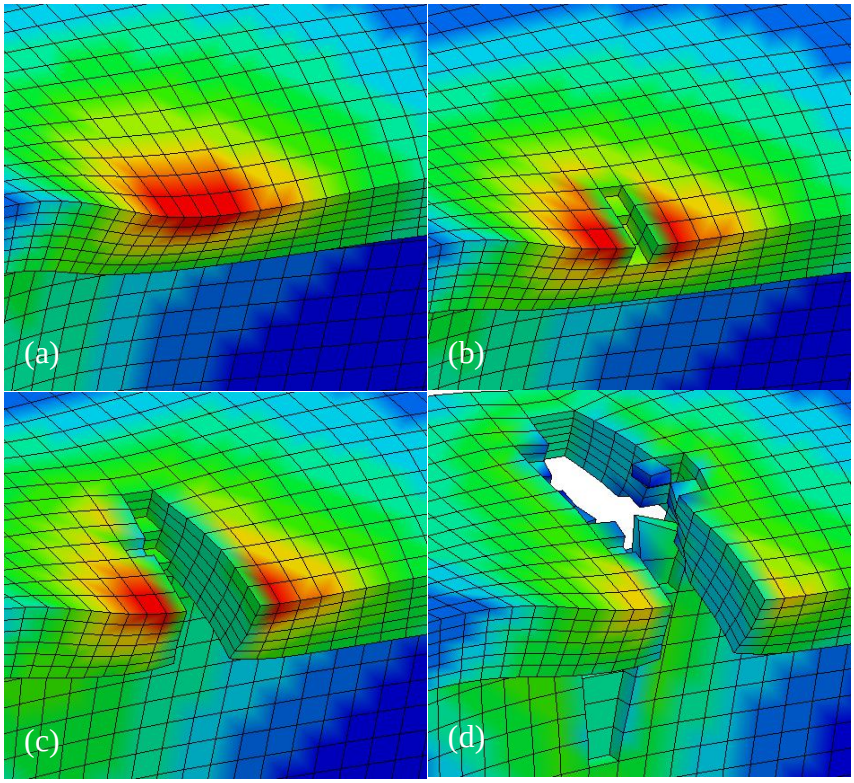


Figure 7.10 –W24x62 RBS for D_c = 0.15 (a) just before fracture initiation, (b) fracture initiation at 1st cycle 4% story drift, (c) fracture propagation at 2nd cycle 4% story drift, (d) and fracture propagation at 1st cycle 4.7% story drift.

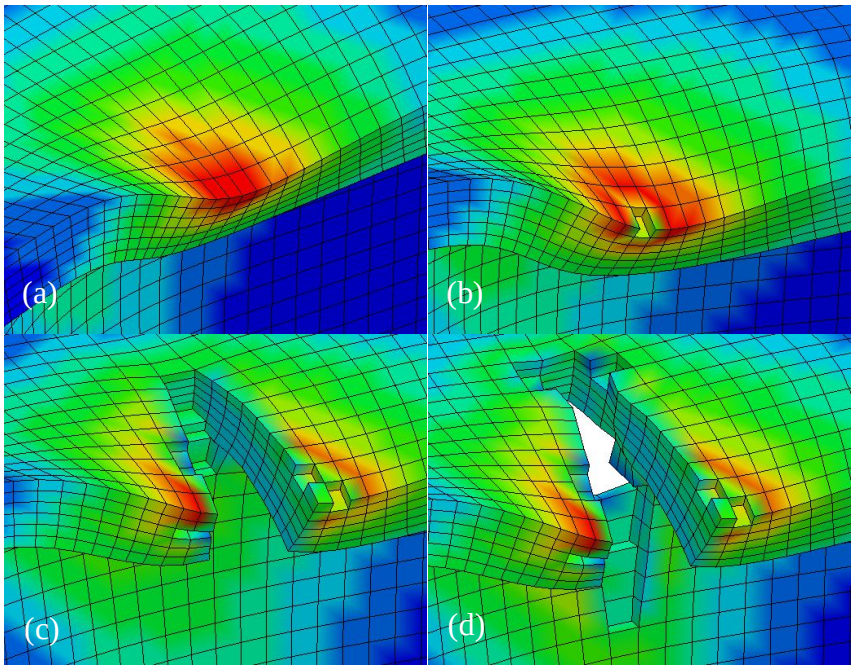


Figure 7.11 –W24x62 RBS for D_c = 0.30 (a) just before fracture initiation, (b) fracture initiation at 2nd cycle 4% story drift, (c) fracture propagation at 1st cycle 4.7% story drift, (d) and fracture propagation at 2nd cycle 4.7% story drift.

The load-deformation plot from the LS-DYNA computational model of the W24x62 RBS specimen are shown in Figure 7.12 for critical damage, D_c, values of 0.15 and 0.30 respectively. It is noticed the model with lower critical damage value (D_c = 0.15) resulted in premature cyclic degradation compared to the model with higher critical damage value (D_c = 0.30).

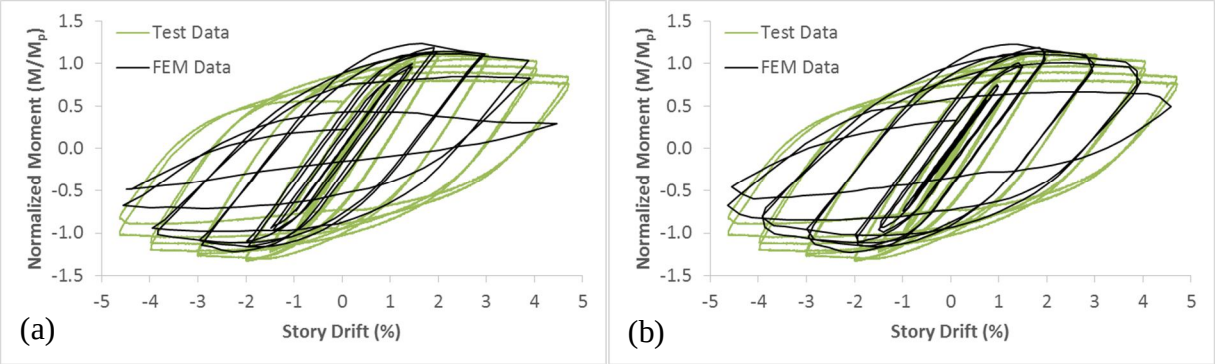


Figure 7.12 – Validation of FEM analysis using CDPM with experimental data for W24x62 specimen with RBS using (a) D_c = 0.15, and (b) D_c = 0.30.

Fracture initiation occurs one cycle before the ductile tear propagated in the LS-DYNA FE models. While in the actual tests the difference between the fracture initiation (second cycle of 3% story drift) and the ductile tear propagation (second cycle of 4.7% story drift) was four cycles. The mechanism of ductile tear propagation, starting from the fracture initiation location toward the middle of the flange, in the LS-DYNA FE models matches the actual tests. Also, fracture initiation originated at multiple locations at the flange tip of the compression side of the local buckle for both the FE models and the actual tests. Using a lower value (D_c = 0.15) for critical damage will predict fracture initiation closer to the actual test result but will cause higher cyclic degradation compared to using a higher critical damage value (D_c = 0.30). A good approach is to run a set of FE models for a range of values for critical damage to capture different failure scenarios.

Calibrating of the CDPM parameters using the cyclic bend tests with the support of the uniaxial monotonic tests gave promising results for predicting fracture initiation location and fracture propagation mechanism. While for the prediction of the fracture initiation cycle the CDPM was off by at least one cycle, also the number of cycles between fracture initiation and propagation was

off by four cycles. It is required that more calibration for the CDPM parameters to have a better match to delay the fracture propagation from initiation, and to obtain closer prediction for fracture initiation. For future work also, it is recommended to model and study other specimens tested by Eatherton et al. (2013) and other researchers in which conducted similar types of tests that contain different artifacts and to compare the CDPM results.

CHAPTER 8 RECOMMENDATIONS OF FUTURE WORK

8.1 Introduction

This study uncovered several challenges associated with the proposed methods that deserve further research which constitute the proposed work that can be used in future work. The topics of the proposed work are summarized in this chapter. First, a new generation of cyclic and monotonic bend tests is proposed to overcome all of the challenges and failures observed through this work. Next, a study of artifacts sensitivity is presented for the current cyclic bend tests and also some recommendations and considerations are discussed for the next phase of testing. Finally, a method of demonstrating equivalence is proposed instead of using ULCF models to measure

8.2 New Monotonic and Cyclic Bend Test

A new cyclic test setup will be proposed in this section to be considered for future testing. The main three changes that will be proposed in this section for the cyclic bend tests are changing the roller size to delay the fracture initiation to incorporate a wider range of material thickness, propose a range of material thickness to be tested with different artifacts to set limit states for each artifact based on material thickness, and to propose a monotonic three point bend test to replace the currently used monotonic uniaxial test.

Early fracture initiation was exhibited in thicker specimens (W36x150) especially with specimens with side notches. Delaying the fracture initiation will give a wider range of fracture initiation distribution that will help in understating the effect of each artifact and also to calibrate each fracture parameter. Therefore a bigger roller is proposed that will exhibit less strain during each cycle which will lead in deferring fracture initiation to get a better distribution of fracture initiation for different artifacts. Also, it should maintain the criteria of ULCF for the range of material thickness ranging from 0.25 in. to 1.5 in. A roller diameter of 16 in. will be suitable to meet the ULCF criteria for the range of material thickness mentioned previously. Figure 8.1 shows

a schematic example of the bending action during one cycle for the proposed roller size. This upgrade can be done on the current test cyclic bend test setup.

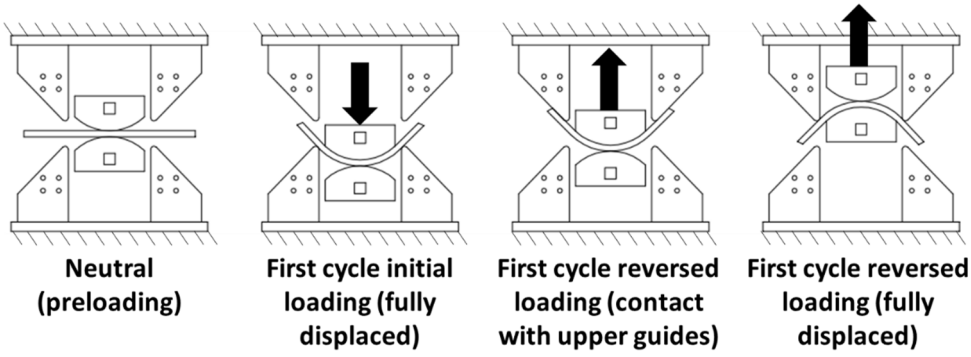


Figure 8.1 – Cyclic bend test bending steps for first cycle of proposed new roller diameter.

A range of different specimen thickness needs to be tested to study the relation between material thickness and different types of artifact. Lee et al. (2012) studied the tensile properties and the hardness of steel around the PAF and welded shear stud. The effected zone for a PAF and a welded shear stud is 0.24 in. measured from the face of the PAF and shear stud and this was measured by the difference in hardness values. Based on the study conducted by Lee et al. (2012) testing a specimen with a thickness of 0.25 in. will be an appropriate start to set a limit state for certain artifacts based on material thickness due to the damage they cause by changing the material properties which might lead to premature fracturing. Therefore a set of four material thickness needs to be studied ranging from relatively thin to thicker specimens and they are 0.25 in., 0.5 in, 1.0 in., and 1.5 in. This will ensure that an appropriate range of material thickness is covered and this will help to study and investigate different artifacts effects.

A monotonic three point bend test needs to be conducted with the same width as the specimens used in the cyclic bend tests. Replacing the uniaxial monotonic testing with a monotonic three point bend test and using the same material dimensions will give a similar failure pattern. This will improve the calibration of the $VGI_{monotonic}^{critical}$ or even if using the method of demonstrating equivalence. This type of testing is explained and used for many other applications to test material ductility there are many test setups mentioned in ASTM E290-14. An example of the proposed

test setup is presented in Figure 8.2. The diameter of the plunger must be as small as 2 in. to ensure that fracture initiation occurs. A plunger with a 2 in. diameter will result in estimated maximum strain values of 0.228 and 0.320 in./in. at the extreme fiber for W24x62 (0.59 in.) and W36x150 (0.94 in.) specimens respectively. Also the artifacts can be located at the tension side and be observed by a high definition camera to capture the fracture initiation and its propagation. It is recommended to test at least three different specimen geometries, an unnotched specimen, a small notch (R = 0.25 in.) and a large notch (R = 1.00 in.). Those are the same specimen geometries tested for the cyclic bend tests. Strain values can be measured accurately using a set of targets points at the side of the specimen. The target points can be placed using a pen at 0.1 in. spacing and a 0.02 in. diameter. A high definition camera is required to photograph and monitor the target points during bending deformation and displacement.

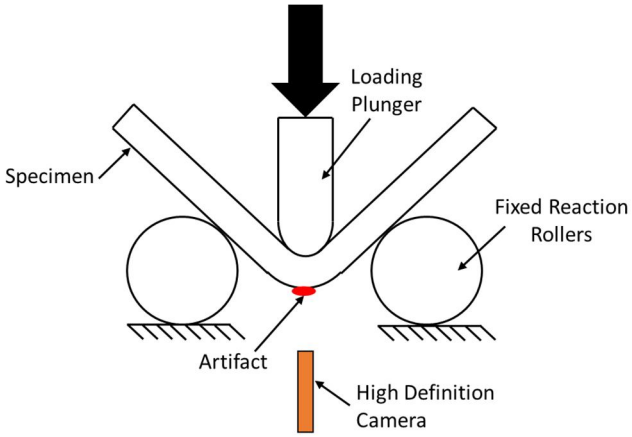


Figure 8.2 – Proposed monotonic three point bend test to replace the current monotonic uniaxial tensile test.

8.3 Artifact Sensitivity to Material Thickness

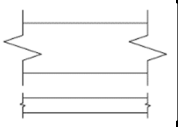
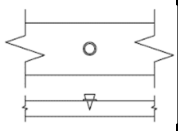
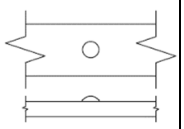
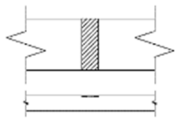
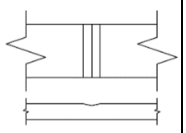
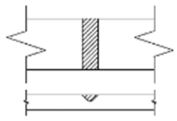
The effect of artifacts on material thickness is studied in this section based on the results of the cyclic bend tests. Also some recommendations and considerations are discussed for the next phase of testing. Five artifacts have been tested as part of this study (PAF, PW, GFW, NGT, and NWG) for two different material thicknesses W24x62 (t = 0.59 in.) and W36x150 (t = 0.94 in.). All of the artifacts used causes degradation in the specimen performance and premature fracture

initiation. Premature fracture initiation is dependent on the type of artifacts used, thickness of the material, and the amount of plastic strain being applied at the extreme fiber during cyclic testing. To relate each artifact damage impact to the material thickness an effective damage factor that measures the percentage across the material thickness for each artifact is being introduced. The effective damage uses the effected damage depth divided by the material thickness. Also, the normalized damage volume is calculated for the unotched cycle bend tests. This was calculated by calculating the effected damage volume for an artifact divided over the volume of the specimen for a 2 in. strip across the length of the specimen. This will help in comparing and understand the volumetric damage caused by the artifact. All of the artifacts effective damage factors that was used in the cyclic bent test is presented in Table 8.1.

Based on the effective damage factor it is noticed that more damage is exhibited on thinner specimens. Some artifacts are more sensitive to the material thickness since they have less footprint due to effective damage from artifacts. Any artifact that contained any type of weld an effected depth damage of 0.24 in. was used such as the PW, GFW, and NWG. This value was adopted from a study conducted by Lee et al (2012). Welds contain complex residual stress with fatigue precracking. For the NWG the effective damage was calculated by adding the 0.25 in. notch depth and the damage of 0.24 in. resulting in a total of 0.49 in. effected damage depth, and it resulted in the highest effective damage depth among all of the other artifacts in this study. Despite that NWG had the highest effective damage value, but it performed better than other artifacts, such as NGT, GFW, and PW. One of the most common defects in welded joints is the lack of fusion between the parent metal and the weld. Some defects can be detected by visual inspection by either a crack or some visible voids on the surface. In many cases the lack of fusion is visually undetectable and requires non-destructive methods using x-ray or ultrasonic inspection methods. This defect can occur in the NWG and cause premature failure due to the lack of fusion in the region between the base metal and the weld.

The PW and GFW shared similar effective damage parameter and also similar behavior throughout the cyclic bend tests. This can be concluded that despite if the weld is a puddle weld or a continuous weld on the surface of the extreme fiber the same damage is being exhibited throughout the material thickness.

Table 8.1 – Artifacts effective damage depth relative to material thickness and effective damage volume for cyclic bend tests unotched specimens

Artifact Type		Effected Damage Depth (in.)	Effected Damage Volume (in.^{3})	Specimen Flange Thickness and Width (in.)	Normalized Damage Depth (%)	Normalized Damage Volume (%)
1) No Artifact		N/A	N/A	W24x62 t = 0.59 w = 2.95	0%	0%
			N/A	W36x150 t = 0.94 w = 4.7	0%	0%
2) Powder Actuated Fasteners (PAF)		0.39	0.537	W24x62 t = 0.59 w = 2.95	66%	15%
			0.537	W36x150 t = 0.94 w = 4.7	41%	6%
3) Puddle Welds (PW)		0.24	0.265	W24x62 t = 0.59 w = 2.95	41%	8%
			0.265	W36x150 t = 0.94 w = 4.7	26%	3%
4) Ground Fillet Weld (GFW)		0.24	0.517	W24x62 t = 0.59 w = 2.95	41%	15%
			0.823	W36x150 t = 0.94 w = 4.7	26%	9%
5) Notch Ground to Taper (NGT)		0.125	0.230	W24x62 t = 0.59 w = 2.95	21%	7%
			0.367	W36x150 t = 0.94 w = 4.7	13%	4%
6) Notch Welded and Ground Smooth (NWG)		0.49	1.236	W24x62 t = 0.59 w = 2.95	83%	36%
			1.969	W36x150 t = 0.94 w = 4.7	52%	22%

The NGT had the least effective damage value but performed poorly throughout the cyclic bend tests. This can be related to the stress concentration exhibited at the v-notch tip. During the cyclic bend tests, this artifact was aggressively replicated by applying the v-notch throughout the whole width of the specimen. In future testing, this artifact can be grinded 1.0 in. at the center of the specimen rather than across the whole width of the specimen. Also, the notch size will have the similar dimensions for all the range of material thicknesses to be tested in the future which makes it more consistent for comparing the results. Theoretical stress concentration factor in elastic range, K_t, for a notch is used to study the relation of material thickness for cyclic bend tests. Figure 8.3 and Equations 8.1 and 8.2 presents the theoretical stress concentration factor equations and explanation for the v-notch. α is the notch angle in degrees, and K_{tu} is the stress concentration for a u-notch and is presented in Equation 8.2. For further information about the theoretical stress concentration for a v-notch refer to Young and Budynas (2002).

The theoretical stress concentration factor, K_t, for the W24x62 and W36x150 NGT is 1.72 and 0.998 respectively. Looking at the theoretical stress concentration results the W36x150 (thicker specimen) exhibited less stress concentrations than the W24x62 (thinner specimens). This can be related to the cyclic bend test results since the since the W36x150 NGT specimens outperformed the W24x6 specimens due to the lower stress concertation values at the v-notch. The average initiation cycle for the W24x62 and the W36x150 was 1.3 and 1.7 respectively. It can be concluded that the damage being exhibited on the specimens is related to the higher stress concentration at the v-notch for the thinner specimens compared to the thicker specimens which is dependent on the material thickness.

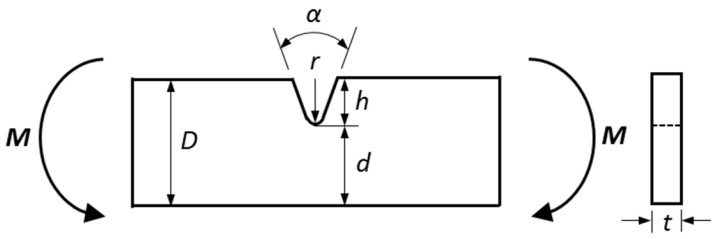


Figure 8.3 – Single notch on one side diagram

$$K_t = 1.11\,K_{tu} - \left[-0.0159 + 0.2243\left(\frac{\alpha}{150}\right) - 0.4293\left(\frac{\alpha}{150}\right)^2 + 0.3609\left(\frac{\alpha}{150}\right)^3\right]K_{tu}^2 \quad (8.1)$$

$$K_{tu} = C_1 + C_2\left(\frac{h}{D}\right) + C_3\left(\frac{h}{D}\right)^2 + C_4\left(\frac{h}{D}\right)^3 \quad (8.2)$$

$0.5 \le \frac{h}{r} \le 2.0$ $\qquad$ $2.0 \le \frac{h}{r} \le 20.0$

$C_1 = 1.795 + 1.481\left(\frac{h}{r}\right) - 0.211\left(\frac{h}{r}\right)^2$ $\qquad$ $C_1 = 2.966 + 0.502\left(\frac{h}{r}\right) - 0.009\left(\frac{h}{r}\right)^2$

$C_2 = -3.544 - 3.677\left(\frac{h}{r}\right) + 0.578\left(\frac{h}{r}\right)^2$ $\qquad$ $C_2 = -6.475 - 1.126\left(\frac{h}{r}\right) + 0.019\left(\frac{h}{r}\right)^2$

$C_3 = 5.459 + 3.691\left(\frac{h}{r}\right) - 0.565\left(\frac{h}{r}\right)^2$ $\qquad$ $C_3 = 8.023 + 1.253\left(\frac{h}{r}\right) - 0.020\left(\frac{h}{r}\right)^2$

$C_4 = -2.678 - 1.531\left(\frac{h}{r}\right) + 0.205\left(\frac{h}{r}\right)^2$ $\qquad$ $C_4 = -3.572 - 0.634\left(\frac{h}{r}\right) + 0.010\left(\frac{h}{r}\right)^2$

The PAF had the second highest effective damage value, after the NWG, with a damage depth of 0.39 in. It showed the best performance in the cyclic bend tests among the other tested artifacts. Although the effected damage is deeper the most of the artifacts but it had caused the least damage. From a study by Lee et al. (2012) for the same PAF, traces of melted zinc from the galvanized surface of the PAF which melted due to the heat exhibited by the friction between the PAF and base material during installation were noticed. Also, it was stated that the PAF was strongly fixed in the base metal with residual stress around it, and this was confirmed by the difference in hardness values around the PAF. During the cyclic bend tests, the W36x150 showed a delay in average fracture initiation in relative to the W24x62 specimens and this was due to the penetration depth of the PAF in relation to the flange thickness, but the W24x62 specimens outperformed the W36x150 specimens at the average fracture cycle.

Some artifacts are more sensitive to the material thickness than others, this can be related to the method those artifacts are placed and the amount of damage they exhibit. Artifacts that require welding cause changes in the material proprieties in the area surrounding the artifact (HAZ), some of the artifacts cause high stress concentration at the tip of a notch. Selecting the

artifacts limitation if testing cannot be conducted can be done based on the effected damage depth. If the effected damage depth exceeds the material thickness a bigger section must be used or a different attachment type or repair method can be used. More testing needs to be conducted for a range of different material thicknesses and to study a variety of artifact behavior. For future testing, it is recommended to test a minimum of five specimens with different notch sizes. Those tests can be broken to two monotonic bend test, which is proposed as part of the new test setup, and three cyclic bend tests. Repeat any outlier or suspicious results to have a set of results that represents the actual behavior of the artifact with different material thicknesses.

8.4 Method of Demonstrating Equivalence

Instead of using low cycle fatigue models, an alternative approach to showing that a connection with artifacts is acceptable is by demonstrating that the fracture resistance is at least as good as another artifact that has already been shown acceptable through full-scale testing. In this case, a set of monotonic tests and bend tests on flat plate specimens (e.g. three of each) with a new artifact could be tested. The resistance to fracture would be quantified based on the elongation at fracture for monotonic coupons, the cycles to fracture initiation for cyclic bend test specimens, and the cycles to full fracture in the bend test specimens. The resistance to fracture would then be compared to the fracture resistance of specimens with artifacts that have already been shown through full-scale testing to satisfy SMRF qualification criteria. If the resistance to fracture is at least as high as the artifacts that have already been shown acceptable, then by equivalence, then it would be highly likely that the new artifact would also satisfy SMRF qualification criteria.

This approach of demonstrating equivalence requires full-scale tests including benchmark artifacts. For instance, Eatherton et al. (2014) demonstrated that W24x62 and W36x150 specimens with and without RBS were capable of satisfying SMRF qualification with a grid of PAF over the flanges. Since monotonic tension tests and cyclic bend tests were also conducted on specimens with the same PAF, the resulting fracture resistance (measured as described in the previous paragraph) can be used as a baseline for evaluating other artifacts.

Since specimens with PAF have higher fracture resistance than other artifacts tested, it may be desirable to qualify other artifacts. If it is desired to create additional benchmark artifacts, full-scale testing is required. It is recommended that full-scale testing include both RBS and non-RBS connection configurations. Including specimens with at least two beam sections with different depth and flange thickness is useful for understanding the sensitivity of the fracture resistance to flange thickness and to inelastic strain demands (which vary with beam depth). Applying the artifact in a relatively dense pattern over the flanges and webs will make it likely that an artifact will be located at the inside of a local buckle which has been shown to be the typical fracture initiation location. Spacing of the artifacts should be selected as small as possible while limiting the interaction between adjacent artifacts.

CHAPTER 9 SUMMARY AND CONCLUSIONS

9.1 Summary

A framework was developed for evaluating the effect of artifacts (fasteners and defects) on the fracture behavior of seismic structural systems. The proposed framework starts with monotonic uniaxial tension tests and cyclic bend tests on flat plate specimens including the artifact. Complimentary finite element models are subjected to the same loading conditions up to the time fracture initiation was observed in the tests. Stress and strain data that is infeasible to measure in the tests, is extracted from the FE model results and used to calibrate fracture parameters ($VGI_{monotonic}^{critical}$ and λ). These fracture parameters can be used in the low cycle fatigue model known as the Cyclic Void Growth Model (CVGM) to predict ductile fracture initiation in structural systems subjected to earthquake loading.

To facilitate the calibration of fracture parameters for steel elements with artifacts, a testing method was devised wherein a flat steel plate is subjected to reversed cyclic inelastic bending. The flat plate specimen is cyclically bent around opposing rollers thus imposing cycles with constant curvature amplitude and therefore constant amplitude of extreme fiber strains. Fracture in seismic structural systems typically occurs at buckling locations that are subjected to large inelastic bending strains. Thus, a cyclic bending test is expected to better capture the strain distribution at critical locations than cyclic axial tests.

The proposed framework was applied to bare steel specimens and five artifact types including powder actuated fasteners, puddle welds, ground fillet welds, notches ground to taper, and notches filled with weld and ground smooth. Powder actuated fasteners and puddle welds represent typical deck attachments or attachment of nonstructural elements to the structural steel beam. The other three artifact types are methods described in AWS D1.8 (AWS 2012) for repairing notches, nicks, and gouges in the protected zone of seismic resisting structural systems.

9.1.1 Monotonic Uniaxial and Cyclic Bend Tests

A total of forty-eight uniaxial monotonic and cyclic bend tests were conducted. Specimens were cut from the flanges of W24x62 (0.59 in. thick) and W36x150 (0.94 in. thick) beams which were tested previously by Eatherton et al. (2013) in full-scale moment connection tests.

Monotonic tests showed that all artifacts led to a reduction in elongation at fracture. The puddle welds, fillet weld ground smooth, notch welded and ground, powder actuated fastener, and the notch ground to taper exhibited average elongations that were 89%, 85%, 76%, 68%, and 58% of the bare steel specimens, respectively. One specimen for each artifact type and material thickness is conducted for the monotonic tests. This was due to the shortage of material and it is inadequate to capture the behavior of each artifact tested and more tests needs to be conducted for each artifact.

Cyclic tests also showed a reduction in the number of cycles to fracture initiation and cycles to full fracture for specimens with artifacts as compared to bare steel specimens. The average number of cycles to fracture initiation were 5.3, 2.5, 3.0, 2.3, 1.5, and 2.3 for the bare steel, powder actuated fasteners, puddle welds, ground fillet welds, notches ground to taper, and notches filled with weld and ground smooth, respectively. The average number of cycles to full fracture of the specimen were 8.7, 6.4, 5.0, 4.3, 2.7, and 4.5 for the bare steel, powder actuated fasteners, puddle welds, ground fillet welds, notches ground to taper, and notches filled with weld and ground smooth, respectively.

The effect of several artifacts on fracture initiation and propagation was found to be sensitive to flange thickness. For instance, powder actuated fasteners installed in 0.59 in. thick material caused a bump on the back side where the tip was near the surface. Fracture was found to initiate at this location at a cycle number that was 28% of the cycle during which fracture initiated in bare steel specimens. On the other hand, fracture initiation for 0.94 in. thick specimens occurred in similar cycles regardless of whether they included powder actuated fasteners. The effect of puddle welds on fracture behavior was also found to be highly sensitive to thickness. Fractures initiated earlier in cyclic 0.59 in. thick specimens with puddle welds than bare specimens, but the fractures occurred on the side opposite the puddle weld. It is hypothesized that reduced

low cycle fatigue fracture resistance of thinner puddle weld specimens may have been due to a redistribution of inelastic strains (because of stronger material and more cross-sectional area at the puddle weld side) leading to larger inelastic strains on the face of the specimen opposite the puddle weld. Similar to PAF, fracture initiation and full fracture of 0.94 in. thick puddle weld specimens occurred at a similar cycle as bare steel specimens. The other three artifacts (ground fillet welds, notches ground to taper, and the notches filled with weld and ground smooth) also showed sensitivity to specimen thickness with the fracture resistance of thicker specimens less affected than thinner specimens. However, the thicker specimens for these three artifacts resisted less cycles to failure than the bare steel specimen.

A study was conducted to examine the cumulative theoretical fiber strain for the W24x62 (0.59 in.) and W36x150 (0.94 in.) to observe if there is any relation related to the thickness of the material and fracture initiation. Strain at the extreme fiber was calculated using the pure bend test curvature design method which assumes that plane sections remain plane for the first half cycle at the tension side. For the first half cycle, the extreme fiber strain were 0.051 in./in. and 0.079 in./in. for the 0.59 in. and 0.94 in. specimens respectively. The average cumulative strain values for the 0.59 in. and 0.94 in. specimens were 0.725 in./in. and 0.685 in./in. respectively. Although there is a significant difference in the extreme fiber strain between the 0.59 in. and 0.94 in. specimens but the average cumulative strain for the six tested groups were similar despite that some artifacts were dependent on the material thickness.

The effective damage depth for the five artifacts tested was studied to measure the sensitivity of the specimens with these artifacts to low cycle fatigue. Some artifacts behavior varied and was related to the specimen thickness. An approach using the effective damage depth was used to quantify the damage caused by the artifact in relation to the specimen thickness, and it uses the effected damage depth divided by the material thickness. Effective damage values for the 0.59 in. specimens were 66%, 41%, 41%, 21%, and 83% for the powder actuated fasteners, puddle welds, ground fillet weld, notch ground to taper, and notch welded and ground smooth, respectively. For the 0.94 in. specimens the effective damage values were 41%, 26%, 26%, 13%, and 52% for the powder actuated fasteners, puddle welds, ground fillet weld, notch ground to taper, and notch welded and ground smooth, respectively. Powder actuated fastener, and notch ground to taper are

sensitive to material. Meanwhile, the puddle welds, and the ground fillet weld were less dependent to the material thickness compared to the Powder actuated fastener, and notch ground to taper. On the other hand, the notch welded and ground smooth resulted in the highest effective damage depth but it performed some artifacts with lower effective damage depth but they are more prone to lack of fusion between the parental metal and the weld which will cause premature fracture. A conclusion can be stated that some artifacts are more sensitive to the material thickness than others, and this can be related to the method those artifacts are placed, stress concentrations, and the amount of damage they exhibit. The effect of residual stresses is also another factor that is related to the damage caused by the artifacts but it was an unclear the amount of residual stresses exhibited by the artifacts and the impact on fracture initiation and propagation. More testing is required for a range of different material thickness to measure the sensitivity of the artifacts to the material thickness.

9.1.2 Calibration of LCF Fracture Parameters to Predict Fracture

The results of the monotonic and cyclic tests were used in conjunction with complimentary finite element models to calibrate the CVGM fracture parameters. The calculated $VGI_{monotonic}^{critical}$ values for 0.59 in. specimens with artifacts were 0.23, 1.55, 0.23, 0.07, and 0.14 for the powder actuated fasteners, puddle welds, ground fillet weld, notch ground to taper, and notch welded and ground smooth, respectively. Similar trends were found for the 0.94 in. thick specimens with artifacts as the values for $VGI_{monotonic}^{critical}$ were found to be 0.26, 0.44, 0.36, 0.17, and 0.38 for the powder actuated fasteners, puddle welds, ground fillet weld, notch ground to taper, and notch welded and ground smooth, respectively. The calibration of the cyclic degradation parameter, λ, resulted in negative values for most artifacts implying that cyclic loading, instead of causing a degradation in fracture resistance, causes an increase in fracture resistance. Since this is implausible, it is concluded that more research is required to understand cyclic degradation with artifacts and that a value of λ=0 was more appropriate than a negative value.

After the unsuccessful calibration of the cyclic degradation parameter, λ, for some of the artifacts which resulted in negative values, further investigation was conducted. Two out of five artifacts were selected as part of this study and they were the powder actuated fastener and the

notch ground to taper. Those artifacts were included in the FE model to recalibrate the $VGI_{monotonic}^{critical}$ and the cyclic degradation parameter, λ, for those two artifacts. The $VGI_{monotonic}^{critical}$ values for 0.59 in. and 0.94 in. specimens with powder actuated fastener were 3.37 and 2.76 respectively. For the notched ground to taper the $VGI_{monotonic}^{critical}$ values for 0.59 in. and 0.94 in. specimens were 3.46 and 1.50 respectively. The higher $VGI_{monotonic}^{critical}$ values of the 0.59 in. specimens in relative to the 0.94 in. can be related to the material thickness sensitivity. Calibrating the cyclic degradation parameter, λ, for the powder actuated fasteners for the 0.59 in. and 0.94 in. specimens were 0.71 and 0.531 respectively. For the notched ground to taper the cyclic degradation parameter, λ, values for 0.59 in. and 0.94 in. specimens were 1.36 and 0.715 respectively. Adding the artifacts in both the monotonic uniaxial and cyclic bend tests FE model resulted in positive cyclic degradation values. Also, the $VGI_{monotonic}^{critical}$ values were higher when the artifacts were accounted in the FE model for the monotonic uniaxial test compared to the models with no artifacts. One of the solutions to overcome the negative cyclic degradation parameter is to model the artifacts in the FE models.

The calibrated fracture parameters were used to predict fracture initiation in full-scale specimens tested by Eatherton et al. (2013). Reasonable agreement was found between the cycles for which fracture initiation was observed in full-scale tests and the cycle predicted using the proposed framework (generally within 2 cycles). The calibrated fracture parameters for all five artifacts were used to predict when fracture would initiate at the worst case location in the SMRF connection (inside of the local buckle). It was predicted that for SMRF connections without a reduced beam section, the artifacts (except for the notch ground to taper) would lead to fracture initiation during the SMRF qualification cycle (1st cycle at 4% story drift) or after. The non RBS connection with notch ground to taper was predicted to initiate fracture in the 2nd cycle of 3% story drift. SMRF connections with reduced beam section and artifacts were predicted to experience fracture initiation as early as the 1st cycle at 3% story drift. However, fracture initiation was not associated with loss of load carrying capacity in full-scale testing. It is therefore necessary to consider fracture propagation in predicting whether these connections would satisfy SMRF qualification criteria.

Width effect study was conducted on monotonic uniaxial tests to measure the impact of width results to the actual test result and to resolve the negative value of the cyclic degradation parameter, λ, for some artifacts. A specimen width similar to the cyclic bend tests was used of 2.95 in. and 4.7 in. for the 0.59 in. and 0.94 in. specimens respectively. The specimens that were tested are bare, powder actuated fastener, and notched ground to taper for both 0.59 in. and 0.94 in. specimens. Increasing the width of the monotonic uniaxial coupons resulted in an increase of failure strains for the 0.59 in. specimens for the bare, powder actuated fastener, and notched ground to taper by 13%, 42%, and 36% respectively. For the 0.94 in. specimens the failure strains also increased for the bare, powder actuated fastener, and notched ground to taper by 9%, 34%, and 19% respectively. Also a slight increase in ultimate stress was noticed ranging from 1 to 2 % for both of the 0.59 in. and 0.94 in. specimens for the wider specimens. It is noticed that the wider specimens with artifacts resulted in higher failure strains from the bare specimens for both of the 0.59 in. and 0.94 specimens. Also, this increase in elongation will result in a larger critical monotonic void growth index, $VGI_{monotonic}^{critical}$, that may result in a positive cyclic degradation parameter, λ, and it might also have an impact on the fracture initiation results.

Different ULCF models have been investigated to predict fracture initiation. First a modification to the CVGM cyclic strength degradation parameter, λ, was tested. The calibration process is explained in Chapter 5. This new approach resulted in higher cyclic strength degradation parameter, λ, compared to the classical CVGM approach. Both the classic and the modified CVGM use the same $VGI_{monotonic}^{critical}$ values. The calibration was conducted on the circumferentially notched round bar tests and the 0.59 in. specimens with no artifacts for the cyclic bend tests with λ values of 0.30 and 0.63. Those values are greater than the values using the classical CVGM the cyclic strength degradation parameter, λ, which means that fracture initiation will be predicted earlier using the modified CVGM approach. Although the new cyclic strength degradation parameter values will predict fracture initiation earlier but for the W24x62 specimen with RBS in the full-scale tests predicted fracture initiation at the same cycle that was predicted using the classical CVGM.

The SWDM is another ULCF model that was investigated in this study. This model was developed by Smith et al. (2014) and it is a modified version of the CVGM which was previously

developed by Kanvinde and Deierlein (2007). The model is explained and the fracture parameters used in our calibration process are presented in Chapter 5. Applying this model in full-scale tests presented similar results to the classical CVGM fracture initiation predictions for the W24x62 specimen but for the W36x150 specimen with RBS fracture initiation was predicted earlier by three cycles. For the W24x62 specimen with RBS fracture initiation was predicted approximately two cycles, at second cycle of 4% story drift, after fractures were observed on the actual tests. While for the W36x150 specimen with RBS fracture initiation was predicted approximately one cycle, at first cycle of 4% story drift, before fractures were observed on the actual tests.

Another numerical fracture model used was the CDPM which was developed by Dufailly and Lemaitre (1995). This model is implemented in FE software LS-DYNA under the material model of MAT_DAMAGE_3 (MAT_153) and it can be calibrated to predict fracture initiation and propagation by element removal. Monotonic uniaxial test data was used to calibrate CDPM parameters for the 0.59 in. and 0.94 in. specimens for fracture initiation and propagation. Those calibrated CDPM parameters were later used as a baseline to calibrate fracture initiation for the cyclic bend tests. All of the CDPM parameters used to calibrate the uniaxial monotonic bare tests for 0.59 in. specimens were used except the critical damage, D_c. Two values for the critical damage, D_c, were calibrated using the cyclic bend test data. Notched specimen (*R025* and *R100*) shared the same D_c value of 0.15, while the unnotched specimen (*R000*) had a D_c value of 0.30.

The CDPM was applied only on one specimen, W24x62 RBS with no artifacts, out of the twelve specimens previously conducted by Eatherton et al. (2013) since it exhibited fracture with proper support of the fracture initiation and propagation. For the model with critical damage, D_c, value of 0.15, fracture initiation was predicted approximately one cycle after fractures were observed to form in the full-scale tests. While for the critical damage, D_c, value of 0.30, fracture initiation was predicted approximately two cycles after fractures were observed to form. The fracture initiation locations for the full-scale tests were captured in the FE models. They were located at the compression side of the flange local buckle in all of the three W24x62 RBS specimens tested by Eatherton et al. (2013) and the FE models. One of the locations out of multiple in which fracture initiation proceeded into a ductile tear propagating from the tip of the flange toward the middle of the flange at the center of the RBS. This was simulated by multiple elements

removed at the same time step in the FE model. The mechanism of fracture propagation in LS-DYNA is similar to the brittle fracture observed at the full-scale tests. Using a lower value (D_c = 0.15) for critical damage will predict fracture initiation closer to the actual test result but will cause higher cyclic degradation compared to using a higher critical damage value (D_c = 0.30). A good approach is to run a set of FE models for a range of values for critical damage to capture different failure scenarios.

Calibrating the CDPM parameters using the cyclic bend tests with the support of the uniaxial monotonic tests gave promising results for predicting fracture initiation locations and fracture propagation mechanism. Despite that the CDPM was off by at least one cycle, and also it was conservative in predicting the number of cycles between fracture initiation and propagation and it was off by four cycles from the full-scale test result. For future work also, it is recommended to model and study other specimens tested by Eatherton et al. (2013) and other researchers that conducted similar types of tests that contain different artifacts and to compare the test results with the CDPM results.

9.1.3 Recommendations of Future Work

A new cyclic test setup is proposed for future testing. The proposed changes are using a larger roller size for the cyclic bend tests to delay the fracture initiation for thicker specimens and also to incorporate a wider range of material thickness, proposing a range of material thickness to be tested with different artifacts to set limit states for each artifact based on material thickness, and finally to propose a monotonic three point bend test to replace the currently used monotonic uniaxial test. A bigger roller with a diameter of 16 in. is selected to maintain the ULCF criteria for the range of material thickness ranging from 0.25 in. to 1.5 in. A monotonic three point bend tests is also proposed with a plunger diameter of 2 in. to ensure that fracture initiation occurs at the extreme fiber of the specimen which is similar to the cyclic bend tests. Also, using the same width of the specimens that are tested using the cyclic bend tests. This will enable a consistent calibration for the ULCF models since the failure location and mechanism is the identical. A plunger size of 2 in. will result in an estimated value of maximum strain at the extreme fiber of 0.228 in. and 0.320 in./in. for 0.59 in. and 0.94 in. specimens. For future testing, it is recommended to test a minimum

of five specimens with different notch sizes. Those tests can be broken to two monotonic bend tests and three cyclic bend tests accounting for repeating any test with suspicious results.

Instead of using low cycle fatigue models, an alternative approach to showing that a connection with artifacts is likely to satisfy SMRF qualification criteria based on coupon testing was also proposed based on demonstrating equivalence. If an artifact is shown to have similar or less effect on fracture resistance (measured by monotonic elongation at fracture, cycles to fracture initiation, and cycles to full fracture in bend tests) as compared to an artifact already shown acceptable through full-scale testing, then by equivalence it would be expected to satisfy SMRF qualification also. This approach to demonstrating acceptability of an artifact does not suffer from the challenges listed above for the low cycle fatigue model approach, but does require a set of benchmark artifacts to be proven acceptable through full-scale testing.

9.2 Conclusion

Ideally, fracture parameters are constant for a material but fracture parameters were different for each artifact. Also, it was noticed that one of the fracture parameters, cyclic degradation parameter, for the bare cyclic bend test and the CNT specimens were different. This can be related to the time step and the location in which fracture initiates. In the case of the bend tests fracture initiation occurs at the surface of the specimen, while for uniaxial tests it occurs at the center of the specimen and propagates to the surface. This delay could be more prone to cause inconsistency in fracture parameters between bend tests and uniaxial tests.

The effect of several artifacts on fracture initiation and propagation was found to be sensitive to many factors that needs to be further investigated. Mainly artifacts are sensitive to the material thickness, insertion method, stress concentration, and the effected damage volume exhibited by the artifact. Some of the repair methods allowed in the protected zone region cause more damage than prohibited attachments or fasteners.

The equivalent plastic strain and stress triaxiality are sensitive to the width of specimen and if the artifact is modeled in the FEM. Even if the load-displacement curve of the specimens

are relatively similar. Therefore, adding the artifacts in any analysis is essential to capture the actual equivalent plastic strain and stress triaxiality.

The three LCF models used were dependent on the equivalent plastic strain and stress triaxiality in addition to other fracture parameters. Some models such as the CVGM and SWDM required certain material testing to calibrate fracture parameters, while the CDPM fracture parameters can be calibrated using FE software in which it is implemented. In this work, the monotonic and cyclic bend tests were used to calibrate three LCF models to predict fracture initiation. The developed framework was able to evaluate the effect of artifacts on SMRF plastic hinge regions using economical coupon tests. All of the models are capable of predicting fracture initiation and propagation using element removal using FE modeling.

REFERENCES

ABAQUS. (2012). *Version 6.12.* Providence, RI: Dassault Systémes Simulia Corp.

Abbas, E.K., and Eatherton, M.R. (2014). "Test Method For Evaluating The Effect of Artifacts on Seismic Behavior of Moment Frames". *10th U.S. National Conference on Earthquake Engineering.* Anchorage, AK.

Adey, B. T., Grondin, G. Y., and Cheng, J. J. (2000). "Cyclic Loading of End Plate Moment Connections". *Candian Journal of Civil Engineering*, Vol. 27, No. 4, pp. 682-701.

AISC. (2010). *ANSI/AISC 341-10 Seismic Provisions for Structural Steel Buildings.* Publishes by AISC.

Anderson, T. L. (2004). *Fracture Mechanics: Fundamentals and Applications.* Boca Raton, FL: CRC Press.

Armstrong, P. J., and Frederick, C. O. (1966). *"A Mathematical Representation of the Multiaxial Bauschinger Effect".* Berkeley, UK: (No. CEGP Report RD/B/N731). Berkeley Nuclear Laboratories, Research & Development Department.

ASTM A370-12a. (2012). *A370-12a Standard Test Methods and Definitions for Mechanical Testing of Steel Products.* ASTM.

ASTM A6/A6M-12. (2012). *A6/A6M-12 Standard Specification for General Requirements for Rolled Structural Steel Bars, Plates, Shapes, and Sheet Piling.*

AWS D1.8/D1.8M. (2009). *An American National Standard " Structural Welding Code – Seismic Supplement"* . American Welding Society.

Brewster, D. (1816). On The Communication of The Structure of Doubly Refracting Crystals to Glass, Muriate of Soda, Fluor spar, and Other Substances, by Mechanical Compression

and Dilatation. *Philosophical Transactions of the Royal Society of London*, Vol. 106, pp. 156-178.

Chen, S. J., and Chao, Y. C. (2001). Effect of Composite Action on Seismic Performance of Steel Moment Connections with Reduced Beam Sections. *Journal of Constructional Steel Research*, Vol. 57, No. 4, pp. 417-434.

Chen, W. F., and Patel, K. V. (1981). Static Behavior of Beam-to-Column Moment Connections. *Journal of the Structural Division*, Vol. 107, No. 9, pp. 1815-1838.

Chi, B., and Uang, C. M. (2002). "Cyclic Response and Design Recommendations of Reduced Beam Section Moment Connections With Deep Columns". *Journal of Structural Engineering*, Vol. 128, No. 4, pp. 464-473.

Civjan, S. A., Engelhardt, M. D., & Gross, J. L. (2000). Retrofit of Pre-Northridge Moment-Resisting Connections. *Journal of Structural Engineering*, Vol. 126, No. 4, pp. 445-452.

D'Escata Y. and Devaux, J.C. (1979). *Numerical Study of Initiation, Stable Crack Growth and Maximum Load with a Ductile Fracture Criterion Based on the Gowth of Holes.* Philadelphia: ASTM STP 668, American Society of Testing and Materials.

Dufailly, J., and Lemaitre, J. (1995). Modeling Very Low Cycle Fatigue. *International Journal of Damage Mechanics*, Vol. 4, No. 2, pp. 153-170.

Eatherton, M. R., Toellner, B. W., Watkins, C. E., and Abbas, E. (2013). *Experimental Investigation on the Effect of Powder Actuated Fasteners on Seismic Performance of Moment Connections.* Blacksburg, VA: Virginia Tech SEM Report Series. Report No. CE/VPI-ST-13/05.

Engelhardt, M. D., and Husain, A. S. (1993). Cyclic-Loading Performance of Welded Flange-Bolted Web Connections. *Journal of Structural Engineering*, Vol. 119, No. 12,pp. 3537-3550.

Engelhardt, M. D., Fry, G., Johns, S., Venti, M., and Holliday, S. (2000). *Behavior and design of radius-cut, reduced beam section connections.* SAC Report No. SAC/BD-00/17.

Griffith, A. A. (1921). The Phenomena of Rupture and Flow in Solids. *Philosophical Transactions of the Royal Society of London. Series A, Containing Papers of a Mathematical or Physical Character*, Vol. 221, pp. 163-198.

Hajjar, J.F., Leon, R.T., Gustafson, M.A., and Shield, C.K. (1998). "Seismic Response of Composite Moment-Resisting Connections. II: Behavior". *ASCE Journal of Structural Engineering*, Vol. 124, No. 8, pp. 877-885.

Hancock, J. W., and Mackenzie, A. C. (1976). On the Mechanics of Ductile Fracture in High Strength Steels Subjected to Multiaxial States of Stress. *Journal of the Mechanics and Physics of Solids*, Vol. 14, No. 2, pp. 147-169.

Huang, Y. and Mahin, S. A. (2010). *Simulating the Inelastic Seismic Behavior of Steel Braced Frames Including the Effects of Low-Cycle Fatigue.* Berkeley, CA: Pacific Earthquake Engineering Research Center. Report No. PEER 2010/104.

Kanvinde, A. M. (2004). *"Micromechanical Simulation of Earthquake-Induced Fracture in Steel Structures".* Stanford, CA: Stanford University.

Kanvinde, A. M., and Deierlein, G. G. (2006). The Void Growth Model and The Stress Modified Critical Strain Model to Predict Ductile Fracture in Structural Steels. *Journal of Structural Engineering*, Vol. 132, No. 12, pp. 1907-1918.

Kanvinde, A. M., and Deierlein, G. G. (2007). Cyclic Void Growth Model to Assess Ductile Fracture Initiation in Structural Steels Due to Ultra Low Cycle Fatigue . *Journal of Engineering Mechanics,* Vol. 133, No. 6, pp. 701-712.

Kanvinde, A.M. and Deierlein, G.G. (2004). *Micromechanical Simulation of Earthquake Induced Fracture in Steel Structures.* Stanford, CA, Stanford University: Blume Center Report No. 145.

Lee, C. H., Jeon, S. W., Kim, J. H., and Uang, C. M. (2005). Effects of Panel Zone Strength and Beam Web Connection Method on Seismic Performance of Reduced Beam Section Steel Moment Connections. *Journal of Structural Engineering*, Vol. 131, No. 12, pp. 1854-1865.

Lee, M., Kobayashi, G., and Tagawa, Y. (2012). “Comparative Study on Effect of Powder Actuated Nail and Stud Welding on Steel Member". *15 World Conference of Earthquake Engineering, Lisbon 2012.*

Lemaitre, J. (1986). Local Approach of Fracture. *Engineering Fracture Mechanics*, Vol. 25, No. 5, pp. 523-537.

Lemaitre, J., and Chaboche, J.L. (1994). *Mechanics of solid materials.* Cambridge, UK: Cambridge University Press.

Leon, R. T., Hajjar, J. F., and Gustafson, M. A. (1998). Seismic Response of Composite Moment-Resisting Connections. I: Performance. *Journal of Structural Engineering*, Vol. 124, No. 8, pp. 868-876.

McClintock, F. A. (1968). Local Criteria for Ductile Fracture. *International Journal of Fracture*, Vol. 4, No. 2, pp. 101-130.

Mudry, F. (1983). Methodology and Applications of Local Criteria for the Prediction of Ductile Tearing. *Elastic--Plastic Fracture Mechanics*, pp. 263-283.

Myers, A. T. (2009). *"Testing and Probabilistic Simulation of Ductile Fracture Initiation in Structural Steel Components and Weldments".* Stanford, CA: Stanford University. Report No. 170.

Parfitt, J., and Chen, W. F. (1976). Tests of Welded Steel Beam-to-Column Moment Connections. *Journal of the Structural Division*, Vol. 102, No. 1, pp. 189-202.

Paris, P. C., and Erdogan, F. (1963). A Critical Analysis of Crack Propagation Laws. *Journal of Fluids Engineering*, Vol. 85, No. 4, pp. 528-533.

Pineau, A. (1992). Global and Local Approaches of Fracture—Transferability of Laboratory Test Results to Components. In A. Argon, *In Topics in Fracture and Fatigue* (pp. pp. 197-234). New York: Springer.

Popov, E. P., and Pinkney, B. R. (1969). Cyclic Yield Reversal in Steel Building Connections. *Journal of the Structural Division*.

Rice, J. R., and Tracey, D. M. (1969). "On the Ductile Enlargement of Voids in Triaxial Stress Fields". *Journal of the Mechanics and Physics of Solids*, Vol. 17, No. 3, pp. 201-217.

Ricles, J. M., Fisher, J. W., Lu, L. -W., & Kaufmann, E. J. (2002). "Development of Improved Welded Moment Connections for Earthquake-Resistant Design". *Journal of Constructional Steel Research, Vol. 58*, 565-604.

Ricles, J. M., Mao, C., Lu, L. W., and Fisher, J. W. (2002). Inelastic Cyclic Testing of Welded Unreinforced Moment Connections. *Journal of Structural Engineering*, Vol. 128, No. 4, pp. 429-440.

Saykin, V. V., Nguyen, T. H., Hajjar, J. F., Deniz, D., and Song, J. (2014). "Validation of a Finite Element Approach to Modeling of Structural Collapse of Steel Structures.". *Structures Congress 2014*, (pp. 2162-2173). Boston, MA.

Schijve, J. (2001). *Fatigue of structures and materials.* Dordrecht: Kluwer Academic.

Smith, C. M., Deierlein, G., and Kanvinde A. M. (2014). *A Stress-Weighted Damage Model for Ductile Fracture Initiation in Structural Steel Undercyclic Loading and Generalized Stress States.* Stanford, CA: Stanford University, The John A. Blume Earthquake Engineering Center. Report No. 187.

Uang, C. M., Yu, Q. S. K., Noel, S., and Gross, J. (2000). Cyclic Testing of Steel Moment Connections Rehabilitated with RBS or Welded Haunch. *Journal of Structural Engineering*, Vol. 126, No. 1, pp. 57-68.

Young, W. C., and Budynas, R. G. (2002). *Roark's formulas for stress and strain.* New York: McGraw-Hill.

Youssef, N. F. G., Bonowitz, D., and Gross, J. L. (1995). *Survey of Steel Moment-Resisting Frame Buildings Affected by the 1994 Northridge Earthquake.* US National Institute of Standards and Technology.

APPENDIX A DESCRIPTION OF BEND TEST FRACTURES

The results of the cyclic bend tests are grouped based on the artifact, then specimen thickness and notch radius. See Table 3.3 for specimen names which consist of four numbers. The first number corresponds to the nominal depth of the beam from which the specimen was taken (W24 for W24x62 and W36 for W36x150). The artifact identification can take six values (B = bare steel, PAF = powder actuated fasteners, PW = puddle welds, GFW = fillet welds ground smooth, NGT = notches ground to taper, and NWG = notches filled with weld and ground smooth) followed by the specimen number for that artifact series (1 through 3). The third number corresponds to the specimen thickness (T59 for 0.59 in. and T94 for 0.94 in.) and the final number corresponds to the radius of the side notches in the specimen (R000 for no notch, R025 for 0.25 in. radius, R100 for 1.00 in. radius).

A.1 No Artifact (B)

Six bare steel bend specimens were tested (three W24x62 and three W36x150). These tests act as control tests with which to compare the effect of the five artifacts being tested. As expected, the bare steel specimens survived more cycles prior to fracture initiation than specimens with artifacts. Also expected was that the 0.59 in. thick specimens could undergo more cycles prior to fracture initiation than 0.94 in. thick specimens because the extreme fiber strains are considerably smaller. The side notch radius also had a noticeable effect on the fracture behavior with smaller radius notches causing earlier fracture initiation.

Specimen W24-B1-T59-R000

After 18 cycles fracture initiation was observed at the center of the bottom side of the specimen at multiple locations. Fracture propagated throughout the bottom side until complete fracture occurred at cycle 27. The rate of the crack growth was very small compared to other specimens and it is shown in Figure A.1 the fracture initiation at cycle 18 and the complete fracture cycle 27.

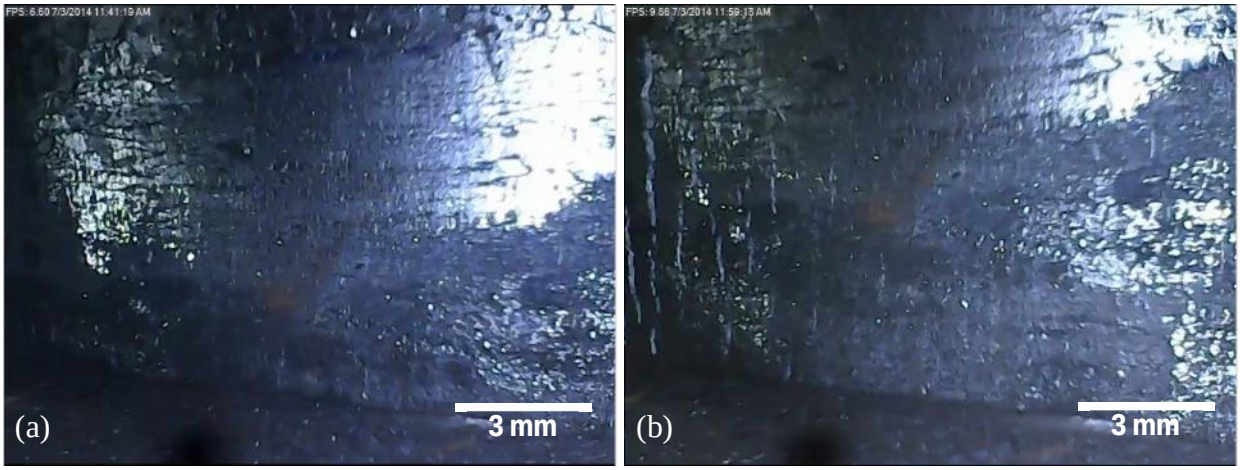


Figure A.1 – (a) Fracture initiation at multiple locations at the bottom of Specimen W24-B1-T59-R000 on cycle 18, (b) complete fracture at the bottom of the specimen at cycle 27.

Specimen W24-B2-T59-R025

Fracture initiated at multiple locations at the bottom side of the specimen on cycle 3. On cycle 5 fracture propagated at multiple locations on the bottom side and complete fracture occurred while the specimen was at tension on the bottom side. Fracture initiation and final fracture is shown in Figure A.2.

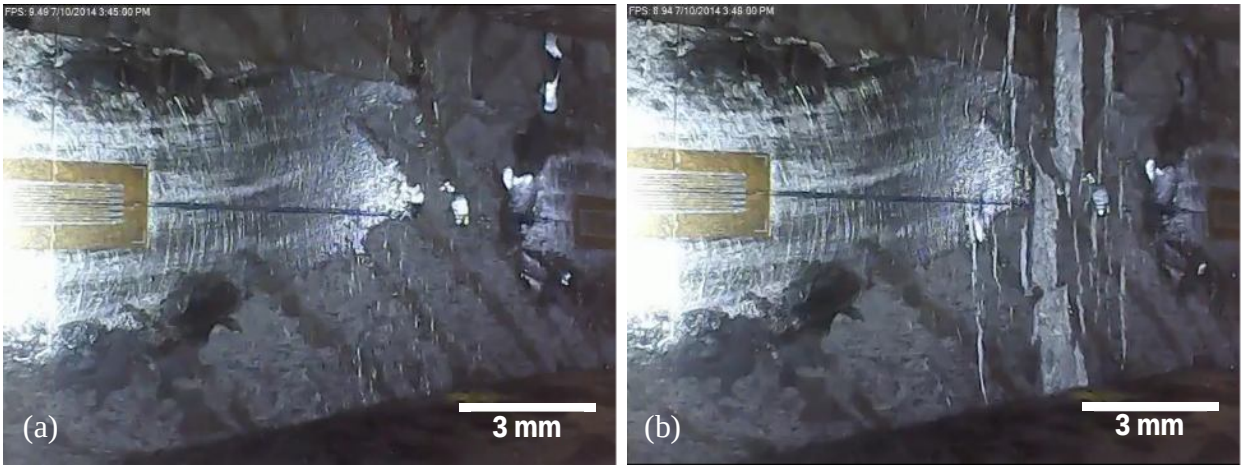


Figure A.2 – (a) Fracture initiation at multiple locations at the bottom of Specimen W24-B2-T59-R025 on cycle 3, (b) complete fracture at the bottom side of the specimen at cycle 5.

Specimen W24-B3-T59-R100

Fracture initiated at multiple locations at the bottom side of the specimen on cycle 4 as shown in Figure A.3. On cycles 5 and 6 fracture propagated at multiple locations on the bottom side. On the top side, fracture initiated at multiple locations at cycle 5 and continued to propagate until complete fracture occurred at cycle 7 while the top side of the specimen was in tension as shown in Figure A.4.

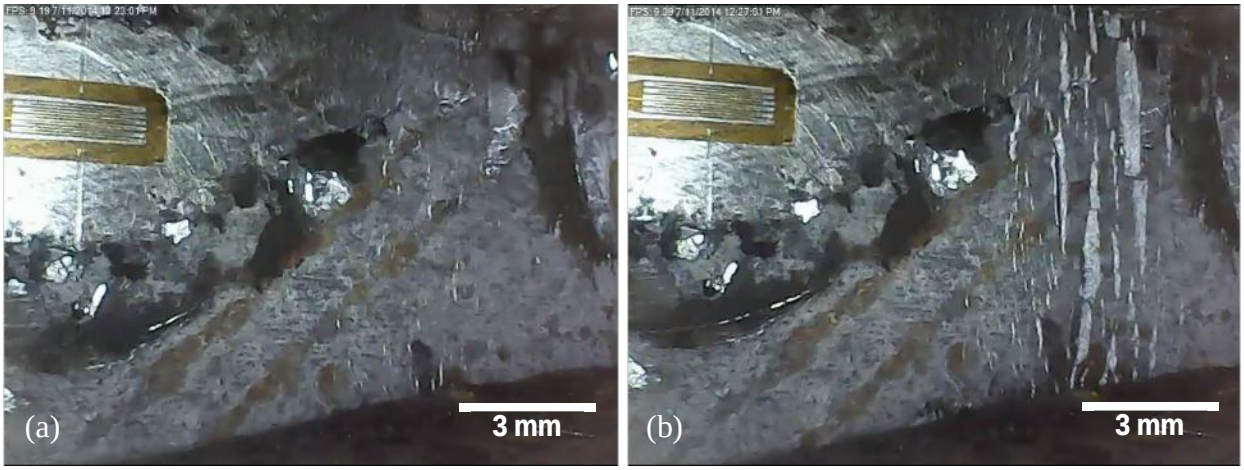


Figure A.3 – (a) Fracture initiation at multiple locations at the bottom of Specimen W24-B3-T59-R100 on cycle 4, (b) fracture propagation at multiple locations on cycle 6 at the bottom of the specimen cycle 6 before complete fracture occurred.

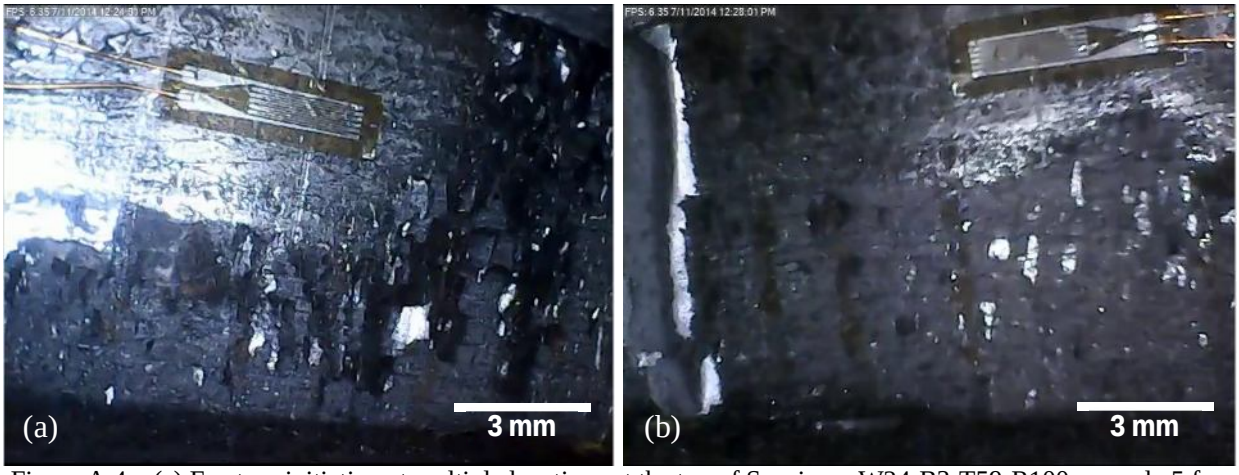


Figure A.4 – (a) Fracture initiation at multiple locations at the top of Specimen W24-B3-T59-R100 on cycle 5 from the top left camera, (b) complete fracture at the center of the top side of Specimen W24-B3-T59-R100 on cycle 7 from the top right camera.

Specimen W36-B1-T94-R000

Fracture initiated at the center of the top side of the specimen at cycle 4 at multiple locations. Fracture propagated throughout the bottom side until complete fracture occurred at cycle 7 while the bottom of the specimen was at tension. Figure A.5 shows the fracture initiation and the complete fracture. The rate of the crack growth was very small compared to other specimens.

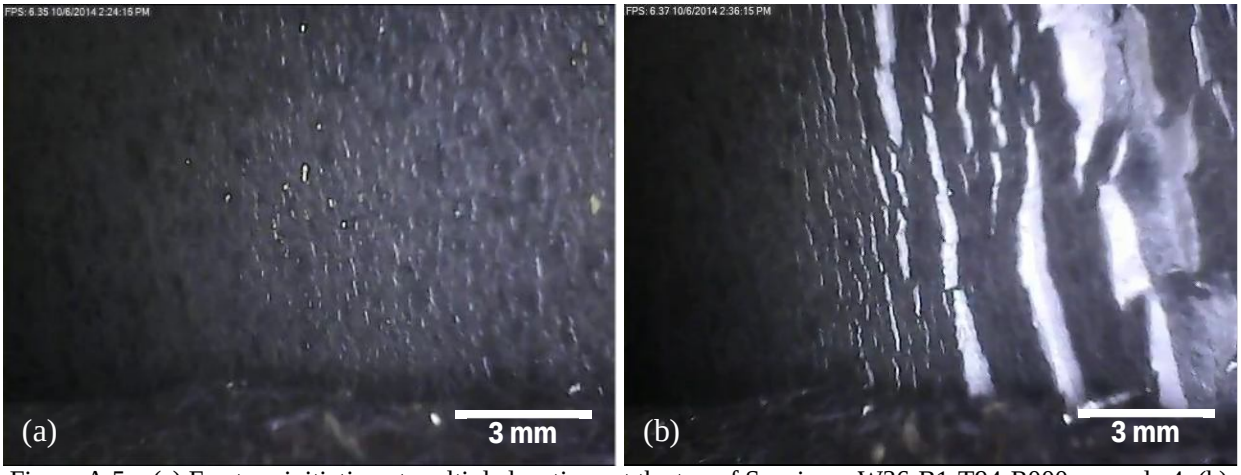


Figure A.5 – (a) Fracture initiation at multiple locations at the top of Specimen W36-B1-T94-R000 on cycle 4, (b) fracture at cycle 7 while the top of the specimen is at compression (top view camera).

Specimen W36-B2-T94-R025

Fracture initiated at multiple locations at the top side of the specimen closer to the side notch on cycle 1 as shown in Figure A.6 (a). On cycle 2 fracture propagated from the side notch on the top side and complete fracture occurred while the specimen was at tension on the top side as shown in Figure A.6 (b).

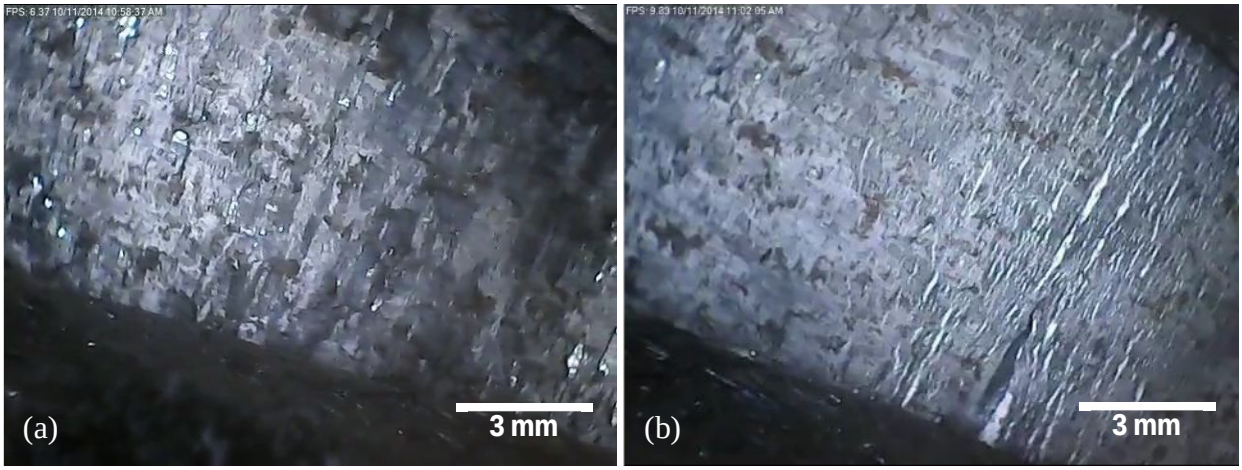


Figure A.6 – (a) Fracture initiation at multiple locations at the top side of Specimen W36-B2-T94-R025 on cycle 1, (b) fracture propagation at cycle 2

Specimen W36-B3-T94-R100

Fracture initiated at multiple locations at the top side of the specimen on cycle 2 and complete fracture occurred at the beginning of cycle 3 while the top of the specimen was in tension as shown in Figure A.7. On the bottom side, fracture initiated at multiple locations at cycle 2 as shown in Figure A.8.

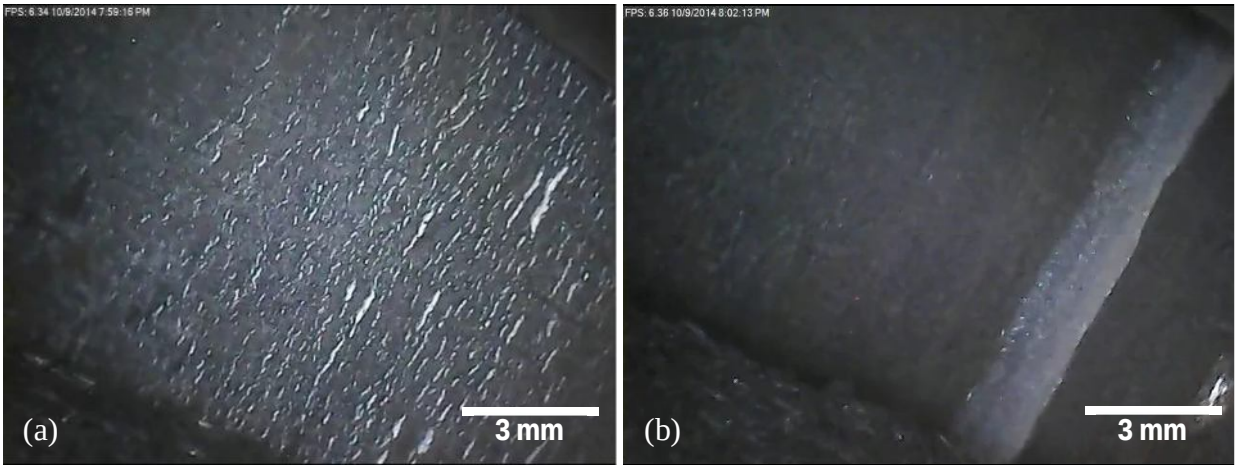


Figure A.7 – (a) Fracture initiation at multiple locations at the top of Specimen W36-B3-T94-R100 on cycle 2, (b) complete fracture occurred at the beginning of cycle 3 at the center of the specimen.

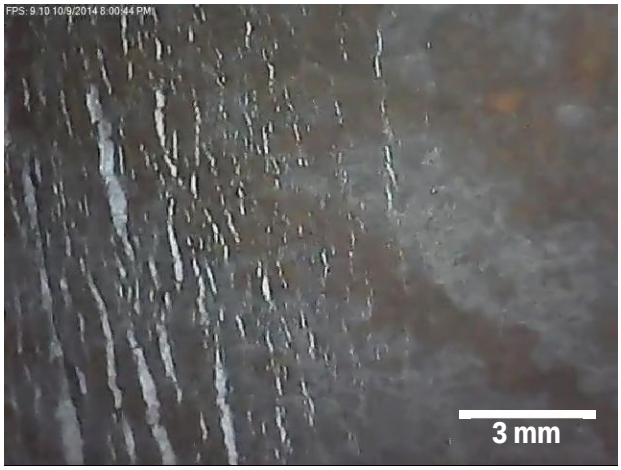


Figure A.8 – Fracture initiation at multiple locations at the bottom of Specimen W36-B3-T94-R100 on cycle 2

A.2 Powder Actuated Fasteners (PAF)

A total of six specimens installed with PAF were tested (three W24x62 and three W36x150). One of the two artifacts were tested previously by Eatherton el al. (2013) in full-scale tests were PAFs. Conducting tests with those artifacts will be helpful to measure the effectiveness of the cyclic bend tests in the prediction of fracture initiation with the full-scale results. The PAFs used in this study were Hilti X-ENP-19 L15 Nails and they were shot into test specimens with a 0.22 caliber Hilti DX 76-PTR tool. Three criteria discussed previously were met for each PAF placed to make sure it is in compliance.

The W24x62 specimens showed signs of early fracture initiation due to the PAF causing damage, a small hump, at the bottom side of the specimen. For the W24x62 unnotched specimen (*W24-PAF1-T59-R000*), despite the early fracture initiation but there was an excessive resistance to final fracture with a slow fracture propagation rate. Complete fracture occurred for the W24x62 specimen while the bottom side of the specimen was at tension, although there were signs of fracture initiation near the head of the PAF.

For the W36x150 specimens, all of the specimens fracture initiation was first noticed near the head of the PAF. Most of the W24x62 and W36x150 specimens fractured while the bottom

side was at tension. Changing the notch size also had a noticeable effect on the fracture behavior for the W24x62 but not for the W36x150 specimens.

Specimen W24-PAF1-T59-R000

The specimen was cycled to 18 cycles before fracture occurred at the center of the specimen. When the PAF was placed at the top of the specimen, a small hump at the bottom of the specimens was noticed due to the PAF placement. At cycle 3 a fracture initiated at the bottom tip of the indentation caused by the PAF as shown in Figure A.9. Signs of PAF dislocation were noticed at cycle 12 while cycling the specimen, although there were no signs of fracture initiation near the head of the PAF. Fracture initiation was noticed near the head of the PAF at cycle 15. The fracture propagation at the head of the PAF can be clearly seen in Figure A.10. Although fracture initiation have occurred at multiple location at the center of the specimen early during testing, but the fracture propagation was controlled at the bottom of the artifact.

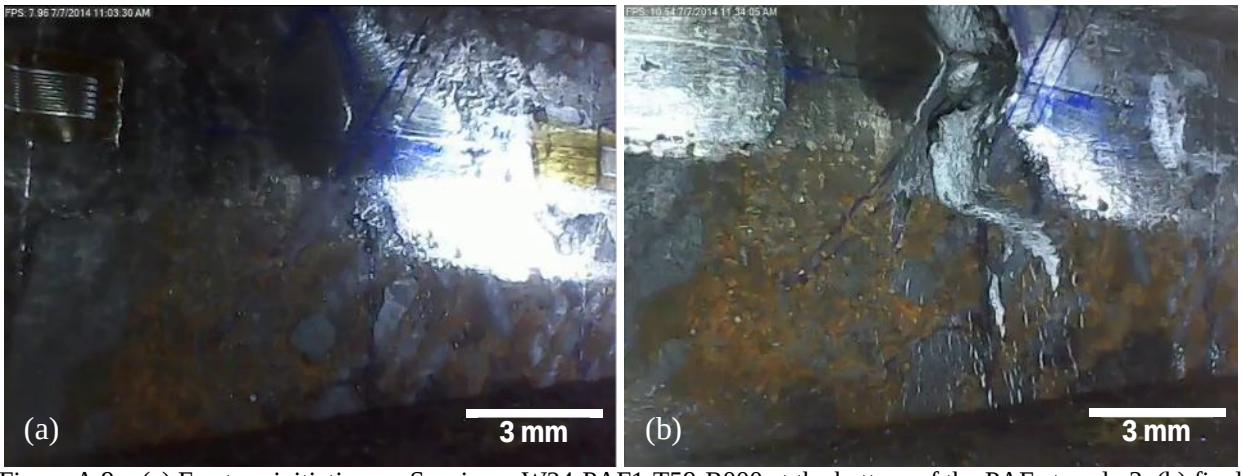


Figure A.9 – (a) Fracture initiation on Specimen W24-PAF1-T59-R000 at the bottom of the PAF at cycle 3, (b) final fracture at cycle 18.

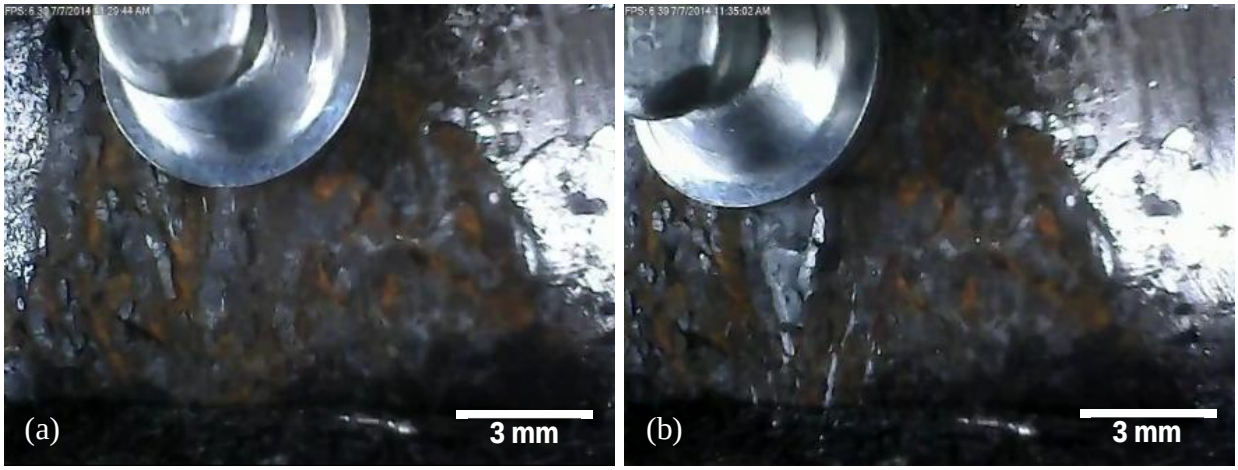


Figure A.10 – (a) Fracture initiation on Specimen W24-PAF1-T59-R000 at the top of the PAF at cycle 15, (b) final fracture at cycle 18 propagating from the PAF.

Specimen W24-PAF2-T59-R025

The specimen was cycled to 4 cycles before fracture occurred at the center of the specimen. When the PAF was placed at the top of the specimen, a small hump at the bottom of the specimens was noticed due to the PAF placement. At cycle 2 a fracture initiated at the bottom tip of the indentation caused by the PAF as shown in Figure A.11. Fracture initiation signs were noticed around the end of the PAF at cycle 3. Signs of PAF dislocation were noticed at cycle 3 while cycling the specimen, although there were no signs of fracture initiation near the head of the PAF. Fracture initiation was noticed near the head of the PAF at cycle 4. The fracture propagation at the head of the PAF can be clearly seen in Figure A.12. While the top of the PAF was at compression complete fracture occurred.

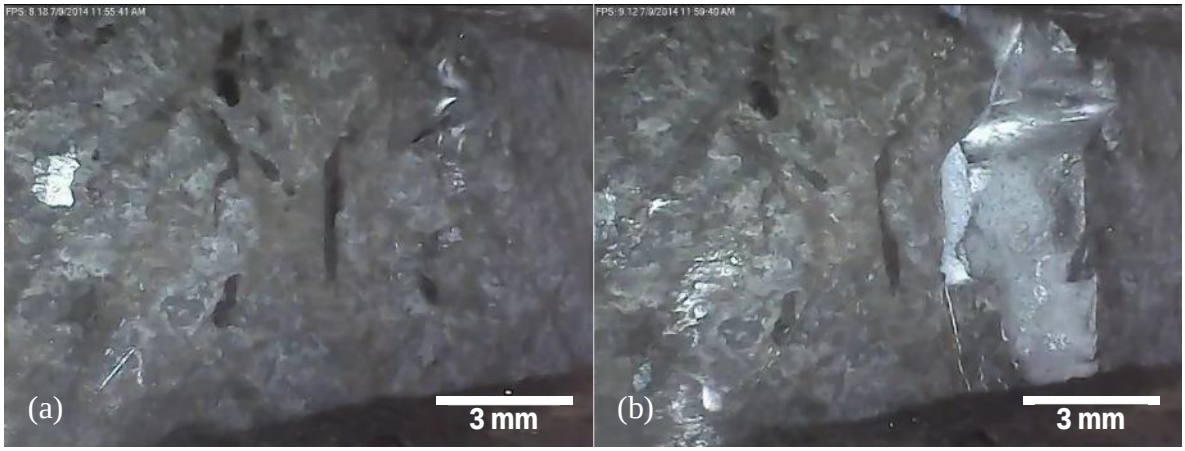


Figure A.11 – (a) Fracture initiation on Specimen W24-PAF2-T59-R025 at the bottom of the PAF at cycle 2, (b) cycle 4 complete fracture at bottom of PAF.

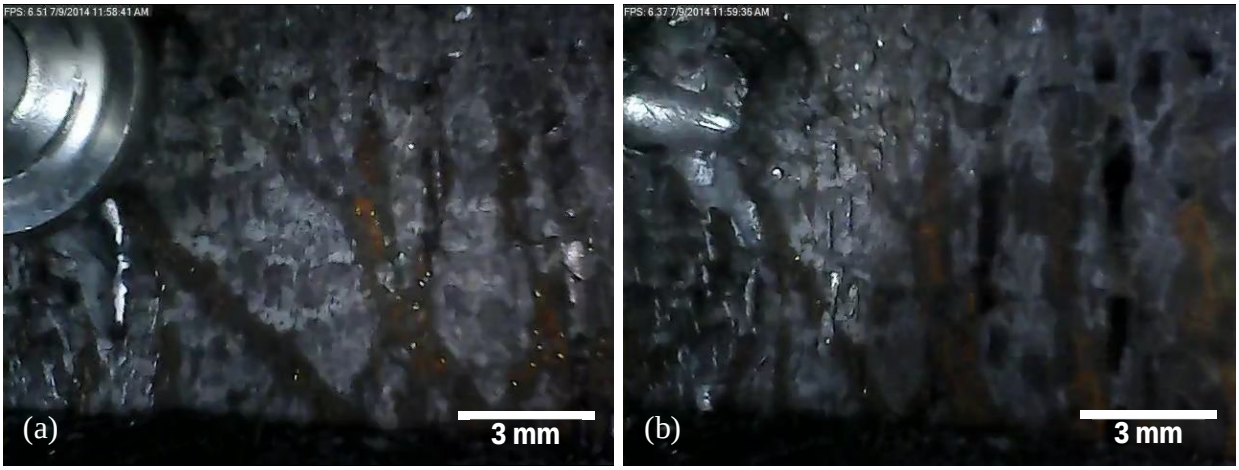


Figure A.12 – (a) Cycle 4 top of PAF while in tension, (b) top of PAF at compression when complete fracture occurred.

Specimen W24-PAF3-T59-R100

The specimen was cycled to 5 cycles before fracture occurred at the center of the specimen. When the PAF was placed at the top of the specimen, a small hump at the bottom of the specimens was noticed due to the PAF placement. At cycle 3 fracture initiated at multiple locations at the bottom of the specimen, also a fracture is initiated at the bottom tip of the indentation caused by the PAF as shown in Figure A.13. At cycle 4 the fracture propagated at the center of the specimen at the PAF end. Fracture initiation signs were noticed in the area around the head of the PAF at

cycle 4 with no signs of fracture initiating from the PAF. Signs of PAF dislocation were noticed at cycle 5 with a rapid fracture propagation initiating at the head of the PAF as shown in Figure A.14. Complete fracture occurred while the top of the PAF head was at compression at the end of cycle 5.

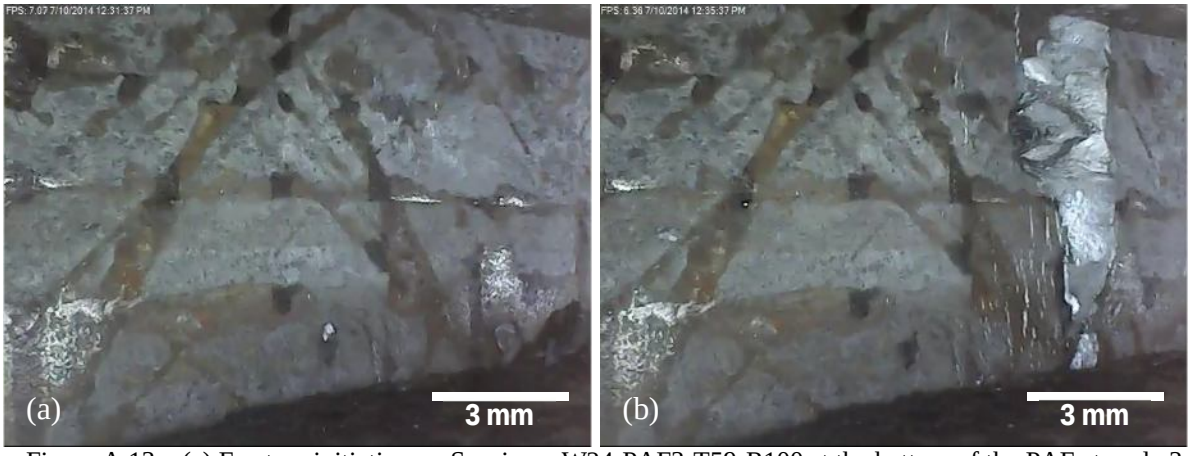


Figure A.13 – (a) Fracture initiation on Specimen W24-PAF3-T59-R100 at the bottom of the PAF at cycle 3, (b) complete fracture on Specimen W24-PAF2-T59-R100 at the bottom of the PAF at cycle 5.

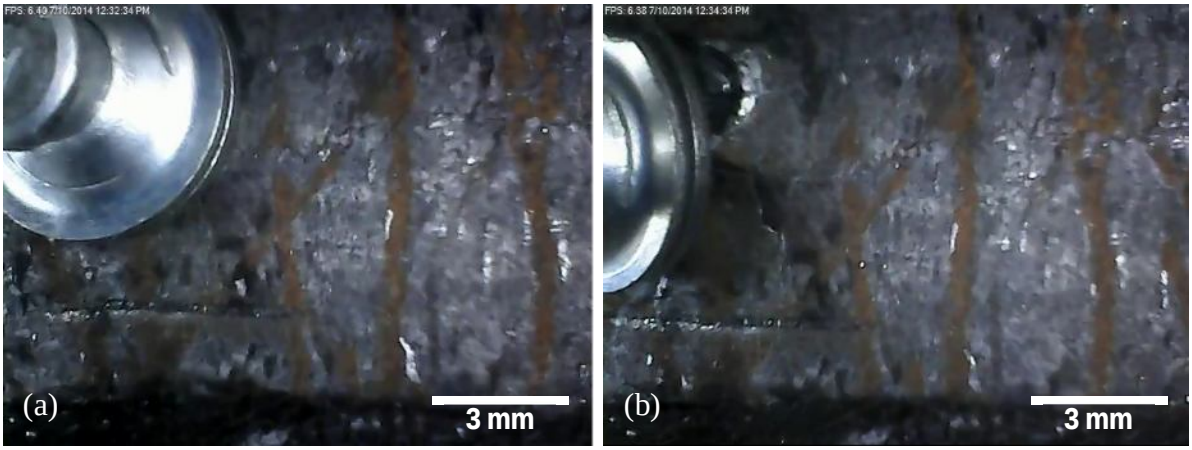


Figure A.14 – (a) Cycle 4 top of PAF while in tension showing signs of fracture initiation around the PAF, (b) cycle 5 top of PAF showing signs of fracture propagated 5mm.

Specimen W36-PAF1-T94-R000

The specimen was cycled to 6 cycles before fracture occurred at the center of the specimen. When the PAF was placed at the top of the specimen, there was no hump noticed at the bottom of

the specimen. At cycle 4 a fracture is initiated at the top of the specimen near the PAF as shown in Figure A.15. Signs of fracture propagation near the head of the PAF and PAF dislocation were noticed at cycle 5 while cycling the specimen. Fracture initiation was noticed at the bottom side of the specimen at cycle 4 and propagated at cycle 5 as shown in Figure A.16.



Figure A.15 – (a) Fracture initiation on Specimen W36-PAF1-T94-R000 at the top of the PAF at cycle 4, (b) complete fracture occurred at the top side of the specimen near the PAF at the beginning of cycle 6.

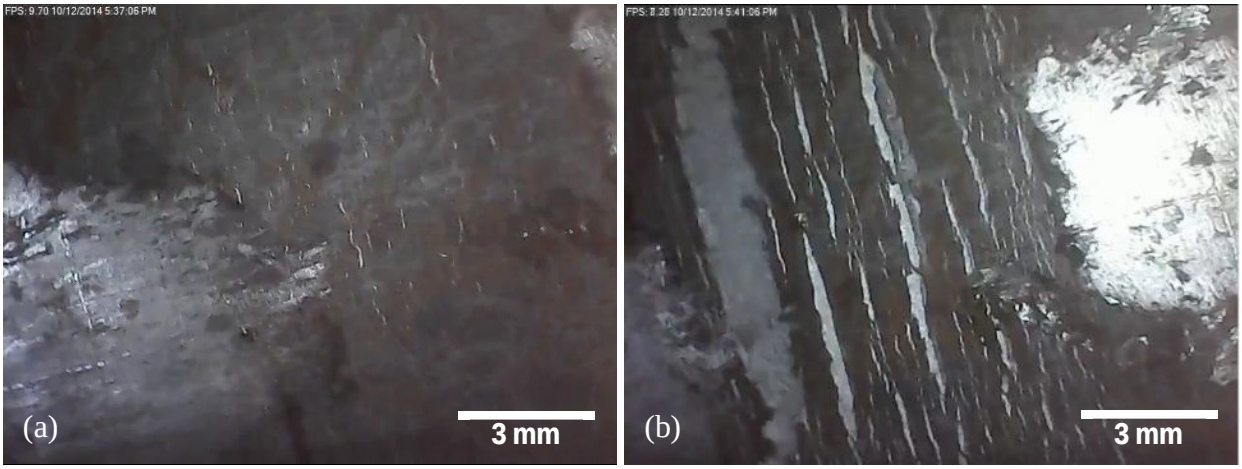


Figure A.16 – (a) Fracture initiation on Specimen W36-PAF1-T94-R000 at the bottom side of the PAF at cycle 4, (b) fracture propagation can be clearly noticed in cycle 5 at the center of the specimen.

Specimen W36-PAF2-T94-R025

The specimen was cycled to 2 cycles before fracture occurred at the center of the specimen. Fracture initiation occurred at cycle 2 and propagated quickly throughout cycle 2 at the top of the specimens originating at the head of the PAF causing the PAF to dislocate at the peak displacement while the top of the specimen was at tension as shown in Figure A.17. Complete fracture occurred at the bottom side of the specimen at cycle 2 at the peak displacement while the bottom side was at tension. The phase of fracture initiation and propagation occurred instantaneously at the bottom side of the specimen.

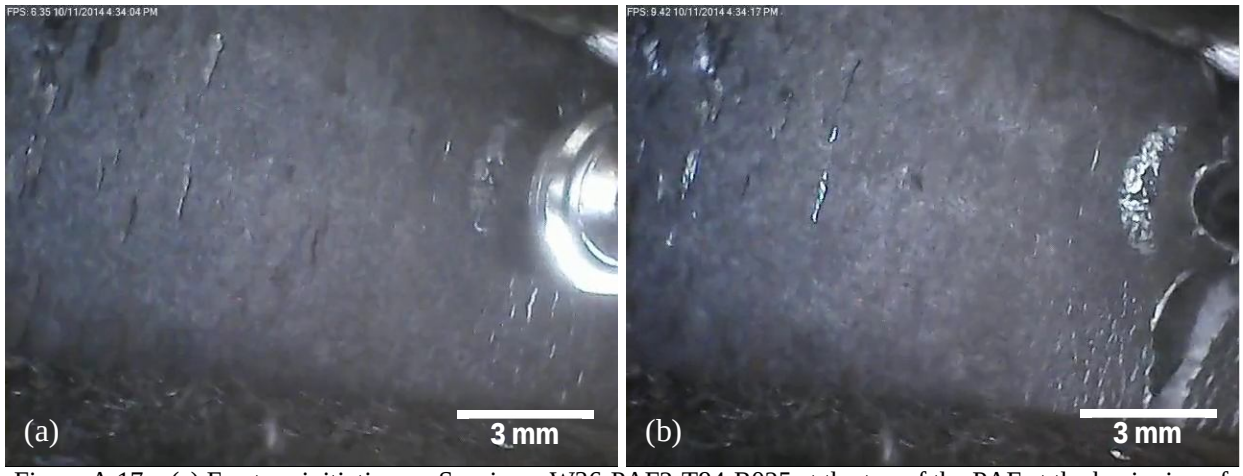


Figure A.17 – (a) Fracture initiation on Specimen W36-PAF2-T94-R025 at the top of the PAF at the beginning of cycle 2, (b) fracture propagated at peak displacement at cycle 2.

Specimen W36-PAF3-T94-R100

The specimen was cycled to 3 cycles before fracture occurred at the center of the specimen. Fracture initiation occurred at cycle 2 and propagated quickly throughout cycle 2 at the top of the specimens originating at the head of the PAF causing the PAF to dislocate at the peak displacement while the top of the specimen was at tension as shown in Figure A.18. Also, fracture initiated at the bottom of the specimen on cycle 2 as shown in Figure A.19. Complete fracture occurred at the top side of the specimen were the PAF is located at the beginning of cycle 3 while the PAF was at tension before reaching the peak displacement.

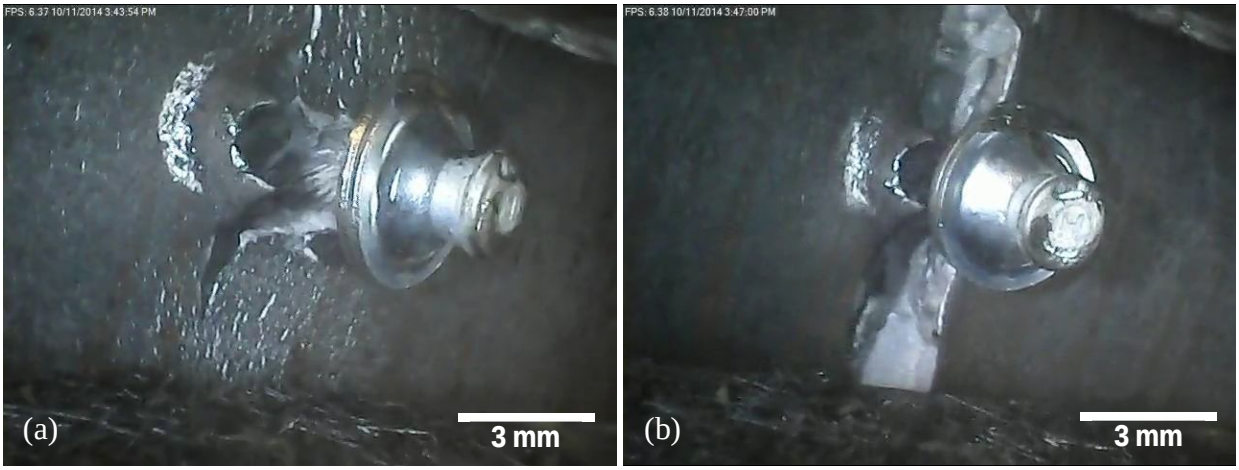


Figure A.18 – (a) Fracture initiation on Specimen W36-PAF3-T94-R100 at cycle 2 at the top side of the PAF while in tension showing signs of fracture initiation around the PAF, (b) cycle 3 top of PAF showing signs of fracture propagated and complete fracture.

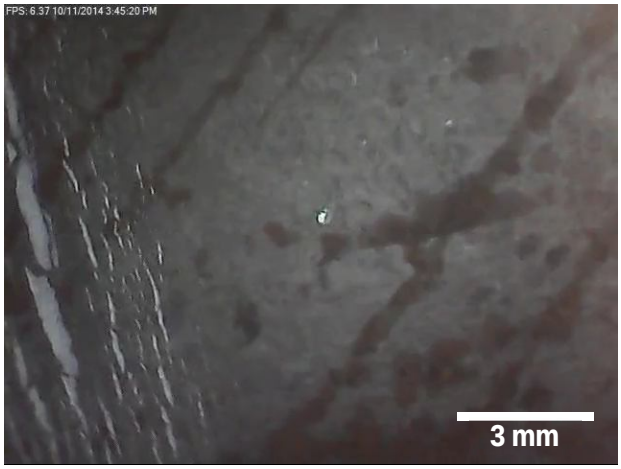


Figure A.19 – Fracture initiation on the bottom side of Specimen W36-PAF3-T94-R100 at cycle 2 while in tension showing signs of fracture initiation.

A.3 Puddle Welds (PW)

A total of six specimens with PW were tested (three W24x62 and three W36x150). One of the two artifacts were tested previously by Eatherton el al. (2013) in full-scale tests were PAFs and PWs. The W24x62 specimens showed better fracture resistance than the W36x150 specimens for both the notched and unnotched. All of the specimens showed signs of fracture initiation at the Heat Affected Zone (HAZ), although final fracture propagation occurred at the bottom side of the PW. Those fracture initiations at the HAZ caused some area loss which weakened the specimen

causing the final fracture. Changing the notch size for the W24x62 specimens also had a noticeable effect on the fracture behavior. While for the W36x150 notched specimens (R = 0.25 and 1.00 in.), both of them exhibited fracture initiation at similar cycles while the bottom side was at tension although fracture initiation was noticed at the HAZ of the PW. Changing the notch size did not change the fracture behavior for the W36x150 specimens.

Specimen W24-PW1-T59-R000

The specimen was cycled to 9 cycles before fracture occurred at the center of the specimen. Fracture initiation occurred at multiple locations at the center of the specimen at cycle 5. Complete fracture occurred at the bottom center of the specimen while it was in tension at cycle 9. Fracture initiation and final fracture is shown in Figure A.20. For this test, the top of the specimen were the PW is located could not be monitored since the floor deck covered the area around the PW.

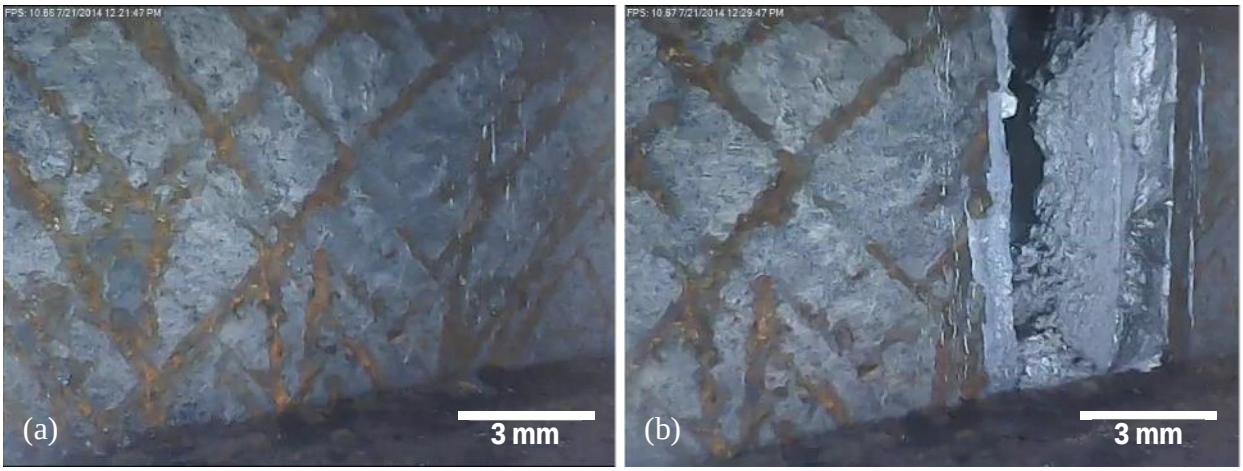


Figure A.20 – (a) Multiple fracture initiation on Specimen W24-PW1-T59-R000 at the bottom of the PW at cycle 5 while at tension, (b) complete fracture occurred on Specimen W24-PW1-T59-R000 at the bottom of the PW at cycle 9 while at tension.

Specimen W24-PW2-T59-R025

Fracture initiation was noticed at cycle 2 at the center of the bottom side of the specimen at multiple locations while the specimen was in tension as shown in Figure A.21. On the top of the specimen near the puddle fracture initiation was noticed at cycle 4 as shown in Figure A.22. Complete fracture occurred on cycle 5 while the bottom of the specimen was in tension.

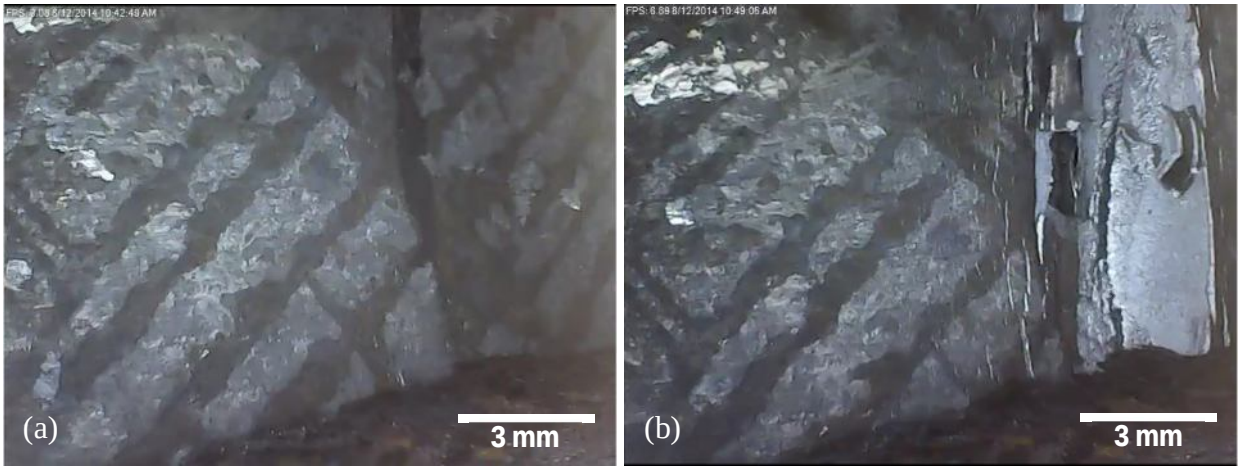


Figure A.21 – (a) Multiple fracture initiation on Specimen W24-PW2-T59-R025 at the bottom of the PW at cycle 2 while at tension, (b) cycle 5 complete fracture occurred at the center.

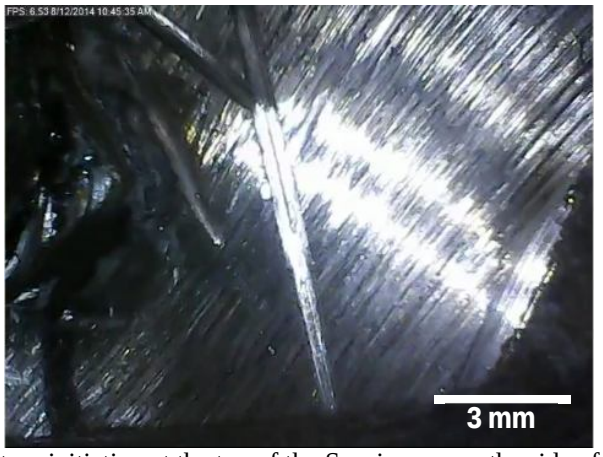


Figure A.22 – Fracture initiation at the top of the Specimen near the side of the PW at cycle 4.

Specimen W24-PW3-T59-R100

Fracture initiation occurred at cycle 3 in the HAZ of the PW as show on Figure A.23. The fracture propagated at the same location until fracture occurred at cycle 5. There were no signs of fracture initiation on the bottom of the specimen.

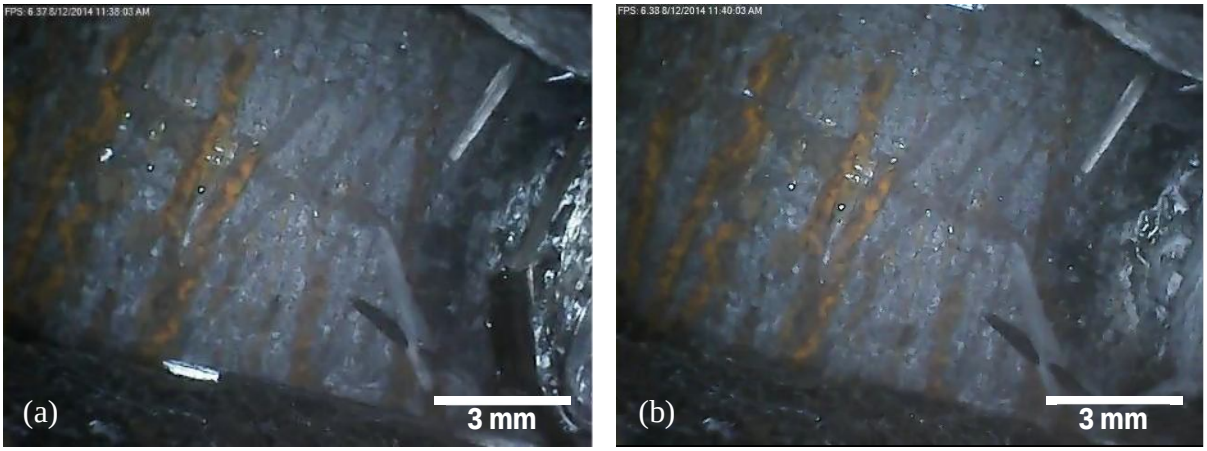


Figure A.23 – (a) Fracture initiation on Specimen W24-PW3-T59-R100 at the HAZ of the PW at cycle 3 while at tension, (b) cycle 4 fracture propagation at the HAZ of the PW.

Specimen W36-PW1-T94-R000

The specimen was cycled to 7 cycles before fracture occurred at the side of the PW. Fracture initiation occurred at multiple locations at the center of the specimen at the top of the specimen at cycle 4. Fracture propagated until complete fracture occurred at cycle 7 while the top side of the specimen was at tension as shown in Figure A.24. At cycle 4, fracture initiation was noticed at the bottom side of the specimen as shown in Figure A.25.

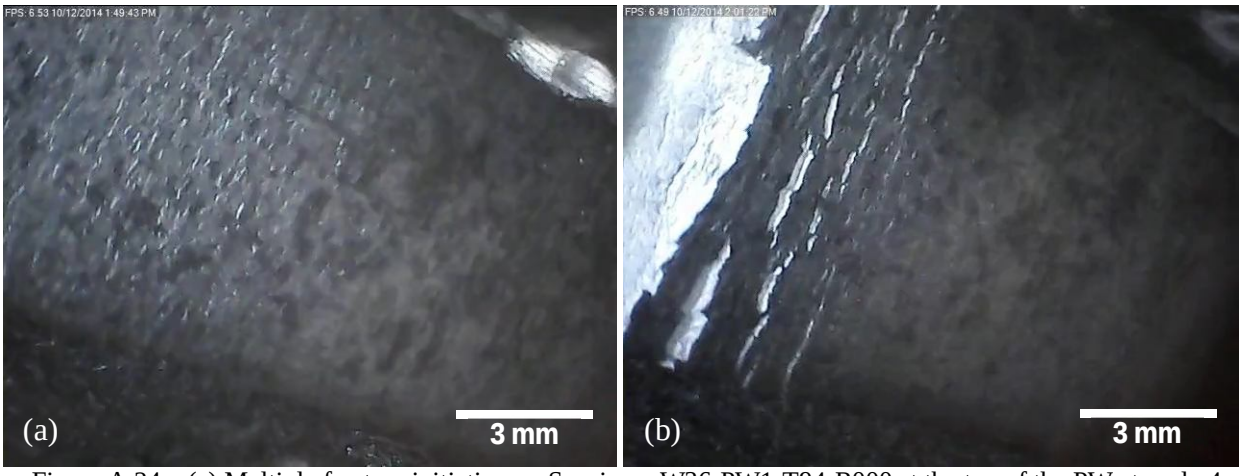


Figure A.24 – (a) Multiple fracture initiation on Specimen W36-PW1-T94-R000 at the top of the PW at cycle 4 while at tension, (b) complete fracture occurred at cycle 7 at the side of the PW.

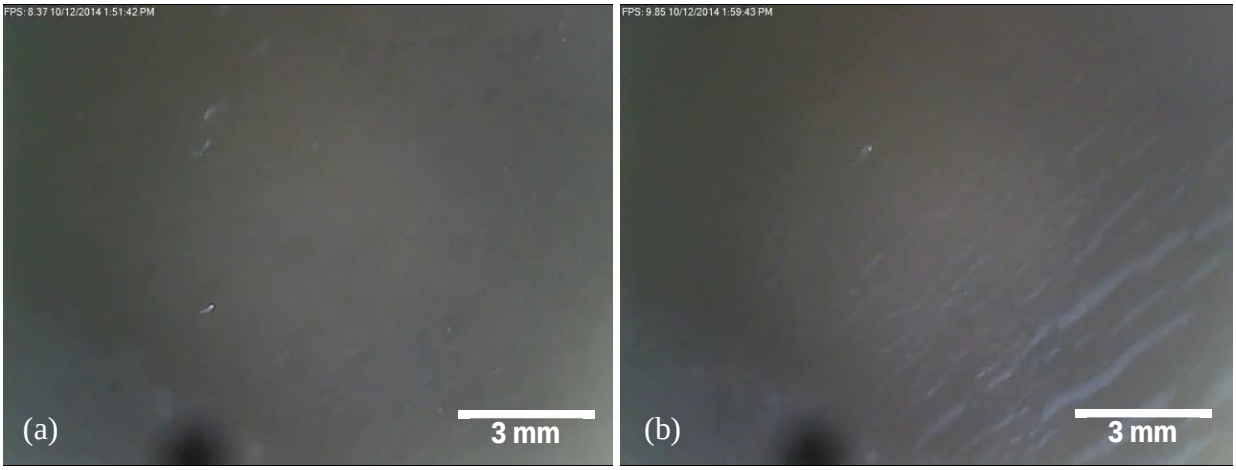


Figure A.25 – (a) Multiple fracture initiation on Specimen W36-PW1-T94-R000 at the bottom of the PW at cycle 4 while at tension, (b) multiple fracture initiation on Specimen W36-PW1-T94-R000 at the bottom of the PW at cycle 6 while at tension.

Specimen W36-PW2-T94-R025

The specimen was cycled to 2 cycles before fracture occurred at the center of the specimen. Fracture initiation occurred at cycle 2 and propagated quickly throughout cycle 2 at the top of the specimens originating at the HAZ of the PW causing the PW to dislocate before reaching the peak displacement while the top of the specimen was at tension as shown in Figure A.26. Complete fracture occurred at the bottom side of the specimen at cycle 2 at before reaching peak displacement while the bottom side was at tension. The phase of fracture initiation and propagation occurred instantaneously at the bottom side of the specimen.

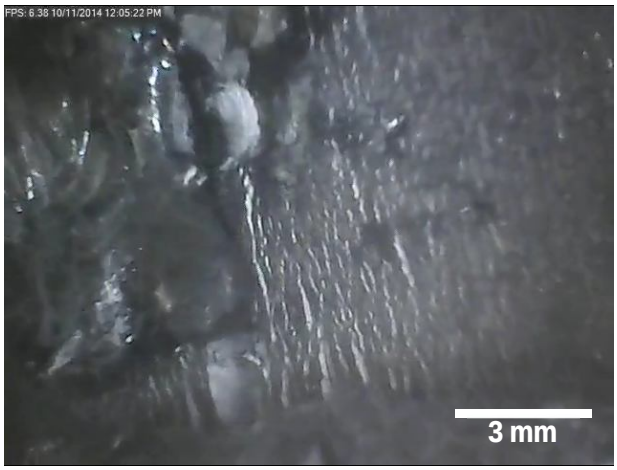


Figure A.26 – Multiple fracture initiation on Specimen W36-PW2-T94-R025 at the top of the PW at cycle 2 while at tension.

Specimen W36-PW3-T94-R100

The specimen was cycled to 2 cycles before fracture occurred at the center of the specimen. Fracture initiation occurred at cycle 2 and propagated quickly throughout cycle 2 at the top of the specimens originating at both sides of the HAZ of the PW causing the PW to dislocate before reaching the peak displacement while the top of the specimen was at tension as shown in Figure A.27. Complete fracture occurred at the bottom side of the specimen at cycle 2 at peak displacement while the bottom side was at tension. The phase of fracture initiation and propagation occurred instantaneously at the bottom side of the specimen.

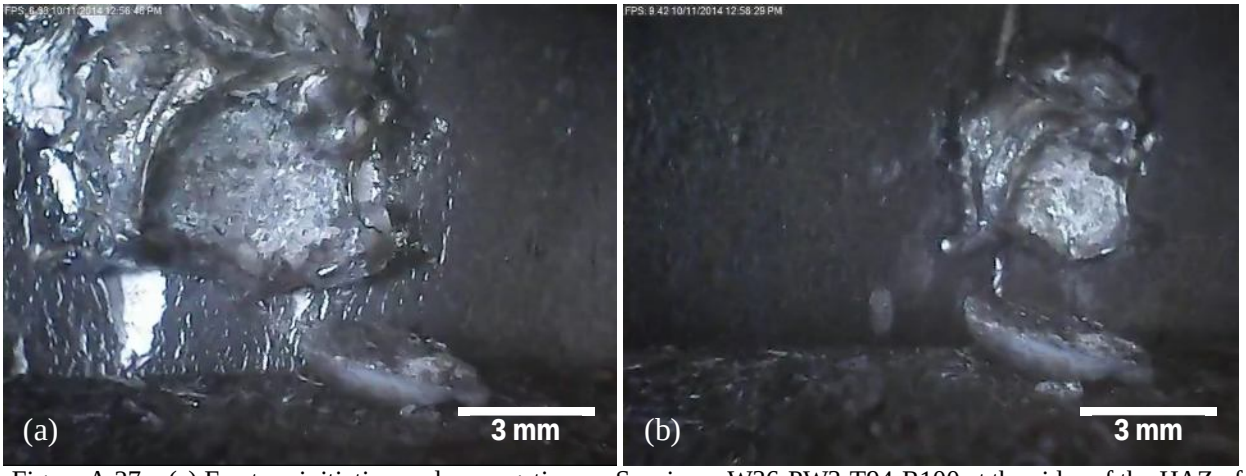


Figure A.27 – (a) Fracture initiation and propagation on Specimen W36-PW3-T94-R100 at the sides of the HAZ of the PW at cycle 2 while at tension, (b) complete fracture at the side of the PW at cycle 2 while the top side of the spcecimen is at compression.

A.4 Ground Fillet Weld (GFW)

A total of six specimens with GFW were tested (three W24x62 and three W36x150). The welds were applied by a qualified lab technician with substantial experience in welding. A detailed process of the GFW preparation is explained in the previous chapter.

The W24x62 specimens showed better fracture resistance than the W36x150 specimens for both the notched and unnotched. Most of the specimens showed signs of early fracture initiation

at the Heat Affected Zone (HAZ), although final fracture propagation occurred at the other side of the GFW. Those fracture initiations at the HAZ caused some area loss which weakened the specimen.

Specimen W24-GFW1-T59-R000

Fracture initiated from the top side of the specimen in the heat affected zone close to the weld at cycle 4. The fracture initiated at both edges of the specimen as shown in Figure A.28. At cycle 7, fracture initiation started at the bottom center of the specimen as shown on Figure A.29. Fracture propagation is controlled from the side of the specimen on cycle 9. The failure origin occurred at the side of the specimen at the top and bottom. The fracture propagated through the specimen after 9 cycles.

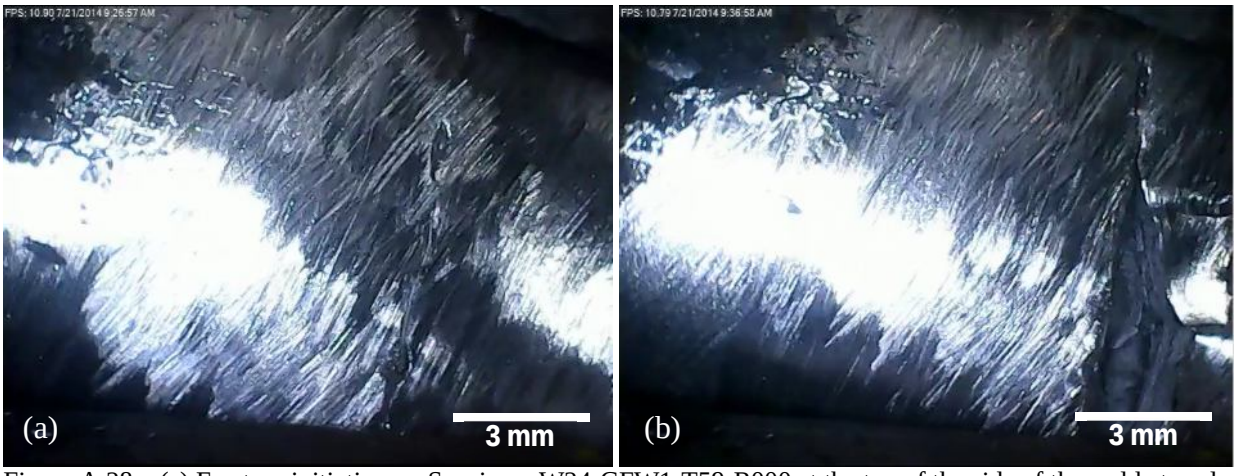


Figure A.28 – (a) Fracture initiation on Specimen W24-GFW1-T59-R000 at the top of the side of the weld at cycle 4 while at tension, (b) fracture propagation on cycle 9.

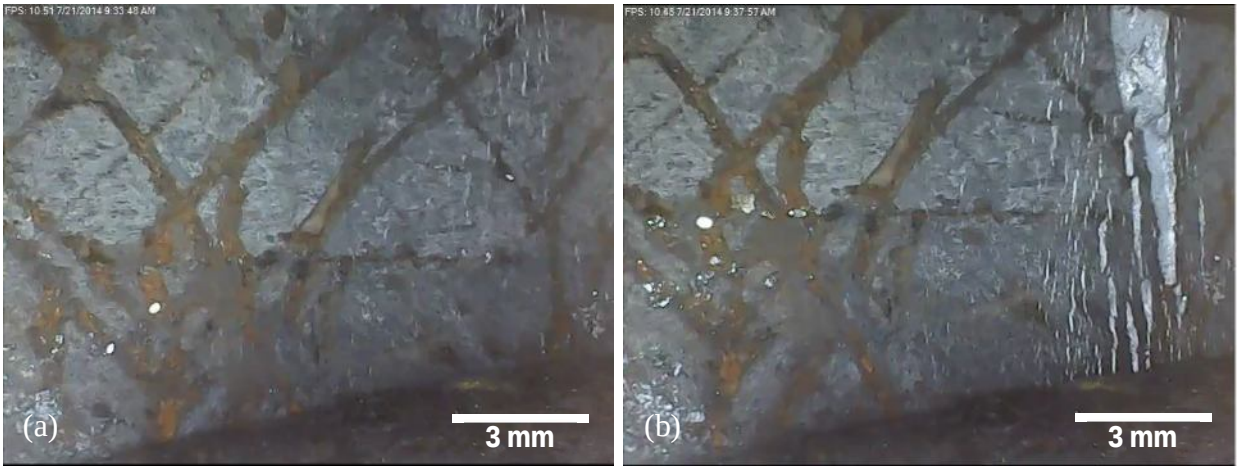


Figure A.29 – (a) Fracture initiation on Specimen W24-GFW1-T59-R000 at the bottom of the specimen at cycle 7 while at tension, (b) fracture propagation at the bottom of the specimen at cycle 9 while at tension.

Specimen W24-GFW2-T59-R025

Fracture initiated at multiple locations at the first half of cycle 2 at the bottom of the specimen. The crack that controlled the fracture propagation is located at the edge notch at the center of the specimen in the heat affected zone of the fillet weld. The fractured propagated to the top of the specimen at the second half of cycle 2. Fracture initiation and complete fracture can be seen in Figure A.30.

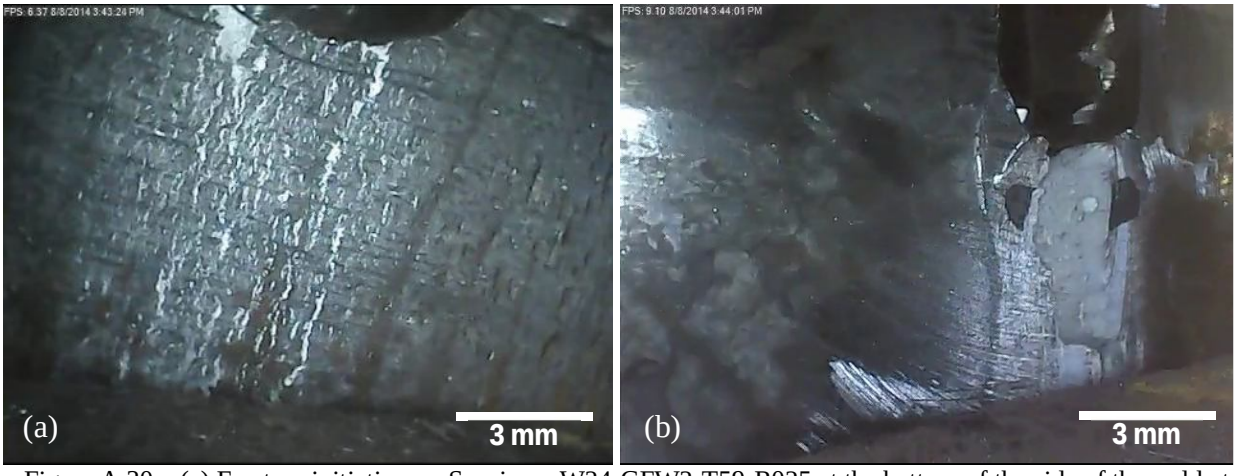


Figure A.30 – (a) Fracture initiation on Specimen W24-GFW2-T59-R025 at the bottom of the side of the weld at cycle 2 while at tension, (b) top of the specimen showing fracture propagation on the second half cycle of cycle 2 in the HAZ.

Specimen W24-GFW3-T59-R100

Fracture initiated at cycle 3 at the top of the specimen in the HAZ. Complete fracture occurred at cycle 5 initiated and propagating the HAZ on the sides of weld located the top of the specimen. Fracture initiated at the bottom of the specimen in cycle 4 while in tension. There were multiple fracture initiation location at the center of the specimen but fracture propagation started the notch. Complete fracture occurred at cycle 5 while the top of the specimen was at tension.

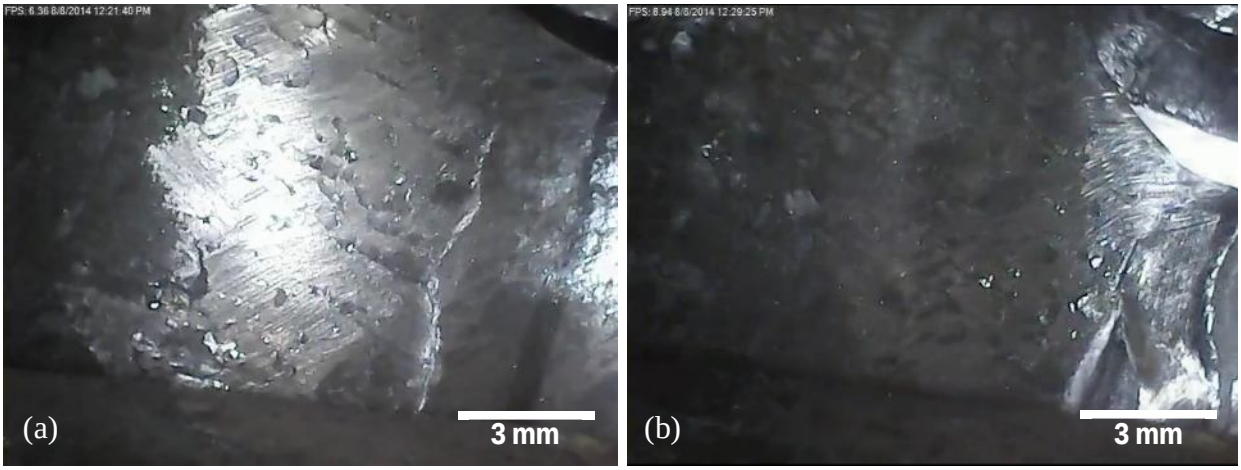


Figure A.31 – (a) Fracture propagation on Specimen W24-GFW3-T59-R100 at the top of the side of the weld at cycle 3 while at tension in the HAZ, (b) top of the specimen showing complete fracture at cycle 5 around the weld in the HAZ.



Figure A.32 – Multiple fracture initiation cracks at the bottom of the Specimen controlled by a fracture propagation from the notch.

Specimen W36-GFW1-T94-R000

Fracture initiated from the top side of the specimen in the heat affected zone close to the weld at cycle 3. The fracture initiated at multiple locations of the specimen but propagated at one side of the HAZ as shown in Figure A.31. At cycle 3, fracture initiation started at the bottom center of the specimen as shown on Figure A.32. The failure origin occurred at the side of the GFW in the HAZ of the specimen located at the top of the specimen. Fracture propagated from the top to the bottom side of the specimen while the top side of the specimen was at tension causing the specimen to fracture at cycle 6.



Figure A.33 – (a) Fracture initiation on Specimen W36-GFW1-T94-R000 at the top of the side of the weld at cycle 3 while at tension, (b) complete fracture occurred at cycle 6 while top of the specimen was at tension.

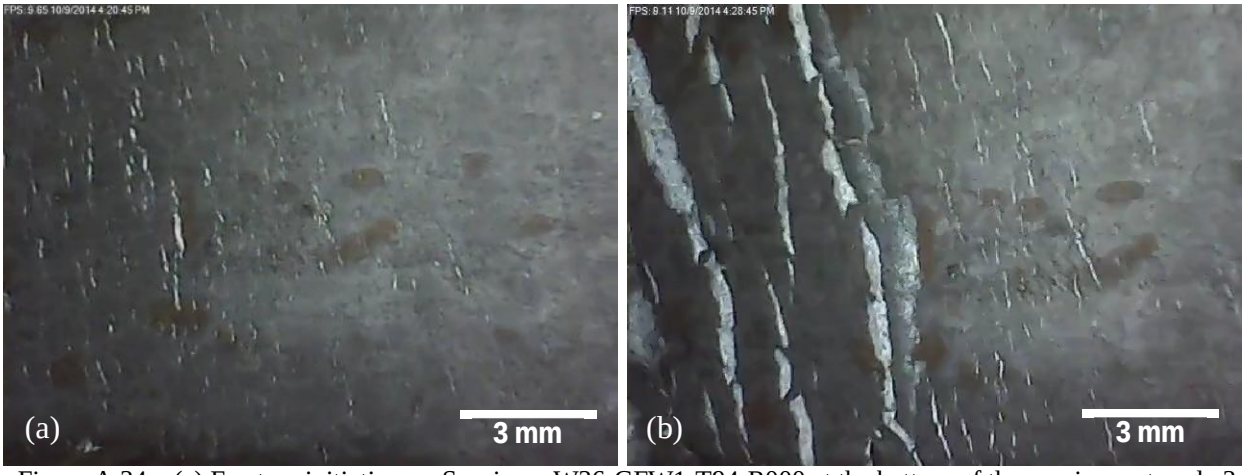


Figure A.34 – (a) Fracture initiation on Specimen W36-GFW1-T94-R000 at the bottom of the specimen at cycle 3 while at tension, (b) fracture propagation on Specimen W36-GFW1-T94-R000 at the bottom of the specimen at cycle 5 while at tension.

Specimen W36-GFW2-T94-R025

Fracture initiated at multiple locations at the first half of cycle 1 at the top of the specimen. The crack that controlled the fracture propagation is located at the edge notch at the center of the specimen in the heat affected zone of the fillet weld as shown in Figure A.35 and Figure A.36. The fracture propagated to the bottom of the specimen at the first half of cycle 2. Complete fracture occurred at the second half of cycle 2 while the top of the specimen was at compression. Rapid fracture propagation occurred at the bottom of the specimen without showing sign of fracture initiation at the previous cycle while the bottom side was at tension.

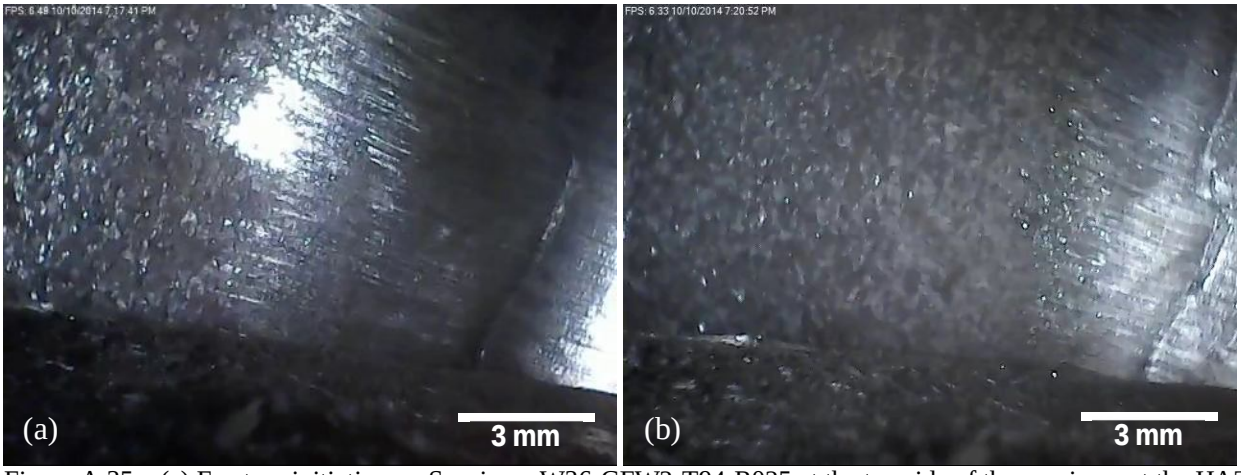


Figure A.35 – (a) Fracture initiation on Specimen W36-GFW2-T94-R025 at the top side of the specimen at the HAZ of the GFW at cycle 1 while at tension, (b) top of the specimen showing fracture propagation on the first half cycle of cycle 2 in the HAZ.



Figure A.36 – Top of the specimen showing two fracture origin locations at the HAZ of the GFW on the first half cycle of cycle 2 in the HAZ.

Specimen W36-GFW3-T94-R100

Fracture initiated at multiple locations at the first half of cycle 1 at the top of the specimen. The crack that controlled the fracture propagation is located at the edge notch at the center of the specimen in the heat affected zone of the fillet weld as shown in Figure A.37. The fracture propagated to the bottom of the specimen rapidly causing complete fracture at the peak of the first half of cycle 2. No signs of fracture initiation was noticed at the bottom side of the specimen.

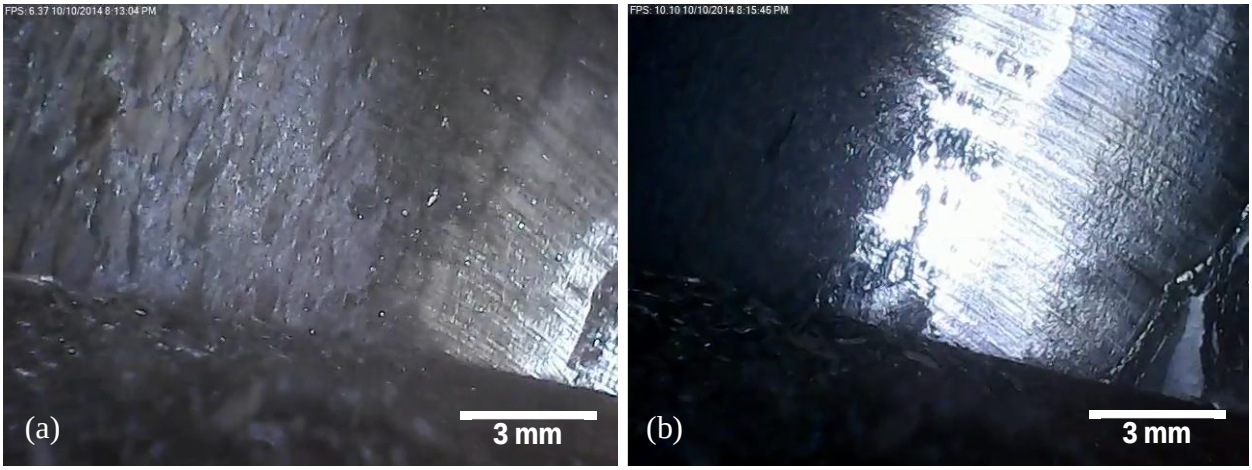


Figure A.37 – (a) Fracture propagation on Specimen W36-GFW3-T94-R100 at the top of the side of the weld at cycle 1 while at tension in the HAZ, (b) top of the specimen showing fracture propagation on cycle 2 while at tension in the HAZ.

A.5 Notch Ground to Taper (NGT)

A total of six specimens with NGT were tested (three W24x62 and three W36x150). The grinding was performed using a grinder, for more detailed process of the NGT preparation is explained in the previous chapter.

Both of the W24x62 and W36x150 specimens showed poor performance in fracture resistance. All of the specimens showed signs of early fracture initiation and propagation at the center of the notch.

Specimen W24-NGT1-T59-R000

Fracture initiated at the center of the ground notch at cycle 2 at multiple locations causing multiple fracture propagation locations as shown in Figure A.38. At bottom of the specimen, fracture initiation was noticed at multiple locations at the center during cycle 2 as shown in Figure A.39. On cycle 3 the fracture propagated at multiple locations at the bottom center of the specimen. Complete fracture occurred at cycle 5 when the ground notch side (top of the specimen) was at tension.

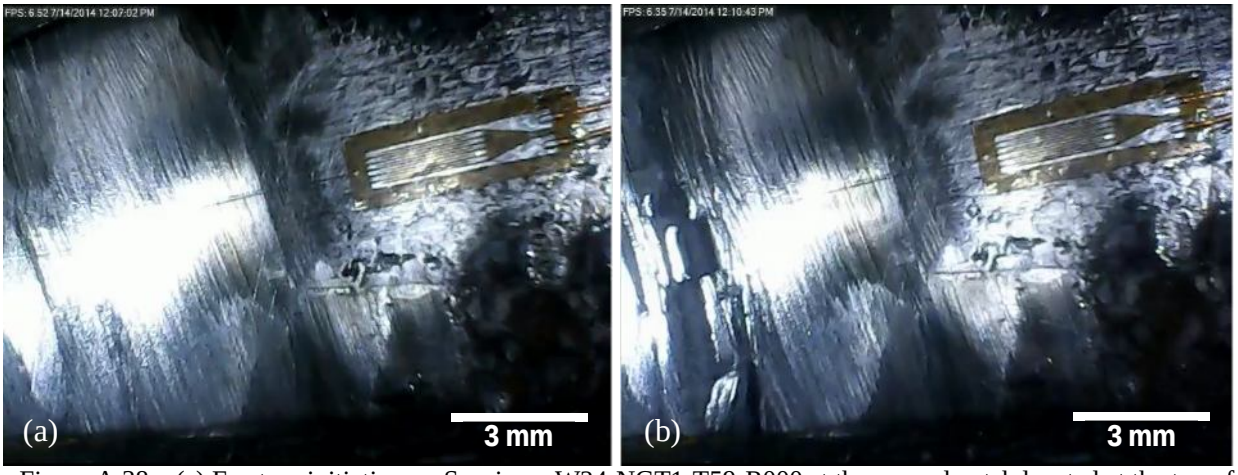


Figure A.38 – (a) Fracture initiation on Specimen W24-NGT1-T59-R000 at the ground notch located at the top of the specimen at cycle 2 while at tension, (b) fracture propagation at multiple locations in at the center of the ground notch on cycle 4 while at tension.

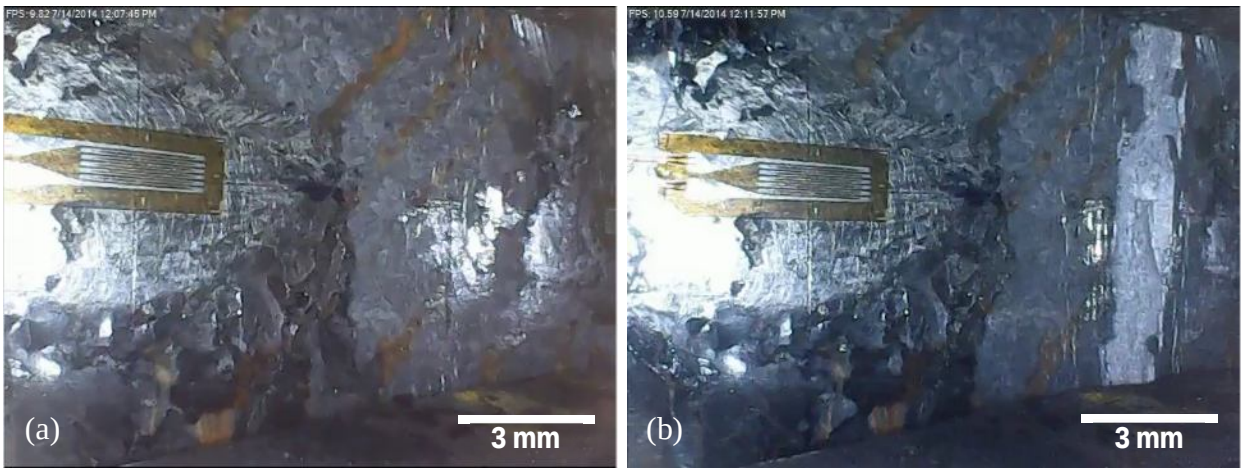


Figure A.39 – (a) Fracture initiation on Specimen W24-NGT1-T59-R000 at the bottom of the specimen at cycle 2 while at tension, (b) complete fracture at cycle 4 at the bottom center of the specimen.

Specimen W24-NGT2-T59-R025

Fracture initiation was noticed at cycle 1 on the center of the ground notch and at the side of the specimen as shown in Figure A.40. Fracture initiation was noticed at the edge of the bottom side of the specimen near the notch as shown in Figure A.41. A rapid fracture propagation at the center of the ground notch occurred at cycle 2 until complete fracture occurred.

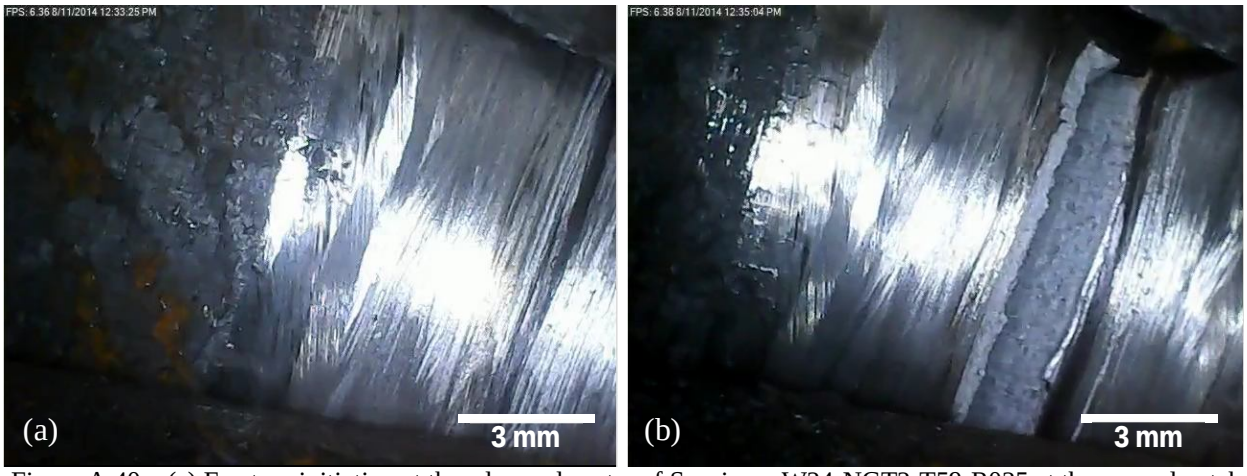


Figure A.40 – (a) Fracture initiation at the edge and center of Specimen W24-NGT2-T59-R025 at the ground notch located at the top of the specimen at cycle 1 while at tension, (b) complete fracture at the center of the ground notch on cycle 2 while at tension.



Figure A.41 – Fracture initiation at multiple locations near notch at the bottom side of Specimen W24-NGT2-T59-R025 at cycle 1 while at tension.

Specimen W24-NGT3-T59-R100

Fracture initiation was noticed at cycle 1 on the center of the ground notch towards the edge of the specimen as shown in Figure A.42. No signs of fracture initiation was noticed at the bottom side of the specimen in cycle 1 at tension as shown in Figure A.43. A rapid fracture propagation at the center of the ground notch occurred at cycle 2 until complete fracture occurred.

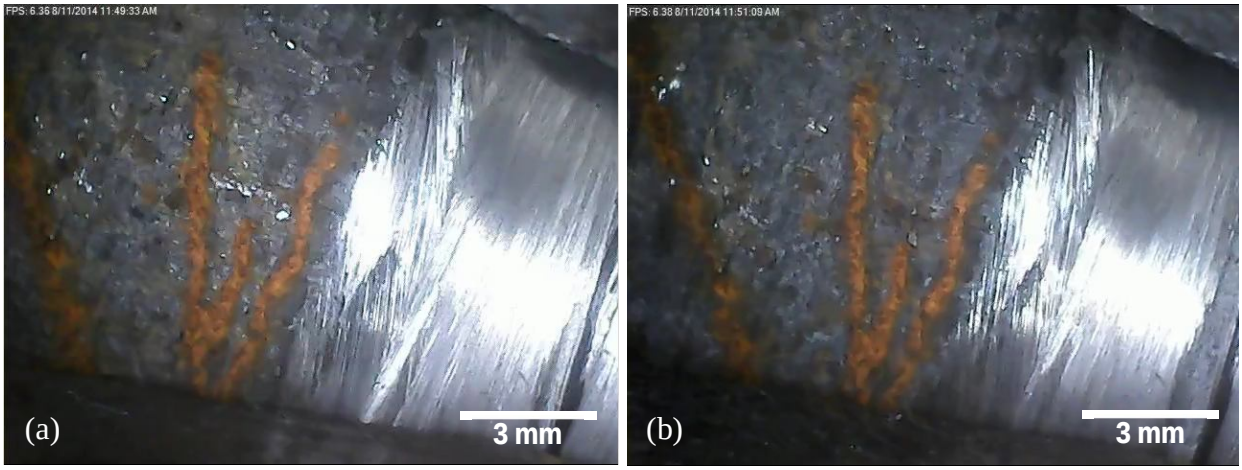


Figure A.42 – (a) Fracture initiation at the center of Specimen W24-NGT3-T59-R100 at the ground notch located at the top of the specimen at cycle 1 while at tension, (b) complete fracture at the center of the ground notch on cycle 2 while at tension.



Figure A.43 – No signs of fracture initiation at the bottom side of Specimen W24-NGT2-T59-R025 at cycle 1 while at tension.

Specimen W36-NGT1-T94-R000

Fracture initiated at the center of the ground notch at cycle 2. Rapid fracture propagation occurred at the center of the ground notch at the first half of cycle 3 until complete fracture occurred at the peak displacement while the top side of the specimen was at tension as shown in Figure A.44.

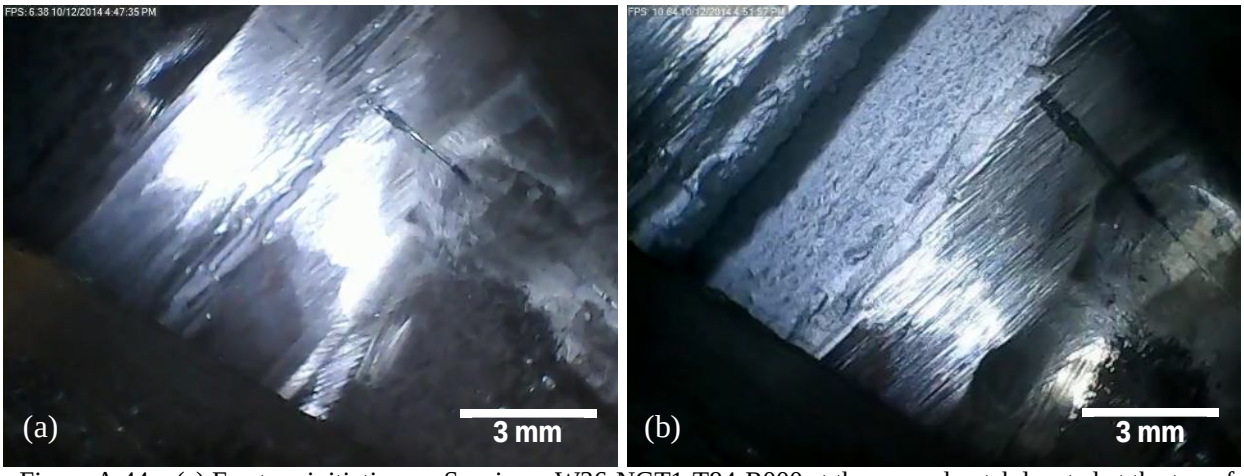


Figure A.44 – (a) Fracture initiation on Specimen W36-NGT1-T94-R000 at the ground notch located at the top of the specimen at cycle 2 while at tension, (b) a rapid fracture propagation at the center of the ground notch on cycle 3 while at tension.

Specimen W36-NGT2-T94-R025

Fracture initiation was noticed at cycle 2 on the center of the ground notch as shown in Figure A.45. Complete fracture occurred at the first half of cycle 2 at peak displacement.

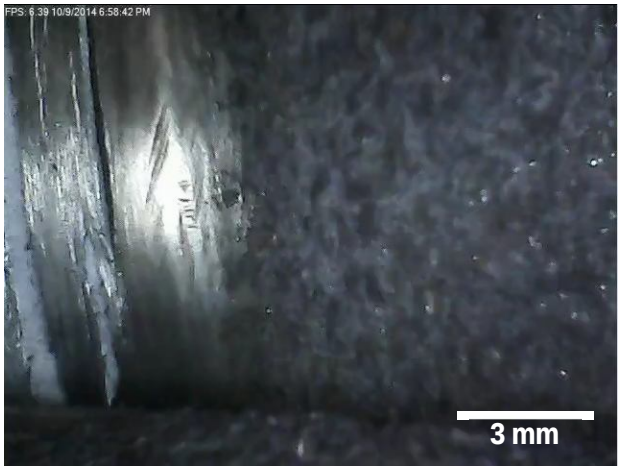


Figure A.45 – Fracture initiation at the top side of Specimen W36-NGT2-T94-R025 at multiple locations at the ground notch originating from the side notch at cycle 2 while at tension

Specimen W36-NGT3-T94-R100

Fracture initiation was noticed at cycle 1 on the center of the ground notch as shown in Figure A.46. Complete fracture occurred at the peak displacement of the first half of cycle 2.

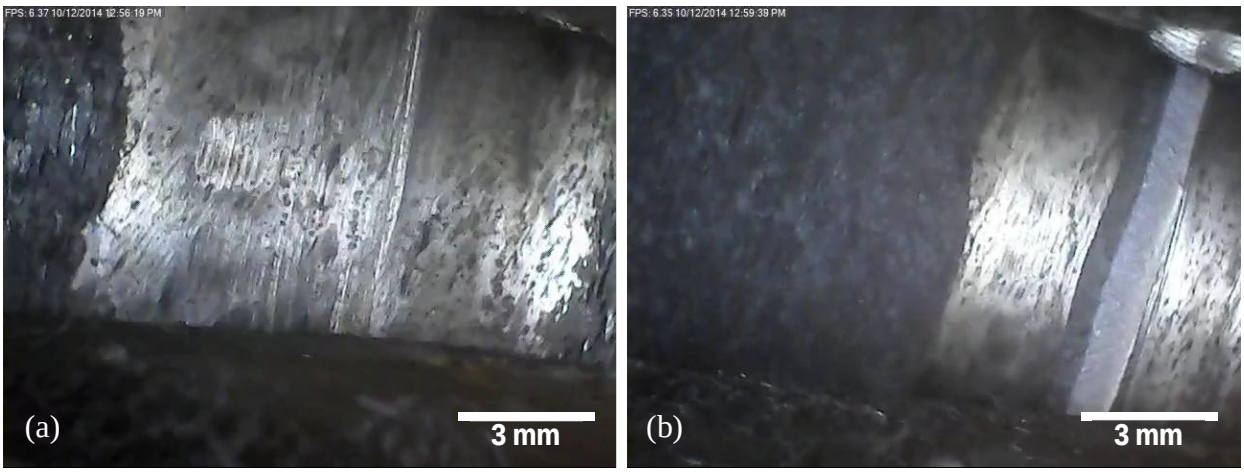


Figure A.46 – (a) Fracture initiation at the center of Specimen W36-NGT3-T94-R100 at the ground notch located at the top of the specimen at cycle 1 while at tension, (b) complete fracture at the center of the ground notch on cycle 2 while at tension.

A.6 Notch Welded and Ground Smooth (NWG)

A total of six specimens with NWG were tested (three W24x62 and three W36x150). The notches were performed using a grinder followed by filling the notch with weld which was applied by a qualified lab technician with substantial experience in welding. A detailed process of the NWG preparation is explained in the previous chapter.

There was a noticeable difference in the fracture resistance of the W24x62 unnotched specimen (*W24-NWG1-T59-R000*) compared with the other five tested specimens. All of the specimens showed signs of early fracture initiation at the HAZ between the notch and the weld. Those fracture initiations at the HAZ were the root cause for the premature occurrence of complete fracture causing some area loss which led to weakening the specimen.

Specimen W24-NWG1-T59-R000

Fracture initiated at the edge of the top of the specimen in the region were the weld is in contact with the base material at cycle 4 as shown in Figure A.47. At cycle 12 fracture initiation was noticed at the center of the bottom side of the specimen as shown in Figure A.48. Complete fracture of the section occurred at cycle 14 propagating from the top of the specimen as shown in Figure A.47.

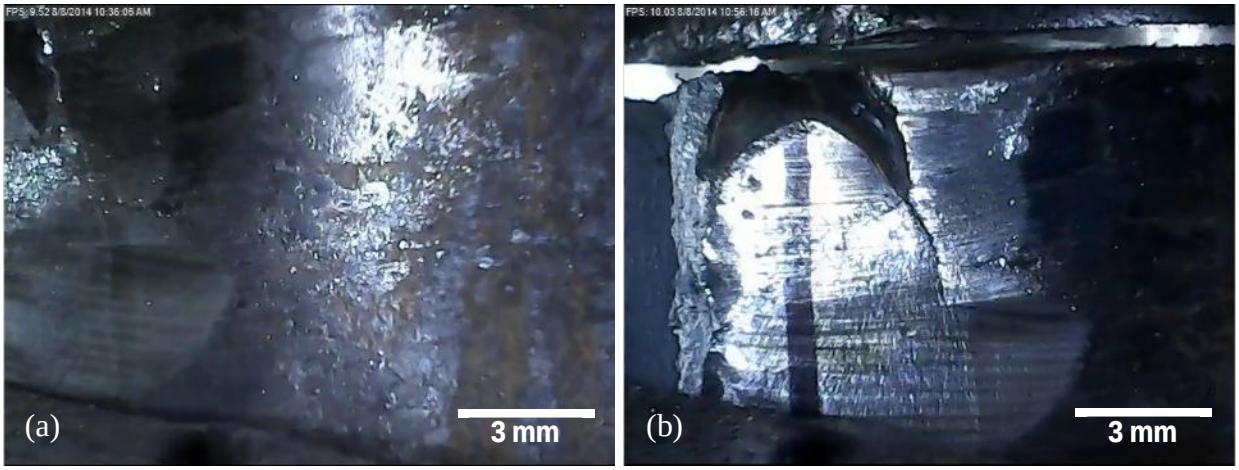


Figure A.47 – (a) Fracture initiated at the edge of the top side of Specimen W24-NWG1-T59-R000 at the region between the weld and the base metal on cycle 4 at tension, (b) complete fracture at edge of weld (HAZ) at cycle 14

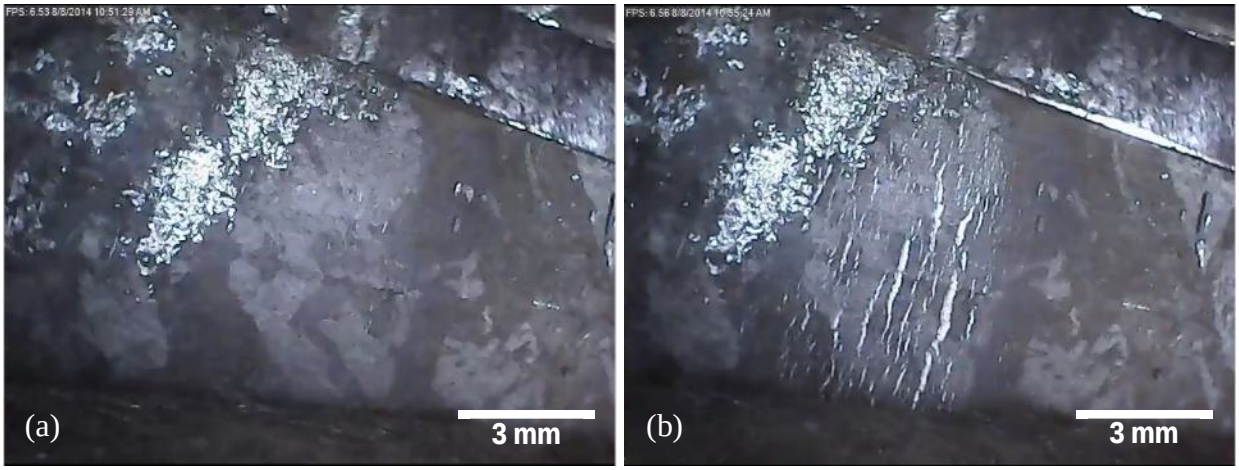


Figure A.48 – (a) Fracture initiation at the center of the bottom side of Specimen W24-NWG1-T59-R000 on cycle 12 at tension, (b) cycle 14 just before fracture.

Specimen W24-NWG2-T59-R025

Fracture initiated at the top of the specimen on cycle 2 at the center of the region were the weld is in contact with the base material at cycle 2 as shown in Figure A.49. At the bottom side of the specimen, fracture initiated at the edge at cycle 2 as shown in Figure A.50. On cycle 3, fracture propagated from the edge towards the center with multiple fracture initiation at the center of the specimen until complete fracture occurred.

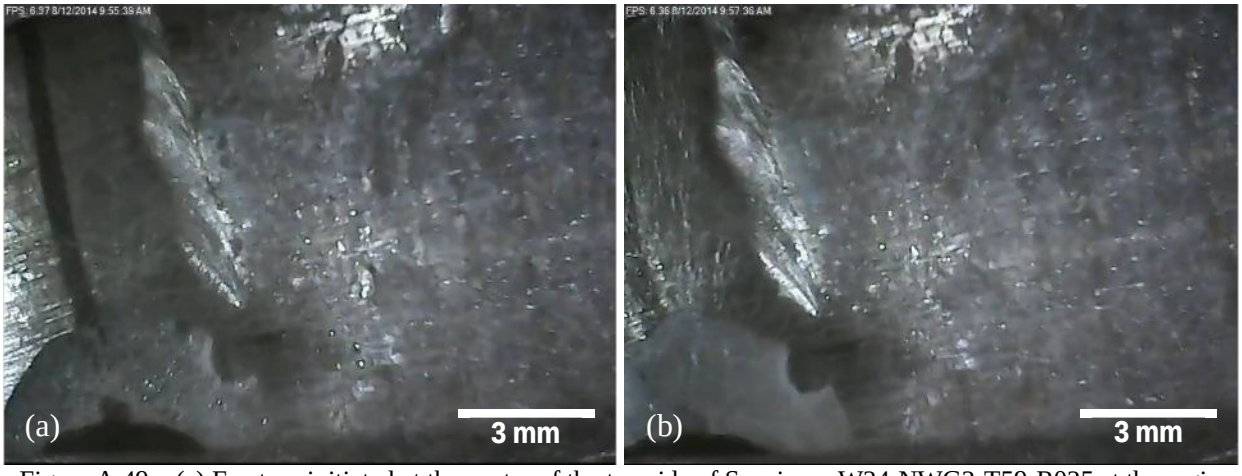


Figure A.49 – (a) Fracture initiated at the center of the top side of Specimen W24-NWG2-T59-R025 at the region between the weld and the base metal on cycle 2 at tension, (b) fracture propagation on the edge with fracture initiation cracks at the center on cycle 3 intension.

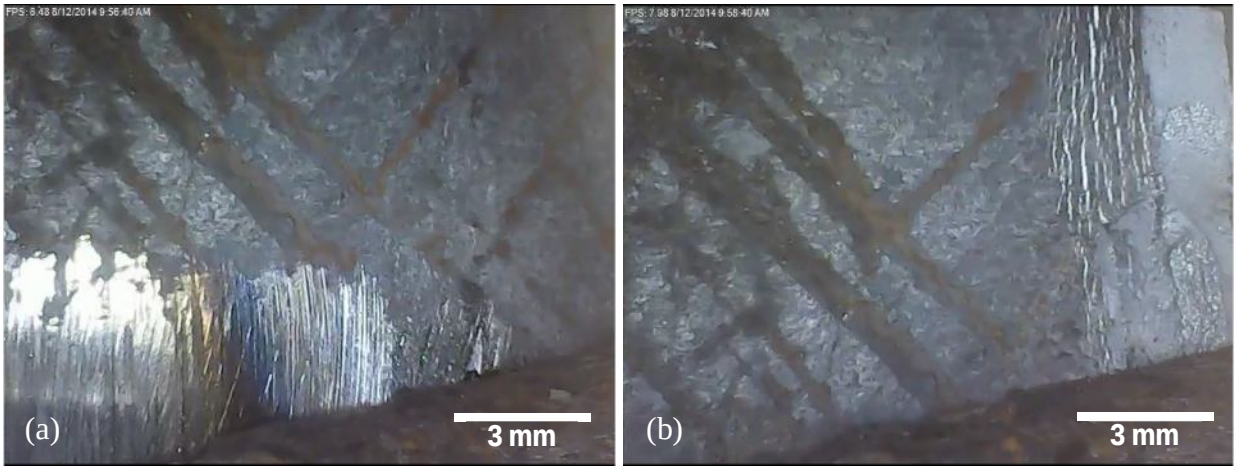


Figure A.50 – (a) Fracture initiated at the edge of the bottom side of Specimen W24-NWG2-T59-R025 on cycle 2 at tension, (b) fracture propagation on the edge with fracture initiation cracks at the center on cycle 3 intension

Specimen W24-NWG3-T59-R100

Fracture initiated at cycle 2 on the top side of the specimen at the center of the region were the weld is in contact with the base material as shown in Figure A.51. At cycle 3, fracture propagation continued from the origin in which fracture initiation was noticed as shown in Figure A.52. Fracture initiation occurred at the bottom side of the specimen at multiple locations at cycle 3 at tension. Complete fracture of the specimen occurred while the top side of the specimen was at tension on cycle 4.

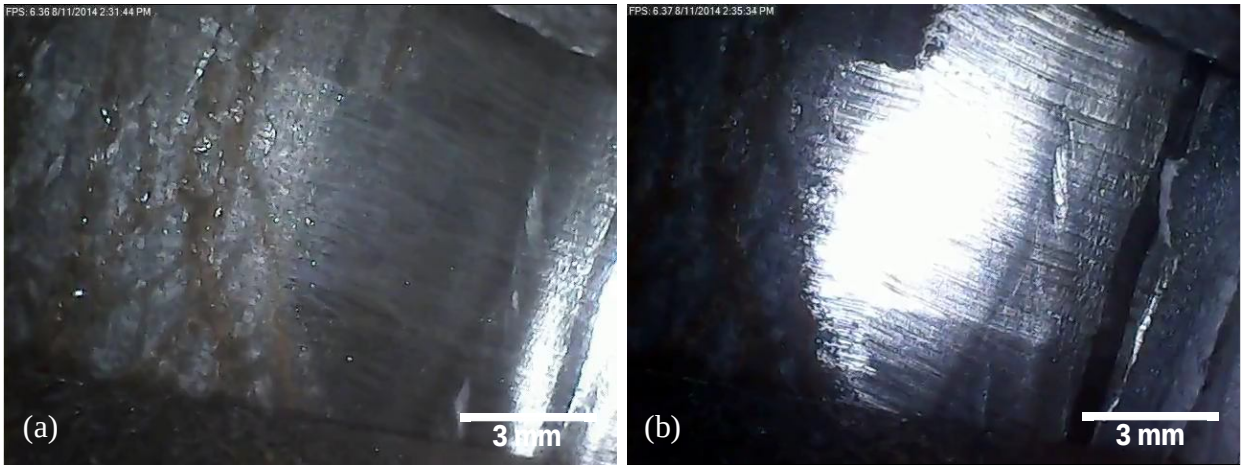


Figure A.51 – (a) Fracture initiated at the edge of the top side of Specimen W24-NWG3-T59-R100 at the region between the weld and the base metal on cycle 2 at tension, fracture propagation on the edge towards the center of the specimen on cycle 3 in tension, (b) complete fracture occurred at cycle 4 while the top side of the specimen was in tension.

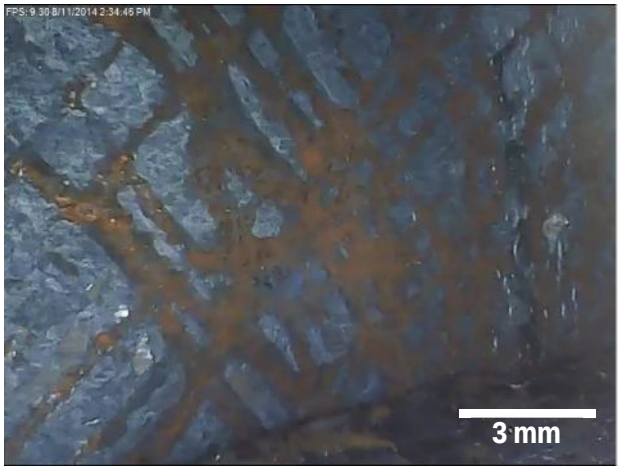


Figure A.52 – Fracture initiated at multiple locations at the bottom side of Specimen W24-NWG3-T59-R100 on cycle 3 at tension.

Specimen W36-NWG1-T94-R000

Fracture initiated at the edge of the top of the specimen in the region were the weld is in contact with the base material at cycle 2 as shown in Figure A.53 (a). Complete fracture of the section occurred at cycle 3 propagating from the top of the specimen as shown in Figure A.53 (b).

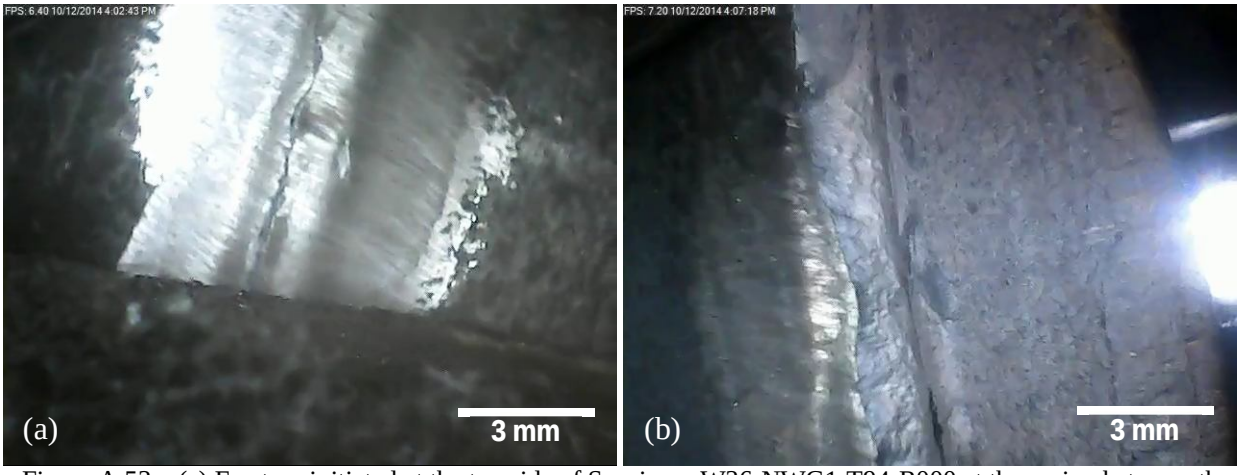


Figure A.53 – (a) Fracture initiated at the top side of Specimen W36-NWG1-T94-R000 at the region between the weld and the base metal on cycle 2 at tension, (b) complete fracture at edge of weld (HAZ) at cycle 3

Specimen W36-NWG2-T94-R025

Fracture initiated at the HAZ at the top side of the specimen originating at the side notch and rapidly propagating until the top side was at peak displacement causing a complete fracture at the first half of cycle 2 as shown in Figure A.54.

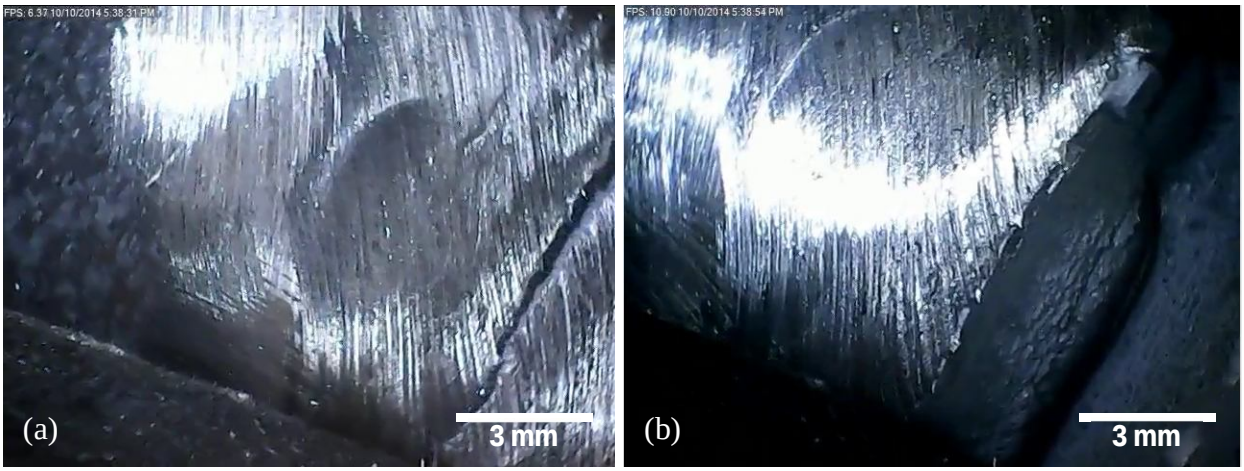


Figure A.54 – (a) Fracture initiated at the top side of Specimen W36-NWG2-T94-R025 at the region between the weld and the base metal on cycle 2 at tension, (b) complete fracture at edge of weld (HAZ) at cycle 2 at peak displacement.

Specimen W36-NWG3-T94-R100

Fracture initiated at the HAZ at the top side of the specimen originating at the side notch and rapidly propagating until the top side was at peak displacement causing a complete fracture at the first half of cycle 2 as shown in Figure A.55.

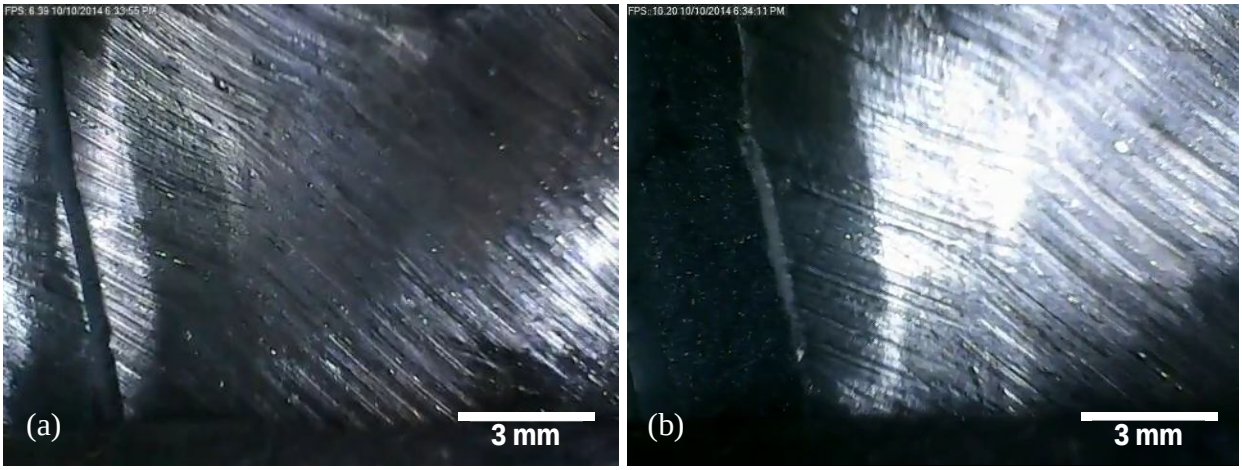


Figure A.55 – (a) Fracture initiated at the top side of Specimen W36-NWG3-T94-R100 at the region between the weld and the base metal on cycle 2 at tension, (b) complete fracture at edge of weld (HAZ) at cycle 2 at peak displacement.

A.7 W24 and W36 Specimens Dimensions

The width and thickness of each specimen was measured at two different locations for all of the W24x62 and W36x150 bend test specimens and are presented in Table A.1 and Table A.2.

Table A.1 – Bend test dimensions for W24x62 specimens with different artifacts.

Artifact Type	**Flange Thickness**	**Artifact Name**	**Width (in.)**		**Thickness (in.)**	
1) No Artifact	0.59 in. (W24x62)	W24-B1-T59-R000	3.012	2.970	0.542	0.536
		W24-B2-T59-R025	2.977	2.954	0.579	0.581
		W24-B3-T59-R100	2.967	2.957	0.581	0.579
2) Powder Actuated Fasteners (PAF)	0.59 in. (W24x62)	W24-PAF1-T59-R000	3.079	2.994	0.538	0.540
		W24-PAF2-T59-R025	2.999	2.946	0.551	0.546
		W24-PAF3-T59-R100	2.938	2.951	0.592	0.587
3) Puddle Welds (PW)	0.59 in. (W24x62)	W24-PW1-T59-R000	2.966	2.983	0.581	0.589
		W24-PW2-T59-R025	2.962	2.966	0.542	0.546
		W24-PW3-T59-R100	2.964	2.949	0.580	0.573
4) Ground Fillet Weld (GFW)	0.59 in. (W24x62)	W24-GFW1-T59-R000	2.987	3.011	0.576	0.575
		W24-GFW2-T59-R025	2.962	2.953	0.572	0.569
		W24-GFW3-T59-R100	2.959	2.886	0.571	0.576
5) Notch Ground to Taper (NGT)	0.59 in. (W24x62)	W24-NGT1-T59-R000	2.971	2.942	0.533	0.534
		W24-NGT2-T59-R025	2.944	2.956	0.542	0.545
		W24-NGT3-T59-R100	2.964	2.991	0.572	0.571
6) Notch Welded and Ground (NWG)	0.59 in. (W24x62)	W24-NWG1-T59-R000	2.952	2.945	0.543	0.545
		W24-NWG2-T59-R025	2.972	2.962	0.548	0.543
		W24-NWG3-T59-R100	2.882	2.951	0.545	0.548
		Average	2.965		0.560	

Table A.2 – Bend test dimensions for W36x150 specimens with different artifacts.

Artifact Type	Flange Thickness	Artifact Name	Width (in.)		Thickness (in.)	
1) No Artifact	0.94 in. (W36x150)	W36-B1-T94-R000	4.655	4.680	0.936	0.957
		W36-B2-T94-R025	4.661	4.728	1.012	0.973
		W36-B3-T94-R100	4.710	4.649	0.951	0.952
2) Powder Actuated Fasteners (PAF)	0.94 in. (W36x150)	W36-PAF1-T94-R000	4.706	4.726	0.965	0.952
		W36-PAF2-T94-R025	4.687	4.675	0.916	0.899
		W36-PAF3-T94-R100	4.670	4.686	0.901	0.904
3) Puddle Welds (PW)	0.94 in. (W36x150)	W36-PW1-T94-R000	4.739	4.742	0.951	0.952
		W36-PW2-T94-R025	4.687	4.744	0.828	0.825
		W36-PW3-T94-R100	4.692	4.660	0.967	0.950
4) Ground Fillet Weld (GFW)	0.94 in. (W36x150)	W36-GFW1-T94-R000	4.703	4.671	0.901	0.900
		W36-GFW2-T94-R025	4.705	4.629	0.862	0.819
		W36-GFW3-T94-R100	4.660	4.679	0.952	0.951
5) Notch Ground to Taper (NGT)	0.94 in. (W36x150)	W36-NGT1-T94-R000	4.674	4.707	0.865	0.820
		W36-NGT2-T94-R025	4.718	4.699	0.973	1.016
		W36-NGT3-T94-R100	4.720	4.771	0.909	0.901
6) Notch Welded and Ground (NWG)	0.94 in. (W36x150)	W36-NWG1-T94-R000	4.565	4.645	0.949	0.951
		W36-NWG2-T94-R025	4.698	4.709	0.873	0.829
		W36-NWG3-T94-R100	4.781	4.664	0.972	1.014
		Average	4.692		0.924	

APPENDIX B TESTING DATA

B.1 Monotonic Axial Tests Data

Load displacement plots for the monotonic tests with artifacts for both the W24x62 (0.59 in. thick) and W36x150 (0.94 in. thick) specimens.

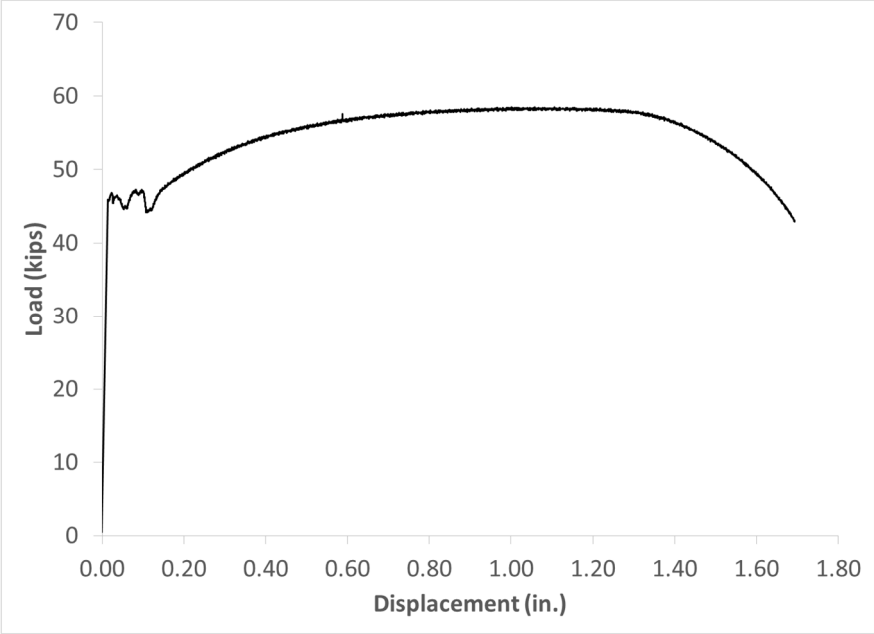


Figure B.1 – Load displacement for W24x62 specimen with No Artifact (B)

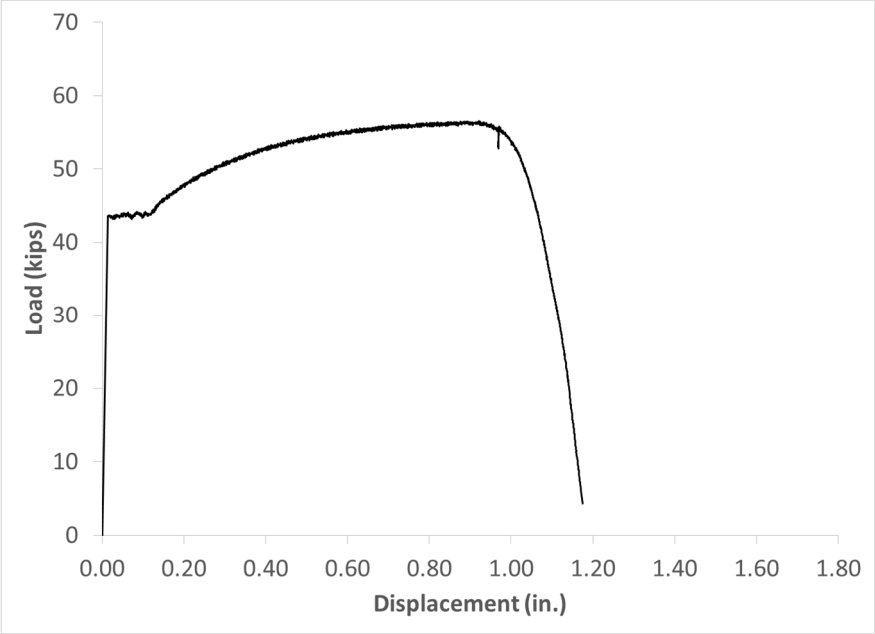


Figure B.2 – Load displacement for W24x62 specimen with Powder Actuated Fasteners (PAF)

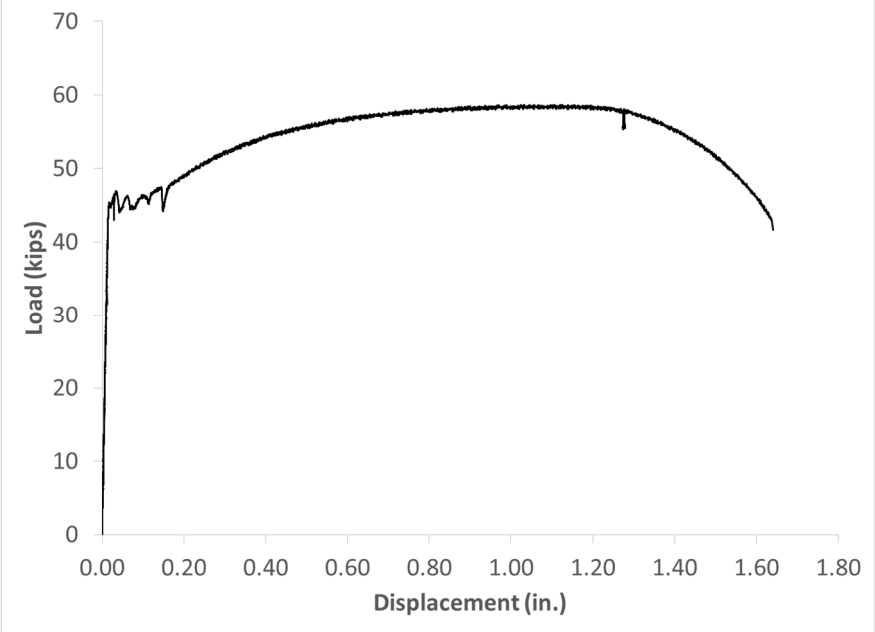


Figure B.3 – Load displacement for W24x62 specimen with Puddle Welds (PW)

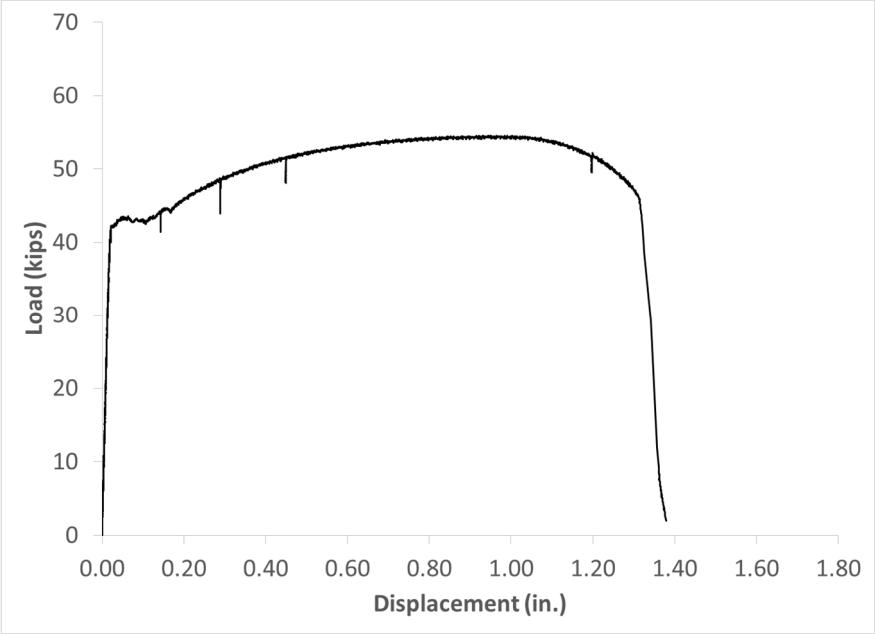


Figure B.4 – Load displacement for W24x62 specimen with Ground Fillet Weld (GFW)

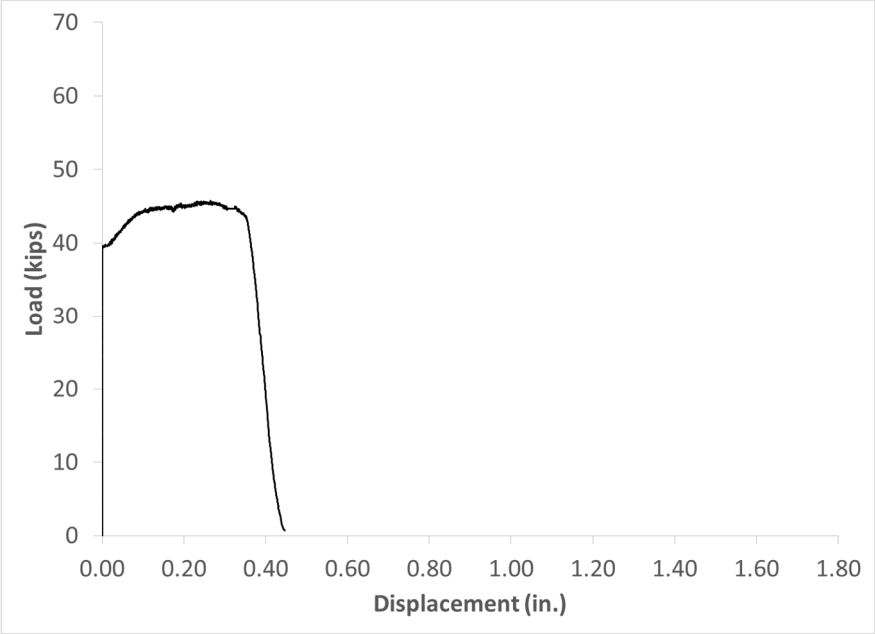


Figure B.5 – Load displacement for W24x62 specimen with Notch Ground to Taper (NGT)

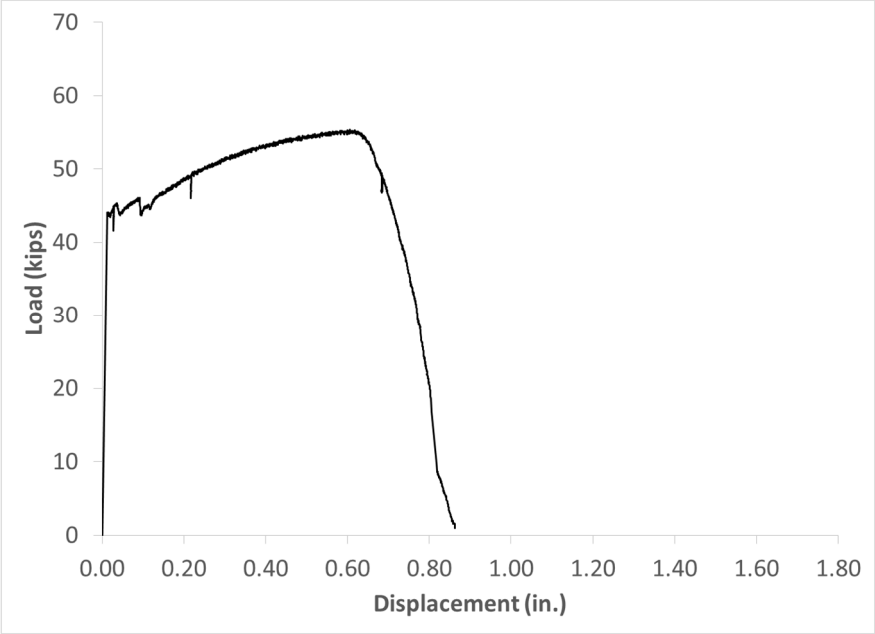


Figure B.6 – Load displacement for W24x62 specimen with Notch Welded and Ground Smooth (NWG)

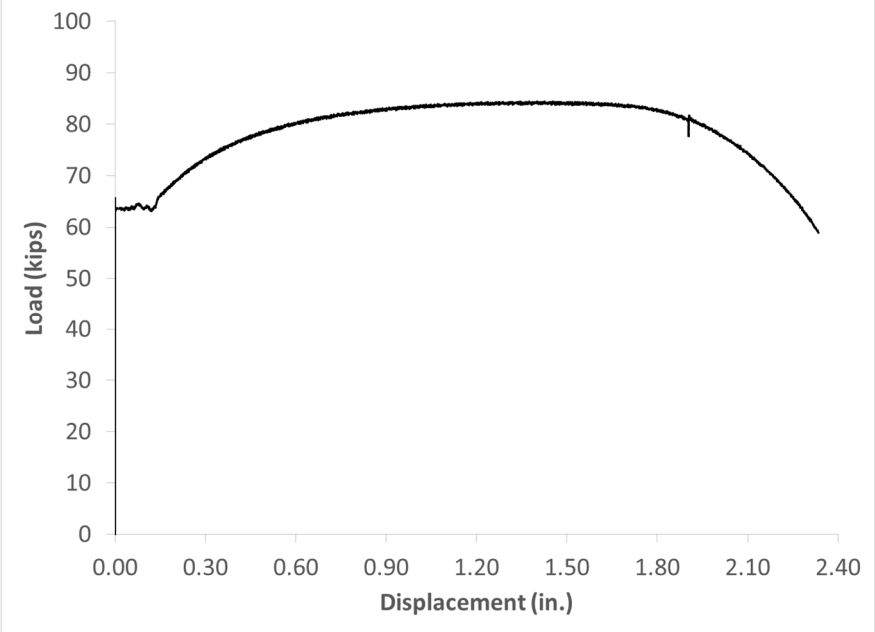


Figure B.7 – Load displacement for W36x150 specimen with No Artifact (B)

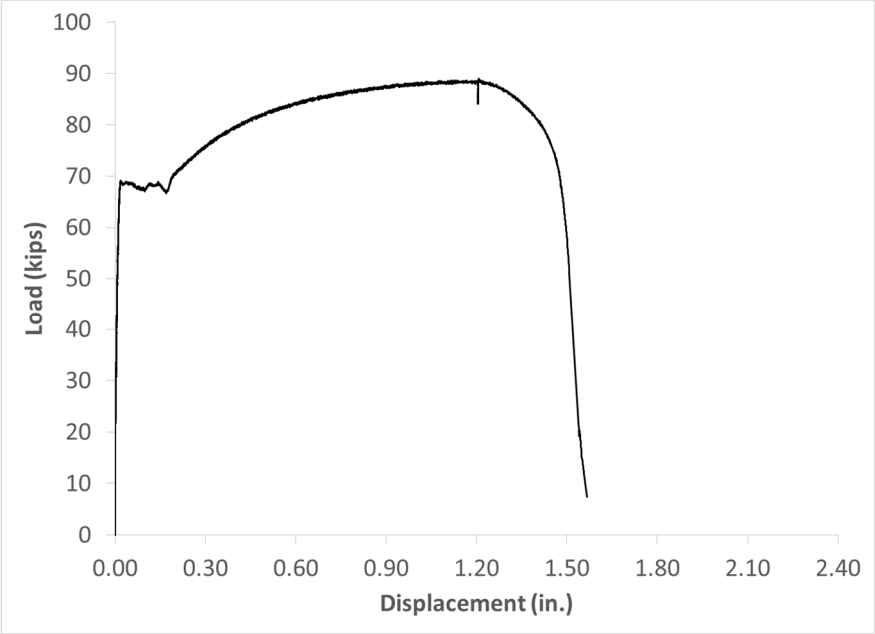


Figure B.8 – Load displacement for W36x150 specimen with Powder Actuated Fasteners (PAF)

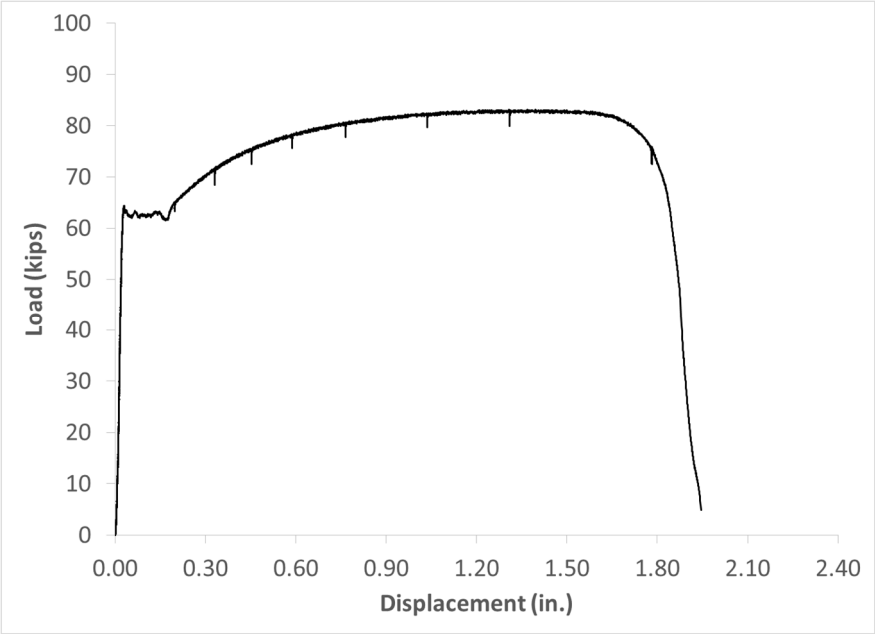


Figure B.9 – Load displacement for W36x150 specimen with Puddle Welds (PW)

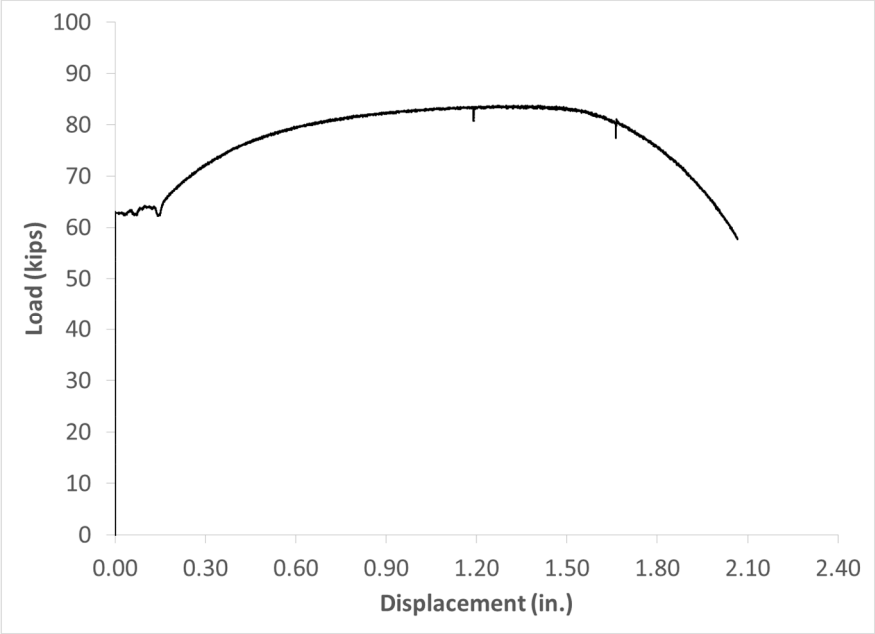


Figure B.10 – Load displacement for W36x150 specimen with Ground Fillet Weld (GFW)

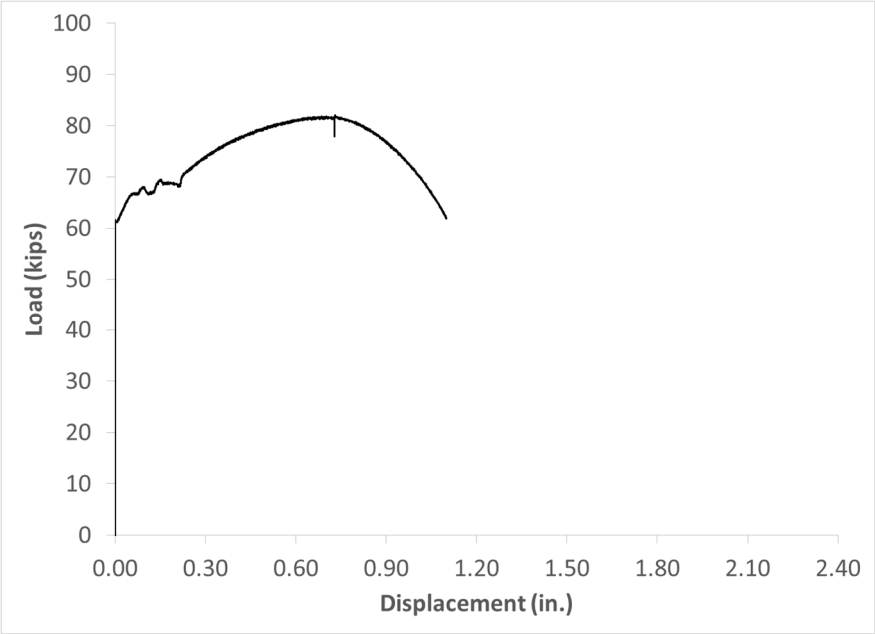


Figure B.11 – Load displacement for W36x150 specimen with Notch Ground to Taper (NGT)

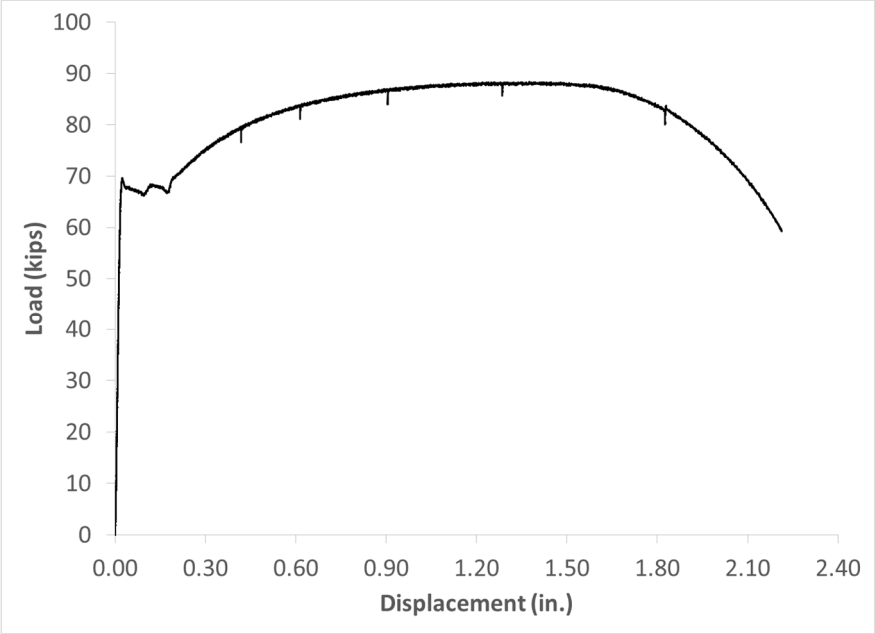


Figure B.12 – Load displacement for W36x150 specimen with Notch Welded and Ground Smooth (NWG)

B.2 Cyclic Bend Tests Data

Load displacement plots for the cyclic bend tests with artifacts for both the W24x62 (0.59 in. thick) and W36x150 (0.94 in. thick) specimens.



Figure B.13 – Load displacement for Specimen W24-B1-T59-R000



Figure B.14 – Load displacement for Specimen W24-B2-T59-R025

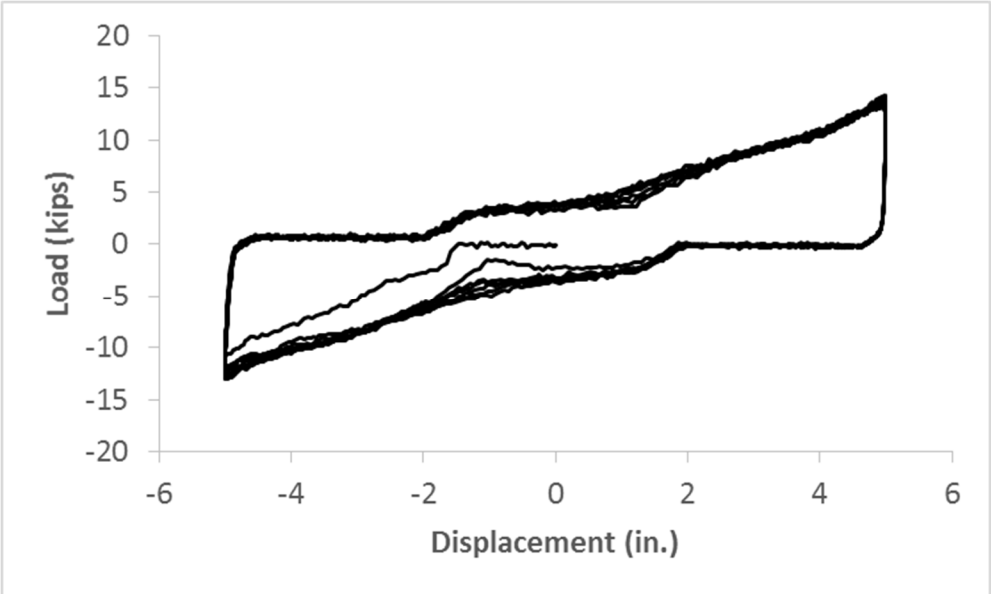


Figure B.15 – Load displacement for Specimen W24-B3-T59-R100

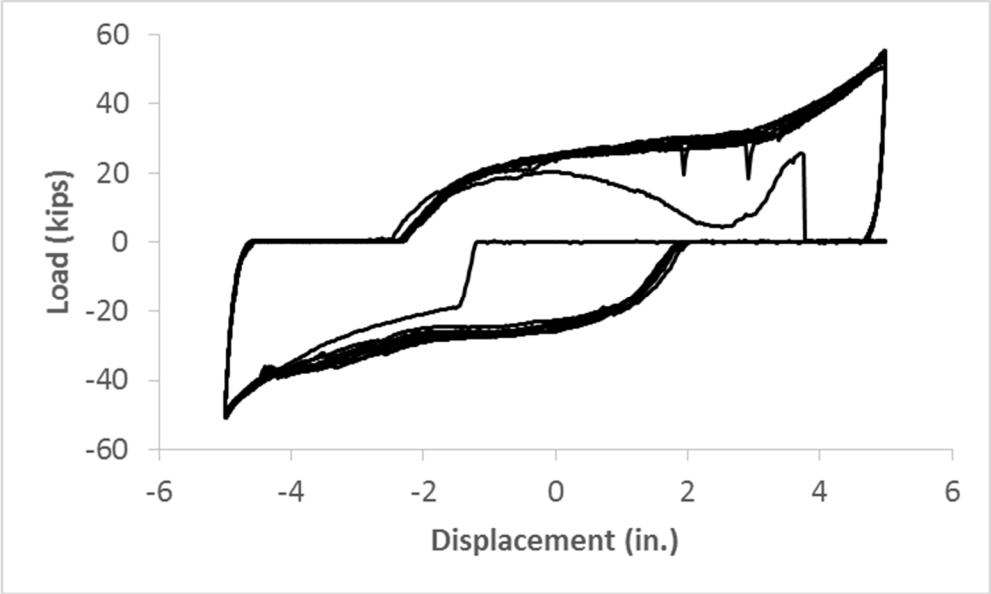


Figure B.16 – Load displacement for Specimen W36-B1-T94-R000

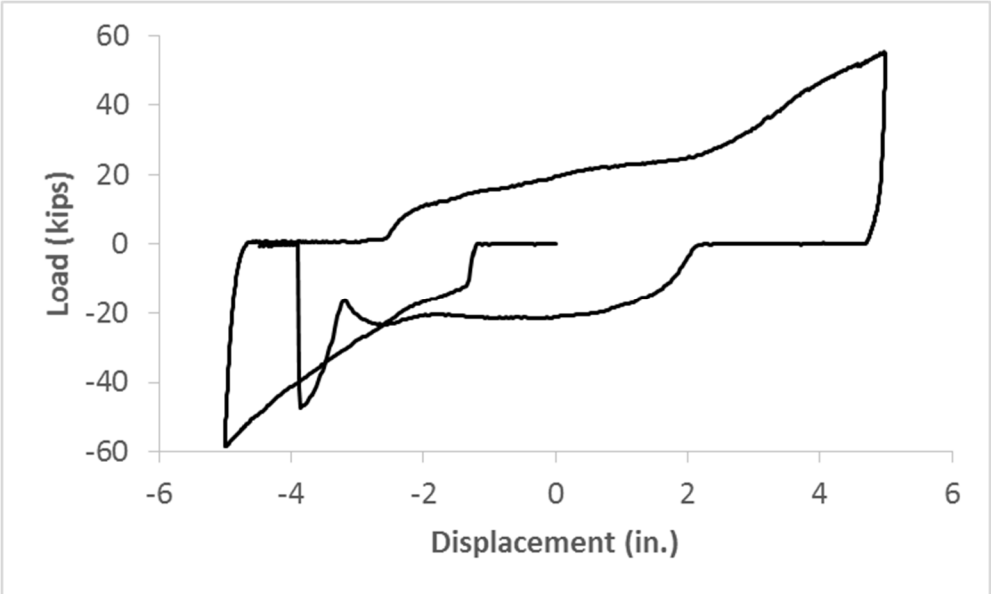


Figure B.17 – Load displacement for Specimen W36-B2-T94-R025

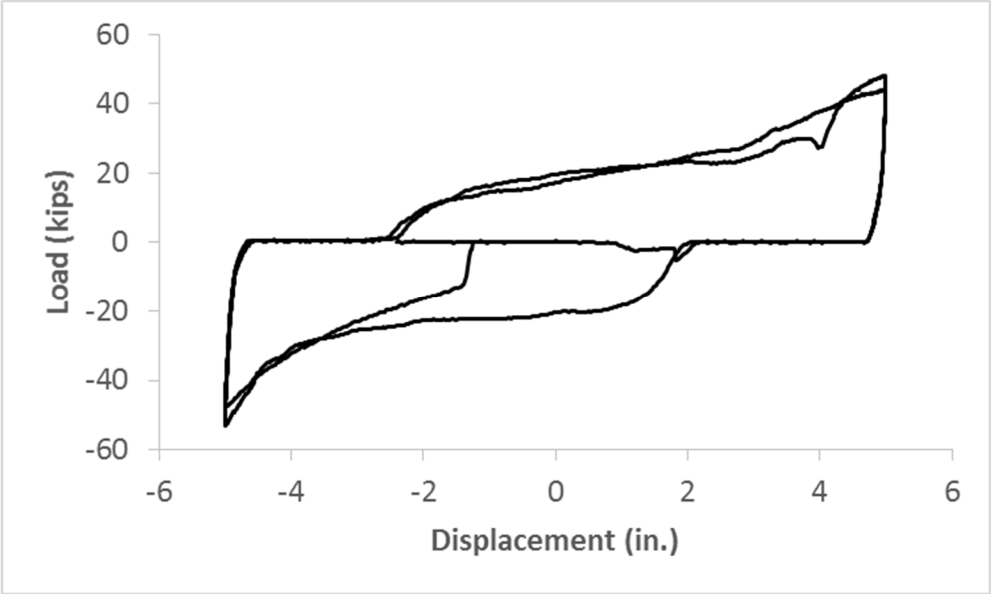


Figure B.18 – Load displacement for Specimen W36-B3-T94-R100

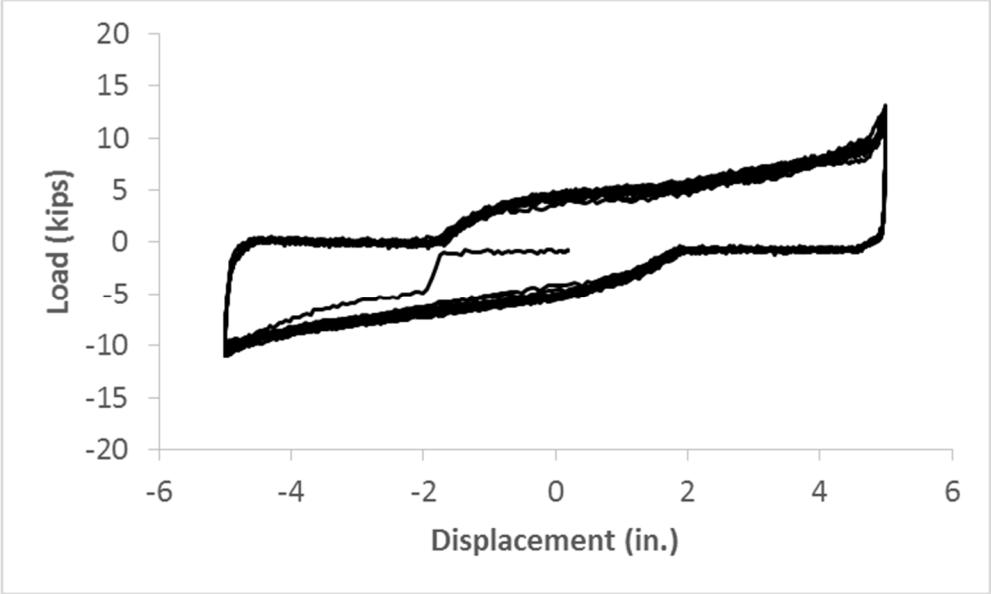


Figure B.19 – Load displacement for Specimen W24-PAF1-T59-R000

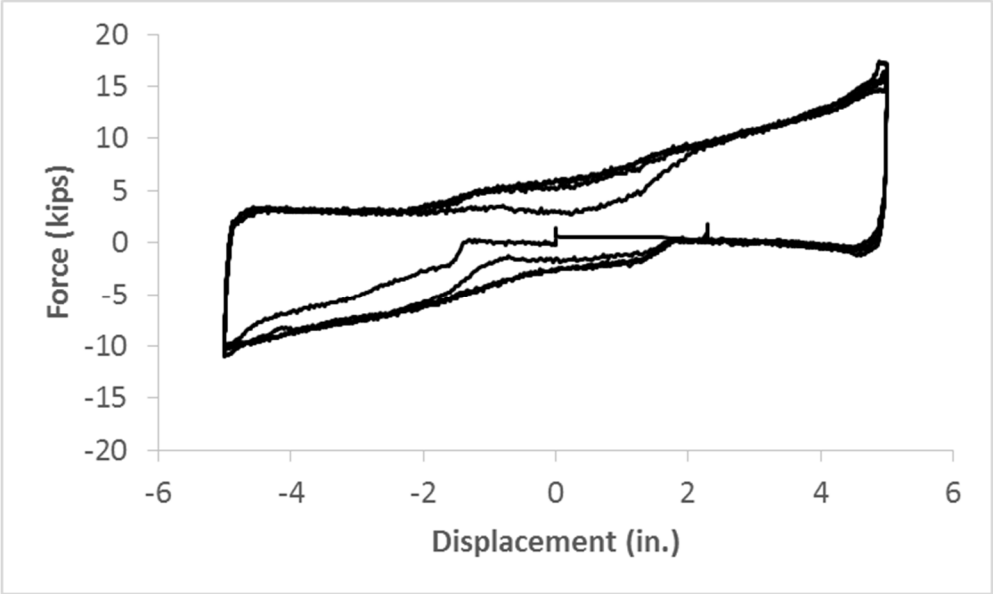


Figure B.20 – Load displacement for W24-PAF2-T59-R025

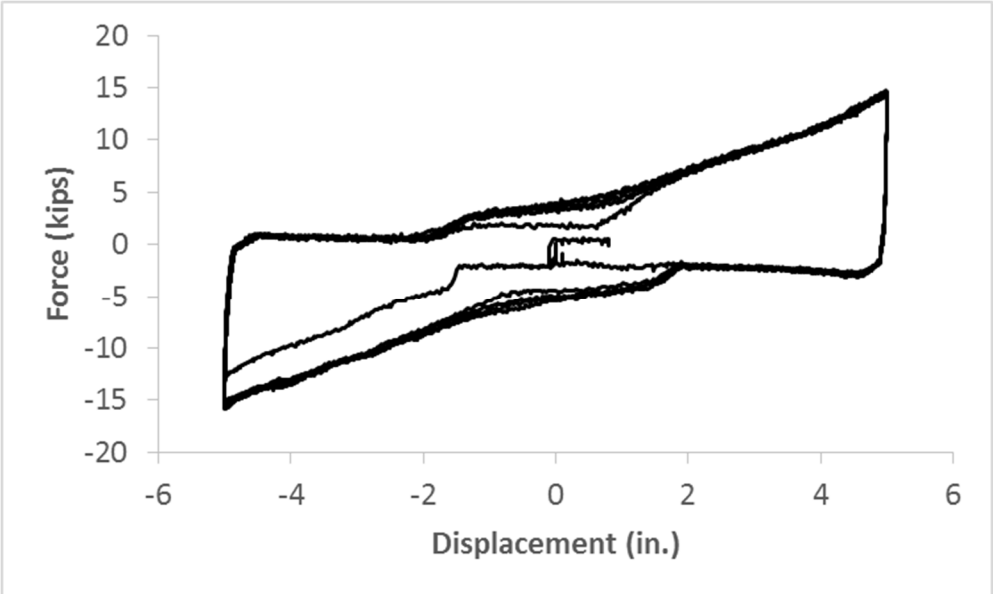


Figure B.21 – Load displacement for W24-PAF3-T59-R100



Figure B.22 – Load displacement for W36-PAF1-T94-R000



Figure B.23 – Load displacement for W36-PAF2-T94-R025

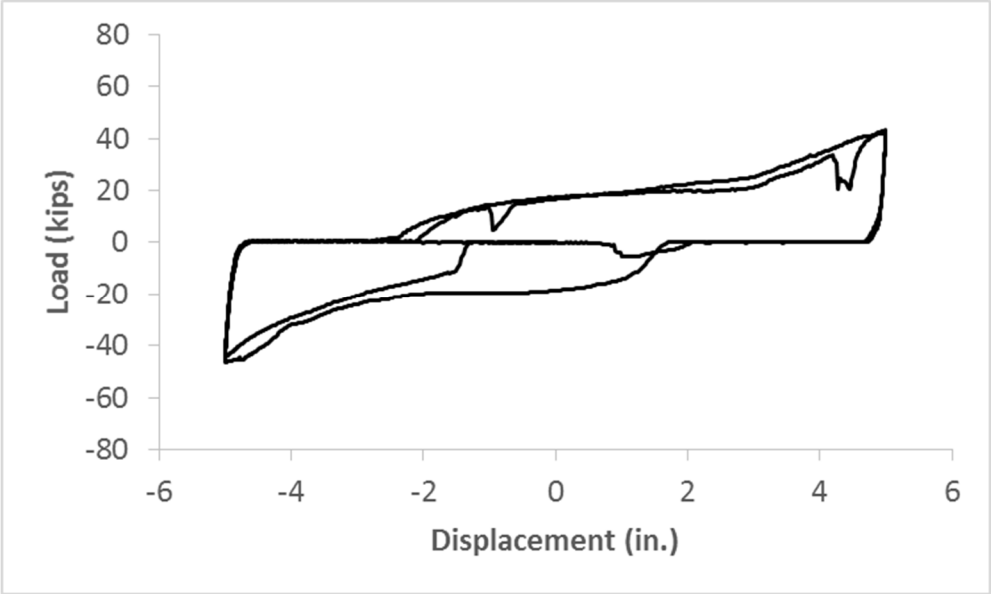


Figure B.24 – Load displacement for W36-PAF3-T94-R100

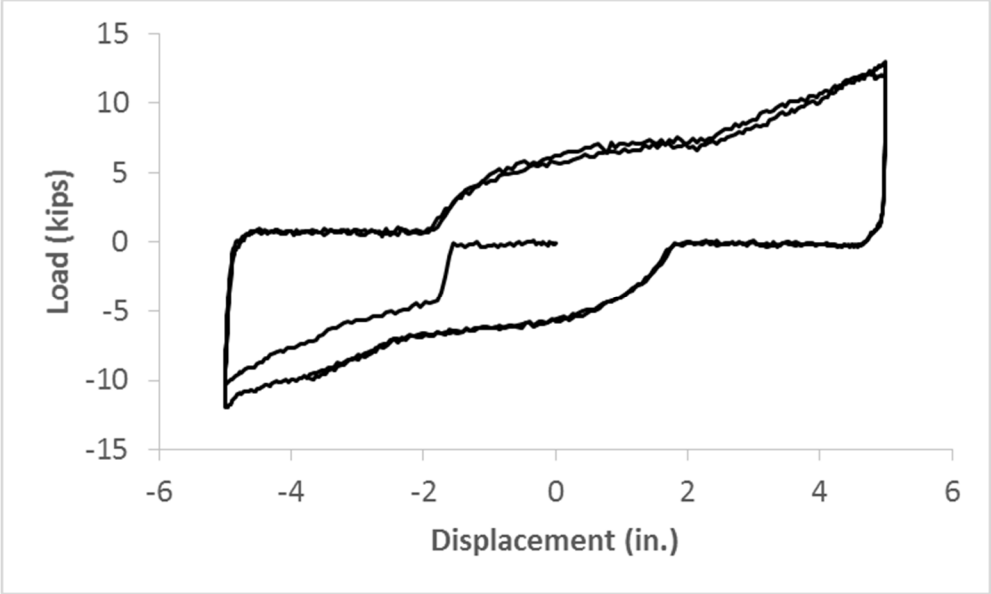


Figure B.25 – Load displacement for Specimen W24-PW1-T59-R000

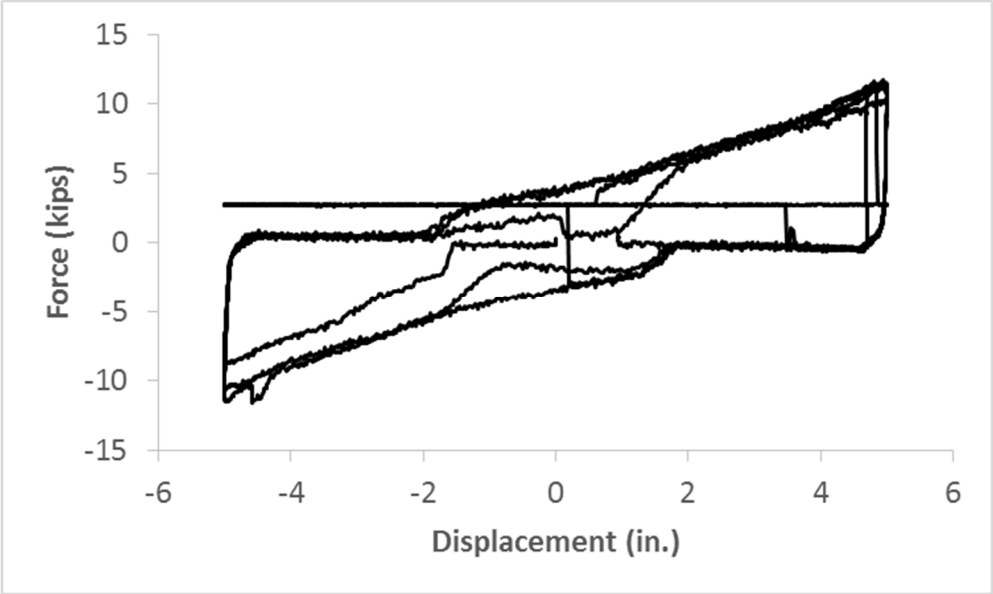


Figure B.26 – Load displacement for W24-PW2-T59-R025

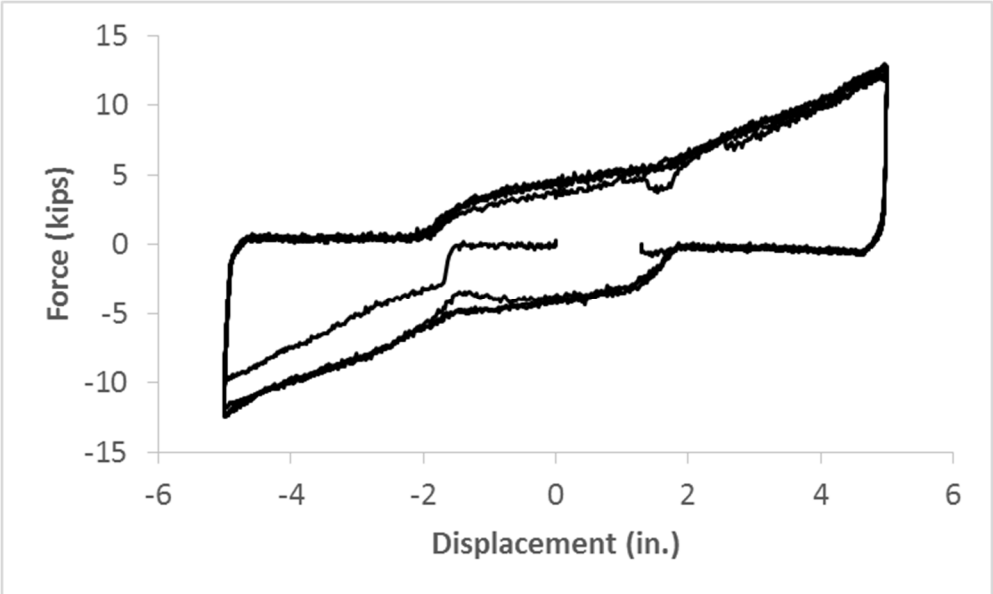


Figure B.27 – Load displacement for W24-PW3-T59-R100



Figure B.28 – Load displacement for W36-PW1-T94-R000

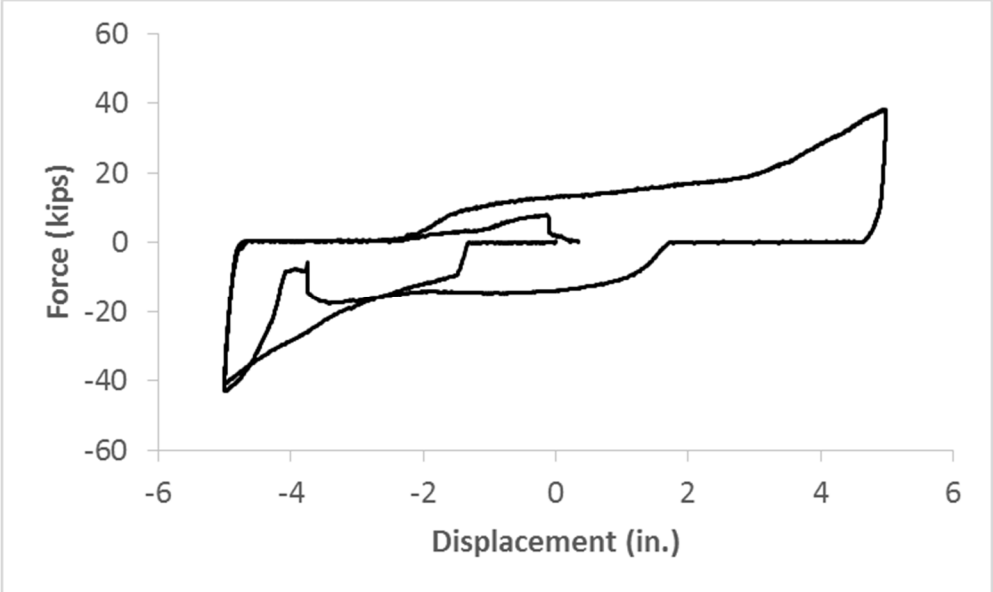


Figure B.29 – Load displacement for W36-PW2-T94-R025

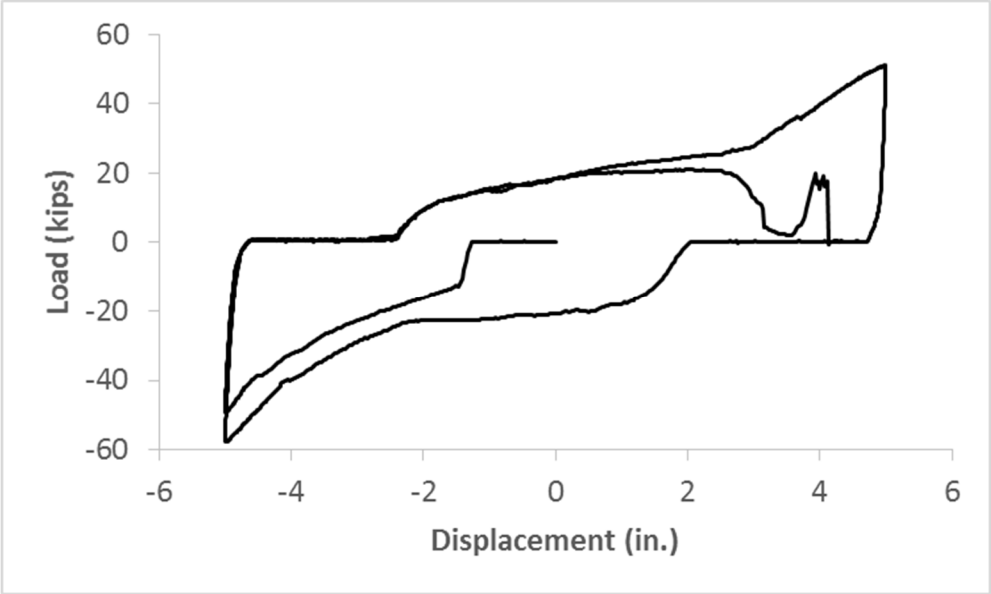


Figure B.30 – Load displacement for W36-PW3-T94-R100

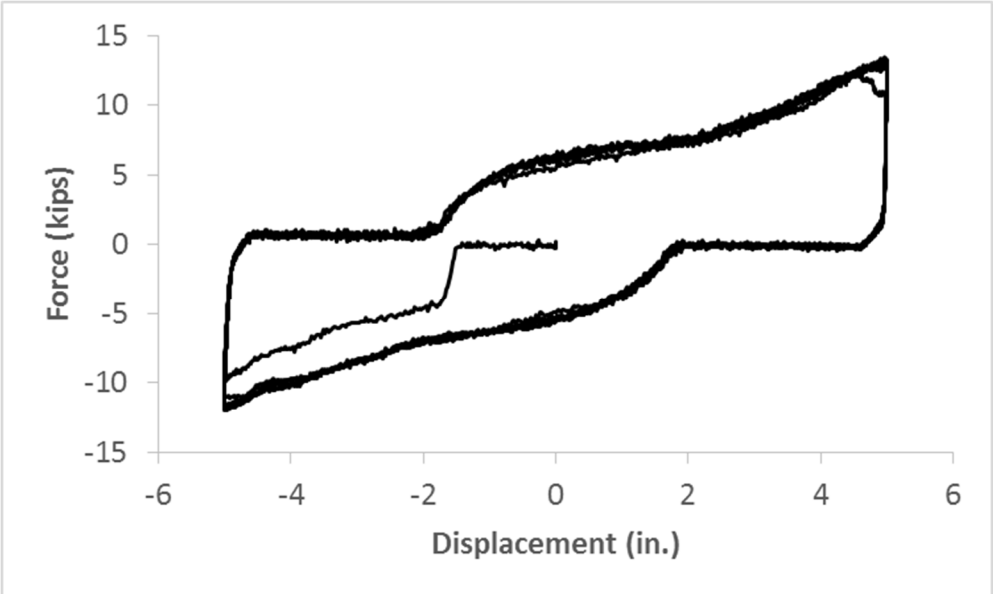


Figure B.31 – Load displacement for Specimen W24-GFW1-T59-R000

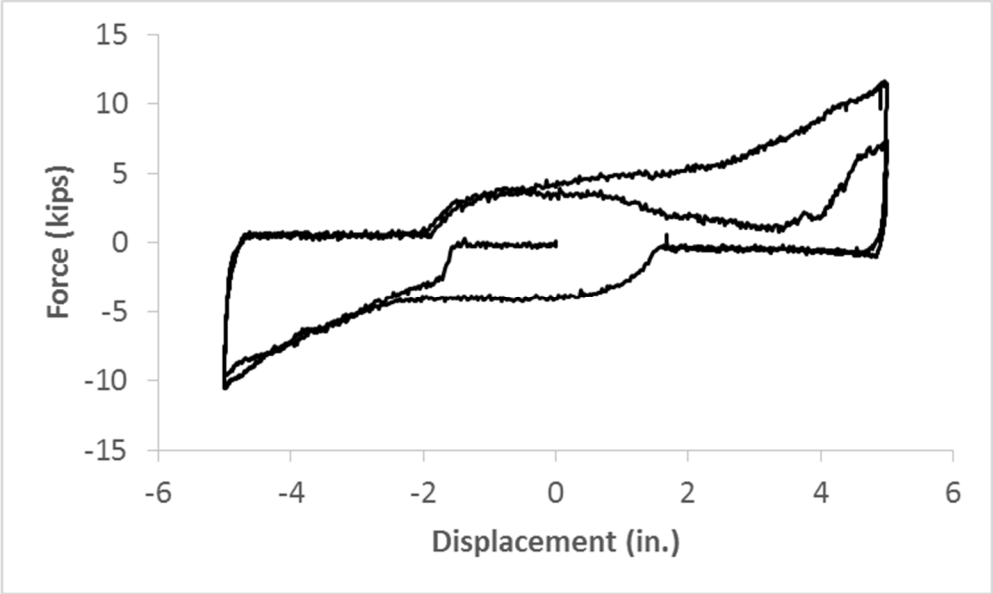


Figure B.32 – Load displacement for W24-GFW2-T59-R025

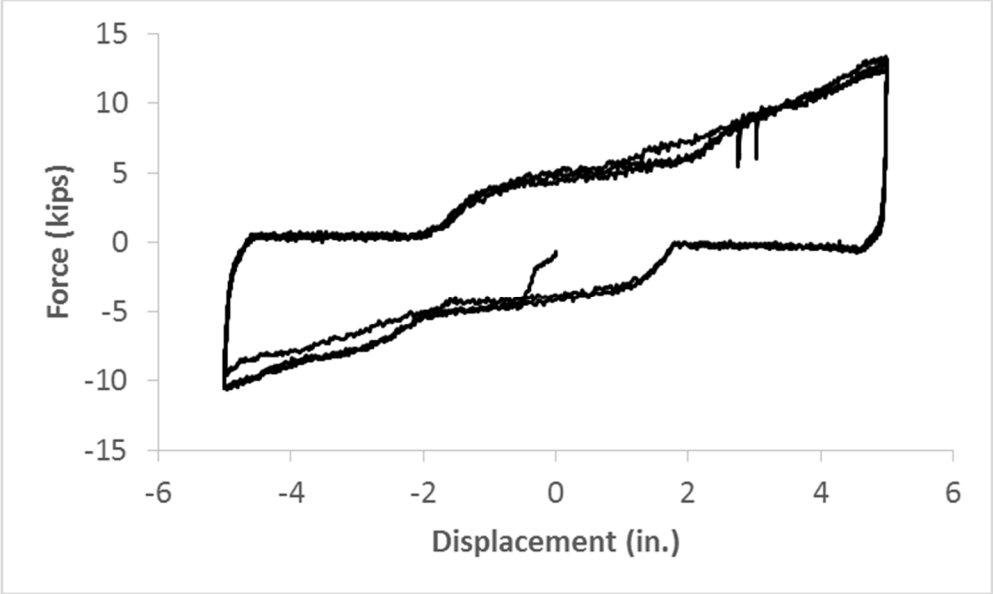


Figure B.33 – Load displacement for W24-GFW3-T59-R100



Figure B.34 – Load displacement for W36-GFW1-T94-R000



Figure B.35 – Load displacement for W36-GFW2-T94-R025

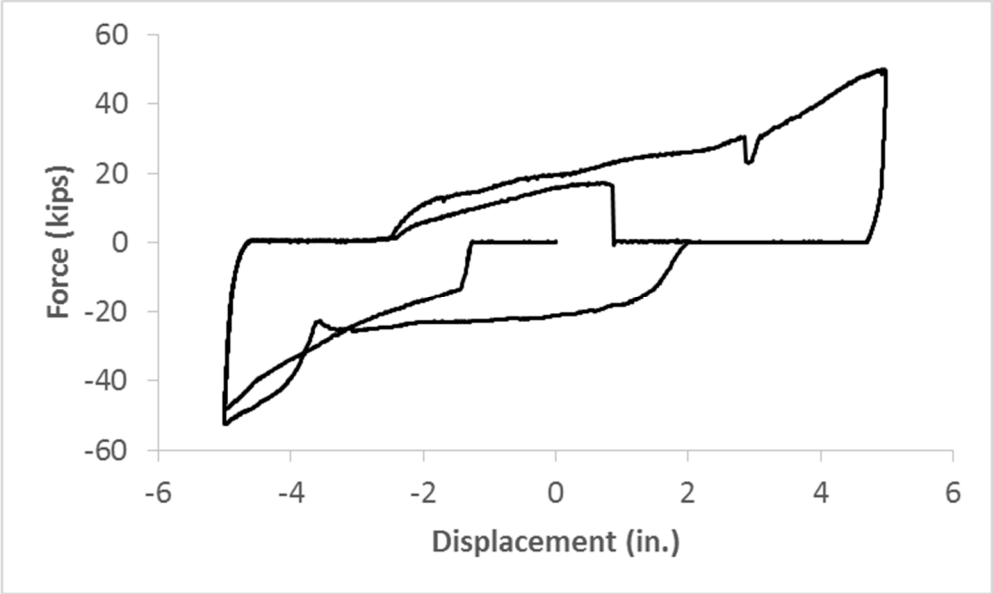


Figure B.36 – Load displacement for W36-GFW3-T94-R100

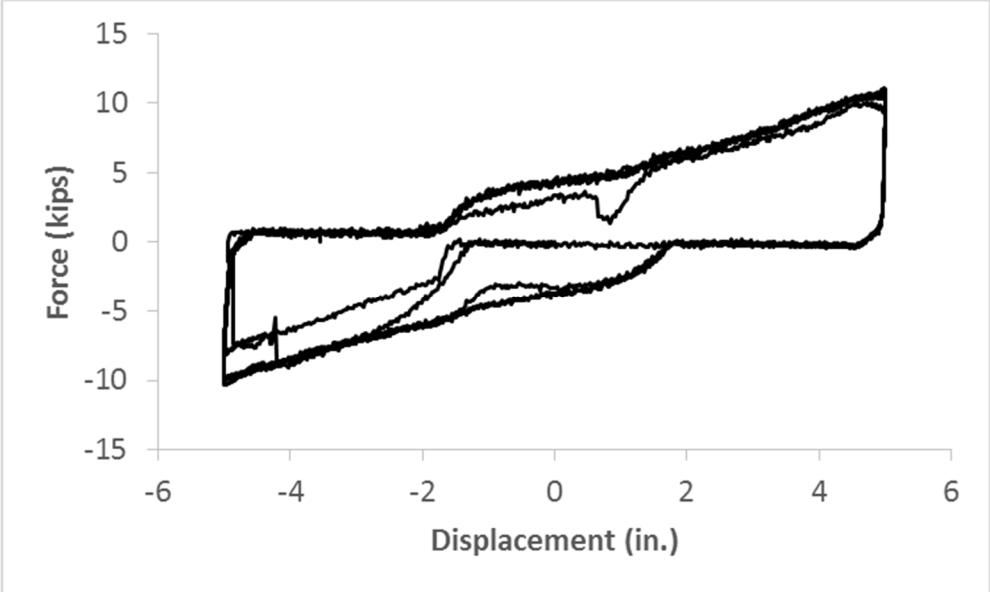


Figure B.37 – Load displacement for Specimen W24-NGT1-T59-R000

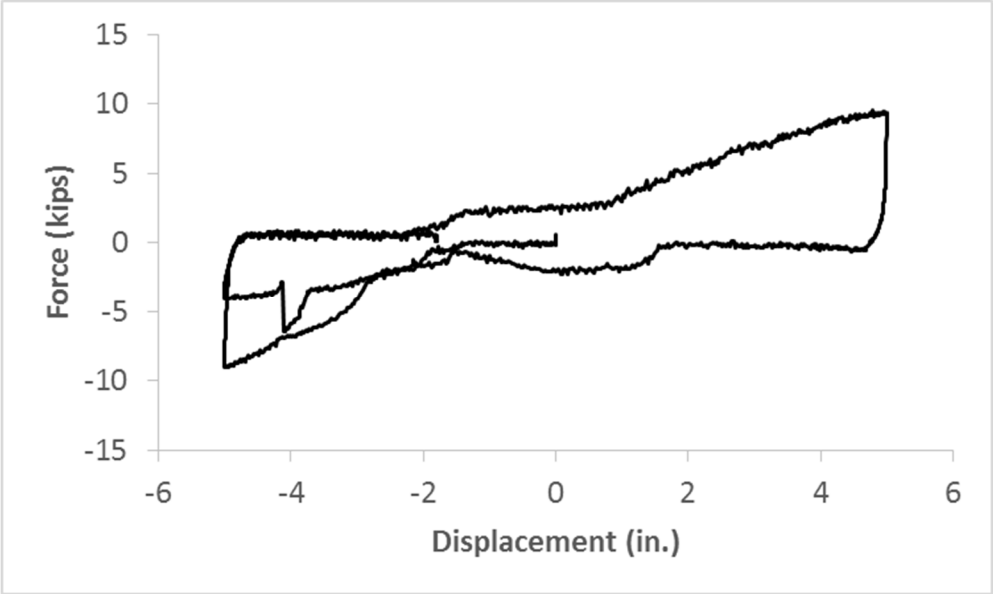


Figure B.38 – Load displacement for W24-NGT2-T59-R025

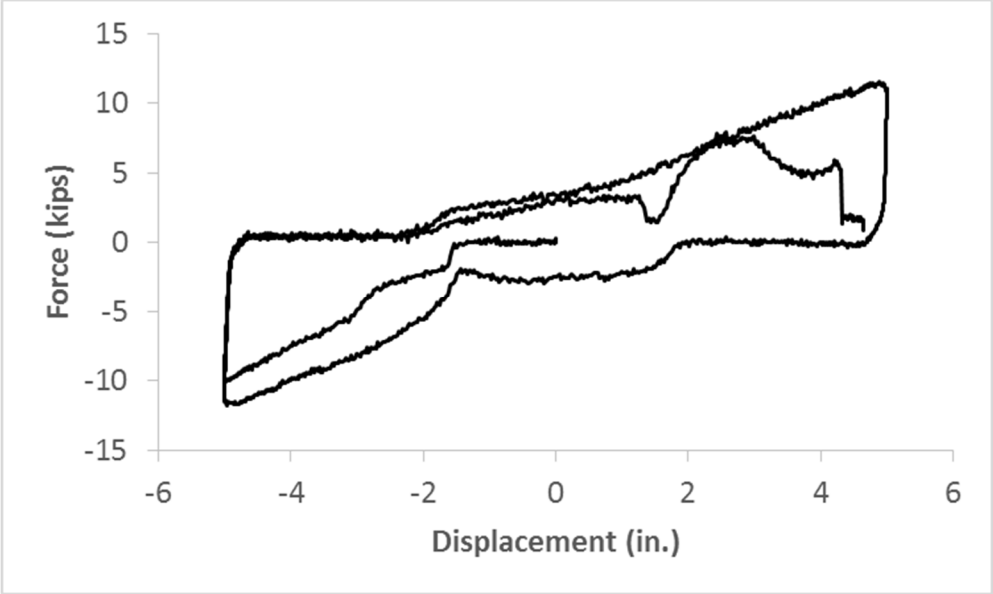


Figure B.39 – Load displacement for W24-NGT3-T59-R100



Figure B.40 – Load displacement for W36-NGT1-T94-R000

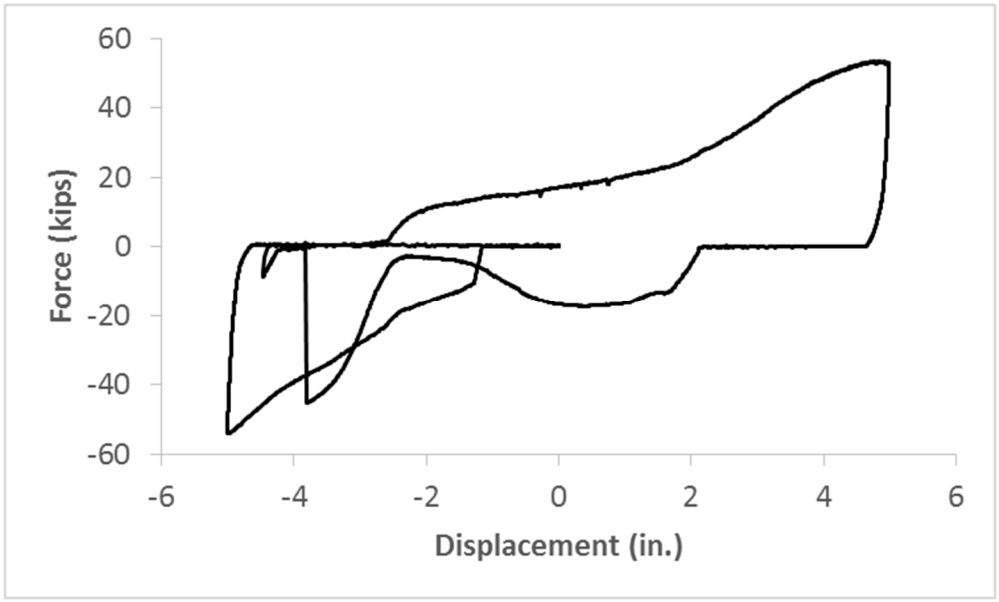


Figure B.41 – Load displacement for W36-NGT2-T94-R025

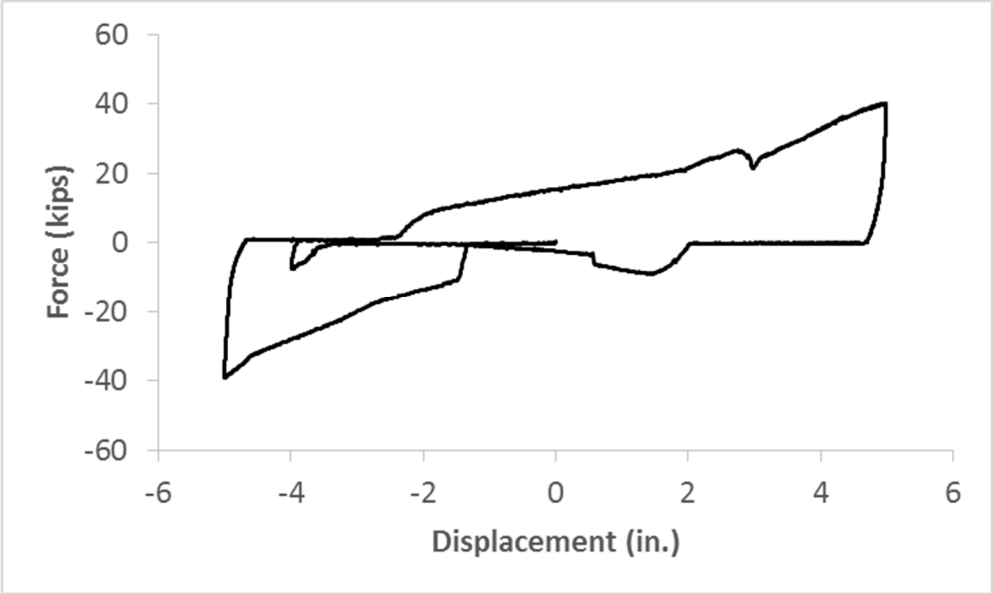


Figure B.42 – Load displacement for W36-NGT3-T94-R100

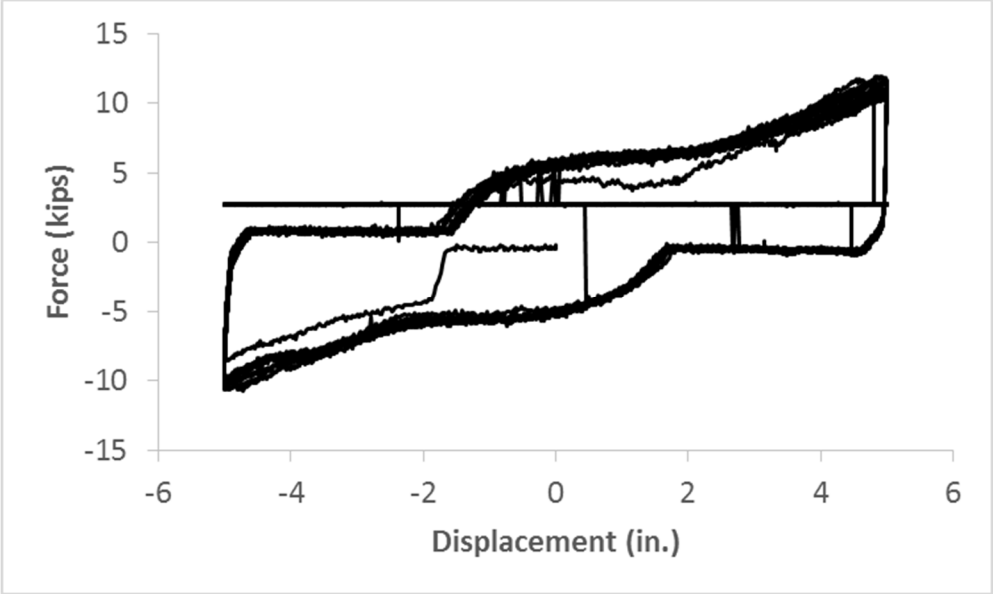


Figure B.43 – Load displacement for Specimen W24-NWG1-T59-R000

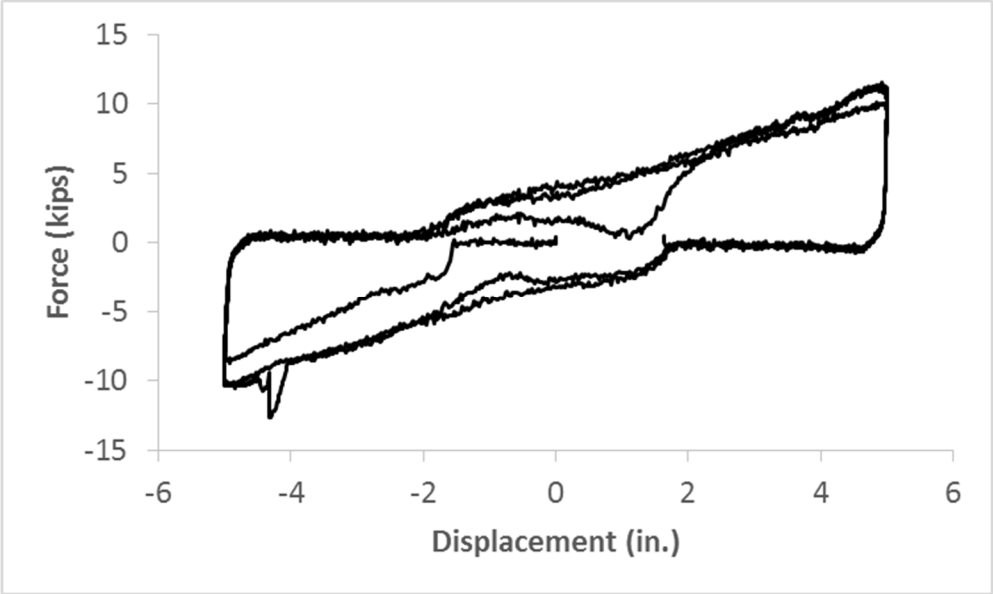


Figure B.44 – Load displacement for W24-NWG2-T59-R025



Figure B.45 – Load displacement for W24-NWG3-T59-R100



Figure B.46 – Load displacement for W36-NWG1-T94-R000

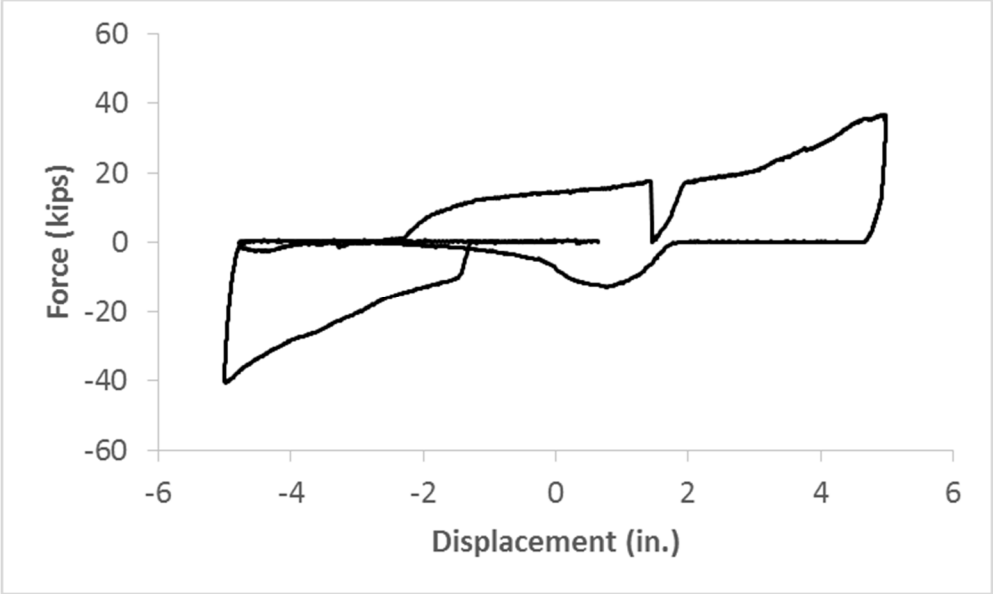


Figure B.47 – Load displacement for W36-NWG2-T94-R025

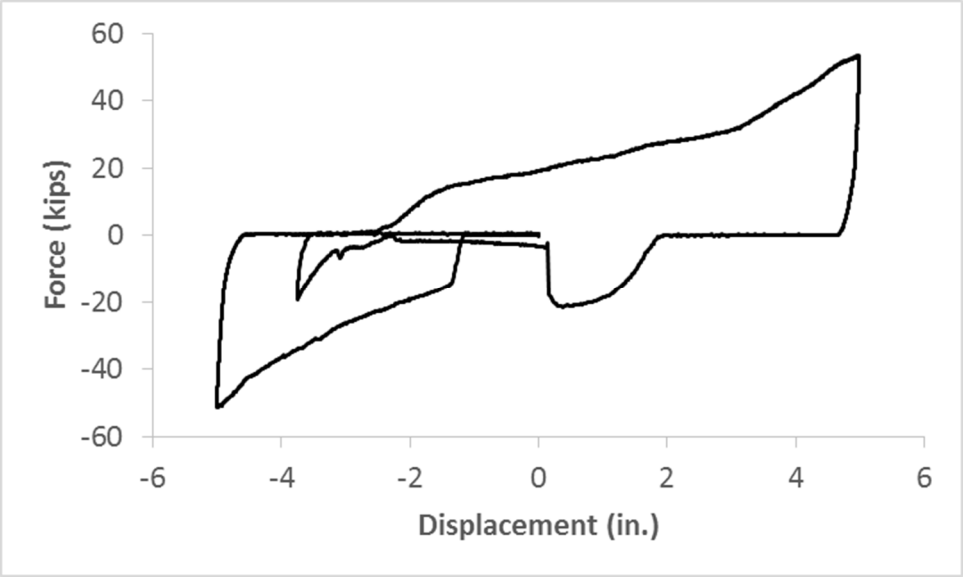


Figure B.48 – Load displacement for W36-NWG3-T94-R100

APPENDIX C CALIBRATION OF DEGRADATION COEFFICIENT

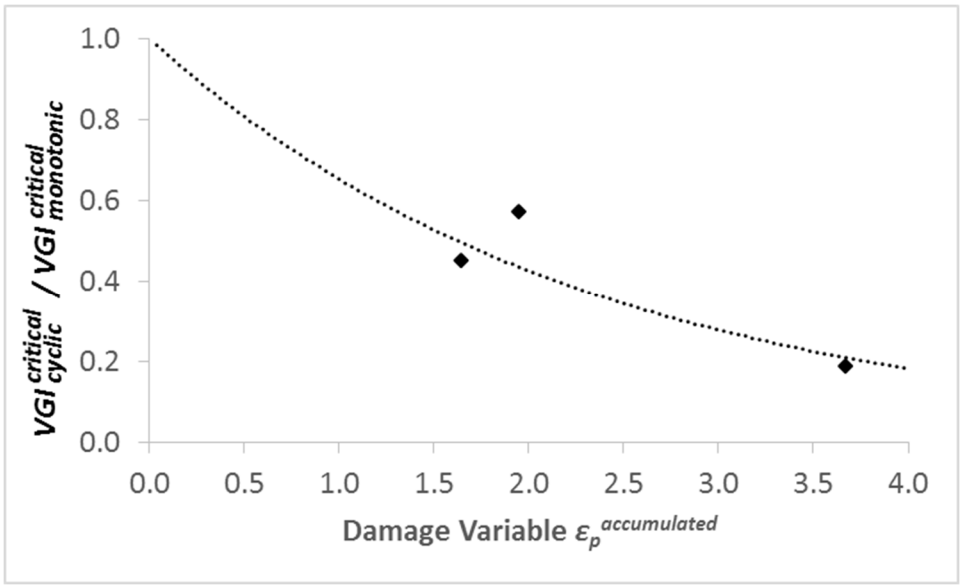


Figure C.1 – Curve fit scatter plot and curve fit to calculate λ for W24x62 with no artifact.

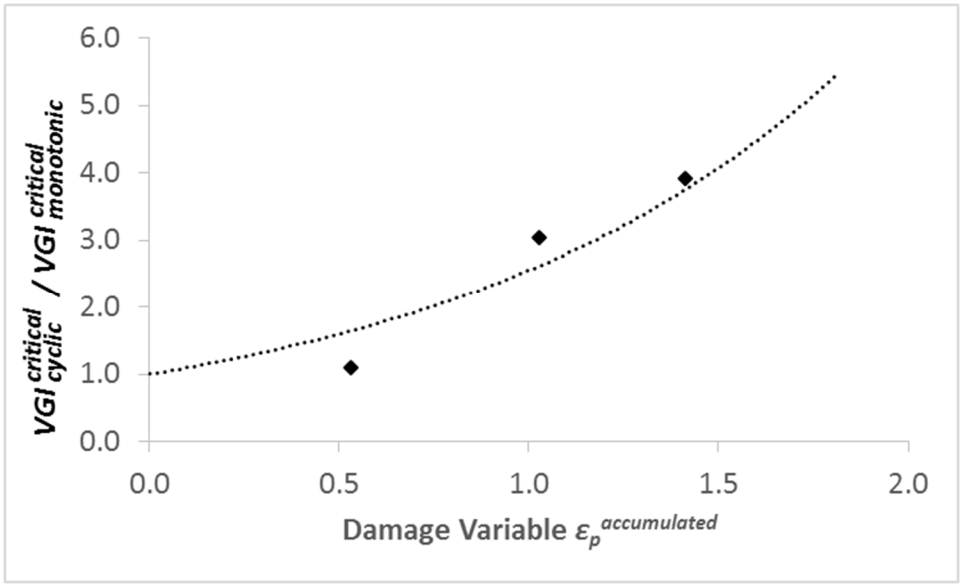


Figure C.2 – Curve fit scatter plot and curve fit to calculate λ for W24x62 with PAF.

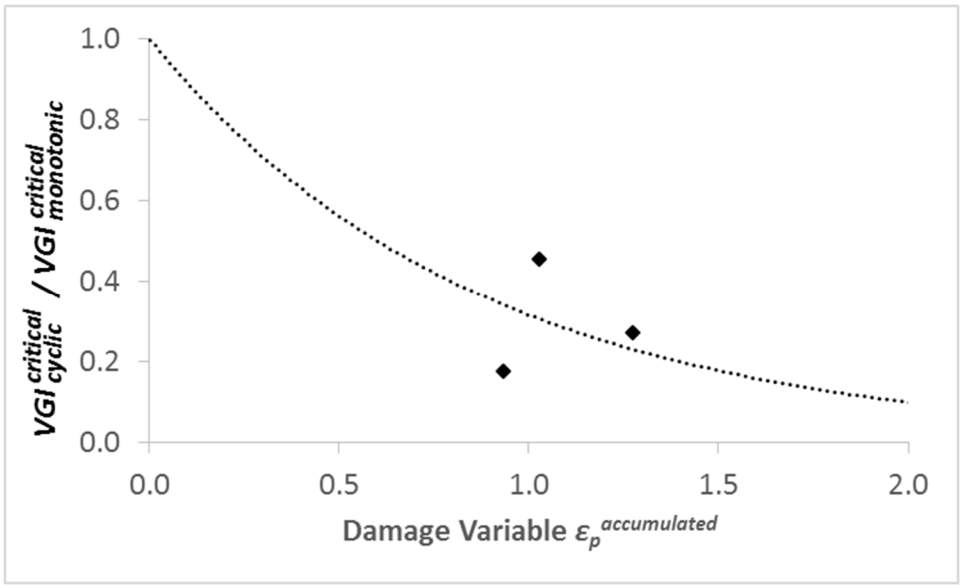


Figure C.3 – Curve fit scatter plot and curve fit to calculate λ for W24x62 with PW.

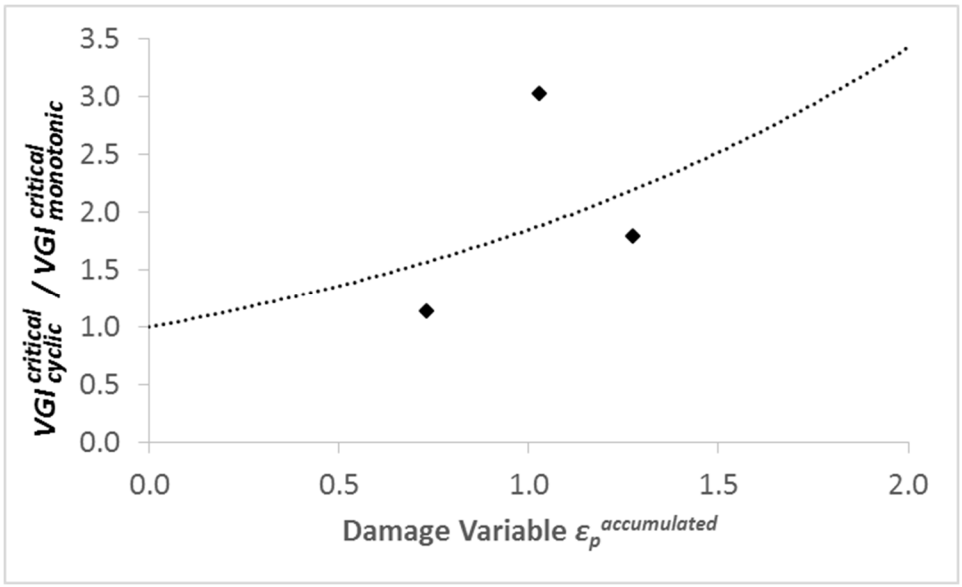


Figure C.4 – Curve fit scatter plot and curve fit to calculate λ for W24x62 with GFW.

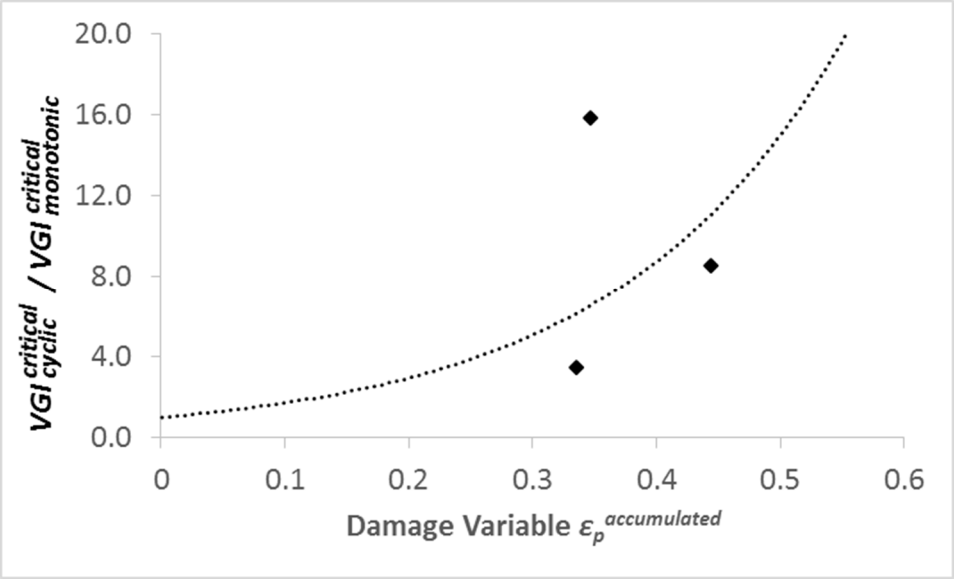


Figure C.5 – Curve fit scatter plot and curve fit to calculate λ for W24x62 with NGT.

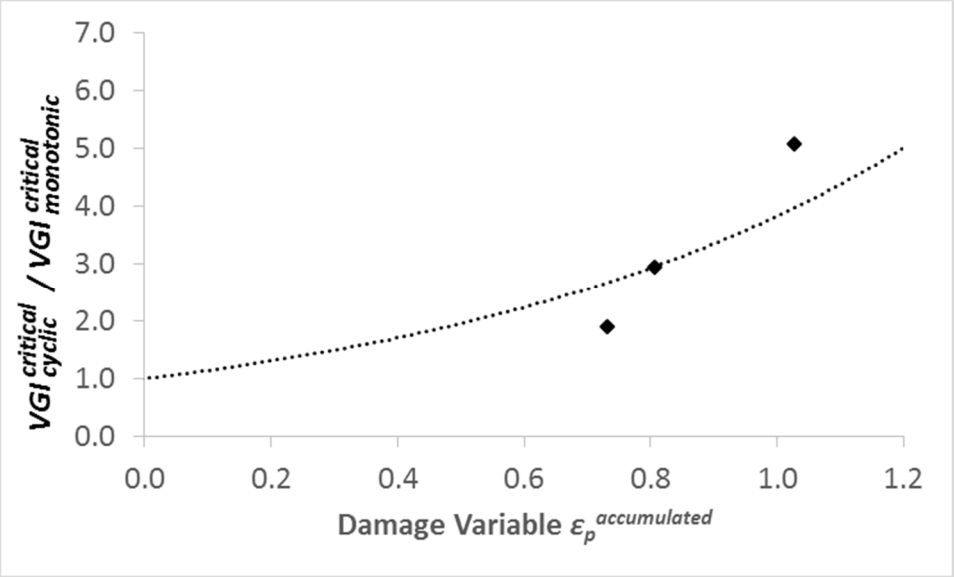


Figure C.6 – Curve fit scatter plot and curve fit to calculate λ for W24x62 with NWG.

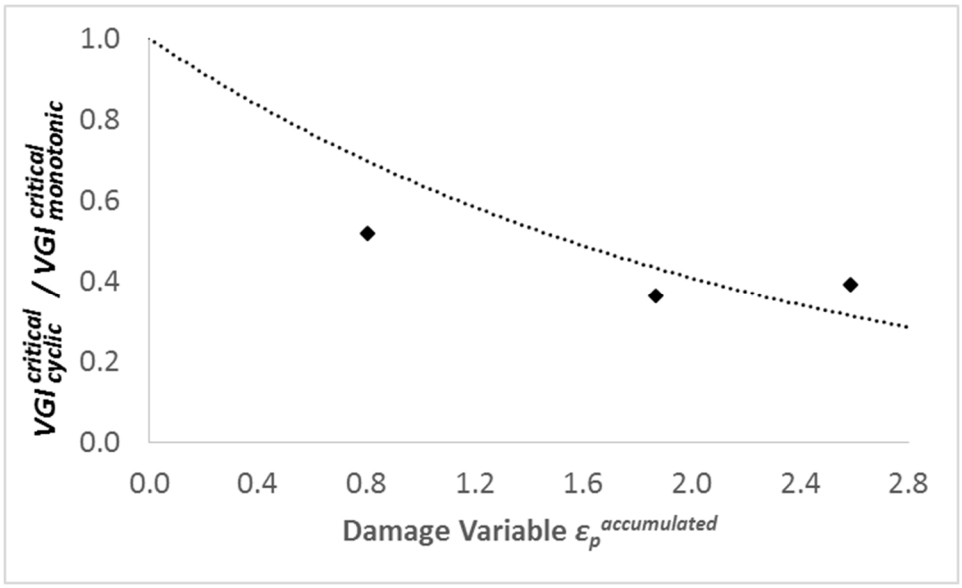


Figure C.7 – Curve fit scatter plot and curve fit to calculate λ for W36x150 with no artifact.

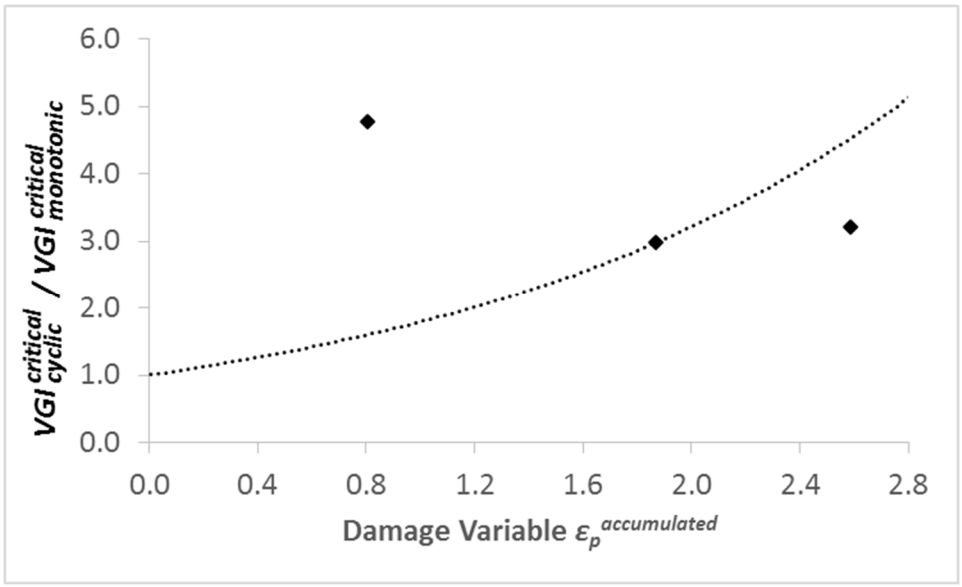


Figure C.8 – Curve fit scatter plot and curve fit to calculate λ for W36x150 with PAF.

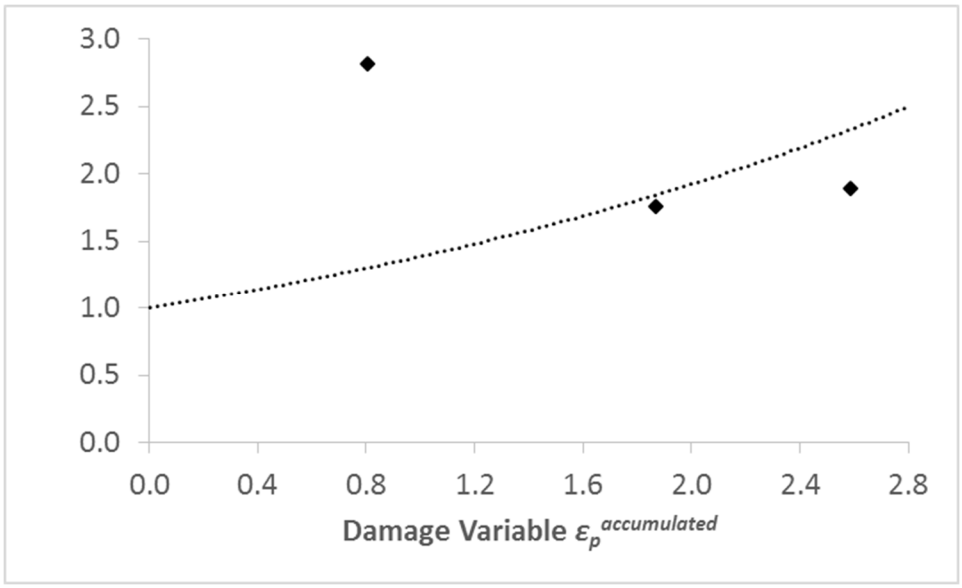


Figure C.9 – Curve fit scatter plot and curve fit to calculate λ for W36x150 with PW.

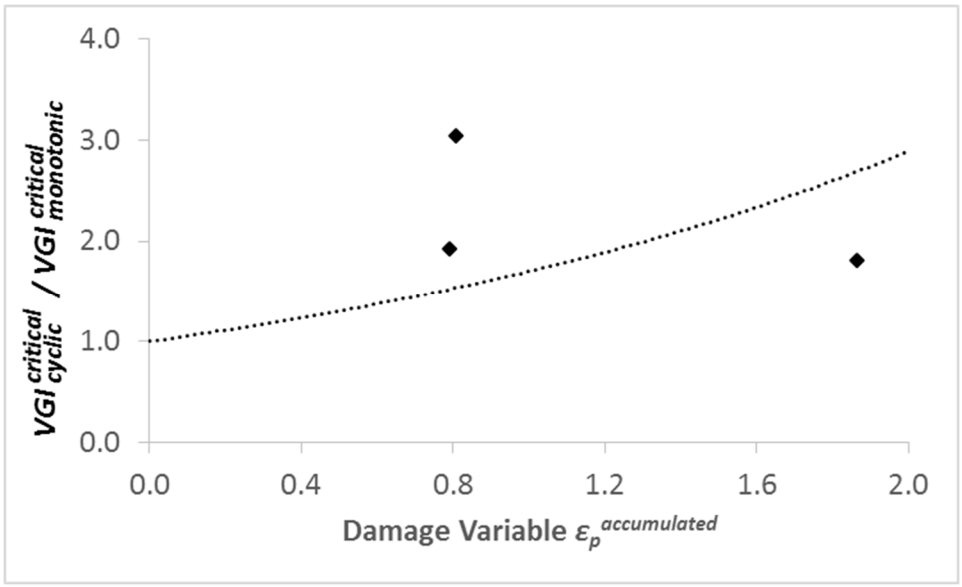


Figure C.10 – Curve fit scatter plot and curve fit to calculate λ for W36x150 with GFW.

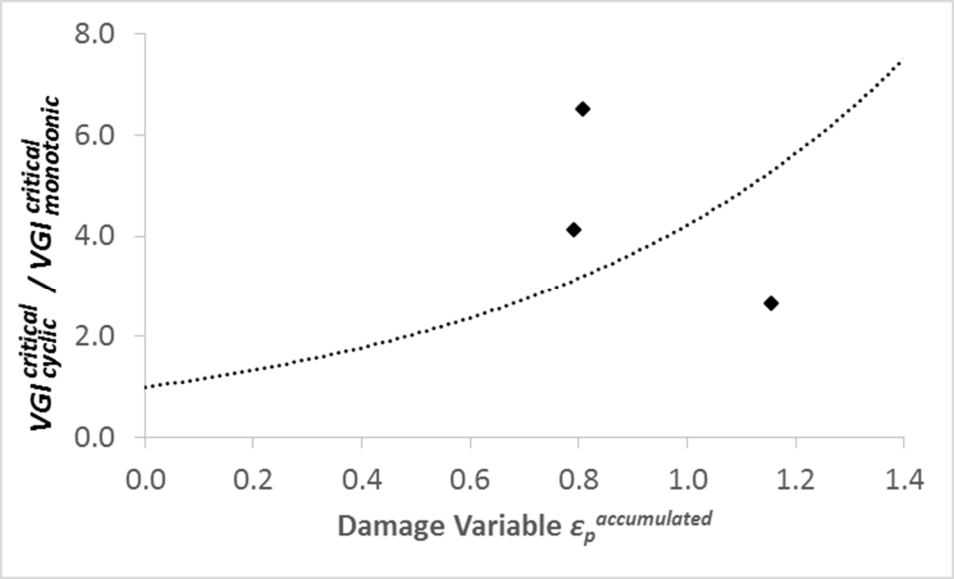


Figure C.11 – Curve fit scatter plot and curve fit to calculate λ for W36x150 with NGT.

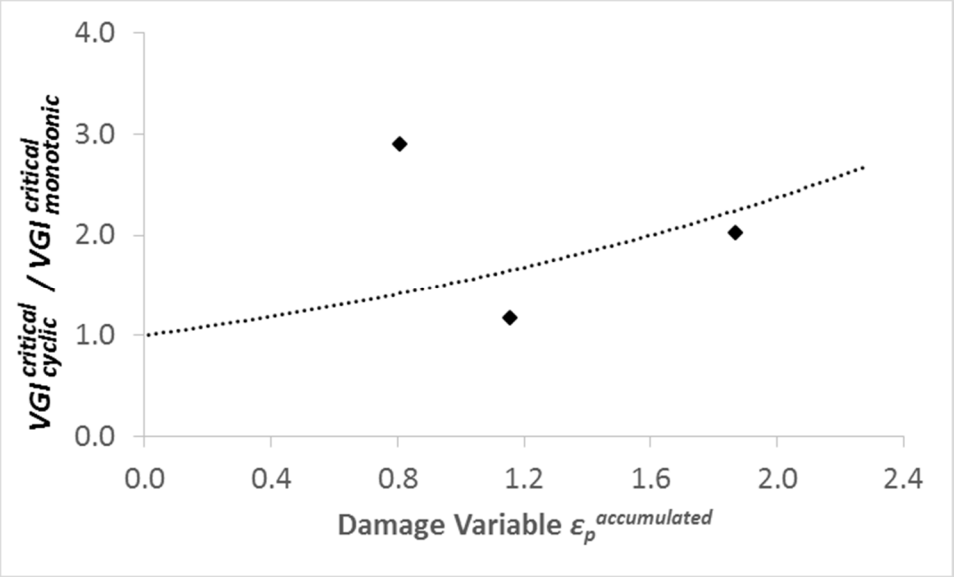


Figure C.12 – Curve fit scatter plot and curve fit to calculate λ for W36x150 with NWG.

APPENDIX D FULL-SCALE FRACTURE INITIATION

D.1 Fracture Initiation Location Based on Worst Case

Locations of fracture initiation at worse case locations in which fracture will initiation will be observed.

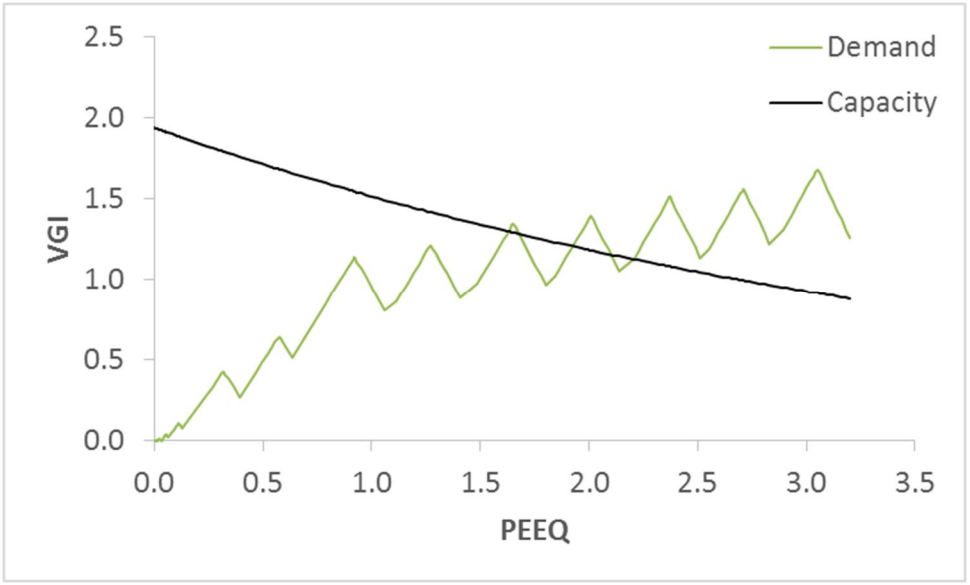


Figure D.1 – CVGM fracture initiation prediction at worst case for W24x62 with no artifact using round notched tests fracture parameters from W36x150 flanges.

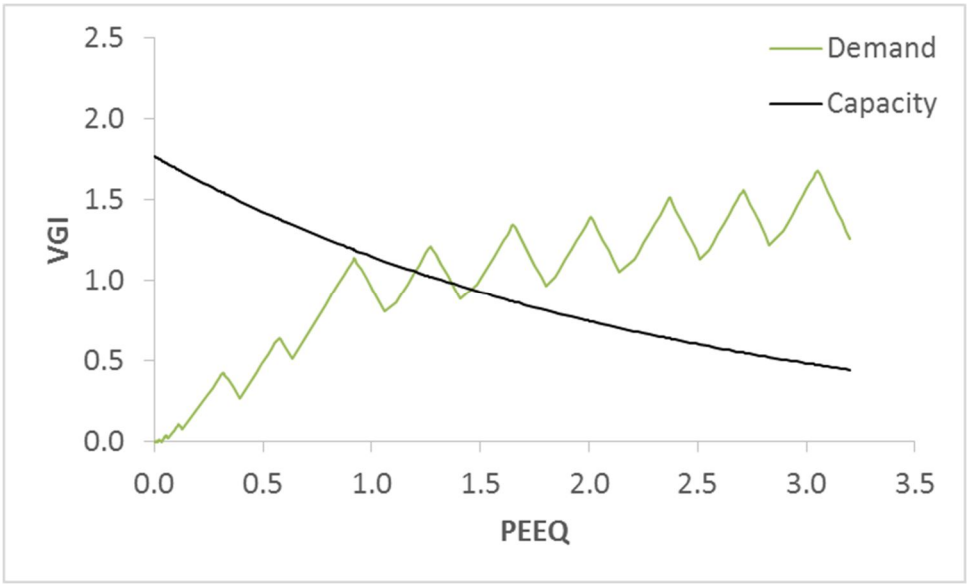


Figure D.2 – CVGM fracture initiation prediction at worst case for W24x62 with no artifact (from cyclic bend tests).

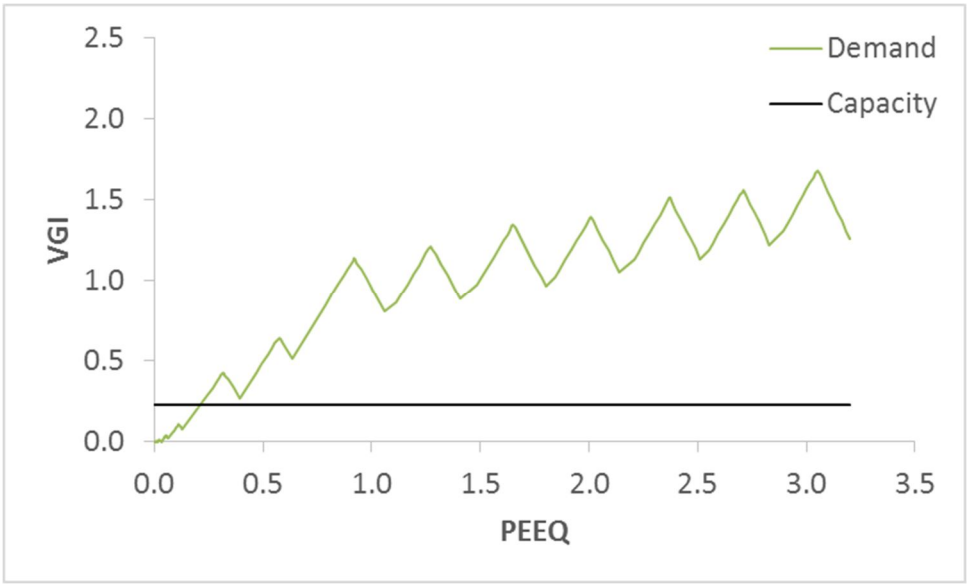


Figure D.3 – CVGM fracture initiation prediction at worst case for W24x62 with PAF.

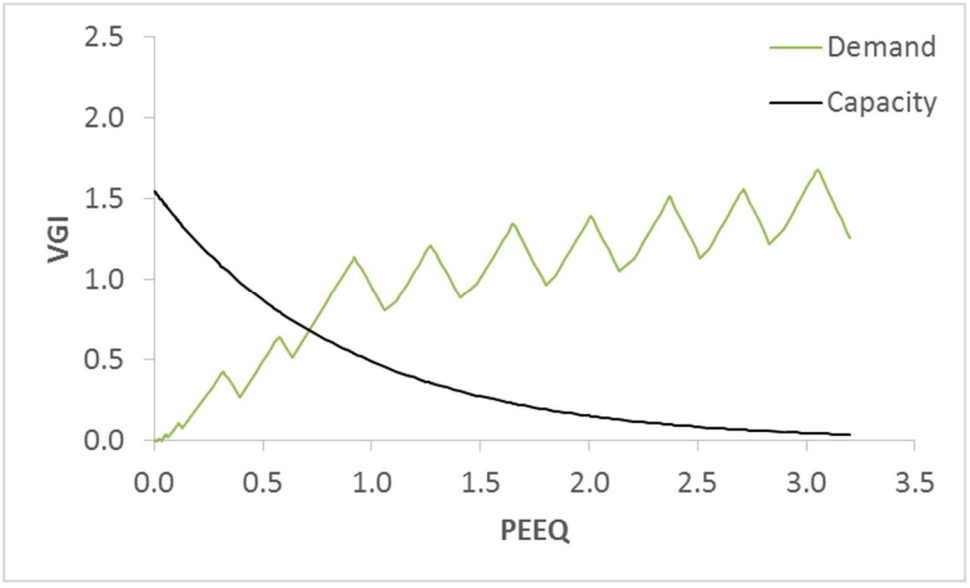


Figure D.4 – CVGM fracture initiation prediction at worst case for W24x62 with PW.

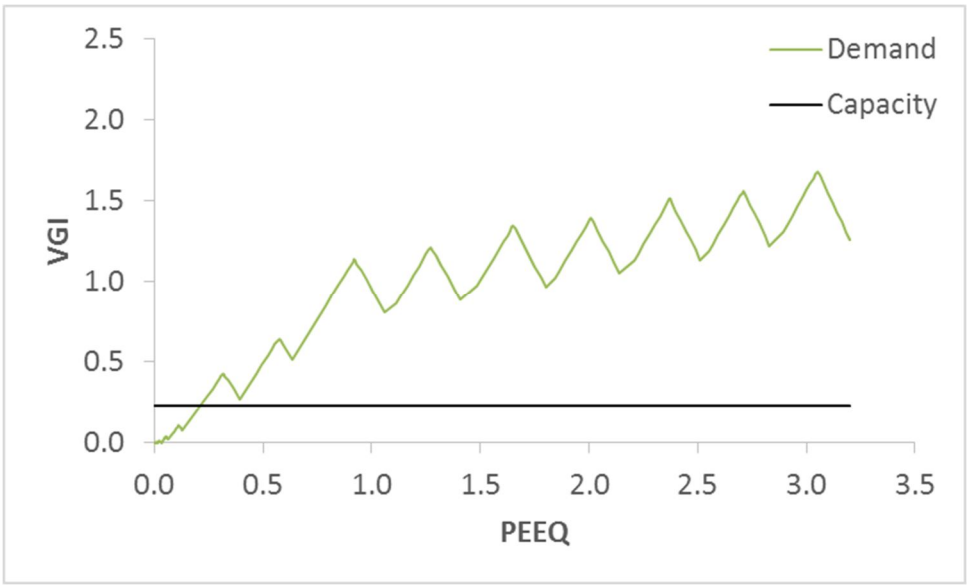


Figure D.5 – CVGM fracture initiation prediction at worst case for W24x62 with GFW.

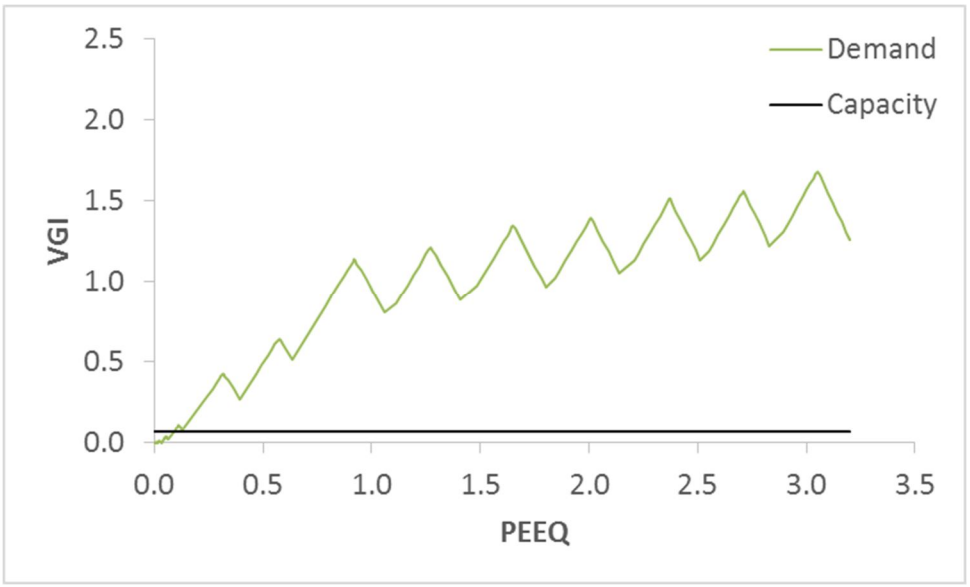


Figure D.6 – CVGM fracture initiation prediction at worst case for W24x62 with NGT.

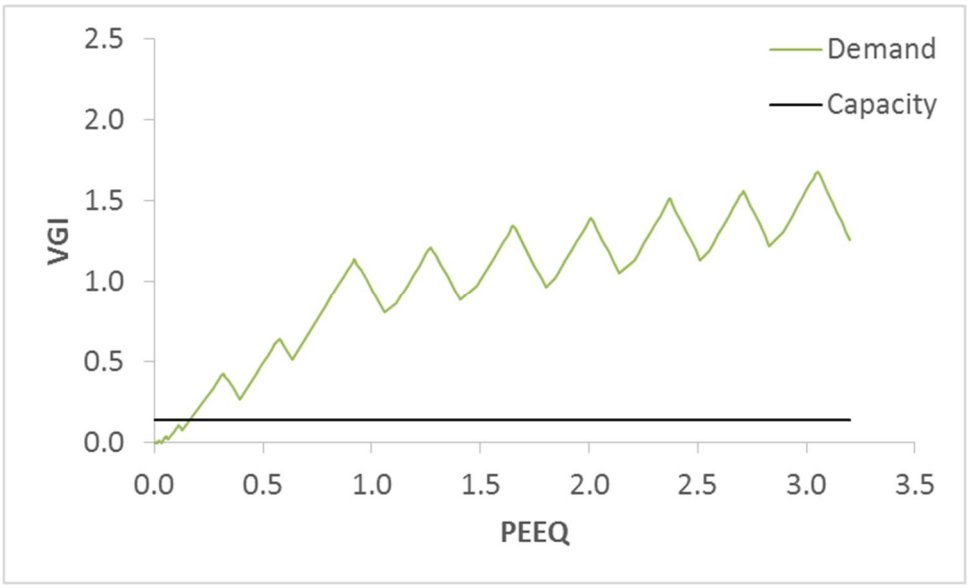


Figure D.7 – CVGM fracture initiation prediction at worst case for W24x62 with NWG.

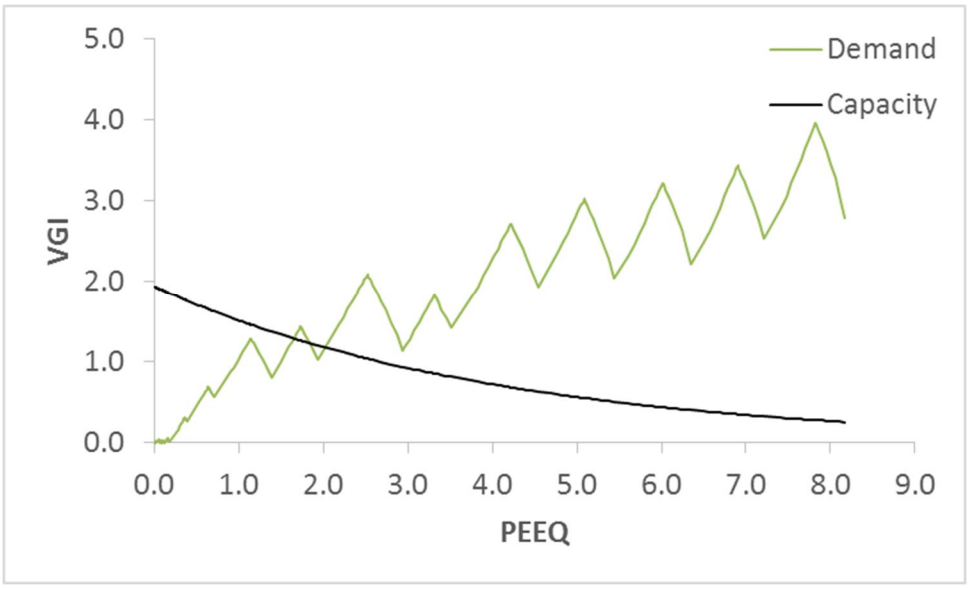


Figure D.8 – CVGM fracture initiation prediction at worst case for W24x62 RBS with no artifact using round notched tests fracture parameters from W36x150 flanges.

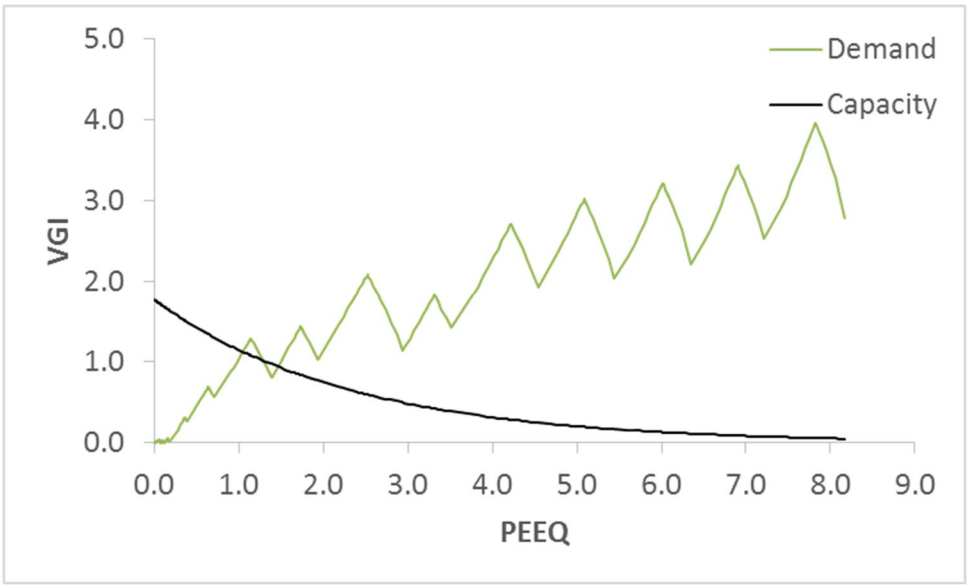


Figure D.9 – CVGM fracture initiation prediction at worst case for W24x62 RBS with no artifact (from cyclic bend tests).

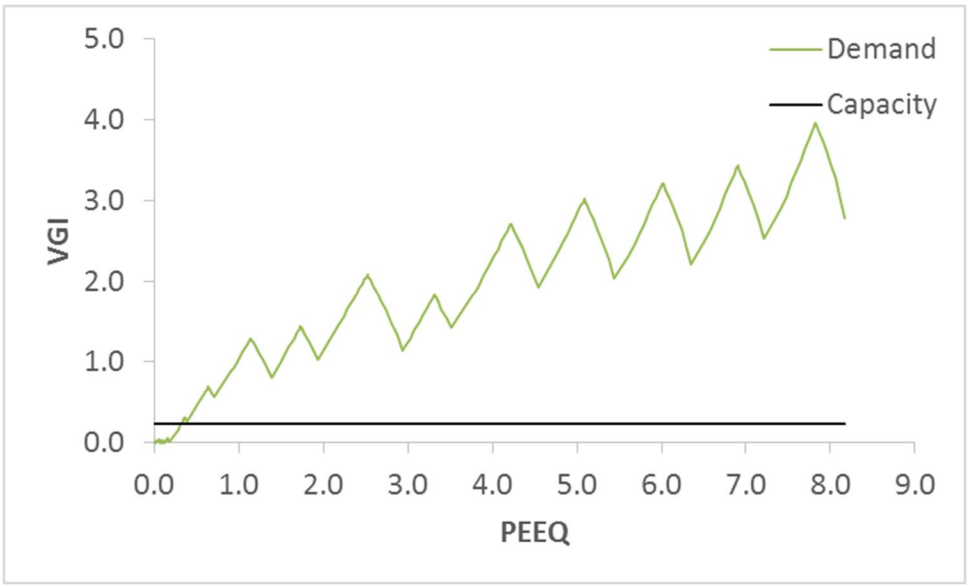


Figure D.10 – CVGM fracture initiation prediction at worst case for W24x62 RBS with PAF.

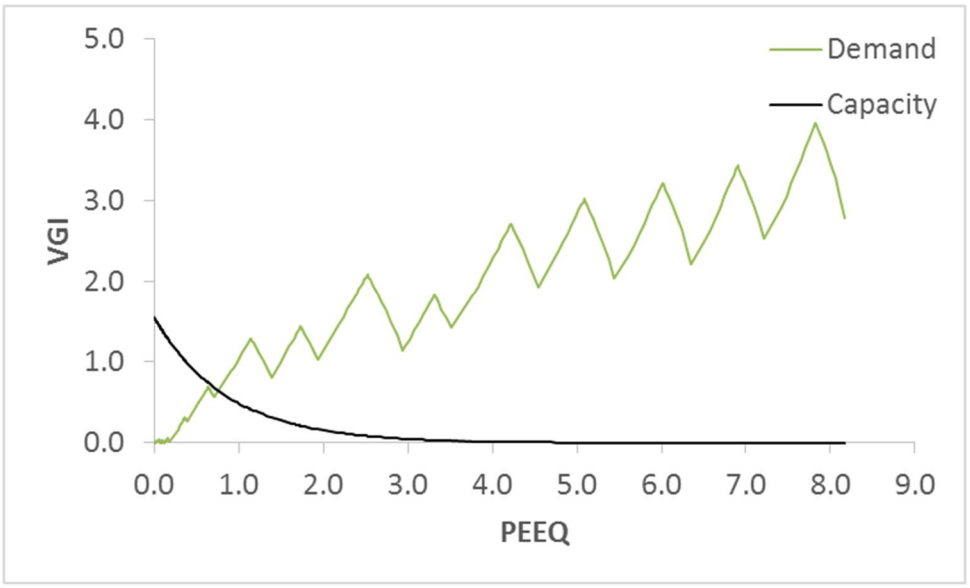


Figure D.11 – CVGM fracture initiation prediction at worst case for W24x62 RBS with PW.

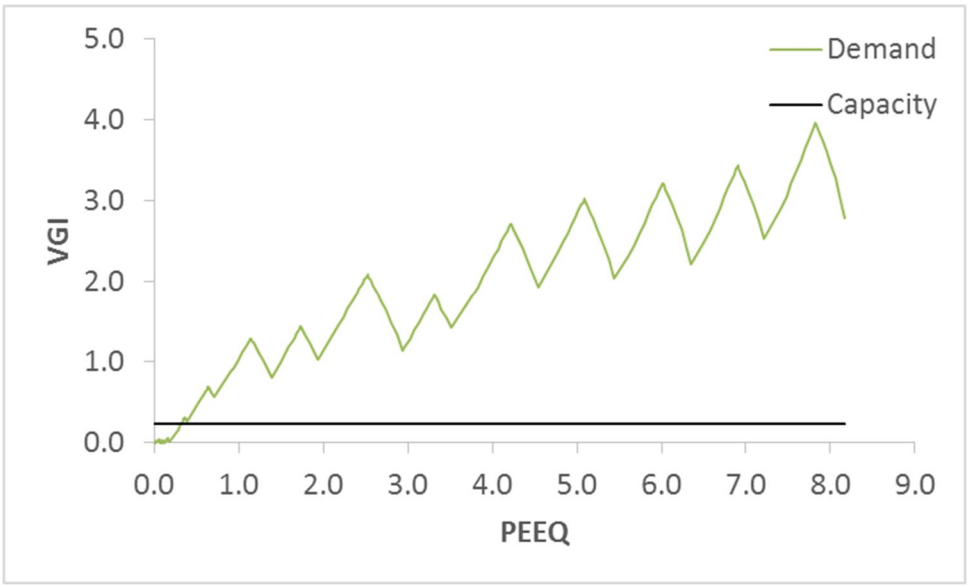


Figure D.12 – CVGM fracture initiation prediction at worst case for W24x62 RBS with GFW.

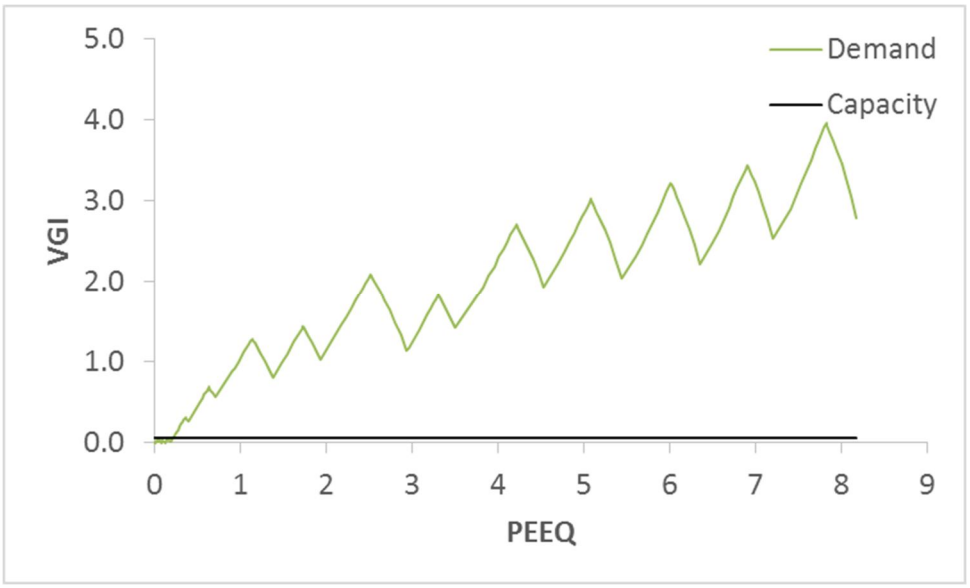


Figure D.13 – CVGM fracture initiation prediction at worst case for W24x62 RBS with NGT.

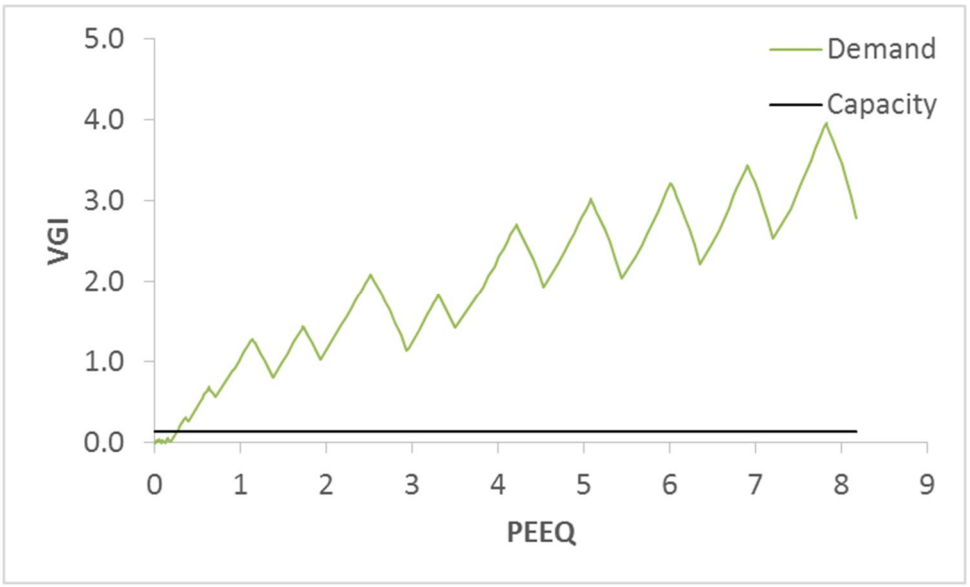


Figure D.14 – CVGM fracture initiation prediction at worst case for W24x62 RBS with NWG.

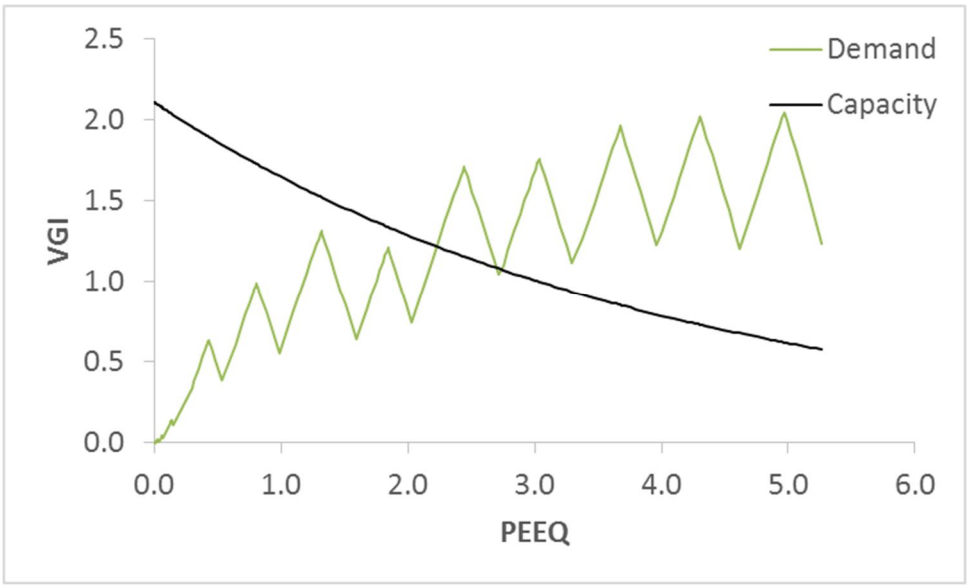


Figure D.15 – CVGM fracture initiation prediction at worst case for W36x150 with no artifact using round notched tests fracture parameters from W36x150 flanges.

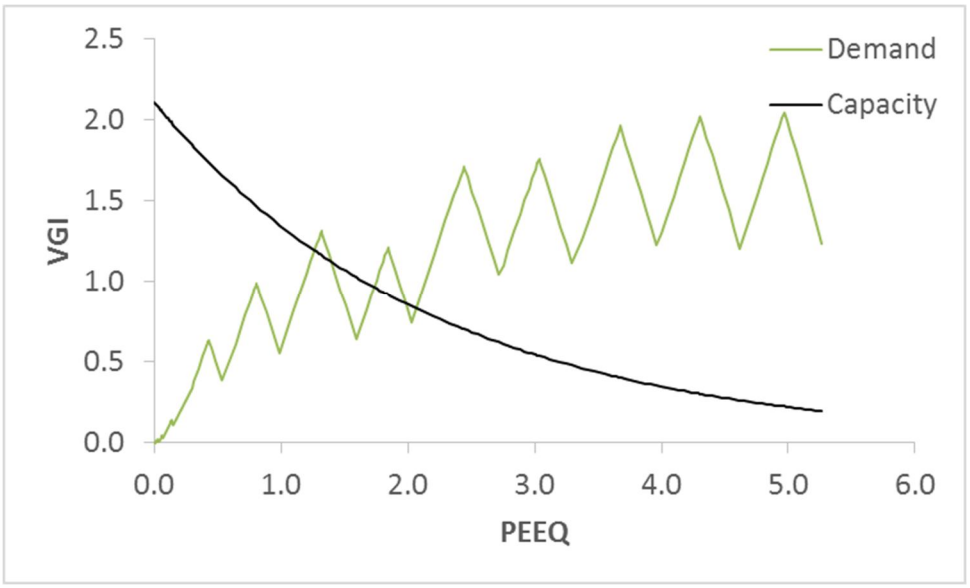


Figure D.16 – CVGM fracture initiation prediction at worst case for W36x150 no artifact (from cyclic bend tests).

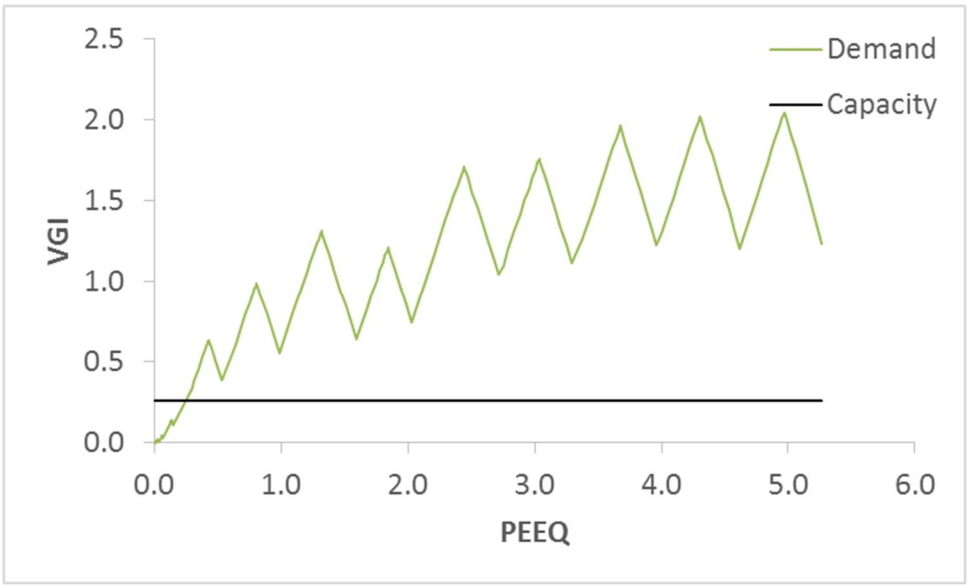


Figure D.17 – CVGM fracture initiation prediction at worst case for W36x150 with PAF.

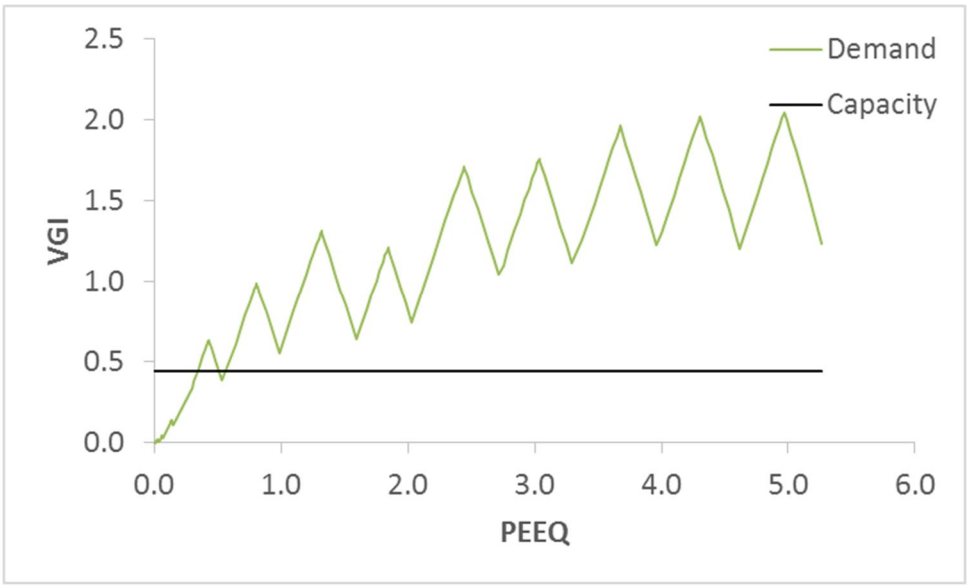


Figure D.18 – CVGM fracture initiation prediction at worst case for W36x150 with PW.

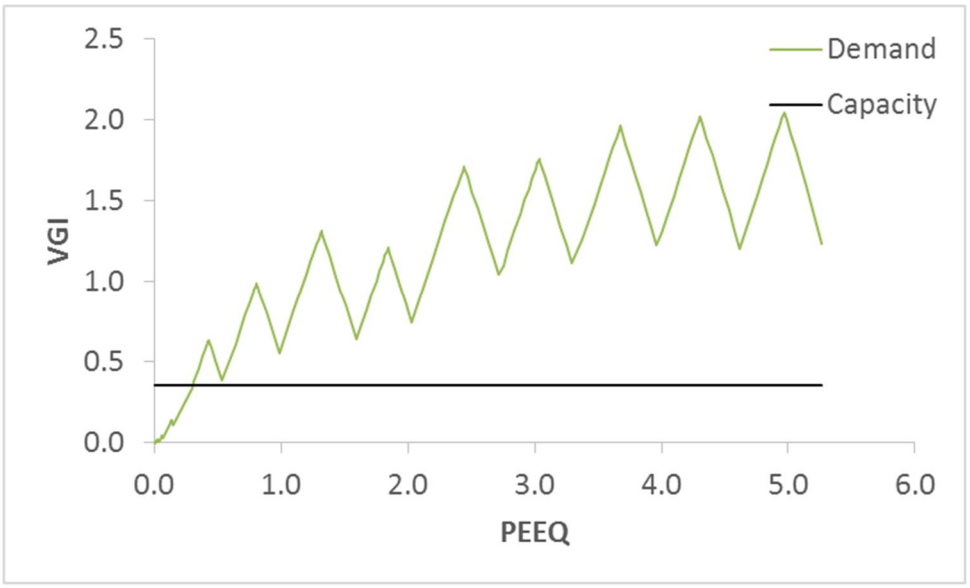


Figure D.19 – CVGM fracture initiation prediction at worst case for W36x150 with GFW.

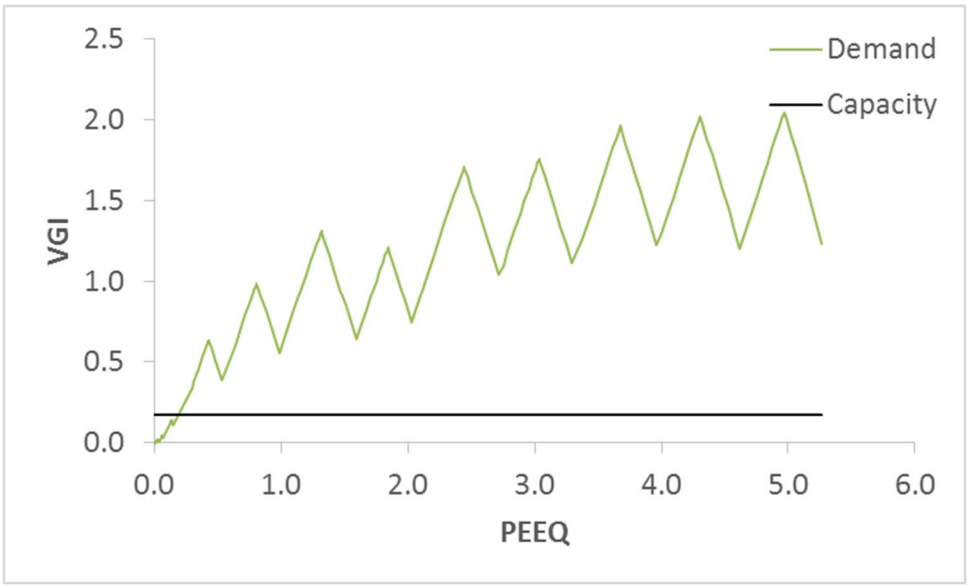


Figure D.20 – CVGM fracture initiation prediction at worst case for W36x150 with NGT.

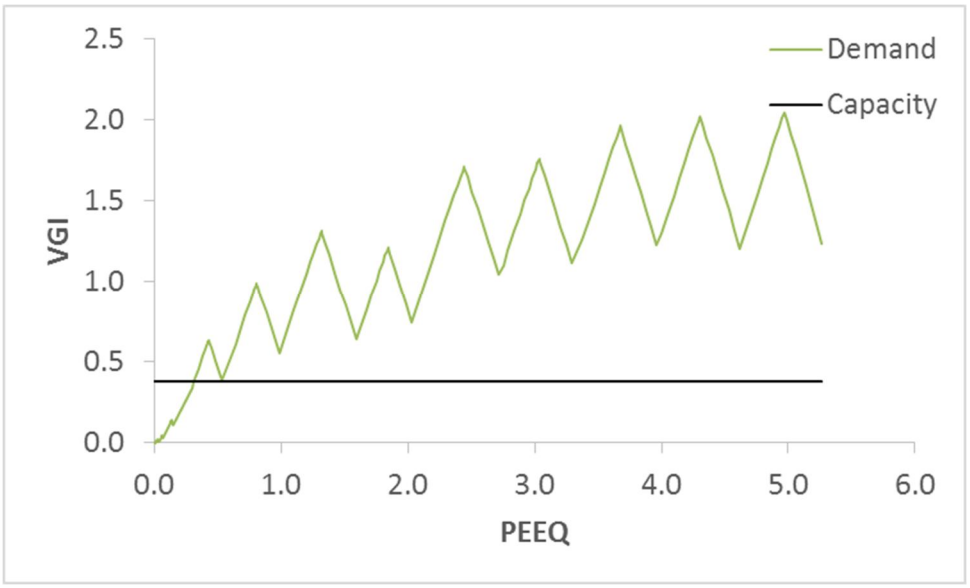


Figure D.21 – CVGM fracture initiation prediction at worst case for W36x150 with NWG.

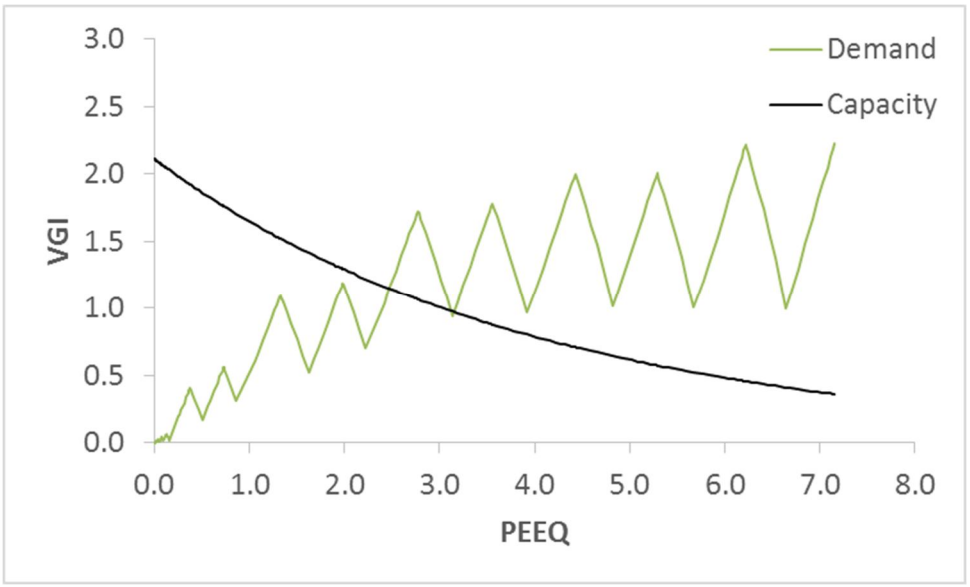


Figure D.22 – CVGM fracture initiation prediction at worst case for W36x150 RBS with no artifact using round notched tests fracture parameters from W36x150 flanges.

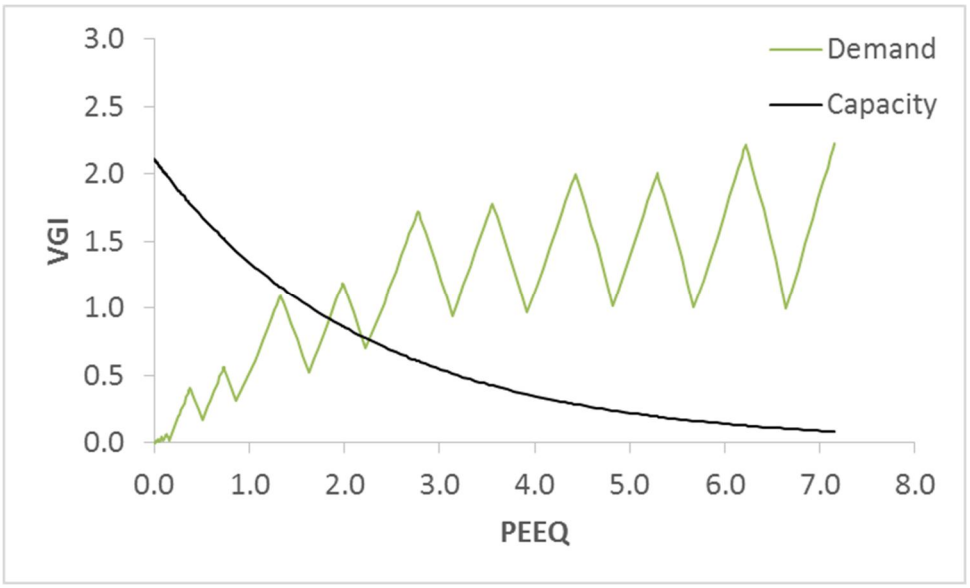


Figure D.23 – CVGM fracture initiation prediction at worst case for W36x150 RBS with no artifact (from cyclic bend tests).

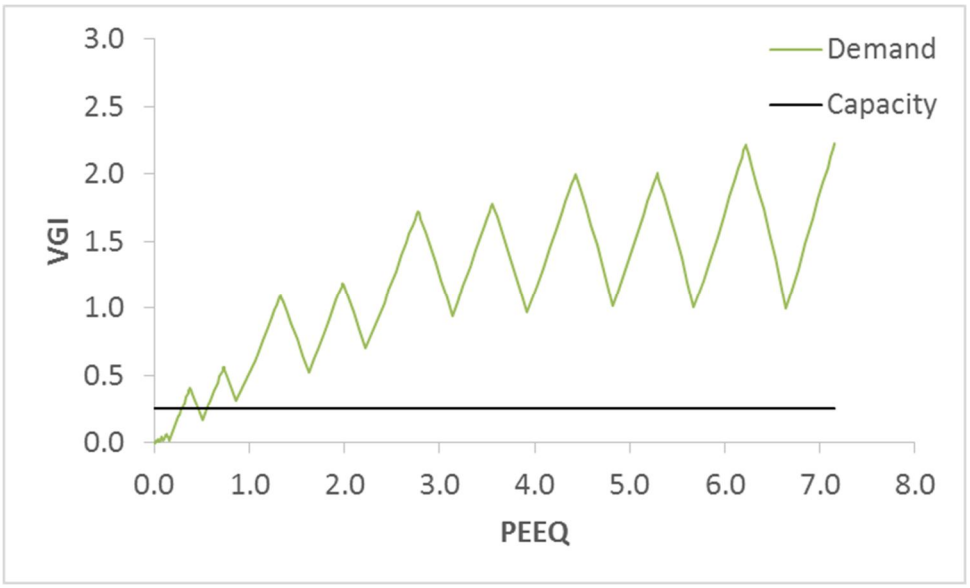


Figure D.24 – CVGM fracture initiation prediction at worst case for W36x150 RBS with PAF.

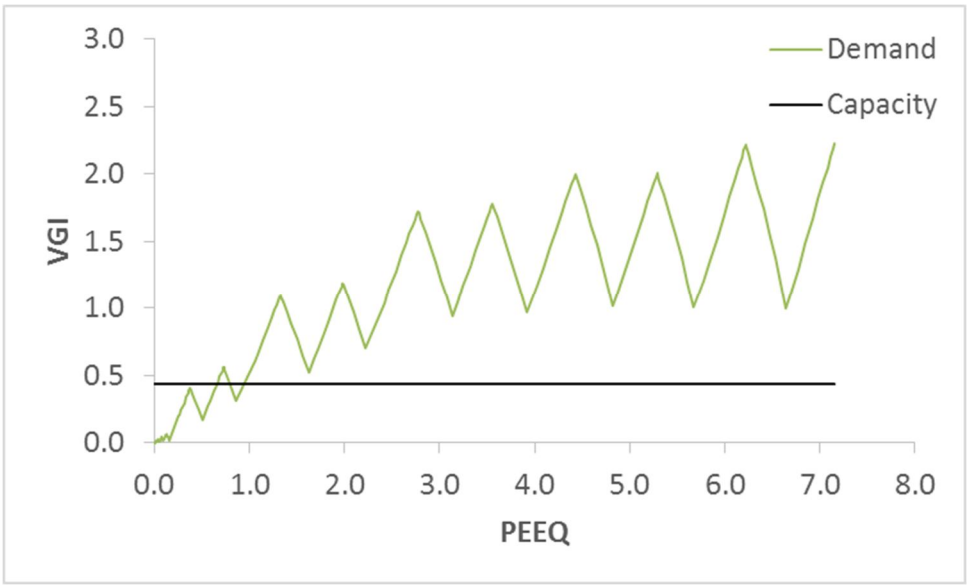


Figure D.25 – CVGM fracture initiation prediction at worst case for W36x150 RBS with PW.

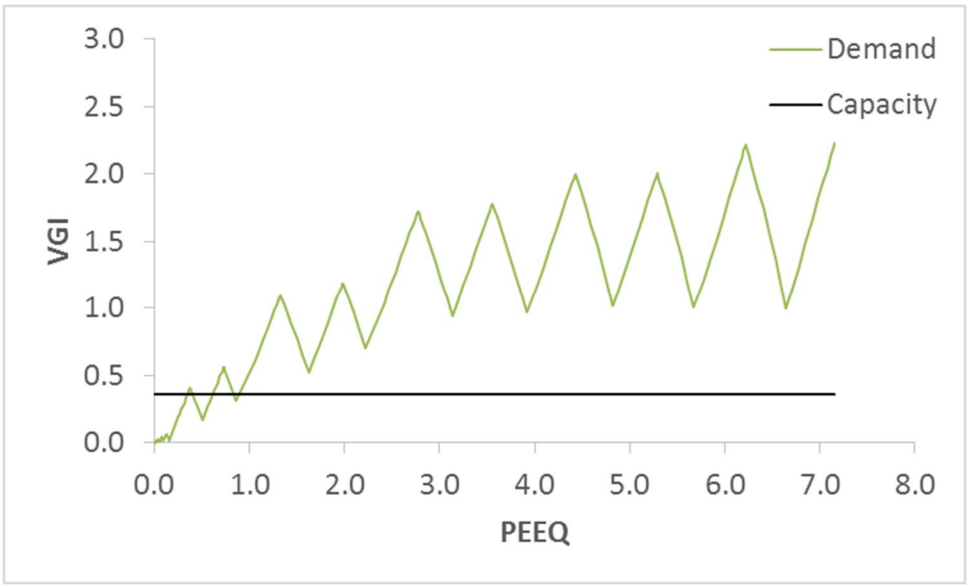


Figure D.26 – CVGM fracture initiation prediction at worst case for W36x150 RBS with GFW.

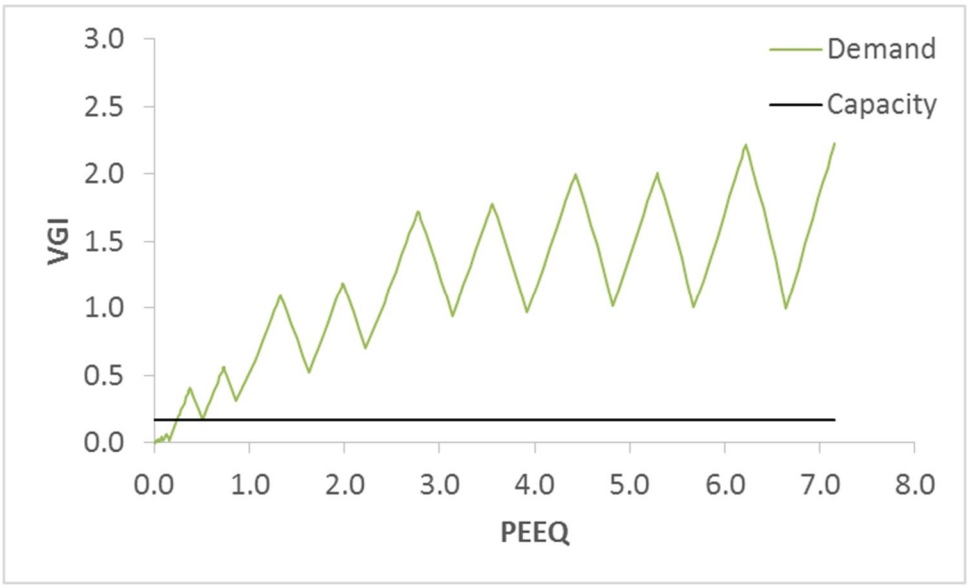


Figure D.27 – CVGM fracture initiation prediction at worst case for W36x150 RBS with NGT.

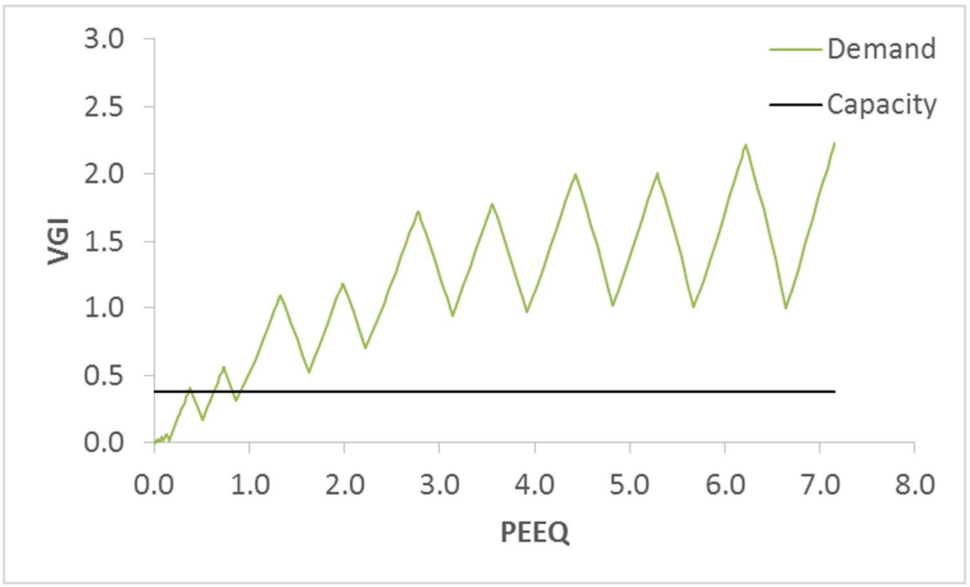


Figure D.28 – CVGM fracture initiation prediction at worst case for W36x150 RBS with NWG.

D.2 Fracture Initiation at the Center of the Flange

Locations of fracture initiation at worse case location at the center of the flange in the protected zone region in which fracture will initiation will be observed.

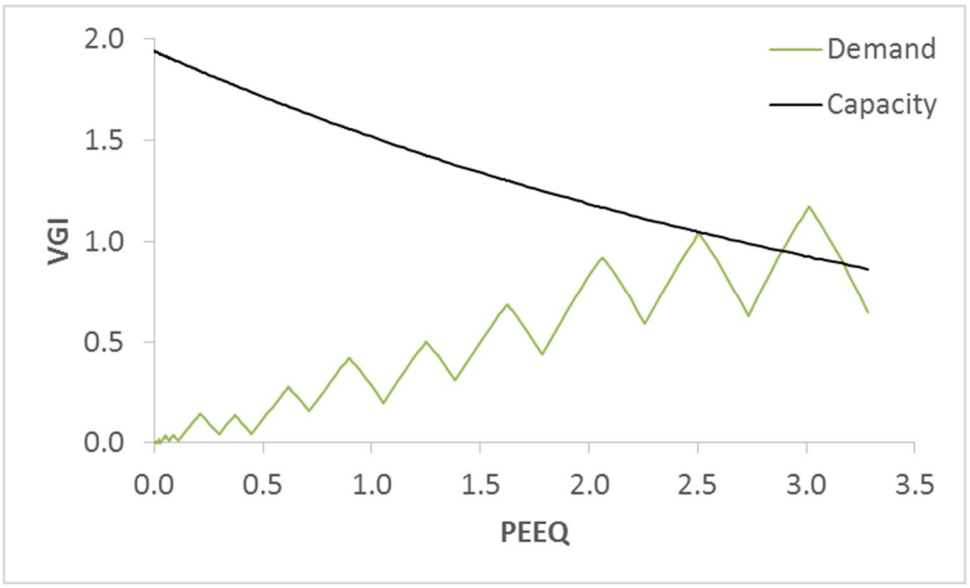


Figure D.29 – CVGM fracture initiation prediction at worse case location at the center of the flange for W24x62 with no artifact using round notched tests fracture parameters from W36x150 flanges.

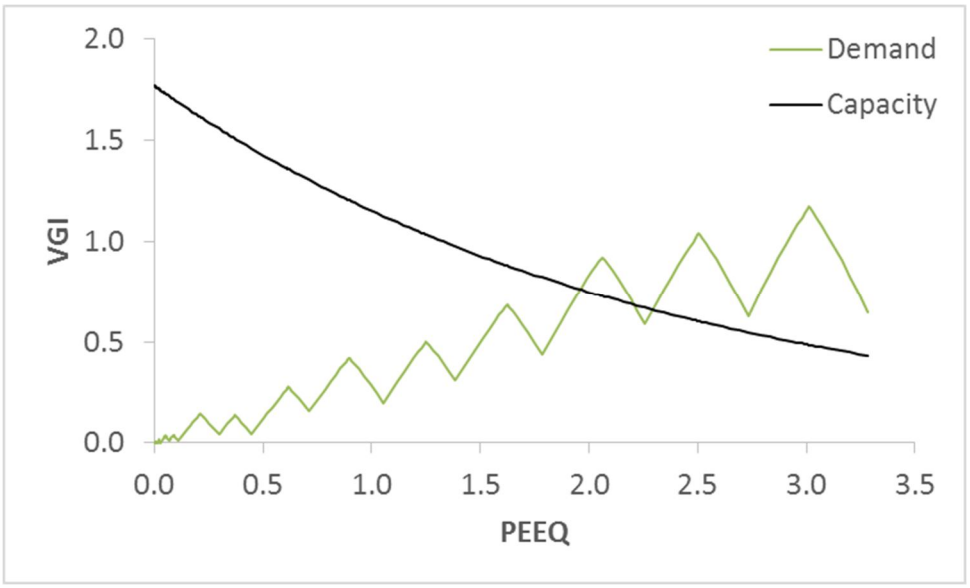


Figure D.30 – CVGM fracture initiation prediction at worst case location at the center of the flange for W24x62 with no artifact (from cyclic bend tests).

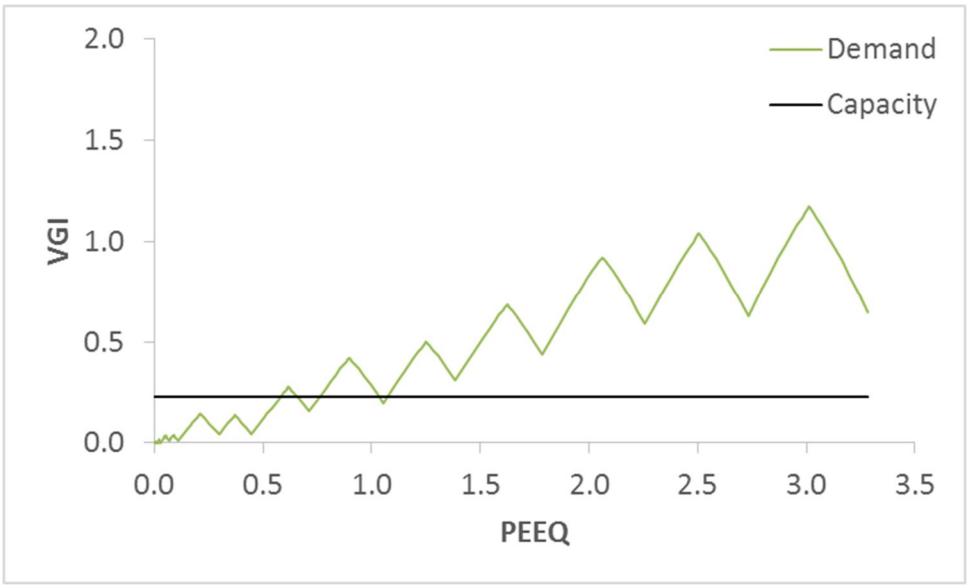


Figure D.31 – CVGM fracture initiation prediction at worst case location at the center of the flange for W24x62 with PAF.

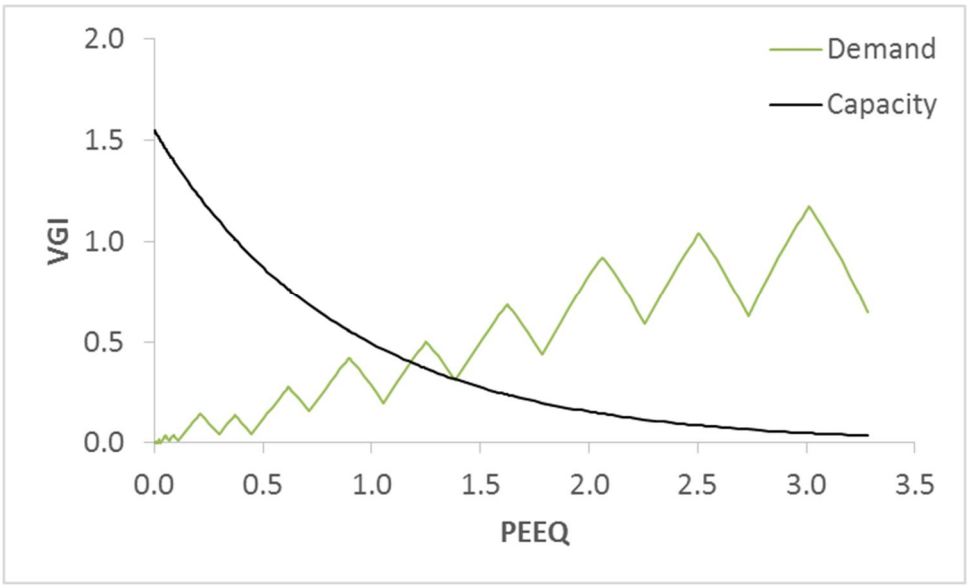


Figure D.32 – CVGM fracture initiation prediction at worst case location at the center of the flange for W24x62 with PW.

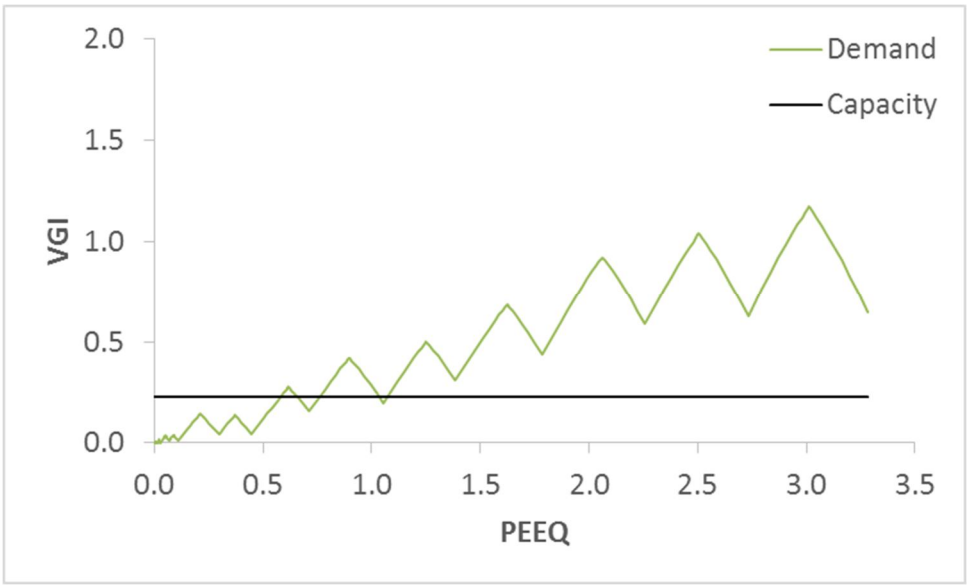


Figure D.33 – CVGM fracture initiation prediction at worst case location at the center of the flange for W24x62 with GFW.

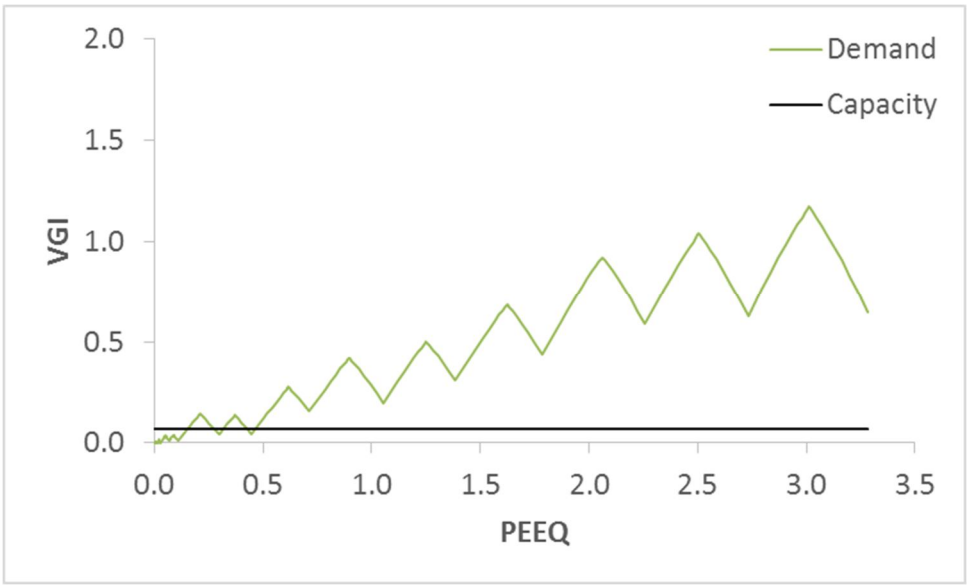


Figure D.34 – CVGM fracture initiation prediction at worst case location at the center of the flange for W24x62 with NGT.

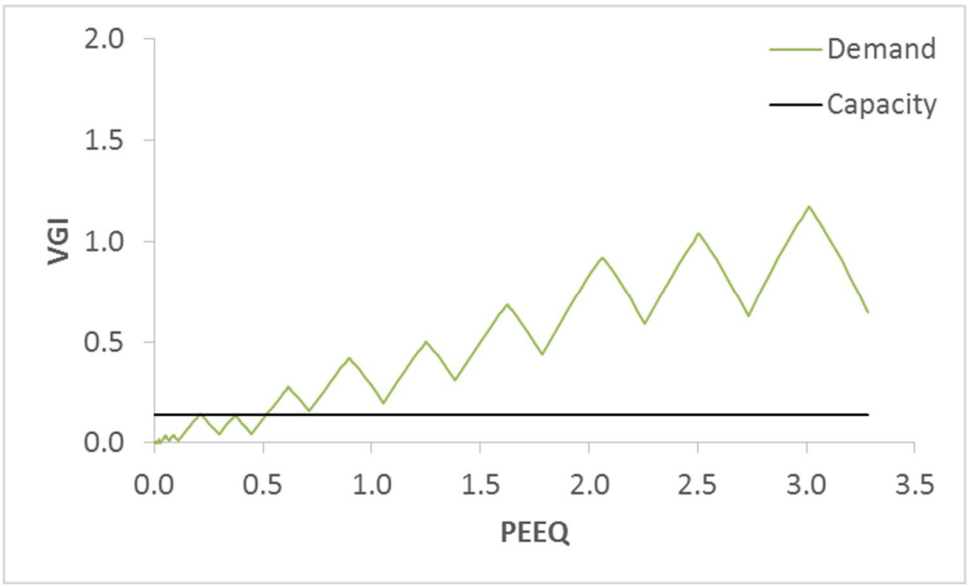


Figure D.35 – CVGM fracture initiation prediction at worst case location at the center of the flange for W24x62 with NWG.

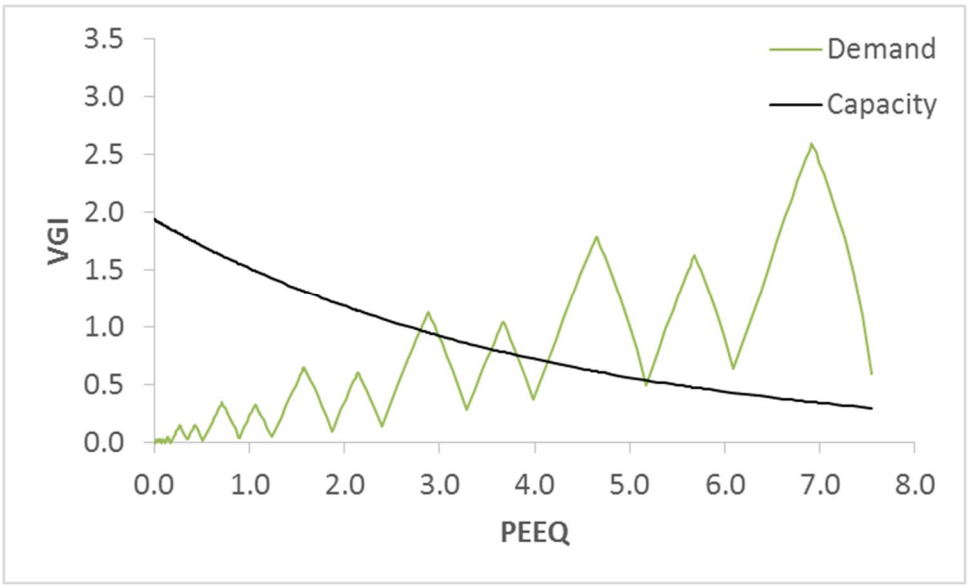


Figure D.36 – CVGM fracture initiation prediction at worst case location at the center of the flange for W24x62 RBS with no artifact using round notched tests fracture parameters from W36x150 flanges.

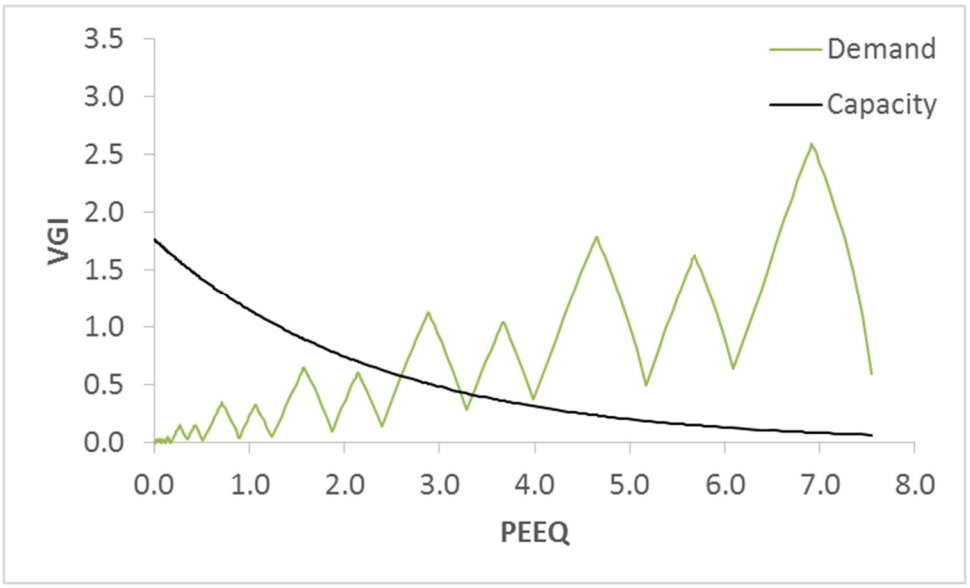


Figure D.37 – CVGM fracture initiation prediction at worst case location at the center of the flange for W24x62 RBS with no artifact (from cyclic bend tests).

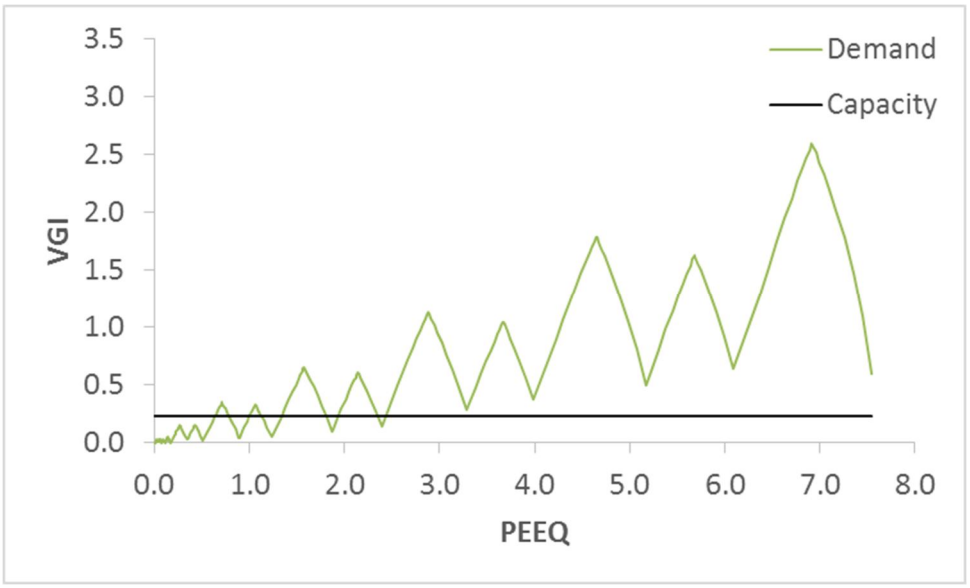


Figure D.38 – CVGM fracture initiation prediction at worst case location at the center of the flange for W24x62 RBS with PAF.

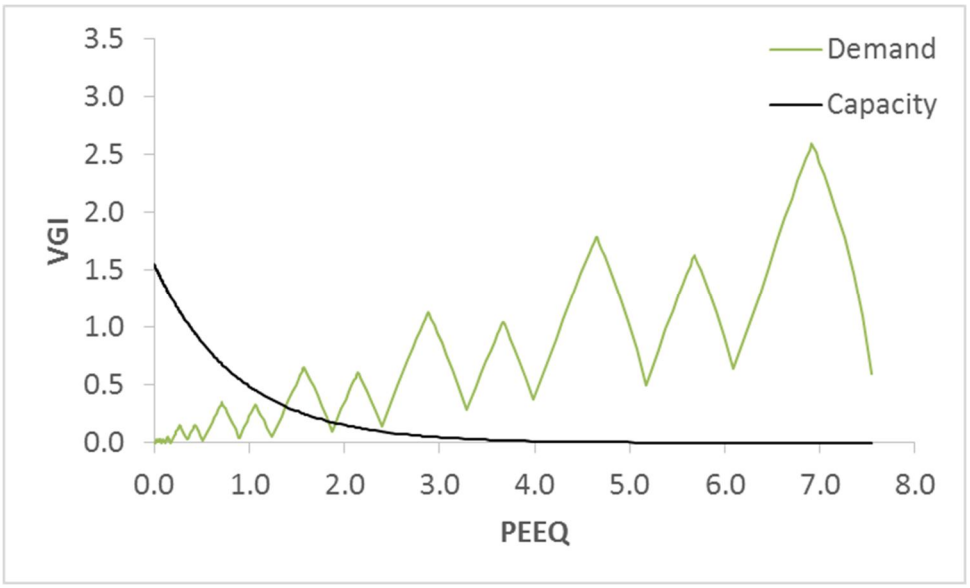


Figure D.39 – CVGM fracture initiation prediction at worst case location at the center of the flange for W24x62 RBS with PW.

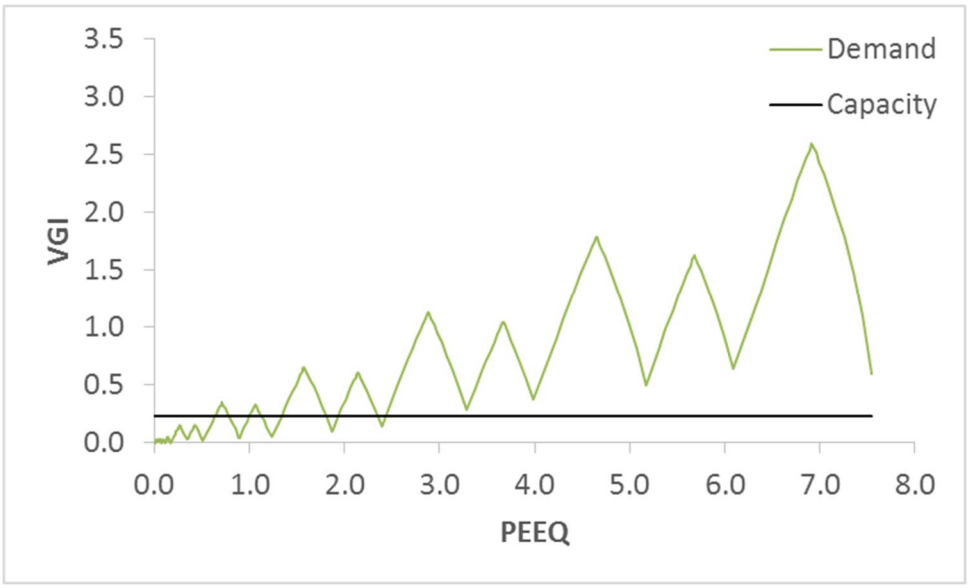


Figure D.40 – CVGM fracture initiation prediction at worst case location at the center of the flange for W24x62 RBS with GFW.

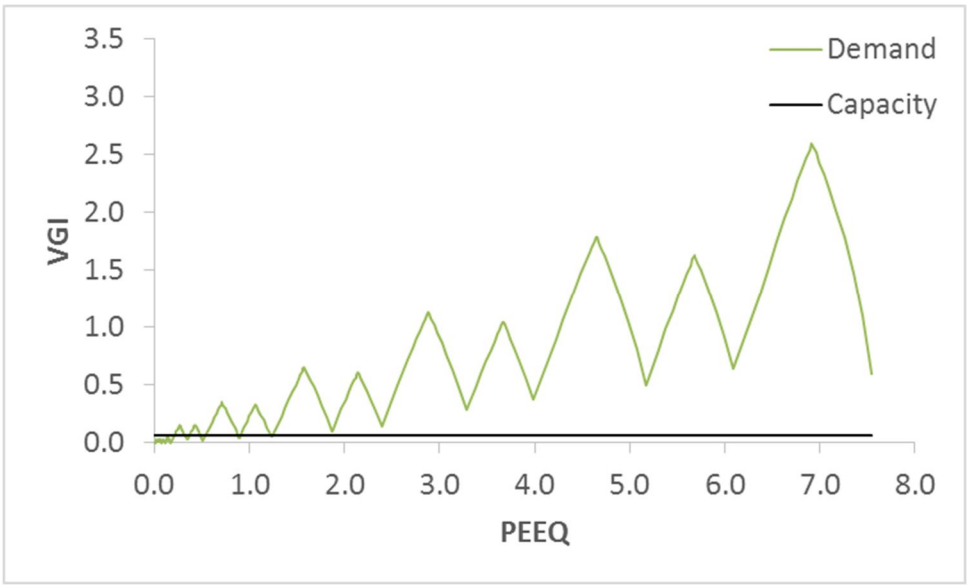


Figure D.41 – CVGM fracture initiation prediction at worst case location at the center of the flange for W24x62 RBS with NGT.

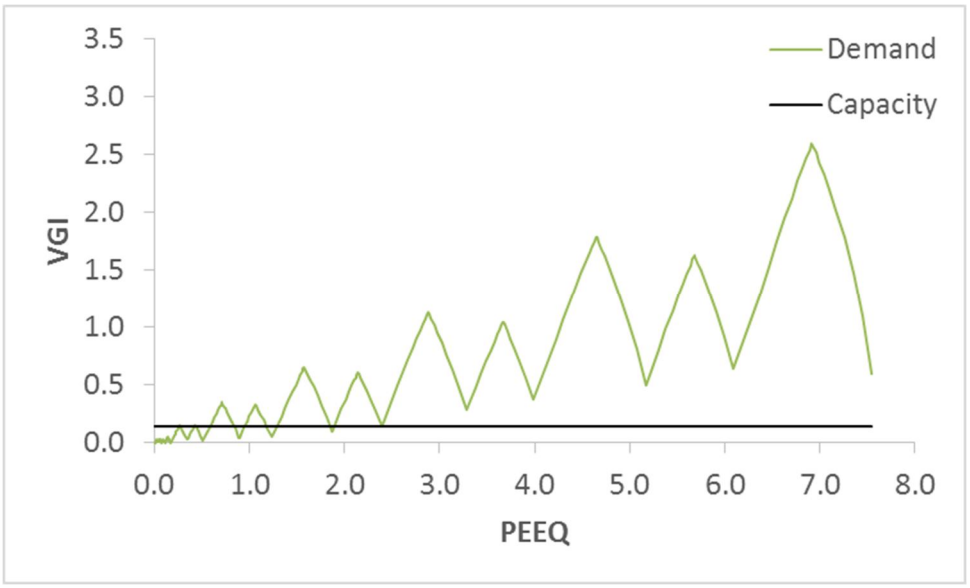


Figure D.42 – CVGM fracture initiation prediction at worst case location at the center of the flange for W24x62 RBS with NWG.

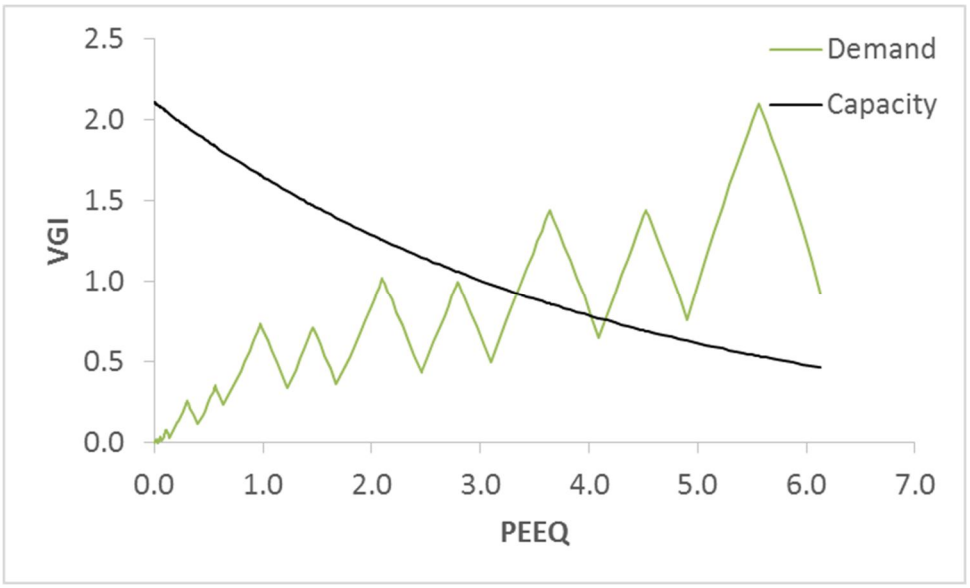


Figure D.43 – CVGM fracture initiation prediction at worst case location at the center of the flange for W36x150 with no artifact using round notched tests fracture parameters from W36x150 flanges.

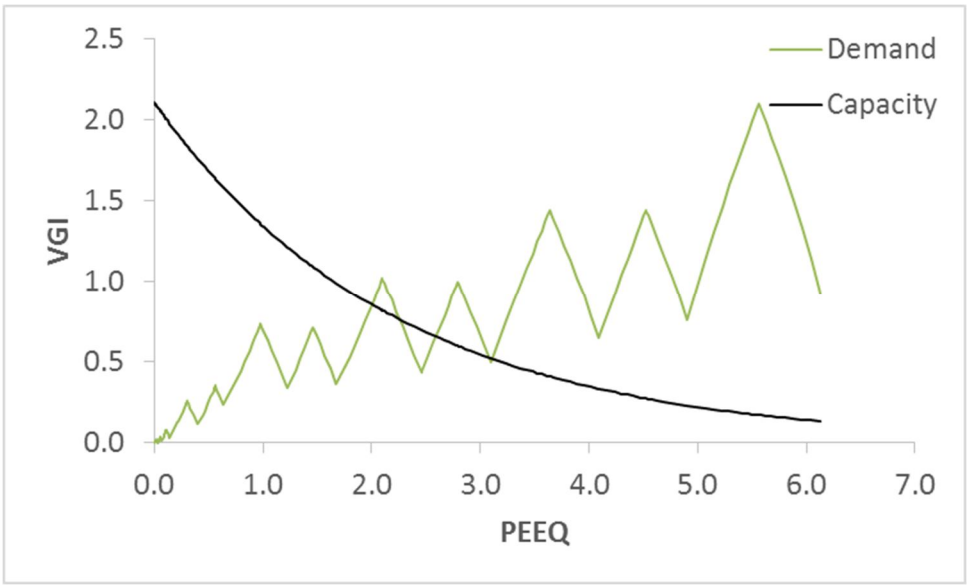


Figure D.44 – CVGM fracture initiation prediction at worst case location at the center of the flange for W36x150 no artifact (from cyclic bend tests).

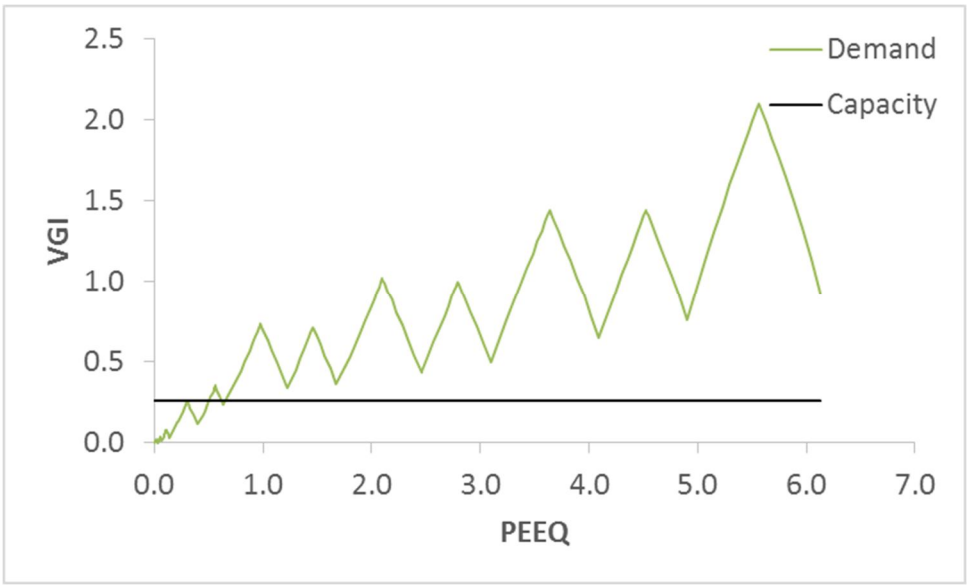


Figure D.45 – CVGM fracture initiation prediction at worst case location at the center of the flange for W36x150 with PAF.

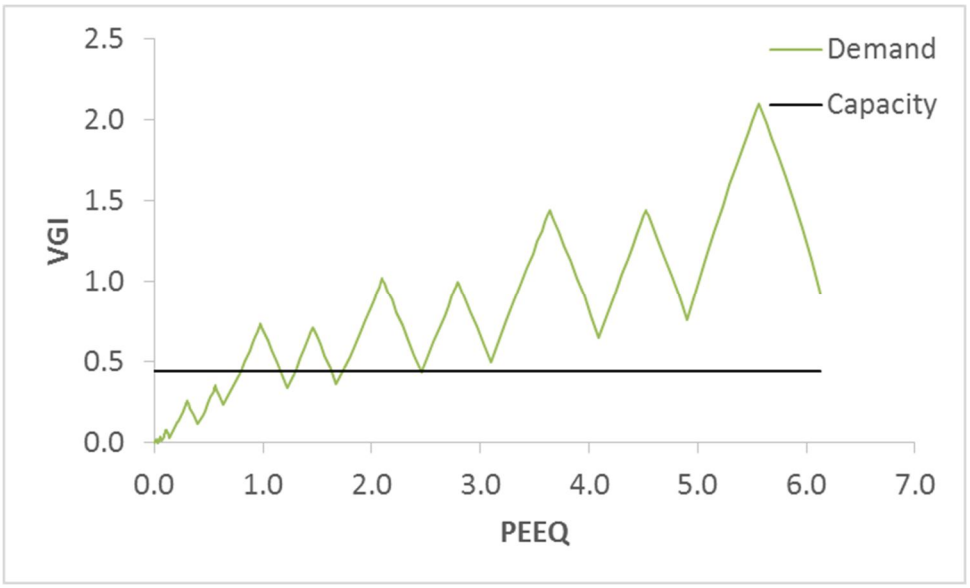


Figure D.46 – CVGM fracture initiation prediction at worst case location at the center of the flange for W36x150 with PW.

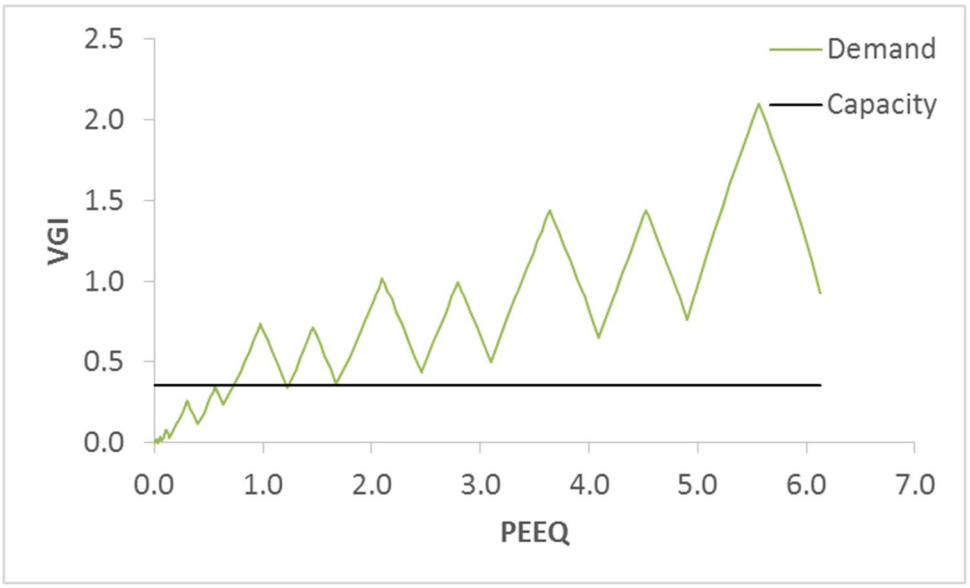


Figure D.47 – CVGM fracture initiation prediction at worst case location at the center of the flange for W36x150 with GFW.

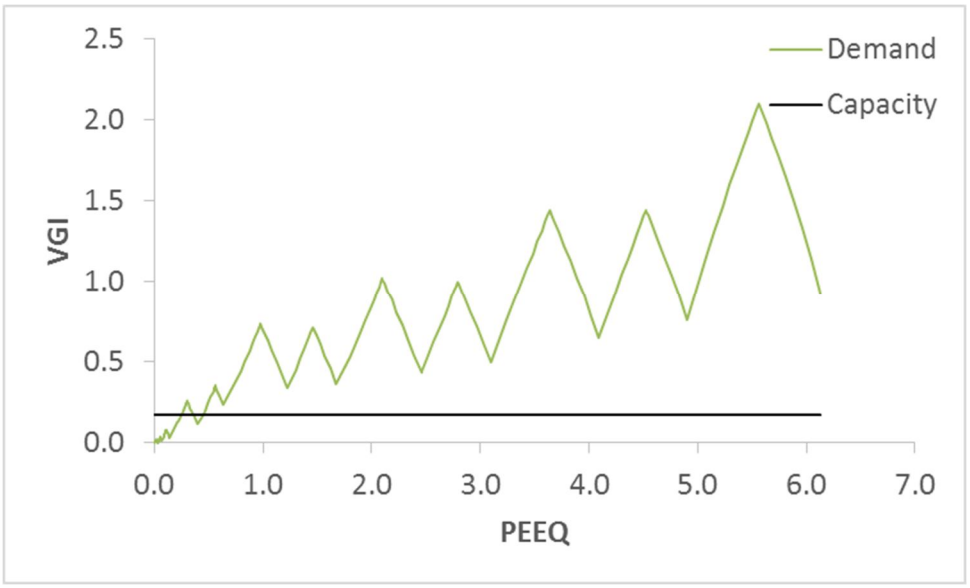


Figure D.48 – CVGM fracture initiation prediction at worst case location at the center of the flange for W36x150 with NGT.

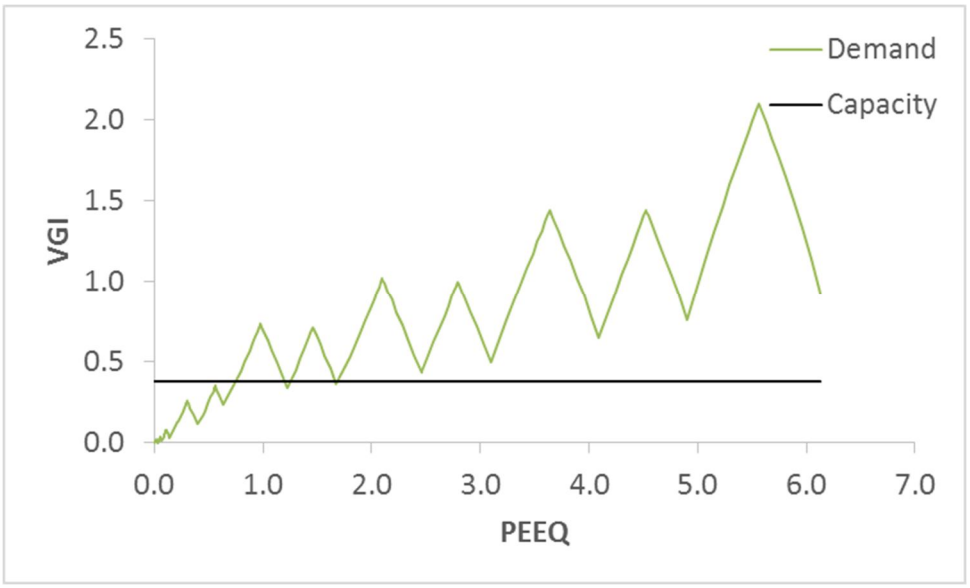


Figure D.49 – CVGM fracture initiation prediction at worst case location at the center of the flange for W36x150 with NWG.

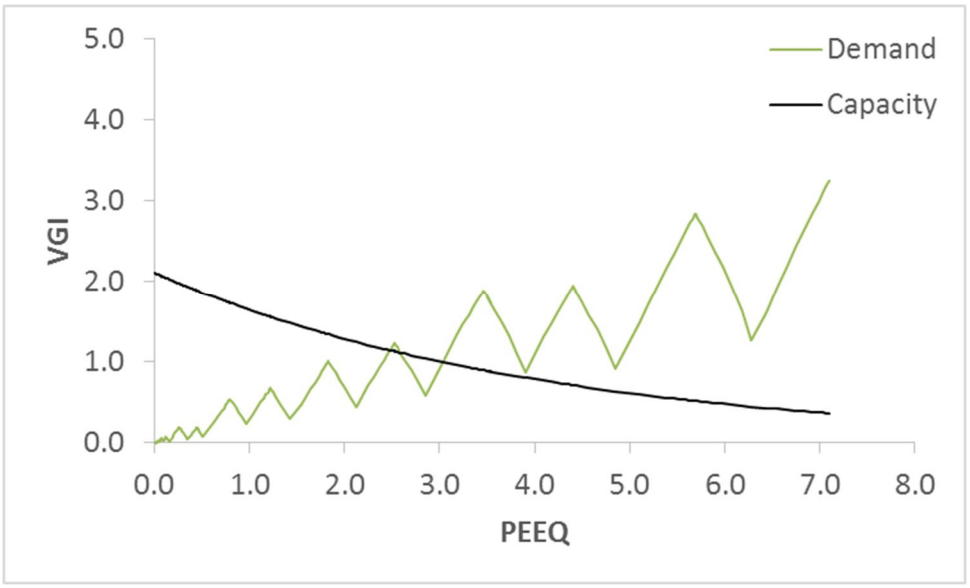


Figure D.50 – CVGM fracture initiation prediction at worst case location at the center of the flange for W36x150 RBS with no artifact using round notched tests fracture parameters from W36x150 flanges.

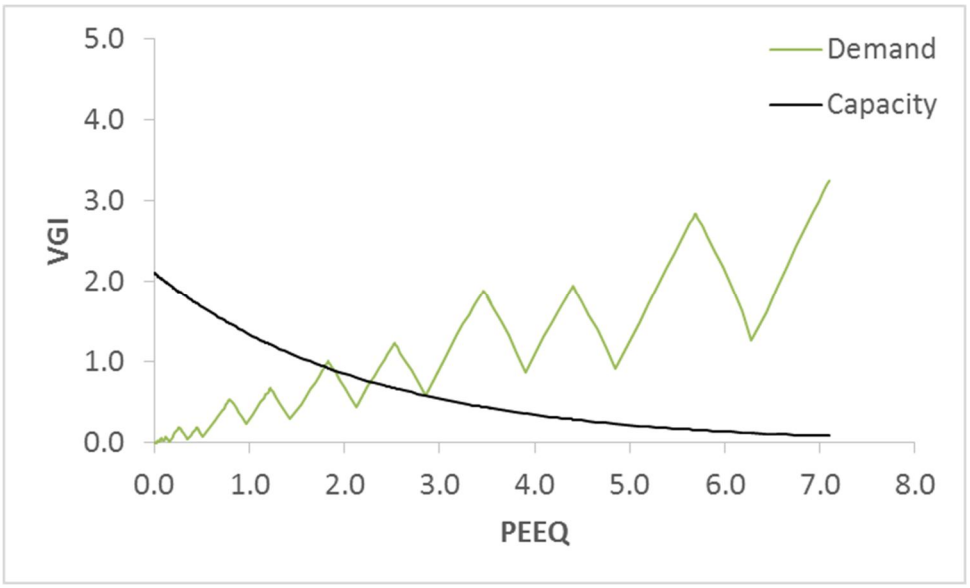


Figure D.51 – CVGM fracture initiation prediction at worst case location at the center of the flange for W36x150 RBS with no artifact (from cyclic bend tests).

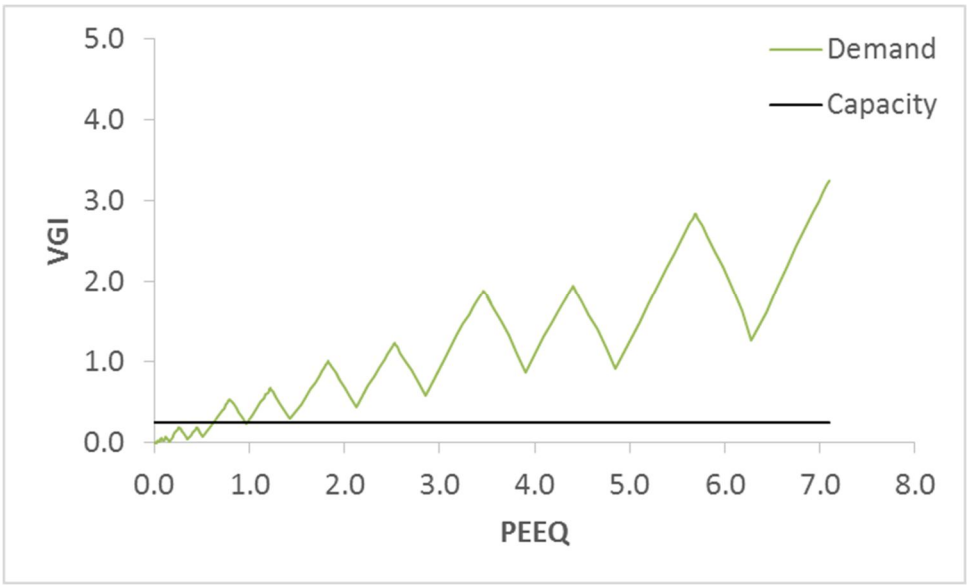


Figure D.52 – CVGM fracture initiation prediction at worst case location at the center of the flange for W36x150 RBS with PAF.

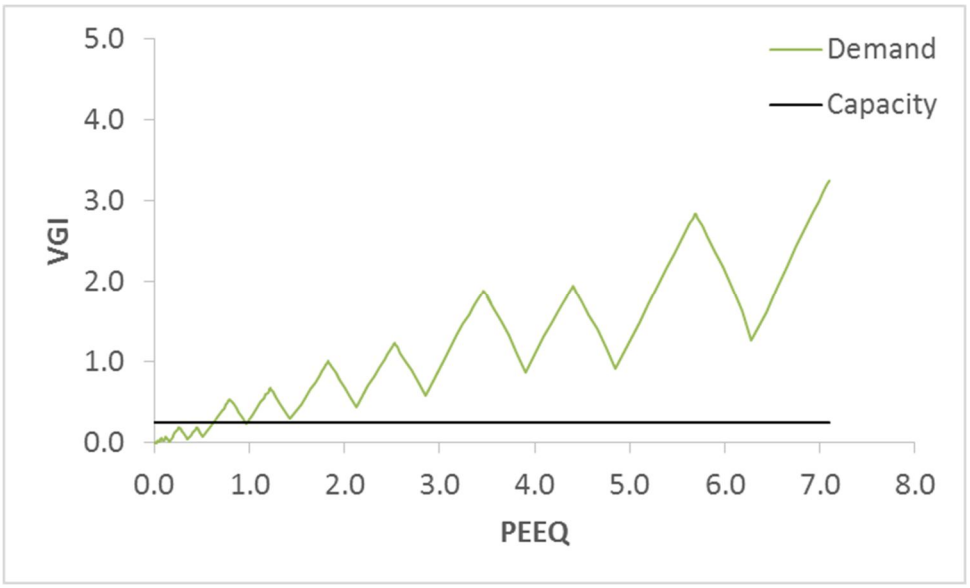


Figure D.53 – CVGM fracture initiation prediction at worst case location at the center of the flange for W36x150 RBS with PW.

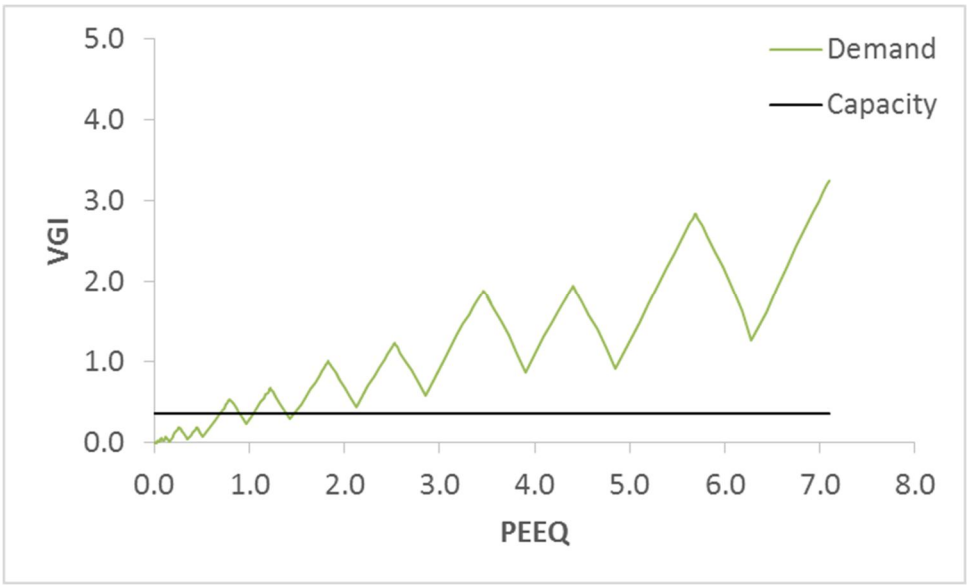


Figure D.54 – CVGM fracture initiation prediction at worst case location at the center of the flange for W36x150 RBS with GFW.

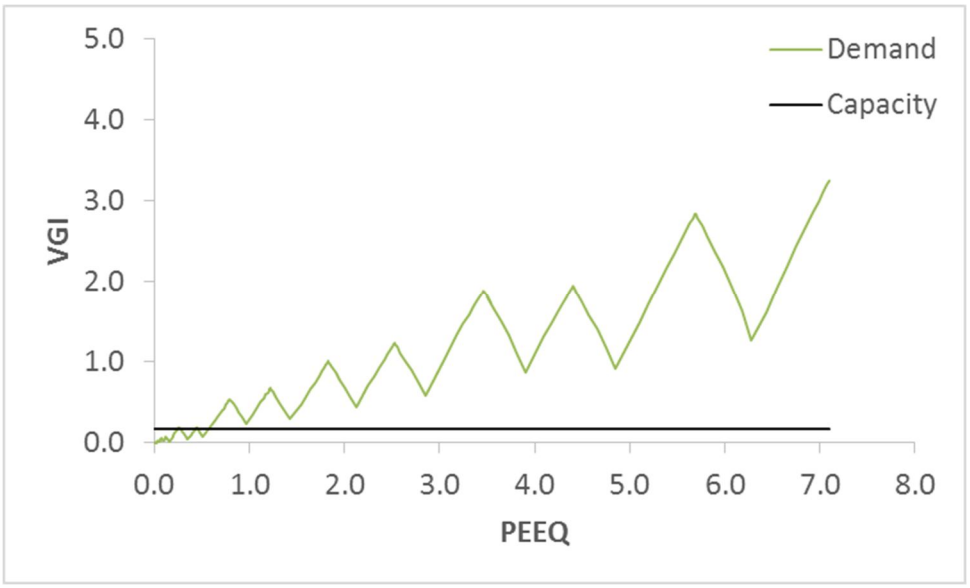


Figure D.55 – CVGM fracture initiation prediction at worst case location at the center of the flange for W36x150 RBS with NGT.

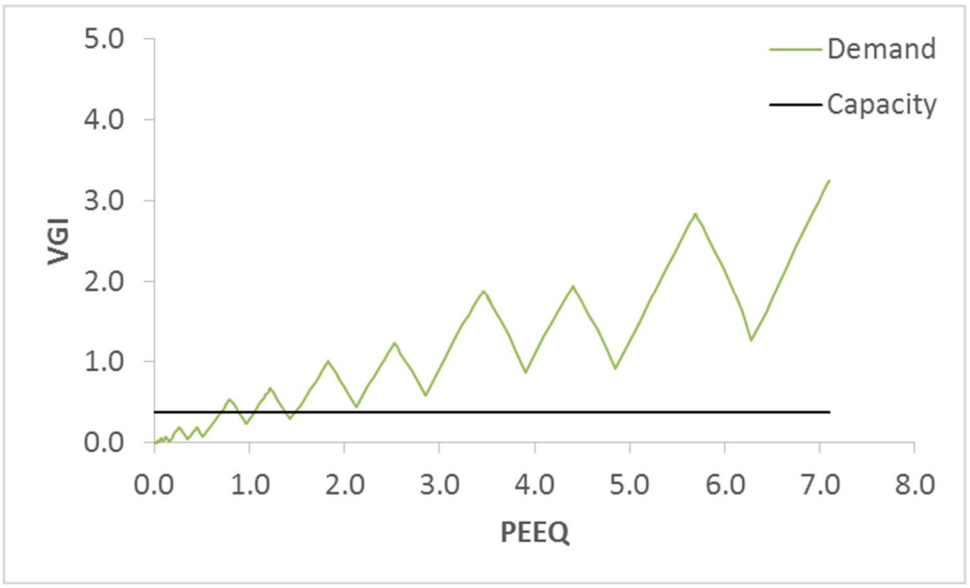


Figure D.56 – CVGM fracture initiation prediction at worst case location at the center of the flange for W36x150 RBS with NWG.

APPENDIX E STRAIN GRADIENTS FROM STRAIN GAGES

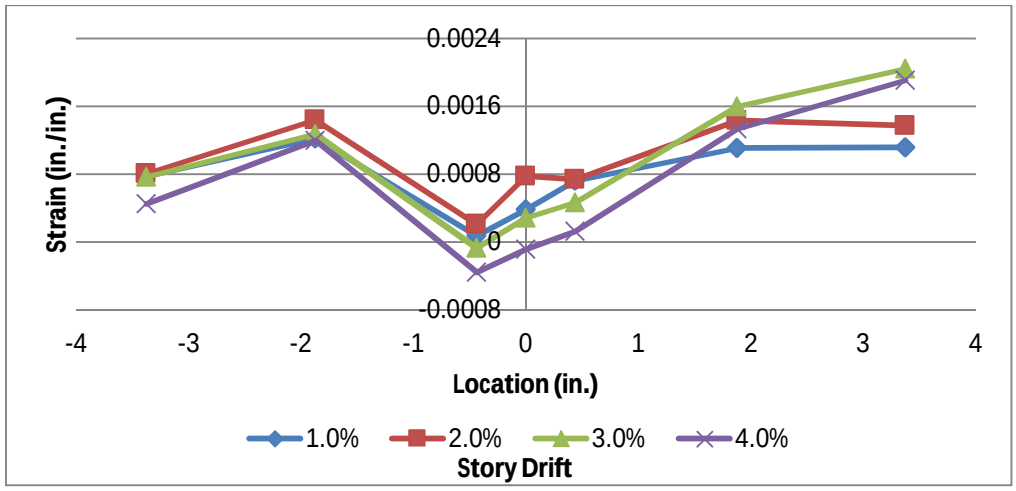


Figure E.1 – Specimen 1 (W24x62 with RBS and No Fasteners) Top Flange Strain Data Line 1

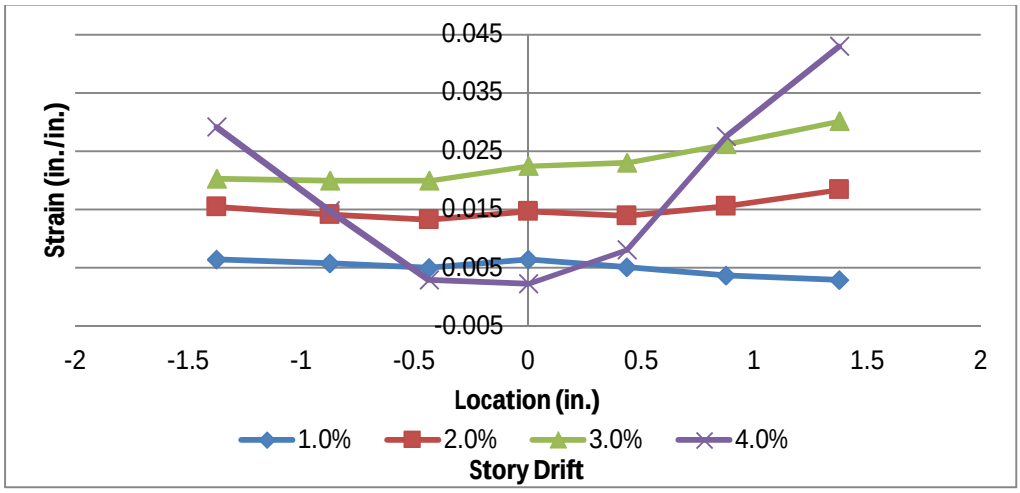


Figure E.2 – Specimen 1 (W24x62 with RBS and No Fasteners) Top Flange Strain Data Line 2

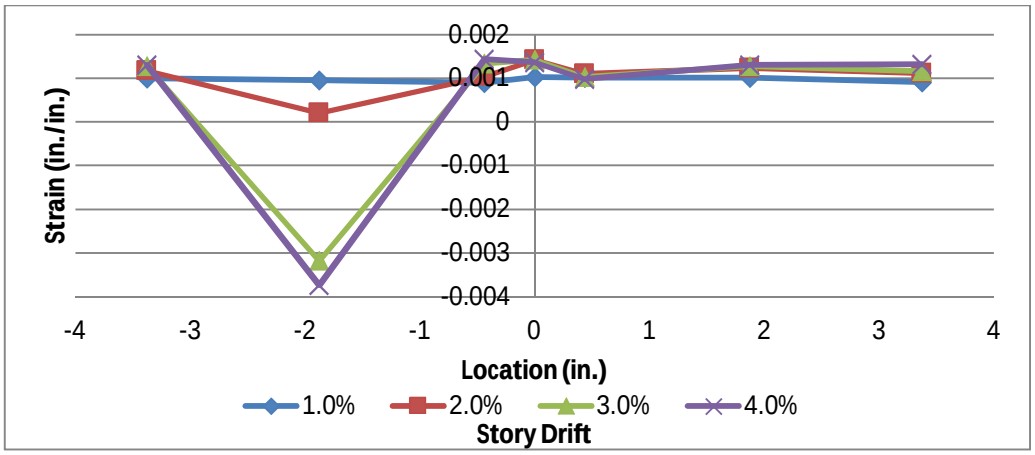


Figure E.3 – Specimen 1 (W24x62 with RBS and No Fasteners) Top Flange Strain Data Line 3

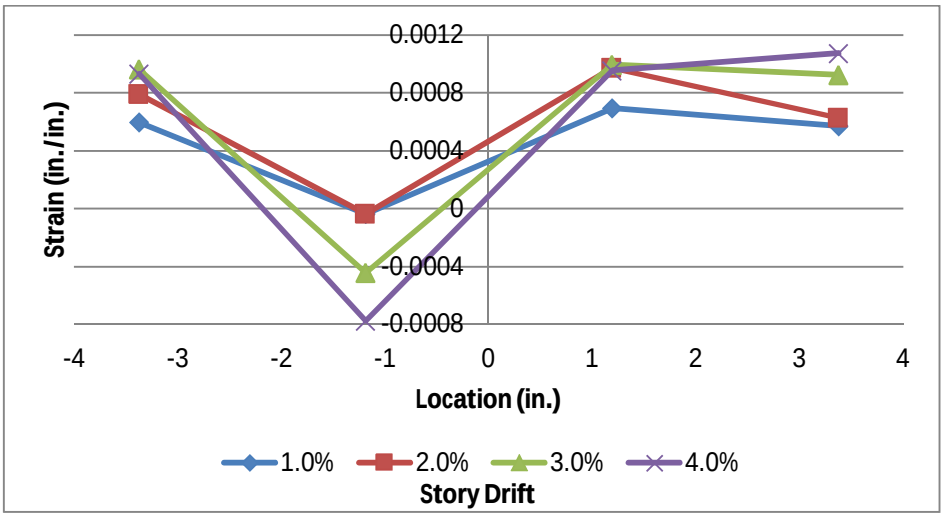


Figure E.4 – Specimen 1 (W24x62 with RBS and No Fasteners) Underside of Top Flange Strain Data Line 1

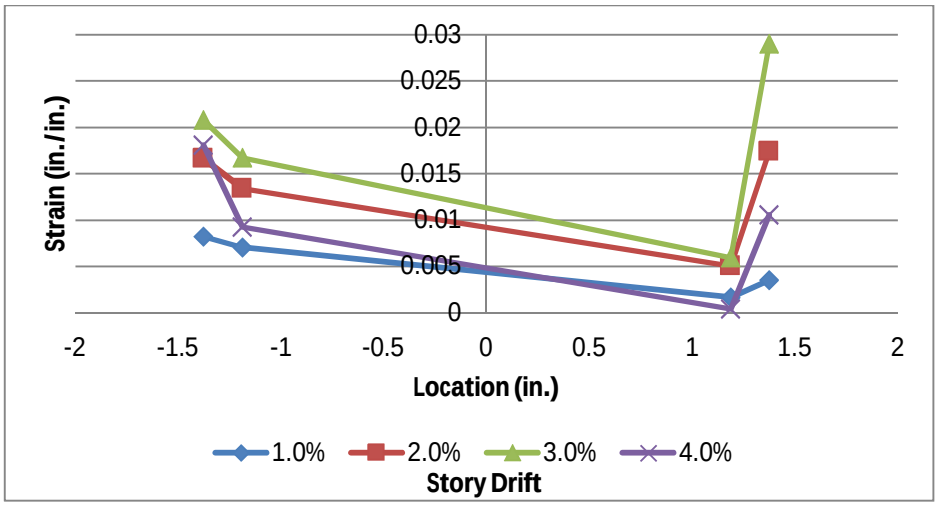


Figure E.5 – Specimen 1 (W24x62 with RBS and No Fasteners) Underside of Top Flange Strain Data Line 2

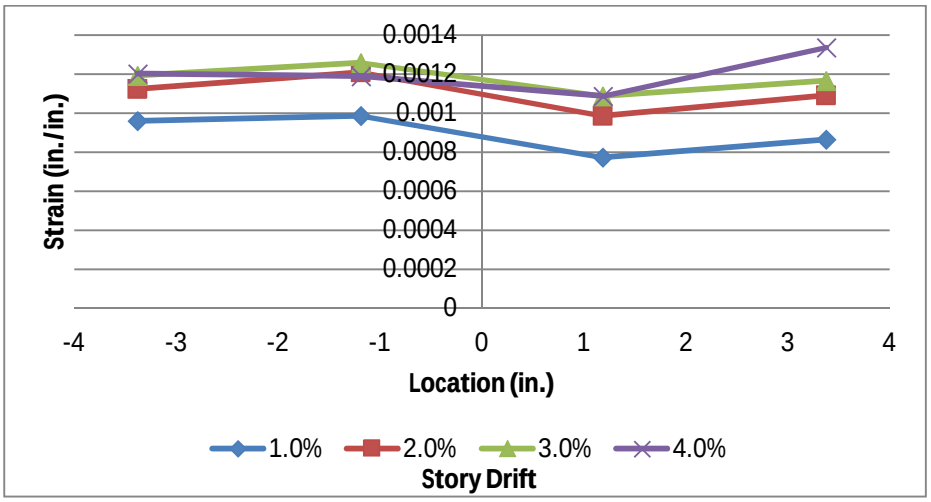


Figure E.6 – Specimen 1 (W24x62 with RBS and No Fasteners) Underside of Top Flange Strain Data Line 3

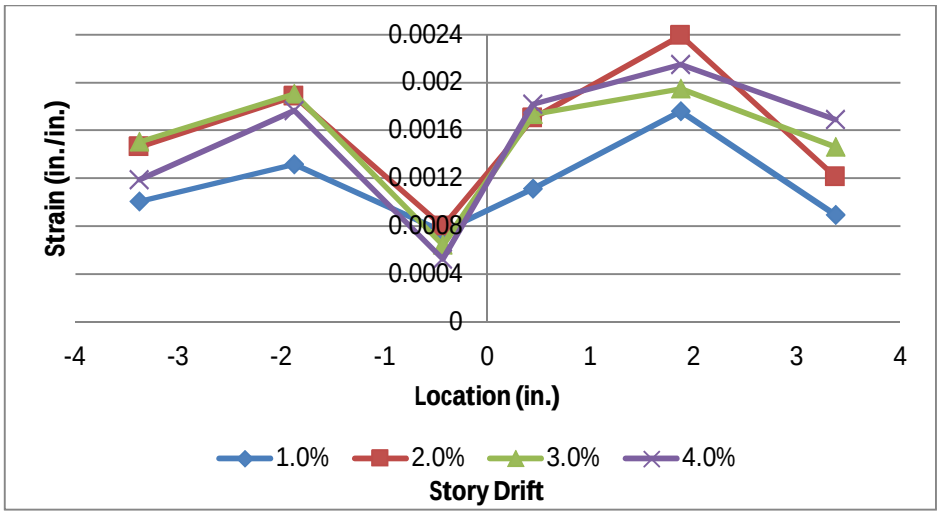


Figure E.7 – Specimen 2 (W24x62 with RBS and PAFs at 12 in.) Top Flange Strain Data Line 1

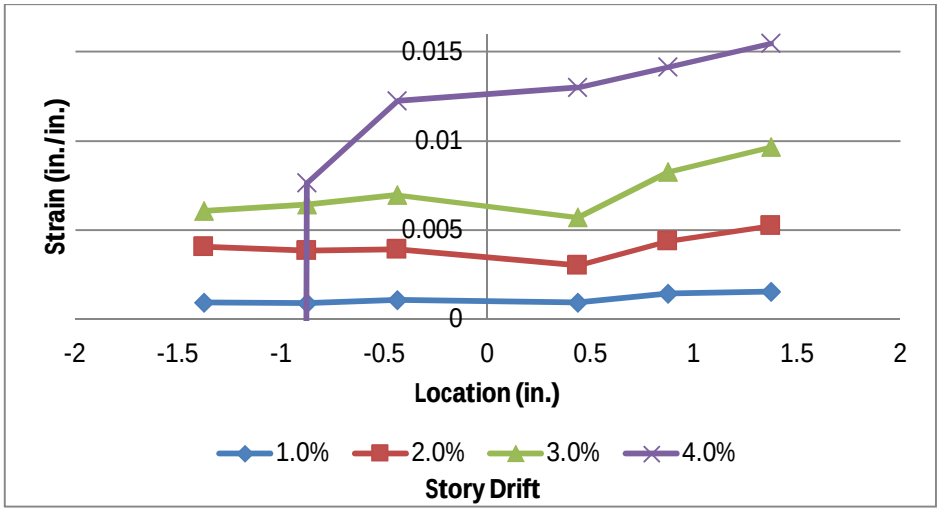


Figure E.8 – Specimen 2 (W24x62 with RBS and PAFs at 12 in.) Top Flange Strain Data Line 2

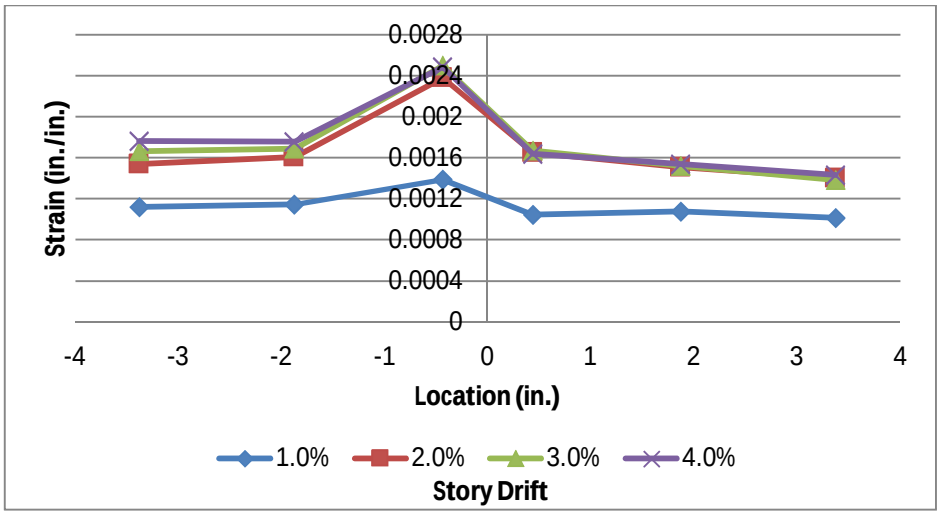


Figure E.9 – Specimen 2 (W24x62 with RBS and PAFs at 12 in.) Top Flange Strain Data Line 3

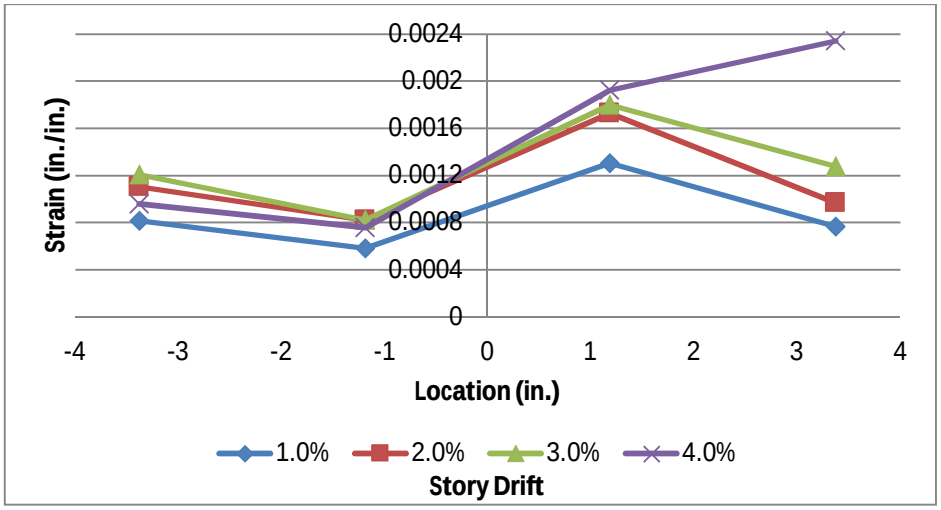


Figure E.10 – Specimen 2 (W24x62 with RBS and PAFs at 12 in.) Underside of Top Flange Strain Data Line 1

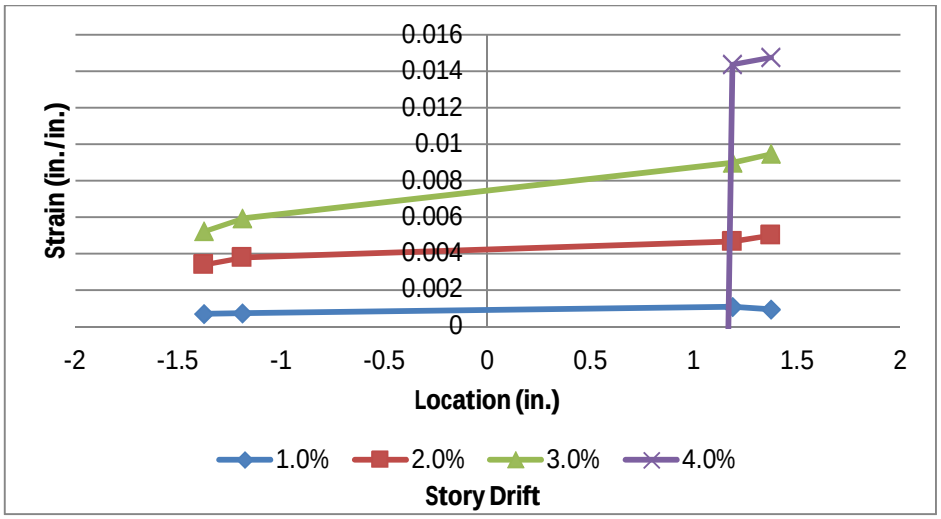


Figure E.11 – Specimen 2 (W24x62 with RBS and PAFs at 12 in.) Underside of Top Flange Strain Data Line 2

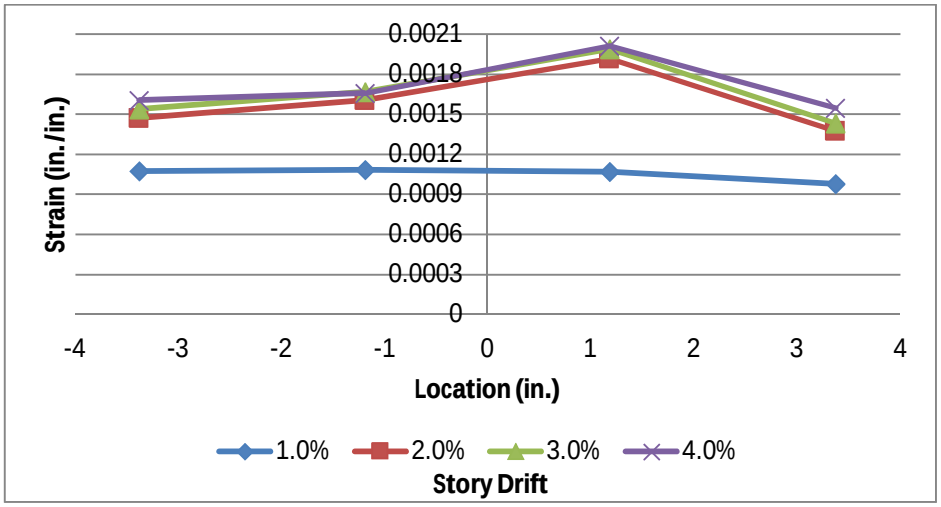


Figure E.12 – Specimen 2 (W24x62 with RBS and PAFs at 12 in.) Underside of Top Flange Strain Data Line 3

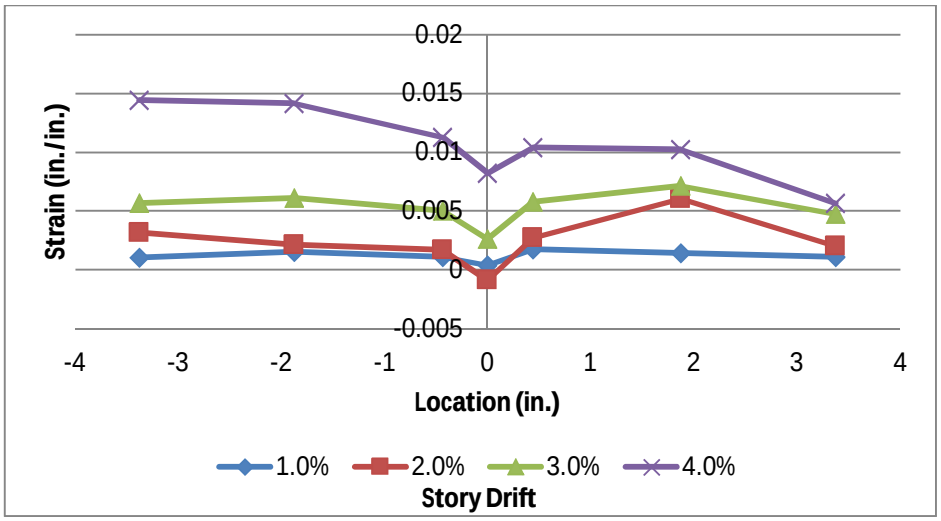


Figure E.13 – Specimen 3 (W24x62 with No RBS and No Fasteners) Top Flange Strain Data Line 1

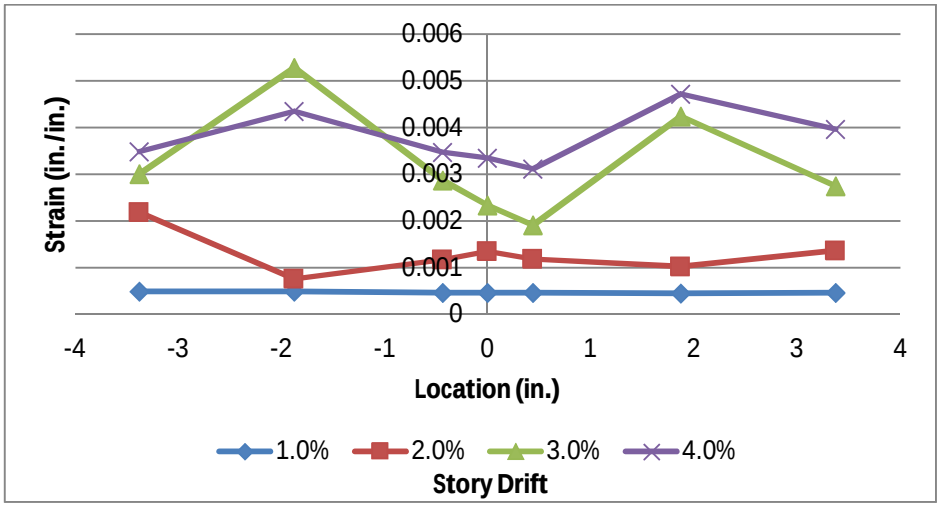


Figure E.14 – Specimen 3 (W24x62 with No RBS and No Fasteners) Top Flange Strain Data Line 2

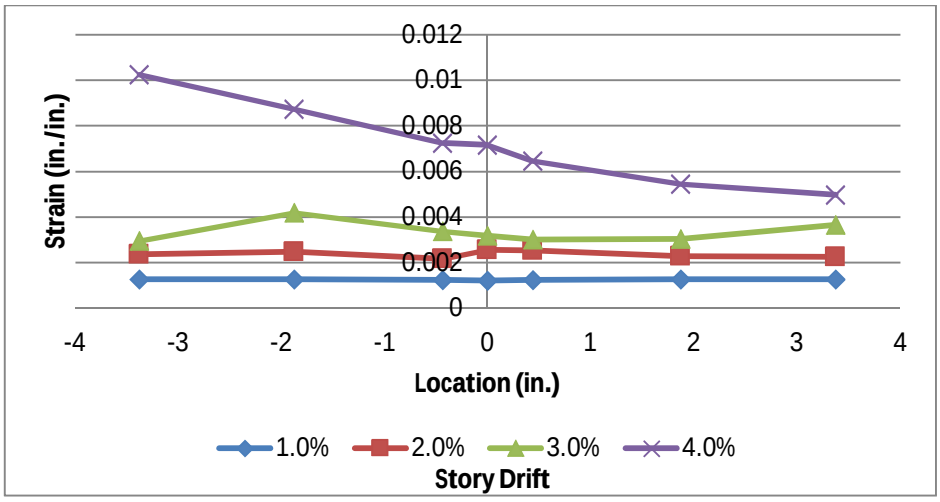


Figure E.15 – Specimen 3 (W24x62 with No RBS and No Fasteners) Top Flange Strain Data Line 3

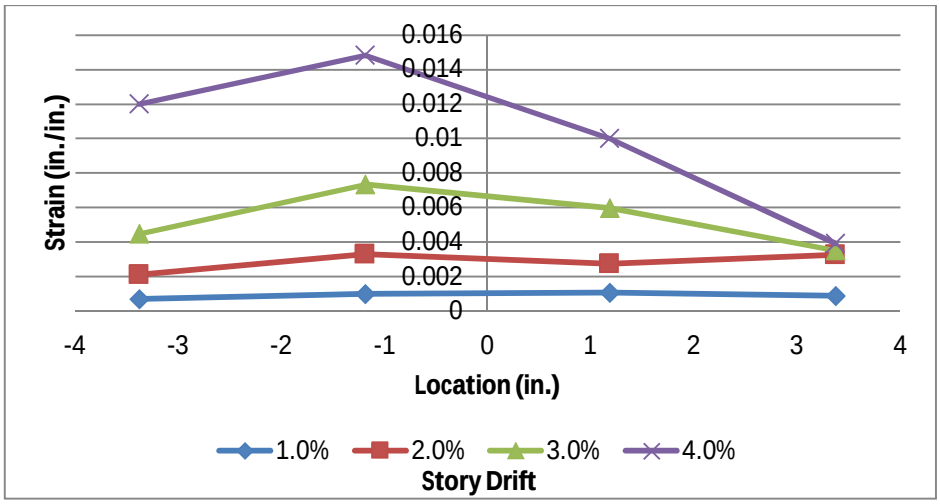


Figure E.16 – Specimen 3 (W24x62 with No RBS and No Fasteners) Underside of Top Flange Strain Data Line 1

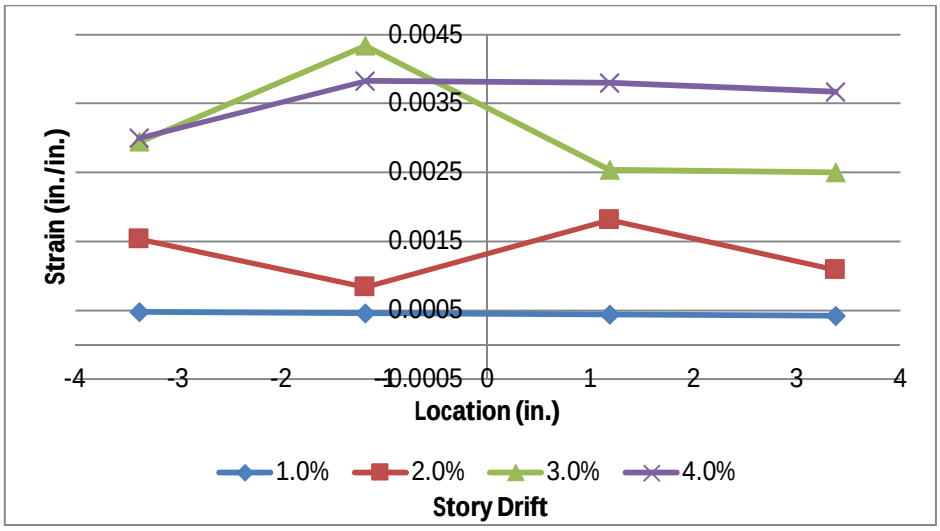


Figure E.17 – Specimen 3 (W24x62 with No RBS and No Fasteners) Underside of Top Flange Strain Data Line 2

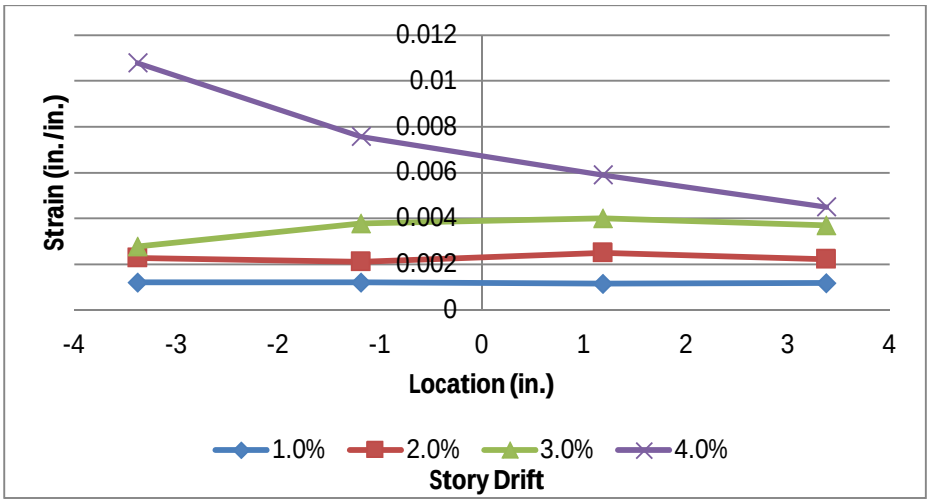


Figure E.18 – Specimen 3 (W24x62 with No RBS and No Fasteners) Underside of Top Flange Strain Data Line 3

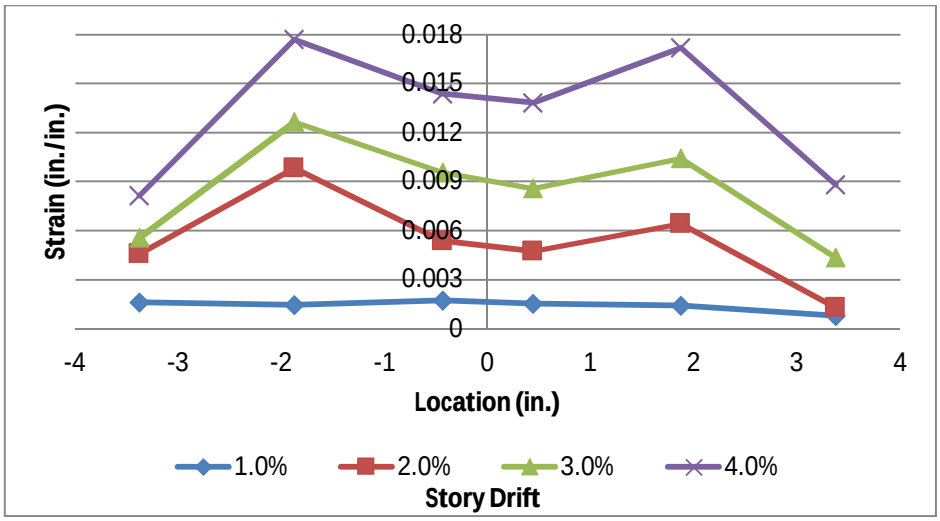


Figure E.19 – Specimen 4 (W24x62 with No RBS and PAFs at 12 in.) Top Flange Strain Data Line 1

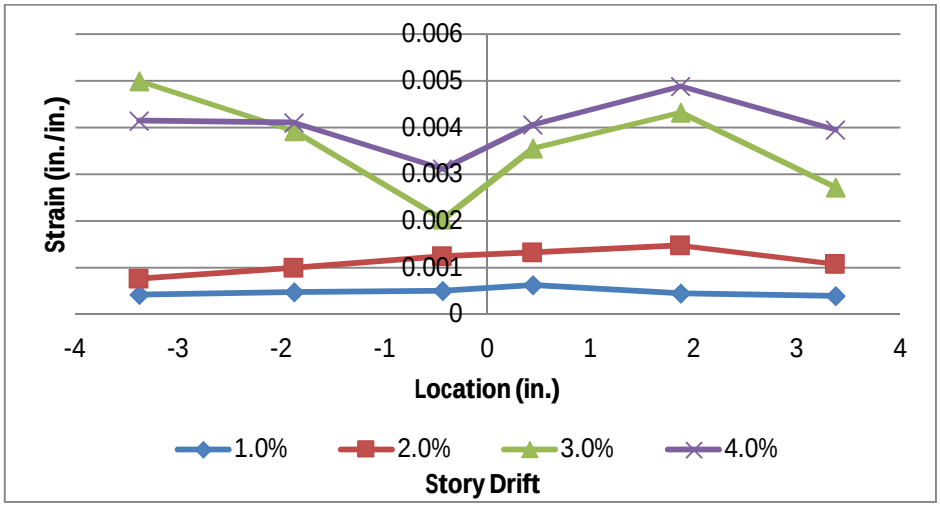


Figure E.20 – Specimen 4 (W24x62 with No RBS and PAFs at 12 in.) Top Flange Strain Data Line 2

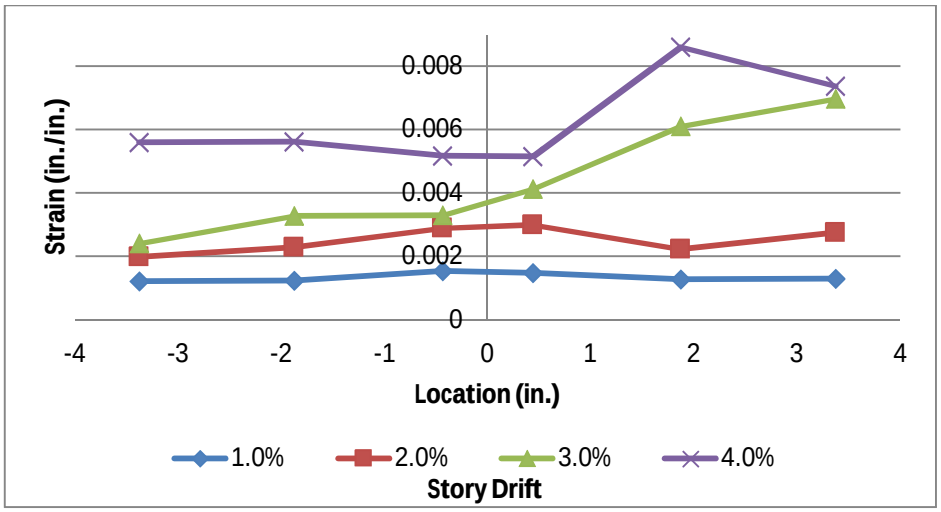


Figure E.21 – Specimen 4 (W24x62 with No RBS and PAFs at 12 in.) Top Flange Strain Data Line 3

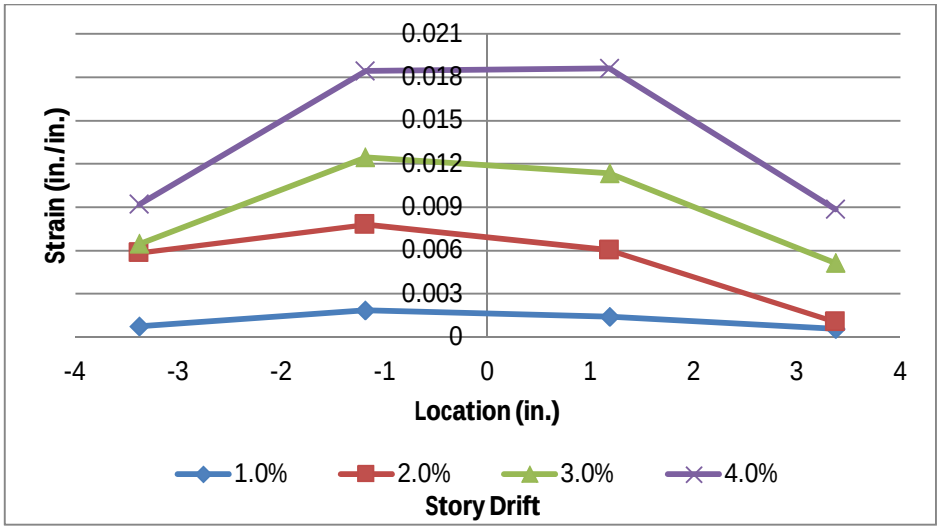


Figure E.22 – Specimen 4 (W24x62 with No RBS and PAFs at 12 in.) Underside of Top Flange Strain Data Line 1

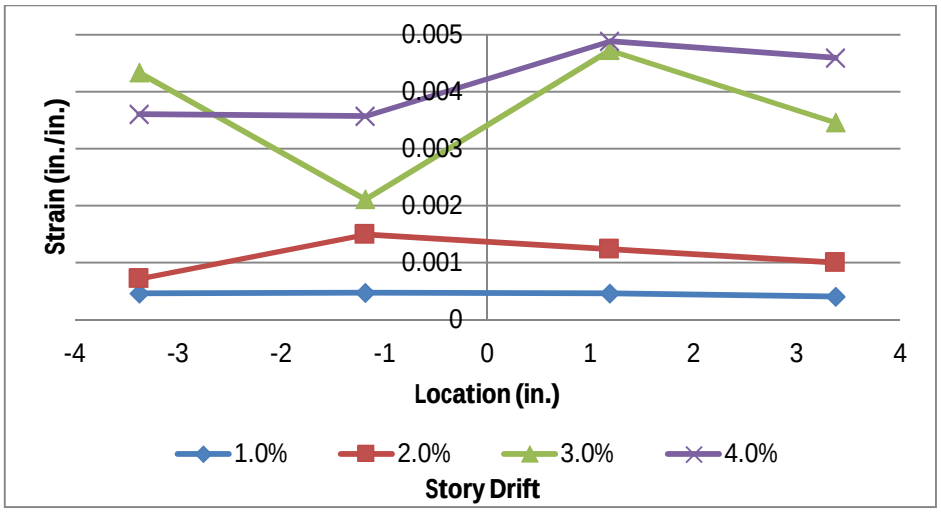


Figure E.23 – Specimen 4 (W24x62 with No RBS and PAFs at 12 in.) Underside of Top Flange Strain Data Line 2

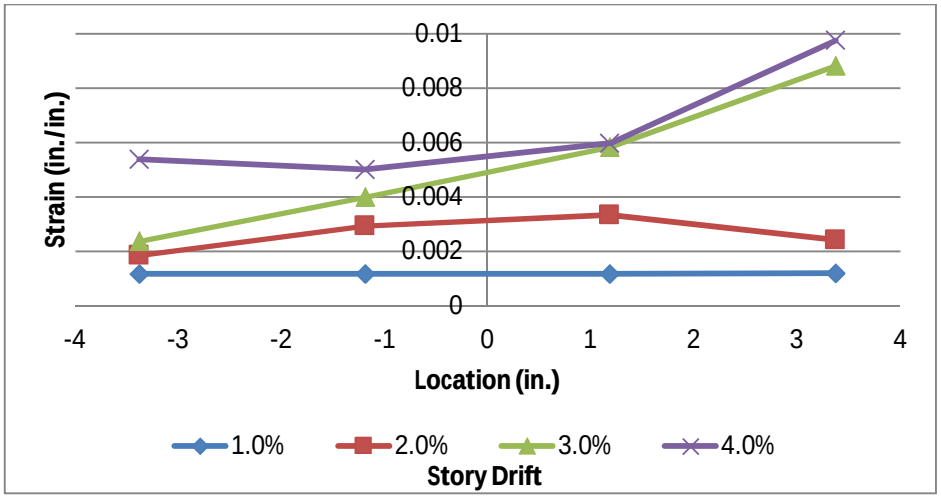


Figure E.24 – Specimen 4 (W24x62 with No RBS and PAFs at 12 in.) Underside of Top Flange Strain Data Line 3

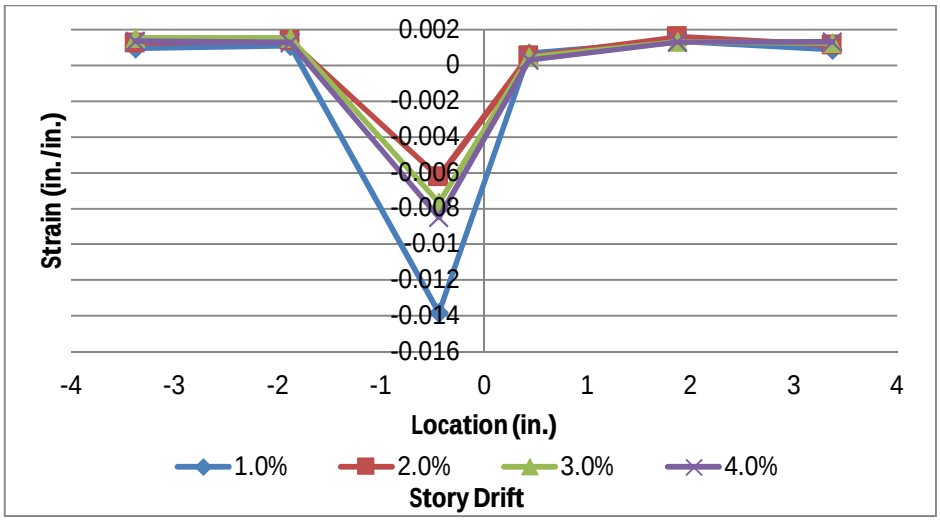


Figure E.25 – Specimen 5 (W24x62 with RBS and Puddle Welds at 12 in.) Top Flange Strain Data Line 1

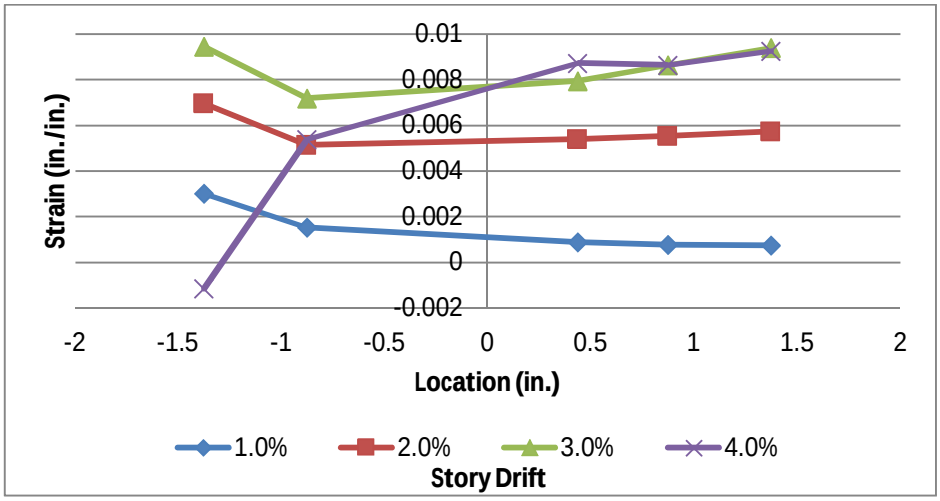


Figure E.26 – Specimen 5 (W24x62 with RBS and Puddle Welds at 12 in.) Top Flange Strain Data Line 2

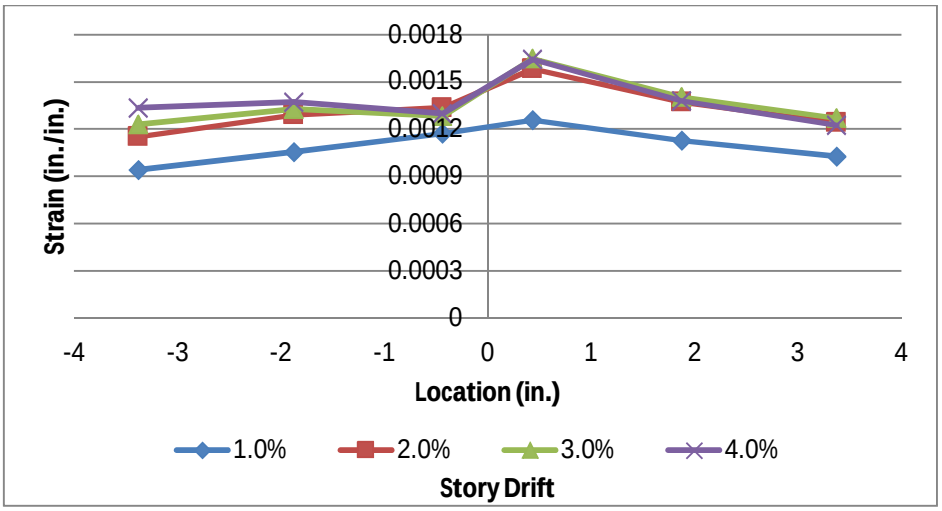


Figure E.27 – Specimen 5 (W24x62 with RBS and Puddle Welds at 12 in.) Top Flange Strain Data Line 3

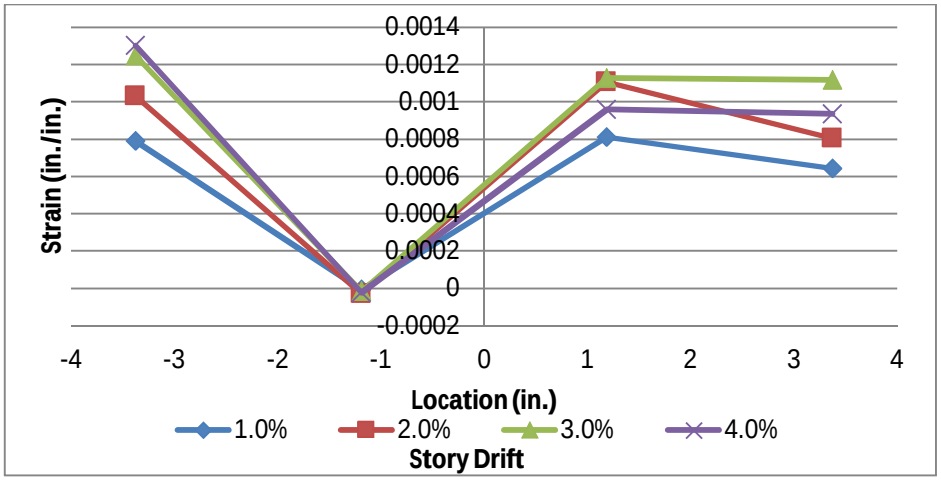


Figure E.28 – Specimen 5 (W24x62 with RBS and Puddle Welds at 12 in.) Underside of Top Flange Strain Data Line 1

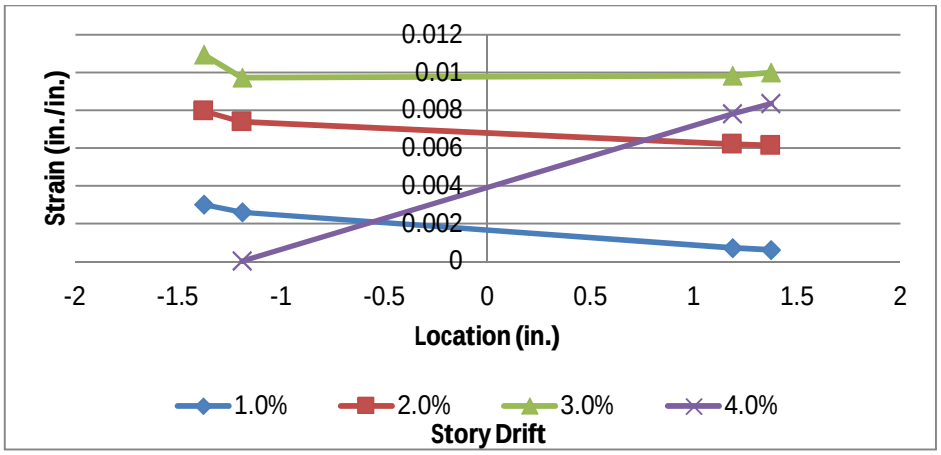


Figure E.29 – Specimen 5 (W24x62 with RBS and Puddle Welds at 12 in.) Underside of Top Flange Strain Data Line 2

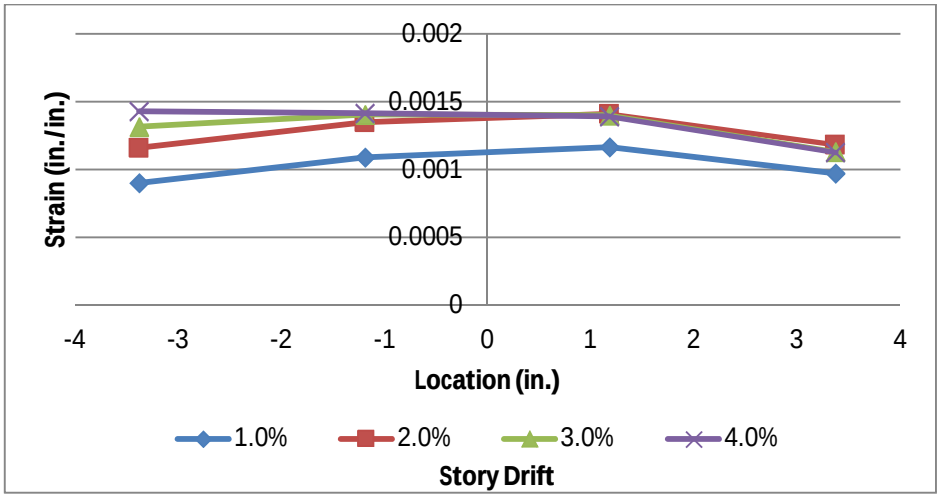


Figure E.30 – Specimen 5 (W24x62 with RBS and Puddle Welds at 12 in.) Underside of Top Flange Strain Data Line 3

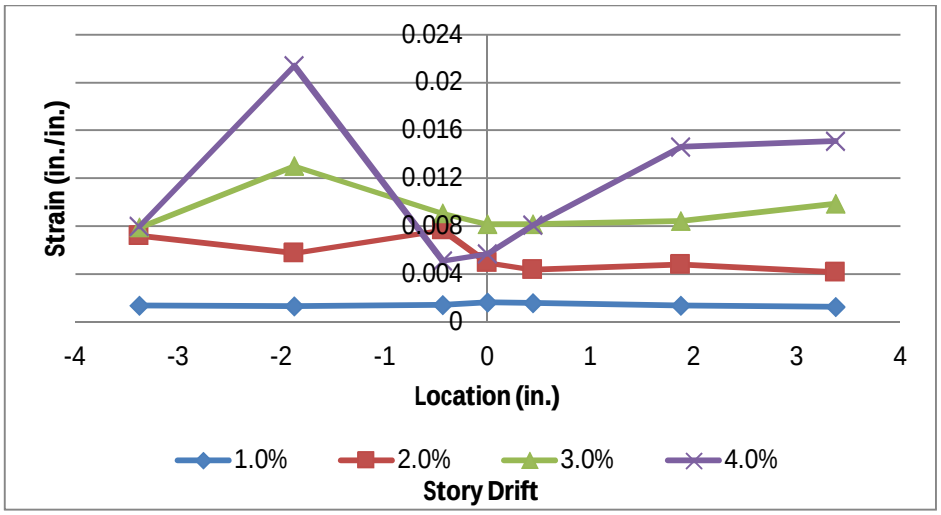


Figure E.31 – Specimen 6 (W24x62 with No RBS and Grid of PAFs) Top Flange Strain Data Line 1

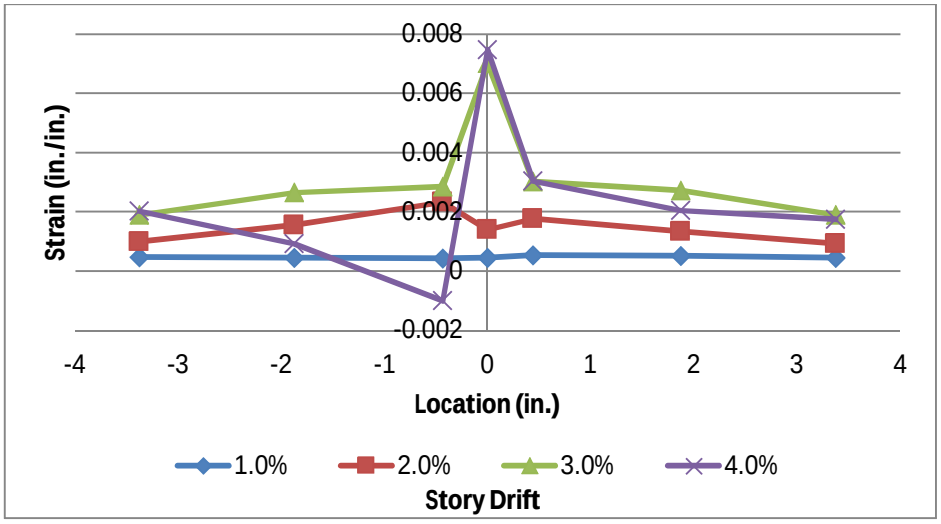


Figure E.32 – Specimen 6 (W24x62 with No RBS and Grid of PAFs) Top Flange Strain Data Line 2

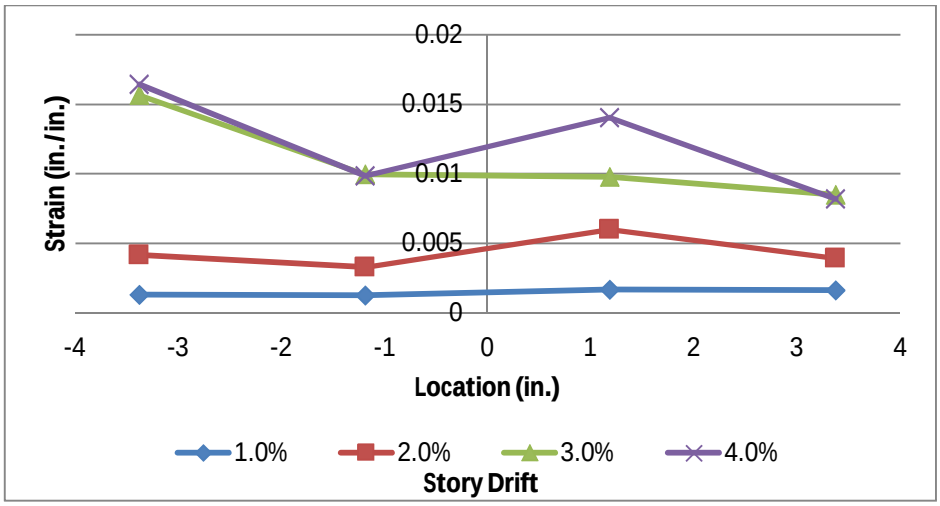


Figure E.33 – Specimen 6 (W24x62 with No RBS and Grid of PAFs) Underside of Top Flange Strain Data Line 1

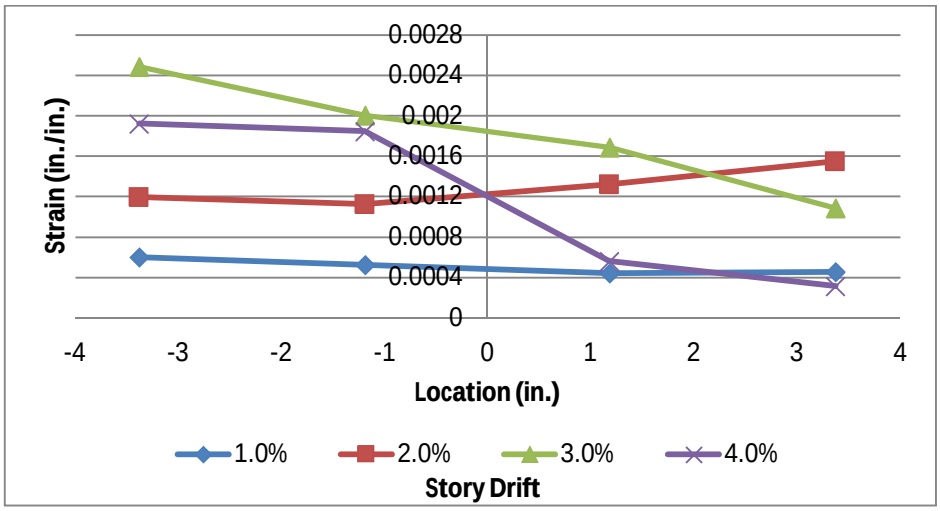


Figure E.34 – Specimen 6 (W24x62 with No RBS and Grid of PAFs) Underside of Top Flange Strain Data Line 2

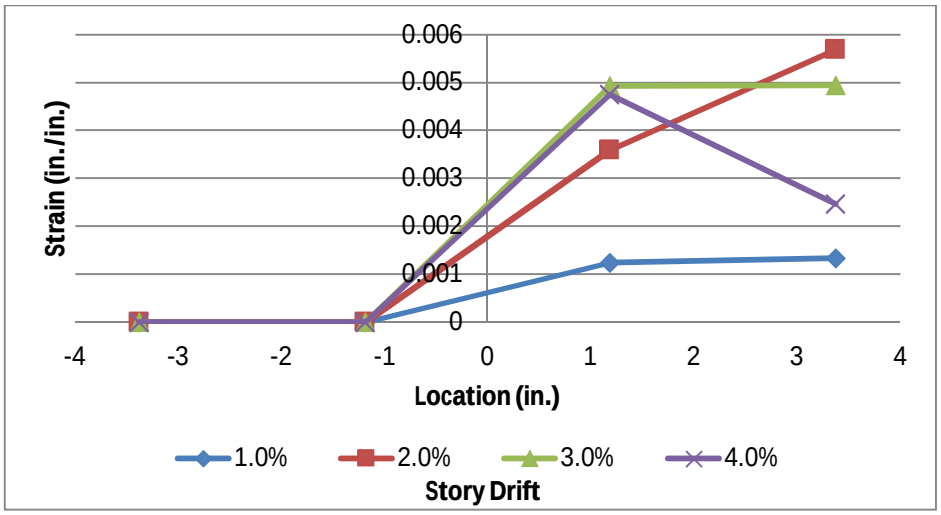


Figure E.35 – Specimen 6 (W24x62 with No RBS and Grid of PAFs) Underside of Top Flange Strain Data Line 3

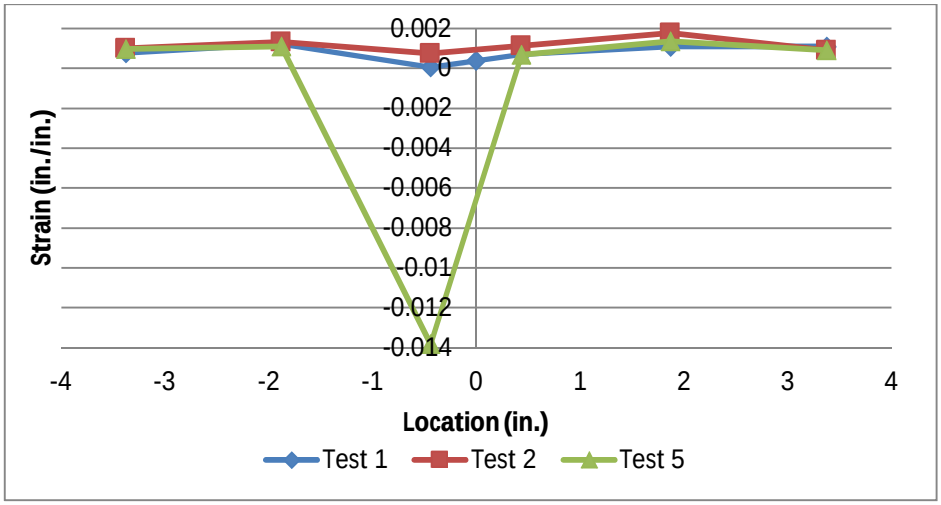


Figure E.36 – RBS24 (Specimen 1, 2 and 5) Top Flange Strain Data Line 1 at 1% Story Drift

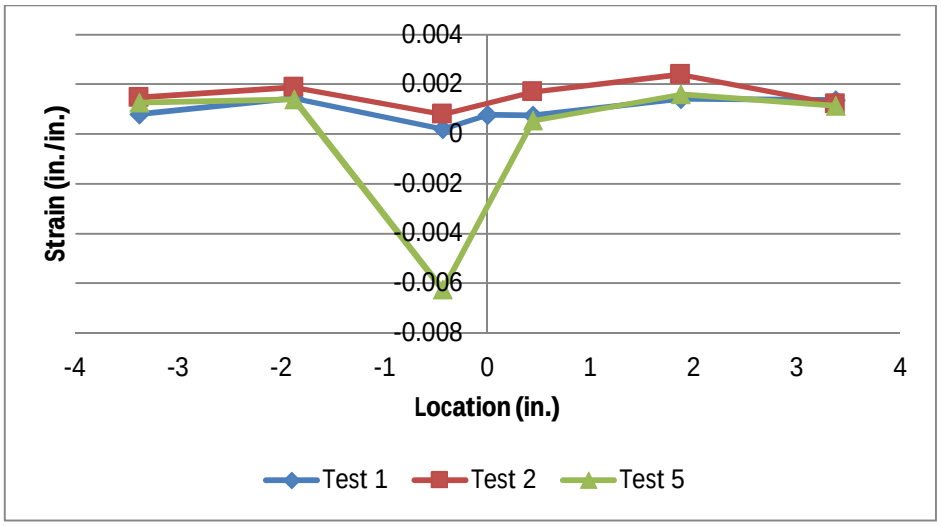


Figure E.37 – RBS24 (Specimen 1, 2 and 5) Top Flange Strain Data Line 1 at 2% Story Drift

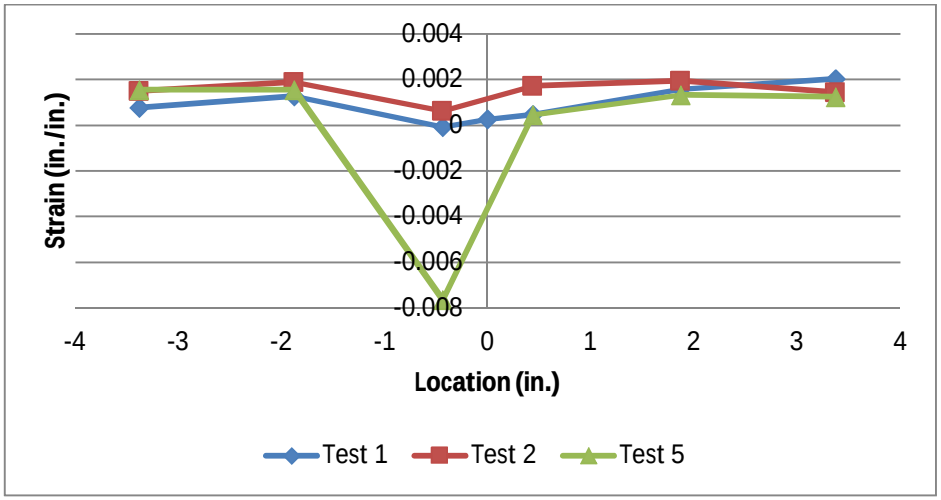


Figure E.38 – RBS24 (Specimen 1, 2 and 5) Top Flange Strain Data Line 1 at 3% Story Drift

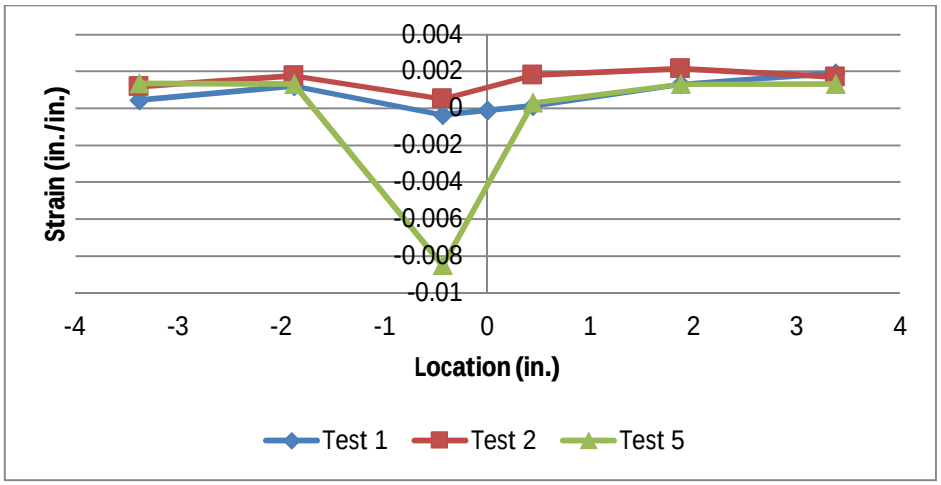


Figure E.39 – RBS24 (Specimen 1, 2 and 5) Top Flange Strain Data Line 1 at 4% Story Drift

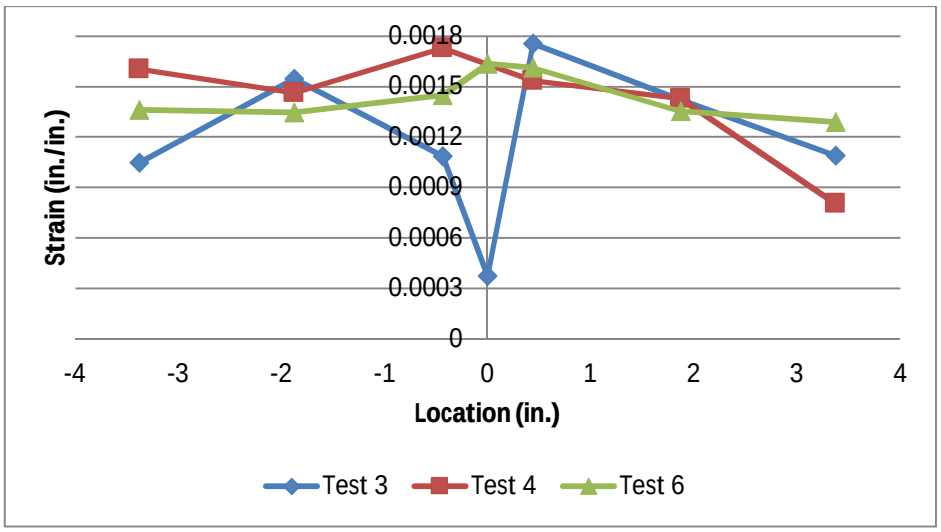


Figure E.40 – W24 (Specimen 3, 4 and 6) Top Flange Strain Data Line 1 at 1% Story Drift

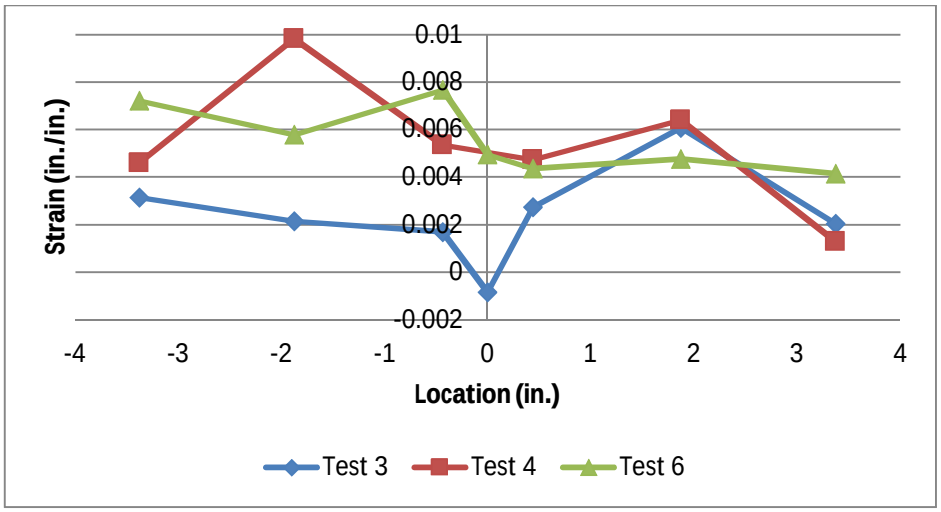


Figure E.41 – W24 (Specimen 3, 4 and 6) Top Flange Strain Data Line 1 at 2% Story Drift

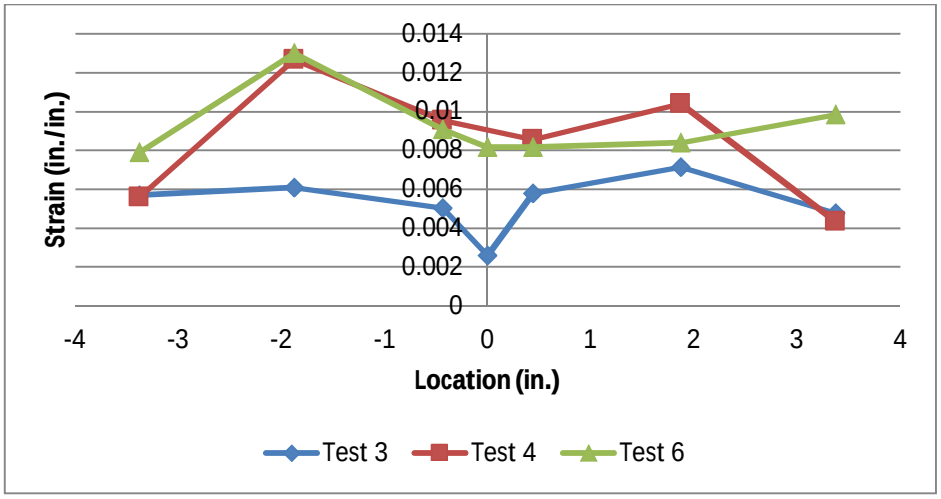


Figure E.42 – W24 (Specimen 3, 4 and 6) Top Flange Strain Data Line 1 at 3% Story Drift

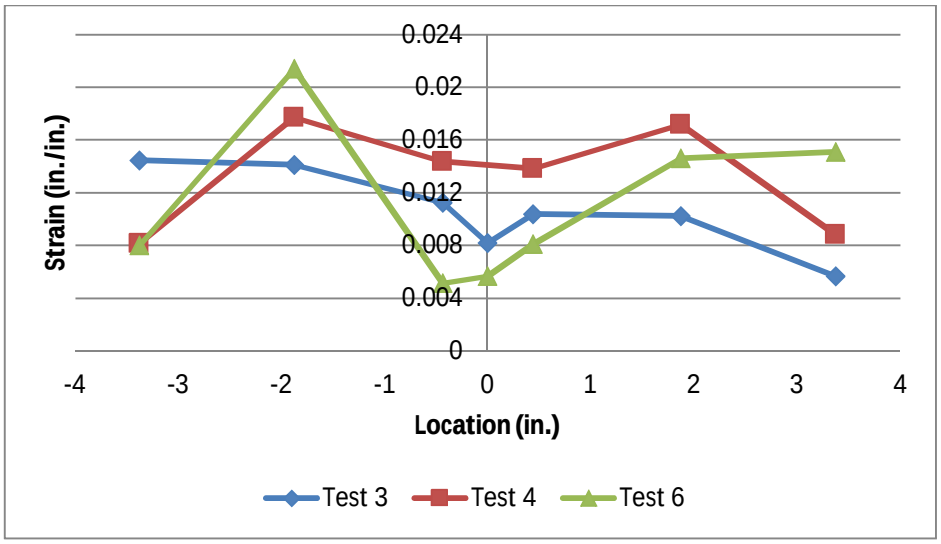


Figure E.43 – W24 (Specimen 3, 4 and 6) Top Flange Strain Data Line 1 at 4% Story Drift

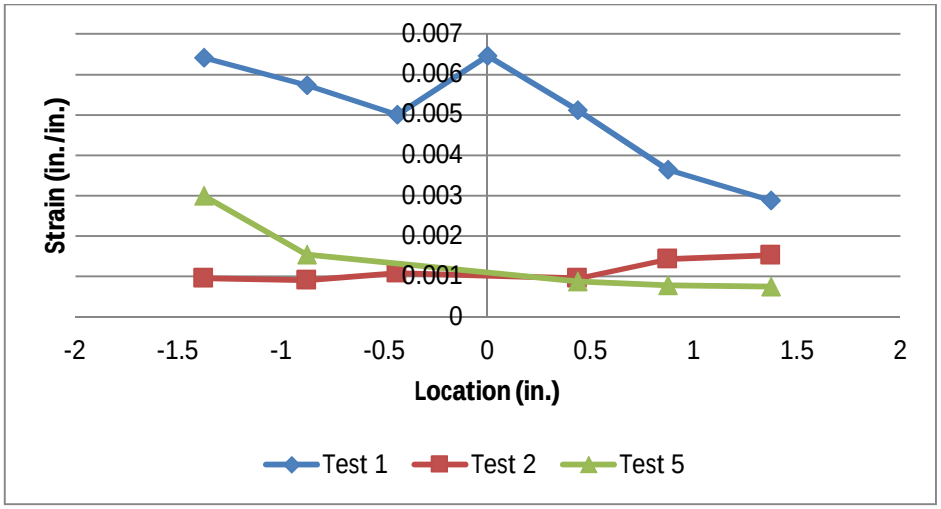


Figure E.44 – RBS24 (Specimen 1, 2 and 5) Top Flange Strain Data Line 2 at 1% Story Drift

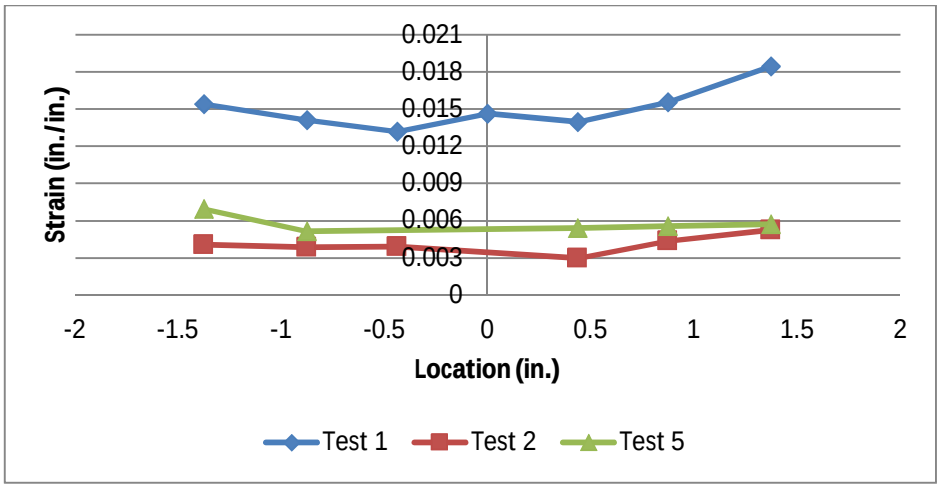


Figure E.45 – RBS24 (Specimen 1, 2 and 5) Top Flange Strain Data Line 2 at 2% Story Drift

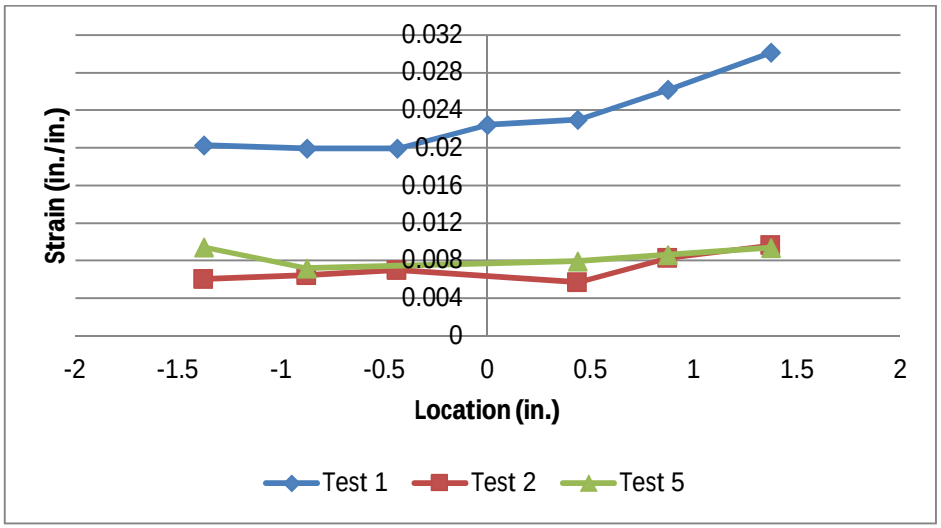


Figure E.46 – RBS24 (Specimen 1, 2 and 5) Top Flange Strain Data Line 2 at 3% Story Drift

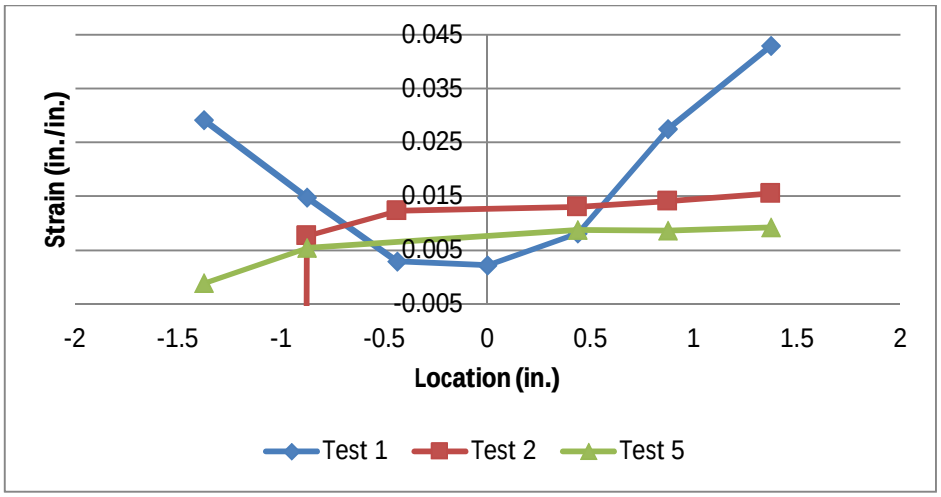


Figure E.47 – RBS24 (Specimen 1, 2 and 5) Top Flange Strain Data Line 2 at 4% Story Drift

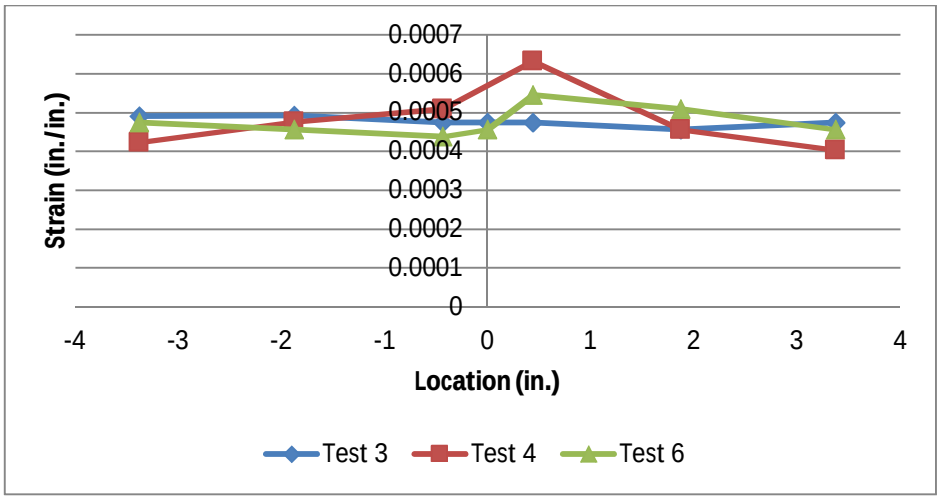


Figure E.48 – W24 (Specimen 3, 4 and 6) Top Flange Strain Data Line 2 at 1% Story Drift

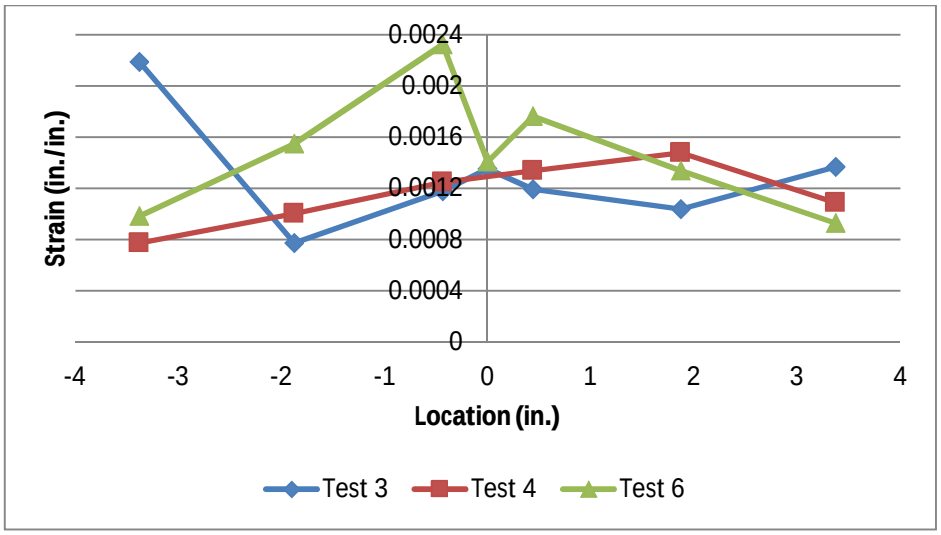


Figure E.49 – W24 (Specimen 3, 4 and 6) Top Flange Strain Data Line 2 at 2% Story Drift

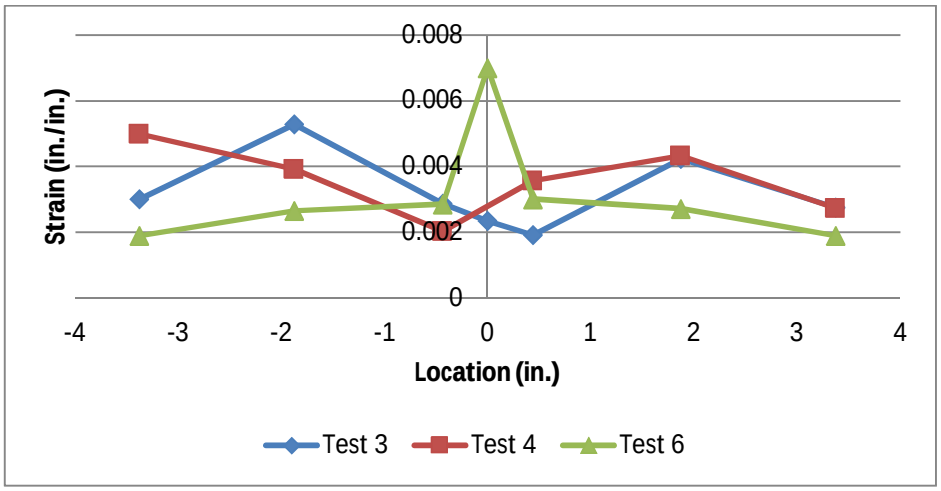


Figure E.50 – W24 (Specimen 3, 4 and 6) Top Flange Strain Data Line 2 at 3% Story Drift

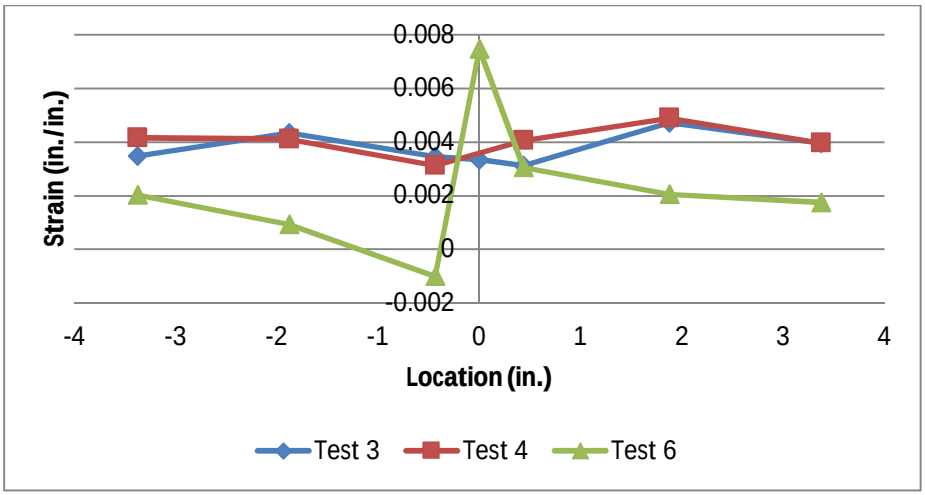


Figure E.51 – W24 (Specimen 3, 4 and 6) Top Flange Strain Data Line 2 at 4% Story Drift

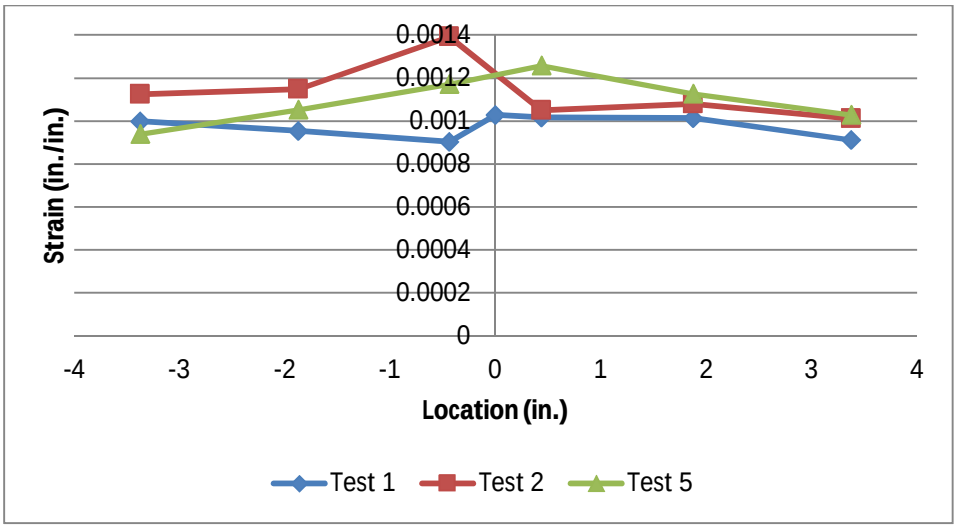


Figure E.52 – RBS24 (Specimen 1, 2 and 5) Top Flange Strain Data Line 3 at 1% Story Drift

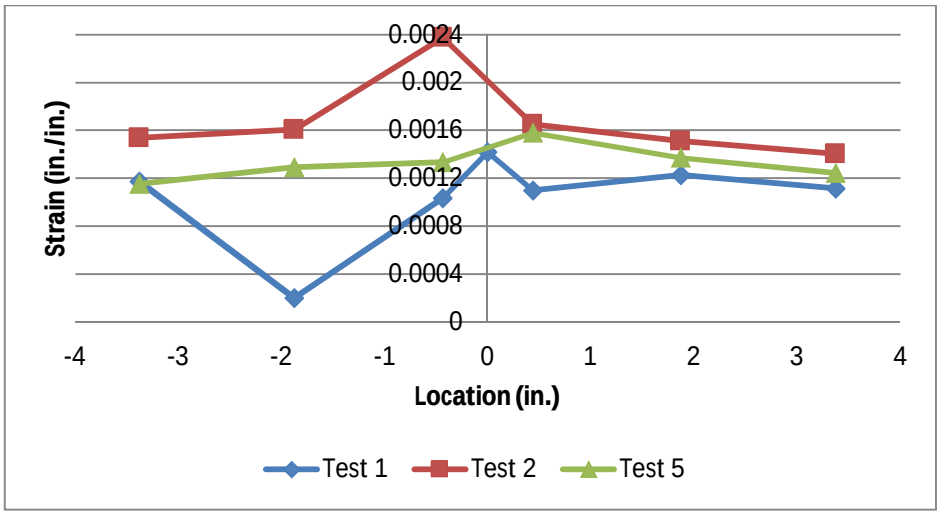


Figure E.53 – RBS24 (Specimen 1, 2 and 5) Top Flange Strain Data Line 3 at 2% Story Drift

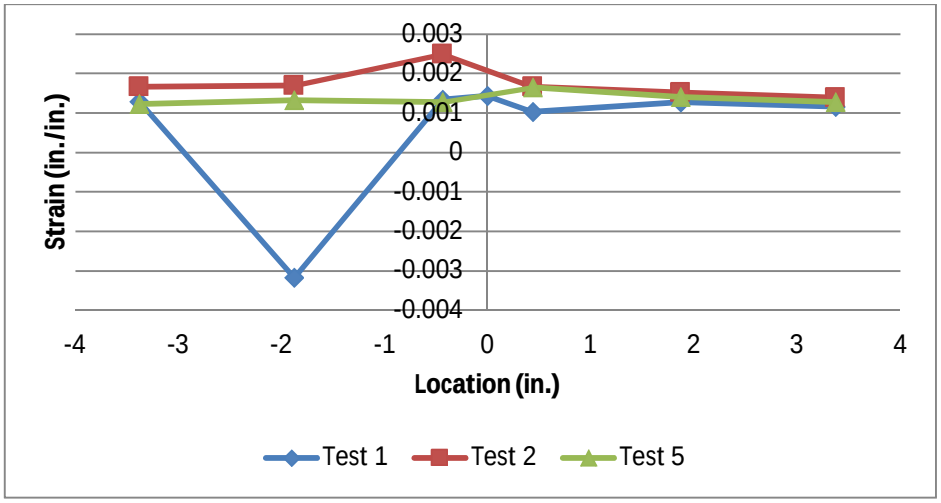


Figure E.54 – RBS24 (Specimen 1, 2 and 5) Top Flange Strain Data Line 3 at 3% Story Drift

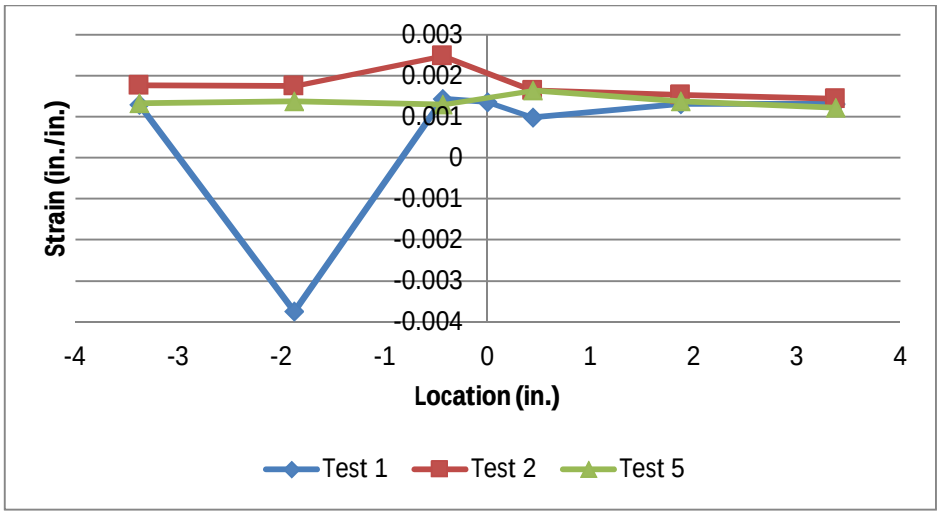


Figure E.55 – RBS24 (Specimen 1, 2 and 5) Top Flange Strain Data Line 3 at 4% Story Drift

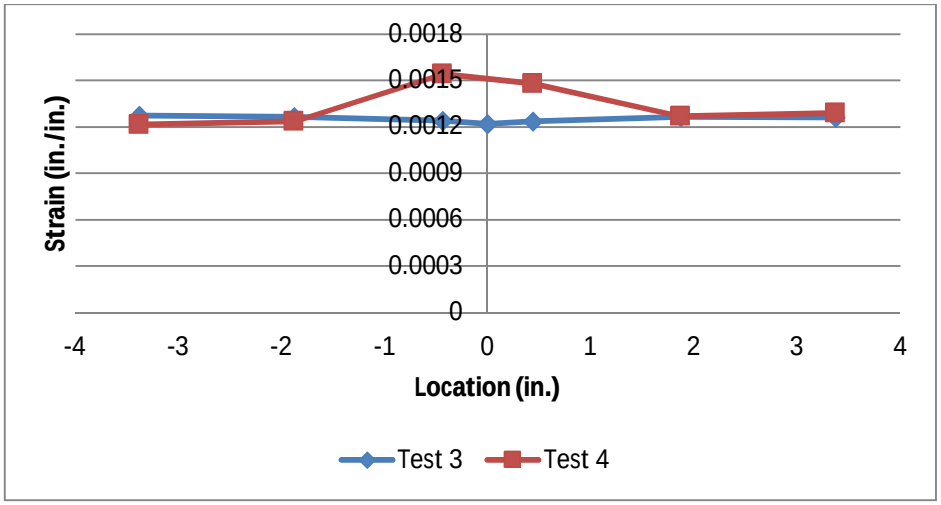


Figure E.56 – W24 (Specimen 3, 4 and 6) Top Flange Strain Data Line 3 at 1% Story Drift

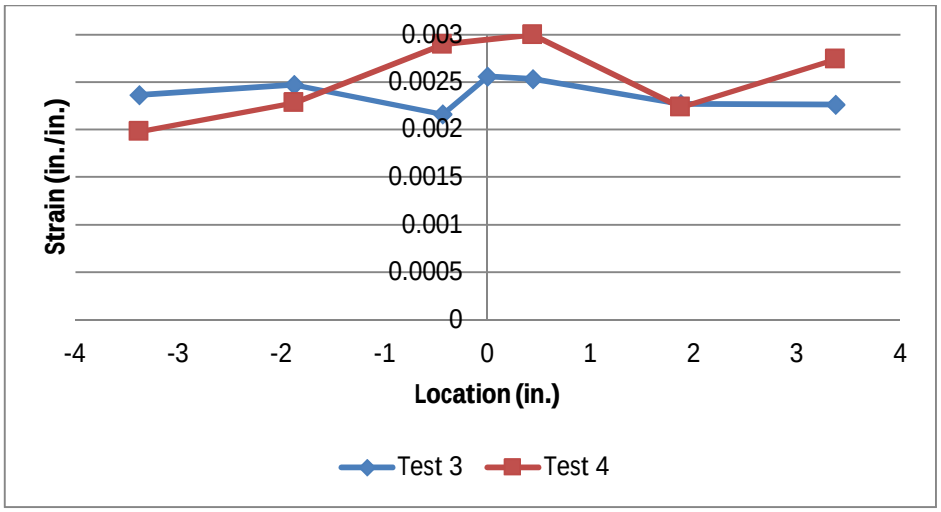


Figure E.57 – W24 (Specimen 3, 4 and 6) Top Flange Strain Data Line 3 at 2% Story Drift

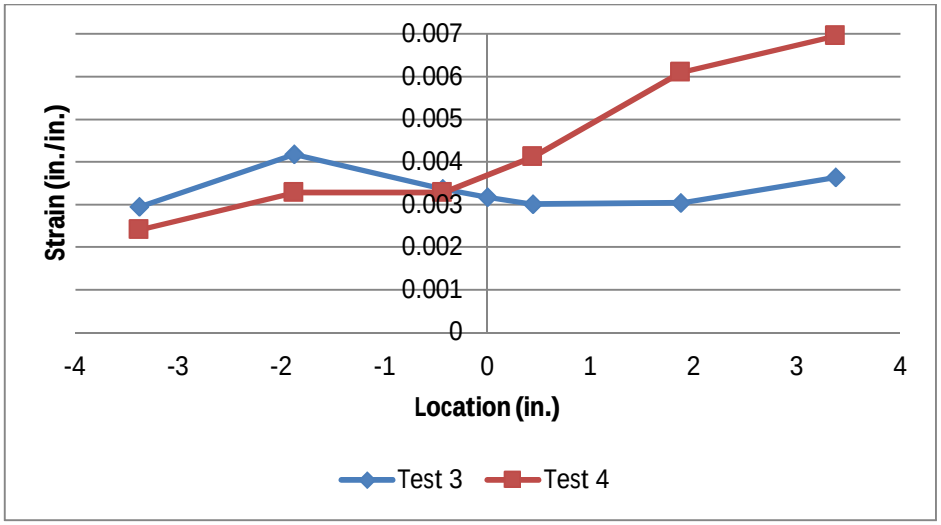


Figure E.58 – W24 (Specimen 3, 4 and 6) Top Flange Strain Data Line 3 at 3% Story Drift

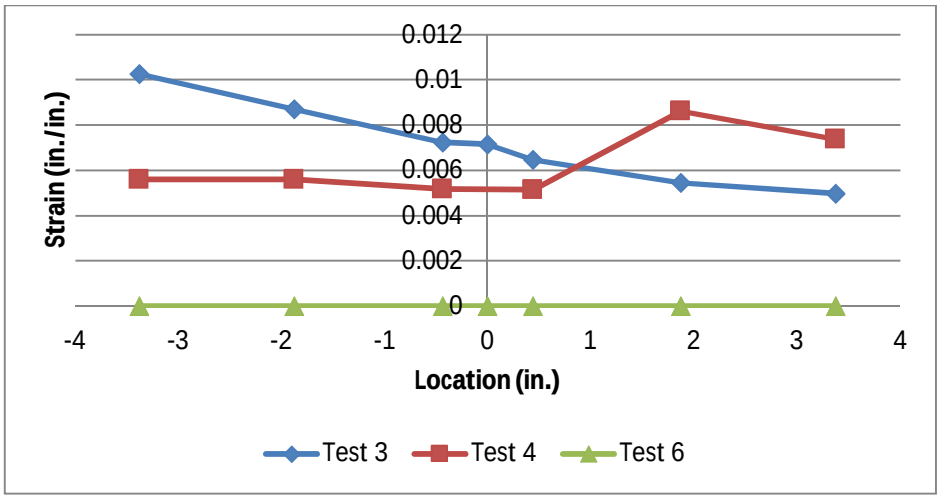


Figure E.59 – W24 (Specimen 3, 4 and 6) Top Flange Strain Data Line 3 at 4% Story Drift

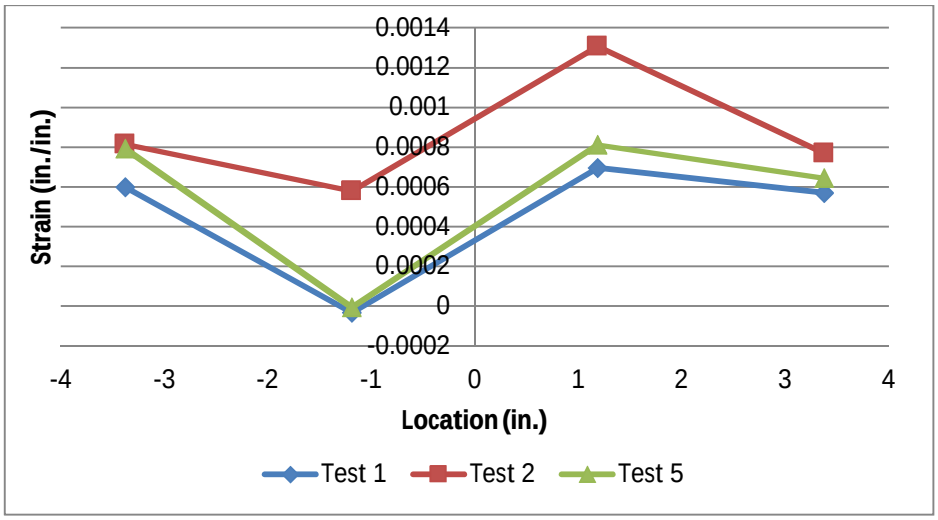


Figure E.60 – RBS24 (Specimen 1, 2 and 5) Underside of Top Flange Strain Data Line 1 at 1% Story Drift

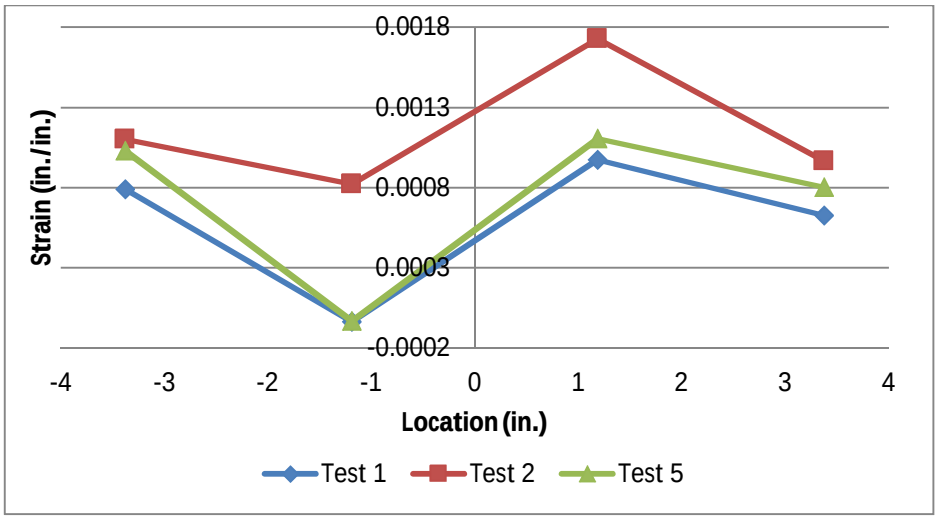


Figure E.61 – RBS24 (Specimen 1, 2 and 5) Underside of Top Flange Strain Data Line 1 at 2% Story Drift

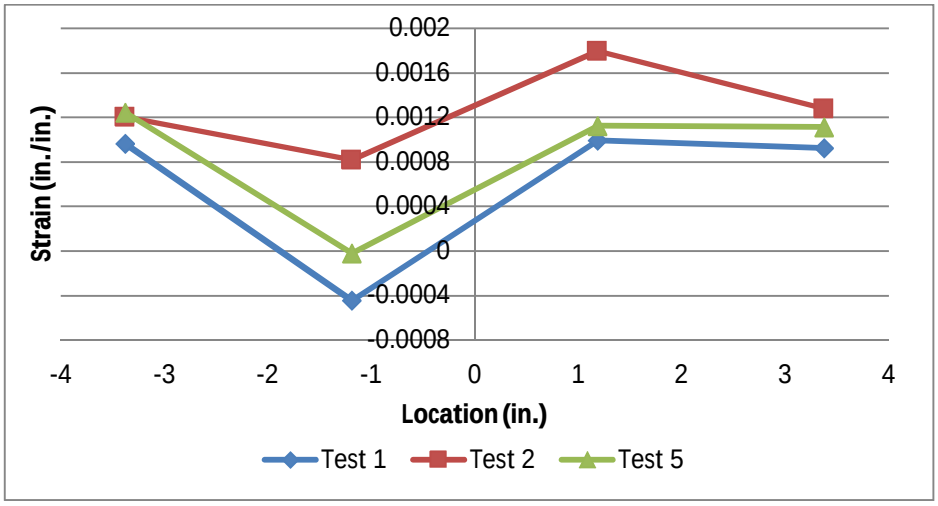


Figure E.62 – RBS24 (Specimen 1, 2 and 5) Underside of Top Flange Strain Data Line 1 at 3% Story Drift

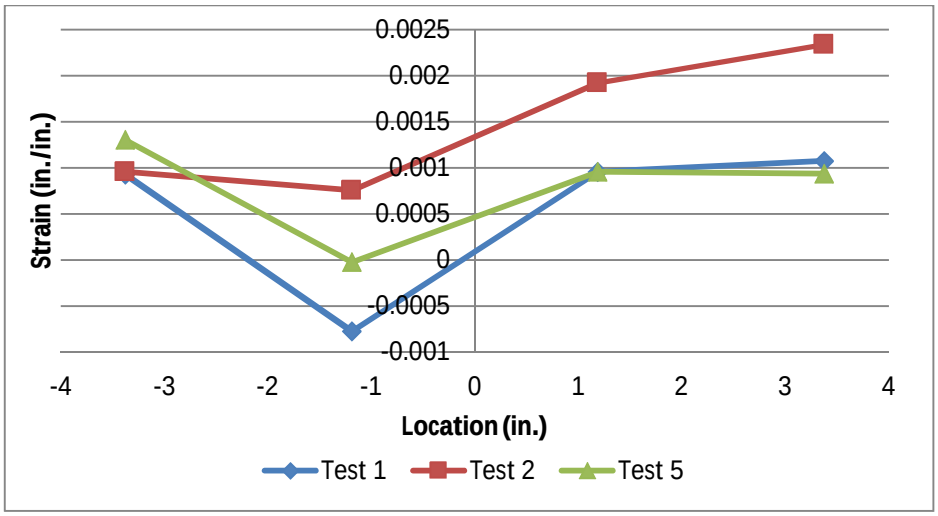


Figure E.63 – RBS24 (Specimen 1, 2 and 5) underside of top flange strain data line 1 at 4% Story Drift

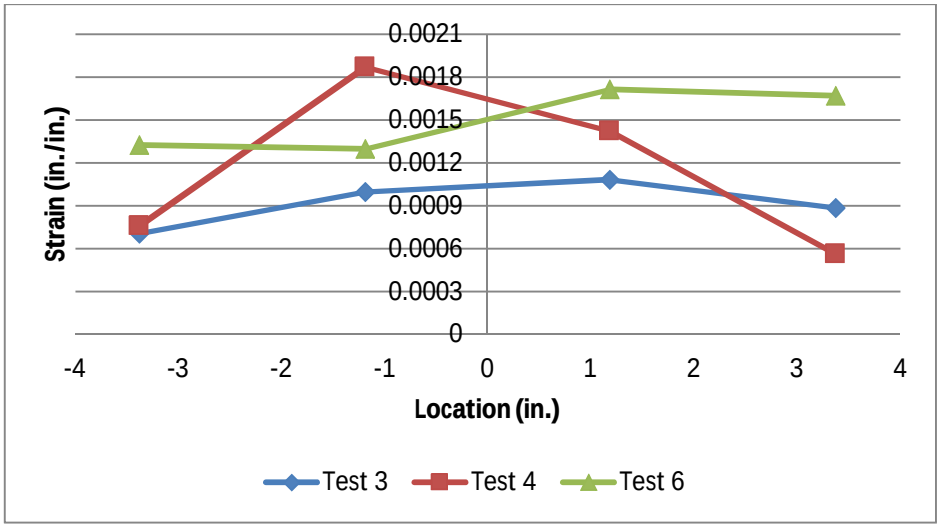


Figure E.64 – W24 (Specimen 3, 4 and 6) underside of top flange strain data line 1 at 1% Story Drift

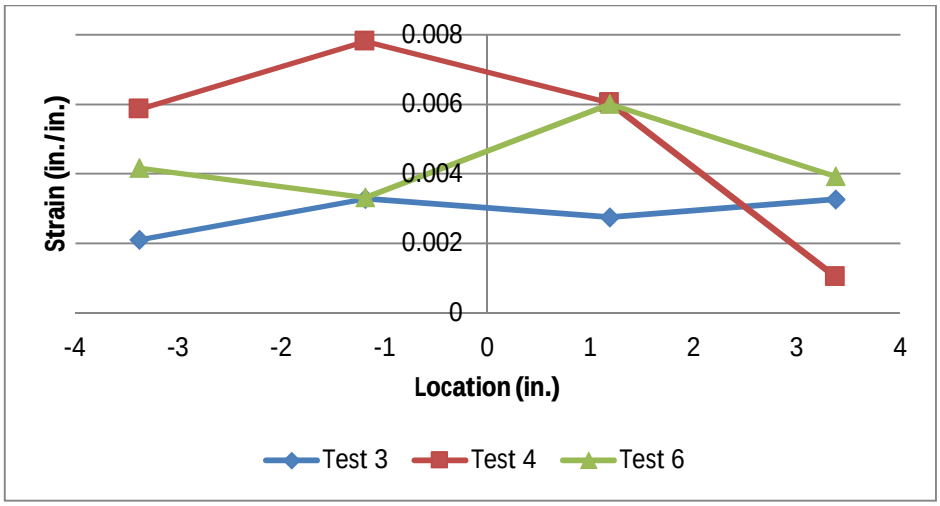


Figure E.65 – W24 (Specimen 3, 4 and 6) Underside of Top Flange Strain Data Line 1 at 2% Story Drift

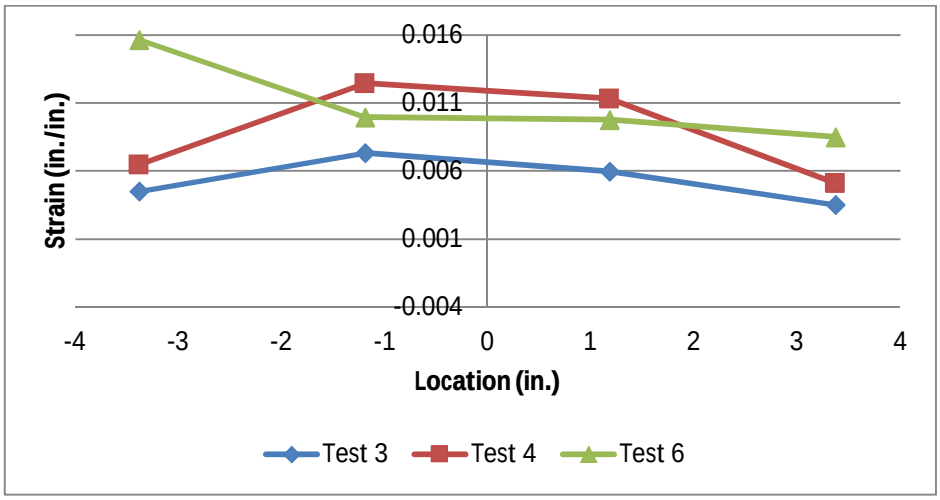


Figure E.66 – W24 (Specimen 3, 4 and 6) Underside of Top Flange Strain Data Line 1 at 3% Story Drift

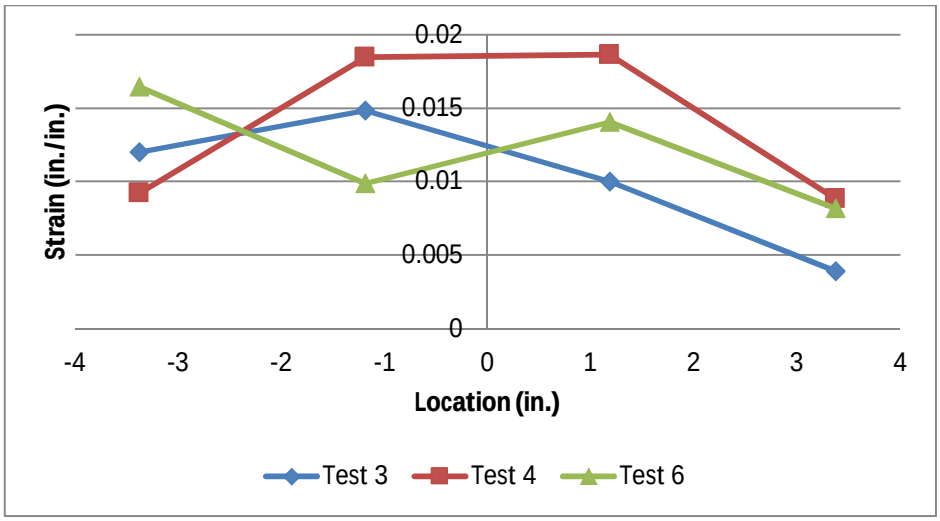


Figure E.67 – W24 (Specimen 3, 4 and 6) Underside of Top Flange Strain Data Line 1 at 4% Story Drift

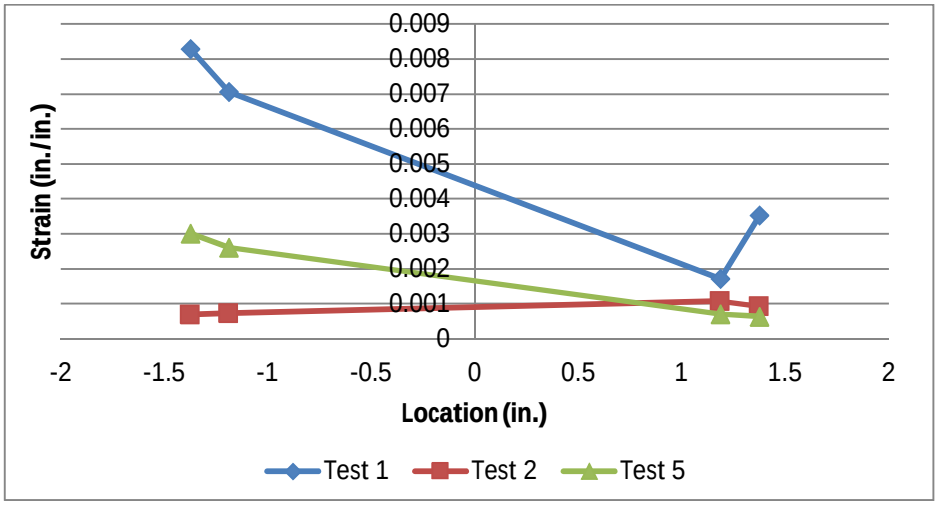


Figure E.68 – RBS24 (Specimen 1, 2 and 5) Underside of Top Flange Strain Data Line 2 at 1% Story Drift

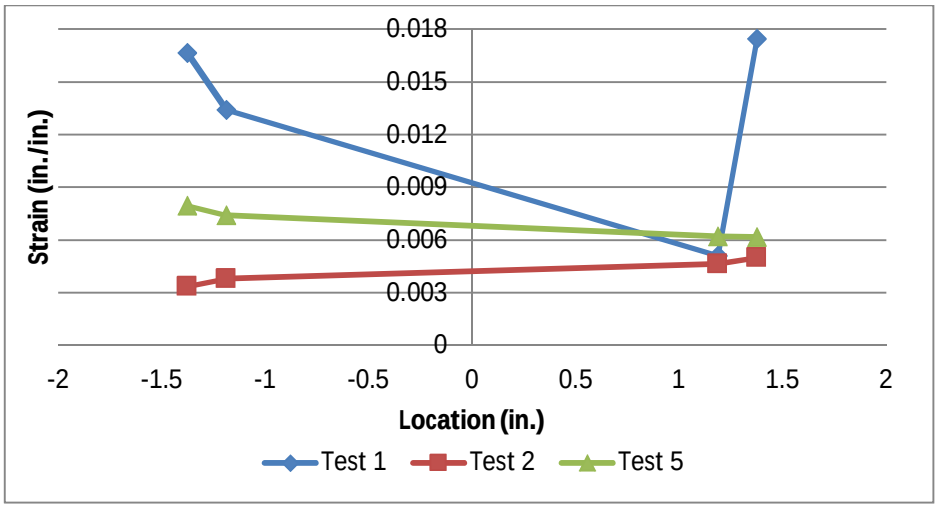


Figure E.69 – RBS24 (Specimen 1, 2 and 5) Underside of Top Flange Strain Data Line 2 at 2% Story Drift

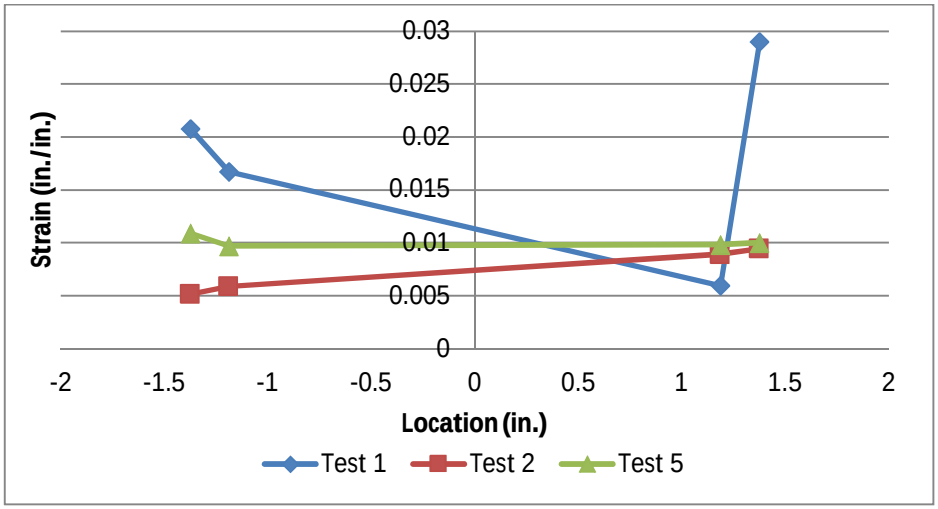


Figure E.70 – RBS24 (Specimen 1, 2 and 5) Underside of Top Flange Strain Data Line 2 at 3% Story Drift

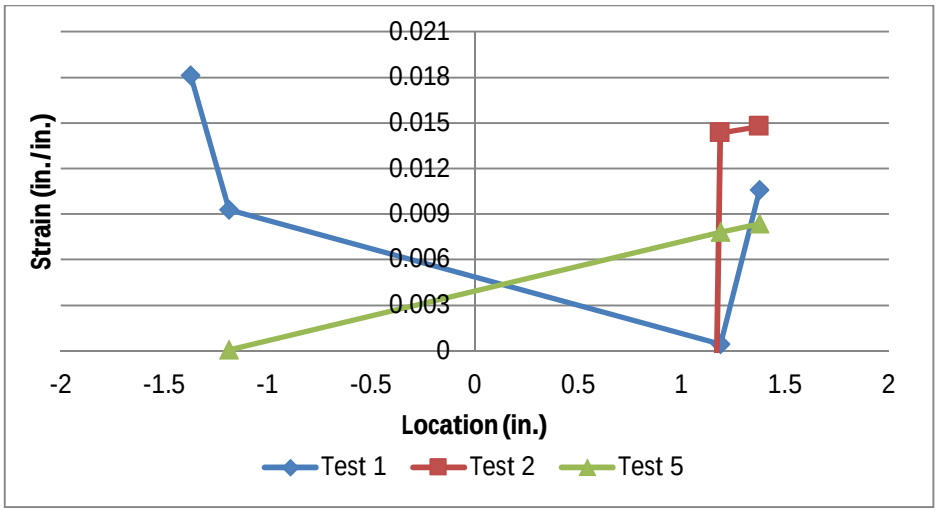


Figure E.71 – RBS24 (Specimen 1, 2 and 5) Underside of Top Flange Strain Data Line 2 at 4% Story Drift

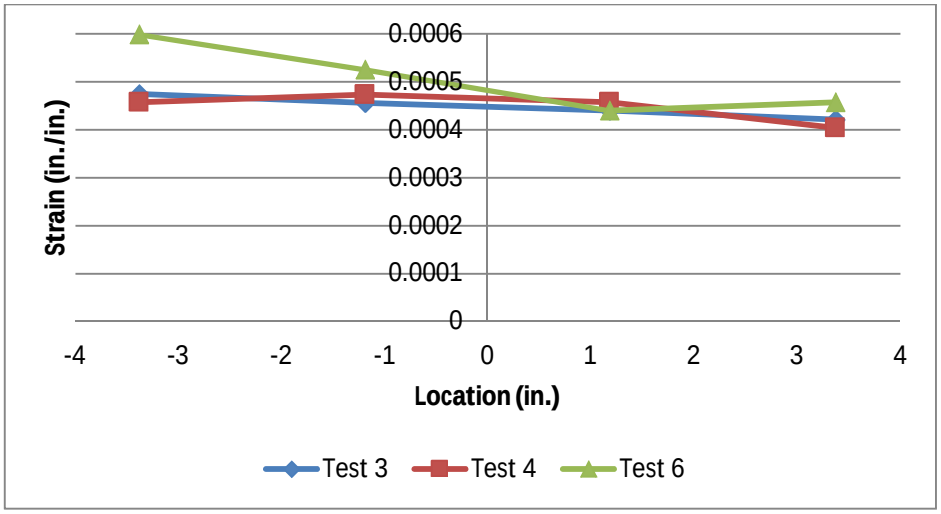


Figure E.72 – W24 (Specimen 3, 4 and 6) Underside of Top Flange Strain Data Line 2 at 1% Story Drift

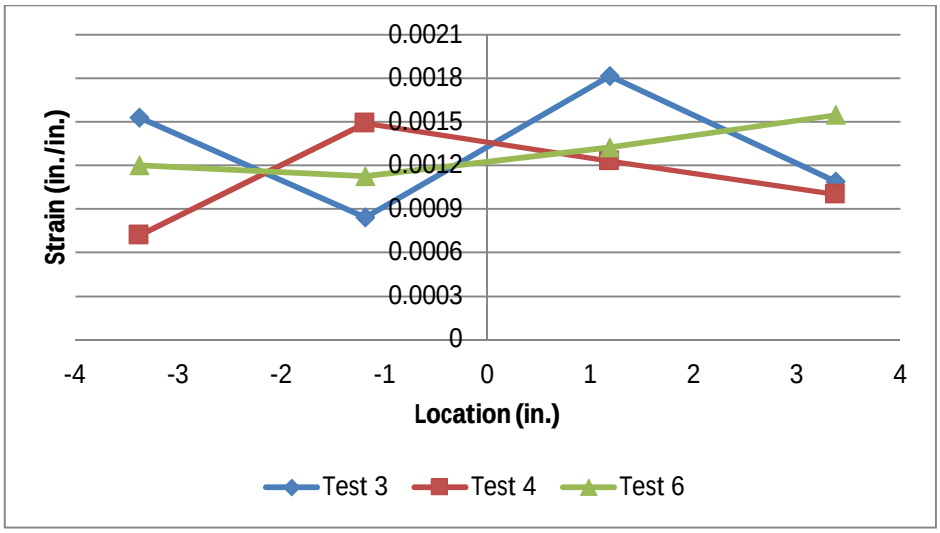


Figure E.73 – W24 (Specimen 3, 4 and 6) Underside of Top Flange Strain Data Line 2 at 2% Story Drift

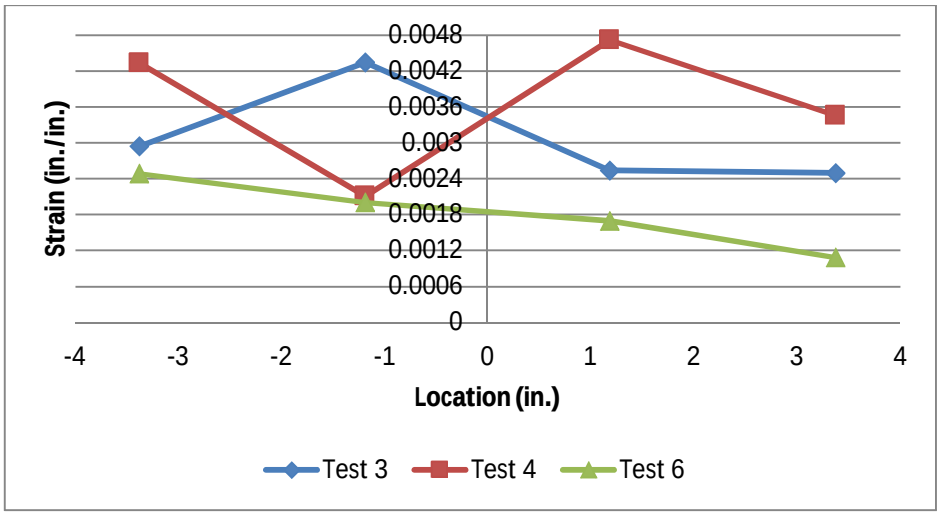


Figure E.74 – W24 (Specimen 3, 4 and 6) Underside of Top Flange Strain Data Line 2 at 3% Story Drift

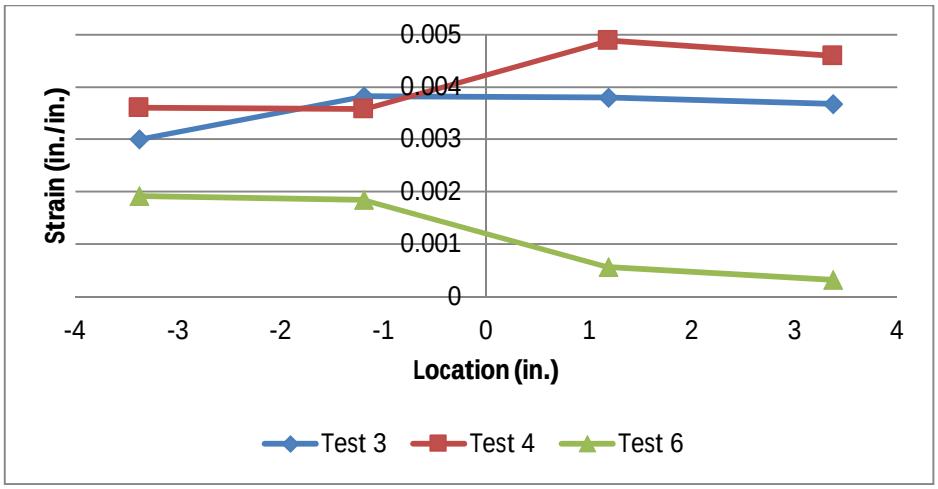


Figure E.75 – W24 (Specimen 3, 4 and 6) Underside of Top Flange Strain Data Line 2 at 4% Story Drift

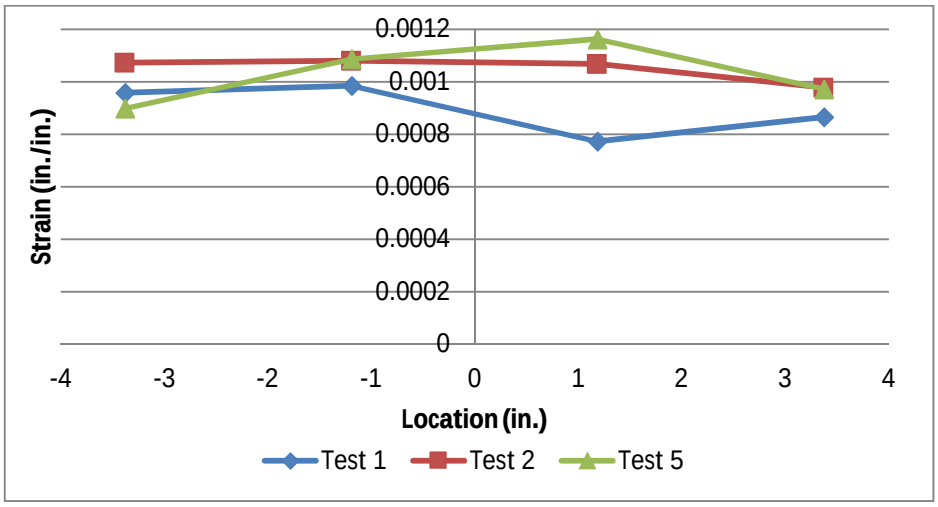


Figure E.76 – RBS24 (Specimen 1, 2 and 5) Underside of Top Flange Strain Data Line 3 at 1% Story Drift

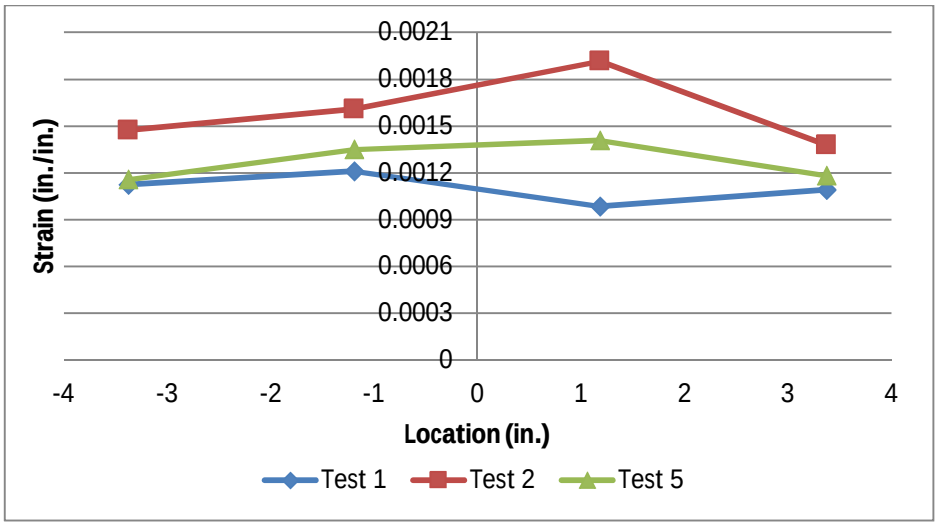


Figure E.77 – RBS24 (Specimen 1, 2 and 5) Underside of Top Flange Strain Data Line 3 at 2% Story Drift

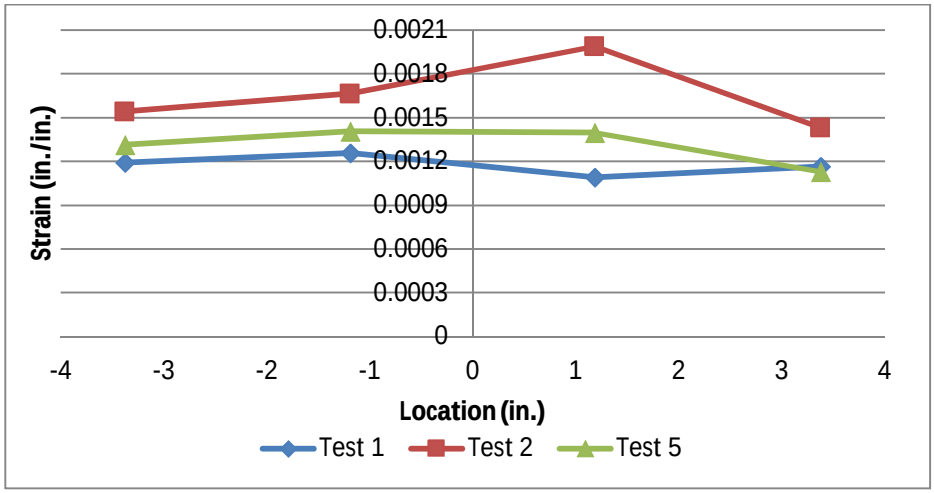


Figure E.78 – RBS24 (Specimen 1, 2 and 5) Underside of Top Flange Strain Data Line 3 at 3% Story Drift

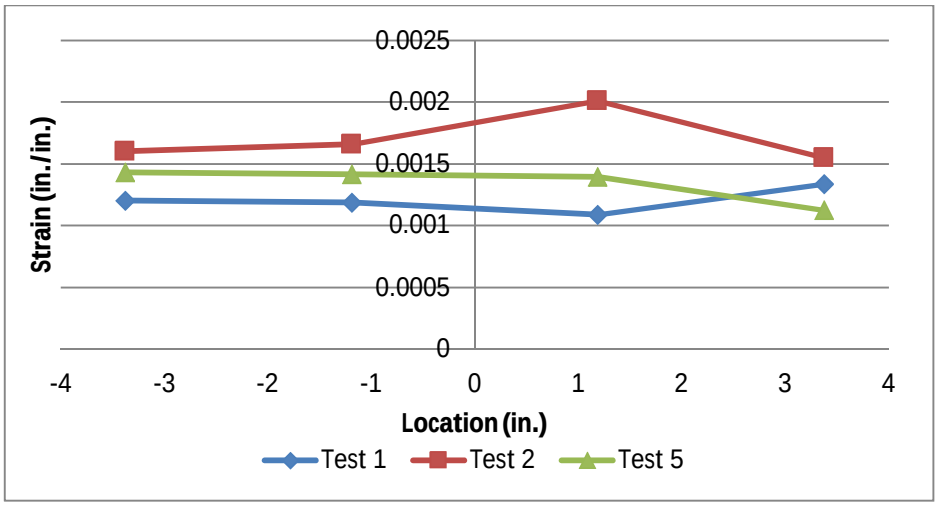


Figure E.79 – RBS24 (Specimen 1, 2 and 5) Underside of Top Flange Strain Data Line 3 at 4% Story Drift

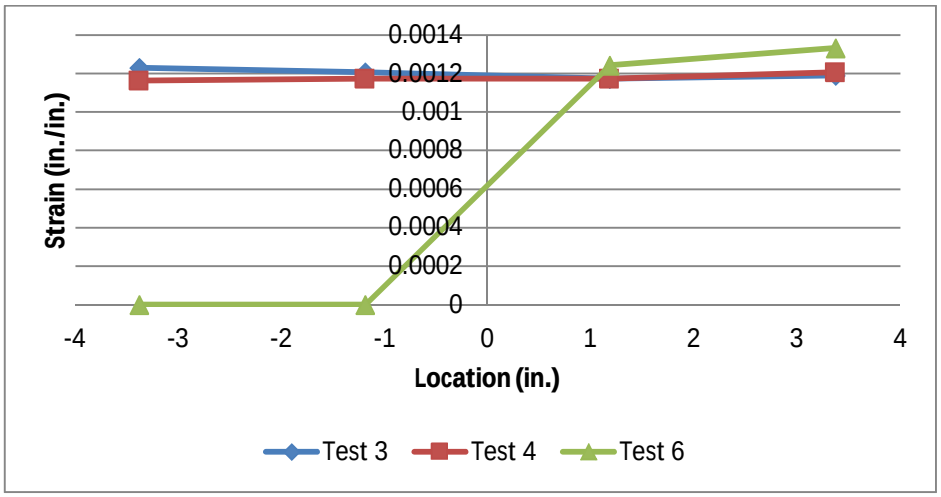


Figure E.80 – W24 (Specimen 3, 4 and 6) Underside of Top Flange Strain Data Line 3 at 1% Story Drift

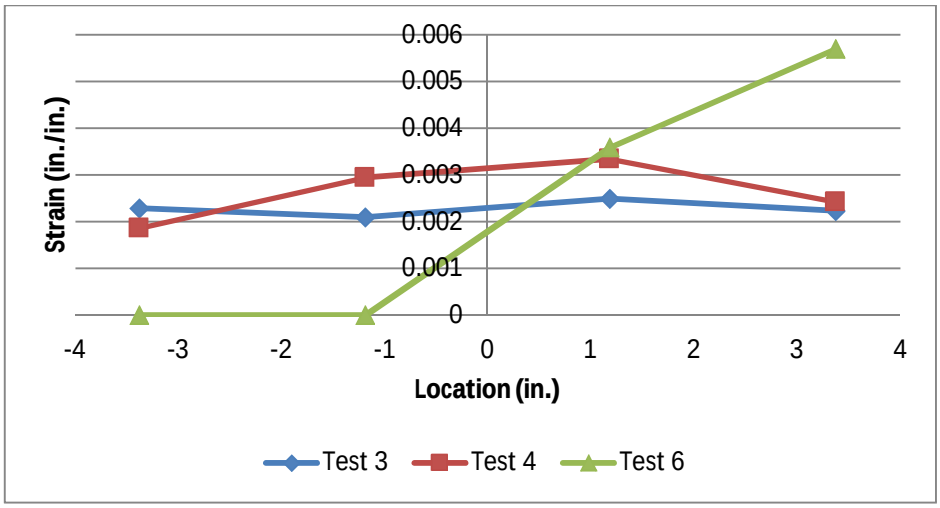


Figure E.81 – W24 (Specimen 3, 4 and 6) Underside of Top Flange Strain Data Line 3 at 2% Story Drift

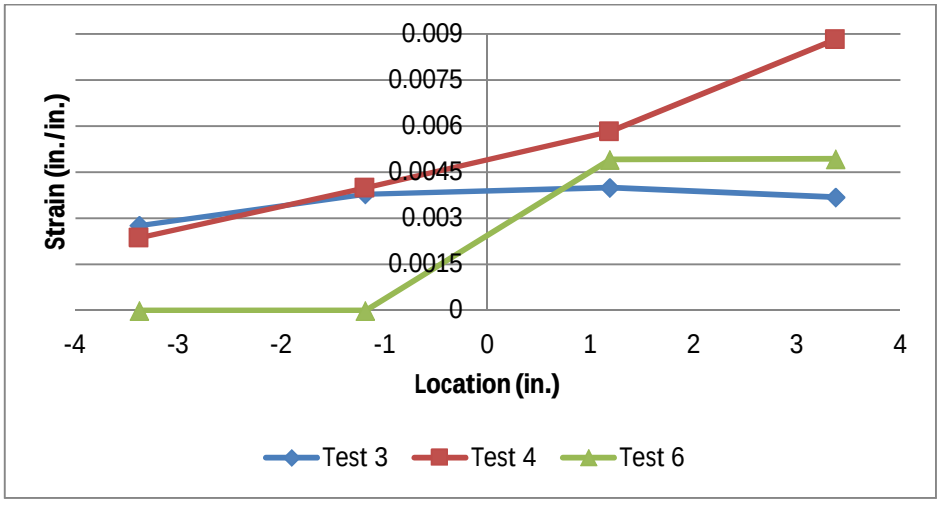


Figure E.82 – W24 (Specimen 3, 4 and 6) Underside of Top Flange Strain Data Line 3 at 3% Story Drift

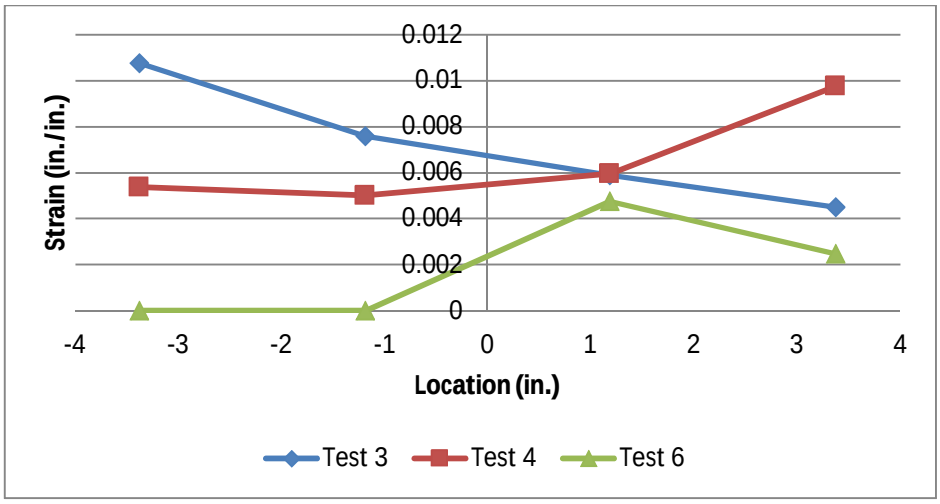


Figure E.83 – W24 (Specimen 3, 4 and 6) Underside of Top Flange Strain Data Line 3 at 4% Story Drift

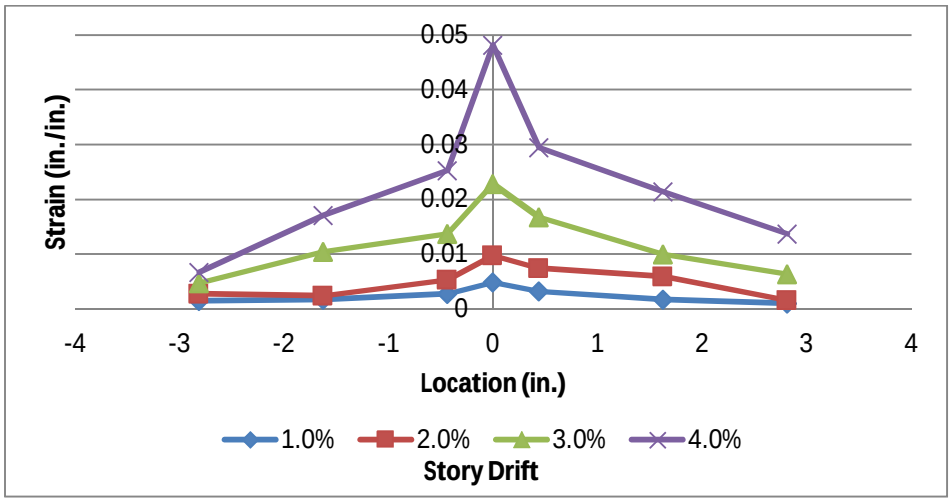


Figure E.84 – Specimen 7 (W36x150 with RBS and No Fasteners) Top Flange Strain Data Line 1

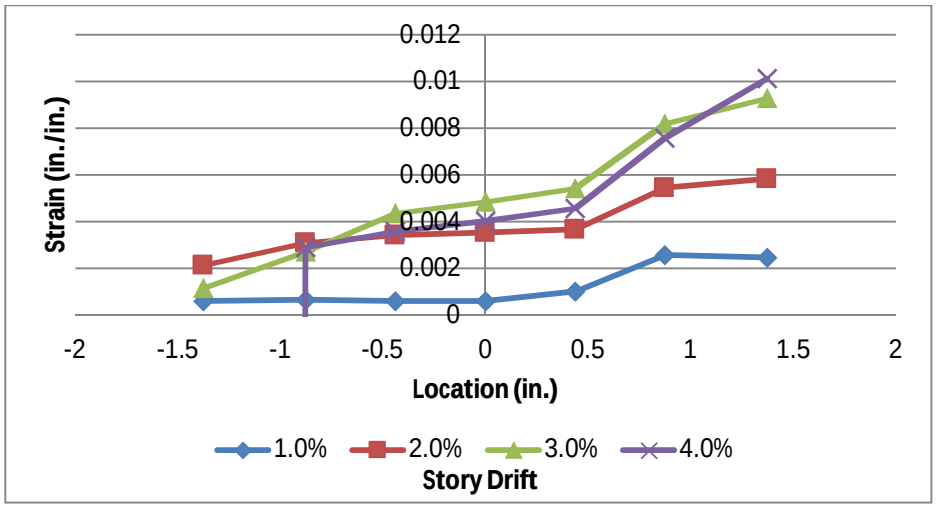


Figure E.85 – Specimen 7 (W36x150 with RBS and No Fasteners) Top Flange Strain Data Line 2

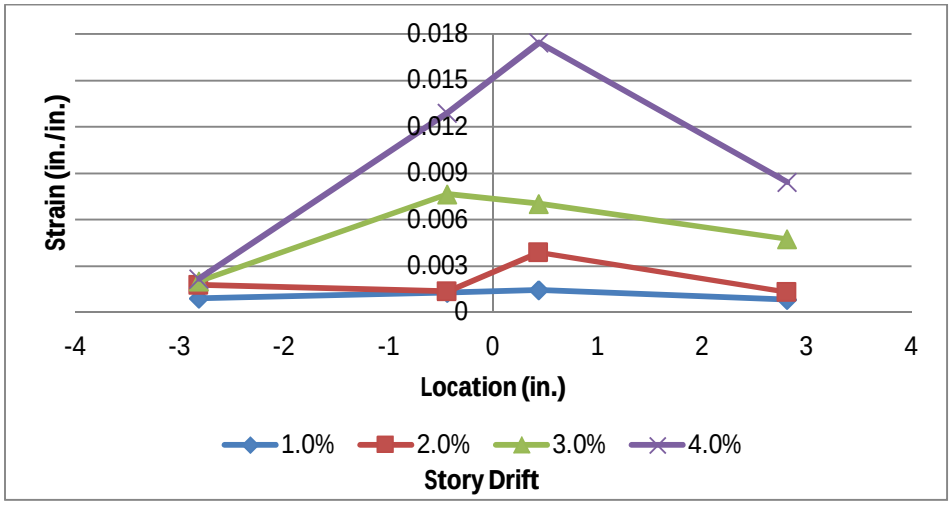


Figure E.86 – Specimen 7 (W36x150 with RBS and No Fasteners) Underside of Top Flange Strain Data Line 1

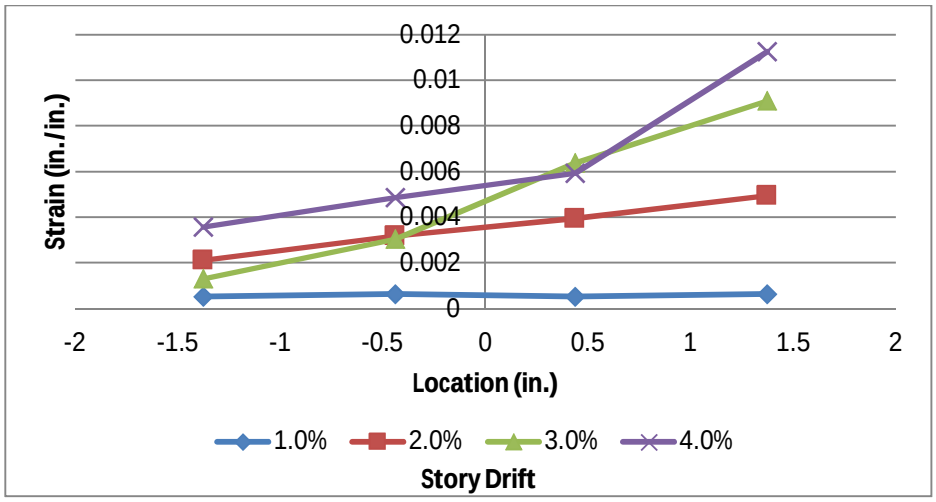


Figure E.87 – Specimen 7 (W36x150 with RBS and No Fasteners) Underside of Top Flange Strain Data Line 2

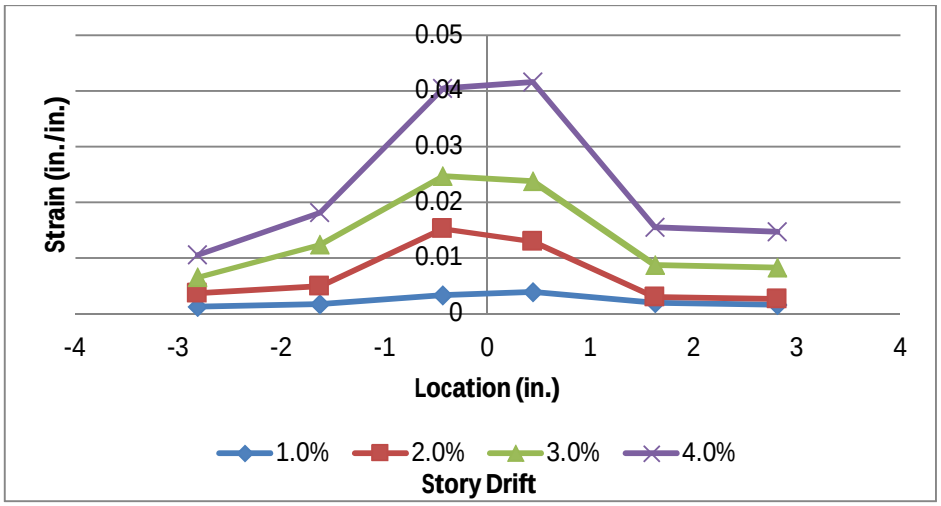


Figure E.88 – Specimen 8 (W36x150 with RBS and Puddle Welds at 12 in.) Top Flange Strain Data Line 1

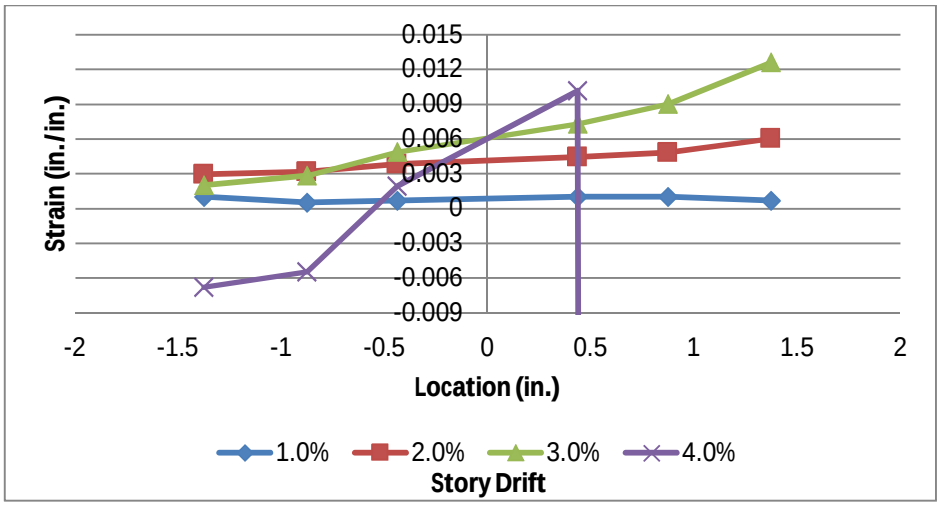


Figure E.89 – Specimen 8 (W36x150 with RBS and Puddle Welds at 12 in.) Top Flange Strain Data Line 2

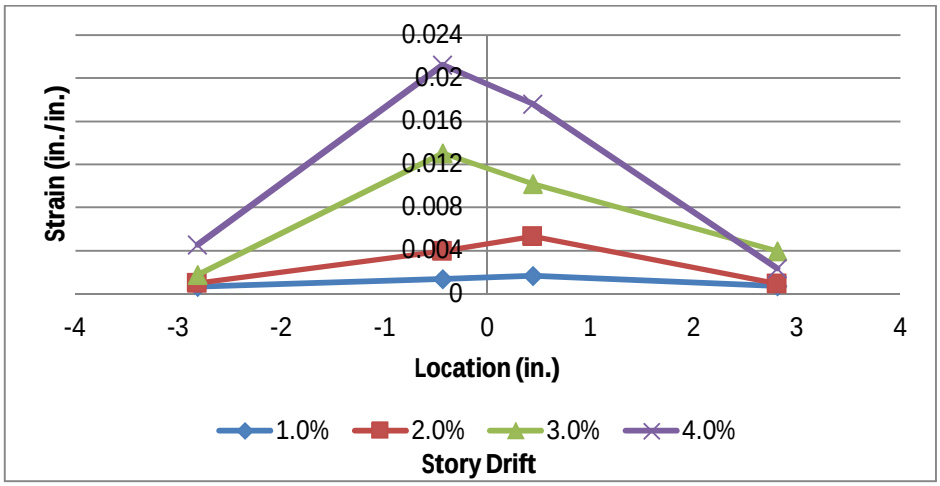


Figure E.90 –Specimen 8(W36x150 with RBS and Puddle Welds at 12 in.) Underside of Top Flange Strain Data Line 1

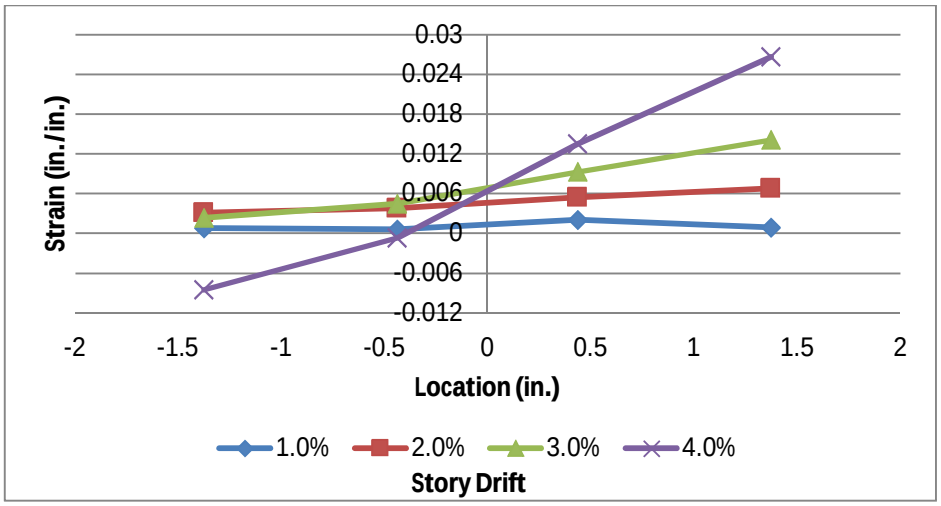


Figure E.91 –Specimen 8(W36x150 with RBS and Puddle Welds at 12 in.) Underside of Top Flange Strain Data Line 2

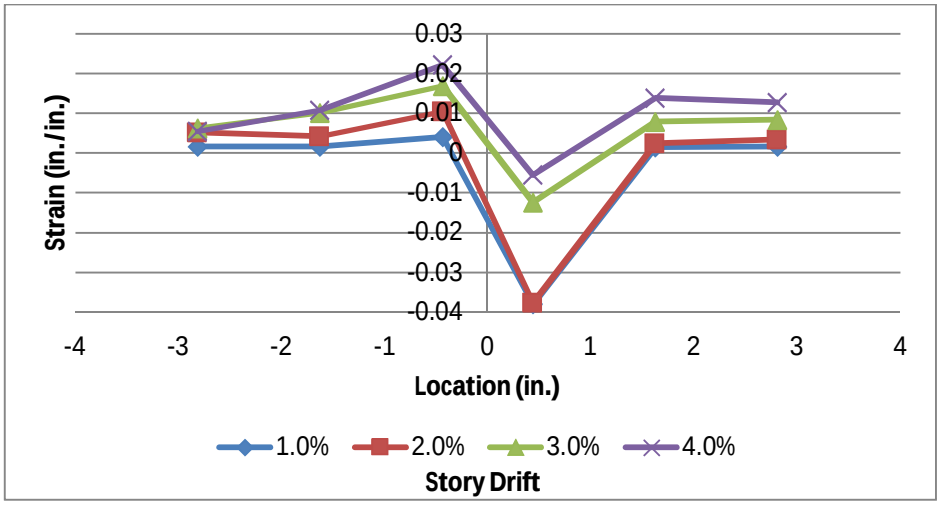


Figure E.92 – Specimen 9 (W36x150 with RBS and Grid of PAFs) Top Flange Strain Data Line 1

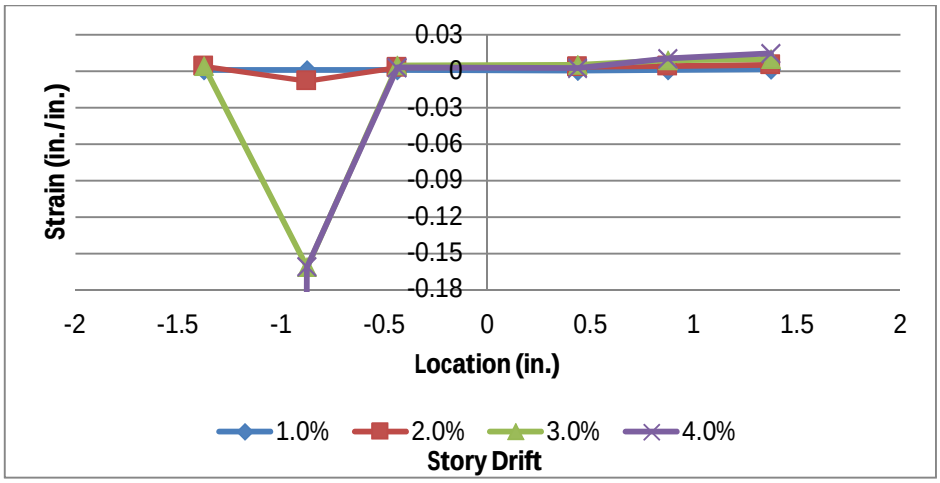


Figure E.93 – Specimen 9 (W36x150 with RBS and Grid of PAFs) Top Flange Strain Data Line 2

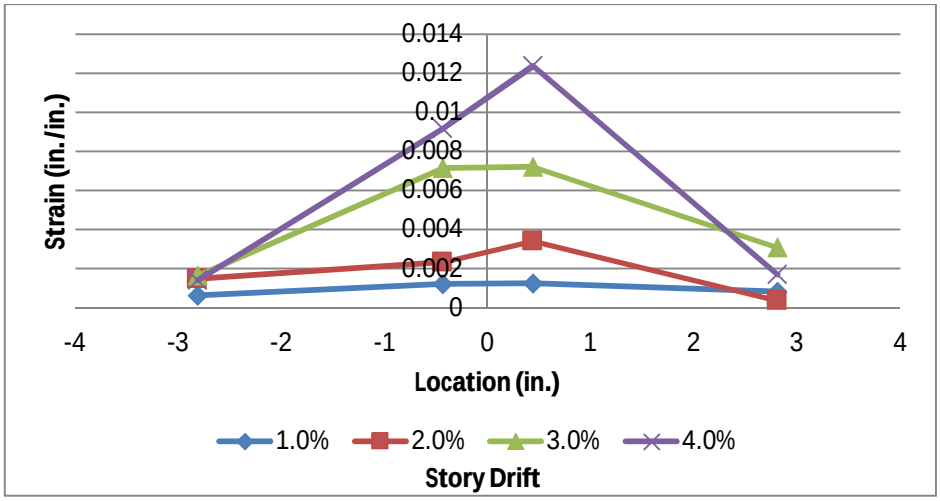


Figure E.94 – Specimen 9 (W36x150 with RBS and Grid of PAFs) Underside of Top Flange Strain Data Line 1

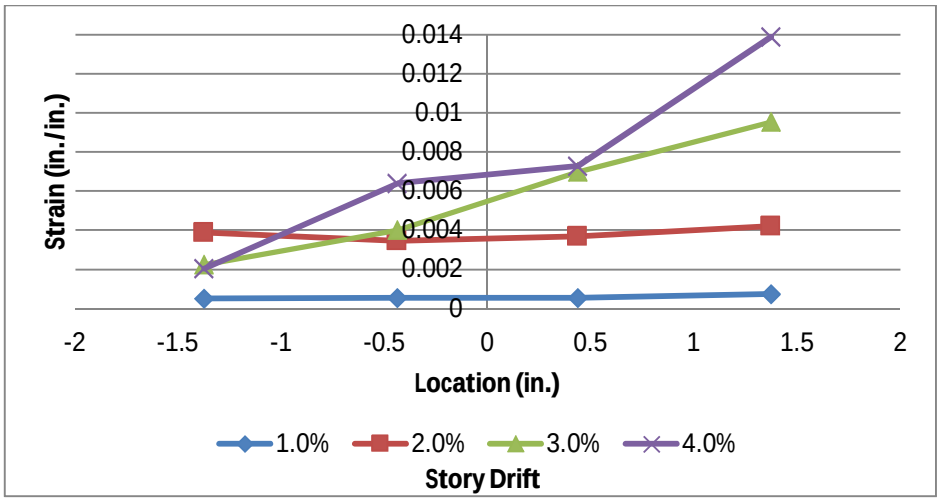


Figure E.95 – Specimen 9 (W36x150 with RBS and Grid of PAFs) Underside of Top Flange Strain Data Line 2

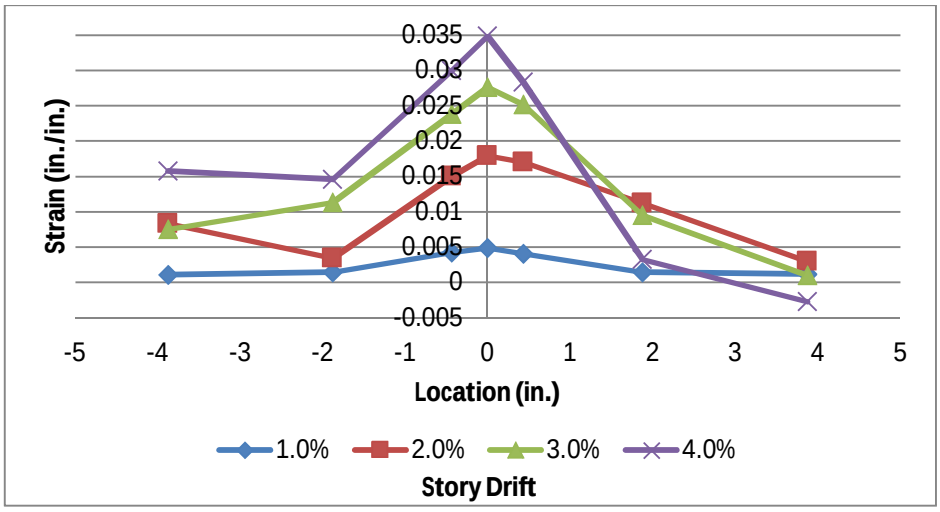


Figure E.96 – Specimen 10 (W36x150 with No RBS and No Fasteners) Top Flange Strain Data Line 1

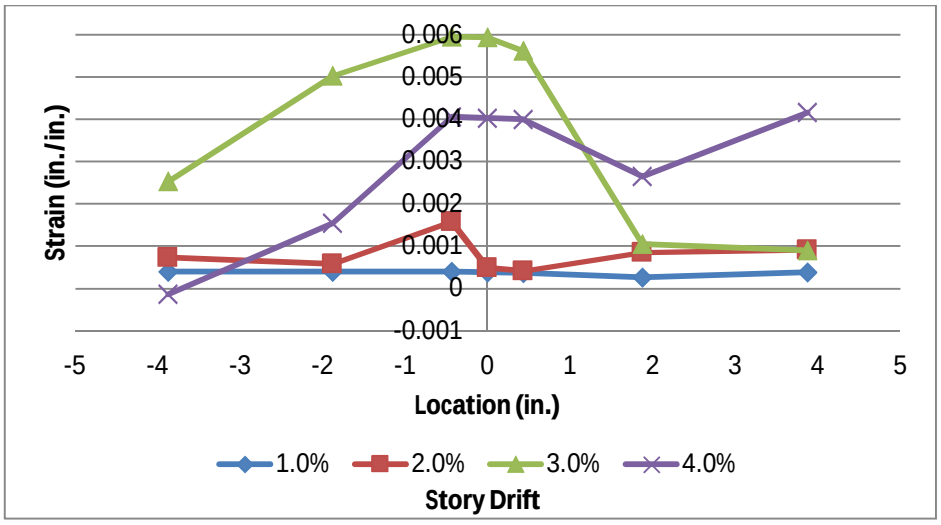


Figure E.97 – Specimen 10 (W36x150 with No RBS and No Fasteners) Top Flange Strain Data Line 2

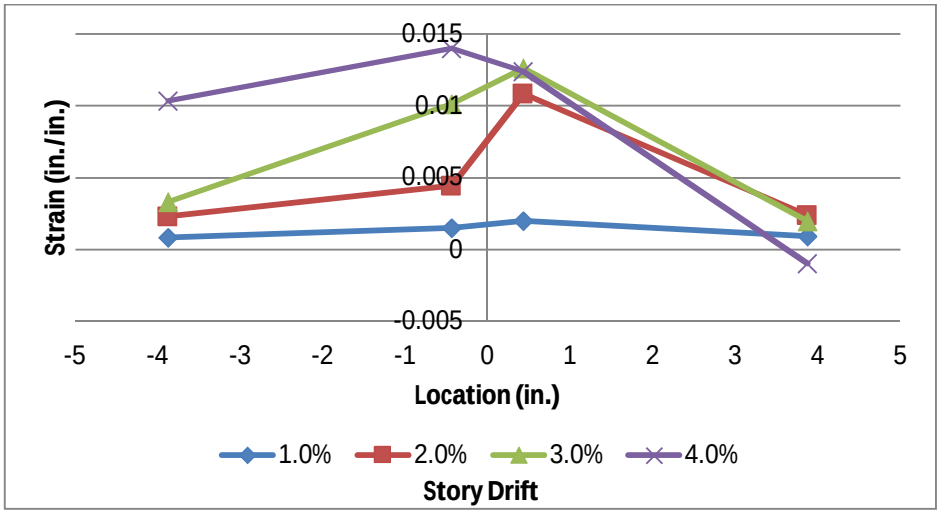


Figure E.98 – Specimen 10 (W36x150 with No RBS and No Fasteners) Underside of Top Flange Strain Data Line 1

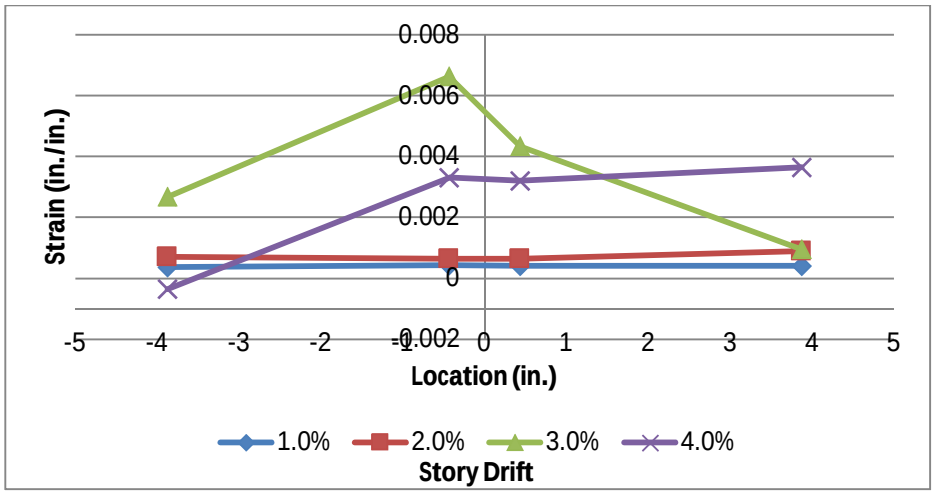


Figure E.99 – Specimen 10 (W36x150 with No RBS and No Fasteners) Underside of Top Flange Strain Data Line 2

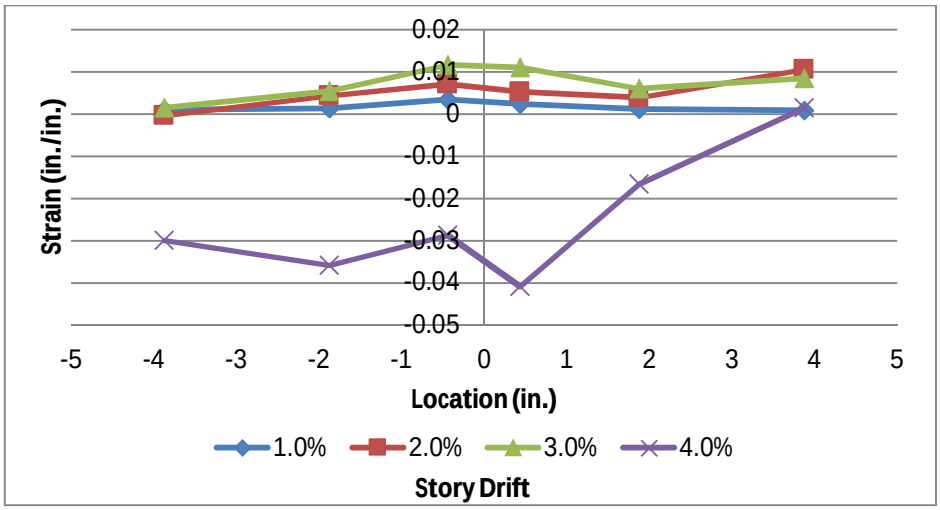


Figure E.100 – Specimen 11 (W36x150 with No RBS and PAFs at 12 in.) Top Flange Strain Data Line 1

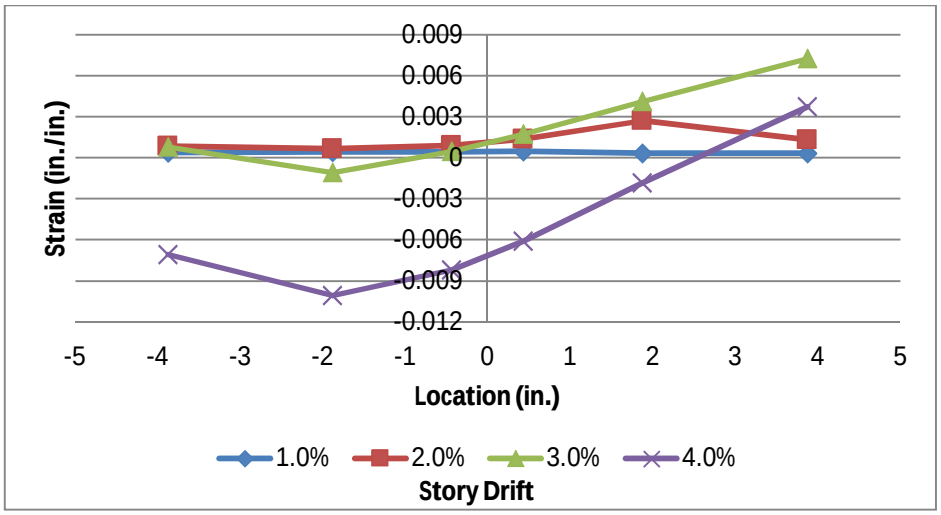


Figure E.101 – Specimen 11 (W36x150 with No RBS and PAFs at 12") Top Flange Strain Data Line 2

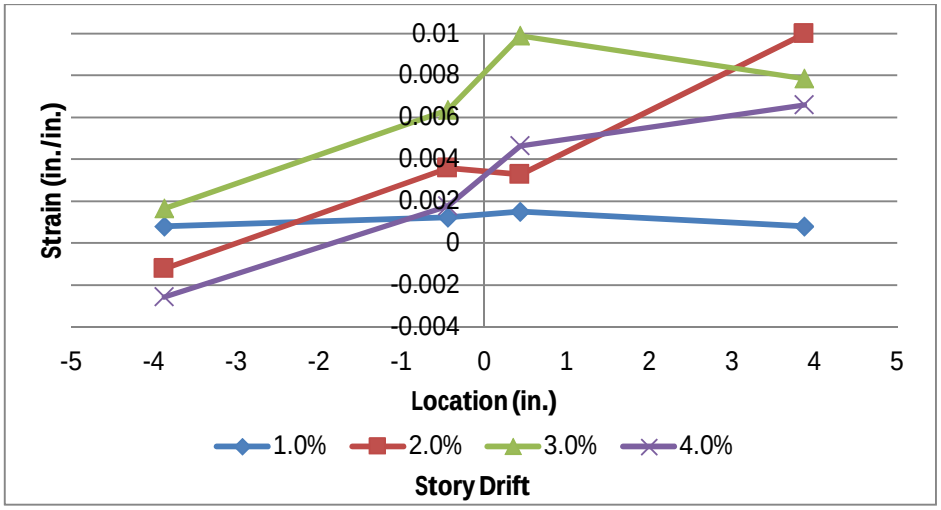


Figure E.102 – Specimen 11 (W36x150 with No RBS and PAFs at 12") Underside of Top Flange Strain Data Line 1

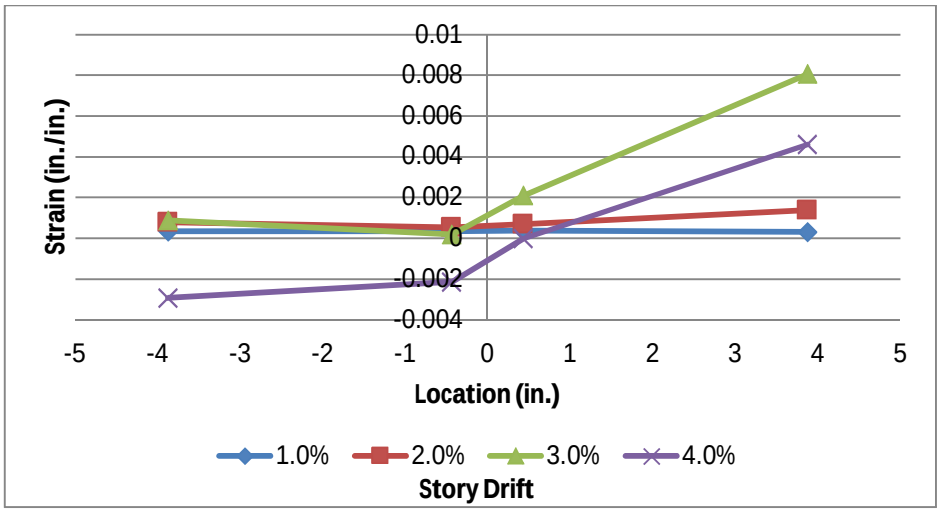


Figure E.103 – Specimen 11 (W36x150 with No RBS and PAFs at 12") Underside of Top Flange Strain Data Line 2

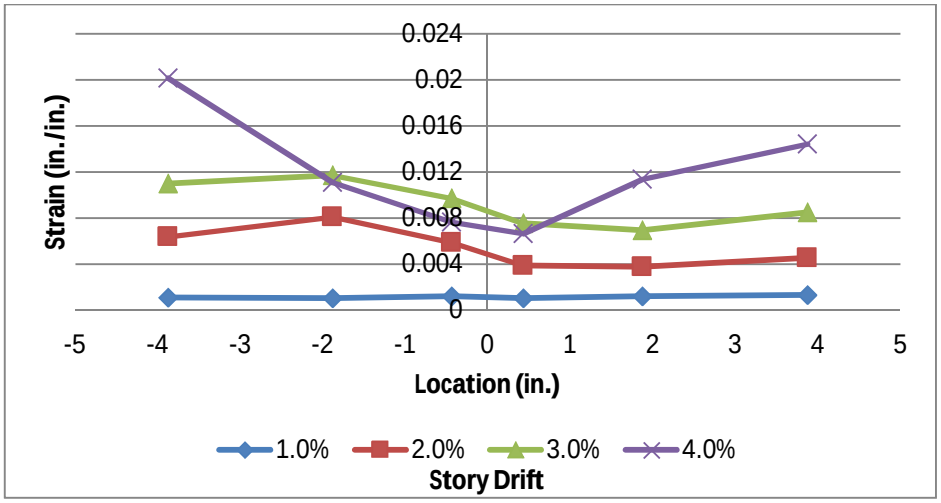


Figure E.104 – Specimen 12 (W36x150 with No RBS and Grid of PAFs) Top Flange Strain Data Line 1

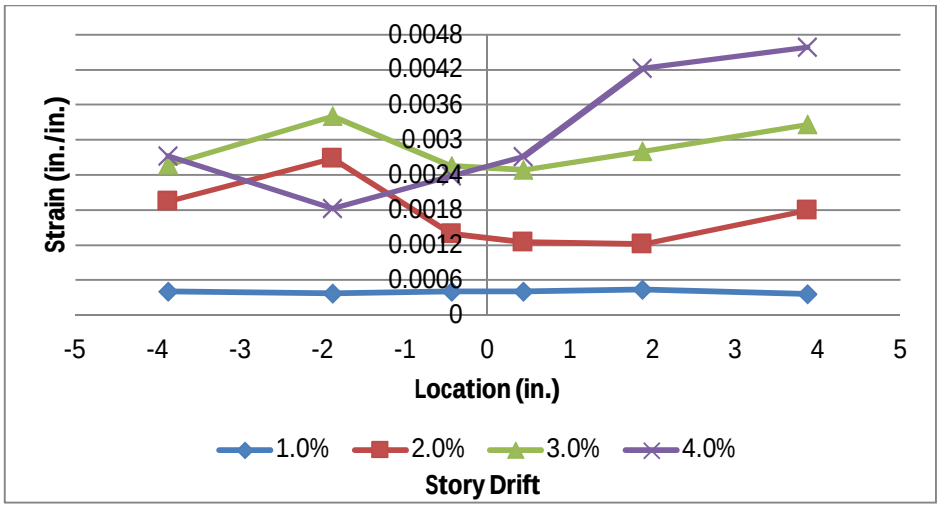


Figure E.105 – Specimen 12 (W36x150 with No RBS and Grid of PAFs) Top Flange Strain Data Line 2

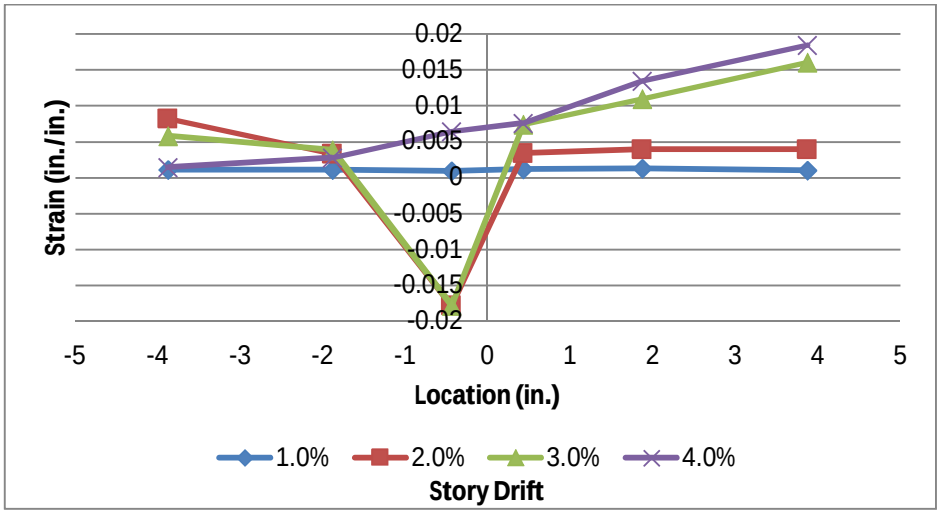


Figure E.106 – Specimen 12 (W36x150 with No RBS and Grid of PAFs) Top Flange Strain Data Line 3

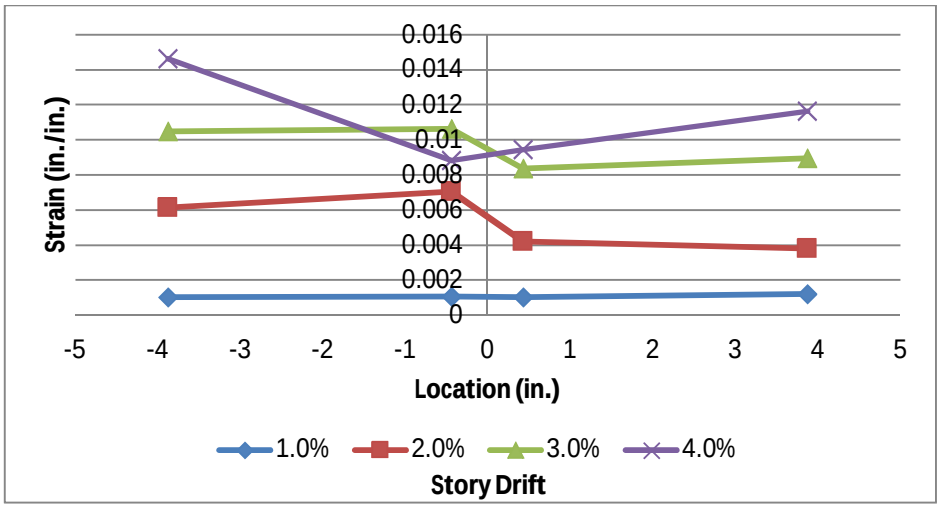


Figure E.107 –Specimen 12(W36x150 with No RBS and Grid of PAFs) Underside of Top Flange Strain Data Line 1

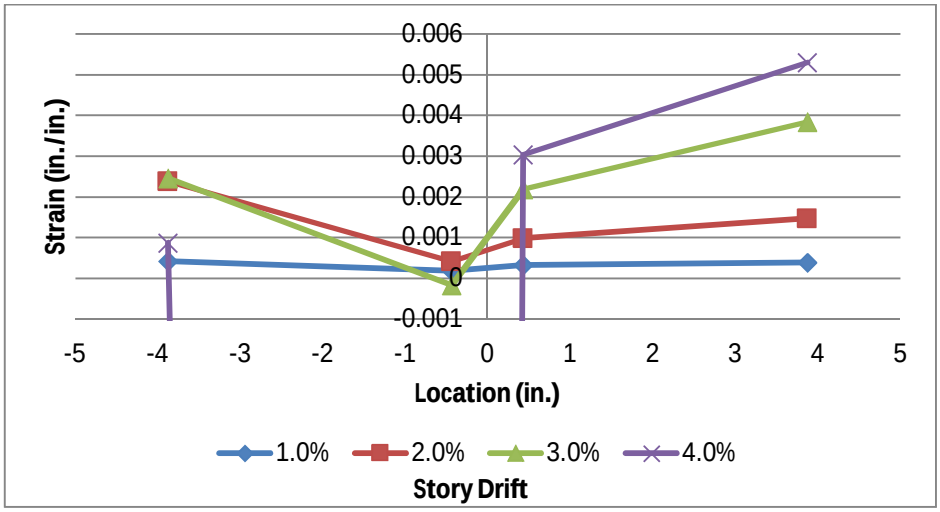


Figure E.108 – Specimen 12(W36x150 with No RBS and Grid of PAFs) Underside of Top Flange Strain Data Line 2

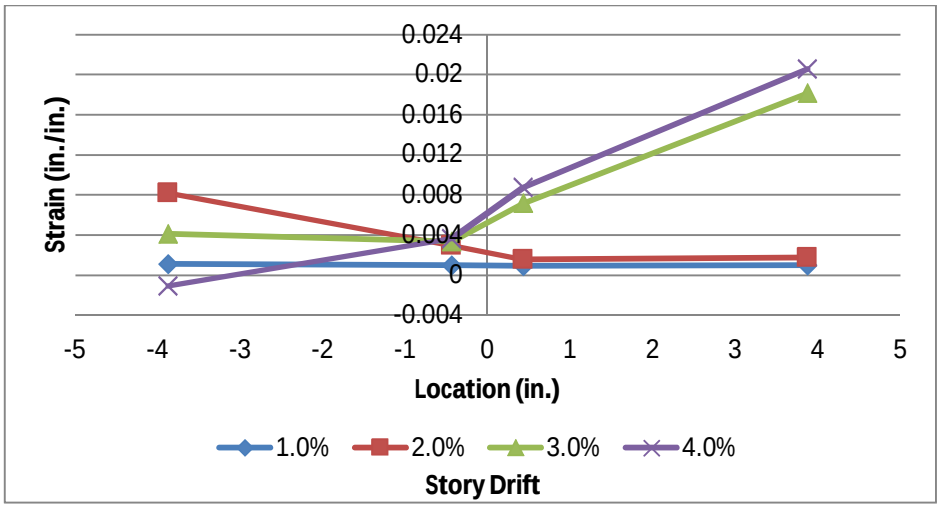


Figure E.109 –Specimen 12(W36x150 with No RBS and Grid of PAFs) Underside of Top Flange Strain Data Line 3

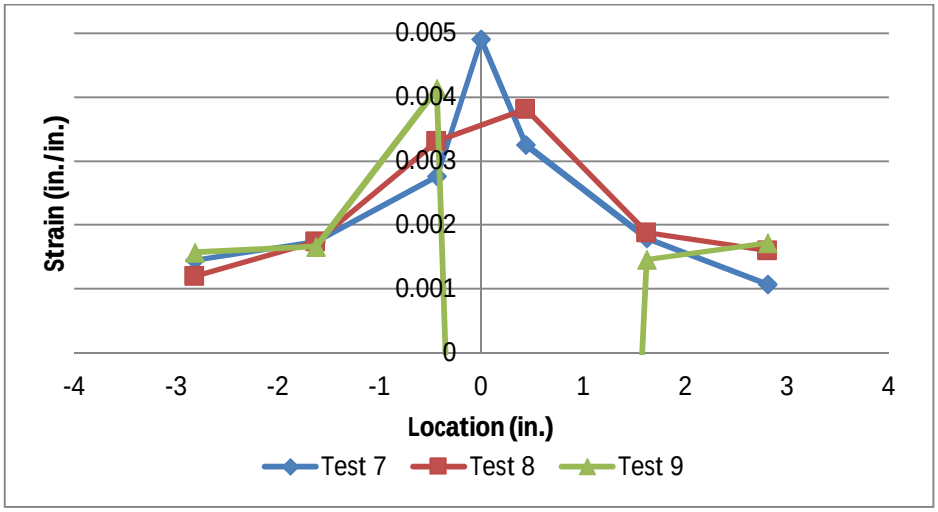


Figure E.110 – RBS36 (Specimen 7, 8 and 9) Top Flange Strain Data Line 1 at 1% Story Drift

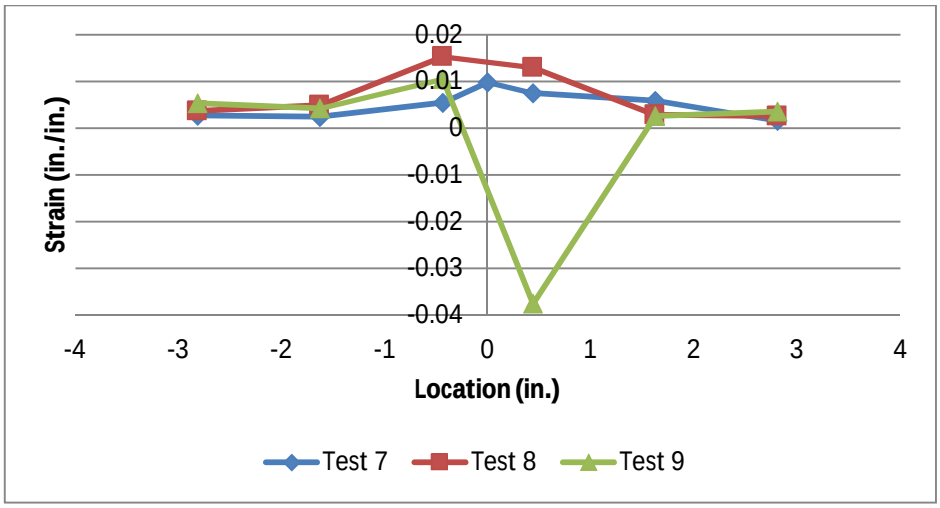


Figure E.111 – RBS36 (Specimen 7, 8 and 9) Top Flange Strain Data Line 1 at 2% Story Drift

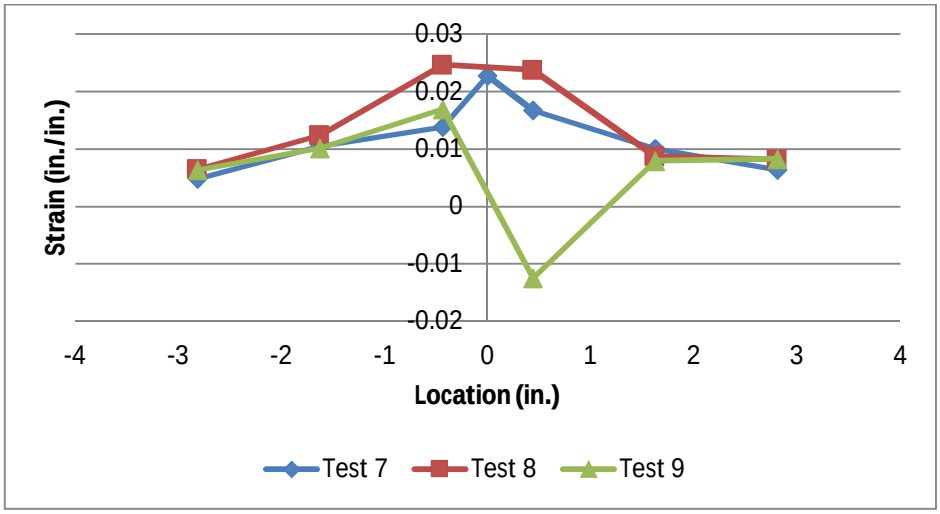


Figure E.112 – RBS36 (Specimen 7, 8 and 9) Top Flange Strain Data Line 1 at 3% Story Drift

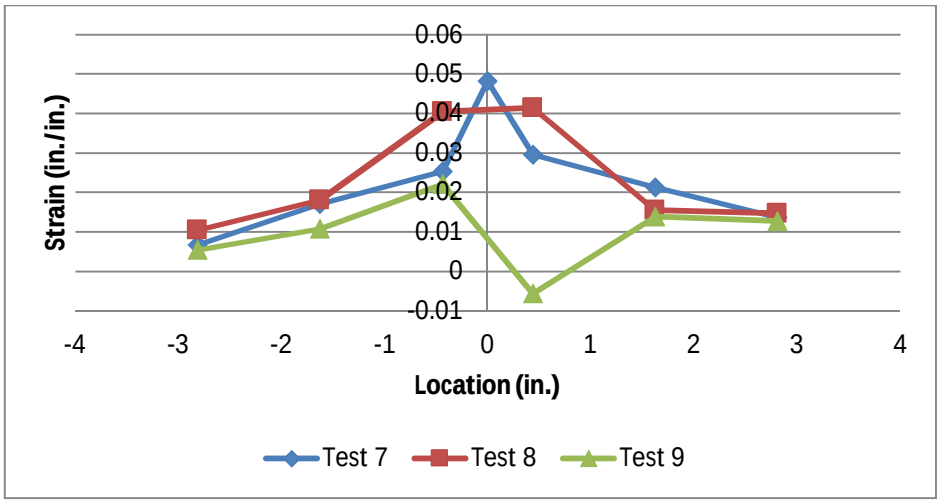


Figure E.113 – RBS36 (Specimen 7, 8 and 9) Top Flange Strain Data Line 1 at 4% Story Drift

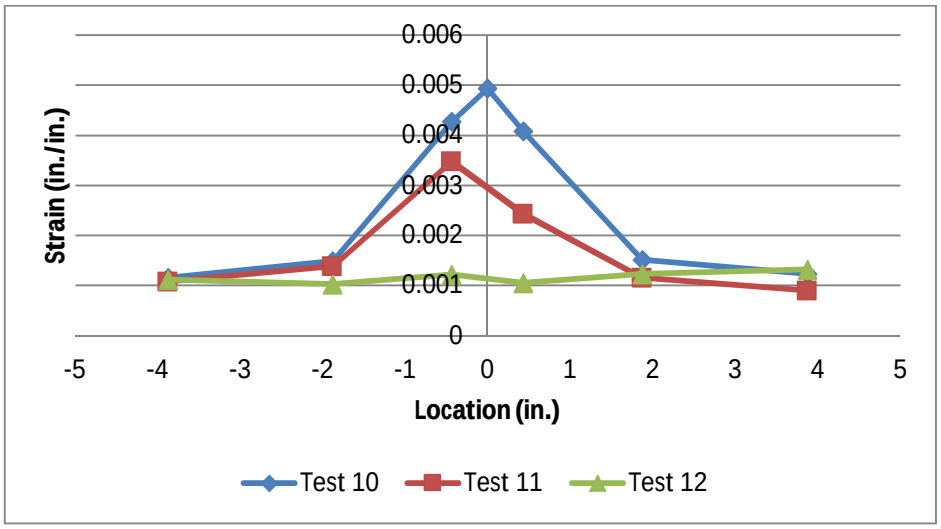


Figure E.114 – W36 (Specimen 10, 11 and 12) Top Flange Strain Data Line 1 at 1% Story Drift

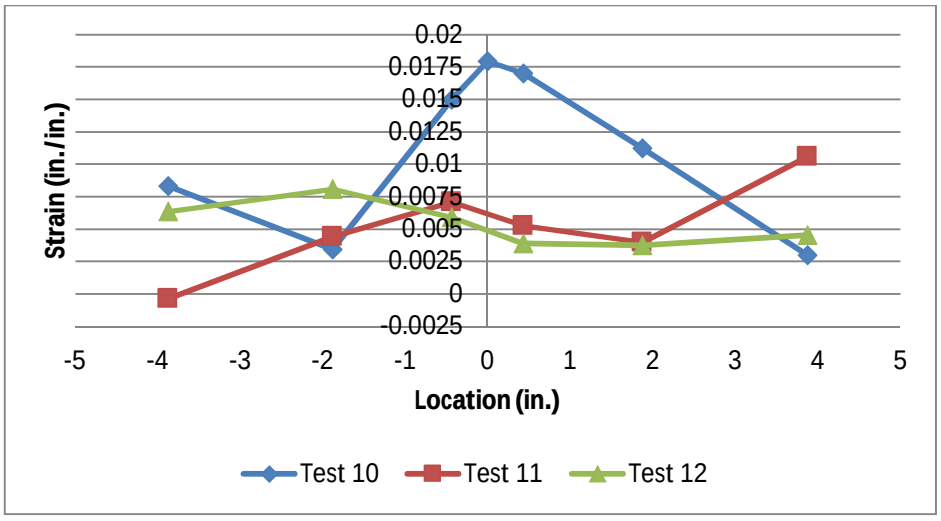


Figure E.115 – W36 (Specimen 10, 11 and 12) Top Flange Strain Data Line 1 at 2% Story Drift

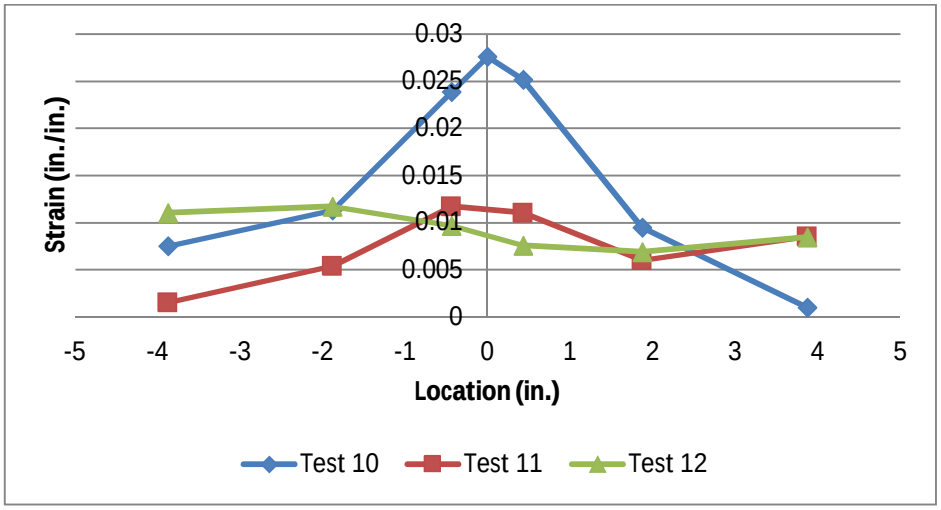


Figure E.116 – W36 (Specimen 10, 11 and 12) Top Flange Strain Data Line 1 at 3% Story Drift

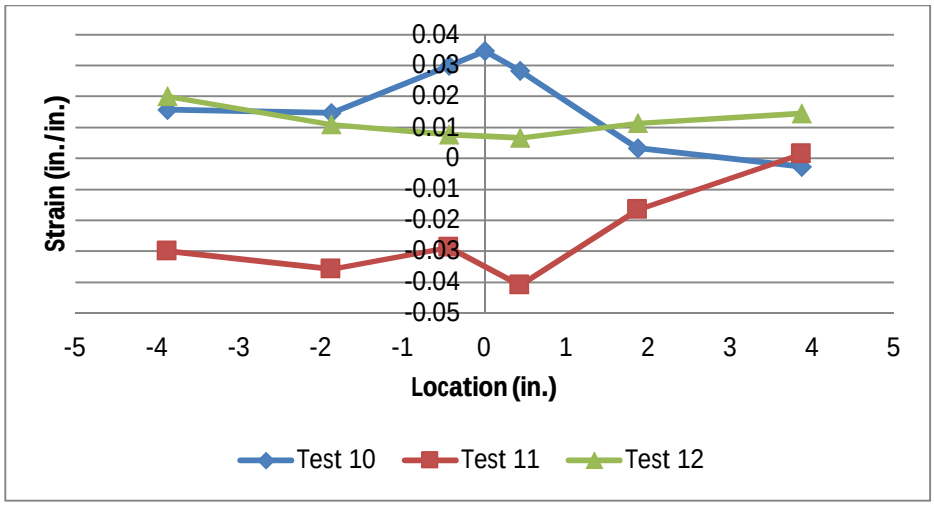


Figure E.117 – W36 (Specimen 10, 11 and 12) Top Flange Strain Data Line 1 at 4% Story Drift

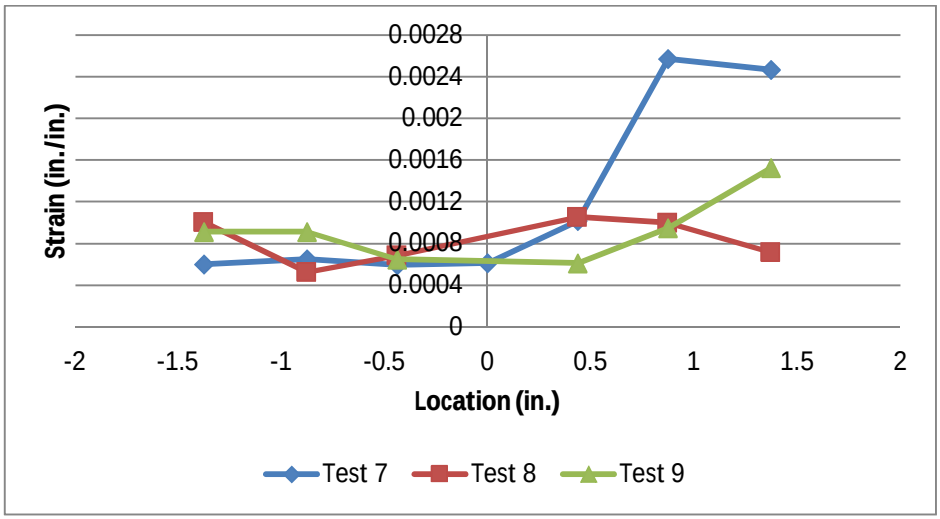


Figure E.118 – RBS36 (Specimen 7, 8 and 9) Top Flange Strain Data Line 2 at 1% Story Drift

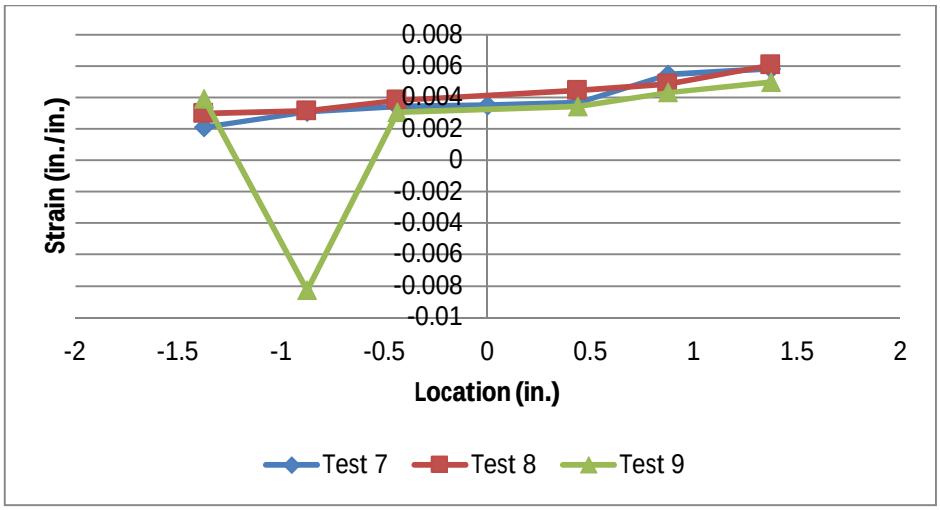


Figure E.119 – RBS36 (Specimen 7, 8 and 9) Top Flange Strain Data Line 2 at 2% Story Drift

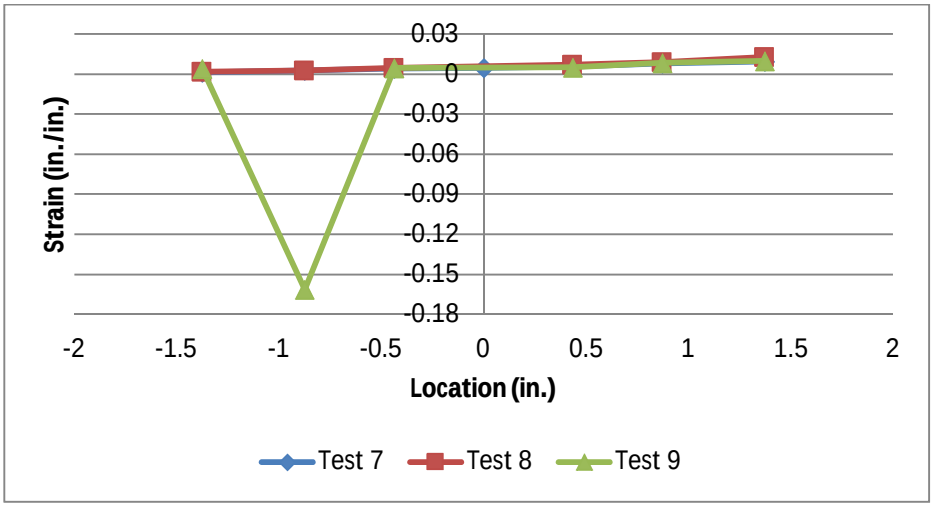


Figure E.120 – RBS36 (Specimen 7, 8 and 9) Top Flange Strain Data Line 2 at 3% Story Drift

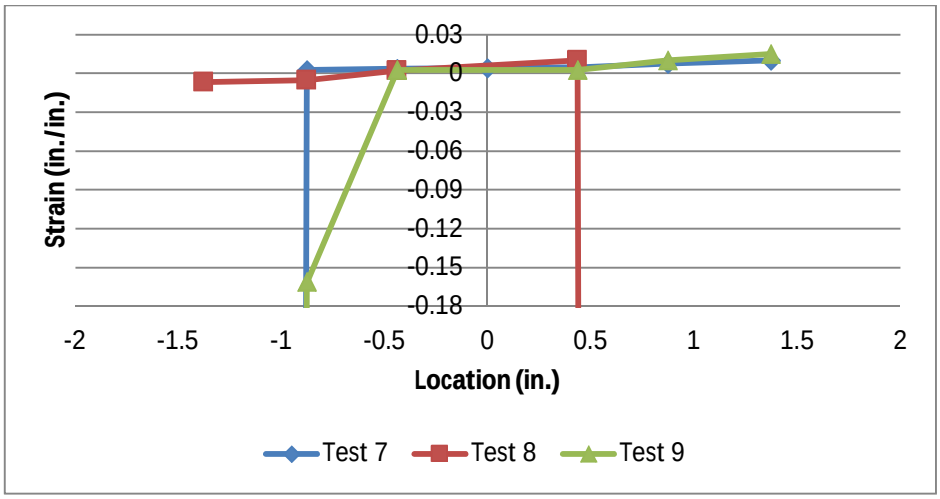


Figure E.121 – RBS36 (Specimen 7, 8 and 9) Top Flange Strain Data Line 2 at 4% Story Drift

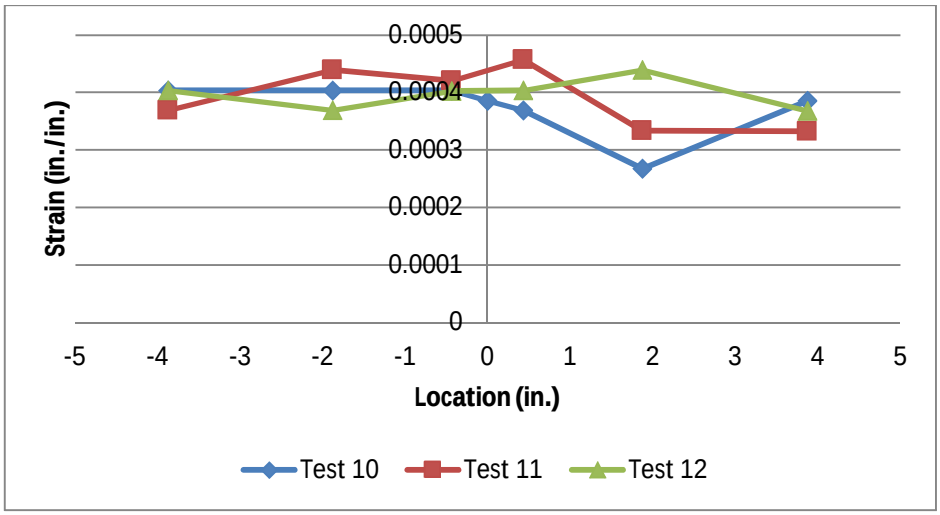


Figure E.122 – W36 (Specimen 10, 11 and 12) Top Flange Strain Data Line 2 at 1% Story Drift

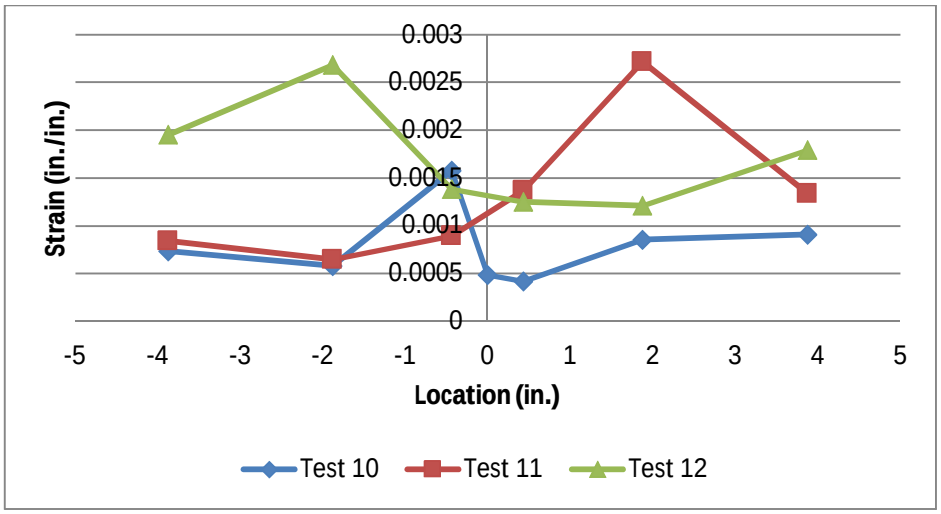


Figure E.123 – W36 (Specimen 10, 11 and 12) Top Flange Strain Data Line 2 at 2% Story Drift

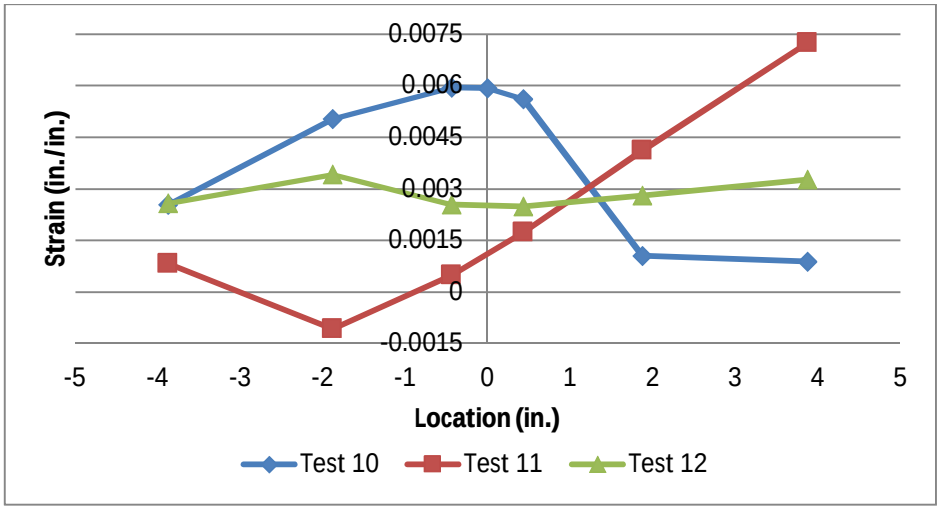


Figure E.124 – W36 (Specimen 10, 11 and 12) Top Flange Strain Data Line 2 at 3% Story Drift

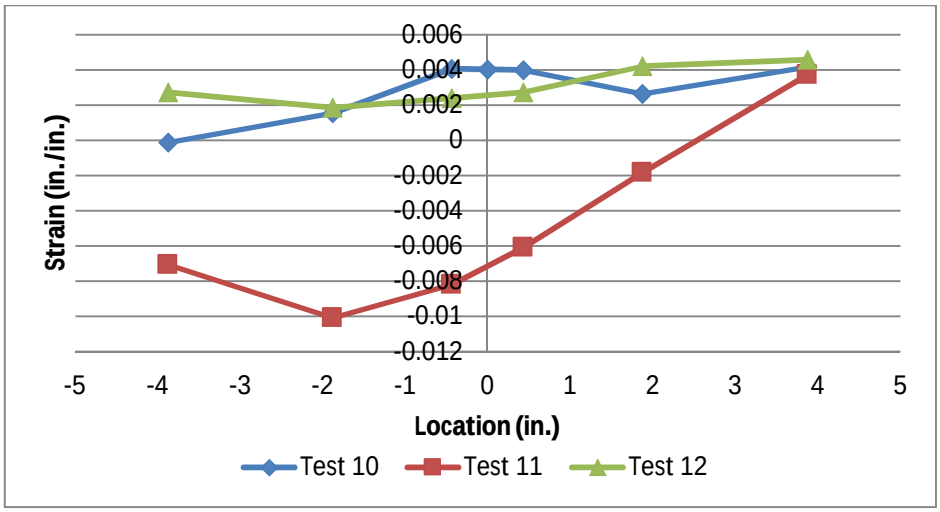


Figure E.125 – W36 (Specimen 10, 11 and 12) Top Flange Strain Data Line 2 at 4% Story Drift

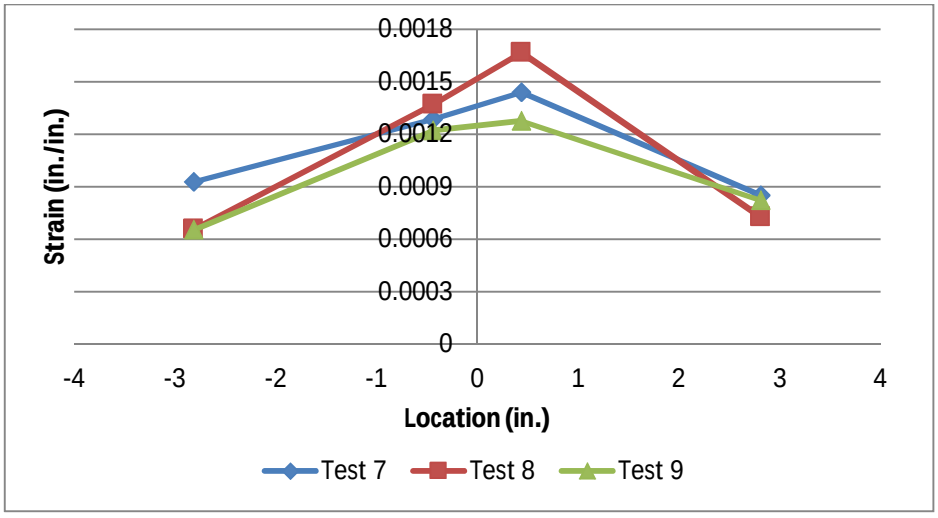


Figure E.126 – RBS36 (Specimen 7, 8 and 9) Underside of Top Flange Strain Data Line 1 at 1% Story Drift

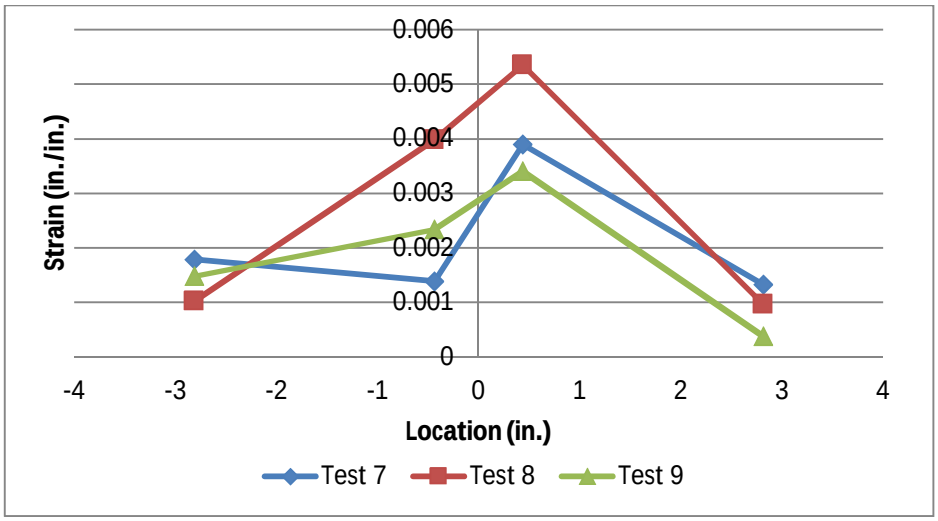


Figure E.127 – RBS36 (Specimen 7, 8 and 9) Underside of Top Flange Strain Data Line 1 at 2% Story Drift

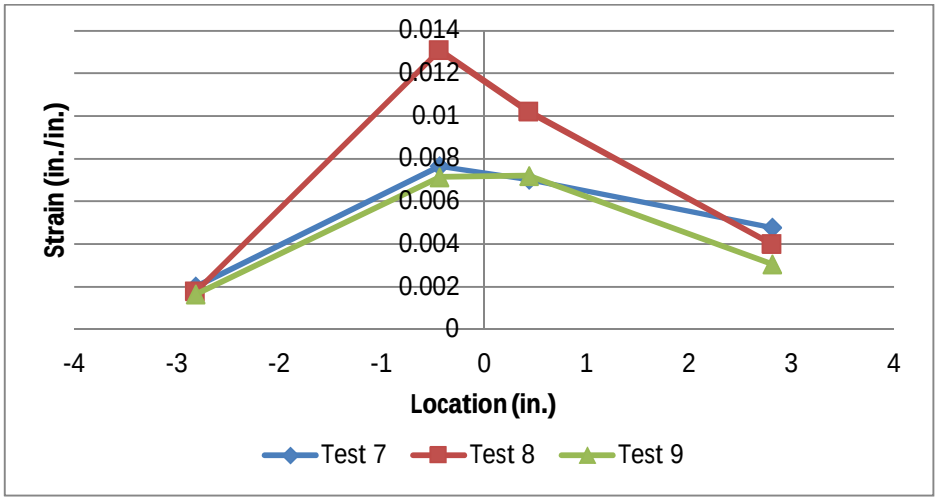


Figure E.128 – RBS36 (Specimen 7, 8 and 9) Underside of Top Flange Strain Data Line 1 at 3% Story Drift

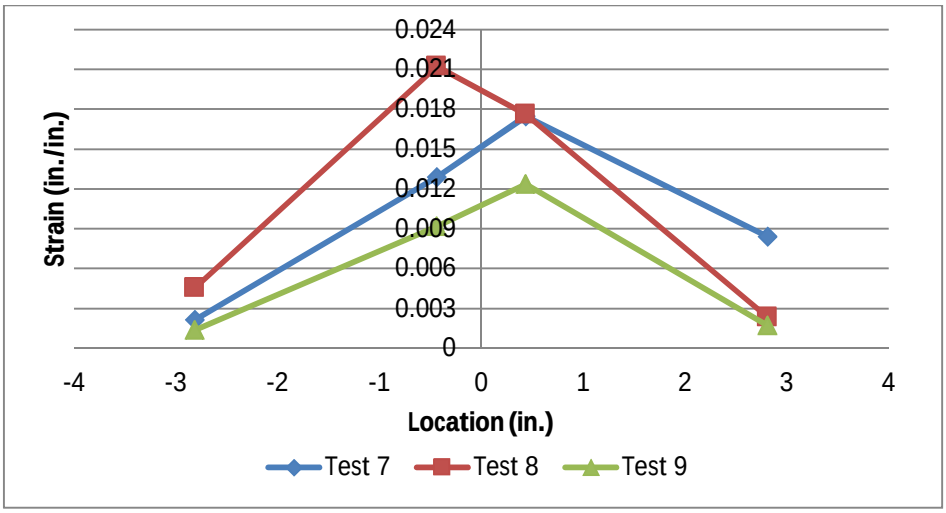


Figure E.129 – RBS36 (Specimen 7, 8 and 9) Underside of Top Flange Strain Data Line 1 at 4% Story Drift

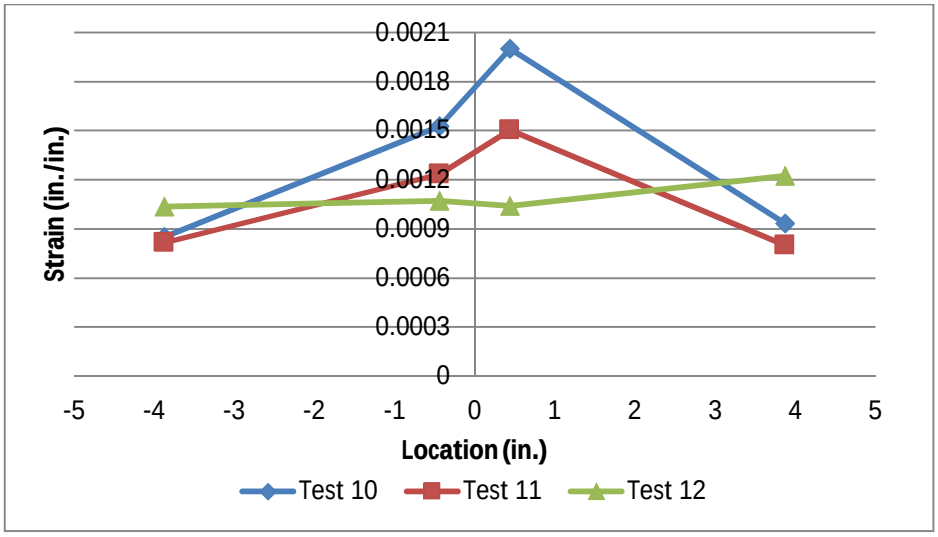


Figure E.130 – W36 (Specimen 10, 11 and 12) Underside of Top Flange Strain Data Line 1 at 1% Story Drift

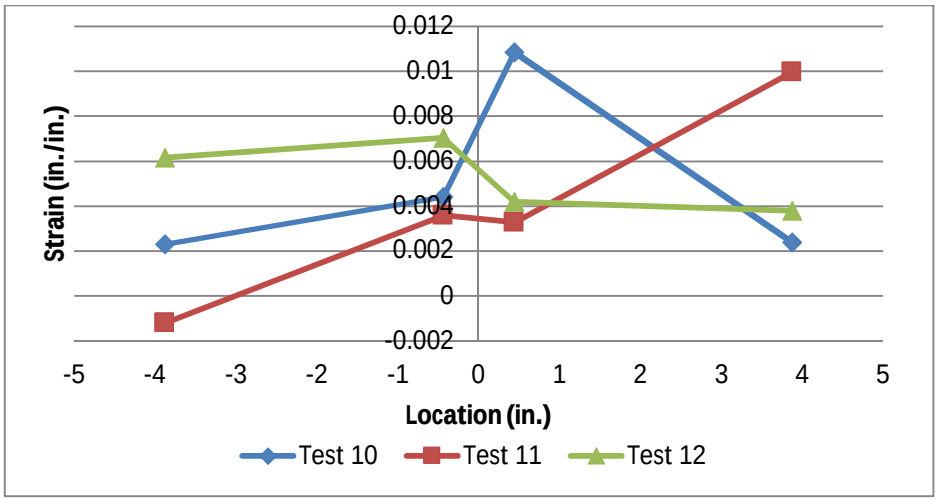


Figure E.131 – W36 (Specimen 10, 11 and 12) Underside of Top Flange Strain Data Line 1 at 2% Story Drift

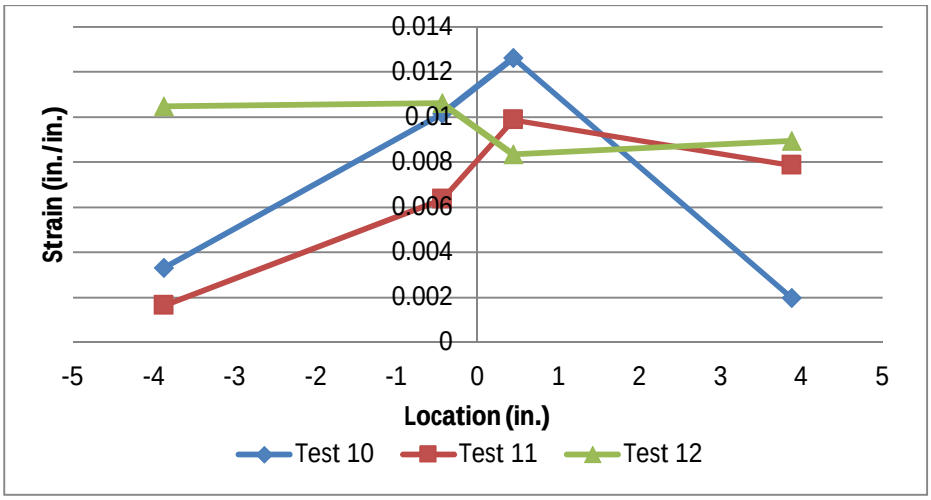


Figure E.132 – W36 (Specimen 10, 11 and 12) Underside of Top Flange Strain Data Line 1 at 3% Story Drift

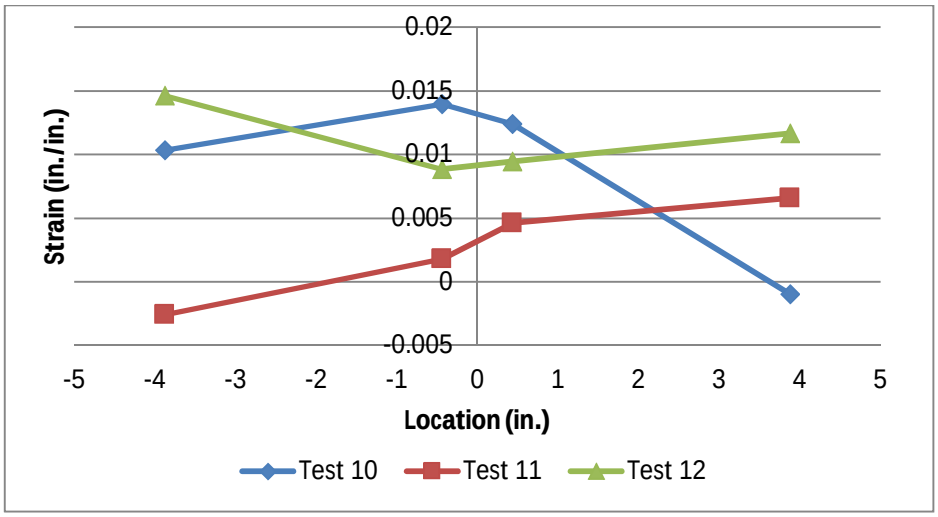


Figure E.133 – W36 (Specimen 10, 11 and 12) Underside of Top Flange Strain Data Line 1 at 4% Story Drift

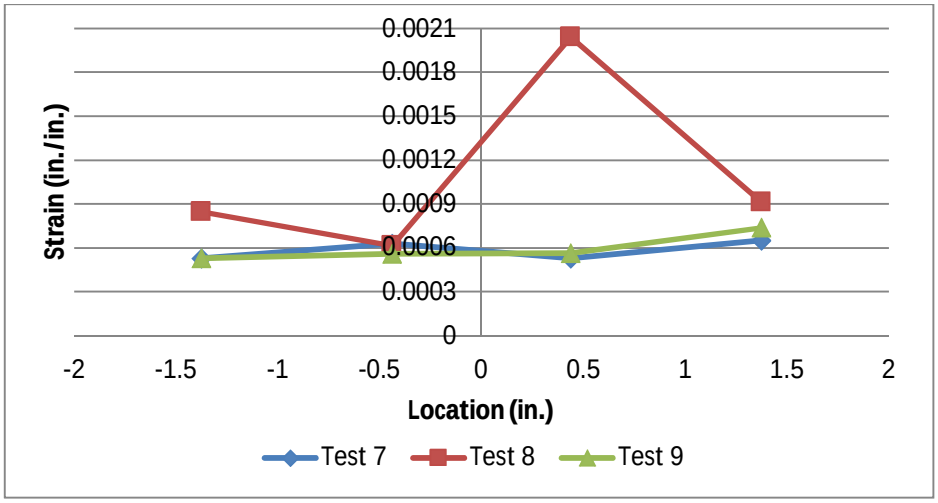


Figure E.134 – RBS36 (Specimen 7, 8 and 9) Underside of Top Flange Strain Data Line 2 at 1% Story Drift

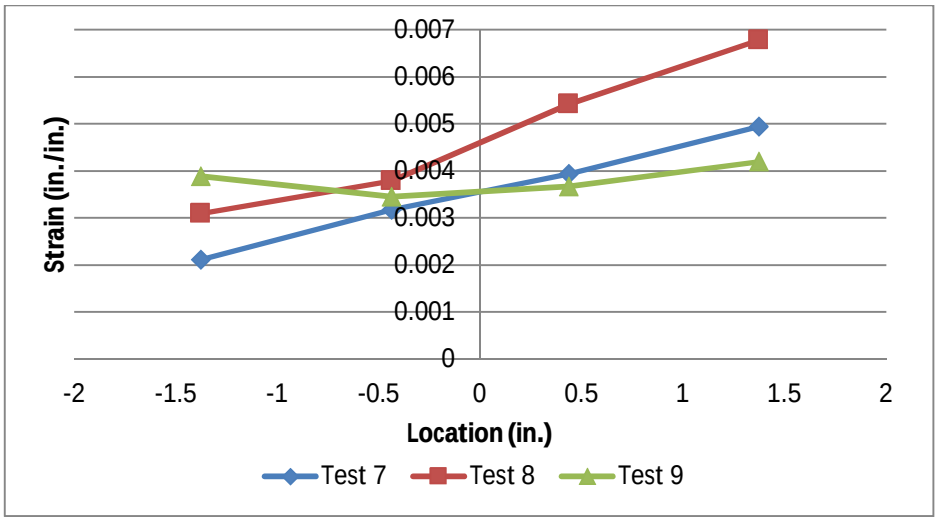


Figure E.135 – RBS36 (Specimen 7, 8 and 9) Underside of Top Flange Strain Data Line 2 at 2% Story Drift

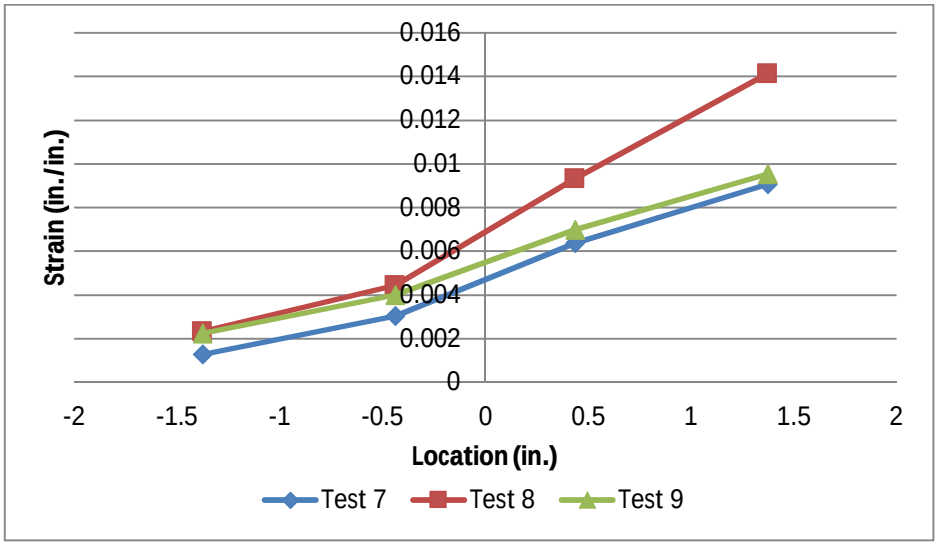


Figure E.136 – RBS36 (Specimen 7, 8 and 9) Underside of Top Flange Strain Data Line 2 at 3% Story Drift

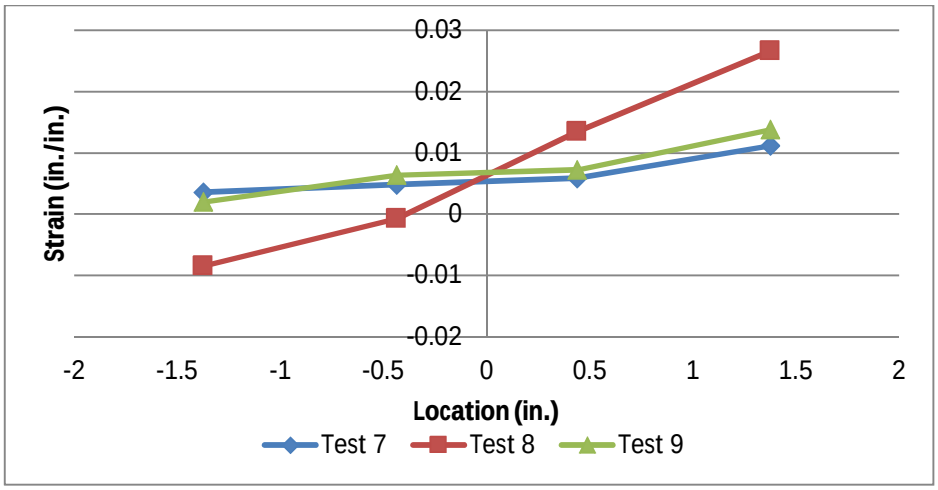


Figure E.137 – RBS36 (Specimen 7, 8 and 9) Underside of Top Flange Strain Data Line 2 at 4% Story Drift

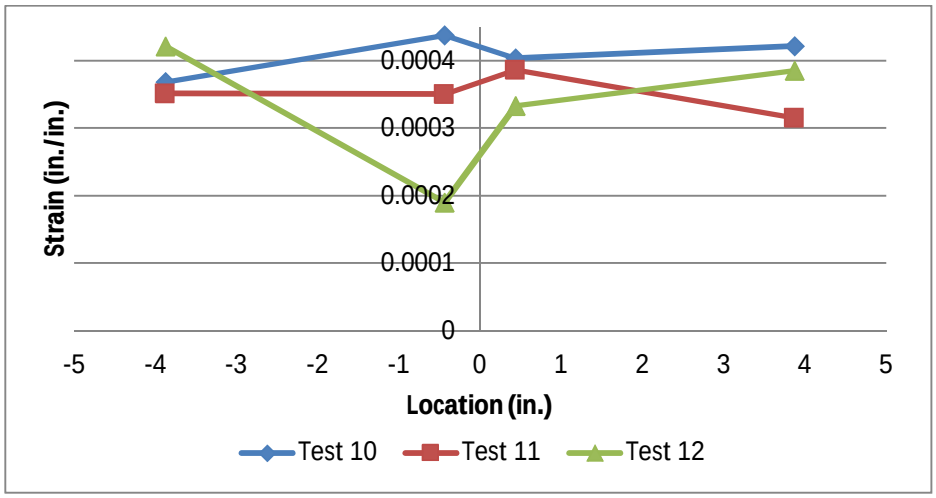


Figure E.138 – W36 (Specimen 10, 11 and 12) Underside of Top Flange Strain Data Line 2 at 1% Story Drift

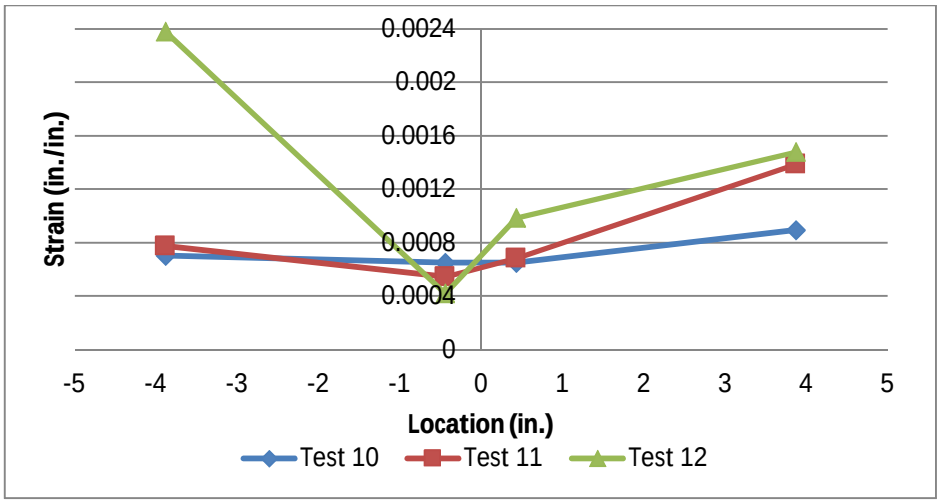


Figure E.139 – W36 (Specimen 10, 11 and 12) Underside of Top Flange Strain Data Line 2 at 2% Story Drift

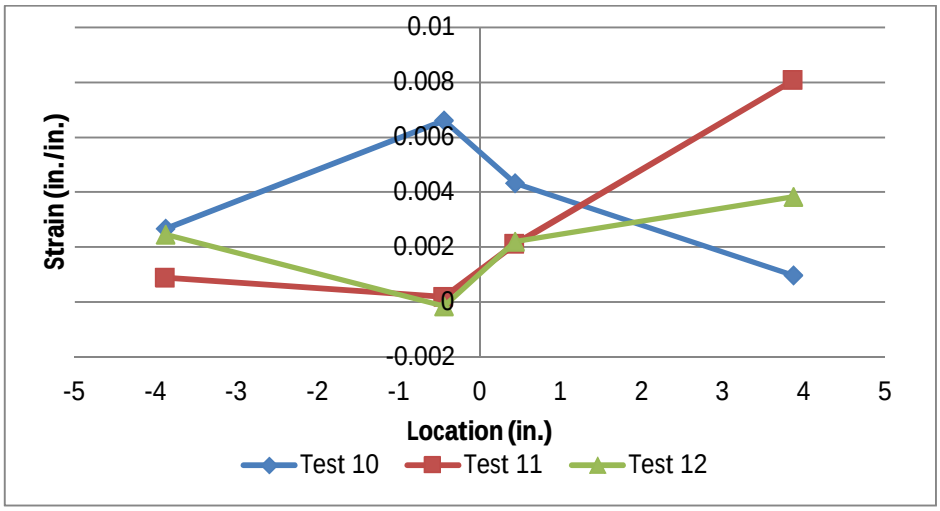


Figure E.140 – W36 (Specimen 10, 11 and 12) Underside of Top Flange Strain Data Line 2 at 3% Story Drift

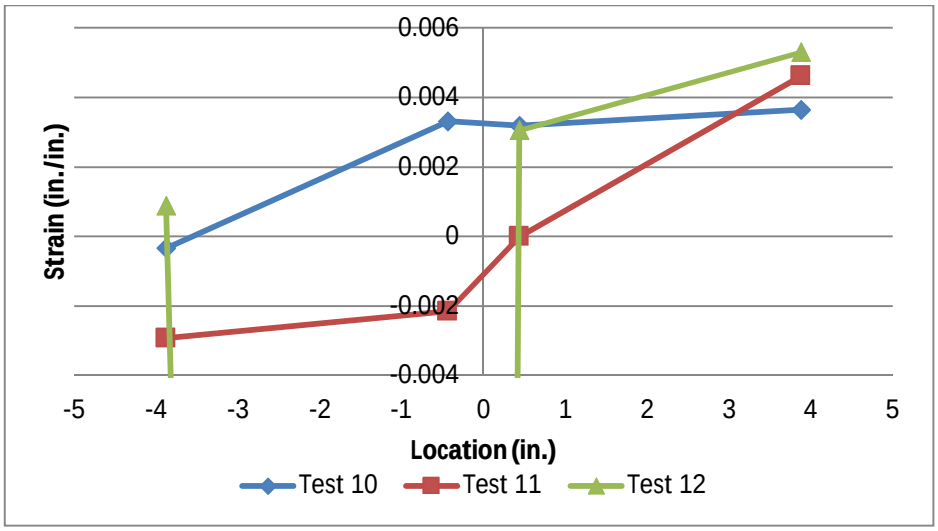


Figure E.141 – W36 (Specimen 10, 11 and 12) Underside of Top Flange Strain Data Line 2 at 4% Story Drift

APPENDIX F FULL-SCALE TEST VALIDATION HYSTERESIS PLOTS

The following FEM analysis for the full-scale tests were run until 4.7% story drift, which was similar to the story drift cycles the full-scale tests were tested to.

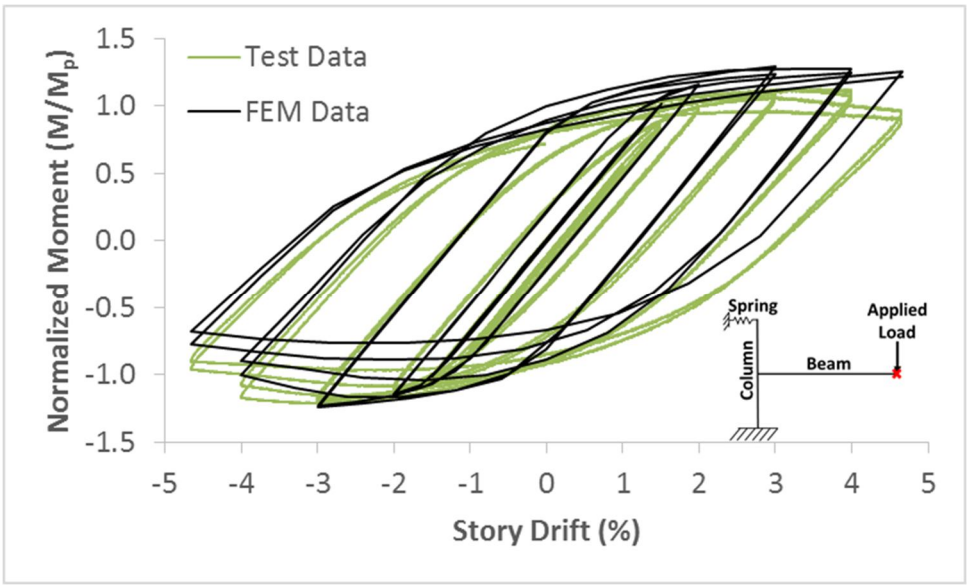


Figure F.1 – Validation of FEM analysis with experimental data for W24x62 specimen.

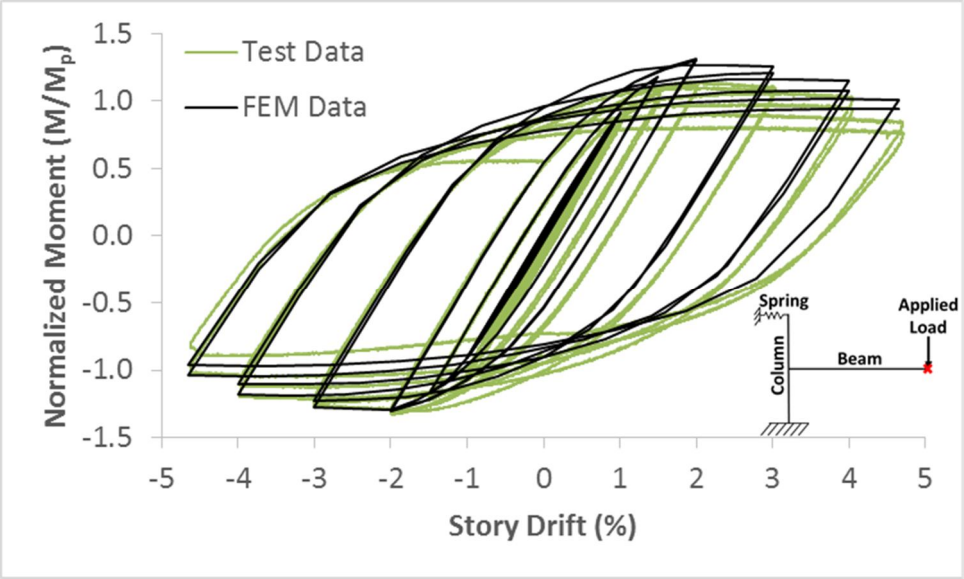


Figure F.2 – Validation of FEM analysis with experimental data for W24x62 specimen with RBS.

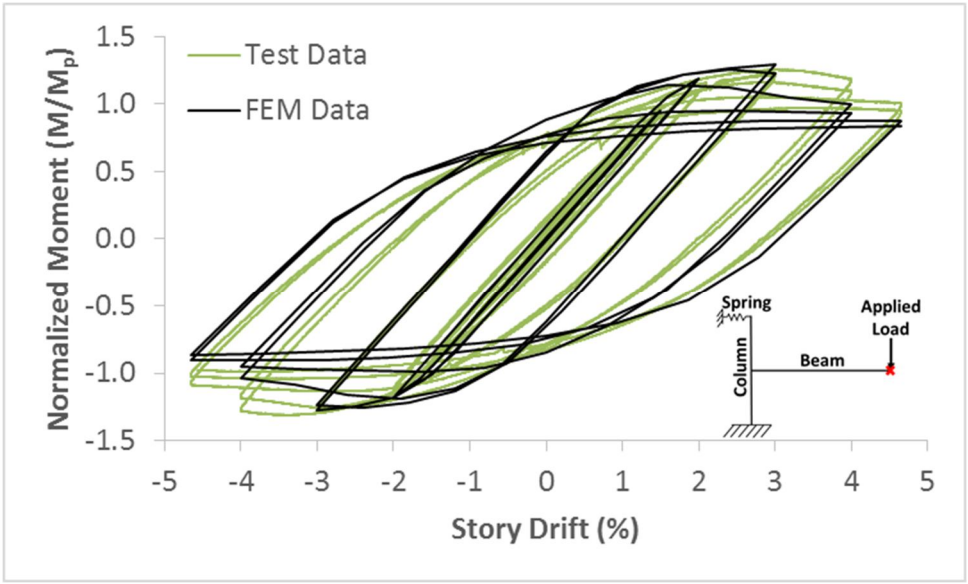


Figure F.3 – Validation of FEM analysis with experimental data for W36x150 specimen.

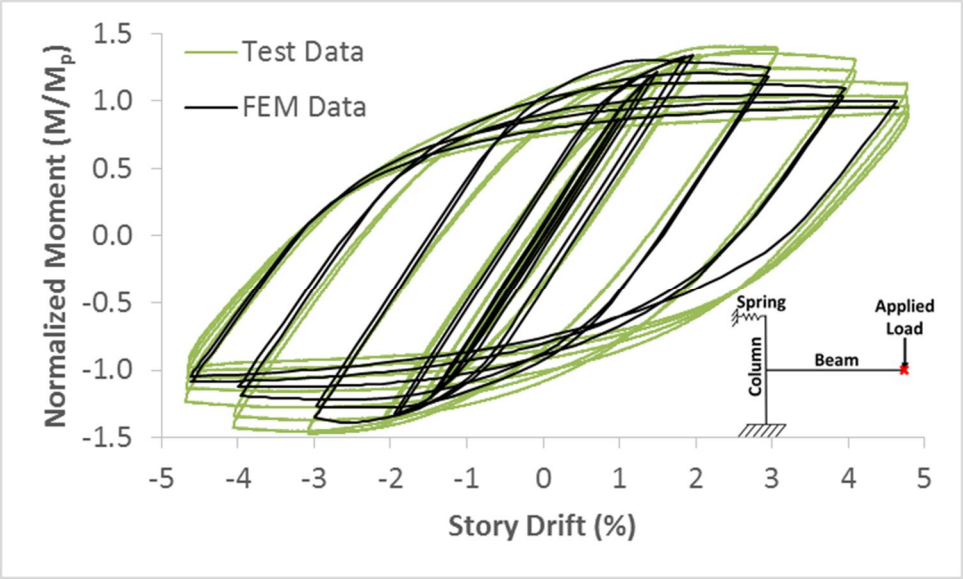


Figure F.4 – Validation of FEM analysis with experimental data for W36x150 specimen with RBS.

APPENDIX G LCF MODELS CALCULATION DEMONSTRATION

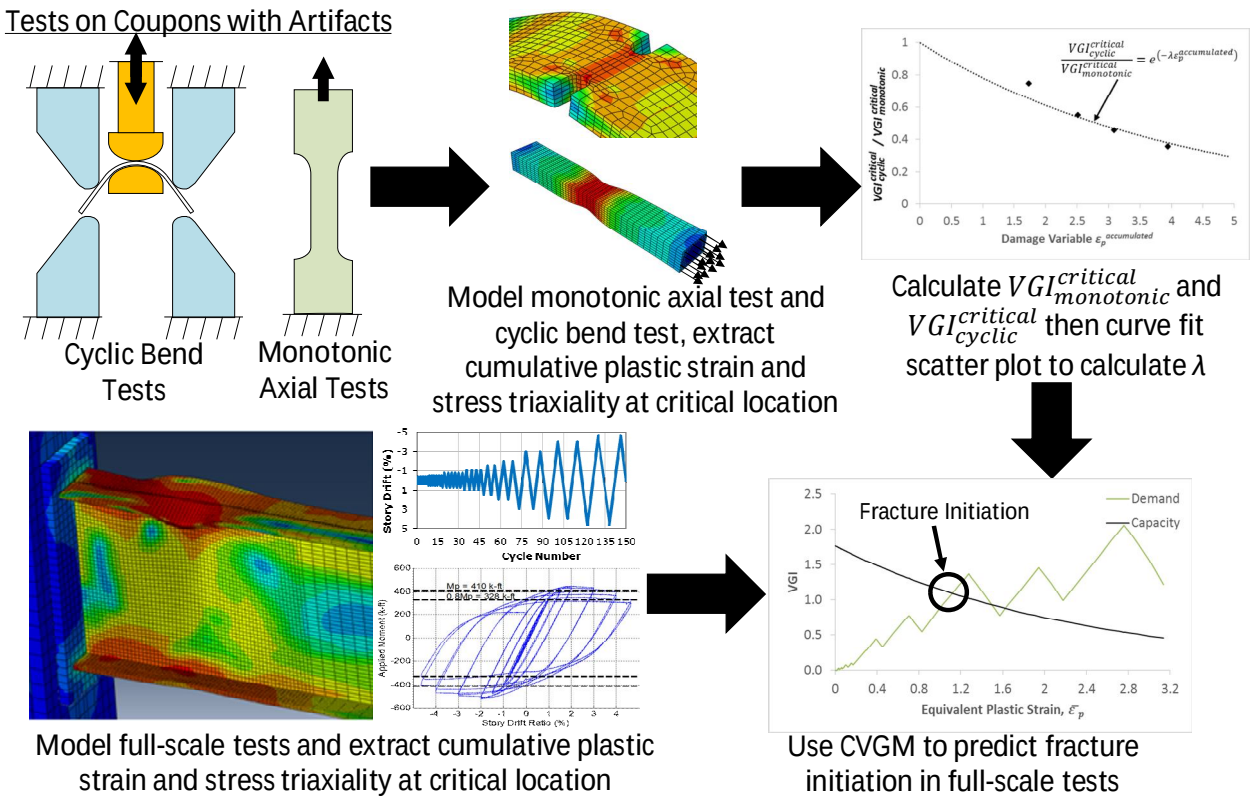


Figure G.1 – Graphical demonstration for CVGM.

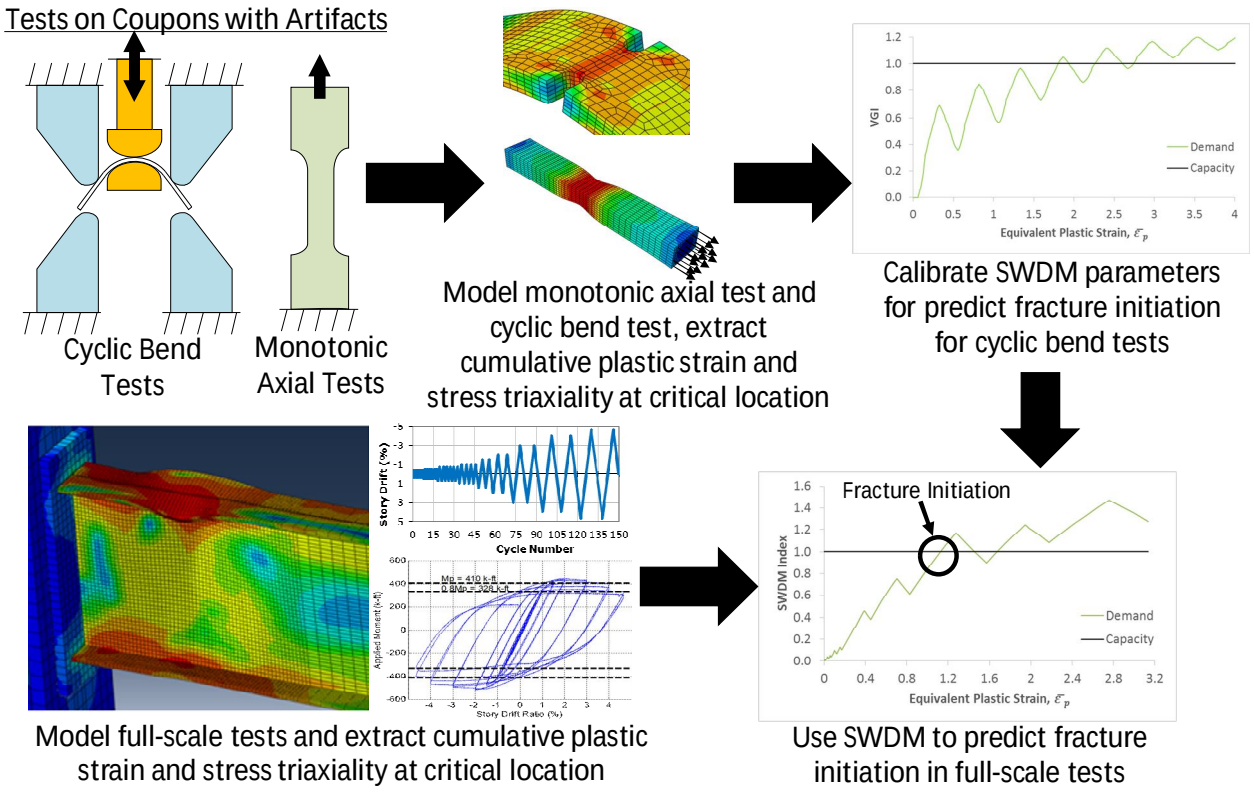


Figure G.2 – Graphical demonstration for SWDM.

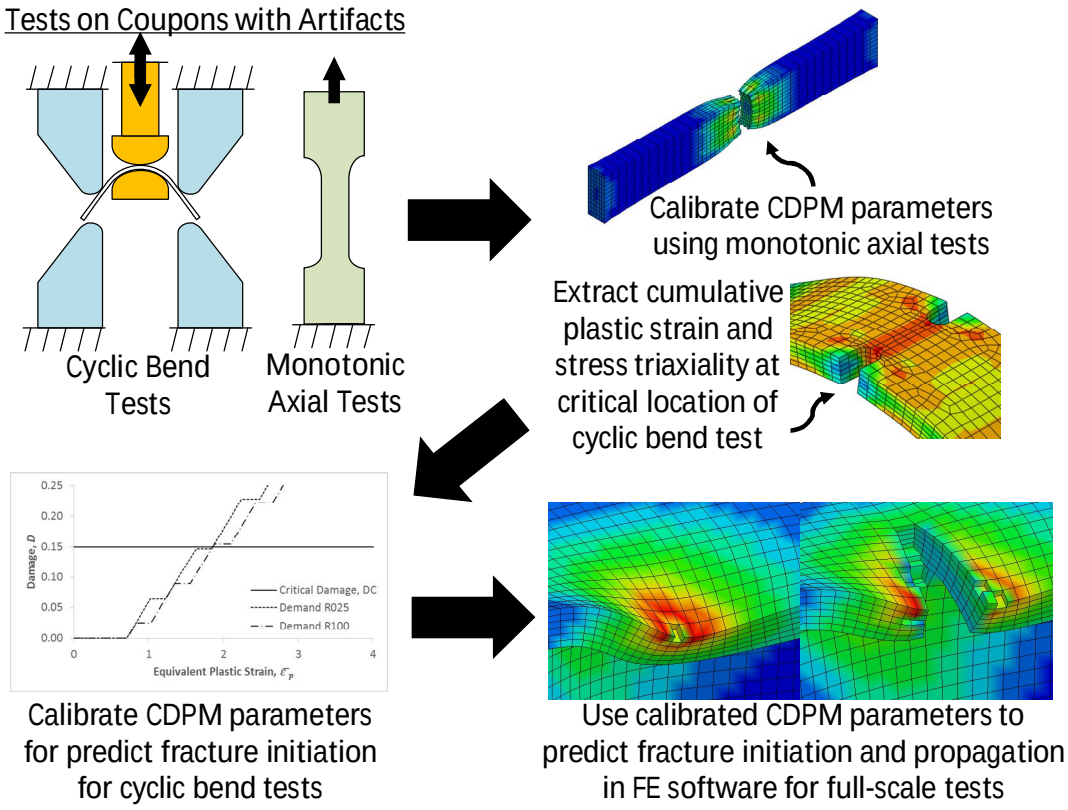


Figure G.3 – Graphical demonstration for CDPM.